GRANEK05

Index of /resources

Name	Last modified	Size	Description
Parent Directory		-	
AA130202.pdf	2013-08-30 12:57	2.2M	
PhD_Bentzen_Andreas.pdf	2013-01-21 14:03	8.4M	
PhD_Carnel_Lode.pdf	2013-05-07 13:11	3.2M	
PhD_Granek_Filip.pdf	2013-04-12 14:06	3.2M	
PhD_Olibet_Sara.pdf	2013-04-18 00:40	14M	
PhD_Petres_Roman.pdf	2013-04-10 15:41	4.2M	

Apache/2.4.25 (Debian) Server at beacon.no Port 443

GRANEK06

HIGH-EFFICIENCY BACK-CONTACT BACK-JUNCTION SILICON SOLAR CELLS

Dissertation

zur Erlangung des Doktorgrades

der Technischen Fakultät

der Albert-Ludwigs-Universität Freiburg im Breisgau

vorgelegt von

Filip Granek

Fraunhofer Institut für Solare Energiesysteme (ISE)

Freiburg im Breisgau

2009

Dekan:	Prof. Dr. Hans Zappe
Hauptreferent:	Prof. Dr. Oliver Paul
Koreferent:	PD. Dr. Andreas Gombert
Datum der Prüfung:	31 Juli 2009

Table of contents

Table of contents 3

Abstract 9

1 Introduction 11

1.1 Thesis motivation 11

1.2 Thesis outline 12

2 Back-contact silicon solar cells 15

2.1 Introduction 15

2.2 Review of back-contact silicon solar cells 17

2.2.1 Back-contact back-junction (BC-BJ) solar cells 18

2.2.2 Emitter Wrap Through (EWT) solar cells 24

2.2.3 Metallization Wrap Through (MWT) solar cells 25

2.3 Critical parameters of the back-contact back-junction solar cells 26

2.4 Conversion efficiency limitations by intrinsic losses 28

2.4.1 Intrinsic loss mechanisms in silicon 28

2.4.2 Short-circuit current limit 29

2.4.3 Open-circuit voltage limit 31

2.4.4 Efficiency limit 33

3 Measurement methods and numerical simulations 35

3.1 Surface saturation current density 35

3.1.1 Injection dependent lifetime measurements 35

3.1.2 Determination of J_{0s} at low injection 37

3.1.3 Determination of J_{0s} at high injection 38

3.2 Device simulation 39

3.2.1 Two-dimensional numerical simulation 39
3.2.2 One-dimensional numerical simulation 41
3.2.3 Simulation parameters 41
3.3 Measurement table for laboratory size solar cell 43
4 Design and technology 45
4.1 Device structure 45
4.2 n-type bulk Si material 47
4.2.1 Minority carrier diffusion length 49
4.2.2 Influence of the surface potential on the minority carrier lifetime 50
4.3 Processing technology 54
4.4 Metallization 58
4.4.1 Formation of the interdigitated metal grid 59
4.4.2 Thickening of the thin seed metal layer 68
4.5 Solar cell results 70
4.5.1 Laboratory-scale solar cells 70
4.5.2 Industrial-scale solar cells 72
4.6 Conclusions 74
5 Analysis of the laser-fired aluminium emitters 77
5.1 Introduction 77
5.2 Fabrication of LFE and boron emitter cells 78
5.3 Solar cell results 79
5.4 Laser-induced damage zone 80
5.5 Quantum efficiency of the LFE cells 81
5.6 Recombination in the damage zone 82
5.7 Comparison of boron diffusion and LFE emitters 86

5.8 SunsV_{OC} and implied voltage 88
5.9 Optimization of the LFE cells 89
5.10 Conclusion 91
6 Analysis of the loss mechanisms 93
6.1 Introduction 93
6.2 Optical losses 94
6.2.1 Optical losses in the back-contact solar cell 94
6.2.2 Modeling of the optical losses 94
6.2.3 Free carrier absorption 95
6.2.4 Distribution of optical losses 97
6.2.5 Influence of optical losses on the cell efficiency 99
6.3 Recombination losses 100
6.3.1 Modeling of the saturation current densities 100
6.3.2 Influence of recombination losses on the short-circuit current 102
6.3.3 Influence of recombination losses on cell efficiency 103
6.4 Electrical shading 104
6.4.1 Increased lateral transport distance for the minority carriers 104
6.4.2 Light beam induced current mapping 105
6.4.3 LBIC line scans 106
6.4.4 Influence of the electrical shading on the cell efficiency 107
6.5 Resistive losses 107
6.5.1 Modeling of series resistance losses 107
6.5.2 Influence of series resistance losses on cell efficiency 110
6.6 Adding up the individual loss mechanisms 111

6.7 Conclusions 115

7 Front surface passivation using a front surface field 117

7.1 Introduction 117

7.1.1 Surface recombination 117

7.1.2 Surface passivation methods 119

7.2 Influence of the front surface field diffusion profile on the solar cell performance 120

7.3 Surface passivation quality for different FSF diffusion profiles 123

7.3.1 Processing of test structures for the determination of J_{0e} 124

7.3.2 Determination of J_{0e} under high and low injection 127

7.3.3 J_{0e} for different FSF diffusion profiles 128

7.4 Solar cells with different FSF diffusion profiles 131

7.4.1 Solar cell results 131

7.4.2 Analysis of the open-circuit voltage 132

7.4.3 Internal quantum efficiency 133

7.5 Stability of the front surface passivation under UV-light exposure 134

7.5.1 UV-light influence on the front surface passivation 134

7.5.2 Lifetime test structures 135

7.5.3 Solar cell results 137

7.5.4 Regeneration of the UV-degraded solar cells 139

7.6 Conclusion 141

8 Lateral current transport via front n^+ diffused layer 143

8.1 Introduction 143

8.2 Lateral current transport of majority carriers 144

8.3 Variation of the pitch 147

8.4 Solar cell results 148

8.5 Short-circuit current analysis 149
8.6 Fill factor and series resistance 150
8.6.1 Fill factor 150
8.6.2 Pseudo fill factor 150
8.6.3 Conductivity modulation 152
8.6.4 Series resistance 153
8.7 Simulations of the lateral current flow of the majority carriers 154
8.8 Conclusions 157
9 Low-illumination characteristics 159
9.1 Introduction 159
9.2 Analyzed solar cells and methodology 160
9.3 Non-diffused surfaces 162
9.4 Floating emitters 166
9.5 Front surface fields 169
9.6 Conclusions 172
10 Summary and outlook 175
Zusammenfassung und Ausblick 179
Symbols, acronyms and physical constants 183
Bibliography 189
List of publications 203
Acknowledgements 207

Abstract

In this thesis high-efficiency back-contact back-junction (BC-BJ) silicon solar cells for one-sun applications were studied. The focus was put on the development of a low-cost and industrially feasible manufacturing technology in order to utilize the full cost reduction potential of this elegant cell structure. At the same time the performance of the developed solar cells was investigated in details by experimental work, analytical modeling and numerical device simulations. The complex and costly photolithography masking steps were replaced by techniques which are of low cost and relevant for mass production, such as screen-printing of the masking layers and local laser ablation of the dielectric and silicon layers. The highest solar cell efficiency of 21.1 % (J_{SC} = 38.6 mA/cm^2, V_{OC} = 668 mV, FF = 82.0 %) was achieved on 160 µm thick 1 Ω cm n-type FZ Si with the designated area of 4 cm^2. A detailed study of the loss mechanisms limiting the efficiency of the developed back-contact back-junction silicon solar cell was performed. The reduction of the cell efficiency was determined to be 3.9 % abs. due to recombination processes, 2.0 % abs. due to optical losses, 0.3 % abs. due to series resistance effects and 0.7 % abs. due to electrical shading. The developed model of the loss mechanisms is a powerful tool for the further optimization study of the solar cell structure. Positive effects of the phosphorus doped n^+ front surface field (FSF) on the performance of the BC-BJ solar cells were studied in details. These effects are: (i) *Surface passivation and passivation stability:* The optimal surface passivation was obtained with a deep diffused Gaussian phosphorus FSF doping profile with sheet resistance of 148 Ω/sq. In contrast to solar cells without the FSF diffusion, the solar cells with the FSF diffusion profile did not show any performance degradation under exposure to UV illumination. (ii) *Lateral current transport:* The front diffused n^+ layer can be seen as a parallel conductor to the lateral base resistance. This way the lateral base resistance losses can be reduced. (iii) *Low-illumination performance:* The front surface field improves the performance of the BC-BJ solar cells under low illumination intensity. Therefore the BC-BJ cells with FSF seem to be the best ones suited for achieving a high energy yield when also operating under low illumination intensity.

1 Introduction

1.1 Thesis motivation

Today's most used form of energy is fossil energy. However this form of energy is based on limited resources and produces harmful emissions. The climate change caused by the emission of the greenhouse gases, as well as the potential of military conflicts over the remaining limited reserves of the fossil fuels, are two of the major problems, which the humanity is facing at the moment. Therefore the transition from the fossil energy sources to the clean and renewable energy sources is at present one of the greatest challenges for the mankind.

The Earth receives incoming solar radiation with the power of 174×10^{15} W from the Sun. Thus, in just one hour our planet receives enough energy from the Sun, to cover the present global annual energy consumption. Solar irradiation energy is an abundant and widely available source of energy. The solar light can be directly converted into electricity by the photovoltaic cells. During its operation, a solar cell does not produce any emissions or noise. Therefore photovoltaics is a very promising technology in satisfying the future demand for the environmentally friendly energy in a sustainable way.

The production of solar cells is growing rapidly, with an average annual growth rate of 35 % since 1998 [1]. By the end of 2007 the cumulative installed capacity of the photovoltaic systems reached 9.2 GW. Silicon solar cells dominate the market of photovoltaic solar cells and are likely to maintain its dominant market share in the coming years [2]. However the costs of energy produced by photovoltaics are still too high. Therefore the successful dissemination of photovoltaics can be only achieved by further reduction of the manufacturing costs of the photovoltaic systems.

A high impact on the lowering of the manufacturing costs is achieved by improving the efficiency of the silicon solar cells. The progress in the technology of the silicon solar cell enables manufacturing of more advanced and highly-efficient cells. In mass production of the solar cells for one-sun applications, the highest conversion efficiencies of above 22 % are achieved using a structure of a back-contact back-junction solar cells [3]. However since this cell structure is complex, its production is challenging and involves multiple masking steps, which should be able to create small feature sizes and be very well aligned to each other. Photolithography masking, a technology widely used in microelectronics, would meet the above mentioned

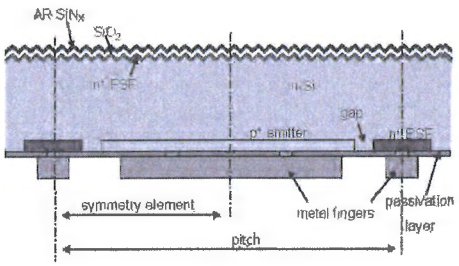
requirement perfectly. However due to its high costs, the application of photolithography is only allowed to the production of the small area concentrator solar cells. Production of the large-area one-sun back-contact back-junction solar cells requires an appropriate low-cost manufacturing technology in order to be able to produce it cost effectively.

Due to the potential of reaching the high-device efficiencies with the low-cost manufacturing technology, the present thesis focuses on the back-contact back-junction silicon solar cell structure. An industrially feasible manufacturing technology of this cell structure is developed. Moreover, based on the presented advanced characterization and modeling of the developed solar cells, further increase of the device efficiency and lowering of its manufacturing costs is possible.

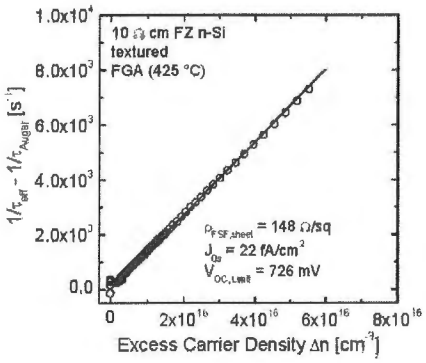
1.2 Thesis outline

The operating principles and the technology of the silicon solar cell are presented in references [4], [5], [6].

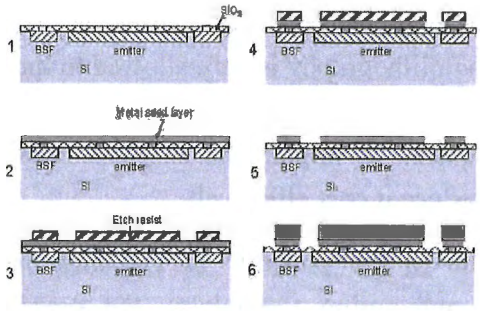
Chapter 2: The thesis starts with a review of advantages and challenges related to the back-contact solar cell structures. Different types of the back-contact solar cells are introduced and a review of the state-of-the-art technology is given. The critical parameters of the back-contact back-junction solar cells are discussed.



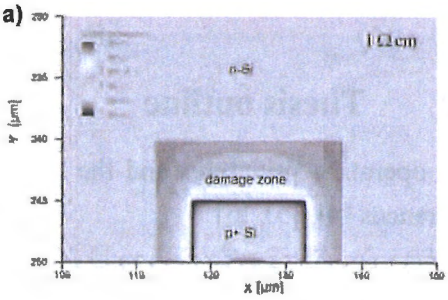
In **chapter 3** two methods for determination of the surface saturation current density under low and high injection are presented. Moreover, the process of the numerical simulations of the back-contact back-junction solar cells using one and two-dimensional simulations is described.



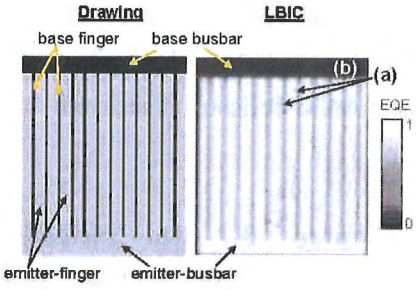
Chapter 4: The technology of the back-contact back-junction silicon solar cells, developed in this work, is presented. The starting material for the cells, n-type silicon material is characterized. Different methods for the formation of the interdigitated contact grid are described in detail. The best results of the developed small, laboratory-size and large, industrial-size solar cells are presented.



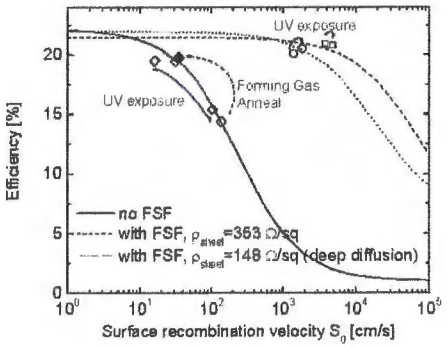
In **chapter 5** the local laser-fired aluminium emitter (LFE) process, an alternative process to boron emitter diffusion, is investigated. The model of the LFE emitters, which includes a laser-induced damage zone, is analysed using a two-dimensional simulation and compared with the experimental solar cell results.



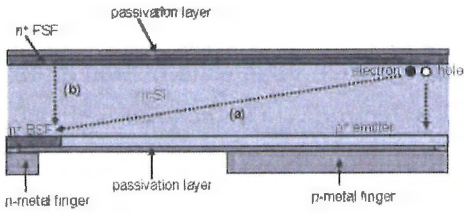
A detailed analysis of the loss mechanisms in the back-contact back-junction silicon solar cells is presented in **chapter 6**. Four main loss mechanisms in the BC-BJ solar cells are described: series resistance, optical losses, recombination losses and electrical shading. The influence of each of the loss mechanisms on the cell efficiency is studied.



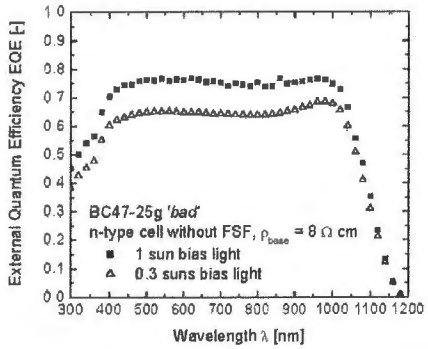
Passivation quality of the different phosphorus-doped front surface field diffusion profiles is analyzed in **chapter 7**. The dark saturation current density of different FSF diffusion profiles is determined under low and high injection. Stability of the test samples and the solar cells under UV exposure is investigated.



Chapter 8: The influence of the large pitch of the n- and p-contact fingers, which is in the range of millimetres, on the series resistance is studied. The application of a phosphorus-doped front surface field (FSF) reduces significantly the lateral base resistance losses. This additional function of the phosphorus-doped FSF is analysed using a comparison between numerical simulation and experimental results.



Chapter 9: The dependence of current and voltage output of three structures of high-efficiency back-junction back-contact silicon solar cells on illumination densities was analyzed in detail. It was shown that, the n-type cell structure with n^+ front surface field enables highest energy yield at low illumination intensity conditions.



2 Back-contact silicon solar cells

The advantages and challenges related to the back-contact solar cell structures are presented. Different types of the back-contact solar cells are introduced and a review of the state-of-the-art technology is given. The influence of the bulk lifetime and the front surface recombination velocity on the efficiency of the back-contact solar cells is discussed. The calculation of the conversion efficiency limit of crystalline silicon solar cells is presented.

2.1 Introduction

Back-contact solar cells exhibit both polarities of the metal electrodes (emitter and base electrodes) on the back cell side. Due to this fact the back-contact solar cells exhibit some major advantages over the conventional solar cell with metal contact on the front side. The advantages are:

- Zero shading due to absence of the metallization grid on the front side. This leads to an increased short-circuit current (J_{SC}) of the cell;
- Due to the absence of the front side metal grid, the front surface can be optimized for optimum light trapping and surface passivation properties, without having to allow for the low contact resistance. This way the front surface recombination can be reduced and light trapping improved;
- Reduction of the series resistance of the metallization grid. Both contact grids are placed on the rear side, therefore the metal finger width is not limited by its shading properties;
- Potentially easier and fully automated co-planar interconnection of the back-contact solar cells in the module assembly process. Recently a novel inline assembly of the solar modules with the back-contact solar cells has been introduced by Späth et al. [7];
- The solar cell packaging density in the solar module can simultaneously be increased, thereby increasing the total area efficiency of the module. A module with back-contact solar cells with a record efficiency of 20.1 % was recently presented by De Ceuster et al. [3].
- Attractive, uniform appearance of the finished modules, which is especially of importance in the building integrated photovoltaics (BIPV).

Thanks to the above mentioned advantages the conversion efficiency of the back-contact solar cells is potentially increased compared to conventional solar cells. Also the costs of the photovoltaic energy produced by the module with back-contact solar cells can be therefore reduced.

However, there are also some challenges and risks related to the back-contact solar cell structure. There challenges and risks are:

- The processing of back-contact solar cells requires a few structuring steps. This makes the processing procedure more challenging and complicated than in the case of the conventional solar cells;
- Risk of fatal shunting between the p- and n- electrodes due to errors in the masking processes. Therefore the requirements of high positioning accuracy and resolution are imposed on the masking steps. That results in an increase of the cost of these processes;
- If the analyzed back-contact solar cell structure possesses all collecting p-n junction on the back side (back-contact back-junction solar cell structure), then a high minority carrier lifetime in the base material is required in order to enable high solar cell efficiencies. Therefore the starting silicon material needs to be of high quality and its quality needs to be maintained during the whole solar cell processing sequence;
- Simultaneously the front surface recombination velocity needs to be kept low in the finished device in order to enable high efficiencies. More information on the issues of the minority carrier lifetime in the base material and the surface recombination velocity are presented in section 2.3.

The high material quality and the complicated processing technology result in the increase of the manufacturing costs. Therefore the efficiency of the processed back-contact solar cell needs to be high, in order to balance the increased costs.

The issues of the complicated processing technology and the requirement of reaching high conversion efficiencies are addressed in this work. In the following chapters a development of a high-efficiency back-contact back-junction solar cell structure using industrially applicable processing technology, including the masking technology, together with an advanced solar cell characterization are presented. However before going into the results of the solar cells developed in this work, a review of the back-contact silicon solar cell will be given in the next section.

2.2 Review of back-contact silicon solar cells

A conventional solar cell is presented in Figure 2-1. This solar cell possesses metal contact on both cell sides. The cell structure shown in Figure 2-1 is a passivated emitter rear locally diffused (PERL) solar cell structure, which enabled reaching the highest efficiency of the silicon solar cell under one-sun illumination intensity. The record efficiency of 24.7 % was demonstrated by Zhao et al. [8] on monocrystalline silicon. Using mulitcrystalline silicon the record efficiency of 20.3 % was obtained by Schultz et al. [9]. These cells feature: a selective doping profiles underneath metal contacts for low contact recombination, passivated front and rear surfaces, well textured front surface with an antireflection coating for low front surface reflection and flat, highly reflective rear for light-trapping, low front contact shading. These are the required ingredients for a high-efficiency design and they are also applicable for the back-contact back-junction cell structure. A review of the recent activities in the industrial application of high-efficiency silicon solar is given by Glunz [10], [11].

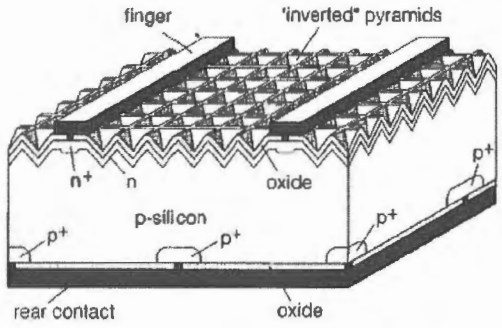


Figure 2-1 The passivated emitter, rear locally-diffused PERL cell which reached record efficiency of 24.7 % (from [8]).

The backside contacted solar cells, which exhibits both polarities of metal contacts on the back side, can be divided into three major categories:

- Back-Contact Back-Junction (BC-BJ) solar cells (section 2.2.1), also called Interdigitated Back Contact (IBC) solar cells, which have both contacts and the collecting junction placed on the back side of the cell;
- Emitter Wrap Through (EWT) solar cells (section 2.2.2), in which the front surface collecting junction is connected to the interdigitated contacts on the back surface via laser-drilled holes;

- Metallization Wrap Through (MWT) solar cells (section 2.2.3), in which the front surface collecting junction and the front metallization grid are connected to the interconnection pads on the back surface via laser-drilled holes.

A short review of the above mentioned categories of the back-contact solar cells is presented in the following subsections. For a more detailed review of back-contact solar cells the reader is refered to the paper of Van Kerschaver and Beaucarne [12]. The topic of this work are back-contact back-junction solar cells. Therefore a detailed review of the development efforts in the field of this solar cell structure done by different groups will be given here.

2.2.1 Back-contact back-junction (BC-BJ) solar cells

The concept of the back-contact back-junction solar cells, also called interdigitated back contact (IBC), was introduced in 1975 by Schwartz and Lammert [13], [14]. This cell structure is shown in Figure 2-2.

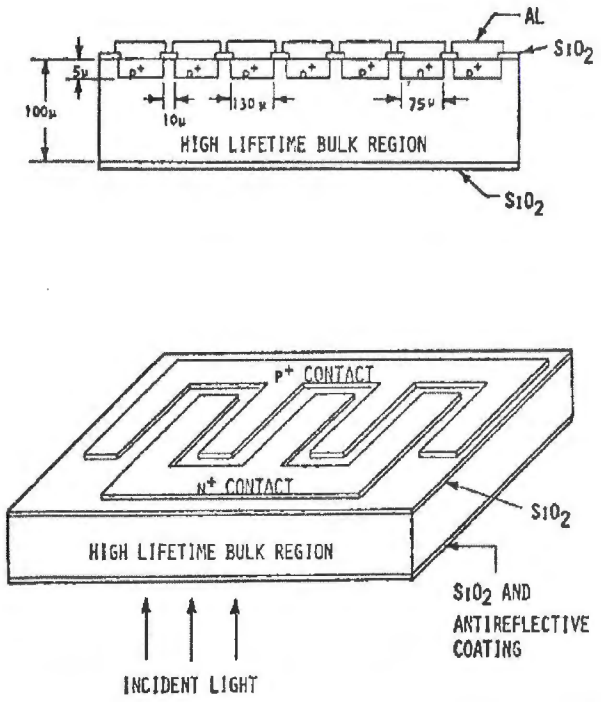


Figure 2-2 The structure of the interdigitated back contact IBC solar cell (from [13]).

Both emitter and base metal contacts are placed on the back cell side in a form of an interdigitated grid. Also the emitter and back surface field diffusions are in the form of the interdigitated grid. Due to such design this device possesses all of the above

mentioned advantages. At first the IBC solar cells were designed for operating in the high-concentration systems. An efficiency of 17 % was achieved under 50-suns concentration [13].

In 1984 Swanson et al. [15] introduced a point contact silicon solar cell, which is similar to the IBC solar cell. The main difference is that in the point contact solar cell the rear side diffusions are limited to an array of small points, as schematically shown in Figure 2-3. By reducing of the area of the highly diffused regions on the back cell side, the dark saturation current of the doped areas could be reduced significantly. Thus, the output voltage and the efficiency of the cell could be increased.

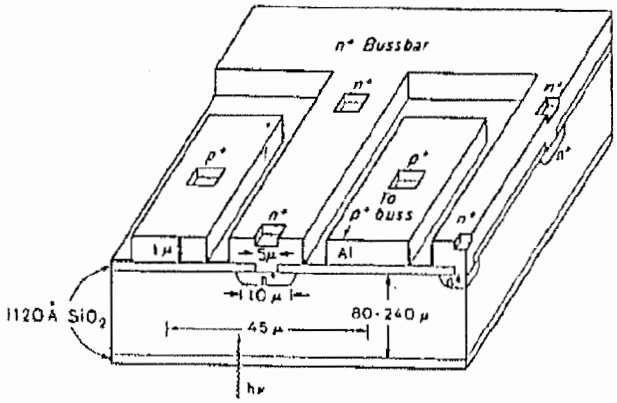


Figure 2-3 Structure of a point contact solar cell (from [15]).

The photovoltaic group at Stanford University led by Prof. Swanson has made the most significant contributions in the field of the IBC cells. Thus, the developments of the back-side contacted cells made by this group are presented in the following:

Non-textured point contact *concentrator solar cell* achieved an efficiency of 19.7 % under 88-suns concentration in 1984 [15]. In 1986 a further optimized point contact solar cell with an efficiency of 27.5 % under 100 suns concentration was achieved by Sinton et al. [16]. Shortly after, an increased device cell efficiency up to 28 % under 150 suns was after presented by Sinton et al. [17]. In 1988 Sinton et al. [18] reported point contact solar cells with an efficiency of 28.4 % at power densities up to 200 suns. The area of these solar cells was 0.15 cm^2.

The back-contact back-junction solar cell structure was also optimized for the applications under standard *one-sun illumination*. In 1985 Verlinden et al. [19] presented an IBC solar cell with a one-sun illumination efficiency of 21 %. One year later Sinton et al. [16] introduced a point contact solar cell with 22.2 % one-sun

efficiency with the area of 0.15 cm^2. However this efficiency was corrected down to 21.7 % after the publication [20].

King et al. [20] presented a first medium-area (8.5 cm^2) point contact solar cell with the front and back surface fields with the top efficiency of 22.3 %. In this solar cell a novel *multi-level metallization scheme*, introduced by Verlinden et al. [21], [22], was applied. This metallization scheme allowed for realization of large-area solar cells in which series resistance is not dependent on solar cell area. In 1991 a record one-sun efficiency of 22.7 % on a 37.5 cm^2 point contact solar cell was reported by King et al. [23].

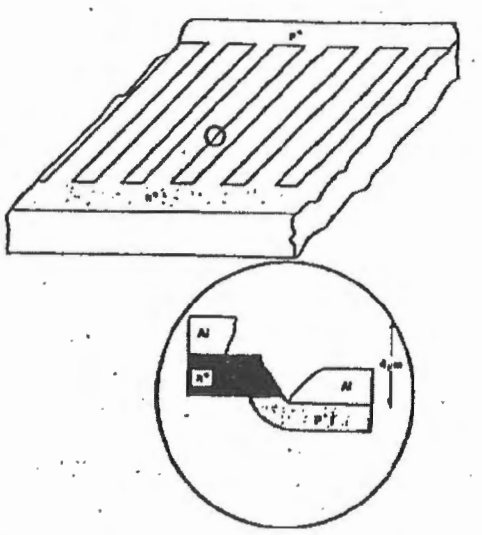


Figure 2-4 Simplified back-side solar cell. The illuminated side is on the bottom in this figure. The mesa trench, which allows for self-aligned metal contact separation is shown in the inset (from [24]).

The processing of the interdigitated grid of the rear side diffusions, contact openings and the metal grid of the point contact solar cells requires four to six patterning steps [24]. Thus, this processing sequence is complex, which results in high manufacturing costs. In 1988 a *self-aligned method* to for an interdigitated contact grid was introduced [18]. In 1990 Sinton et al. [24] presented a simplified back-side solar cell (schematically shown in Figure 2-4), which used this self-aligned contact separation and allowed for reduction of the masking steps to one. For the simplified processing sequence a 10.5 cm^2 one-sun solar cell with an efficiency of 21.9 % was reported.

The Sunpower Corporation was founded in 1985 by Prof. Swanson in order to commercialize to high-efficiency back-contact silicon solar cells developed by the

research group of Stanford University. A pilot production of large area (35 cm^2) back-contacted solar cells with an efficiency of 21 % was reported by Sinton et al. [25]. 7000 solar cells of this type, with an average efficiency of 21.1 %, were manufactured for the Honda solar-car *Dream*, which won the World Solar Challenge race in 1993 [26]. The processing of these solar cells required five photolithography masking steps.

In a following study of Sunpower the back-contact solar cell design, especially the *edge passivation* and the *substrate doping*, were optimized. This resulted in a record one-sun efficiency of 23.2 % reported in 1997 by Verlinden et al. [27]. In 2002 the process simplifications, which eliminated one third of the major processing steps and resulted in reduction of the fabrication costs by 30 %, were reported by Cudzinovic et al. [28]. The process simplifications led to 0.6 % absolute efficiency decrease.

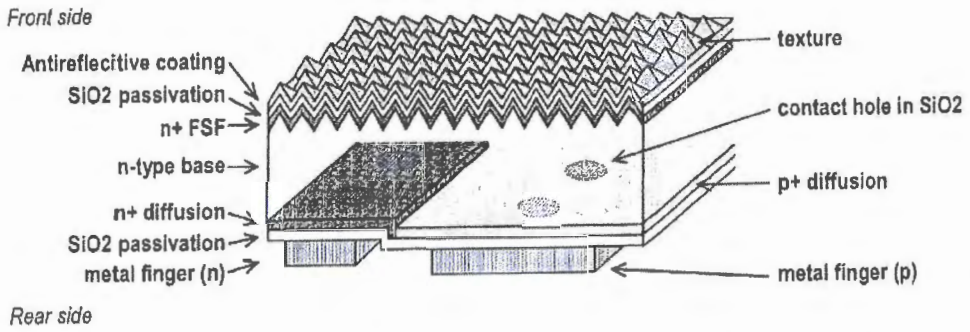


Figure 2-5 Schematic diagram of the Sunpower's A-300 solar cell (from [29]).

In 2004 a manufacture of the large-area (149 cm^2) *A-300 back-contact solar cells* was introduced by Mulligan et al. [29]. A maximum cell efficiency of the A-300 solar cells of 21.5 % was achieved. A schematic diagram of the Sunpower's A-300 solar cell is shown in Figure 2-5. McIntosh et al. [30] found that the n-type silicon material with thickness of 160 to 280 μm and resistivity of 2 to 10 Ω cm was optimal for the A-300 cells. Also the light trapping of this cell type was studied in details by McIntosh et al. [31].

A high volume production of a *new generation of the A-300* back-contact cells with an record average efficiency of 22.4 % was introduced in 2007 by De Ceuster et al. [3]. The new generation back-contact solar cells achieve the highest efficiency silicon solar cells in mass production up to date. In the same paper a record module efficiency of 20.1 % using back-contact solar cells was reported.

In a recent lecture Prof. Swanson [32] announced a new record efficiency of 23.4% of a large area (149 cm^2) back-contact solar cell developed by the R&D department of Sunpower. Details of the improvements that have been applied to this solar cell design and to the processing technology are not known.

Simultaneously to the development efforts at Stanford University and Sunpower, there other groups which are working on the high-efficiency back-contact back-junction solar cell devices. At Fraunhofer ISE a rear-contacted (RCC) silicon solar cell with line contacts were processed using the photolithography masking. A schematic diagram of a RCC cell is shown in Figure 2-6. An efficiency of 22.1 % was reported by Dicker et al. [33], [34].

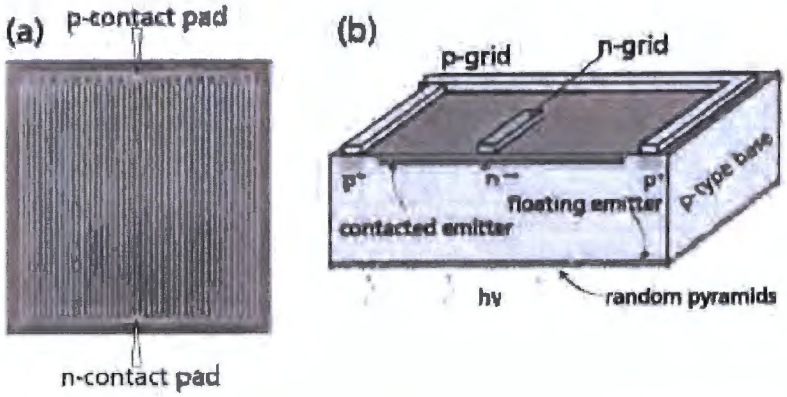


Figure 2-6 Structure of the RCC fabricated at Fraunhofer ISE. (a) View of the rear side of the RCC showing the interdigitated contact pattern. (b) Details of the solar cell structure, with the cell shown upside down (from [33]).

For the applications under concentrated sunlight a rear-line-contacted concentrator cell (RCLL) was developed by Mohr [35]. This cell structure is based on the RCC solar cell design. A maximum efficiency of 25 % at illumination intensity of 100 suns was achieved [36].

A low-cost approach to the BC-BJ solar cell structure was developed by Guo [37] from the UNSW. The *Interdigitated Backside Buried Contact* (IBBC) solar cell, shown in Figure 2-7, is processed without the use of photolithography. The laser-grooved buried contact technology is applied. A maximum one-sun efficiency of 19.2 % was reported by Guo et al. [38].

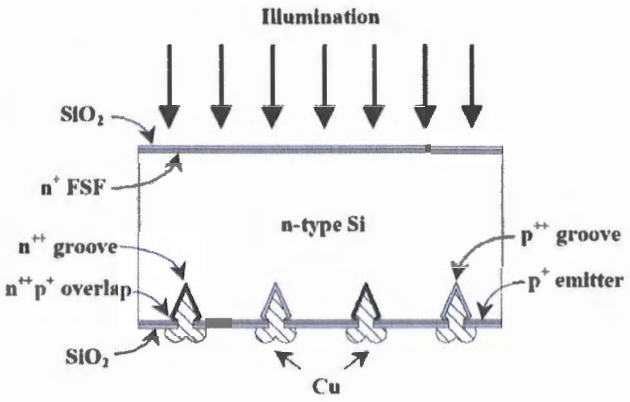


Figure 2-7 Schematic cross section of the n-type IBBC solar (from [38]).

Another very promising low-cost BC-BJ solar cell structure was developed by Engelhart at al. [39], [40] from the ISFH. The *RISE* (*Rear Interdigitated contact scheme, metalized by a Single Evaporation*) solar cell structure is schematically presented in Figure 2-8. The RISE solar cell is fabricated using a mask-free process, in which the laser ablation of Si and laser ablation of protective coatings are applied. With this cell structure a designated area efficiency of 22 % was achieved on a 4 cm^2 laboratory solar cell.

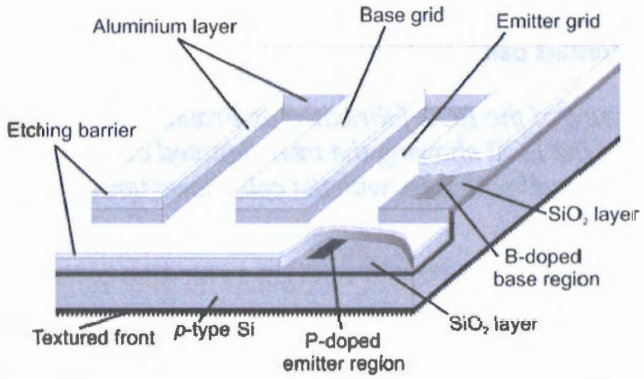


Figure 2-8 Schematics of the RISE back junction solar cell. (from [39]). The illuminated side is on the bottom in this drawing.

Furthermore, large-area high-efficiency back-contact solar cells for a mass production are being developed by Q-Cells within the *Quebec* project. In 2006 Huljic et al. [41] reported maximum efficiency of 21 % for laboratory scale 4 cm^2 on low cost Cz-Si wafers. In 2007 Huljic et al. [42] presented large area (100 cm^2) BC-BJ solar cell with an efficiency of 20.5 %. In the same presentation plans for a technology transfer to a pilot production were announced.

One of the very promising developments in the field of back-contact solar cells, is the application of the of *amorphous/crystalline silicon* (a-Si/c-Si) *hetero-junction structures*. Due to its superior surface passivation properties the a-Si/c-Si hetero-junctions have the potential to significantly increase the voltage of a solar cell. Hetero-junction back-contact solar cells are being developed by a number of research groups [43], [44], [45].

2.2.2 Emitter Wrap Through (EWT) solar cells

The concept of the emitter wrap through EWT solar cell was introduced by Gee et al. [46], [47]. The concept is based on an emitter which is diffused on the front and back side of the cell. The front and back emitters and connected through laser-drilled and emitter-diffused holes. The EWT cell concept is schematically shown in Figure 2-9.

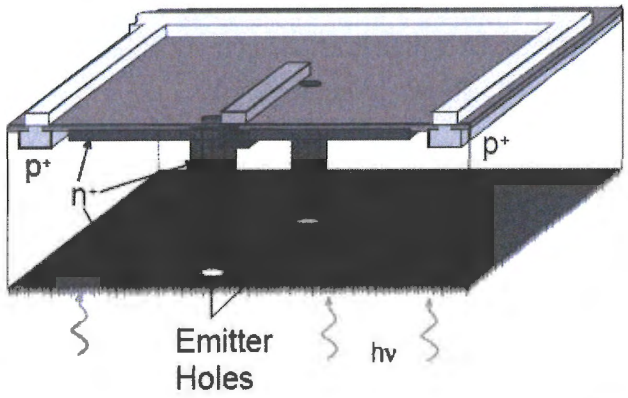


Figure 2-9 Schematic diagram of an emitter wrap through EWT solar cell. The illuminated side is facing down in the picture (from [48]).

The advantages of the EWT solar cell are comparable to the ones of back-contact back-junction solar cells: (i) complete elimination of front contact grid shading, and (ii) the possibility of the co-planar interconnection. However there exists one major advantage of the EWT cells over the BC-BJ cells. Due to the presence of the p-n junction on the front and on the back cells side, the average distance of the minority carriers to the emitter is significantly reduced. This results in the much lower required minority carrier lifetime in the bulk than in the case of BC-BJ cells. It is therefore possible to reach high efficiencies with EWT cells even with a low quality bulk Si, what is not possible in the case of BC-BJ cells. A comparison of the influence of the bulk lifetime on the solar cell efficiency for the BC-BJ and EWT solar cells is presented by Kray [48] and Engelhart [40].

Advent Solar reported manufacturable EWT solar cells with efficiencies of 14 % on mc-Si and 16 % on mono-Si using only low-cost processing [49]. At the University of Konstanz a low-cost EWT solar cell process was developed and an efficiency of 13.6 % on Cz-Si was achieved [50], [51]. At Fraunhofer ISE an EWT solar cell processed using photolithography masking achieved 18.7 % on Cz-Si [52] and 21.4 % on FZ-Si [53]. At ISFH a large area (92 cm^2) RISE-EWT (Rear Interdigitated Single Evaporation Emitter Wrap-Through) solar cell was developed. A maximum efficiency of 21.4 % on FZ-Si was reported by Hermann et al. [54]. Q-Cells presented a large area (92 cm^2) EWT solar cell on mc-Si with an efficiency of 17.1 % [55].

2.2.3 Metallization Wrap Through (MWT) solar cells

The metallization wrap through (MWT) solar cell concept [56] shows the closest similarity to a conventional solar cell structure. The emitter and the front side metallization fingers are located on the front surface. However, the busbars are placed on the back side of the cell. The front side metal fingers are connected to the busbar on the rear side through the laser drilled holes, which are filled with the metal. The MWT cell concept is schematically shown in Figure 2-10.

Due to the fact that in the processing of the MWT solar cells standard screen-printing technology can be applied, the transition from the processing sequence of a conventional soar cell to a MWT solar cell is not complicated. Furthermore, the MWT cell concept offers advantages over the conventional solar cell. Thanks to the removal of the front side busbars, the front contact shading is reduced. Simultaneously, the co-planar interconnection is possible since both contact polarities are placed on the back side.

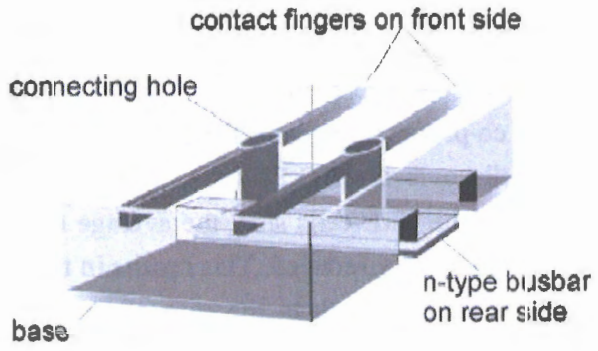


Figure 2-10 Schematic drawing of a MWT cell (from [57]).

The MWT cell structure is being successfully developed by different groups: Van Kerschaver et al. [58] from IMEC presented a module based on screen-printed MWT solar cells with an efficiency of 14.7 %. At ECN a pin-up module concept was introduced by Bultman et al. [59]. Weeber et al. [60] from the ECN group presented mc-Si MWT cells with an area of 225 cm^2 and an efficiency of 16.7 %. At Fraunhofer ISE a mc-Si MWT solar cell with an area of 156 cm^2 and an efficiency of 16.2 % was presented by Clement et al. [61]. Joos et al. [62] from the group of University of Konstanz presented Cz-Si MWT solar cells with an area of 25 cm^2 and an efficiency of 17.5 % and Knauss et al. [57] presented large area (243 cm^2) Cz-Si MWT cells with an efficiency up to 16.7 %.

2.3 Critical parameters of the back-contact back-junction solar cells

As already mentioned in section 2.1, one of the challenges related to the back-contact back-junction solar cell structure is the requirement of a high minority carrier lifetime in the silicon bulk (τ_{bulk}) and a low front surface recombination velocity (S_{front}). Without fulfilling these requirements, high device efficiencies cannot be achieved.

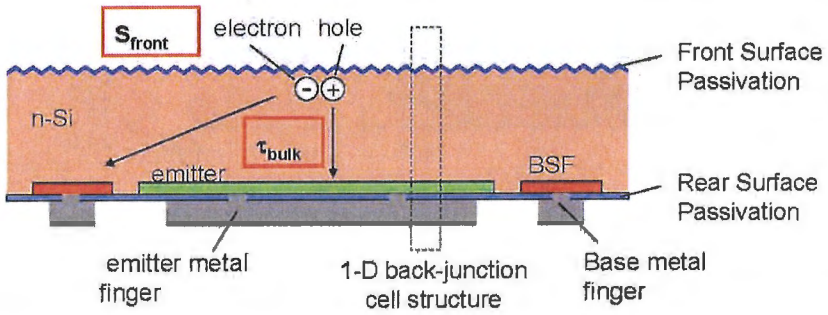


Figure 2-11 *Schematic cross-section of an n-type high-efficiency back-contact back-junction silicon solar cell (sketch not to scale). Two most critical parameters for this cell type, namely the front surface recombination velocity (S_{front}) and the minority carriers lifetime in bulk (τ_{bulk}) are also shown.*

In silicon solar cells most of the photogeneration occurs at the front side of the cell (schematically shown in the Figure 2-11). But in the back-junction cell structure, the p-n junction is located on the back cell side. Therefore the light generated carriers can be easily lost by recombining at a poorly passivated front surface, instead of reaching the back junction. Moreover, even if the front surface is well passivated, a risk of recombination within the bulk silicon exists. The carriers which need to diffuse

through the wafer thickness can recombine in the bulk silicon before reaching the back junction if the bulk lifetime of the minority carriers is insufficient. Therefore, τ_{bulk} and S_{front} are the two most critical parameters in the back-contact back-junction solar cell structure.

In order to show the importance of these two critical parameters in the back-contact back-junction solar cell structure, a one-dimensional back-junction cell structure (marked in Figure 2-11) was simulated using simulation program PC1D [63]. Both critical parameters τ_{bulk} and S_{front} were varied in a wide range in order to analyze their influence on the solar cell efficiency. In the simulations the device thickness of 200 µm was chosen. The simulation results are shown in Figure 2-12.

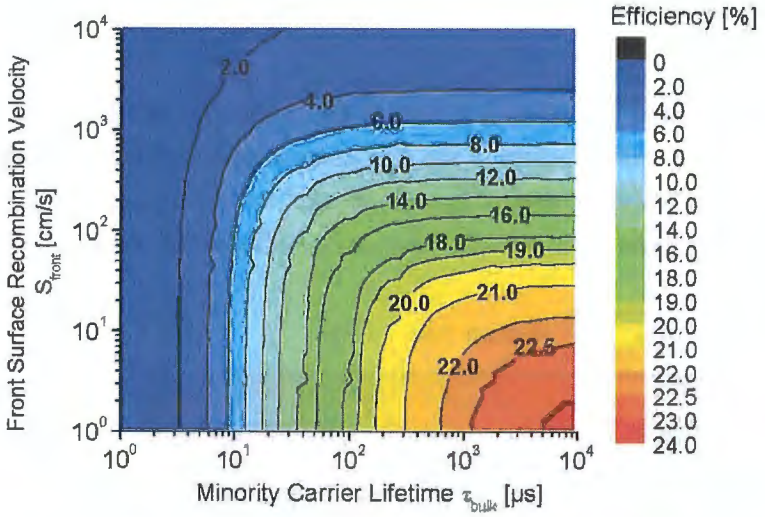


Figure 2-12 Simulations of the efficiency of a one-dimensional back-junction solar cell structure in a wide range of carriers lifetime and front surface recombination velocity. The thickness of the simulated device is 200 µm. The resistivity of the n-type base is 1 Ωcm and the p-type rear emitter has a sheet resistance of 30 Ω/sq. Simulations were performed using PC1D [63].

Based on the simulation results presented in Figure 2-12 the requirements on the τ_{bulk} and S_{front} can be quantified. In order to achieve conversion efficiencies above 22 %, the front surface recombination velocity should be less than 10 cm/s. At the same time the minority carrier lifetime in the bulk material should be higher than 700 µs, which for the base resistivity of 1 Ω cm corresponds to a diffusion length of 900 µm. As a rule of thumb it can be assumed that the diffusion length of the minority carriers in the bulk should be at least four times greater than the wafer thickness in order to allow for high efficiencies in this solar cell concept. As can be seen in Figure 2-12 the conditions of

low S_{front} and high τ_{bulk} need to be fulfilled simultaneously in order to reach high device efficiencies. Even a minor deterioration of one of the critical parameters will lead to a significant efficiency decrease.

It is therefore essential to be able to fulfill the above mentioned requirements when developing a back-contact back-junction solar cell structure. Without having realized the conditions of low S_{front} and high τ_{bulk}, any other developments and optimization efforts on the BC-BJ structure will be fruitless. The analysis of the minority carrier lifetime in the bulk is presented in section 4.2. The front surface recombination velocity of the analyzed solar cell structure was investigated in chapter 7.

2.4 Conversion efficiency limitations by intrinsic losses

The thermodynamic limit of the conversion efficiency of a single bang-gap photovoltaic converter was found to be 33 % [64], [65] for a band-gap of silicon (1.12 eV) and the AM1.5 spectrum. Using actual parameters for intrinsic recombination the efficiency limit is reduced to 30 % [65]. Swanson [66] calculated a theoretical limit of efficiency of a silicon solar cell of 29 %.

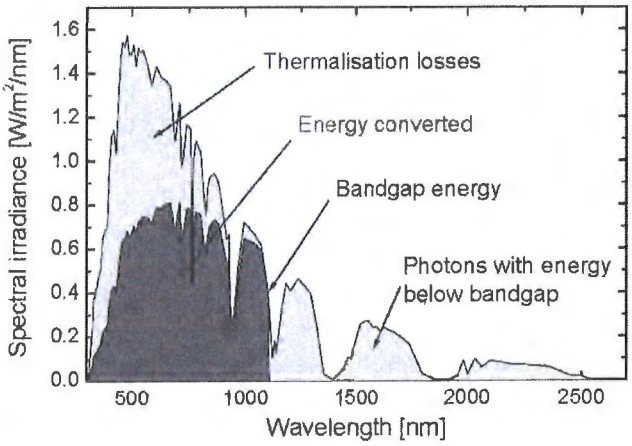


Figure 2-13 Spectral irradiance of the AM1.5G spectrum. The fraction of the spectrum that can be converted by a single-junction silicon solar cell is marked with dark grey.

2.4.1 Intrinsic loss mechanisms in silicon

The above mentioned conversion efficiency of a single junction silicon solar cell is primarily limited due to the following intrinsic loss mechanisms:

- Photons with energy smaller than the band gap (1.12 eV) of silicon do not have enough energy to generate electron hole pairs.
- Photons with energy equal or exceeding the band gap will generate electron-hole pairs. However, photon energy exceeding 1.12 eV will be lost due to the thermalization process. These two effects are schematically shown in Figure 2-13.
- The maximum open-circuit voltage is smaller than 1.12 V (band gap in Si). This is caused by the fact that not the separation of band gap, but the separation of the quasi-Fermi levels defines the open-circuit voltage [5].
- The maximum power that can be generated by a solar cell is smaller than the product of open-circuit voltage and short-circuit current. The current-voltage (IV) curve of a solar cell does not have a rectangular shape (see for example Figure 4-23). Due to the exponential dependence of current with voltage, which is caused by the non-avoidable recombination currents, the fill factor (FF) is limited to about 85 %.

Moreover, the absorption of incoming photons in silicon strongly depends on the energy of the photons (see Figure 2-13). For the low energy photons ($\lambda > 1000$ nm) the absorption coefficient is very low, and the absorption length increases strongly. Therefore, even with optimal light trapping schemes, for a finite thickness of the silicon wafer not all incoming photons with appropriate energy will generate electron-hole pairs (see section 2.4.2).

In the following sections a calculation of the efficiency limit of an ideal single junction silicon solar cell with finite thickness and a particular base doping will be presented. In the ideal solar cell only the recombination mechanisms which are intrinsic and non-avoidable in silicon will be considered. These are: radiative and Auger recombination. The technology related recombination losses such as surface recombination, recombination in the highly doped regions of the solar cell or the recombination through the defect and/or impurities in a non-perfect silicon bulk are not taken into account here.

2.4.2 Short-circuit current limit

Short-circuit current (J_{SC}) of a solar cell is a function of the absorption of the incoming photons within the solar cell. In an ideal solar cell the technology related optical effects are not considered. These effects are front surface reflection, metallization grid

shading, transmission through the silicon wafer and parasitic absorption in the dielectric layers or in the highly doped silicon regions.

For the calculation of the limit to the short-circuit current only the intrinsic optical loss effect in the silicon wafer is considered. This effect is the finite maximal average path length of the incoming photons within the silicon wafer. Tiedje et al. [65] and Brendel [67] showed that for the optimal light trapping, the maximal average path length of the incoming light within the silicon wafer (l) can be approximated with:

$$l \approx 4\, n_{Si}(\lambda) W \tag{2.1}$$

where W is the wafer thickness, λ is the wavelength of light and $n_{Si}(\lambda)$ is the wavelength dependent refraction index of silicon.

Knowing the maximum average path length of the incoming light in silicon, the maximum limit on the short-circuit current ($J_{SC,limit}$) as a function of the wafer thickness can be calculated. In order to calculate $J_{SC,limit}$, the solar spectrum needs to be integrated with the absorption coefficient in silicon, assuming the maximum average path of the incoming light calculated with equation (2.1):

$$J_{SC,limit}(W) = \frac{q}{hc} \int \lambda\, I_{AM1.5G}(\lambda) \left[1 - \exp(-4\alpha_{Si}(\lambda) n_{Si}(\lambda) W)\right] d\lambda \tag{2.2}$$

where q is the elementary charge, h is the Planck constant, c is velocity of light in vacuum, $\alpha_{Si}(\lambda)$ is the wavelength dependent absorption coefficient of silicon, $I_{AM1.5G}(\lambda)$ is the energy flux density of the incoming light.

In Figure 2-14 the calculated maximal short-circuit current as a function of wafer thickness is presented. For the complete AM1.5G spectrum a maximal J_{SC} of nearly 46 mA/cm^2 is possible. However, due to the finite path length of the incoming light, the actual J_{SC} limit is lower. The calculations of J_{SC} limit for the case of optimal light trapping (as obtained using the maximal average path length calculated with Eq. 2.1 and then with Eg. 2.2) and for the case of no light trapping (i.e. the path length of the incoming light in silicon equals wafer thickness l=W) are shown as well. For the optimum light trapping and a wafer thickness of 150 µm the J_{SC} limit equals 44 mA/cm^2. However, if no light trapping is applied, then the J_{SC} limit is reduced to 38.6 mA/cm^2.

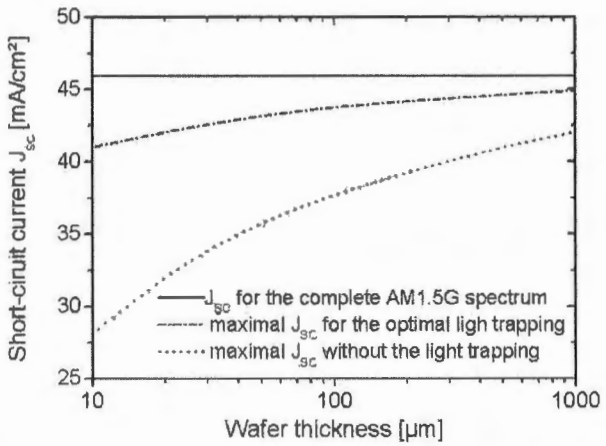


Figure 2-14 Maximum possible short-circuit current in the silicon solar cell under AM1.5G spectrum, as a function of wafer thickness.

2.4.3 Open-circuit voltage limit

Open-circuit voltage (V_{OC}) of a solar cell is limited by the recombination rate of the electron-hole pairs. In an ideal solar cell only the recombination mechanisms, which are intrinsic and non-avoidable in silicon, take place. These intrinsic recombination mechanisms in silicon are the radiative recombination and the Coulomb-enhanced Auger (CE Auger) recombination.

The influence of the intrinsic recombination processes, as well as the limitations of short-circuit current, on the V_{OC} and efficiency of the ideal solar cell can be modelled using the approach of Kerr [68]. The following equation enables calculation of the current –voltage (J-V) characteristics of an ideal solar cell:

$$J(V,W,N_D) = J_{\mathrm{SC,limit}}(W) - qWR_{\mathrm{int}}(V,W,N_D) \tag{2.3}$$

where J is the current and V is the voltage of the solar cell, N_D is the doping concentration of the silicon wafer, R_{int} is the intrinsic recombination rate and the $J_{SC,limit}$ is the short-circuit current calculated in the previous section.

The intrinsic recombination rate can be calculated using the parameterisation of the radiative (R_{rad}) and CE-Auger ($R_{CE\text{-}Auger}$) recombination by Kerr and Cuevas [69], [70] using the following equation:

$$\begin{aligned} R_{\mathrm{int}}(V,W,N_D) &= R_{CE\text{-}Auger} + R_{Rad} = \\ &= n_i^2 e^{\frac{qV}{k_B T}} \left(1.8\times10^{-24} n_0^{0.65} + 6\times10^{-25} p_0^{0.65} + 3\times10^{-27}[\Delta n(V)]^{0.8} + (1-P_{PR}(W))B_R\right) \end{aligned} \tag{2.4}$$

where n_0 and und p_0 are the equilibrium concentrations of electron and holes expressed in units of cm^{-3}, Δn is the injection density and B_R is the radiative recombination coefficient. The photon recycling (i.e. the re-absorption of the radiatve recombination radiation in the solar cell and generation of an electron-hole pair) is considered, with P_{PR} describing the photon recycling rate.

Derivation of the equation (2.4) is done under assumption of the Narrow-Base approximation of Green [71]. Assuming that Fermi levels of electrons and holes are constant within the solar cell base. Then the equation (2.5) is valid

$$np = (n_0 + \Delta n)(p_0 + \Delta n) = n_i^2 e^{\frac{qV}{k_B T}} \tag{2.5}$$

For the calculations of the recombination rate of the intrinsic recombination mechanism the parameters summarized in Table 2-1 were applied. The limit to the open-circuit voltage can be then calculated using the equation (2.3) for the condition of $J(V_{OC}) = 0$.

Table 2-1 Parameters used for the modeling of the intrinsic recombination in silicon.

Parameter	Value
T	300 K
n_i	1.0×10^{10} cm^{-3} [80]
B_R	4.73×10^{-15} $cm^3 s^{-1}$ [72]
P_{PR}	0.79 @ W= 150 µm [70]
p_0	$p_0 = \frac{n_i^2}{N_D}$
n_0	N_D
Δn	$\Delta n(V) = \frac{1}{2}\sqrt{(n_0^2 + p_0^2)^2 - 4\left((n_0 - p_0) - n_i^2 e^{\frac{qV}{k_B T}}\right)} - \frac{1}{2}(n_0 - p_0)$

The limit of the open-circuit voltage calculated for different wafer thicknesses and different base doping density of an n-type solar cell is shown in Figure 2-15. For the cell thickness of 150 µm and an n-type base with doping of N_D=5.0×10^{15} cm^{-3} the V_{OC} limit equals 742.5 mV.

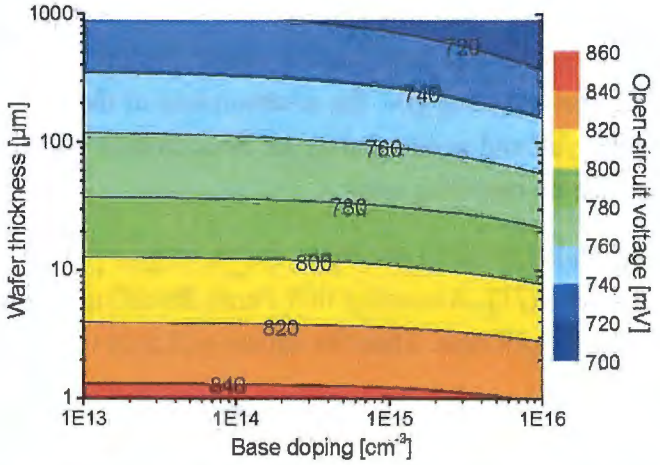


Figure 2-15 *The open-circuit voltage of an n-type silicon solar cell imposed by the intrinsic (radiative and Auger) recombination loss mechanisms. Calculations were done for a wide range of the wafer thicknesses and base doping range.*

Table 2-2 *Efficiency limit of a silicon solar cell with optimal light trapping and only intrinsic recombination mechanisms. Calculations assuming the cell thickness of 150 µm and the n-type base with doping of $N_D=5.0\times10^{15}$ cm^{-3} (base resistivity of 1 Ω cm).*

Cell parameter	Limit by intrinsic losses
efficiency η [%]	28.3
fill factor FF [%]	86.5
open-circuit voltage V_{OC} [mV]	742.5
short-circuit current J_{SC} [mA/cm^2]	44.0

2.4.4 Efficiency limit

By applying the calculated short-circuit current limit and the open-circuit limit into equation (2.3), it is possible to calculate current-voltage characteristics of an illuminated ideal solar cell. Thus, the efficiency limit can be determined.

In Table 2-2 the calculated parameters of an ideal silicon solar cell, with optimal light trapping and only Auger and radiative recombination mechanisms, are shown. The efficiency limit of 28.3 % was calculated assuming the cell thickness of 150 µm and

the n-type base with doping of N_D=5.0×10^{15} cm^{-3} (base resistivity of 1 Ω cm). This wafer thickness and the base doping correspond to the back-contact back-junction solar cells developed in this work. The fill factor was calculated using the one-diode model described by equation (6.8).

The technology related loss mechanisms, which are introduced during the manufacturing of the silicon wafers and the following solar cell processing, will lead to strongly reduced efficiencies of the real solar cells. A detailed comparison of the efficiency limit and the maximal achieved efficiency of the back-contact back-junction solar cell is presented in chapter 6.

3 Measurement methods and numerical simulations

In this chapter, two methods for the determination of the surface saturation current density under low and high-injection are presented. In addition, the process of the numerical simulations of the back-contact back-junction solar cells using one- and two-dimensional simulations is described. The measurement table developed for the electrical characterization of the analyzed solar cells is presented.

3.1 Surface saturation current density

The analysis of the surface passivation quality using different passivation layers (e.g. thermally grown SiO_2, PECVD SiN_X) in the combination with the dopant diffusion requires determination of the surface recombination velocity S and surface saturation current density J_{0s}. The measurement of the saturation current density of the applied diffusion profile is especially required in chapter 7 for the optimization of the n^+ front surface diffusion profile (the so called front surface field - FSF). The method presented below is used to determine the surface saturation current density and can also be applied in order to characterize and optimize both rear side diffusion profiles of the BC-BJ solar cell, i.e. the emitter diffusion, and the back surface field (BSF) diffusion profiles.

3.1.1 Injection dependent lifetime measurements

A direct measurement of the surface recombination velocity S and surface saturation current density J_{0s} is not possible. It is, however, possible to measure the so-called effective lifetime τ_{eff} of minority carriers, which takes into account the recombination mechanisms at the surfaces of the measured sample as well as within its bulk.

The effective lifetime was measured using the photoconductance tool WTC-120 from Sinton Consulting [73]. In this experimental setup, the measured silicon wafer is illuminated by a Xenon flash lamp, which has its spectrum distributed mainly at the wavelengths of 900 to 1000 nm. This near infrared light source allos for a fairly uniform profile of the excess carrier density Δn along the wafer thickness. During the lamp flash, the photoconductance of the measured wafer $\Delta\sigma$ is measured contactlessly by using inductive coupling. At the same time, the light intensity is measured using a reference solar cell, which is placed very close to the measured sample. The excess

carrier density Δn in the sample is calculated from the measured $\Delta\sigma$. Knowing the optical properties of the measured sample allows for the determination of the photogeneration rate within the sample measuring the illumination intensity with a monitor solar cell. After determination of both Δn and photogeneration, τ_{eff} can be calculated as a function of Δn (see for example Figure 3-2). This is possible by applying the generalized evaluation method, which is valid for quasi-steady-state and quasi-transient measurement conditions [74]. The quasi-steady–state photoconductance (QSSPC) method was introduced by Sinton et al. [75].

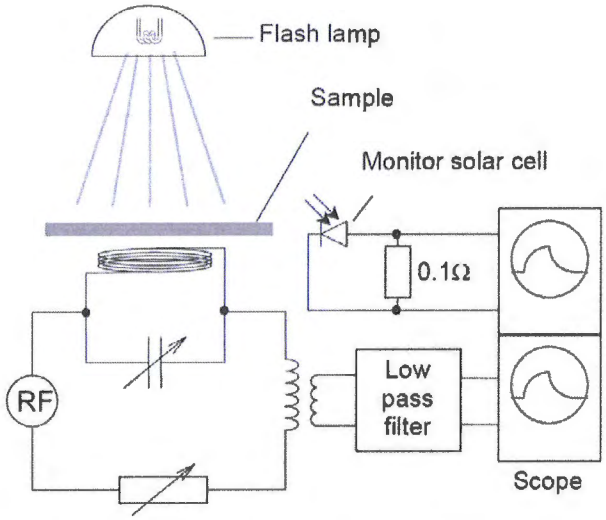


Figure 3-1 Schematic sketch of the photoconductance measurement setup (picture taken from [76])

The measured effective lifetime of the carriers is a function of the recombination in the bulk and at the surfaces of the sample, as shown in equation (3.1).

$$\frac{1}{\tau_{eff}} = \frac{1}{\tau_s} + \frac{1}{\tau_{SRH}} + \frac{1}{\tau_A} + \frac{1}{\tau_{rad}} \tag{3.1}$$

The surface recombination can be described by the surface lifetime τ_s. The volume lifetime τ_b is determined by the Shockley-Read-Hall (SRH) recombination [77], [78], described by the SRH lifetime τ_{SRH}, the Auger recombination τ_A [79] , and the radiative recombination (τ_{rad}).

The sample temperature during the measurements was set to 30°C. For the calculation of recombination parameters, the intrinsic carrier concentration value n_i=1.0 × 10^{10} cm^{-3} [80] was used. In order to determine the surface saturation current density, two methods were applied. J_{0s} was determined under low injection, where

$\Delta n << N_D$, for samples with resistivity of 1 Ω cm and under high injection, where $\Delta n >> N_D$, for 10 Ω cm samples. The same n_i value was used for both analyzed wafer resistivities of 1 and 10 Ω cm. Determination of the J_{0s} from the measured effective lifetime is presented in the next sections.

3.1.2 Determination of J_{0s} at low injection

The effective lifetime τ_{eff} measured under low injection at $\Delta n = 1\times10^{14}$ cm^{-3} was used for the calculations of the surface saturation current density. For samples with resistivity of 1 Ω cm, the dopant concentration equals $N_D = 5\times10^{15}$ cm^{-3}. Therefore, the condition of low injection $\Delta n << N_D$ is satisfied [81].

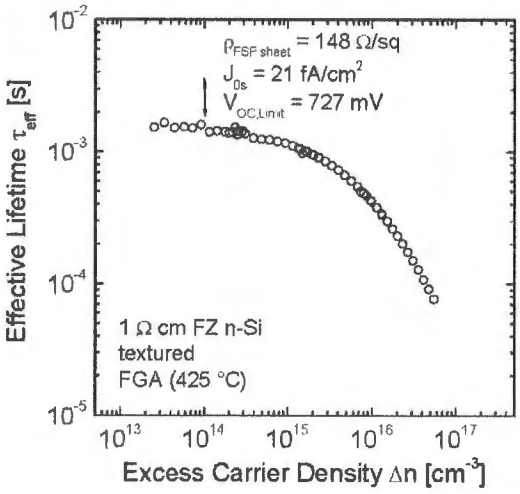


Figure 3-2 Example of QSSPC lifetime measurement of the textured symmetrical test sample with resistivity of 1 Ωcm and front surface field diffusion of 148 Ω/sq. J_{0s} and $V_{OC,\ Limit}$ determined at $\Delta n = 1\times10^{14}$ cm^{-3} are shown.

The surface lifetime τ_s was calculated using the equation (3.2) [82]. For the bulk lifetime τ_b, the intrinsic Auger and radiative recombination was used for the calculation. For the calculation of the Auger lifetime, the model of Kerr [69] was used. For the radiative recombination, the parameterization of Trupke et al. [72] was taken. Omitting the Shockley-Read-Hall bulk recombination results, the upper limit for J_{0s} value is determined as:

$$\frac{1}{\tau_{eff}} = \frac{1}{\tau_b} + \frac{1}{\tau_s} \tag{3.2}$$

For symmetrical lifetime samples, the effective surface recombination velocity S_{eff} can now be calculated using an approximation from Sproul [83]:

$$\tau_s = \frac{W}{2S_{eff}} + \frac{1}{D}\left(\frac{W}{\pi}\right)^2 \tag{3.3}$$

Where S_{eff} takes into account the recombination at the silicon surface as well as the minority carrier's behavior in the highly doped layers at the silicon surface. S_{eff} is defined by del Alamo [84] as:

$$S_{eff} = -\frac{J_p}{q\Delta n} \tag{3.4}$$

Where J_p is the minority carrier current into the surface or from the lowly doped side to the highly doped side of the high-low junction, if a front- and/or back surface field is applied. Using the following equation:

$$J_p = -J_{0s}\frac{\Delta n(N_D + \Delta n)}{n_i^2} \tag{3.5}$$

Thus S_{eff} can be calculated with:

$$S_{eff} = \frac{J_{0s}(N_D + \Delta n)}{qn_i^2} \tag{3.6}$$

With the known S_{eff} value, the J_{0s} can then be calculated using equation (3.7):

$$J_{0s} = \frac{S_{eff} qn_i^2}{(N_D + \Delta n)} \tag{3.7}$$

In Figure 3-2, the example of the measured lifetime curve over a broad injection level is shown.

3.1.3 Determination of J_{0s} at high injection

Surface saturation current density can be also determined under high injection, i.e. at excess carrier densities higher than around ten times the dopant density [81]. Under high injection, where $\Delta n >> N_D$, the recombination of the diffused surfaces together with Auger recombination in the bulk, described by the Auger lifetime τ_A, limits the effective lifetime. One can analyze the inverse effective lifetime corrected for the Auger recombination limit under high injection with the so called *'slope method'* proposed by Kane and Swanson [85]. The slope of the inverse lifetime is then proportional to $2\times J_{0s}$ according to the equation:

$$\frac{1}{\tau_{eff}} - \frac{1}{\tau_A} = \frac{1}{\tau_{SRH}} + \frac{2J_{0s}}{qn_i^2 W}\Delta n \tag{3.8}$$

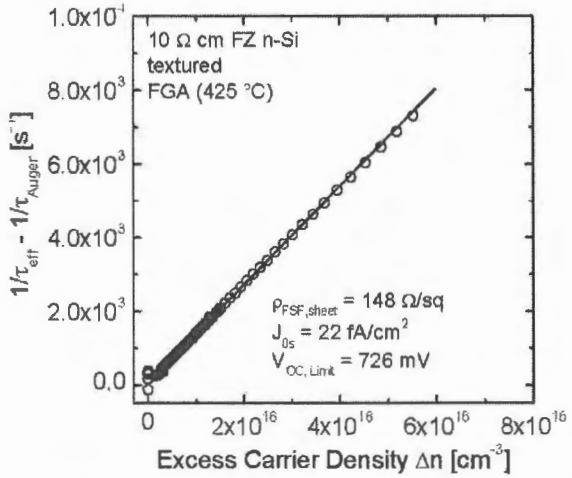


Figure 3-3 Determination of J_{0s} at high injection using the 'slope method'. Example of the determined J_{0s} and $V_{OC,\,Limit}$ for the textured samples with the resistivity of 10 Ω cm and front surface field diffusion of 148 Ω/sq is shown.

The lowly doped, 10 Ω cm samples ($N_D = 4.5\times10^{14}$ cm^{-3}) can be easily measured in high injection using QSSPC equipment. The slope of the inverse lifetime curve at $\Delta n_{hli} = 10\times N_D$ can then be calculated.

An ambipolar Auger coefficient of $C_A = 1.66\times10^{-30}$ cm^{-3}s^{-1} [17] was used for the calculation of the Auger lifetime term ($\tau_A^{-1} = C_A\Delta n^2$). For the determination of the slope of the inverse lifetime curve, a linear fit with measured data points from the range of $\Delta n_{hli} \pm 0.8\times\Delta n_{hli}$ was performed. An example of the determination of J_{0s} for the textured 10 Ω cm test sample under high injection is shown in Figure 3-3.

3.2 Device simulation

3.2.1 Two-dimensional numerical simulation

As shown in Figure 3-4, the structure of the analyzed solar cells is strongly two-dimensional due to the presence of the interdigitated grid of the p- and n-diffusions on the rear cell side. Therefore, for the correct description of the back-contact back-junction solar cell, a two-dimensional modeling and simulations of the device are required.

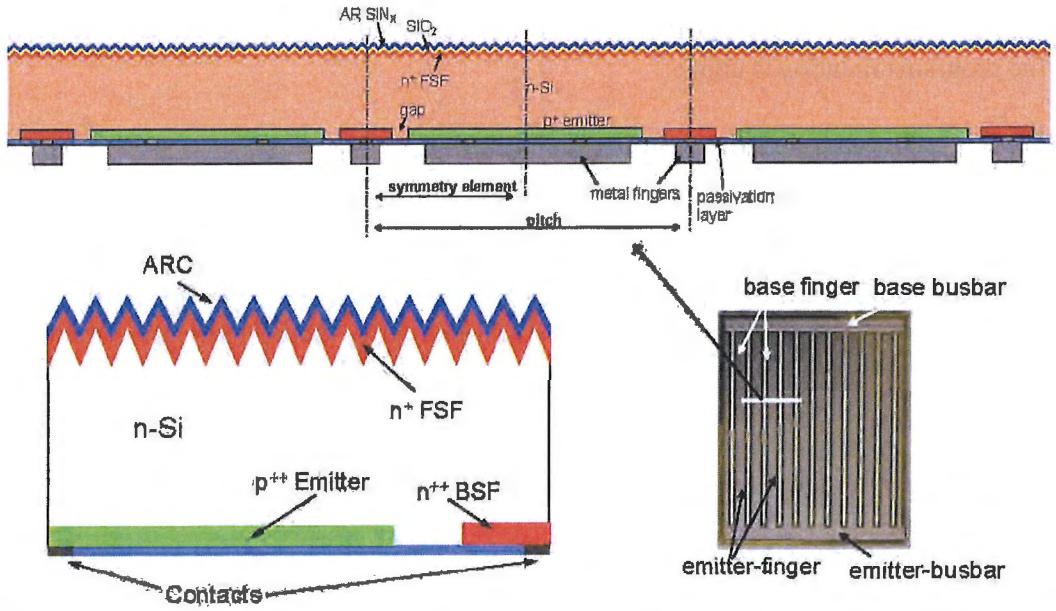


Figure 3-4 Cross-section of the back-contact back-junction silicon solar cell (top). The symmetry element used in two-dimensional simulations (left) as well as a photograph of the rear cell side (right) are shown. The white line in the photograph of the solar cell represents the direction in which the cross-section in the top picture was taken.

The two-dimensional model of the BC-BJ solar cells was developed by Martin Hermle at the Fraunhofer ISE in Freiburg [86]. The simulations of the back-contact back-junction solar cell structure were done by M. Hermle in cooperation with the author of the present thesis.

In two-dimensional simulations, the symmetry element (see Figure 3-4 left) of the solar cell is considered. Different geometry and electrical parameters of the symmetry element are also shown in the diagram. In the simulations, only the active solar cell areas were simulated. The busbar and the edge areas were not taken into account in the simulations presented in this thesis. For the simulation analysis of the influence of the busbars, see the work of M. Hermle [87], [86].

The simulation process starts with the calculation of the generation profile and the optical performance calculations. The simulations of the optical properties of the solar cell are done with the raytracing program *Rayn* [88]. Next, using the program *Mesh* [89], a discretization grid of the symmetry element is created. The semiconductor equations are solved at the nodes of the discretization grid using the *Sentaurus Device* (*SDevice*) [90] program. The whole simulation process is simplified

by the use of the *PVObjects* [91] script in Mathematica, which enables the auditing of the programs mentioned above.

3.2.2 One-dimensional numerical simulation

As previously mentioned, the BC-BJ solar cell has a strongly two-dimensional structure. In many cases, however, simulations using a simplified one-dimensional back-junction solar cell structure (see Figure 3-5) can also describe the effects which occur in the BC-BJ solar cell. The effects which occur in the BC-BJ solar cell and can be well described by the one-dimensional simulation of the back-junction solar cell include:

- Influence of the carrier lifetime on the carrier collection efficiency at the rear junction,
- Influence of the surface concentration and depth of the phosphorus doping profile on the front side (FSF) on the front surface passivation quality.

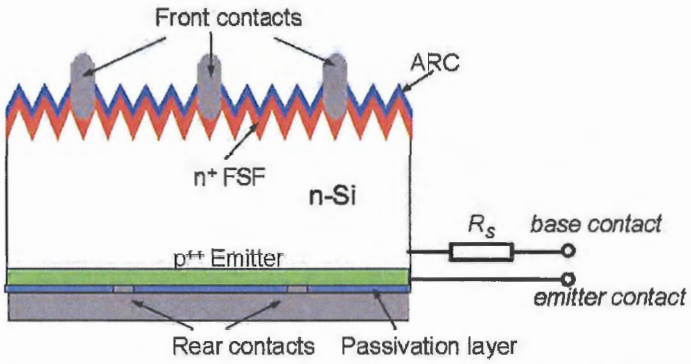


Figure 3-5 Structure of the back-junction cell used in the one-dimensional simulations using device simulation program PC1D [63], [92].

Therefore, the one-dimensional simulations were often applied throughout this thesis. The one-dimensional device simulations were done with the program *PC1D* by Basore and Clugston [63], [92]. The simulations of the optical properties, such as generation profile, reflection, and transmission spectra of the analyzed device were performed using the program *Sunrays* [93]. *Sunrays* is a raytracing program which calculates the generation in the analyzed optical device numerically using the Monte Carlo method.

3.2.3 Simulation parameters

The proper choice of the simulation parameters is essential for a correct simulation. The geometrical parameters as for example thickness and pitch are predefined and thus

easy to access. Most of the electrical parameters as for example doping profiles, bulk lifetime and resistivity have been measured and used for the simulation in this work. Some parameters such as the surface recombination velocity cannot be directly assessed and must be described by models.

The surface recombination velocity S at the doped silicon surfaces depends on the doping profile and the surface dopant concentration. In the one- and two-dimensional device simulations, the highly and lowly doped phosphorus and boron layers with a Gaussian distribution of the impurity concentrations were assumed. For these diffusion profiles with surfaces passivated with thermally grown silicon oxide, the parameterization of Cuevas et al. was taken.

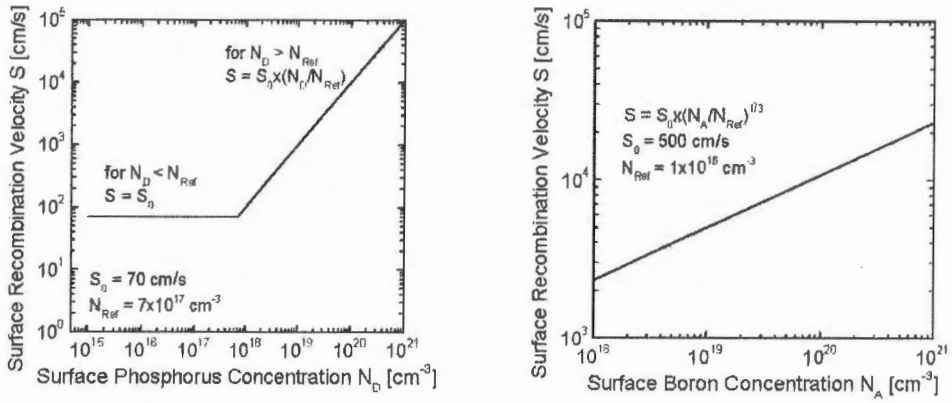


Figure 3-6 Surface recombination velocity as a function of the surface phosphorus (left) and boron (right) concentrations according to parameterization of Cuevas et al. [94], [95].

S for the phosphorus doping according to Ref. [94]:

$$\begin{aligned} S &= S_0 && \text{for } N_D < N_{ref}, \\ S &= S_0(N_D/N_{ref}) && \text{for } N_D \geq N_{ref} \end{aligned} \qquad (3.9)$$

where $S_0 = 70$ cm/s and $N_{ref} = 7 \times 10^{17}$ cm^{-3}

S for the boron doping according to Ref. [95]:

$$S = S_0(N_A/N_{ref})^{1/3} \qquad (3.10)$$

where $S_0 = 500$ cm/s and $N_{ref} = 1 \times 10^{16}$ cm^{-3}

In the left side of Figure 3-6, the surface recombination velocity of the phosphorus doped silicon surfaces and its parameterization according to [94] is shown. The surface recombination velocity dependence with the boron surface concentration and its parameterization according to [95] is shown in the right side of Figure 3-6.

3.3 Measurement table for laboratory size solar cell

Since both p- and n-electrodes of the analyzed solar cell are placed on the rear cell side, the application of the standard measurement table for the electrical characterization of the back-contact solar cells is not possible. A new measurement setup for the laboratory scale BC-BJ cells with an area of 4 cm^2 was developed by the author in the course of this work.

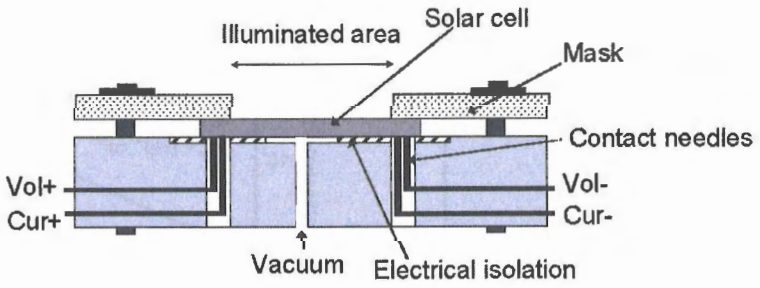


Figure 3-7 Schematic representation of the measurement table for measurement of the back-contact back-junction silicon solar cells.

A schematic drawing of the measurement table developed in this work at Fraunhofer ISE is shown in Figure 3-7. A solar cell is placed on an electrically insulating layer, in order to avoid shunting of the p- and n-electrodes. The finished solar cells are larger than the illuminated area, making it therefore possible to mechanically fix the position of the measured cell with a mask with an illumination area opening of 2×2 cm^2. The contact needles for separate measurement of the current and voltage are placed on the cell busbars from the rear side, through the holes in the measurement table. A three-dimensional AutoCAD design and a photograph of the measurement table developed in this work at Fraunhofer ISE are shown in Figure 3-8.

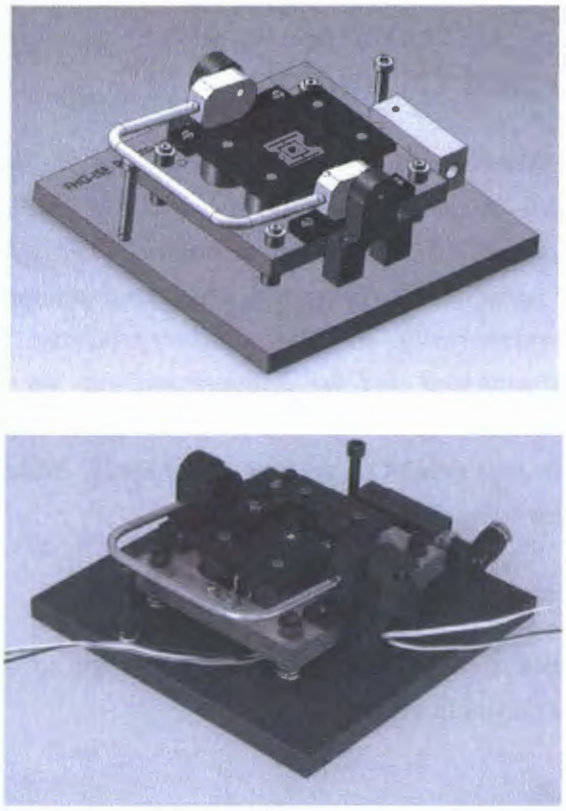


Figure 3-8 Measurement table for measurement of the illuminated and dark current-voltage characteristics of the laboratory size (2×2 cm^2) back-contact back-junction silicon solar cells. AutoCAD design is shown in top graphic and in the bottom graphic a photograph of the finished measurement table is shown.

4 Design and technology

In this chapter the structure and technology of the developed back-contact back-junction silicon solar cell is presented. The minority carrier lifetime of the applied n-type Si material is determined. The solar cell structure was fabricated using newly developed structuring processes, which are using low-cost screen-printing and laser ablation processes. The applied processes are briefly reviewed and the different methods for the formation of the interdigitated grid of the n- and p- metal grids are described in detail. Finally, the best results of the developed small, laboratory size and large, industry size solar cell are presented.

4.1 Device structure

A schematic cross-section of the back-contact back-junction solar cell developed in the frame of this work is shown in Figure 4-1.

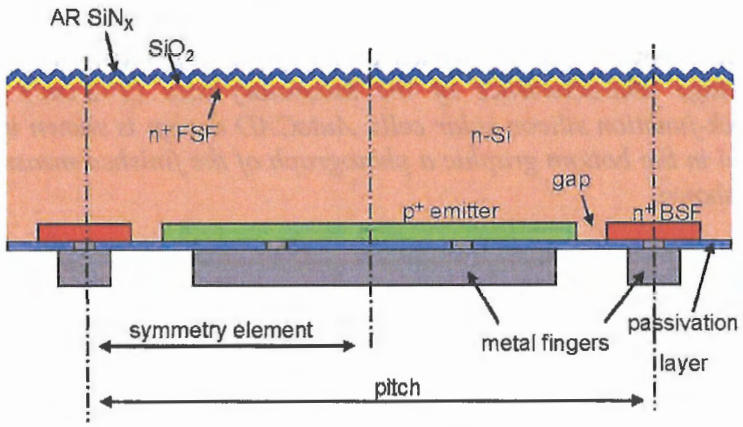


Figure 4-1 Schematic cross-section of the n-type high-efficiency back-contact back-junction silicon solar cell developed in the frame of this thesis (sketch is not to scale). Pitch and symmetry element are shown.

The cells were fabricated from n-type float-zone (FZ) silicon wafers. The thickness of the finished solar cells was about 160 µm. Specific base resistivities of 1 and 8 Ω cm were chosen. The chosen specific base resistance range is believed to be an optimum between two effects: maximization of the carrier lifetime in bulk and reduction of the series resistance losses introduced by the base material. On one hand, the carrier lifetime, which needs to be high in order to enable good collection of the minority

carriers at the rear junction, decreases with increased base doping level and reduced specific base resistance of the base material. On the other hand, the high specific base resistivity results in increased series resistance in the base material, which leads to significant efficiency losses. Details of the silicon material chosen and its characterization are presented in the next section.

The front side is textured with random pyramids and passivated with a lightly doped ($N_{peak} = 5 \times 10^{18}$ cm^{-3}) and deeply diffused (1.4 µm) phosphorus front surface field (FSF). The sheet resistance of the FSF (ρ_{FSF}) equals 148 Ω/sq. The diffusion profile of the FSF was optimized to achieve an optimum front side passivation quality. The presence of the phosphorus doped front surface field (FSF) is one of the key features of the developed device design. Therefore, a comprehensive analysis of the positive effects of the FSF in the BC-BJ solar cells was performed in the frame of this thesis. The presence of the FSF reduces the concentration of the minority carriers at the physical semiconductor surface and thus improves the front surface passivation (chapter 7) and strongly improves the stability of the front surface passivation under UV-light exposure (section 7.5). Furthermore, the FSF enhances the lateral majority carriers current transport and thus reduces the series resistance losses (chapter 8). Finally, the solar cells with the FSF show a linear current response at low-illumination levels, in contrast to cells without the FSF (chapter 9).

The front surface passivation is further improved by a thin thermally grown silicon dioxide layer. Finally a silicon nitride (SiN_x) antireflection (AR) layer is deposited on top of the oxide layer by means of plasma enhanced chemical vapour deposition (PECVD). Passivation properties of the applied front surface field doping profile and the stack system of the SiO_2 and SiN_X layers is investigated in section 7.3

On the cell rear side an interdigitated grid of the p- and n-diffusion areas is formed. Both emitter p^+ and back surface field n^+ diffusions are separated by an undiffused gap. The rear metallization structure also forms an interdigitated grid, as shown in Figure 4-2. The rear cell surface is passivated with silicon oxide. Metal fingers are contacted to the diffused regions via local openings in the passivation layer.

For masking steps on the rear side, such as:

- definition of boron doped emitter area,
- definition of phosphorus doped back-surface-field diffusion area,
- formation of local openings in the dielectric layer for the metal-semiconductor contacts,
- and formation of the interdigitated metal fingers grid,

only industry-relevant screen-printing and laser processes were applied. No photolithography masking steps were introduced to the processing sequence of the investigated cell structure. Due to the fact that more than one masking step was required, and the limited resolution and positioning accuracy of the applied structuring technology, the pitch of the processed cells was chosen to be in the range of 1.3 to 3.5 mm.

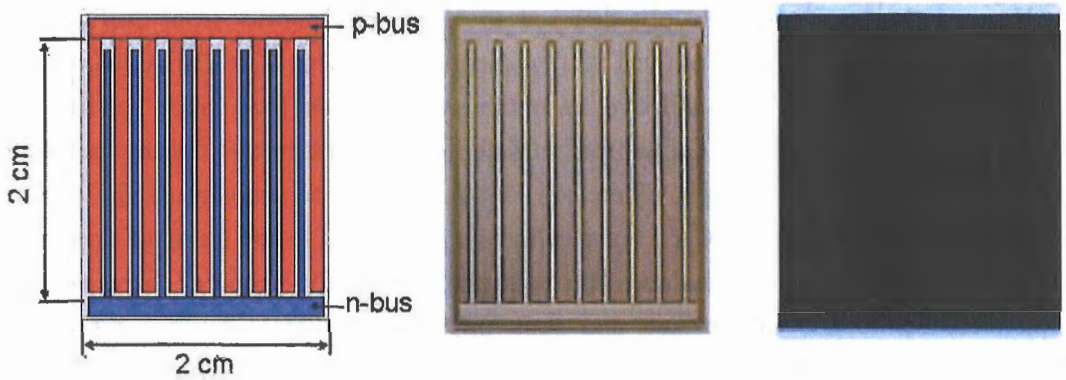


Figure 4-2 Interdigitated grid of the p- and n-metallization fingers of the back-contact back-junction Si solar cell developed in the course of this thesis. The interdigitated grid is schematically shown in the left picture and in the middle the photograph of the rear side of the actual solar cell is shown. In the right a photograph of the cell front side is shown.

Shunting between the tight p- and n-metal finger grids was avoided by a careful design of the metallization process, which is presented in section 4.4.1. The metallization is performed in a two-step process. First, a thin metal layer is deposited and structured to form an interdigitated grid. Secondly, this thin seed metal layer is thickened using an industrially feasible plating process. At the same time the series resistance losses, mainly caused by the lateral carrier transport due to large pitch, could be minimized by application of the high conductivity FSF.

Prior to measurements, the cells were annealed in a forming gas atmosphere and removed from the host wafer by the means of laser cutting. A distance of 500 µm from active cell area was chosen. This distance should allow for strong reduction of the edge recombination losses [96].

4.2 n-type bulk Si material

As previously shown in chapter 2, in order to realize high-efficiency cells using the back- junction cell structure, high minority carrier diffusion lengths are required. The carriers, most of which are generated near the front surface, need to diffuse through the

entire cell thickness in order to be collected by the back-junction. According to the simulations presented in section 2.3, the required diffusion length of the minority carriers should be at least four times larger than the wafer thickness in the back-junction cell type to enable high carrier collection efficiency. Thus, for a solar cell with a thickness of 160 µm, a diffusion length of the minority carriers of at least 640 µm is required.

Phosphorus doped n-type silicon has received increased interest in the PV research community in recent years, due to shortage of the p-type silicon feedstock and due to its high minority carrier lifetime. In many research laboratories front-junction and back-junction silicon solar cells on n-type substrates are being developed.

For example, a front-junction solar cell structure with monocrystalline FZ n-type Si with boron diffused emitter passivated using Al_2O_3 passivation layer developed by Benick et al. achieved an efficiency of 23.2 % [97]. A front-junction cell with oxide passivated boron emitter also developed by Benick et al. achieved an efficiency of 20.4 % [98]. On large area cells of 156×156 mm^2, screen-printed Cz n-type Si, the efficiency of 17.9 % was obtained by Mihailetchi et al. [99]. The application of multicrystalline n-type Si to solar cell processing is also being studied intensivley (see for example the work of Libal et al. [100], Tool et al. [101], and Cuevas et al. [102]). The application of n-type Si to the back-junction cell structure has also been investigated. Zhao et al. demonstrated an efficiency of 22.7 % for FZ n-type Si [103]. Schmiga et al. presented a rear-junction solar with aluminum emitter with an efficiency of 20.1 % [104].

Moreover, in the industry, the highest commercially available solar cells are produced on n-type Si substrates. SunPower Corp. produces back-contact back-junction n-type Si solar cells with efficiencies up to 22.7 % [3]. Sanyo Electric manufactures heterojunction solar cells on n-type c-Si with efficiency of 19.5 % [105].

The advantages of n-type Si when compared to p-type Si are as follows:

- The minority carrier lifetime in p-type boron-doped oxygen-contaminated silicon is strongly reduced under illumination or carrier injection [106], [107], [108]. Due to the lack of boron in n-type Si, no degradation occurs.
- n-type Si has a lower sensitivity to the prominent impurities (e.g. interstitial iron Fe_i,) [109], [110].This is due to strong asymmetry in capture cross section for electron and holes ($\sigma_n >> \sigma_p$).

- For reasons mentioned above, the lifetime of the minority carriers in n-type Si is higher than in the case of p-type Si. For example, extremely high minority carrier lifetime in the range of milliseconds was already reported for n-type multicrystalline silicon by Cuevas et al. [111].

4.2.1 Minority carrier diffusion length

For the determination of the minority carrier lifetime and diffusion length of the n-type FZ Si chosen for processing of the BC-BJ solar cells, lifetime samples were prepared and measured. Planar symmetrical n^+nn^+ test structures are shown in Figure 4-3. Both sides of these samples exhibit a full area shallow n^+ diffusion (ρ_{sheet} = 148 Ω/sq., N_{peak}=5×10^{18} cm^{-3}, depth 1.4 µm) and a full area thermal oxide with thickness of 105 nm. Before the measurements all samples were annealed at forming gas atmosphere (FGA) at the temperature of 425°C (15 min.).

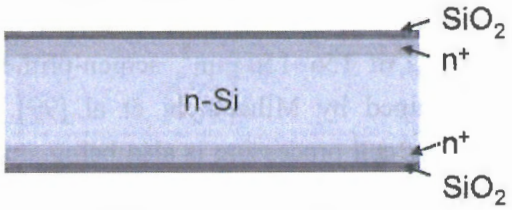


Figure 4-3 n^+nn^+ symmetrical test structures for the measurements of the minority carrier lifetime and diffusion length.

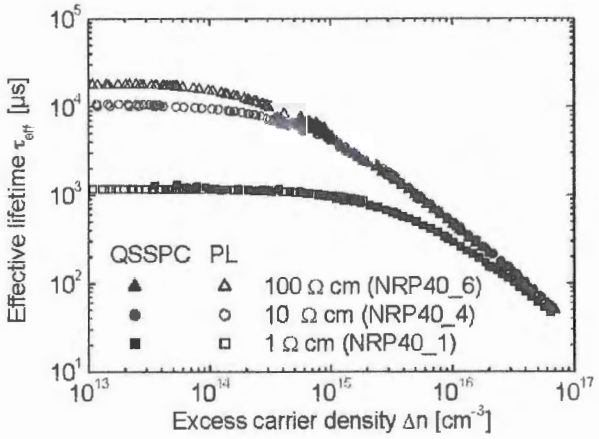


Figure 4-4 Injection-dependent minority carrier lifetime of the planar n^+nn^+ symmetrical samples on FZ n-type Si wafers with different resistivity. The effective carrier lifetime was measured in a wide excess carrier density range using quasi-steady-state photo-conductance (closed symbols) and photoluminescence (open symbols) methods.

The lifetime of all samples was measured in a wide injection density range using two measurement methods. With the quasi-steady–state photo-conductance (QSSPC) method [75], the lifetime was measured in the middle to high injection using the WTC-120 lifetime tester from Sinton Consulting [73]. In the low injection range, the lifetime was measured with the photoluminescence (PL) method [112]. The lifetime results are shown in the Figure 4-4. A good agreement between both measurement methods can be observed.

Table 4-1 *Effective minority carriers lifetime and diffusion length for n-type FZ Si with the specified base resistivity of 1, 10 and 100 Ω cm. Lifetime was measured at injection level of $\Delta n=1\times10^{14}$ cm^{-3}.*

Cell no.	ρ_{base} [Ω cm]	τ_{eff} [ms]	L_{eff} [µm]
NRP40_6	100	18.3	4710
NRP40_4	10	10.1	3492
NRP40_1	1	1.2	1175

Extremely high effective lifetime values of up to 18 ms have been measured for the 100 Ω cm n-type FZ Si at an injection level of $\Delta n=1\cdot10^{14}$ cm^{-3}. As shown in Table 4-1, the lifetime is high enough to realize perfect carrier collection by the back junction for all three investigated resistivities of 1, 10 and 100 Ω cm. Note that actual base resistivities may vary in the range of ± 20 % from the specified resistivity. Even the 1 Ω cm material exhibits lifetime values above 1 ms, resulting in an effective diffusion length (L_{eff}) of about 1200 µm, which is more than 4 times the cell thickness.

4.2.2 Influence of the surface potential on the minority carrier lifetime

In the previous section the analysis of the lifetime samples with diffused FSF and SiO_2 passivation layer was presented. However, as explained in section 3.1, the measured effective lifetime of the minority carriers is not only influenced by the bulk lifetime, but also by the quality of the surface passivation. Therefore, in order to determine the real minority carrier lifetime in the bulk of investigated n-type FZ Si, the effects of the surface recombination should not be taken into account. A significant reduction of the surface recombination can be obtained through application of the field-effect passivation using corona charging [113]. This approach is presented in the following.

Symmetrical n-type lifetime samples with resistivities of 1, 3.5 and 10 Ω cm with both surfaces passivated by a 105 nm thick thermal SiO_2 (shown in Figure 4-5) were processed and annealed at forming gas atmosphere (FGA) at the temperature fo 425°C (15 min.). The effective lifetime of the minorrity carriers was measured using quasi-steady–state photo-conductance (QSSPC) and the results are shown in Figure 4-6. In this measurement no additional corona charging was applied.

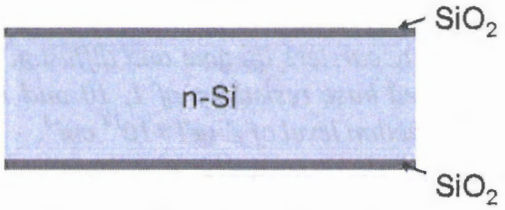


Figure 4-5 FZ n-type symmetrical test structures with thermally grown silicon dioxide passivation layer for the measurements of the minority carrier lifetime.

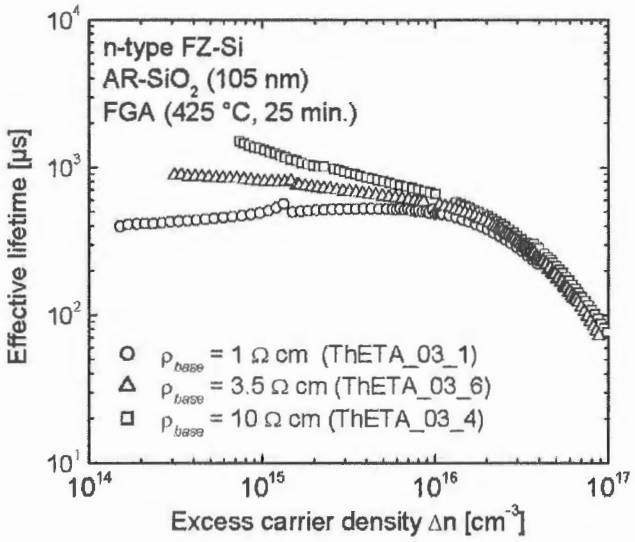


Figure 4-6 Injection-dependent minority carrier lifetime of the planar symmetrical samples on FZ n-type Si wafers with different resistivity. In this measurement no corona charging was applied.

The application of the fixed charges on top of the passivation layer strongly influences lifetime. A charge density in the range between $-3\times10^{12}\,cm^{-2}$ and $3\times10^{12}\,cm^{-2}$ was applied on both sides of the tested samples using a corona charger. The applied charge density corresponds to a surface potential in the range of -15 V to 15 V. The resulting

voltage was measured using the Kelvin Probe technique. The results of the effective lifetime and the surface saturation current density of the tested samples in the wide range of applied charge density are shown in Figure 4-7. The surface saturation current density was determined under low injection using the method presented in section 3.1.2.

The application of the high positive surface potential of 15 V results in the highest τ_{eff} for all three samples analyzed. At the same time, the surface saturation current density is minimal for this surface potential. This is caused by the field-effect passivation of the applied surface potential. The positive charges which are present at the surface repel the positive charge carriers from the surface of the samples. Due to the depletion of the minority carrier concentration at the physical surface, the surface recombination is decreased and does not limit the effective lifetime. Therefore, the measured effective lifetime of the minority carriers is very close to the bulk lifetime.

On the other hand, the application of the negative charges on the surface of the tested samples also leads to an increase of the effective lifetime. However, the maximum lifetime when negative charges are applied is lower than in the case of the positive charges. A strong negative charge induces an accumulation of holes under the surface. Since the capture cross section of holes σ_p of the surface recombination is much smaller than the capture cross section for electrons σ_n, an accumulation of holes is not as effective as accumulation electrons to suppress surface recombination. The lifetime of the tested samples is summarized in Table 4-2.

Table 4-2 Effective minority carriers lifetime and diffusion length for n-type FZ Si with base resistivity of 1, 3.5 and 10 Ω cm for different surface charge density. Lifetime was measured under low injection at $\Delta n = 5\times10^{14}$ cm^{-3}.

		Surface charge density [cm^{-2}]					
		0		3×10^{12}		-3×10^{12}	
Cell name	ρ_{base} [Ω cm]	τ_{eff} [ms]	L_{eff} [μm]	τ_{eff} [ms]	L_{eff} [μm]	τ_{eff} [ms]	L_{eff} [μm]
ThETA03_1	1	0.4	682	5.1	2440	0.9	1020
ThETA03_5	3.5	0.8	980	8.3	3150	2.3	1660
ThETA03_3	10	1.7	1430	10.0	3470	3.1	1940

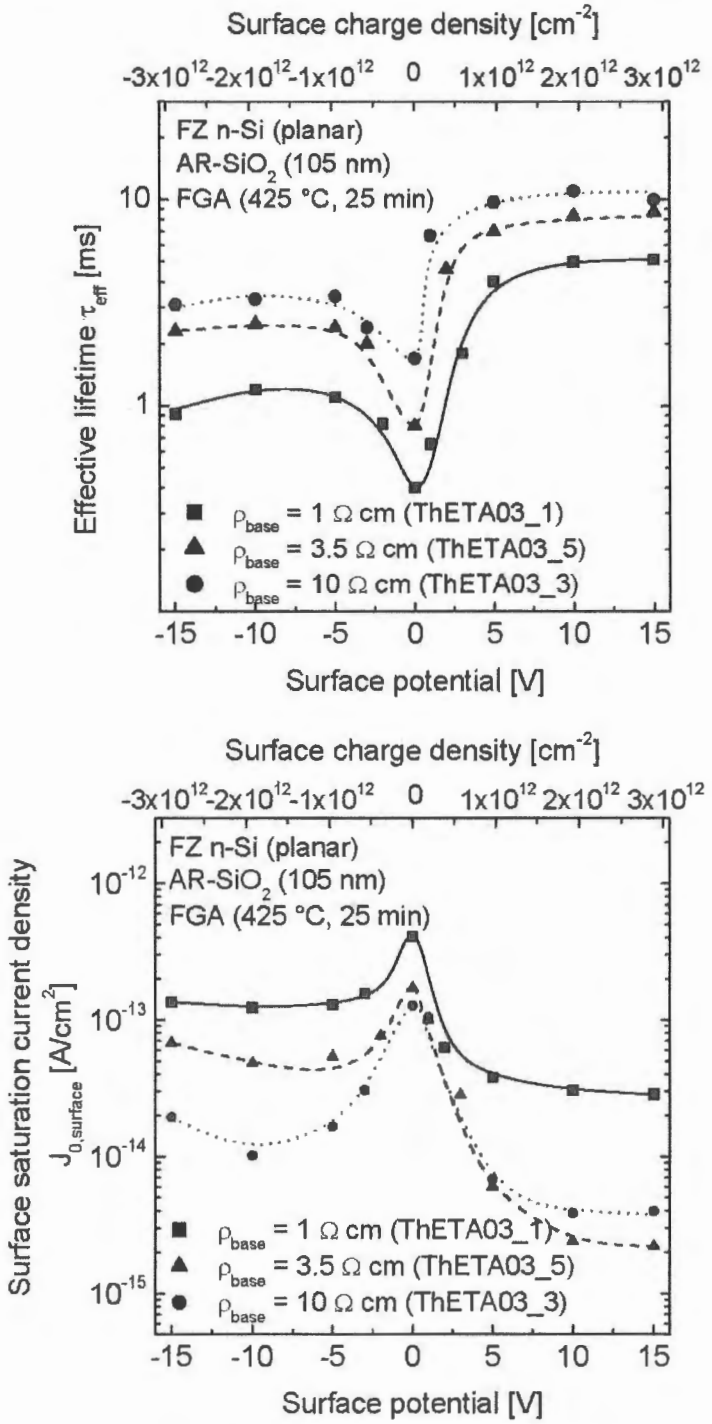


Figure 4-7 Effective lifetime of the minority carriers (top) and the surface saturation current density (bottom) of n-type FZ Si lifetime samples measured in a wide range of surface potential and surface charge density at the outer oxide surface for base resistivity of 1, 3.5 and 100 Ω cm. Lifetime was measured under low injection at $\Delta n = 5 \times 10^{14}$ cm^{-3}. Lines are guides-to-the-eye.

For the lowest surface recombination current density at the surface charge density of 3×10^{12} cm^{-2}, the effective diffusion length of the minority carriers is in the range of 2.4 to 3.5 mm for the tested n-type FZ Si. Thus, the selected Si material is of very high quality and perfectly suited for processing of high-efficiency back-junction solar cells.

4.3 Processing technology

After the selection of the silicon material, next the processing technology to form the solar cell structure, as shown in Figure 4-1 and Figure 4-2, can be to be optimized. The work of the author in the field of development of the processing technology and the sequence of the processing steps was performed in the framework of the research project *Quebec* [41] with the solar cell manufacturing company Q-Cells AG and the Institut für Solarenergieforschung Hameln (ISFH). In the present section the family of processes applied in the processing sequence of the developed back-contact back-junction solar cell is presented. The technology critical to the interdigitated solar cell structure, namely the metallization technology, is presented in more detail in the following section.

Cleaning

In the processing of the high-efficiency solar cells, much attention needs to be given to the cleaning of the processed samples. The introduction of contaminated samples into the high temperature diffusion or oxidation process would be fatal to the sample lifetime. Therefore, the so-called RCA Cleaning [114] procedure was applied. In the first step, the organic impurities and the metals are removed from the silicon surface by wet chemical oxidation in a solution of ammonium hydroxide (NH_4OH) and hydrogen peroxide (H_2O_2). Next, the formed oxide is removed in a diluted hydrofluoric acid (HF) in the so-called HF-Dip. In the second wet oxidation step, in the hydrochloric acid (HCl) and hydrogen peroxide solution, the alkali ions are removed. Again, the formed oxide is removed in a diluted hydrofluoric acid. The samples are rinsed with de-ionized (Di) water after each cleaning step.

Thermal oxidation

The role of the thermal silicon dioxide (SiO_2) layer is to:

a) reduce the surface recombination by passivation of the silicon surface, and

b) form a masking layer for the subsequent local diffusion or contact opening steps.

The typical applied oxidation temperature is 1050°C and the thickness of the applied oxide was around 200 nm for the masking oxide. In the case of the passivation oxide on the front cell side, the thickness was 10 nm and the oxidation temperature was only 850°C.

Phosphorus and boron diffusion

In the processing sequence of the analyzed high-efficiency BC-BJ solar cells, three diffusions in a quartz tube furnace are applied:

a) Formation of the boron emitter from the liquid BBr_3

b) Formation of the phosphorus back-surface field (BSF) from the gaseous $POCl_3$. From the $POCl_3$ in the atmosphere of oxygen O_2 and nitrogen N_2, a phosphorus silicate glass (PSG) is formed on the wafer surface. The phosphorus silicate glass functions as a source of phosphorus during the high temperature diffusion.

c) Formation of the low phosphorus doped front-surface field (FSF) from the gaseous $POCl_3$. A detailed analysis of the applied FSF diffusion profiles is presented in chapter 7.

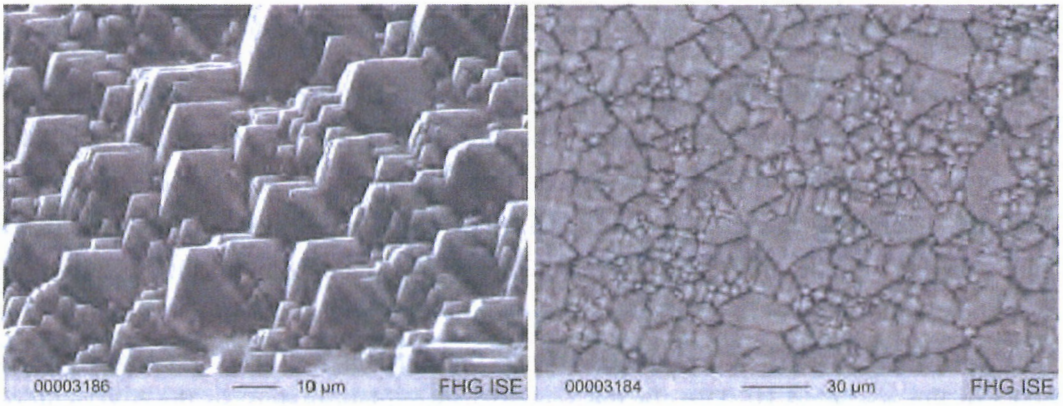


Figure 4-8 Scanning electron microscope (SEM) micrographs of the silicon surface with random pyramids texture with (111)-crystal planes. Side view (left) and top view (right) are shown.

Texture

In order to reduce the optical reflection losses of the solar cells, the front surface is textured. Due to the textured surface, the incident light that is reflected from the wafer surface has an increased chance to be absorbed by hitting the wafer surface again. To form the texture in the case of the monocrystalline silicon, the so called random pyramid texture was applied. In a low concentrated KOH solution, different crystal

planes in silicon are etched at different rates [115]. This way, the structure of the randomly distributed pyramids with different sizes is formed as shown in Figure 4-8.

Deposition of silicon nitride

An antireflection silicon nitride (SiN_X) layer with a thickness of 70 nm is deposited on the front cell side in order to further decrease the reflection losses and increase the front surface passivation quality [116], [117]. The nitride layer is deposited by means of a plasma enhanced chemical vapor deposition (PECVD) process at the temperatures around 400°C [118].

Formation of the interdigitated grid of the emitter and BSF diffusions

As already shown in Figure 4-1 and Figure 4-2, the emitter and BSF diffusions on the rear cell side form an interdigitated grid. In the solar cells, the local diffusions were performed through a masking oxide layer. For the structuring of the masking oxide only industry-relevant technology, such as screen-printing and laser ablation, were applied.

In Figure 4-9 an example of the processing sequence to create local emitter/BSF diffusion by means of laser ablation is shown. First, the whole rear surface is oxidized. Local openings in the oxide layer are then formed by local laser ablation of oxide and a thin silicon layer. Subsequently, the damage induced by the laser into the silicon crystal lattice is etched back in the KOH solution. Finally the emitter/BSF diffusion is performed. The oxide layer acts as a diffusion barrier.

In Figure 4-10 an example of the processing sequence to create local emitter/BSF diffusion by means of screen printing of the etch barrier (etch resist) is shown. First the whole rear surface is oxidized (1). Then the etch resist layer is screen-printed on the wafer surface (2). The openings in etch resist layer correspond to the places where the emitter/BSF diffusion should take place. In the next step (3), the oxide surface which was not covered with etch resist is etched in a diluted HF solution. Next (4), the etch resist layer is removed wet-chemically. Finally (5) the emitter/BSF diffusion is performed. In the developed process first the boron emitter diffusion in performed locally. Next the local phosphorus BSF diffusion is performed.

Due to the limited positioning accuracy and resolution of the applied structuring technology, the pitch of the finished solar cells was in the range of 1.3 to 3.5 mm. The pitch of concentrator solar cells processed with the use of photolithography can be as low as 50 µm [119]. Thus, the application of the low cost structuring technology

results in an increase in pitch by a factor of around 40. The impact of the pitch on solar cell performance is studied in chapters 6 and 8.

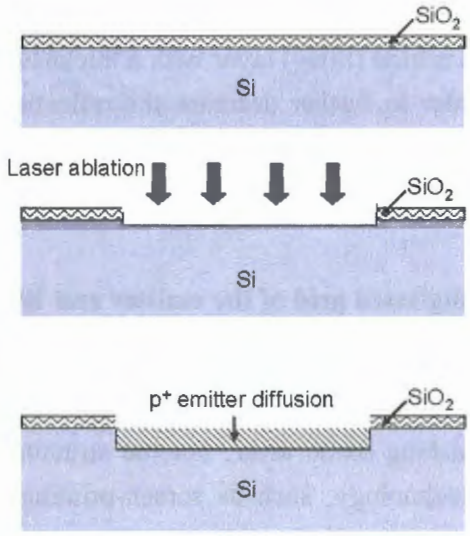


Figure 4-9 Processing sequence for the creation of the local emitter or BSF diffusions using the laser ablation of the silicon oxide layer. In the figure, the rear side of the cell is on top. The front side structure is not shown for simplification. The pictures are not to scale.

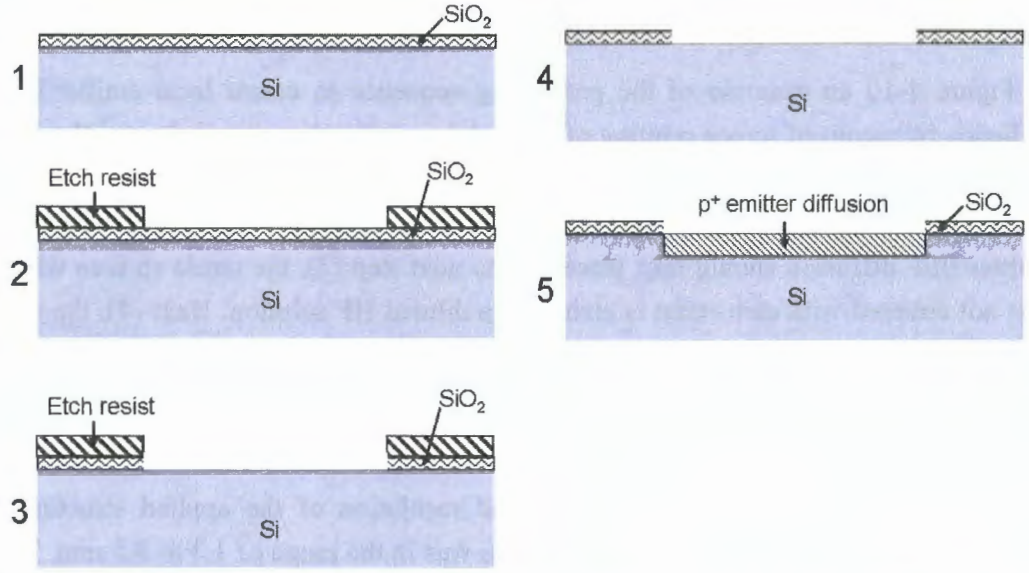


Figure 4-10 Processing sequence for the creation of the local emitter or BSF diffusions using the screen-printing of the masking layers. In the figure, the rear side of the cell is on top. The front side structure is not shown for simplification. The pictures are not to scale.

Formation of the contact openings

The surface recombination velocity of the metal contact to the intrinsic silicon is extremely high in the range of 10^6 cm/s [120] to 10^7 cm/s [121]. However, the surface recombination velocity at the metal contacts can be effectively reduced by the application of highly doped n^{++} or p^{++} silicon regions in the areas of the metal-semiconductor contacts [85]. The size and pitch of the local openings in the dielectric layer on the rear cell side through which the metal-semiconductor contacts are formed, and the diffusion profiles of the emitter and BSF diffusions, need to be carefully optimized [122], [123] in order to minimize the contact-semiconductor recombination losses and the contact resistance losses [124].

The openings of the metal-semiconductor contacts are formed in the same way as already shown in Figure 4-9 and Figure 4-10. Both screen-printing of the etch resist layer and a direct ablation of the dielectric layers were developed and applied in the processing sequence of the solar cells analyzed. The laser ablation of the dielectric layers was intensively investigated by Grohe [125]. Photographs of the rear side cell structure after emitter and BSF diffusions and after the formation of the contact openings in the rear side dielectric layer are shown in Figure 4-11.

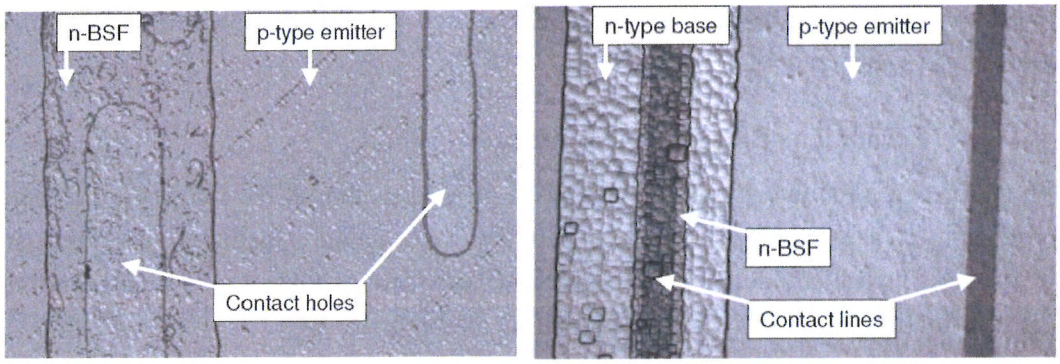


Figure 4-11 Photographs showing details of the rear side pattern prior to solar cell metallization. The emitter and BSF diffusions, as well as the contact openings are marked. The patterns were defined by (left) screen printing and (right) laser processing. For both images the same scaling is used.

4.4 Metallization

In this section the process to form an interdigitated grid of p and n metal electrodes is presented. A two-step metallization scheme was developed and successfully applied to the processing of the BC-BJ solar cells structure. In the first step a thin seed metal

layer is deposited and structured to form an interdigitated grid. In the second step the thin seed metal layer is thickened using an industrially feasible plating process.

The seed metal layer is deposited on the full rear side by the means of a vacuum evaporation process. The seed metal layer consists of a stack of aluminum and silver layers with a total thickness of less than 500 nm. The aluminum layer, which is in direct contact with the silicon wafer, enables formation of good ohmic contact to both the highly doped p-emitter and highly doped n-BSF at the same time [124], [126]. Moreover, the aluminum layer, together with the rear side passivation dielectric layer forms a very effective rear side reflector, enhancing the internal light trapping. The second layer, which is evaporated on top of the Al layer during one evaporation process, is the thin silver layer. Silver acts as a seed layer for the following silver plating process, in which the line resistance will be reduced. Moreover silver enables direct soldering on the finished cell during the solar module assembly.

After deposition of the seed metal layers on the entire rear cell surface, the interdigitated grid of non-shunted p and n-metal grids needs to be formed. Different techniques for the formation of the interdigitated metal gird are presented in section 4.4.1. Next, the thin seed metal layer needs to be thickened, in order to increase the conductivity of the metal fingers. This is accomplished by means of the plating process. The analysis of the required thickness of the finished metallization grid is presented in section 4.4.2.

4.4.1 Formation of the interdigitated metal grid

In the present section different techniques for the formation of the interdigitated metal grid, which are based on the two-step approach called 'seed and growth', are presented. Two methods were developed in the course of this work and successfully applied to the processing of solar cells. These methods are:

- Local etching of the metal layer defined by screen-printed masks
- Lift-off approach and laser-enhanced lift-off using screen-printed masks

Other interesting techniques, which are based on deposition of the thin seed metal layers and thickening them using a plating process, are presented for reference. In all presented methods both p- and n-diffusions, as well as the local contact openings, are already present on the solar cell. Thus, only the formation of the interdigitated metal grid is presented.

Self-aligned metal grid formation on steps in Si surface

A self-aligned technique to separate p- and n-contact grids after full area metal deposition was introduced by Sinton et al. in 1988 [18]. The method is schematically presented in Figure 4-12. In this method, on the rear side of the solar cell the emitter and base areas are placed on different levels on the Si surface, i.e. there is a wafer thickness difference of 5 to around 20 µm between the emitter and base areas, which was created by the local KOH etching.

After the formation of the contact openings, a full area deposition of the metal layer (e.g. Al) with a thickness of few to several tens of micrometers is performed. Next a thin (e.g. 50 nm) layer of the etch barrier (such as Ti or PECVD SiO_2) is deposited on top of the metal layer. Due to steep slopes between emitter and base regions, the thin etch barrier material is thinner and even discontinuous at the slopes. This feature is used in the following etch step, in which the aluminum layer is etched at the slopes where the etch barrier is discontinuous, e.g. in diluted HCl solution. In this manner, no alignment is required for this method. However, the solar cell structure must feature the above mentioned thickness variation structure. The self-aligned method of slopes in the Si surface was also successfully applied by Engelhart in the processing sequence of the RISE solar cell [40].

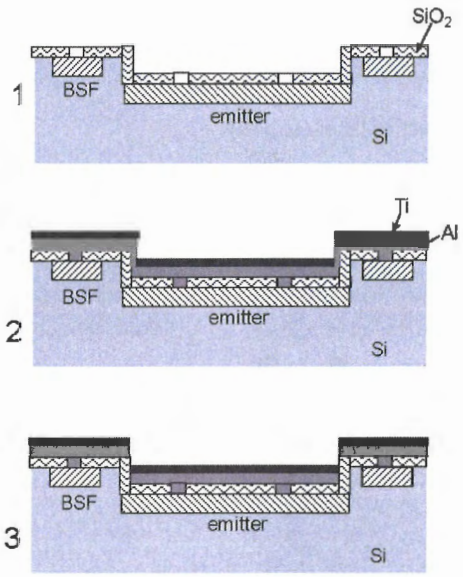


Figure 4-12 Method formation of the interdigitated p-n metal grid using the self aligned process on the high steps in the silicon surface. The method was introduced by Sinton et al. [18]. The front side structure is not shown for simplification. The drawings are not to scale.

Laser ablation of the masking layer and etching of the bulk metal

A contact separation method using a laser ablation of the thin etch barrier was recently introduced by Teppe et al. [127]. This method is schematically shown in Figure 4-13. First a full area metal deposition by means of evaporation or sputtering is applied. Secondly, a thin layer of the etch barrier (here again, a thin PECVD SiO_2 layer can be used for example) is deposited on top of the metal layer. In the next step, the etch barrier and a thin layer of the underlying metal layer is locally removed by means of laser ablation. Finally the metal layer is locally etched back, and the etch barrier is removed.

The advantage of this method is the formation of very thin separation lines between metal fingers, which enables the realization of high metal coverage on the rear cell side, which is needed for good reflection characteristics. Additionally, the application of a thick metal layer below the thin etch barrier removes the risk of introduction of laser damage to the solar cell structure, because all of the laser power will be absorbed in the etch barrier and in the top surface of the metal layer. An example of separation lines created between the metal fingers is shown in Figure 4-14.

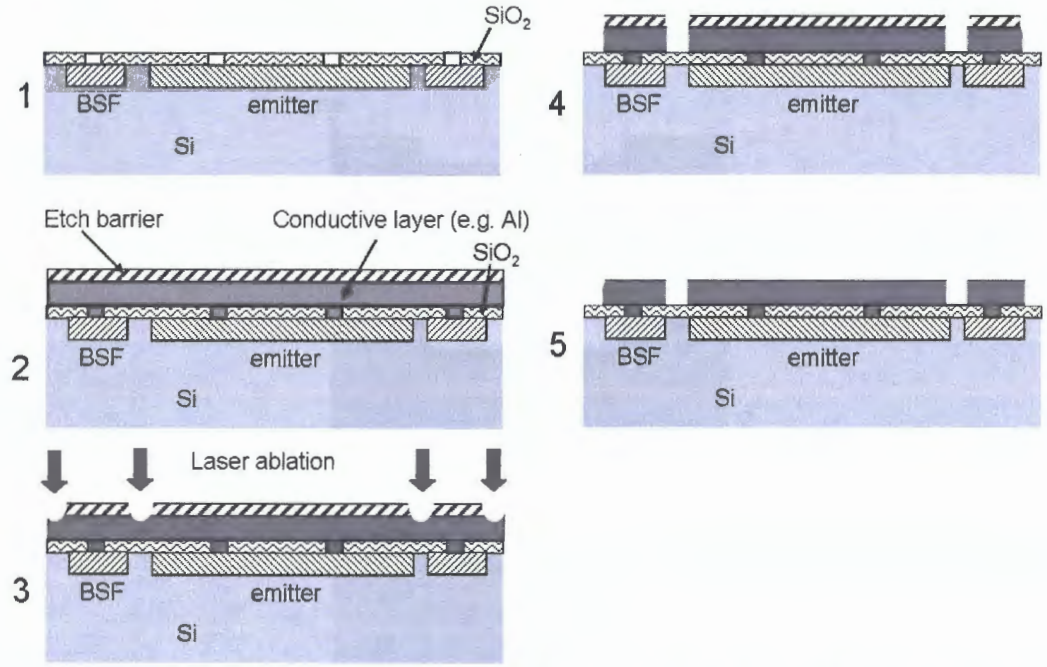
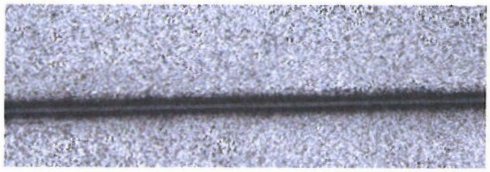


Figure 4-13 Method for contact separation using local laser ablation of an etch barrier and etching of the conductive layer. Method is patented by Teppe et al. [127]. The front side structure is not shown for simplification. The drawings are not to scale.



This method is patented by Mulligan et al. [128] of Sunpower Co. After deposition of a thin seed metal layer, the plating resist is applied on top of the metal layer locally in the locations where the separation between the metal fingers is required. Next, the rear side metal layer is thickened in the electroplating process using Ag or Cu plating baths. The locations covered with the plating resist remain thin after the electroplating process. Next, the plating resist layer is stripped. Now, using the wet chemical etching, the thin metal layer between the thick plated metal fingers can be etched away. Since the seed metal layer is typically thinner than 1 μm, only a very small percentage of the plated metal will be etched away.

The advantage of this process is the elimination of the shunting risk through the formation of metal bridges between p- and n-electrodes during the plating process. On the other hand, if more than one metal is applied in the seed layer, as can be the case in copper plating, then multiple selective etching steps are required, which may increase the complexity of the process.

Local etching of the metal layer through the screen-printed masks (this work)

Another method which uses the screen-printed or inkjet masking layers is presented in Figure 4-16. This method, using screen-printing of the etch barriers, was developed and successfully applied during solar cell processing in the course of this thesis. After the deposition of the thin (less than 1 μm) seed metal layer (Al and Ag), the etch barrier is screen-printed locally on top of the metal layer in the locations where the metal fingers are needed. Next, the local wet chemical etching of the Ag layer is done in diluted HNO_3. In the following step the Al layer is etched back in diluted HCl (see Table 4-3). After etching the metal layer, the etch barrier is stripped and the thin metal fingers are thickened to the required thickness using the Ag plating process.

Table 4-3 Process parameters for the selective etching of the aluminum (thickness of 300 nm) and silver (thickness of 100 nm) seed metal layers, used in the formation of the interdigitated p- and n-metal grids.

Etched metal	Etching Solution	Ratio	Temperature	Time
silver	HNO_3 (69 %) : H_20	1 : 1	room T	30 sec
aluminum	HCl (32 %) : H_20	1.4 : 1	room T	2 to 10 min.

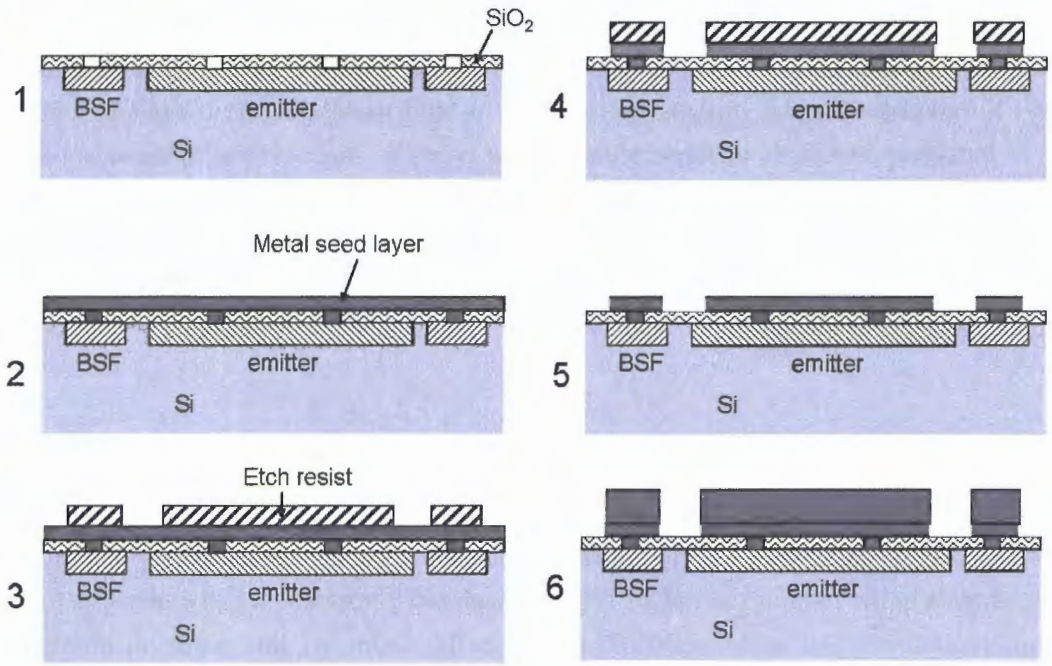


Figure 4-16 Method for contact separation using application of the screen-printed or inkjet etching masks. This method was developed in and successfully applied into the solar cells processing in the course of this thesis. The front side structure is not shown for simplification. The drawings are not to scale.

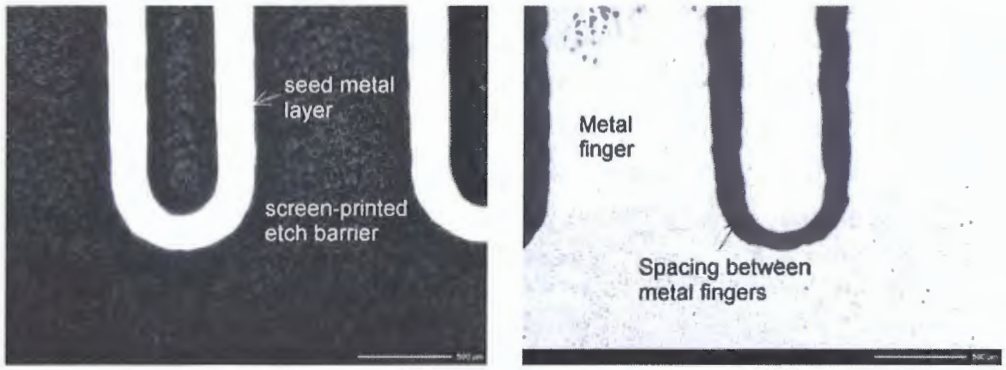


Figure 4-17 Example of the contact separation using the screen-printed etch barrier layers (left). After the local etching of the metal seed layer and etch barrier removal, the contact separation between the metal fingers is created (right). Photographs taken with optical microscope.

An example of the application of the screen-printed etch barrier and the resulting metal finger structure is shown in the Figure 4-17. The presented method has two major risks. These are:

- strong under-etching of the metal fingers underneath the etch barrier if the etching time and uniformity over the whole wafer area are not optimized carefully, and
- formation of metal bridges between the p- and n-metal grids if openings and/or local imperfections in the screen-printing process, such as locally closed opening lines, are formed.

Additionally as in the previous method, if more than one metal is applied in the seed layer, then multiple selective etching steps are required. This would increase the complexity of the process.

Lift-off approach and laser enhanced lift-off (this work)

In microelectronics and in the processing of high-efficiency solar cells, the lift-off method is widely used [129]. However, the use of photolithography to form the structures in the photoresist makes this approach too complicated and expensive for the mass production of solar cells. Therefore in the frame of this work an alternative approach, in which the photolithography was replaced with the low-cost screen-printing process, was developed. In Figure 4-18 the lift-off method is schematically presented.

The screen-printed lift-off resist is locally deposited on the rear cell surface. Next, a thin seed metal layer is deposited. If the slopes of the resist are steep enough, only a very thin layer of the metal is deposited on the slopes. In the next step, the resist is stripped in a liquid solvent. The solvent can penetrate the resist layer through the very thin and non-continuous metal layer at the slopes of the resist. After dissolution of the resist, the metal layer lying on top of the resist is removed and the contact separation is complete. In the final step, the thin seed metal layer is thickened in the plating process.

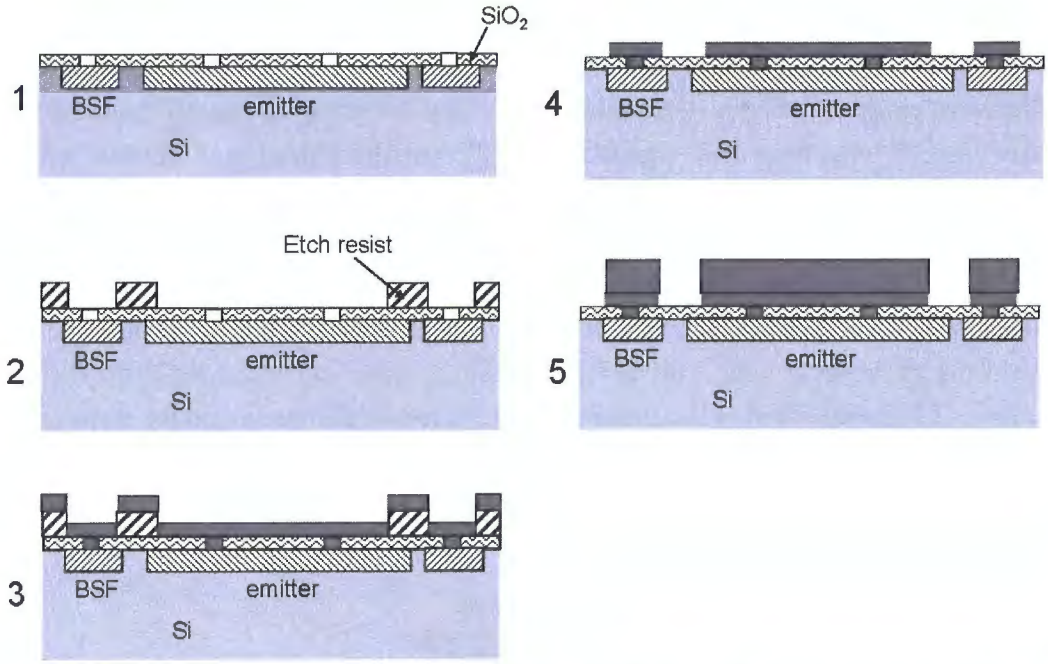


Figure 4-18 Method for contact separation using the lift-off approach with the application of the screen-printed or ink-jetted resist layer. This method was developed in and successfully applied into the solar cells processing in the frame of this thesis. The front side structure is not shown for simplification. The drawings are not to scale.

An example of the contact separation using the lift-off technique with screen-printed resist layer is shown in Figure 4-19. The same screen-printing mask was used here as in the case of Figure 4-17, which resulted in a negative structure of the metal fingers after the lift-off process.

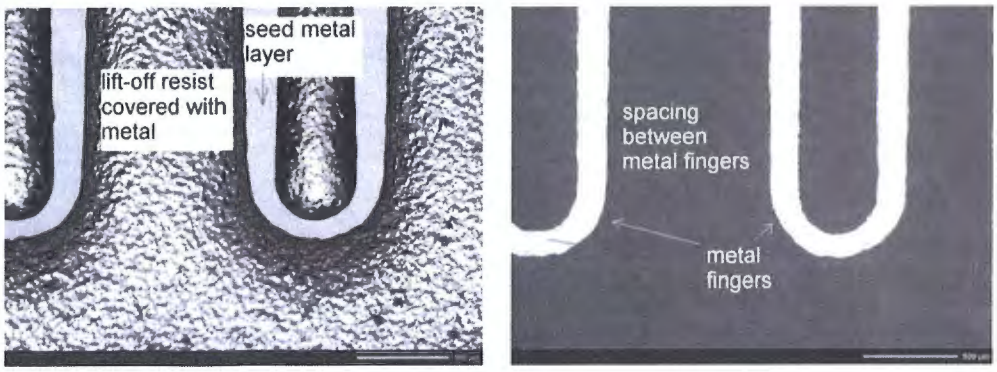


Figure 4-19 Example of the contact separation using the lift-off process with the screen-printed resist layer before (left) and after (right) the lift-off process. Photographs taken with optical microscope.

Unfortunately, due to the fact that the slopes of the screen-printed resist are not steep enough, the metal layer at these slopes is usually dense, and the solvent cannot reach the resist easily (see Figure 4-20). Due to this fact, the stripping time of the resist layer can take a long time and significantly decrease the throughput of this process. Therefore, a modification of the standard lift-off process was introduced in the course of this work. After deposition of the seed metal layer, local openings in the metal layer are formed by means of the laser ablation as schematically shown in Figure 4-20. Thus the transport of the solvent to the resist layer is greatly enhanced, at the same time reducing the process time. This process is called "Laser enhanced lift-off". The laser energy is fully absorbed in the first few micrometers of the metal and the resist layers. Therefore, due to the large thickness of the resist layer (10-30 µm), the laser energy cannot reach the silicon surface and create damage there.

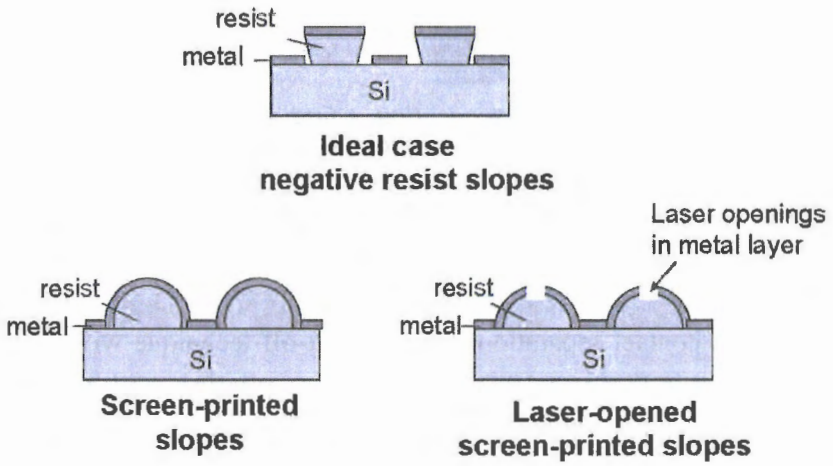


Figure 4-20 Influence of the slope of the resist edges on the lift-off process. The ideal case of the resist with negative slopes is shown in the top picture. The actual slopes of the screen-printed resist are not steep at all (left). The laser ablation process, used to open the metal layer, enhances the speed of lift off process significantly (right).

The advantages of the lift-off process are:

- No risk of under-etching of the metal fingers,
- Removal of the seed metal layers is done in one step. There is no need for selective etching of many metals in the seed layer.

On the other hand, due to the application of the screen-printing process the size of the spacing between the metal fingers is high, in the range of 100 to 300 µm. This is caused by the low positioning accuracy and the resolution of the screen-printing process. The large spacing between the metal fingers increases the optical transmission

losses of the solar cell. The application of screen-printed resist with non-steep slopes requires the introduction of the laser ablation process in order to increase the speed of the lift-off process.

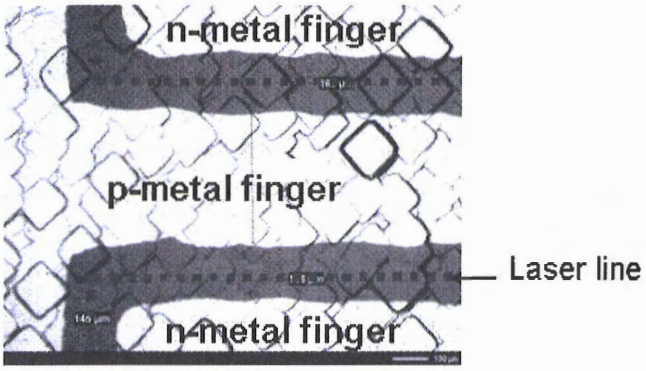


Figure 4-21 Example of the contact separation using the laser enhanced lift-off process with the screen-printed resist layer. Photographs were taken using an optical microscope.

4.4.2 Thickening of the thin seed metal layer

After formation of the interdigitated p- and n-metal seed layer, the thickening of the thin seed metal layer is required in order to increase the conductivity of the metal fingers and reduce the series resistance losses. The influence of the metal finger height on the series resistance and the resulting fill factor of the solar cell can be calculated with the following equations [121]:

$$R_s = \frac{1}{3}\frac{A_F}{B_F H_F}\rho L_F^{\,2} \tag{4.1}$$

$$\Delta FF = FF_0 \frac{R_s J_{sc}}{V_{oc}} \tag{4.2}$$

where A_F is the pitch of the solar cell, B_F is the width of the metal fingers, L_F is the length of the fingers, H_F is the height of the fingers, and ρ is the resistivity of the applied metal. FF_0 is the fill factor of the solar cell not reduced by the series resistance losses and ΔFF is the fill factor loss caused by the series resistance R_S.

The calculated series resistance and the fill factor of the n- and p- metallization grid for two solar cell sizes of 2×2 cm^2 and 12×12 cm^2 with the pitch of 2200 µm are shown in Figure 4-22. For the laboratory cell size of 4 cm^2 a thickness of 2 µm of the metal

fingers is sufficient to reduce the resistance of the metal grid to 0.1 Ω cm^2, which would result in a the fill factor loss of less than 0.5 % absolute. However, for the industrial scale 144 cm^2 solar cells with the length of the metal fingers of 12 cm, the required thickness of the metal fingers is much higher. If 1 % absolute loss in fill factor due to metal resistance is allowed, than the required thickness of the metal fingers is around 35 µm in the case of the application of the silver plating. Using this metal finger thickness, the series resistance of the metallization grid equals 0.2 Ω cm^2. This calculation shows the importance of the thickening of the seed metal layer, especially for industrial size solar cells.

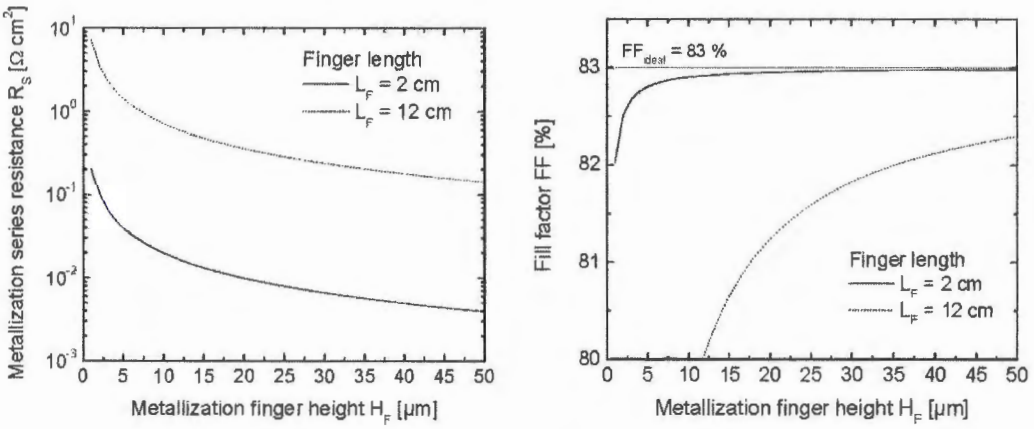


Figure 4-22 Calculated resistance of the interdigitated grid for a pitch of 2200 µm for two solar cell sizes of 2×2 cm^2 and 12×12 cm^2 (left side) for different thickness of the silver fingers. The resulting fill factor for both solar cell sizes is shown in the right graph.

In the developed solar cell process, the thickening of the structured seed metal layer was done using silver plating. A novel approach to thickening the interdigitated grid of the back-contact back-junction solar cells was introduced, in which both electrodes are thickened using different plating mechanisms. The p-electrode is contacted and thickened using the electroplating process in the potassium silver cyanide $K[Ag(CN)_2]$ bath [130]. The n-electrode is not contacted. It is plated using the light-induced plating (LIP) approach in the same chemical bath. LIP was optimized by Mette et al. [131] for the application of thickening the front surface metallization grid of the both-sides contacted solar cells. The p- and n-electrodes are of different width (see Figure 4-2), requiring therefore different thickness to achieve optimal resistance of the total metal grid. Due to the application of two different plating mechanisms during one plating process, the rate of the thickening of both electrodes can be optimized in order to achieve optimum usage of the metal material.

4.5 Solar cell results

The low-cost screen-printing and laser structuring processes described above were successfully applied to the BC-CJ solar cell processing sequence. In the present section the solar cell results, obtained using the described technologies, are presented.

4.5.1 Laboratory-scale solar cells

For laboratory-scale (4 cm^2) solar cell (see Figure 4-2), best conversion efficiency of 21.1 % (designated area measurement) was achieved on 1 Ω cm n-type FZ Si with the pitch of 2200 μm. The illuminated current-voltage characteristics together with the solar cell parameters of the best solar cell are shown in Figure 4-23.

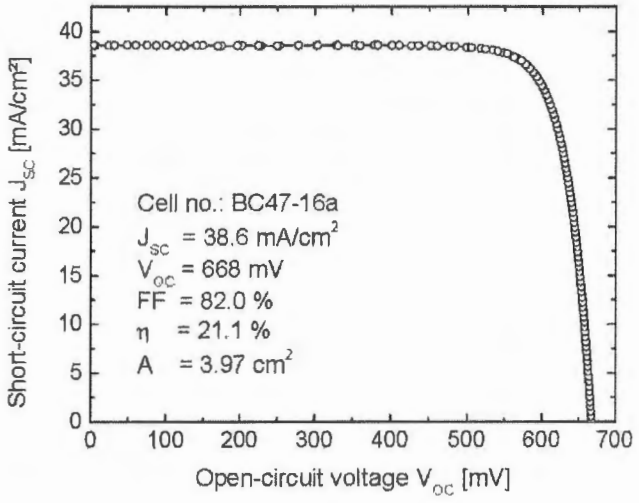


Figure 4-23 Illuminated current-voltage characteristics of the best n-type back-contact back-junction solar cell with the pitch of 2200 μm and the efficiency of 21.1 %. Designated area measurement under AM1.5G spectrum with illumination intensity of 100 mW/cm² and with device temperature of 25 °C. The efficiency was measured at Fraunhofer CalLab.

A very high fill factor value of the finished cell of 82 % indicates low resistive losses. Shunting between the tight p- and n-metal finger grids was avoided by a application of appropriate metallization process (see section 4.4.1). The series resistance losses of lateral carrier transport due to the large pitch could be minimized by application of the high conductivity FSF (see chapter 8 for more details). The total series resistance of the best solar cells is around 0.2 Ω cm^2, which proves a good device design in terms of resistive losses.

The open-circuit voltage of the best cell equals 668 mV. The rather moderate V_{OC} value indicates that a careful optimization of the rear side geometry and the diffusion profiles is required in order to further increase the device efficiency.

The short-circuit current of the best cell reaches nearly 39 mA/cm^2 for 1 Ω cm base resistivity. Analysis of the J_{SC} losses (section 6.2) shows that the optical losses (mainly front surface reflection, escape light and free carrier absorption) and the recombination losses over the base areas are limiting J_{SC}.

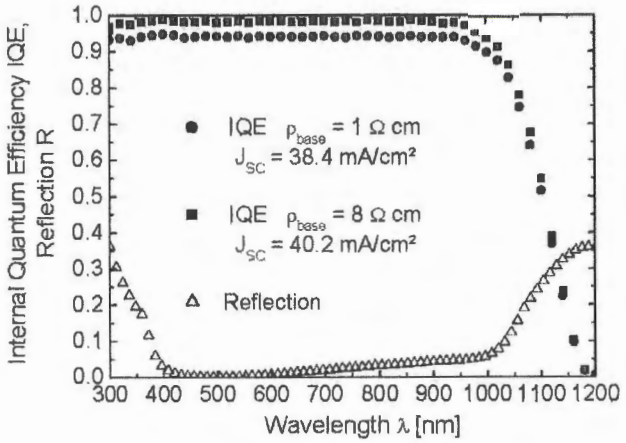


Figure 4-24 Comparison of the internal quantum efficiencies of the BC-BJ solar cells with base resistivity of 1 Ωcm and 8 Ωcm. The cells have a FSF with ρ_{sheet} = 148 Ω/sq and pitch of 2200 µm. The short-circuit current calculated by the integration of the solar spectrum with the external quantum efficiencies are shown in the graph. Note a nearly zero-reflectance at wavelength of around 550 nm due to the absence of the front side metal fingers.

The internal quantum efficiencies (IQE) and reflection (R) of the BC-BJ solar cells with a base resistivity of 1 Ω cm and 8 Ω cm are shown in Figure 4-24. The cell's reflection is very low due to the absence of the front side metallization grid. A nearly zero-reflectance is achieved for wavelengths of around 550 nm. The internal quantum efficiency for both resistivities is high, but does not reach unity. The IQE of the 1 Ω cm cells equals 95 % and for the 8 Ω cm cells it equals 98 %. The decrease of the IQE (5 % for 1 Ω cm cells and 2 % for 8 Ω cm cells) is partially caused by the front surface recombination and the bulk recombination of the minority carriers, which did not reach the rear side p-n junction. The front and rear surface recombination is higher in the case of base material with higher doping concentration [132]. This explains the differences in J_{SC} of solar cells with both base resistivities. However, the analysis presented in section 6.4 indicates that there is another cause for the decrease of IQE,

namely the recombination over the broad areas of base doping, called electrical shading.

Due to the absence of the front side metallization grid, the optical shading losses can be avoided in the BC-BJ solar cells. However, electrical shading is still present due to the rear side recombination in the regions of base busbar and base fingers [87]. A light beam induced current (LBIC) [133] map of the 2×2 cm^2 laboratory solar cell is presented in Figure 4-25. One can clearly recognize the reduced EQE signal over the base fingers and busbar. The EQE drops to nearly zero above the base busbar, even though no optical shading in this region is present. This is due to (a) large lateral distances which the minority carriers need to diffuse in order to be collected by the p-n junction and (b) due to enhanced recombination over the gap and BSF areas which have high saturation current densities. A detailed analysis of the solar cell results and the loss mechanisms is presented in chapter 6.

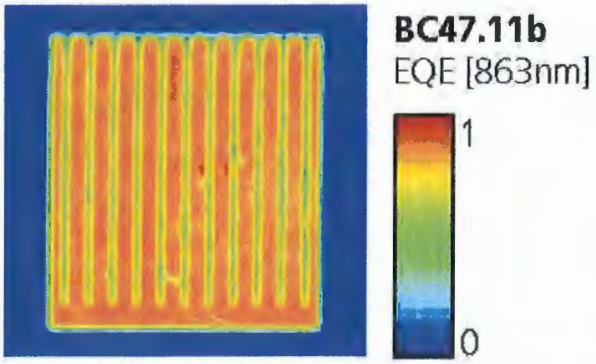


Figure 4-25 LBIC map of the BC-BJ silicon solar cell. The reduced EQE signal above the base fingers and base busbar (top side) are visible. The designated cell area is 2x2 cm^2 and the busbar area is 0.15x2 cm^2. EQE was measured at a wavelength of 863 nm.

4.5.2 Industrial-scale solar cells

In the frame of the *Quebec* [41] project, in which the author of the thesis developed the back-contact back-junction solar cell structure for mass production, large size solar cells were also manufactured. The photographs of a finished large area cell is shown in Figure 4-26.

The best efficiency of 19.2 % was achieved on n-type Cz-Si 5-inch pseudosquare wafers (cell size 147.4 cm^2) with the resistivity of 3 Ω cm. The illuminated current-voltage characteristics, together with the solar cell parameters of the best large size solar cell are shown in Figure 4-27.

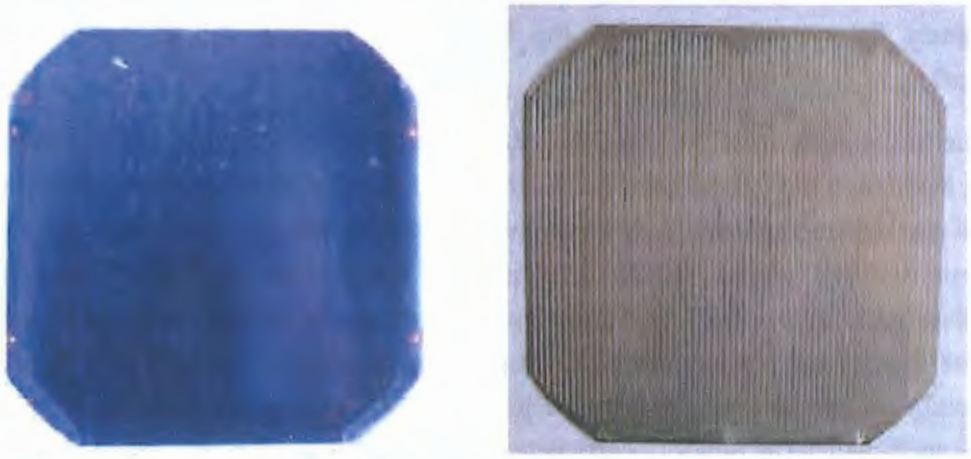


Figure 4-26 Photographs of the front (left) and rear (right) side of the large area back-contact back-junction solar cells developed in the course of the Quebec project at Fraunhofer ISE. Cell area is 147.4 cm²

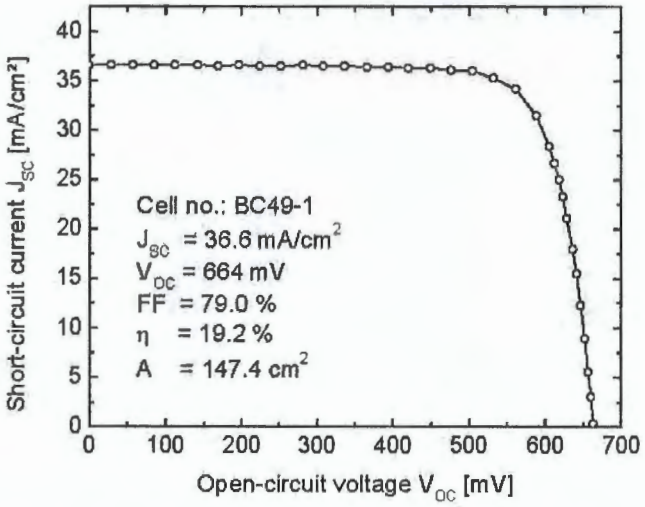


Figure 4-27 Illuminated current-voltage characteristics of the best n-type large size (147.4 cm²) back-contact back-junction solar cell developed at Fraunhofer ISE in the frame of the Quebec project [41]. The solar cell has an efficiency of 19.2 %. Measurement under AM1.5G spectrum with illumination intensity of 100 mW/cm² and with device temperature of 25 °C.

A lower efficiency (19.2 %) of the large area solar cells in comparison to the small laboratory-scale solar cells (21.1 %) is caused mainly by the lower fill factor and lower short-circuit current values. The open-circuit voltage of both solar cells is similar.

The lower FF values are caused by the significantly increased length of the metal fingers from 2 to 12 cm. The metal finger height after the silver plating process is in the range of 10 to 30 µm, which results in a FF loss of about 2 to 3 % absolute (see Figure 4-22). The rather wide spread of the metal finger thickness is caused by the fact the silver plating process of the BC-BJ solar cells was not optimized for large-area solar cells.

The difference in J_{SC} of small and large size solar cells is partially caused by the application of a different silicon material: FZ Si for small cells and Cz Si for large cells. The differences in the minority carrier's lifetime in the bulk of the fully processed cells may cause the J_{SC} differences. Moreover, in the case of the large size solar cells, local imperfections and non-uniformities, which are not avoidable due to manual handling of the large size wafers in the laboratory processing conditions, are present. These local imperfections (e.g. scratches, cracks, and passivation or diffusion non-uniformities) over the whole area of the solar cells are responsible for the locally decreased quantum efficiency of these cells (see Figure 4-28).

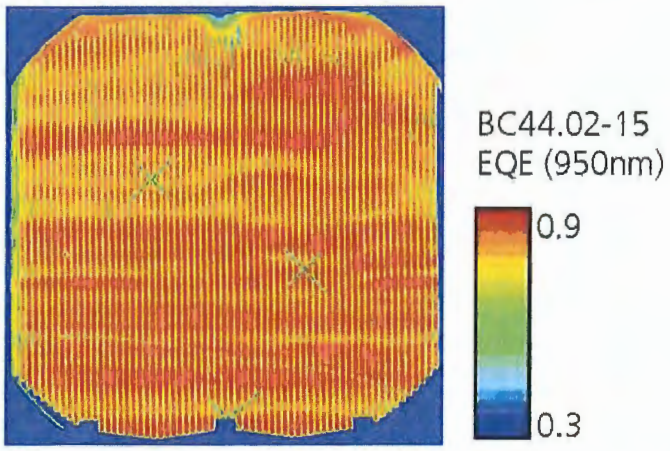


Figure 4-28 LBIC map of the large area BC-BJ silicon solar cell. The reduced EQE signal above the base fingers and base busbar (bottom side) are visible. The solar cell area is 147.4 cm^2. Local defects introduced by the manual handling of the wafer during processing can be recognized.

4.6 Conclusions

The design and the processing technology of the developed high-efficiency back-contact back-junction solar cell were presented. The structuring steps, which are required to form an interdigitated grid of p- and n-diffusions and metal grids, were done using industrially relevant low-cost techniques. Screen-printing of the masking

layers, as well as the local laser ablation of the dielectric and silicon layers, were developed and successfully applied to the solar cell processing sequence.

Solar cells were processed on n-type Si substrates. The applied n-type Si material was intensively examined. Very high minority carrier lifetimes up to 18 ms were measured for the investigated silicon substrates. The determined minority carrier lifetime is high enough to enable realization of the high-efficiency BC-BJ silicon solar cells.

Metallization technology is very critical in the case of the interdigitated metal grid structure, due to the very high risk of shunt formation between the p- and n-metal grids. A review of the existing approaches to form an interdigitated metallization grid on the rear cell side, as well as the two methods which were developed in the frame of this study, were presented. Metallization of the developed solar cells was performed using a laboratory approach consisting of two steps. First a thin (less than 1 μm) seed metal layer was evaporated and structured to form interdigitated grid geometry. Next, a silver plating process was applied to increase the metal finger height and conductivity.

The highest solar cell efficiency of 21.1 % was achieved on 1 Ω cm n-type FZ Si with the designated area of 4 cm^2. For the large area solar cells with an area of 147.4 cm^2, a maximum efficiency of 19.2 % was achieved. A detailed analysis of the solar cell results is presented in the following chapters.

5 Analysis of the laser-fired aluminium emitters

In this chapter the local laser-fired aluminium emitter (LFE) process, an alternative process to boron emitter diffusion, was investigated. The model of the LFE emitters, which includes a laser-induced damage zone, was analyzed using a two-dimensional simulation and compared with the experimental solar cell results. The injection-dependent Shockley-Read-Hall recombination in the direct vicinity of the local back junction influences negatively the cell performance and causes large cell performance differences for varying specific base resistivities of the cells.

5.1 Introduction

The Laser-Fired Contact (LFC) technology developed at Fraunhofer ISE [134] not only provides local contacts through the dielectric passivation layer at the back cell side, but also creates a local aluminium doped region. In the case of p-type cells, this region works as a high-low junction - an effective back surface field (BSF). This feature of the LFC process already enabled fabrication of a 21.9 % p-type solar cell. In addition to application of the LFC process to p-type substrates, an n-type substrate process with the use of the LFC has been introduced by Glunz et al. [135], [136]. The LFC process was used in that case to form local p-n back junctions on the *n-type* substrates, referred to as the laser-fired aluminium emitter (LFE) process.

The LFE process combines three steps in one:

1. Formation of the local openings in a dielectric layer.
2. Formation of the metal-semiconductor contacts, through the local openings.
3. Formation of the local p^+ emitter. Al is alloyed with Si, and a local p^+ emitter is created in the n-type substrate. Thus, the additional emitter diffusion process can be omitted.

Thus, the greatest appeal of the laser-fired p^+ aluminium emitter (LFE) process is the inherent opportunity to create a patterned emitter without additional masking steps. This feature of the LFE process makes it attractive for its application in the back-contact back-junction solar cell structure, where the p^+ emitter is diffused only locally.

Moreover, the LFE process enables the fabrication of high efficiency n-type cells without the use of boron diffusion. Replacement of the boron diffused emitter with the laser fired aluminium emitter could lead to significant reductions in processing time and potentially to a reduction in costs of the manufacturing of back-contact back-junction solar cells. The reason for this is that the boron diffusion is a high-temperature and time consuming process: diffusion temperatures are in the range of 800 - 1100°C, and the process requires several hours. High diffusion temperatures are required because of the low solubility of boron in Si. The solubility of phosphorus [137] is, for example, around one order of magnitude higher than the solubility of boron at the same temperatures [138]. Thus, in order to achieve high surface concentrations of boron, the diffusion process needs to take place at strongly elevated temperatures. In contrast LFE can be performed with the wafer at room temperature. Therefore, the heating of wafers to high diffusion temperatures is not required for this process, as it is in the case of boron emitter diffusion. Additionally, the LFE process is very fast, requiring a processing time in the range of seconds per wafer.

The objective of this chapter is to analyze and gain fundamental knowledge about the LFE process, an alternative process to the emitter formation using boron diffusion. Based on the analysis of the laser-fired Al emitters, the replacement of the boron diffusion with the LFE process could be potentially considered in the processing sequence of the back-contact back-junction solar cells.

5.2 Fabrication of LFE and boron emitter cells

Laser fired aluminium emitters (Figure 5-1 left) and locally diffused boron emitter (Figure 5-1 right) n^+np^+ back junction cells have been fabricated on 250 µm thick FZ n-type 1, 10 and 100 Ω cm Si substrates. The size of the cells is 2x2 cm^2. The cells exhibit a front surface with random pyramids, evaporated front contacts and a phosphorus diffusion (front surface field) with sheet resistance ρ_{sheet}=120 Ω/sq. The front surface is passivated by a 105 nm thick thermal oxide. The rear surface is covered with the same thermal oxide.

Formation of the local p-n junction on the rear side:

- LFE cell: After evaporation of 2 µm thick aluminium layer on the rear surface, the back junction is created by local laser-firing of the aluminium through the oxide layer, resulting in formation of a p^+ emitter and contact/emitter coverage of about 5 %.

- Diffused boron emitter cell: Back junction was formed by local boron diffusion through the oxide structured with photolithography on the rear side, with 1.5 % emitter coverage. The rear surface was then oxidized again and local contact openings were formed using photolithography with 0.2 % contact opening coverage. Finally, a 2 µm thick aluminium layer was evaporated on the rear surface.

The last processing step is a low temperature (425 °C) annealing under forming gas, called FGA process. The process time is 25 min and the concentration of H_2 in N_2 equals 5 %.

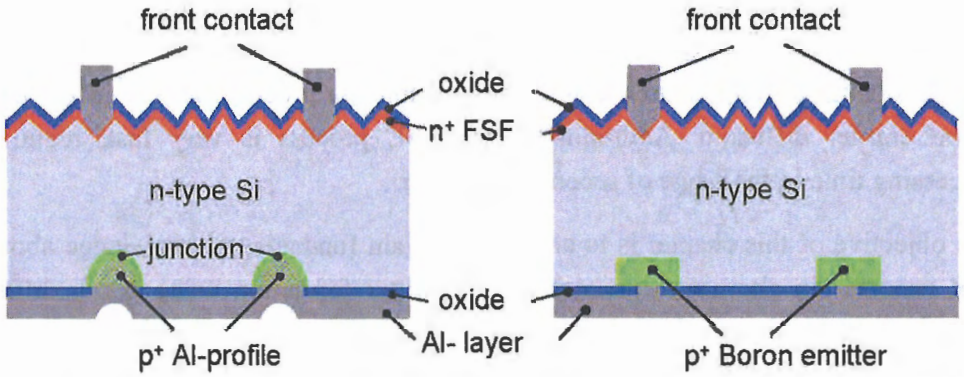


Figure 5-1 Structure of the n-type back-junction LFE cell (left) and the n-type back-junction locally boron diffused cell (right).

5.3 Solar cell results

The best results of different base resistivity n-type LFE cells are summarized in Table 5-1. The best efficiency of 19.4 % was obtained on 100 Ω cm FZ n-type material with the back-junction LFE cells. In the section 5.7, where the comparison of the results of the solar cells with LFE and boron diffused emitters is presented.

In Table 5-1 a very large difference in the performance of the LFE cells with different base resistivities can be observed. Differences of almost 10 mA/cm^2 (i.e. up to more than 20 % relative) in J_{SC} of the 1 and 100 Ω cm cells were measured. At the same time, differences of 30 mV in V_{OC} of cells with 1 and 100 Ω cm base can be seen. It is believed that the laser-induced crystal damage is responsible for limiting the performance of the LFE cells and for causing significant differences in the performance of these cells with different base resistivities. Understanding the differences in performance of the LFE solar cells with different base resistivities is an objective of the analysis presented in the following sections.

Table 5-1 I-V results of the LFE cells fabricated on n-type FZ Si substrates with different resistivities.

Cell no.	ρ_{base} [Ω cm]	V_{OC} [mV]	J_{SC} [mA/cm^2]	FF [%]	η [%]
NRP7_24.2m	100	646.5	39.8	75.1	19.4
NRP7_21.2m	10	639.8	37.9	71.9	17.4
NRP4_23.5	1	616.7	30.2	72.9	13.5

5.4 Laser-induced damage zone

In previous work [135] a concept of a laser-induced damage zone (see Figure 5-2) was introduced in order to explain the decreased V_{OC} of the p-type LFC cells in comparison to the passivated emitter rear locally diffused (PERL) cells with diffused Al BSF. Laser damage to the crystal lattice is caused by rapid melting during the absorption of a very short laser pulse [139] and a subsequent recrystallization of the silicon. The laser-induced defects are known to form recombination centers [140], [139], thus locally reducing the lifetime of the minority carriers.

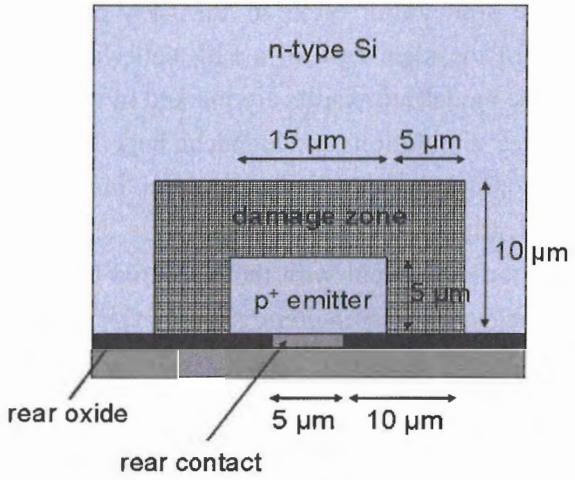


Figure 5-2 Two-dimensional simulation model of an LFC contact with a laser-induced damage zone around the local Al BSF.

The introduction of the damage zone with strongly reduced lifetime into the two-dimensional simulation model enabled very good modelling of the LFC p-type structures and modelling of their performance as a function of different base doping

concentrations. The damage zone implemented in the simulation model has a size of $15 \times 5\ \mu m^2$ and strongly reduced lifetime of $\tau_{local} = 0.3\ \mu s$. The size of the damage zone and the value of τ_{local} were arbitrary chosen in the simulations. The strongly reduced local lifetime in the laser damage zone models the very strong crystal defects and introduction of the metal impurities induced by the laser firing of the Al contacts.

Since in case of the n-type cell the local Al-profile functions as an emitter, the quality of this junction and the quality of the area in the direct vicinity of the junction is has a much bigger impact on the cell performance than in the case of p-type cells, where the Al-profile has the function of a local back-surface-field (LBSF).

5.5 Quantum efficiency of the LFE cells

In Figure 5-3 the measured internal quantum efficiency (IQE) of the LFE cells and the simulated IQEs are presented. Significant differences in the quantum efficiency of the LFE cells with different base doping concentrations cause very large differences in short-circuit current of the measured cells. IQE of the cell with 100 Ω cm base resistivity equals around 97%. At the same time the internal quantum efficiency of the LFE cell with 1 Ω cm base resistivity equals only around 75%. This difference in IQE explains around 20% differences in J_{SC} of these cells.

In the bottom part of Figure 5-3, the IQE of the n-type LFE cells were modeled using two-dimensional device simulation. Next to the LFE cells with the laser-induced damage zone, the IQE of the ideal case of a LFE cell without the damage zone was calculated as well. These modelling results are marked in the graph as 'Ideal Local Al-Diffusion'. In the device simulations an identical bulk lifetime $\tau_{SRH} = 1000\ \mu s$ was used for all three base doping concentrations in order to investigate the influence of the damage zone independently of the bulk effects. The damage zone model enables modeling which is in good agreement with the measured IQEs. It is believed that fine adjustments of the damage zone parameters, such as size and lifetime, may result in even better agreement with the measured values.

In Figure 5-3b, one can compare the influence of the damage zone on the quantum efficiency of the 1 and 100 Ω cm cells. The influence of the damage zone is much bigger for the 1 Ω cm material than in the case of 100 Ω cm, where the damage zone has almost no influence on the quantum efficiency. In the case of the cell with 1 Ω cm base resistivity and with the damage zone model the quantum efficiency is around $7\ \%_{abs}$ lower than the IQE of the cell without the damage zone. The next section deals with the explanation of this effect.

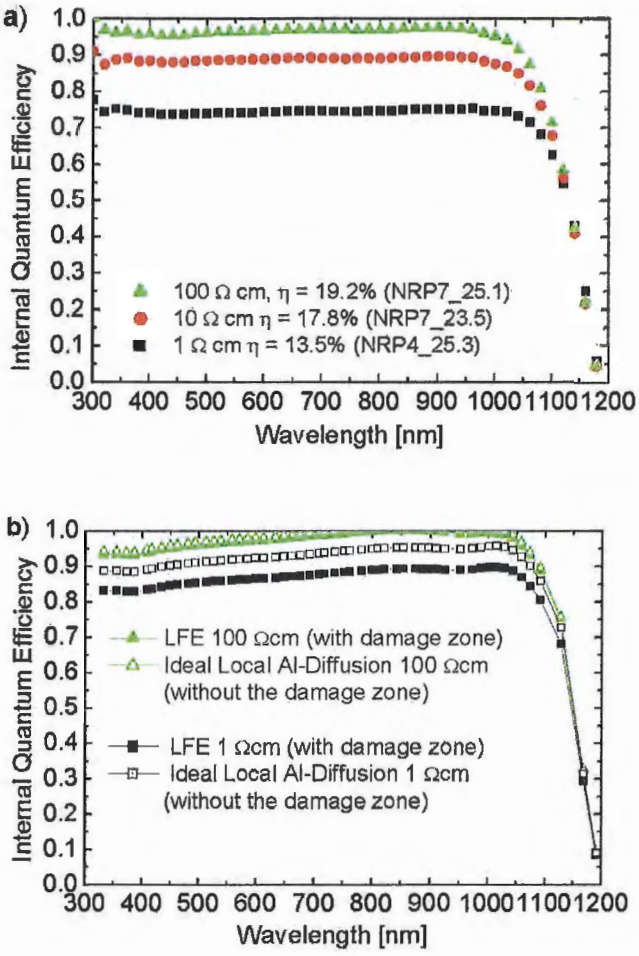


Figure 5-3 Measured (a) and two-dimensional SDEVICE [90] simulation (b) internal quantum efficiencies for the n-type LFE cells of different doping concentration.

5.6 Recombination in the damage zone

Using the damage zone model presented in the previous section, the Shockley-Read-Hall (SRH) recombination rate and the density of the electrons and holes in the direct vicinity of the rear local junction were simulated. The results of the two-dimensional simulations of the SRH recombination rate are shown in Figure 5-4. The LFE cells with base resistivities of 1 and 100 Ω cm were simulated. Additionally, the rear local junction solar cell without the damage zone and with base resistivity of 1 Ω cm was simulated for comparison.

In the results shown in Figure 5-4, a strongly increased recombination rate in the damage zone is observed. The recombination rate in damage zone is around 3 to 4

orders of magnitude higher than in the bulk Si material. Increased SRH recombination in the damage zone results from the very low lifetime of the minority carriers within this zone. In the model, the local minority carrier lifetime inside of the damage zone is set to 0.3 µs. The bulk lifetime is significantly larger and equals 1000 µs.

In the simulation of the cell without the damage zone, shown in Figure 5-4c, the recombination rate is uniform over the whole bulk area. This is the case when a p^+ emitter was created by boron diffusion or by alloying of Al, without the introduction of the stress caused by rapid thermal processing and crystal lattice defects during emitter formation using the LFE process.

An interesting effect can be observed by comparing the recombination rate in the damage zone of the LFE cells with 1 and 100 Ω cm. The recombination rate is there clearly higher in the case of the 1 Ω cm LFE cell than in the case of the 100 Ω cm cell. This effect can be analyzed better when looking at the profiles of the recombination rate taken through the wafer thickness in the middle of the rear local emitter, as shown in Figure 5-5.

The difference in the recombination rate of the cells with different base resistivity can be explained with the injection dependence of the Shockley-Read-Hall carrier lifetime (τ_{SRH}). τ_{SRH} is a function of the carrier injection level and the dopant density. In the case of the 1 Ω cm material, where the injection level is lower than the dopant density (see Figure 5-5a), a low injection level condition occurs ($\tau_{SRH,\,\mathrm{li}}$). However, the dopant density of the 100 Ω cm material is lower than the density of the holes (Figure 5-5 b), thus the 100 Ω cm LFE cell is under high injection ($\tau_{SRH,\,\mathrm{hli}}$).

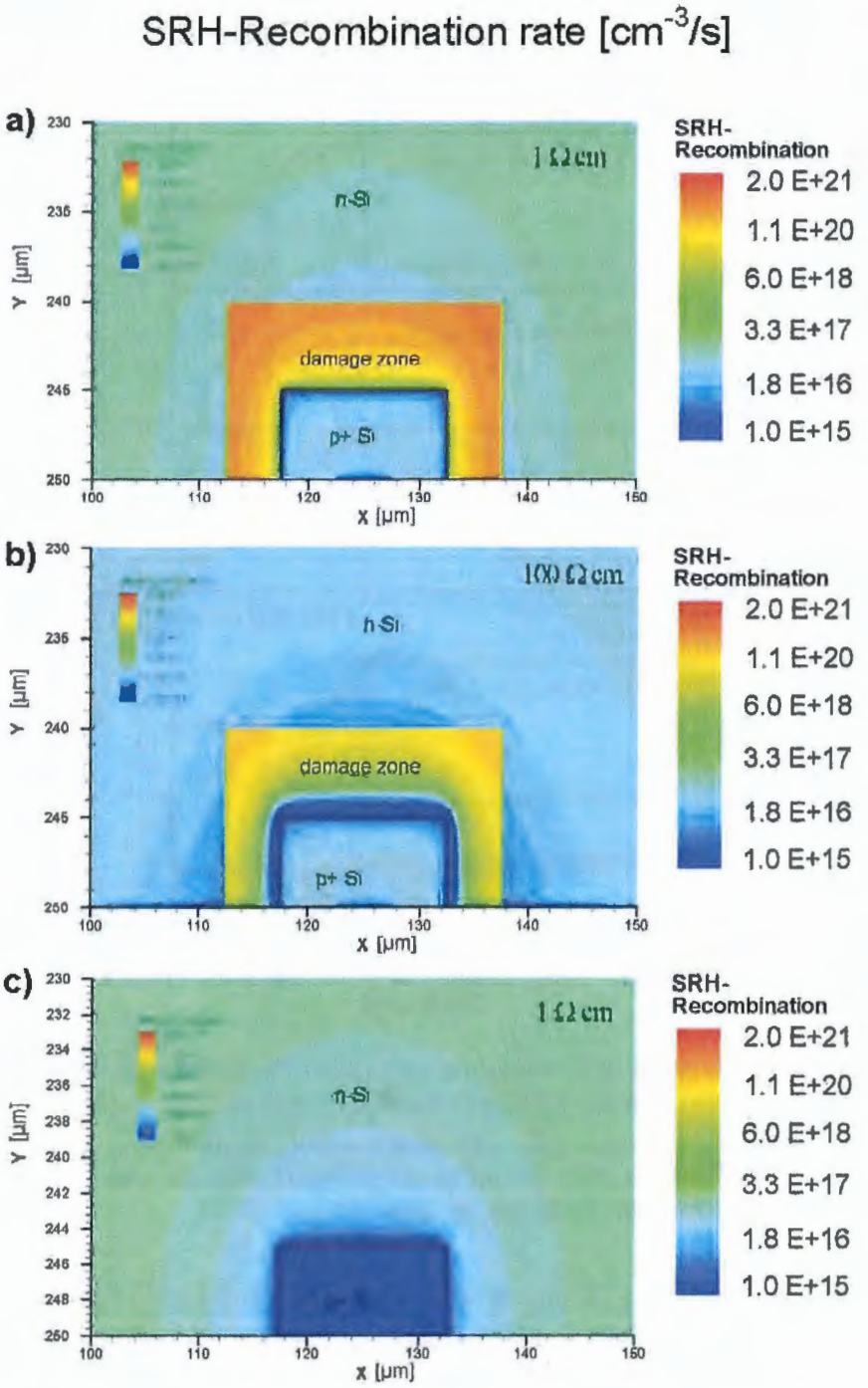


Figure 5-4 Two-dimensional simulation of the SRH-recombination rate under J_{SC} conditions of 1 Ω cm (a) and 100 Ω cm (b) LFE and 1 Ω cm LBSF (c) cells. Recombination was simulated in the vicinity of the local emitter on the rear side. Y-axis represents the thickness of the cell, with front cell surface at Y=0. SHR-recombination rate shown in the colour scale is given in cm^{-3}/s. Note strongly the increased recombination rate in the laser damage zone of the LFE cells (a and b).

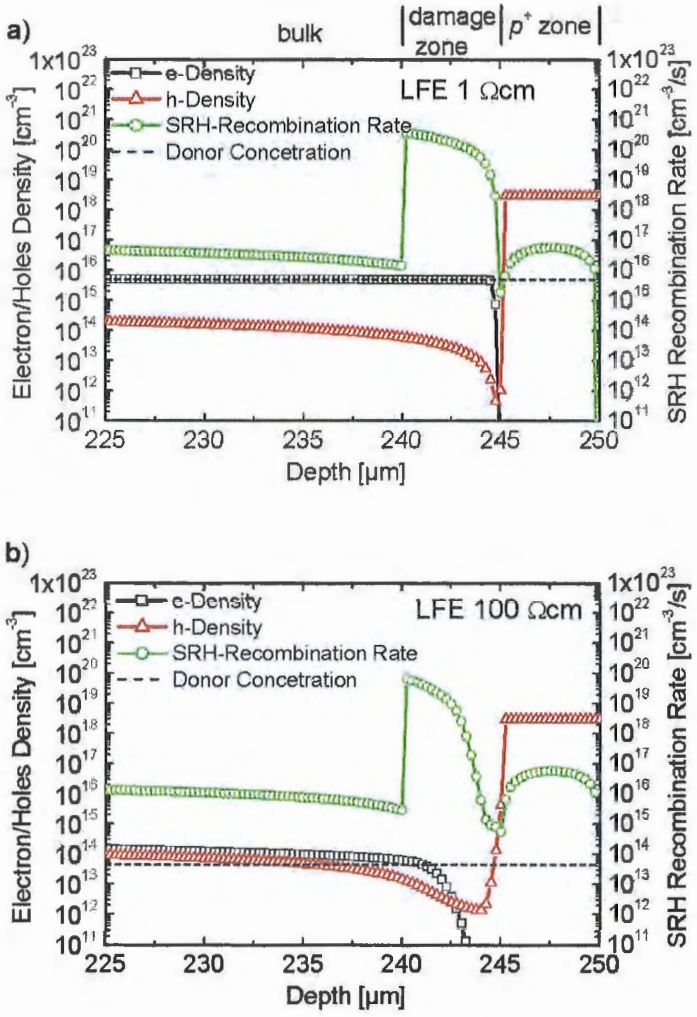


Figure 5-5 Profiles of the recombination rate under J_{SC} conditions of the 1 Ω cm (a) and 100 Ω cm (b) LFE cells taken through the cell thickness at the back surface of the cell (two-dimensional simulation). Note the high recombination rate in the laser-induced damage zone (between 240-245 µm from the cell front surface).

Using the simplified SRH lifetime models under low- and high-level injection [141] and for $\tau_{no} = \tau_{po}$, the low (lli)- and high-level injection (hli) lifetime in n-type Si is:

$$\tau_{SRH,\,\mathrm{lli}} = \tau_{po}$$
$$\tau_{SRH,\,\mathrm{hli}} = \tau_{no} + \tau_{po} \qquad (5.1)$$

Thus both bulk and damage zone lifetime of cells under high injection is significantly higher than under low injection. It is therefore believed that this significant lifetime difference, resulting in a drastic change of the diffusion length in the bulk Si and in the

damage zone, is the reason for the performance difference between the LFE cells processed on the 1 and 100 Ω cm n-type wafers. Results of the simulation prove the hypothesis to be correct. The increased recombination rate of the 1 Ω cm cell in the bulk and inside the damage zone leads to a significant current reduction of these cells compared to 100 Ω cm LFE cells.

5.7 Comparison of boron diffusion and LFE emitters

Further analysis of the influence of the injection dependence bulk and damage zone lifetime on the analyzed cell structure performance is done by direct comparison of the solar cells with LFE emitters (Figure 5-1 left) to cells with local boron diffused emitters (Figure 5-1 right). During the boron diffusion process, the damage zone in the direct vicinity of the local rear junction is not formed. It is therefore expected that, due to the absence of the damage zone, the solar cells with boron diffused emitters will show a different dependence on the current as a function of base doping than with the LFE cells.

Table 5-2 Comparison of the parameters of the LFE and boron diffusion emitter cells on different base resistivities. All cells were processed on the n-type FZ Si substrates. The area of the solar cells is 4 cm^2.

Cell no.	Emitter type	ρ_{base} [Ω cm]	V_{OC} [mV]	J_{SC} [mA/cm^2]	FF [%]	η [%]
NRP46_1d	Boron diffusion	1	599.6	35.1	60.6	12.8
NRP46_4e	Boron diffusion	10	653.1	36.0	74.7	17.6
NRP46_5e	Boron diffusion	100	658.5	37.6	74.2	18.4
NRP46_10f	LFE	1	619.2	31.7	69.8	13.7
NRP46_14b	LFE	10	625.1	35.9	78.0	17.5
NRP46_18b	LFE	100	629.0	37.6	76.3	18.0

As mentioned in section 5.2, a set of the LFE and boron diffused emitter solar cells was processed within the frame of this work. The best results are summarized in Table 5-2. The best efficiency of the back junction with locally diffused boron emitters in this experiment was 18.4 % on the 100 Ω cm substrate resistivity. For comparison, the highest reported efficiency of the n-type back junction solar cell with full area boron emitter is 22.7 %, presented by Zhao et al. [142]. Thus, the full area emitter on the rear

side has a far superior performance than the local rear emitter of this study. Coming back to Table 5-2, the performance of the cells with boron emitters is slightly higher than that of the LFE cells. The variation in FF of the boron emitter cells is caused by processing faults during the photolithography for the rear side contact formation.

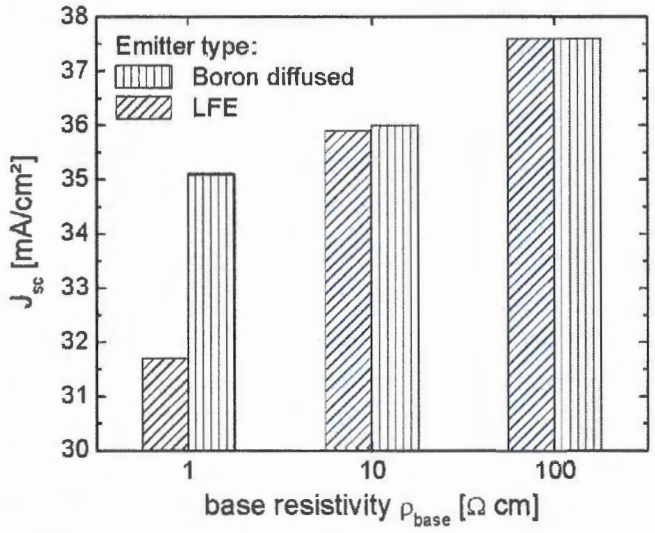


Figure 5-6 Comparison of the short-circuit current of the back-junction cells with LFE and boron diffused emitters on different resistivity substrates.

The V_{OC} values of the LFE cells are around 20 to 30 mV lower than the V_{OC} values of the boron emitter cells. The loss in V_{OC} is caused by the recombination in the damage zone of the LFE cells and by the increased metal contact coverage of LFE cells, which also results in the increased recombination of the minority carriers at the rear surface. In Figure 5-6, direct comparison of J_{SC} of the LFE and boron diffused cells on different substrate resistivities is shown. For a base resistivity of 100 Ω cm, there is no difference in J_{SC} of both cell types. The cell operates under high injection, thus the damage zone lifetime of LFE cells is high enough not to limit the device performance. This result is in good agreement with the device simulations shown in Figure 5-3b. With increasing substrate doping concentration, the J_{SC} of both cell types decreases. This effect is caused by decreased bulk lifetime in the substrate of higher doping concentration. However, for a base resistivity of 1 Ω cm there is a large J_{SC} difference of 3.4 mA/cm^2 between the LFE and boron emitter cells. This effect is again in good agreement with simulations shown in Figure 5-3 b. In the case of 1 Ω cm cells, which operate under low injection, the bulk lifetime in the damage zone is so low that it limits the minority carrier collection at the back junction.

The results mentioned above clearly prove the validity of the model of the laser fired aluminium emitter process, which includes the damage zone with significantly reduced local lifetime.

5.8 SunsV$_{OC}$ and implied voltage

The SunsV$_{OC}$ curves of the fully processed LFE cells, presented in Table 5-1, were measured for a wide light intensity range (Figure 5-7) in order to analyze the cell voltage under low and high injection level conditions.

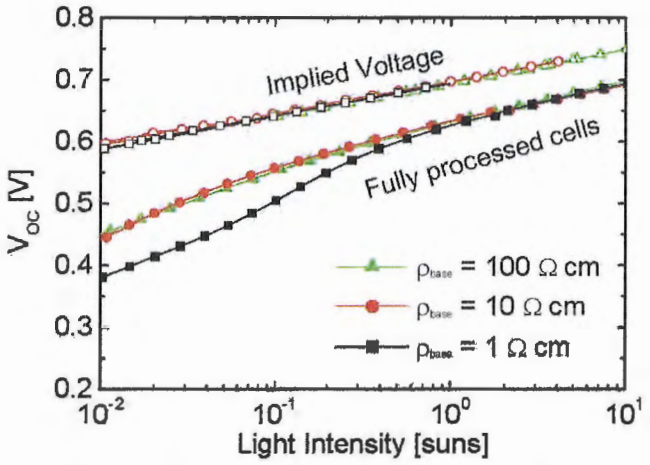


Figure 5-7 Open-circuit voltage (closed symbols) and implied voltage (open symbols) in the wide light intensity range for different resistivity n-type fully processed LFE cells and test samples for determination of the effective minority carrier lifetime.

The excess carrier density in the lifetime samples lead to the separation of the quasi Fermi levels and implies an open circuit voltage. For this experiment the n-type lifetime samples with different base resistivity have been prepared. Both sides of these samples exhibit a full area shallow n^+ diffusion (ρ_{sheet}= 120 Ω/sq.) and a full area 105 nm thick thermal oxide.

The implied voltage of the n-type FZ Si material, used for the solar cell processing, was calculated from the QSSPC lifetime curves. The calculations were performed using equation (5.2) as proposed by Sinton et al. in [75].

$$V_{OC} = \frac{kT}{q} \ln\left(\frac{\Delta p(N_D + \Delta n)}{n_i^2}\right) \tag{5.2}$$

The calculated implied voltage is plotted in Figure 5-7. The symmetrical n-Si lifetime samples, as shown in section 4.2.1, were analyzed. For all resistivities, shape and values of the implied voltage are roughly the same in the range of 700 mV at one sun light intensity. The implied voltage values represent an ideal state, where only bulk recombination (which is low for the good quality n-type material as shown in section 4.2) and the low surface recombination rate plays a role.

In the case of the fully processed LFE cells, the SunsV_{OC} curves are different than the implied voltage curves of the symmetrical lifetime samples. First of all, voltage values are lower. This is attributed to the cell structure, where additional recombination mechanisms such as: (a) front and rear side metal contacts, (b) laser-induced damage zone and (c) texturization are introduced. All these elements reduce the cell voltage to 610-630 mV at light intensity of one sun.

Additionally, one can see an interesting shape of the 1 Ω cm curve of the LFE cell. Under low-injection intensities (light intensities <0.3 Suns), the voltage decreases faster than in the case of higher resistivity cells. It is believed that this effect is caused by a strong decrease in lifetime in the laser damage zone, where under low-injection the SRH recombination dominates – as discussed above.

One would expect a larger J_{SC} vs. Suns than a V_{OC} vs. Suns dependence, because under short-circuit conditions the cells operate at much lower injection levels as compared to open-circuit conditions. Moreover, the short-circuit current of the rear junction cell structure has a much stronger bulk lifetime dependence then the cell voltage. That is why the differences in J_{SC} are much more significant than the V_{OC} differences between 100, 10 and 1 Ω cm cells, as can be seen in Table 5-1. The analysis above has another practical meaning as well. Under low illumination conditions, i.e. more realistic outdoor conditions, the LFE cells will suffer from an drop in efficiency, whereas the boron diffused cells should retain linear characteristics.

5.9 Optimization of the LFE cells

Optimization of the pitch, i.e. distance between the LFE points, was performed. The pitch of laser points was varied in order to find the optimum between two opposing trends:

a) For a smaller laser pitch, the emitter coverage on the rear side increases, which improves carrier collection at the back-junction. Moreover, the decrease of the LFE pitch should also have a beneficial influence on the fill

factor by reducing the lateral series resistance, especially for the cells with a low conductivity substrate.

b) Increasing the pitch of the LFE points results in a decrease of the damage introduced by laser, which should be as small as possible to reduce degradation of the cell performance.

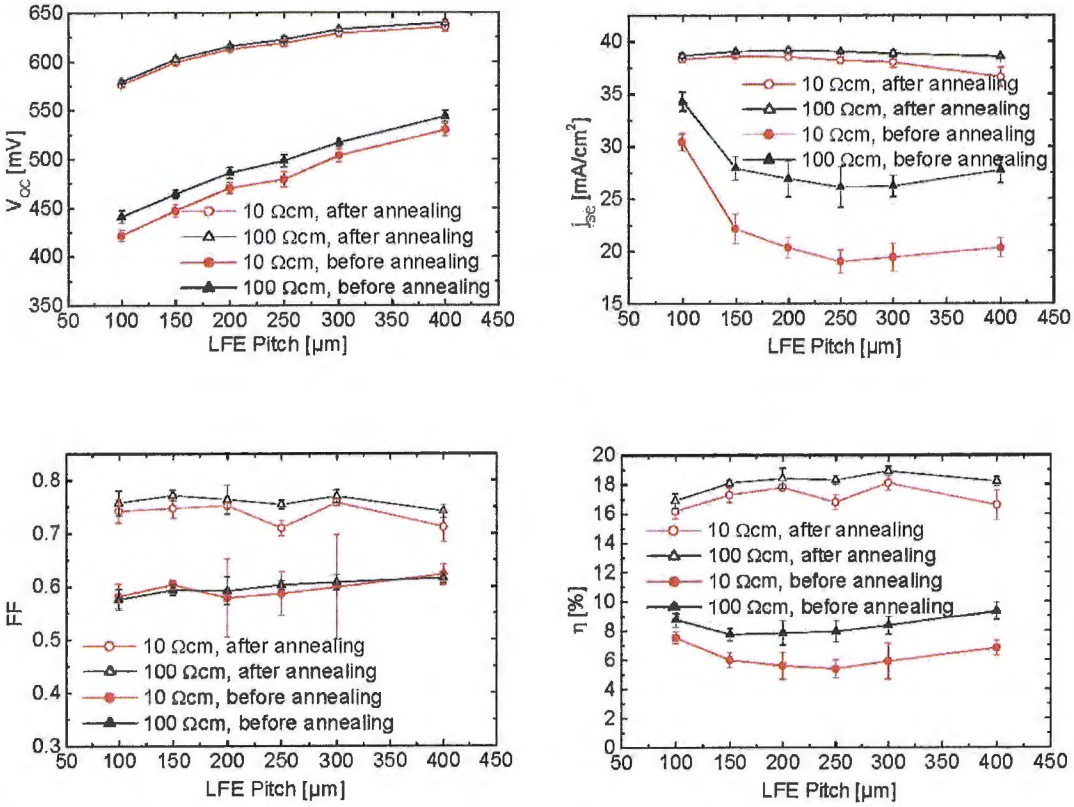


Figure 5-8 Results of the LFE cells processed with different pitch of the laser process. Cell results before and after annealing step are shown. Each data point represents the average of 7-16 cells. Standard deviation of the measurements is also plotted on the graphs.

A pitch of the LFE points in the range between 100 µm and 400 µm was chosen. The minimum pitch of 100 µm allows realization of an almost full area emitter on the rear side (each LFE point is of about 70 µm in diameter). The maximum pitch of 400 µm, on the other hand, is expected to be already too large for a good carrier collection at the back side and therefore lead to strongly reduced performance of the LFE cells. Results of the pitch optimization of the 10 and 100 Ω cm LFE cells are shown in Figure 5-8.

The solar cell parameters before and after the low-temperature (425 °C) annealing are presented. The importance of the annealing to achieve good cell results is clear, as it drastically improves all of the solar cell parameters: open-circuit voltage, short-circuit current, fill factor, and efficiency.

As expected, the cell's voltage improves with increasing pitch, because less damage is introduced by the laser. V_{OC} increased from 575 mV for the pitch of 100 µm to 630 mV for the pitch of 400 µm. Further increase of pitch of the LFE points is expected to lead to further improvement of V_{OC}.

However, with increasing pitch J_{SC} decreases. This is due to the increase of the effective diffusion path for the carriers required to reach the local back junction. When the required diffusion length becomes equal or higher than the effective diffusion length of the carriers, a significant percentage of the minority carriers, which were photogenerated in large lateral distances from the local junction, will recombine before reaching the p-n junction. Detailed analysis of the J_{SC} of the 10 and 100 Ω cm LFE cells shows that the J_{SC} of the 10 Ω cm cells is both lower and decreases more rapidly with the increasing pitch. This is caused by lower diffusion length of the minority carriers in the 10 Ω cm cells compared to 100 Ω cm n-type Si.

The fill factor of the cells is not significantly affected by the pitch in the investigated pitch range. However, a decrease of the FF for the largest pitch of 400 µm can be observed, due to increased lateral series resistance of the LFE cells. The best efficiency of 19.4 % on the 100 Ω cm was realized for the LFE pitch of 300 µm. Both voltage and current of the 100 Ω cm is only slightly better than 10 Ω cm cells, since both cell groups operate under medium- to high- injection and the low-injection conditions do not occur significantly.

5.10 Conclusion

The appealing benefit of the laser-fired p^+ aluminium emitter (LFE) process is the inherent opportunity to create a patterned emitter without additional masking steps. This feature of the LFE process makes it attractive for the application in the back-contact back-junction solar cell structure, where the p^+ emitter is diffused only locally. Therefore, in this chapter the LFE process was investigated and its influence on the solar cell parameters was compared to the solar cells with the traditional boron diffused p^+ emitter.

N-type solar cells with local back-junction were processed on 1, 10 and 100 Ω cm resistivity n-type FZ-Si. Differences in J_{SC} of up to 20 % between 1 and 100 Ω cm

cells were observed. An explanation, based on the experimental and simulation analysis of this effect, was proposed. It is concluded that the injection-dependent Shockley-Read-Hall recombination in the bulk Si and in the laser-induced damage zone determines the LFE cell performance and leads to strong performance differences between cells on different resistivity substrates.

By directly comparing the back-junction cells with LFE and boron diffused emitters, it was shown that the LFE process limits the open-circuit voltage and the short-circuit current of the LFE cells in comparison to the back-junction cells with locally diffused boron emitters. Moreover, due to non-linear behavior of the voltage under low illumination conditions, at the low light intensities the LFE cells will suffer drops in efficiency, whereas the boron diffused cells should remain linear.

Based on the above disadvantages of the LFE emitter formation process, the application of the LFE in the manufacturing of the high-efficiency back-junction solar cells was not further followed in the course of this thesis. On the other hand, if lower device efficiencies are allowed, then it might be interesting to consider the replacement of the boron diffusion by the LFE process in order to reduce the device processing thermal budget and time.

6 Analysis of the loss mechanisms

A detailed analysis of the loss mechanisms in the back-contact back-junction silicon solar cells is presented. Four main loss mechanisms in the BC-BJ solar cells are described: series resistance, optical losses, recombination losses and electrical shading. The influence of each of the loss mechanisms on the cell efficiency is studied. The reduction of the cell efficiency due to the analyzed loss processes was determined to be 3.9 % abs. due to recombination processes, 2.0 % abs. due to optical losses, 0.3 % abs. due to series resistance effects and 0.7 % abs. due to electrical shading.

6.1 Introduction

A back-contact back-junction n-type Si solar cell processed without the use of photolithography with a top efficiency of 21.1 % was developed and demonstrated in the course of this work. In order to better understand the parameters of the best solar cell and to further optimize the cell design, it is crucial to perform a detailed loss analysis. Therefore, the focus of this chapter is to quantify the main loss mechanisms of the developed solar cells and to analyze their influence on the cell efficiency. The loss mechanisms, such as optical, recombination, and resistance losses are analyzed and discussed in the following sections.

Table 6-1 *Solar cell parameters of the best solar cell demonstrated within this work. The parameters of an ideal solar cell with only the intrinsic loss mechanisms are shown for comparison. Cell thickness (W), pitch and base resistivity (ρ_{base}) are given as well.*

	Cell no	ρ_{base} [Ω cm]	W [µm]	Pitch [µm]	V_{OC} [mV]	J_{SC} [mA/cm2]	FF [%]	η [%]
best	BC47-16a	1	160	2200	668	38.6	82.0	21.1
ideal	-	1	160	2200	742	44.0	86.5	28.3

The calculated loss mechanisms limiting device efficiency are compared to the parameters of the best solar cell results achieved experimentally. The best solar cell results were already presented in section 4.5, and are used in this chapter in Table 6-1

for reference. In addition to the experimental results of the best solar cell, the ideal solar cell parameters limited only by intrinsic loss processes are shown in the Table 6-1 as well. The analysis of the intrinsic loss mechanisms in the silicon solar cells, such as radiative and Auger recombination processes and the optical losses due to finite absorption coefficient of the incoming light, were already presented in section 2.4.

6.2 Optical losses

6.2.1 Optical losses in the back-contact solar cell

One of the major advantages of BC-BJ solar cells is the reduction of optical losses due to the absence of the metal finger grid on the front side. This results in a reduction of the front side reflectance and enables an increase of the short-circuit current of this cell type. However, there are still other remaining optical losses in BC-BJ solar cells. These include: (a) primary surface reflectance, (b) escape light, (c) transmission, and (d) parasitic absorption. The parasitic absorption occurs in front side antireflection layers, rear side passivation layers, at the metal contacts and as free-carrier absorption (FCA) in highly doped cell regions (see section 6.2.3 for more details on FCA). All these parasitic absorption effects are non-generating absorption processes and therefore do not contribute to current generation of the solar cell. The analysis of the contribution of each of the optical loss mechanisms to the overall optical losses is the goal of this section.

6.2.2 Modeling of the optical losses

The optical processes which occur in the solar cell, like absorption, reflection, transmission and parasitic absorption, can be simulated with the optical simulation tool *Sunrays* [93]. *Sunrays* is a three dimensional ray tracing program that simulates the optical effects in stack systems of layers with different optical characteristics. It uses a Monte Carlo approach to simulate reflectance, transmission, absorption, and parasitic absorption spectra of the modeled structures. With *Sunrays* it is possible to model optical systems with variable textures and multiple layers. *Sunrays* allows modeling of layers which are varied only vertically. However the BC-BJ solar cells have a strongly two-dimensional structure of the rear cell side. Therefore the modeling of this structure requires a modified simulation approach.

In order to enable simulation of the BC-BJ cell structure with the *Sunrays* program, the analyzed device was split into different, optically one-dimensional unit-cells, as shown in Figure 6-1. Each optical unit-cell was simulated separately. Finally, the individual

optical simulation results of each unit-cell were averaged using area weighted averaging factors. For simplicity reasons of this model, it is assumed that the arrangement of the unit cells is not relevant in this averaging. In reality however it is definitely a more complex problem. With this approach the analysis of the optical effects in different regions of the solar cell is performed.

All of the optical unit-cells (Figure 6-1) have the same optical characteristics on the front surface of the cell and in the bulk of the silicon wafer. The differences among the unit-cells are in the rear surface layer stack systems. The structure of the rear side layers of the chosen unit-cells is as follows:

1. bulk Si / BSF doping / rear passivation layer / Aluminum metallization
2. bulk Si / rear passivation layer
3. bulk Si / emitter doping / rear passivation layer / Aluminum metallization
4. bulk Si / emitter doping / Aluminum metallization
5. bulk Si / emitter doping / rear passivation layer / Aluminum metallization
6. bulk Si / BSF doping / Aluminum metallization

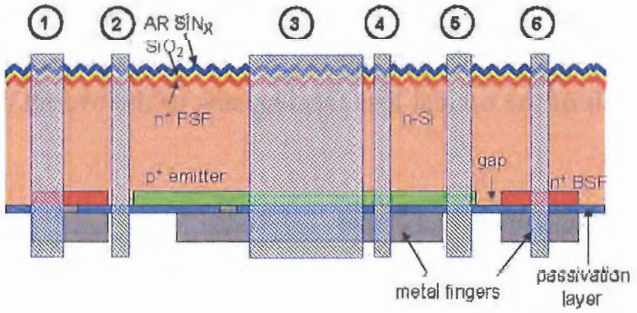


Figure 6-1 Schematic diagram of the different optical unit-cells in back-contact back-junction solar cell structure. Six different optical unit-cells with different rear side structures are shown.

6.2.3 Free carrier absorption

In silicon solar cells there are different light absorption mechanisms. To maximize the conversion efficiency of a photovoltaic device, the desired absorption process is the intrinsic absorption, also called bandgap absorption. In this process, if the energy of the incoming photon is higher than the band gap, then an electron-hole pair can be generated. However, in heavily doped silicon layers, in addition to the bandgap absorption, free carrier absorption (FCA) also occurs. FCA is a process in which the

photon energy is absorbed by free carriers in either conduction or valence bands [143], [144]. In the solar cell the FCA is a parasitic process, which reduces the useful photon flux and reduces the photogenerated current, leading to a reduction in the device's performance. As mentioned above, the FCA process is especially significant in highly doped silicon layers, where the concentration of free carriers is high. The absorption coefficient for the intrinsic silicon and absorption coefficient of the FCA process in highly doped silicon are shown in Figure 6-2. The free carrier absorption coefficient can be calculated using the modeling proposed by Green [121]:

$$\alpha_{FCA} = 2.6\times10^{-18} N_D \lambda^3 + 2.7\times10^{-18} N_A \lambda^2 \qquad (6.1)$$

where N_D and N_A are the doping densities of the n- and p-doped region in cm^{-3} respectively and λ is the wavelength in micrometers.

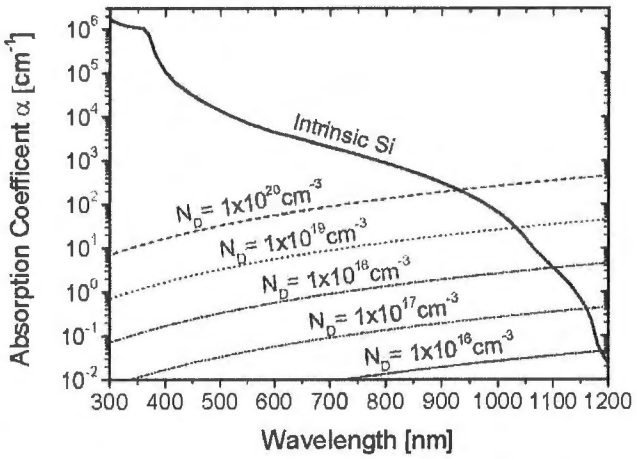


Figure 6-2 Absorption coefficient of intrinsic silicon (thick line) and absorption coefficients of the free carrier absorption process for different donor concentrations (thin lines) calculated with equation (4.1) as a function of wavelength. For the calculated free carrier absorption coefficients, the corresponding donor concentrations are shown.

As can be seen in Figure 6-2, the effect of FCA is especially significant for long wavelengths in the range of 1000 to 1200 nm. In solar cells with good light trapping properties, the light in this wavelength range may pass many times through the wafer thickness and through the highly doped regions at the same time. Thus, the FCA process can significantly contribute to the reduction of the amount of low energy photons available for the photogeneration of electron-hole pairs.

In the *Sunrays*, the FCA process in highly doped cell regions, such as front surface field, back surface field, and emitter doping is not taken into account. In order to analyze the influence of this effect on the optical losses of the BC-BJ cell, an additional layer on the back cell side, possessing the refractive index (n) of silicon, but an absorption coefficient (α_{FCA}) calculated with equation (4.1), was introduced.

6.2.4 Distribution of optical losses

The resulting simulation spectra of reflectance and transmission for a BC-BJ solar cell are shown in Figure 6-3. The experimental results are shown as well. A good agreement between the measured and simulated results indicates that the simulation approach, introduced in the previous section, allows a good description of the device. Note that the reflection is nearly zero at a wavelength of 500 to 600 nm due to the absence of the front side metallization. Another important feature of the analyzed device is the non-zero transmission at long wavelength ranges. Transmission of 5-10 % at 1200 nm is caused by the not fully metalized rear surface. The interdigitated metallization grid covers around 60 % of the rear cell surface. The remaining 40 % of the rear surface is not covered with metal. Therefore the weakly absorbed light can pass through the cell without being absorbed.

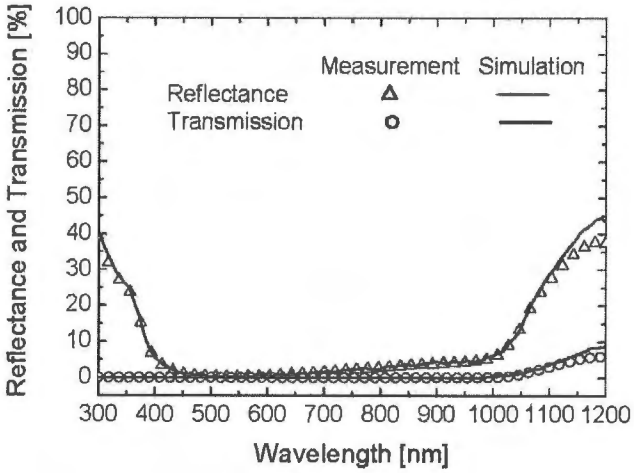


Figure 6-3 *Measured and simulated reflectance and transmission spectra of a back-contact back-junction cell with a pitch of 2200 µm and base resistivity of 1 Ω cm. The simulated reflectance shows good agreement with the measured data. The measurements were done using an integrating sphere set-up.*

According to the optical simulations of the device, the maximal short-circuit current density $J_{SC,opt}$ of 41.1 mA/cm^2 can be generated assuming no recombination and

resistance losses. By comparing the ideal short-circuit current ($J_{SC,ideal}$) shown in Table 6-1 with the $J_{SC,opt}$, a loss in short-circuit current due to the non-intrinsic optical loss mechanisms ($J_{opt,loss}$) can be determined. For a BC-BJ solar cell with 1 Ω cm base resistivity and thickness of 160 µm under AM1.5g illumination, the $J_{opt,loss}$ is 2.93 mA/cm^2.

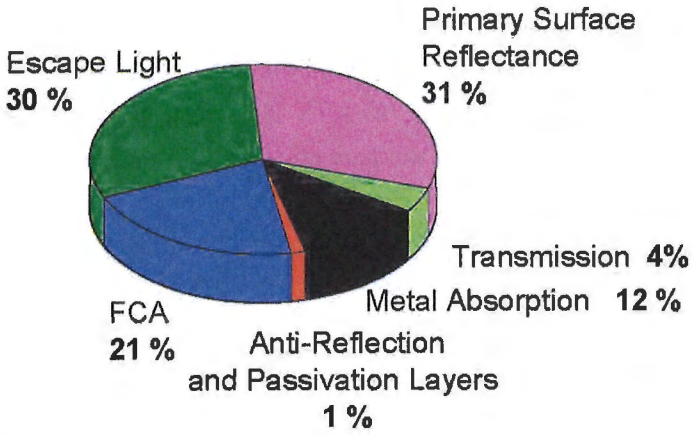


Figure 6-4 Distribution of the modeled optical loss mechanisms in BC-BJ cells with pitch 2200 µm and 1 Ω cm base resistivity under AM1.5g illumination with 0.1 W/cm². Note the significant influence of the free carrier absorption caused by the presence of the highly doped emitter and BSF regions.

In order to quantify the effect of every single layer and process, two simulations are required: one with normal absorption coefficients of every layer, and the other one with an absorption coefficient of a specific layer set to zero for all wavelengths. The difference of the two spectra equals the parasitic absorption in the specific layer. Figure 6-4 shows the modeled distribution of the optical loss mechanisms in the BC-BJ solar cell. The largest loss mechanism is the primary surface reflectance, which accounts for 31 % of all optical losses. The primary surface reflectance is caused by the non-optimal properties of a single layer antireflection coating. The second largest contribution to the optical losses is the escape light (30 %). Escape light is a result of non-ideal light trapping, where light rays are reflected out of the cell after multiple internal reflections in the cell. The next largest loss mechanisms are the free-carrier absorption (21 %) in the highly doped emitter and BSF regions and absorption in the metal layer (12 %). The influence of the FCA process is significant and caused by the large coverage of the highly doped regions (BSF, emitter) on the rear cell side and very good light trapping properties, which result in multiple passes of the long wavelength

light through the highly doped regions. The impact of transmission (4 %) and absorption in antireflection and passivation layers (1 %) is only minor.

One remark about the optimization of the optical device design has to be made. The reduction of one of the optical loss mechanisms will not lead to the increase of the generated photocurrent by the same amount. The increase in J_{SC} will be smaller, because the gain resulting from reduction of one of the optical loss mechanisms will be partially distributed between the other optical loss effects. For example, the replacement of the partial metal coverage on the rear cell side with full area aluminum would lower the transmission losses to zero. However, the reduction of transmission losses will result in the increase of the parasitic absorption in the aluminum.

Table 6-2 Modeled reduction of the solar cell parameters due to optical losses, for a 160 µm thick n-type BC-BJ cell with pitch of 2200 µm and 1 Ω cm base resistivity under AM1.5g illumination with intensity of 0.1 W/cm². The influence of non-intrinsic recombination losses and series resistance losses were not included in the modeling.

		Limit imposed by	
		intrinsic losses	optical losses
J_{SC}	[mA/cm^2]	44.0	41.1
V_{OC}	[mV]	742.5	741.3
FF	[%]	86.5	86.5
η	[%]	28.3	26.3
$\Delta\eta$	[%]		**-2.0**

6.2.5 Influence of optical losses on the cell efficiency

Optical losses reduce the amount of the photo-generated electron-hole pairs, which mainly reduces the short-circuit current density. However, a reduction of J_{SC} causes a reduction in the open-circuit voltage and the fill factor as well. The effect of the reduced V_{OC}, FF and efficiency can be calculated similarly to the calculations made in section 2.4, using the equations below:

$$J(V) = J_{SC,opt} - qWU_{rec,int} \tag{6.2}$$

$$\Delta\eta_{opt} = \eta_{opt} - \eta_{int} \tag{6.3}$$

$J_{sc,opt}$ is the short-circuit current density modeled considering the optical losses. The recombination and resistive losses are not taken into account in this calculation. η_{opt} is the cell efficiency limit imposed by the intrinsic recombination and optical losses and non-intrinsic optical losses calculated with equation (6.2). $\Delta\eta_{opt}$ is the reduction in the cell efficiency due to optical losses. The influence of the non-intrinsic optical losses on the solar cell parameters is summarized in Table 6-2. In the device analyzed, the optical losses cause 2.0 % absolute efficiency loss.

6.3 Recombination losses

6.3.1 Modeling of the saturation current densities

The non-intrinsic recombination losses include the surface recombination, the Auger recombination in highly doped regions of the solar cell, the bulk recombination, and the recombination at metal-semiconductor contacts. Each of the recombination processes can be described by its individual value of the saturation current density J_0. The total saturation current density of the solar cell can then be calculated as an area-weighted sum of the saturation current densities of the different cell regions.

The saturation current densities of the highly doped regions (emitter, BSF) for both passivated and metalized case were taken from the literature. The references used for different doping types are listed in Table 6-3. The published values of J_0 for highly doped regions with different sheet resistance were fitted. According to the fit function, the J_0 values for the sheet resistance of the doping profiles applied in the analyzed cell structure were calculated.

The saturation current densities of the bulk [145] and the gap regions can be calculated analytically by using the equations (3.2) and (6.5) respectively:

$$J_{0,Bulk} = \frac{qWn_i^2}{N_{Bulk}\tau_{Bulk}} \tag{6.4}$$

$$J_{0,Gap} = \frac{qn_i^2 S_{Gap}}{N_{Bulk}} \tag{6.5}$$

where n_i is the intrinsic carrier concentration, N_{base} is the doping density of the bulk, τ_{bulk} is the lifetime of the minority carriers in the bulk and S_{Gap} is the surface recombination velocity of the gap region. S_{Gap} was calculated according to the model of Cuevas et al. [94] and for a base doping of N_{base}=5×10^{15} cm^{-3}, which corresponds to base resistivity of 1 Ω cm, thus S_{Gap}= 70 cm/s. The saturation current density of the

front surface field doping was experimentally determined in section 7.3. Therefore, the experimental result for $J_{0,FSF}$ obtained in this work was applied here.

The area weighted results are summarized in Table 6-3. The total saturation current density of the solar cell equals 227 fA/cm^2. The largest contribution is due to passivated and metalized emitter doping, which account for 47.1 % of the total J_0. Such a high emitter saturation current contribution is caused by the large coverage of the emitter on the rear cell side and high doping level of the emitter profile. The relatively small contribution of the highly recombinative contacted areas is caused by the very small area coverage of the metal-semiconductor contacts, which totals 5 % for both contact polarities.

Table 6-3 *Modeled saturation current densities and their contributions to the overall J_0. Calculations were made for an n-type BC-BJ cell with 1 Ω cm base resistivity and 148 Ω/□ sheet resistance of the FSF. The saturation current densities were area weighted proportionally to their coverage on respective surfaces. Literature sources for the saturation current densities are given. J_0 values were calculated for n_i=1×10 cm^{-3} and T=25°C.*

	Reference	Area weighted J_0 [fA/cm^2]	Fraction of $J_{0,total}$ [%]
Boron Emitter (passivated)	[95], [85], [146]	98	43.3
Boron Emitter (metallized)	[85]	8.6	3.8
Phosphorus BSF (passivated)	[147], [148]	30	13.1
Phosphorus BSF (metallized)	[147]	7	2.9
Bulk	[145]	26	11.3
Gap regions	[94]	37	16.4
Phosphorus FSF (passivated)	this work	21	9.2
$J_{0,total}$		**227**	**100**

6.3.2 Influence of recombination losses on the short-circuit current

A general analysis of the influence of the two most important parameters of the back-junction solar cell structure, namely the front surface recombination S_{front} and the diffusion length of the carriers L, on the short-circuit current was already presented in section 2.3. Here the specific calculations of the J_{SC} losses due to measured S_{front} and L are presented. The 1-dimensional expression for the short-circuit current of the back-junction solar cell structure in the case of n-type base doping and monochromatic illumination with light of absorption coefficient α is given by [149]:

$$J_p(\alpha) = qF_{ph}(1-R)\left(\frac{\alpha L_p}{\alpha^2 L_p^{\,2}-1}\right)\cdot \left[\frac{\left(\frac{S_{front}L_p}{D_p}+\alpha L_p\right)-e^{-\alpha W}\left[\frac{S_{front}L_p}{D_p}\cosh\left(\frac{W}{L_p}\right)+\sinh\left(\frac{W}{L_p}\right)\right]}{\frac{S_{front}L_p}{D_p}\sinh\left(\frac{W}{L_p}\right)+\cosh\left(\frac{W}{L_p}\right)}-\alpha L_p e^{-\alpha W}\right] \tag{6.6}$$

where J_p is the hole current density, q the elementary charge, D_p the electron diffusion coefficient, F_{ph} the incident monochromatic photon flux density, R is the reflection coefficient, S_{front} is the front surface recombination velocity, L_p is the hole diffusion length, W is the wafer thickness. Integration of J_p for the whole light spectrum results in a short-circuit current density as a function of L_p and S_{front}.

Table 6-4 *Influence of the non-perfect collection efficiency of the carriers in on the short-circuit current density of the back-junction solar cell structure. J_{SC} losses due non-zero front surface recombination velocity and finite carrier lifetime was calculated for S_{front}=6.6 cm/s, τ_{bulk}=1 ms, ρ_{base}=1 Ω cm, W=160 µm.*

τ_{bulk} [ms]	S_{front} [cm/s]	J_{SC} [mA/cm^2]	ΔJ_{SC} [mA/cm^2]
∞	0	41.1	-
1	0	40.6	-0.5
∞	6.6	40.8	-0.3
1	6.6	40.3	**-0.8**

Using the equation (6.6) and the light absorption simulated with *Sunrays* as described in section 6.2.2, the short-circuit current losses due to non-zero recombination at the front surface and due to finite bulk lifetime of the carriers were calculated. Calculations were performed for base resistivity of 1 Ω cm, wafer thickness of 160 µm, S_{front}=6.6 cm/s was calculated using equation (6.7) and the measured saturation current density of the front surface field $J_{0,FSF}$=21 fA/cm^2 as shown in Table 6-3.

$$S_{front} = \frac{J_{0,FSF} N_{Bulk}}{q n_i^2} \tag{6.7}$$

The carrier lifetime in bulk τ_{bulk}=1 ms was assumed. The results are summarized in Table 6-4. The finite carrier lifetime causes 0.5 mA/cm^2 loss in J_{SC}. The non-zero front surface recombination results in another 0.3 mA/cm^2 loss in J_{SC}. Together both effects lead to 0.8 mA/cm^2 loss in J_{SC} and the maximal short-circuit current, resulting from optical and recombination losses ($J_{SC,rec}$), equals 40.3 mA/cm^2.

6.3.3 Influence of recombination losses on cell efficiency

The effect of the modeled saturation current densities on the open-circuit voltage and the cell efficiency can be calculated with the one-diode model:

$$J(V) = J_{SC,rec} - J_{0,total}\left(e^{qV/kT} - 1\right) \tag{6.8}$$

Where $J_{SC,rec}$ is the maximal short-circuit current resulting in optical and recombination losses. The influence of the $J_{0,total}$ on the V_{OC} can be calculated by transforming the one-diode equation:

$$V_{OC} = \frac{kT}{q} \ln\left(\frac{J_{SC,rec}}{J_{0,total}} + 1\right) \tag{6.9}$$

A good agreement between the analytically determined and measured V_{OC} can be observed. The open-circuit voltage calculated with equation (6.9) for T=25°C equals 666.3 mV. This result is very close to the V_{OC} of the best solar cell, which as shown in Table 6-1 equals 668 mV.

When the total saturation current density $J_{0,total}$ is determined, it is possible to calculate the influence of the recombination losses on the efficiency of the solar cell. Two calculations are needed. First, the efficiency limit (η_{opt}) due to intrinsic recombination losses and due to optical losses needs to be calculated (as shown in previous section).

Secondly, using equation (6.8), the efficiency limit imposed by non-intrinsic recombination losses (η_{rec}) can be determined. The difference between both efficiency limits is the efficiency reduction, which is caused only by the non-intrinsic recombination losses:

$$\Delta\eta_{rec} = \eta_{rec} - \eta_{opt} \tag{6.10}$$

where $\Delta\eta_{rec}$ is the reduction of the cell efficiency caused by the non-intrinsic recombination processes. The influence of the non-intrinsic recombination processes on the solar cell parameters is summarized in Table 6-5. The non-intrinsic recombination losses are causing an efficiency loss of 3.8 % absolute. However, it should be noted that the influence of the recombination losses in form of electrical shading on the short circuit current was not taken into account here. The influence of electrical shading losses on the short-circuit current was determined experimentally in section 6.4.

Table 6-5 Modeled reduction of the cell parameters caused by the non-intrinsic recombination processes for the BC-BJ cell of this thesis with pitch 2200 µm and 1 Ωcm base resistivity under AM1.5g illumination.

		Limit imposed by	
		intrinsic and optical losses	recombination losses
J_{SC}	[mA/cm^2]	41.1	40.3
V_{OC}	[mV]	741.3	666.3
FF	[%]	86.5	84.1
η	[%]	26.3	22.5
$\Delta\eta$	[%]		**-3.8**

6.4 Electrical shading

6.4.1 Increased lateral transport distance for the minority carriers

In back-contact solar cells, optical shading losses of the metallization grid can be avoided. However, electrical shading losses [150], [87] are still present due to the large

lateral dimensions on the rear cell side and due to the increased recombination rate in the regions of base busbar and base. The impact of this recombination on V_{OC} was already modeled in the previous section. In this section the impact of electrical shading on J_{SC} losses will analyzed. In Figure 6-5, a symmetry element of the BC-BJ solar cell is shown schematically. For the minority carriers that were photogenerated far away form the p-n junction, the large lateral dimensions of the BSF and non-diffused gap regions increase the required diffusion length before reaching the emitter. If the lateral dimensions of the base areas on the rear side are too large, or if the minority carrier lifetime is too low, then the carriers generated far away from the emitter may recombine before reaching the emitter. This results in a reduction of the quantum efficiency in the rear side regions of the solar cell that are not covered by an emitter.

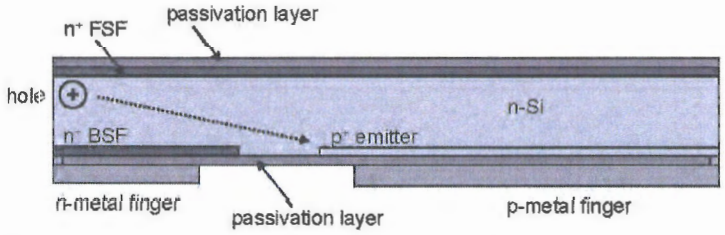


Figure 6-5 Increased lateral diffusion path for the minority carriers which were photogenerated far away from the p-n junction can lead to the recombination of these carriers before reaching the emitter. A symmetry element of the BC-BJ solar cell is shown.

6.4.2 Light beam induced current mapping

A light beam induced current (LBIC) [133] map of the 2×2 cm^2 laboratory solar cell is presented in Figure 6-6. One can clearly recognize the reduced EQE signal over the base fingers and busbar. The EQE drops down to nearly zero above the base busbar, even though no optical shading in this region is present. This effect is caused by (a) large lateral distances which the minority carriers need to diffuse in order to be collected by the p-n junction and (b) by the enhanced recombination over the gap and BSF areas which have high saturation current densities.

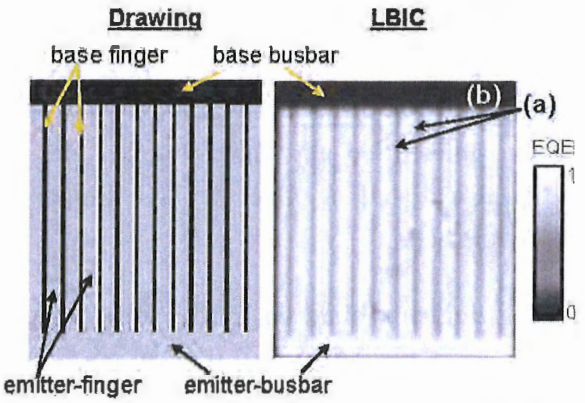


Figure 6-6 Sketch (left) and LBIC map (right) of the rear side of the BC-BJ silicon solar cell. The reduced EQE signal above the base fingers (a) and base busbar (b) are visible. The active cell area is 2x2 cm² and the busbar area is 0.15x2 cm².

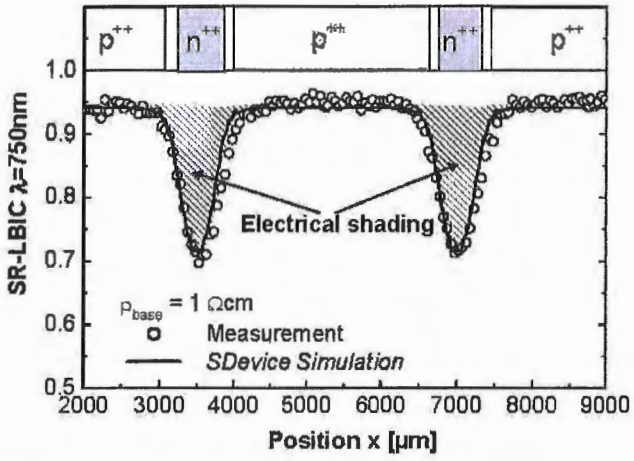


Figure 6-7 Measured and simulated external quantum efficiency line scans of a BC-BJ solar cells with 1 Ω cm base resistivity and a pitch of 3500 µm. Line scans were measured perpendicular to the p-n grid. The width of the p^{**} (emitter) diffusion and the n^{++} (BSF) diffusion are shown in the graph. The EQE was measured at a wavelength of 750 nm. The influence of electrical shading on the quantum efficiency is marked with thin lines.

6.4.3 LBIC line scans

In order to quantify the influence of the electrical shading over the base fingers (gap and BSF areas) on the solar cell efficiency, light beam induced current (LBIC) line scans were measured perpendicular to the p-n grid at a wavelength of 750 nm. The results are shown in Figure 6-7. A solar cell with a base resistivity of 1 Ω cm was

measured. The pitch of the cell analyzed was 3500 µm. The width of the p^{++} (emitter) diffusion and the n^{++} (BSF) diffusion are shown in the graph. Next to the measured LBIC signal, the 2D device simulation results are plotted in the graph. The EQE drops down above the BSF and undiffused gap regions (areas marked with thin lines in Figure 6-7) due to the electrical shading. Over the base fingers, the EQE drops from 0.95 down to 0.70 for 1 Ω cm cells.

6.4.4 Influence of the electrical shading on the cell efficiency

In order to determine the influence of the electrical shading losses on the solar cell's efficiency, the LBIC line scans shown in Figure 6-7 were integrated. The LBIC signal reduction over the base doping causes a 3.3 % absolute reduction of internal quantum efficiency for $\rho_{base} = 1\ \Omega$ cm. By making a simplified assumption that the electrical shading is equal for all wavelengths in the absorbed light spectrum, the short circuit current loss of 1.4 mA/cm^2 caused by electrical shading can be assumed. The maximal J_{SC} reduces from 40.3 to 38.9 mA/cm^2. The resulting efficiency loss caused by the reduction of J_{SC} equals 0.7 % absolute. Thus, the minority carrier recombination in the area of the rear side BSF and undiffused gap causes a significant efficiency loss in the analyzed device. Novel structures of a back-contact back-junction solar cells is which the electrical shading losses can be significantly reduced or even eliminated were recently proposed by Harder et al. [151] and Granek et al. [152].

6.5 Resistive losses

6.5.1 Modeling of series resistance losses

The series resistance (R_S) of BC-BJ solar cells can be described analytically by a network of several resistance elements connected in series as shown in Figure 6-8. The analyzed solar cells operate close to high-injection or under high-injection at maximum power point (MPP) conditions. Therefore both carrier types have to be included in the analysis of the series resistance.

In Figure 6-8, the extreme case for an electron and a hole is shown, where the lateral distance to the metal contacts is at a maximum. The resulting model is a quasi-one-dimensional model of the series resistances in the BC-BJ solar cell. This model is built of the lateral and vertical resistances in the bulk, the lateral resistance of the emitter and the back surface field, the metal-semiconductor contact resistances, and the resistance of the metallization fingers and busbar. The influence of the front n^+ diffused layer on the lateral current transport of the majority carriers was taken into account as parallel resistances to the base lateral resistance. A detailed analysis of the

influence of the front n^+ diffused layer on the lateral current transport is given in chapter 8. The descriptions of the individual resistance elements, as shown in Figure 6-8, are given in Table 6-6. The resistance of the individual resistance elements was calculated similarly to the series resistance model of the concentrator BC-BJ solar cells described in [35].

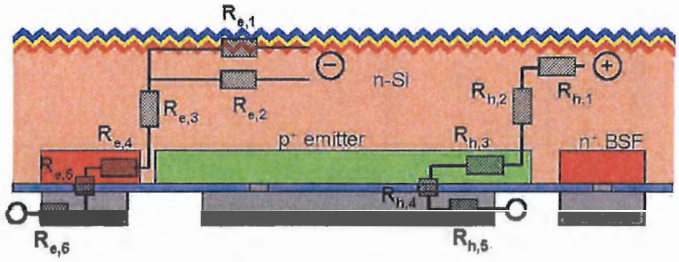


Figure 6-8 *Schematic diagram of the series resistance elements in BC-BJ solar cell that contribute to the analytical resistance model. The influence of the front surface field on the minority carriers (holes) lateral current transport was modeled using a parallel connection of lateral base and front surface field resistances.*

Table 6-6 *Explanation of the resistance symbols used in the quasi-one-dimensional resistance model shown in Figure 6-8.*

electrons		holes	
$R_{e,1}$	lateral FSF resistance	$R_{h,1}$	lateral base resistance
$R_{e,2}$	lateral base resistance	$R_{h,2}$	vertical base resistance
$R_{e,3}$	vertical base resistance	$R_{h,3}$	lateral emitter resistance
$R_{e,4}$	lateral BSF resistance	$R_{h,4}$	p-contact resistance
$R_{e,5}$	n-contact resistance	$R_{h,5}$	p-metal finger resistance
$R_{e,6}$	n-metal finger resistance		

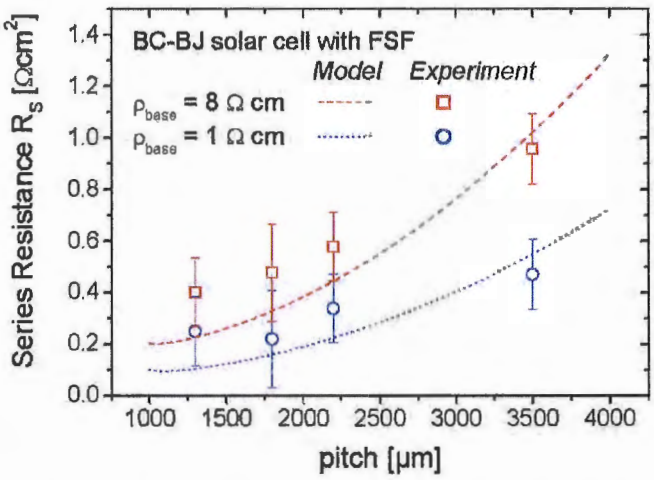


Figure 6-9 *Series resistance of the BC-BJ solar cells with FSF (ρ_{sheet} = 148 Ω/□) and base resistivity of 1 and 8 Ω cm for different pitches. Analytical modeling results (lines) and the experimentally determined series resistance (points) together with the error bars are shown. The conductivity modulation in the base under the maximum power point was taken into account. The size of the solar cells was 2×2 cm^2.*

The series resistance of the BC-BJ solar cells calculated analytically, using the series resistance model presented above, was compared to the experimentally determined series resistance of the processed solar. The series resistance of the fully processed solar cells was determined by comparing the SunsV_{OC} curve [153] with the one-sun IV-curve. For more details on this method to determine series resistance, see for example Ref. [154]. The analytical and experimentally determined series resistance of the BC-BJ solar cells with different base resistivity and pitch are shown in Figure 6-9. A good agreement between the analytical model and experimental data can be observed, proving the accuracy of the analytical model. The increase of R_S with increasing pitch is caused by a strong increase of the lateral base resistance with increasing pitch. See chapter 8 for more details on lateral base resistance issues.

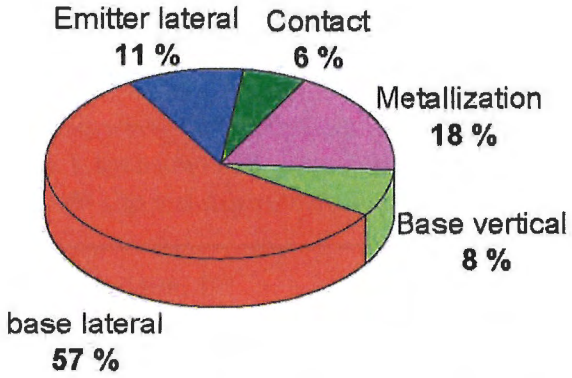


Figure 6-10 Distribution of the modeled series resistance in BC-BJ cells with pitch of 2200 µm, sheet resistance of the FSF of 148 Ω/□ and 1 Ω cm base resistivity. A solar cell with a size of 2×2 cm² was modeled. The total series resistance equals 0.18 Ω cm².

The distribution of the series resistance components in a BC-BJ cell with 1 Ω cm base resistivity, front surface field ($\rho_{FSF,sheet}$ = 148 Ω/□) and pitch of 2200 µm is shown in Figure 6-10. The lateral base resistance is the dominat resistance loss mechanism, contributing to 57 % of the total series resistance. The impact of lateral base resistance is very high due to the large lateral current transport distances required in the solar cell with a pitch of 2200 µm. A smaller pitch would decrease the lateral paths of the charge carriers and therefore reduce the lateral base resistance. It would be difficult, however, to decrease the pitch while using the low cost structuring technology. The impact of the metal fingers equals only 18 %, due to the small finger length in the cell size of 2×2 cm². The contribution of the metallization losses to the total series resistance will increase with an upscaling of the cell design to the production standard sizes of 12.5×12.5 cm² or larger. The total series resistance equals 0,18 Ω cm².

6.5.2 Influence of series resistance losses on cell efficiency

The series resistance causes a reduction of voltage at the maximum power point and therefore reduces the fill factor of the solar cell. The effect of the reduction of FF caused by R_S can be described using an approximation proposed by Green [4]:

$$FF_{Rs} = FF_{rec}\left(1 - R_S \frac{J_{SC}}{V_{OC}}\right) \tag{6.11}$$

where FF_{Rs} is the fill factor resulting from series resistance, optical and recombination losses, FF_{rec} is the fill factor limit imposed by the optical and recombination losses, not affected by resistance losses, R_S is the series resistance given in Ω cm², J_{sc} is the short-

circuit current density limited by the optical losses, and V_{OC} is the reduced open-circuit voltage limited by optical and recombination losses.

Table 6-7 Modeled reduction of the cell parameters caused by the series resistance for a BC-BJ cell with pitch 2200 µm and 1 Ωcm base resistivity and front surface field with sheet resistance of 148 Ω/□.

		Limit imposed by	
		intrinsic, optical and recombination (including electrical shading) losses	resistance losses
J_{SC}	[mA/cm^2]	38.9	38.9
V_{OC}	[mV]	666	666
FF	[%]	84.1	83.0
η	[%]	21.8	21.4
$\Delta\eta$	[%]		**-0.3**

Due to the low value of the series resistance, its influence on the short-circuit current was not taken into account. The reduction of the solar cell parameters resulting from the influence of the series resistance is summarized in Table 6-7. Series resistances of 0.18 Ω cm^2 causes fill factor loss of 1.1 % absolute; in this case, this results in a efficiency reduction of 0.3 % absolute.

6.6 Adding up the individual loss mechanisms

The presented model gives an overview of the different loss mechanisms in the back-contact back-junction solar cell structure developed in this work. The main results of the modeled solar cell efficiency are schematically shown in Figure 6-11 and summarized in Table 6-8. The evolution of the calculated current-voltage characteristics of the solar cell structure after stepwise introduction of the different loss mechanisms is presented in Figure 6-12.

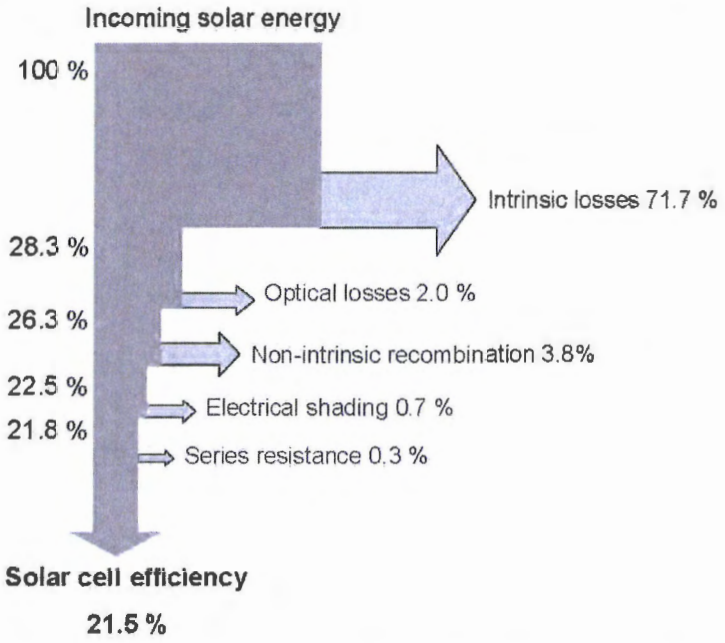


Figure 6-11 Schematic drawing showing the influence of different loss mechanisms on the reduction of the efficiency of the analyzed back-contact back-junction solar cell.

As can be seen in Table 6-8, a very good agreement between the modeled solar cell parameters and the experimental results of the best solar cell can be observed, proving the accuracy of the developed model. Both the modeled short-circuit current and the modeled open-circuit voltage are very close to the measured solar cell parameters. A slightly higher modeled fill factor may be a result of the fact that the edge effects, shunt resistance losses and the recombination in the space charge region were not taken into account in the calculations. These effects have a detrimental influence on the fill factor, thus introduction of these effects into modelling could result in a lower fill factor, with values closer to the measured one. The modelled overall cell efficiency equals 21.5 %, which is very close to the efficiency of the best solar cell (21.1 %).

The presented model is a powerful tool for the further optimization study of the solar cell structure. Improving the solar cell optics, reduction of the overall recombination losses and minimization/elimination of the electrical shading could enable reaching a solar cell efficiency of above 23 %.

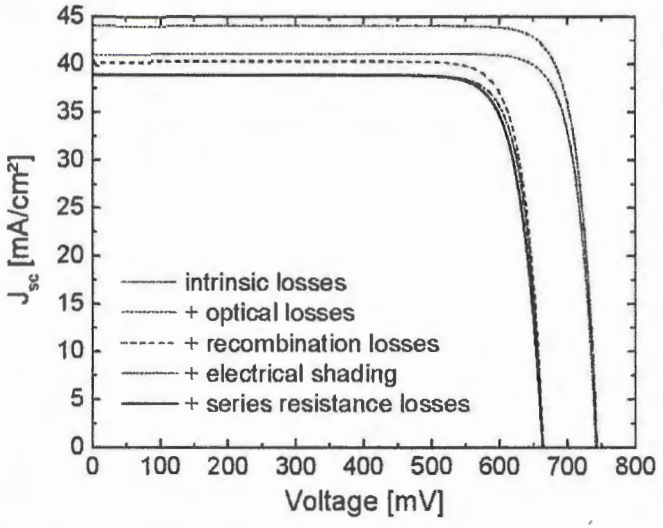


Figure 6-12 Evolution of the current-voltage characteristics of the analyzed BC-BJ solar cell structure after introduction of the different loss mechanisms.

Table 6-8 *Summary of the modeled cell parameters of a 160 µm thick n-type BC-BJ silicon solar cell with pitch of 1800 µm, base resistivity of 1 Ω cm and the FSF with sheet resistance of 148 Ω/□. The influence of different loss mechanisms on the solar cell parameters is shown. The results of the best experimental solar cell are shown for comparison.*

Parameter	Unit	Intrinsic losses	+Optical losses	+Non-intrinsic recombination losses	+Electrical shading losses	+Series resistance losses	Best measured solar cell
J_{SC}	mA/cm^2	44.0	41.1	40.3	38.9	38.9	38.6
ΔJ_{SC}	mA/cm^2	-	-2.9	-0.8	-1.4	0.0	
V_{OC}	mV	742	741	666	666	666	668
ΔV_{OC}	mV	-	-1	-75	0	0	
FF	%	86.5	86.5	84.1	84.1	83.0	82.0
ΔFF	%	-	0.0	-2.6	0.0	-0.91	
η	%	28.3	26.3	22.5	21.8	21.5	21.1
Δη	%	-	-2.0	-3.8	-0.7	-0.3	

6.7 Conclusions

A detailed study of loss mechanisms limiting the efficiency of the back-contact back-junction silicon solar cell developed in this work was presented. The analytical model included the intrinsic, optical, recombination and resistance losses occurring in the actual cell design. The experimental analysis of the electrical shading losses was also introduced to the modeling of the overall solar cell characteristics.

A very good agreement between the modeled solar cell parameters and the experimental results of the best solar cell was obtained, proving the accuracy of the developed model. The main loss sources in the analyzed solar cell structure are the recombination losses, accounting for the absolute efficiency loss of 3.8 %; the optical losses, which cause 2.0 % absolute efficiency loss; and the electrical shading, which causes 0.7 % absolute efficiency loss. Altogether, the analyzed loss mechanisms reduce the solar cell efficiency by 6.8 % absolute from 28.3 % to 21.5 %.

The presented model is a powerful tool for the further optimization study of the solar cell structure. The performed analysis showed that improving the solar cell optics, reduction of the overall recombination losses, and minimization of the electrical shading could enable reaching the solar cell efficiency of 23 %.

7 Front surface passivation using a front surface field

The passivation quality of different phosphorus-doped front surface field diffusion profiles was analyzed. J_{0e} values of different FSF diffusion profiles determined under low and high injection are in a good agreement. The presence of the random pyramids texture increased the J_{0e} by a factor of 1.3 to 1.7. The best solar cell efficiency of 20.8 % was obtained with a deep diffused Gaussian profile of the FSF. Increased doping concentration and depth of the FSF diffusion reduced J_{SC} and V_{OC} of the analyzed cells. The lifetime samples and the solar cells with FSF diffusion are stable under UV exposure in opposition to test structures and solar cells without FSF. The regeneration of the performance of the solar cells without FSF after degradation under UV exposure is possible by a forming gas anneal.

7.1 Introduction

Due to the fact that the p-n junction is placed on the rear surface of the back-contact back-junction solar cells developed and analyzed in the frame of this work, the requirements on the front surface passivation of this cell type are very high. Most of the photo-generation occurs close to the front surface, where the carriers can easily be lost by recombining at a poorly passivated surface. Thus, a low front surface recombination (S_{front}) is one of the critical factors influencing the efficiency of the back-junction cell type. The importance of the high quality of the front surface passivation in the case of the back-junction solar cells was already presented in more details in section 2.3. In the present chapter the quality of the front surface field passivation and its influence on the solar cell stability with respect to ultraviolet light is studied.

7.1.1 Surface recombination

The crystal lattice is severely disturbed at the surface. This results in a large density of the non-saturated bonds, also called 'dangling' bonds. Moreover at the surface the material defects related processing technology such as residues of chemicals and metals depositions are present. At the crystal surface these effects result in a high density of surface states within the bandgap, which cause surface recombination.

In this section the fundamentals of surface recombination are given following Aberle [155]. The recombination rate U_S via a single-level surface state, which is located at an energy E_t, is described by the Shockley-Read-Hall (SRH) theory [77], [78]:

$$U_S = \frac{n_S p_S - n_i^2}{\frac{n_S + n_1}{S_{p0}} + \frac{p_S + p_1}{S_{n0}}} \tag{7.1}$$

with

$$n_1 = n_i \exp\left(\frac{E_t - E_i}{kT}\right), \qquad p_1 = \frac{n_i^2}{n_1},$$
$$S_{n0} = \sigma_n \upsilon_{th} N_{st}, \qquad S_{p0} = \sigma_p \upsilon_{th} N_{st} \tag{7.2}$$

n_S and p_S are the electron and hole concentrations at the surface, S_{n0} and S_{p0} are the surface recombination velocity parameters of electron and holes, σ_n and σ_p are the capture cross sections for electrons and holes, N_{st} is the number of surface states per unit area, E_i is the intrinsic Fermi energy, n_i is the intrinsic carrier density, υ_{th} is the thermal velocity of the charge carriers, k is the Boltzman constant, T is the temperature.

The surface recombination velocity S is defined as $U_S = S\Delta n$, with Δn being the excess carrier density at the surface. In the case of the equal excess densities of electrons and holes at the surface ($\Delta n_S = \Delta p_S$), S can be expressed as [149] :

$$S(\Delta n_S) = \frac{n_0 + p_0 + \Delta n_S}{\frac{n_0 + n_1 + \Delta n_S}{S_{p0}} + \frac{p_0 + p_1 + \Delta n_S}{S_{n0}}} \tag{7.3}$$

Thus, the surface recombination velocity is also influenced by the injection level at the surface (Δn_S) and by the wafer doping (n_0 and p_0).

For the recombination velocity of the p-n junctions and high-low junctions, an effective surface recombination velocity S_{eff} can be defined at a virtual surface. This virtual surface is positioned at the edge of the surface space charge region, located at $x=d$:

$$S_{eff} = \frac{U_S}{\Delta n(x = d)} \tag{7.4}$$

The quality of the emitter or the highly diffused region is expressed using the emitter saturation current density J_{0e}. The relation between S_{eff} and J_{0e} for n^+ diffused regions equals:

$$S_{eff} = \frac{J_{0e}(N_A + \Delta n)}{q n_i^2} \tag{7.5}$$

7.1.2 Surface passivation methods

Analysis of the SRH theory of the surface recombination defined with equation (7.1) indicates that there are two ways to reduce the recombination rate at the silicon surface:

1. The surface recombination rate is proportional to the defect density at the surface (see equation (7.1)). Thus, it is beneficial to reduce the density of the surface states, what can be technologically achieved by growth or deposition of passivation layers. The most widely used examples of the passivation layers in silicon solar cell technology are the thermally grown silicon oxide (SiO_2) and silicon nitride (SiN_X) deposited using the plasma enhanced vapour deposition (PECVD). Both of these passivation layers are applied in the investigated solar cell structure in a form of a stack of passivation layers.

2. The SRH recombination process requires a pair of one electron and one hole. The recombination rate is the highest when the concentration of electrons and holes at the surface is equal. However, if the surface concentration of one of the carrier types is reduced, then the surface recombination rate is also reduced. There are two methods to reduce the concentration of one type of carriers:

   a. One is to implement a doping profile at the surface, which results in a reduction of one carrier type. This can be achieved by the high-temperature diffusion, which will result is a high-low junction [84] or p-n junction, depending on the polarity of the dopant and the silicon substrate. The phosphorus-doped front surface field, applied in the analyzed solar cells, is therefore a high-low junction which passivates the silicon surface by a strong reduction of holes concentration at the surface.

   b. The second method is the application of the field-effect passivation [156]. This can be achieved by electrical charges implemented in the passivation layer.

More details on surface passivation methods for silicon solar cells can be found in a review article of Aberle [155]. In the following, the front surface passivation quality of

the phosphorus doped front surface field combined with a stack system of SiO_2/SiN_X passivation layers will be analyzed.

7.2 Influence of the front surface field diffusion profile on the solar cell performance

A one-dimensional PC1D [63] simulations of a back-junction cell structure as presented in Figure 3-5 are shown in Figure 7-1. The influence of the front surface recombination velocity on the efficiency of the back-junction solar cells with and without front surface field diffusion is obvious: As already shown in section 2.3, with increasing S_{front} the efficiency of the cells without the front surface diffusion decreases rapidly. On the other hand the solar cells with front surface field diffusion profit from the reduction of the effective recombination velocity in a broad $S_{0,front}$ range. A properly designed FSF can therefore improve the efficiency of the back-unction cell for the non-perfectly passivated front surfaces, which is often the case for realistic processing conditions. However, comparing the range of $S_{0,front}$ in which the efficiency remains high for cells with and without FSF should be done carefully and consciously. It should be noted that the $S_{0,front}$ increases rapidly with increasing surface concentration of the phosphorus doping [94]. Therefore the $S_{0,front}$ of the solar cells with FSF diffusion is inherently orders of magnitude higher than in the case of solar cell without FSF diffusion.

The influence of the front surface recombination velocity is visible in the whole wavelength range of the internal quantum efficiency of the back-junction cells as can be seen in Figure 7-2. A lowly doped FSF results in high quantum efficiency. This is because the Auger recombination inside the highly doped region and the surface recombination velocity are low. A proper choice of the front surface field profile is therefore one of the most critical points in the design of the back-contact, back-junction solar cell device.

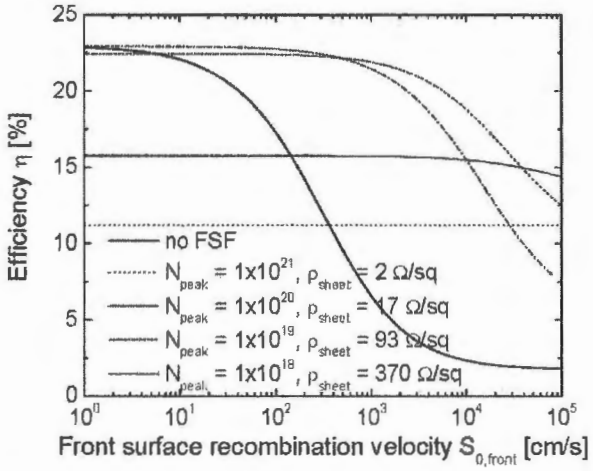


Figure 7-1 Influence of the front surface recombination velocity ($S_{0,front}$) on the efficiency of the back-junction n-type Si solar cells with different phosphorus FSF diffusion profiles (one-dimensional PC1D simulations). In simulations of the doping profiles a depth factor of 0.5 was used.

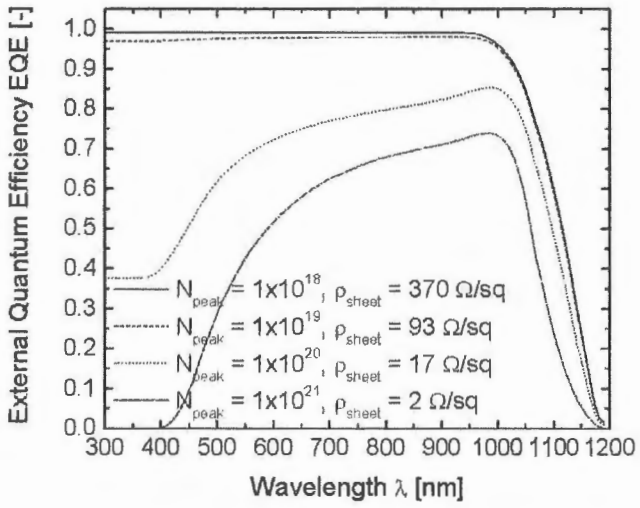


Figure 7-2 Internal quantum efficiency of an n-type back-junction solar cells for different front surface field diffusion profiles. $S_{0,front}$ calculated accordingly to model of Cuevas et al. [94] was assumed for this PC1D simulations. Depth factor of the diffusion profiles equals 0.5 in all simulations.

The importance of the selection of the appropriate diffusion profile for surface passivation is presented in the Figure 7-3. PC1D modelling results of the emitter saturation current density for both metalized and passivated Gaussian phosphorus

diffusion profiles are shown. The sheet resistance of the simulated diffusion profiles is presented in Figure 7-4.

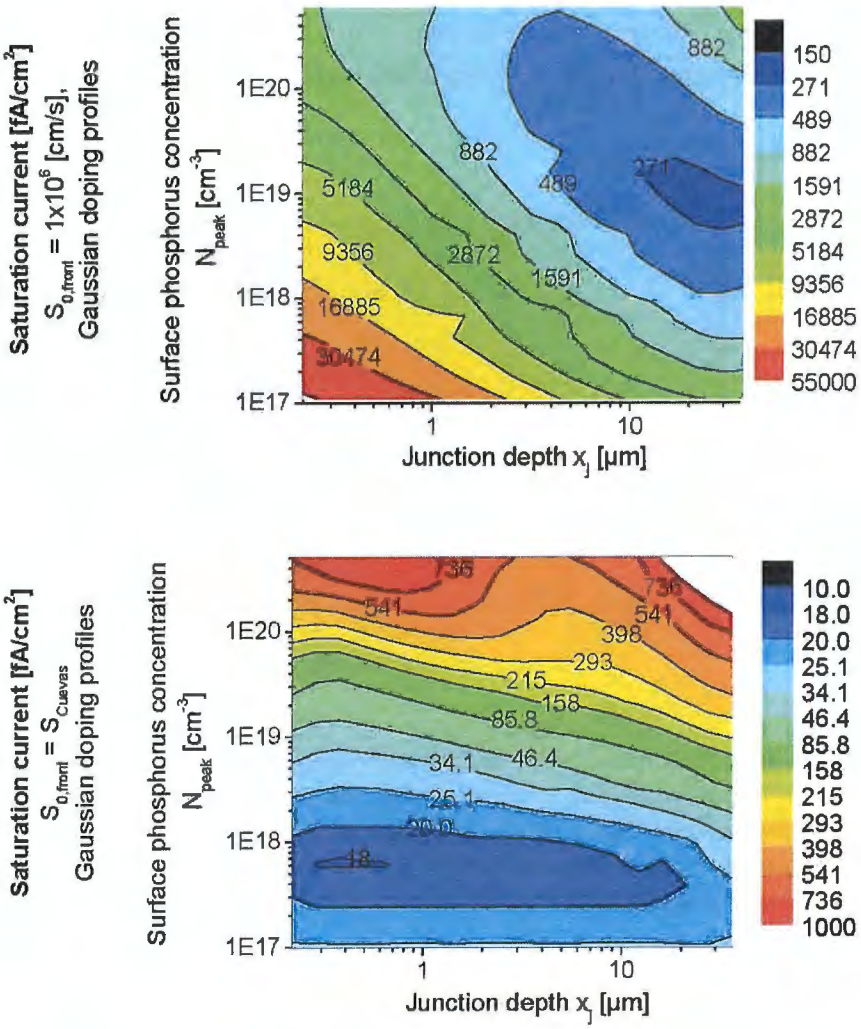


Figure 7-3 Emitter saturation current densities (J_{0e}) of the phosphorus doped Gaussian diffusion profiles calculated in a wide range of surface phosphorus concentration and junction depth. On top the case of the metalized diffusion profiles with $S_{0,front}=1\times10^6$ cm/s is presented. On the bottom graph, the case of the passivated diffusion profiles is shown. For the passivated emitter the $S_{0,front}$ was calculated using the model of Cuevas et al. [94], which was presented in 3.2.3. Note that the emitter saturation current density is presented in a logarithmic scale. The calculations were done using PC1D [63].

From the simulations it is clear that for the poorly passivated surfaces, highly doped and deep diffusion profiles are optimal in order to minimize the surface recombination (see Figure 7-3 top), with sheet resistance of about 10 Ω/sq. On the other hand, for the well passivated surfaces, an optimal diffusion profile is lowly doped and shallow (see Figure 7-3 bottom), with the sheet resistance of around 200 to 800 Ω/sq. These results are in a good agreement with the analytical modelling of del Alamo et al. [157].

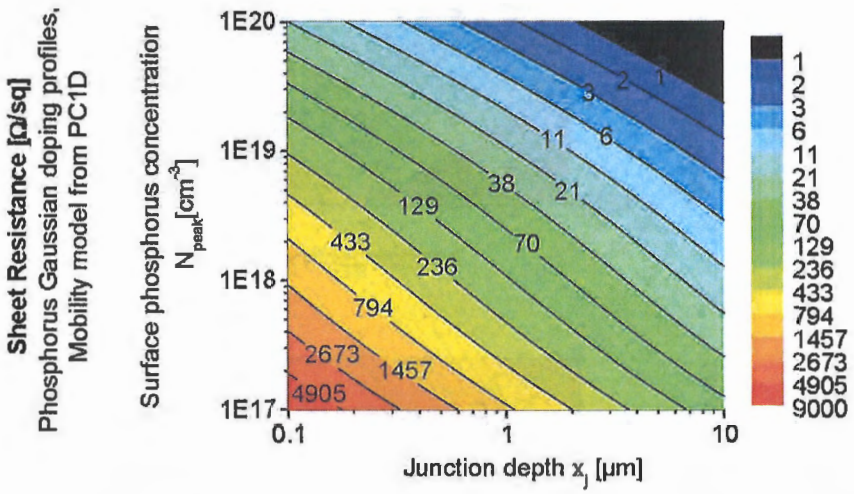


Figure 7-4 Sheet resistance of the phosphorus doped Gaussian diffusion profiles in a wide range of surface phosphorus concentration and junction depth. For the calculation of sheet resistance an electron mobility model of PC1D program [63] was taken. Note that the sheet resistance is presented in a logarithmic scale.

7.3 Surface passivation quality for different FSF diffusion profiles

King et al. [148], [20] and Cuevas et al. [147] studied the saturation current densities of the phosphorus doped emitters. In their work the Gaussian phosphorus profiles were analyzed using n^+pn^+ test structures. In the present work the focus is to analyze the FSF diffusion profiles on the n-type base, therefore in contrast to both authors here the n^+nn^+ samples with front surface field, without the p-n junction, were studied. Error-function diffusion profiles are formed by only a short oxidation step after phosphorus diffusion. The deep diffused Gaussian profile on the other hand, is a result of a long post diffusion oxidation process times and temperatures.

7.3.1 Processing of test structures for the determination of J_{0e}

Symmetrical n^+nn^+ test structures (see Figure 7-5) for lifetime measurements were processed on 250 µm thick n-type FZ-Si wafers. Base resistivities of 1 and 10 Ω cm were selected for this study. This base resistivity range is of interest for the high-efficiency back-junction back-contact solar cells processed in the frame of this study. The advantage of using high quality n-type FZ-Si is the very high bulk lifetime, as was already shown in section 4.2. Due to the high minority carrier lifetimes, the recombination in bulk material is minimum and the carrier lifetime is almost entirely limited by the surface recombination. This way an accurate determination of the surface recombination effects is possible.

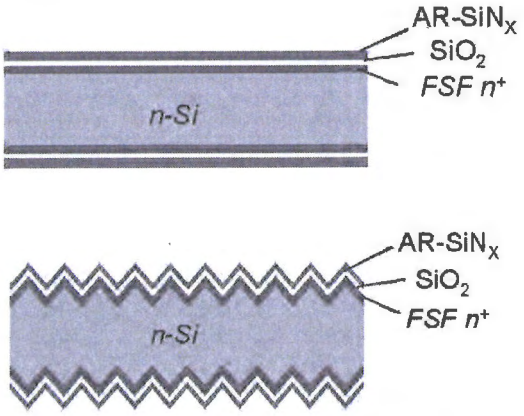


Figure 7-5 Symmetrical n^+nn^+ test structures for the lifetime measurements and the determination of the surface recombination current density. Test structures with planar (top) and textured (bottom) surfaces were processed.

Test samples with untextured (planar) and textured surfaces (random pyramids) were processed. The front surface field was created on both sample sides by a tube furnace phosphorus diffusion form liquid $POCl_3$ source. The phosphorus diffusion time was fixed for all diffusion profiles and the diffusion temperature was varied in the range from 780 to 840°C. This resulted in different n^+ error-function dopant profiles. The resulting diffusion profiles measured for planar samples are shown in Figure 7-6.

Next, the phosphorus glass was etched back in HF solution. For selected samples a deep Gaussian phosphorus profile (called 'deep diffusion') was created by a dry thermal oxidation at 1050°C to form a 105 nm thick antireflection SiO_2 layer. The high oxidation temperature caused redistribution of the phosphorus atoms and transition from the error-function dopant profile to Gaussian profile. The thick oxide was then etched-back in HF solution. Next, the thermal oxide of the planed thickness of about

10 nm for the passivation of the silicon surface was grown during a short dry oxidation process at the temperature of 850°C. Due to the short oxidation time and its low temperature, the doping profiles were not changed significantly.

The parameters such as sheet resistance (ρ_{sheet}), surface phosphorus concentration (N_S) and depths of the diffusion profile (x_j) of the resulting diffusion profiles are summarized in Table 7-1. The sheet resistance of the FSF doping was calculated by integrating the dopant profiles using the mobility model from Masetti et al. [158].

All wafers were processed in one oxidation step. However the oxide growth rate is different on differently doped surfaces [159]. This resulted in the oxide thickness variation of all samples in the range from 10 to 40 nm. Next, the antireflection 70 nm thick PECVD silicon nitride coating was deposited. Finally all samples were annealed at forming gas atmosphere (FGA) at the temperature of 425°C for 15 min.

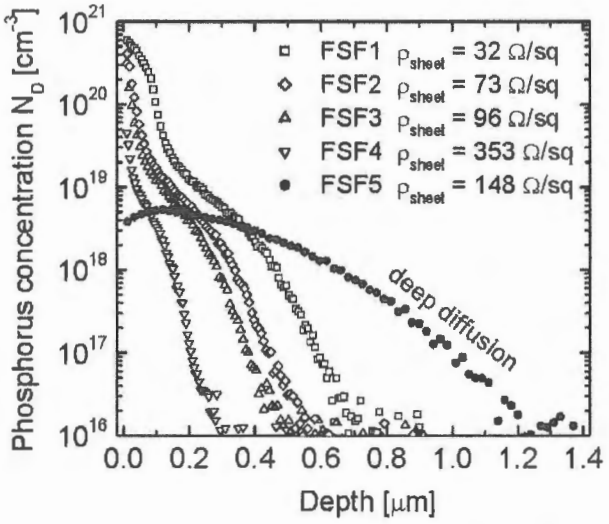


Figure 7-6 Secondary ion mass spectometry (SIMS) profiles of the studied phosphorus dopant profiles measured for untextured samples after all high temperature processing steps.

Table 7-1 *Parameters of the analyzed phosphorus doped front surface field diffusion profiles.*

Profile	Type	ρ_{sheet} [Ω/sq]	N_S [cm^{-3}]	x_j [µm]
FSF1	erfc	32	6.0×10^{20}	0.78
FSF2	erfc	73	4.0×10^{20}	0.66
FSF3	erfc	96	3.2×10^{20}	0.56
FSF4	erfc	353	4.5×10^{19}	0.38
FSF5	Gauss	148	3.8×10^{18}	1.44

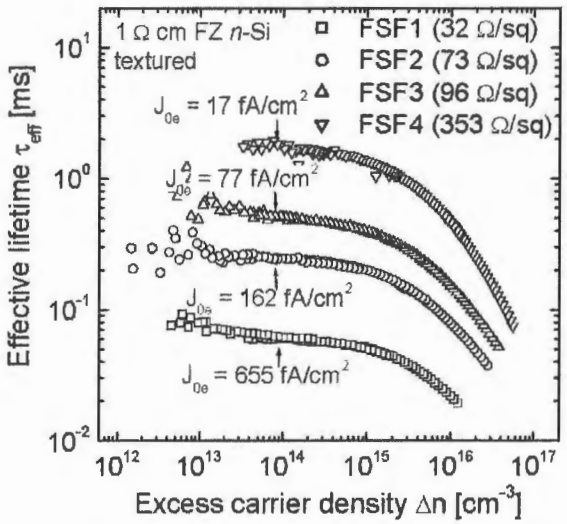


Figure 7-7 *Determination of the emitter saturation current density under low injection for different front surface field diffusion profiles. J_{0e} is determined at $\Delta n = 1\times10^{14}$ cm^{-3}.*

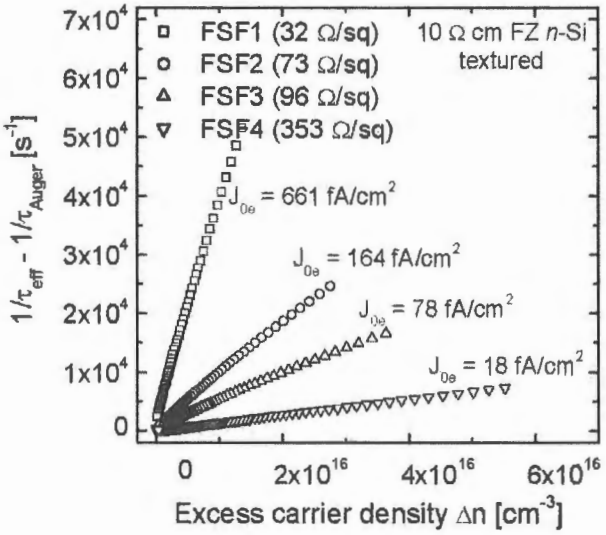


Figure 7-8 Determination of the emitter saturation current density under high injection for different front surface field diffusion profiles. J_{0e} is determined using the slope method.

7.3.2 Determination of J_{0e} under high and low injection

In order to determine the saturation current density of the phosphorus doped front surface field areas (J_{0e}) of the analyzed front surface field diffusion profiles, two methods were applied. J_{0e} was determined under low level injection for 1 Ω cm samples and using the *slope method* under high level injection for 10 Ω cm samples. This way a direct comparison of J_{0e} values determined by both methods was possible. Both methods for determination of J_{0e} under low and high injection are presented in section 3.1 Because of the different SiO_2 thicknesses of samples with different n^+ dopant profile, the optical factor required for QSSPC measurements had to be calculated for all samples. After measuring the oxide thickness, the optical factor was calculated using *SUNRAYS* [93].

Next to J_{0e}, the V_{OC} limit imposed by $J_0 = J_{0e}$ was calculated with the equation (2.1) for all determined J_{0e} ($J_{SC} = 40$ mA/cm^2 was assumed). For calculation of $V_{OC,\,limit}$ the standard testing temperature of 25°C was assumed. The $V_{OC,\,Limit}$ is the maximum V_{OC} that can be achieved with the used passivation. The influence of the bulk recombination was neglected in calculation of $V_{OC,\,limit}$.

$$V_{OC,limit} = \frac{kT}{q}\ln\left(\frac{J_{SC}}{J_0}+1\right) \tag{7.6}$$

Examples of the determination of the emitter saturation current density of the analyzed FSF diffusion profiles are shown in Figure 7-7 for the low injection case and in Figure 7-8 for the slope method in high injection.

7.3.3 J_{0e} for different FSF diffusion profiles

The determined J_{0e} values together with the corresponding $V_{OC,\,Limit}$ are summarized in Table 7-2 for the untextured samples and in Table 7-3 for the textured samples. A very good agreement between J_{0e} results determined under high injection using the slope method for the 10 Ω cm samples and in low injection for the 1 Ω cm samples was obtained. This shows that both methods enable a very good determination of J_{0e} of the samples with front surface field. The presence of p-n junction is not required to determine the recombination currents of the n^+ diffused regions [147]. Both methods of determination of J_{0e} proved also to be independent of the base doping.

Table 7-2 Summary of the J_{0e} results for the planar lifetime samples with different FSF diffusions. J_{0e} results for the 1 and 10 Ω cm samples determined under low and high injection respectively are shown together with the corresponding $V_{OC,\,limit}$.

			ρ_{base} = 1 Ω cm low-injection		ρ_{base} = 10 Ω cm high-injection	
Profile	Type	ρ_{sheet} [Ω/sq]	J_{0e} [fA/cm²]	$V_{OC,limit}$ [mV]	J_{0e} [fA/cm²]	$V_{OC,limit}$ [mV]
FSF1	erfc	32	404	652	414	651
FSF2	erfc	73	118	683	128	681
FSF3	erfc	96	61	700	69	697
FSF4	erfc	353	11	744	12	742
FSF5	Gauss	148	12	741	16	734
no FSF	-	-	3[i]	774	3[i]	774

[i] For the non-diffused surfaces a surface saturation current density J_{0s} was determined instead of diffusion saturation currant density J_{0e}.

Table 7-3 *Summary of the J_{0e} results for the textured lifetime samples with different FSF diffusions. J_{0e} results for the 1 and 10 Ωcm samples determined under low and high injection respectively are shown together with the corresponding $V_{OC,\ limit}$.*

			ρ_{base} = 1 Ω cm low-injection		ρ_{base} = 10 Ω cm high-injection	
Profile	Type	ρ_{sheet}	J_{0e}	$V_{OC,limit}$	J_{0e}	$V_{OC,limit}$
		[Ω/sq]	[fA/cm²]	[mV]	[fA/cm²]	[mV]
FSF1	erfc	32	655	639	661	639
FSF2	erfc	73	162	675	166	674
FSF3	erfc	96	77	694	90	690
FSF4	erfc	353	17	733	20	729
FSF5	Gauss	148	21	727	22	726
no FSF	-	-	15[i]	736	17[i]	733

Extremely low J_{0e} = 3 fA/cm² for the non-diffused surface were measured. This proves that stack system of the thin (10 nm) thermal oxide and PECVD SiN_X (70 nm) passivation is very effective. Phosphorus diffusion introduces increased Auger recombination and SRH recombination due to crystal defects [147], [160]. That is why J_{0e} of samples with FSF are higher than for samples without FSF for the untextured surfaces. Of the investigated diffusions deep Gaussian diffusion (148 Ω/sq) and shallow error-function (353 Ω/sq) diffusion result as expected in the lowest J_{0e} values. These are the two doping profiles with the lowest surface phosphorus concentration.

For textured surfaces J_{0e} is as expected higher than for the untextured samples. This is due to larger surface area of the textured samples and could also be caused by a different phosphorus concentration at the tops and bottoms of the pyramids as proposed by Glunz at al. [161]. For the textured samples with FSF the V_{OC} higher than 720 mV are possible when only the front surface recombination is regarded. Such a good surface passivation with thin SiO_2 and antireflection SiN_X layers have enabled processing of back-junction back-contact solar cells with efficiencies greater than 21 % as presented in this thesis.

Table 7-4 Comparison of the J_{0e} values for textured and planar samples for different front surface field doping profiles.

Profile	Type	ρ_{sheet}	$J_{0e,planar}$	$J_{0e,textured}$	$\frac{J_{0e,textured}}{J_{0e,planar}}$
		[Ω/sq]	[fA/cm^2]	[fA/cm^2]	[mV]
FSF1	erfc	32	404	655	1.62
FSF2	erfc	73	118	162	1.37
FSF3	erfc	96	61	77	1.26
FSF4	erfc	353	11	17	1.54
FSF5	Gauss	148	12	21	1.75
no FSF	-	-	3[i]	15[i]	5.00

Comparison of the J_{0e} data in Table 7-4 of the planar and textured samples indicates that the J_{0e} increases by a factor of 1.3–1.7 when going from a planar to a textured surface. This is similar to the increase measured by Kerr et al. [162] and by Moschner et al. [163] and is consistent with the increase in surface area by a factor of 1.73 compared to a planar surface.

A strong J_{0e} dependence of the sheet resistance is shown in Figure 7-9. The J_{0e} of the error-function diffusions could be very well fitted with a linear fit in the broad sheet resistance range. Deep Gaussian diffusion seems to have a different dependence of the ρ_{sheet}. It is concluded that this effect is due to differences in surface phosphorus concentration between error function profiles and the deep diffused Gaussian profiles.

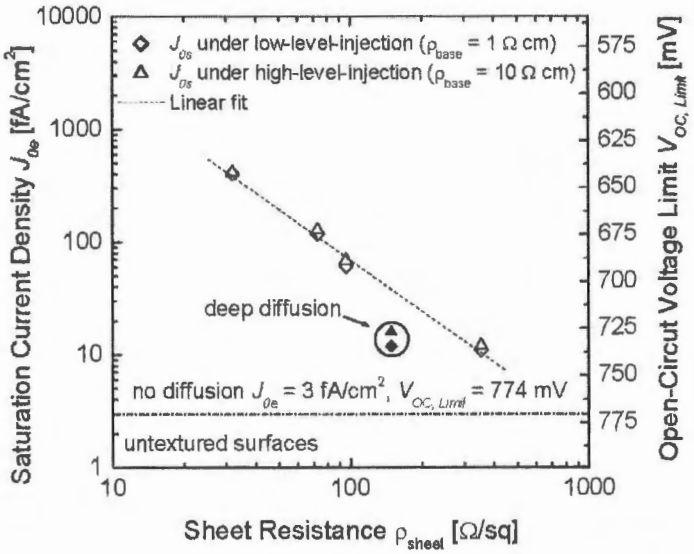


Figure 7-9 *J_{0e} and $V_{OC, Limit}$ as a function of sheet resistance of the n^+ diffusion for the untextured samples. J_{0e} of the sample without FSF is shown for comparison.*

7.4 Solar cells with different FSF diffusion profiles

Back-contact back-junction n-type silicon solar cells were processed with different FSF diffusion profiles. Thus, the influence of the FSF profile on the solar cell performance could be analyzed. The solar cells structure together with the processing technology is presented in chapter 4. Solar cells were processed on 1 Ω cm FZ n-type wafers. The thickness of the finished cells was about 160 µm. The active cell area was 4 cm^2.

7.4.1 Solar cell results

The current-voltage (I-V) parameters of the best solar cells for each FSF diffusion profile are summarized in Table 7-5. The diffusion profiles are labelled corresponding to the data presented in Table 7-1. The pitch of the analyzed cells was 1800 µm, with an emitter width of 1200 µm and a base width of 600 µm. The highest efficiency of 20.8 % was achieved on base resistivity of 1 Ω cm and deep diffused FSF (FSF5). The best efficiency of the BC-BJ solar cell processed without the FSF was 19.7 %. However, it should be noted the solar cells without the FSF diffusion had a very large distribution of the efficiency in the range of 10 to almost 20 %. This shows the importance of the stable front surface passivation quality. The distribution of the solar cell efficiency of the cells with FSF diffusion was much lower, in the range of 2 to 4 %

absolute. For the deeply diffused FSF profile the efficiency distribution was is the range of 0.5 % absolute.

The FSF doping has an influence primarily on the short-circuit current density and the open-circuit voltage as can be seen in Table 7-5. J_{SC} increases from 34.1 mA/cm^2 for the 73 Ω/sq FSF, to 38.1 mA/cm^2 for the deep diffused 148 Ω/sq FSF diffusion. At the same time V_{OC} increases from 647 mV to 663 mV due to reduction of the overall J_0 caused by reduction of the J_{0e} on the front side. The FF of the cells is on a high level of 81 to 82 % and is not being influenced by the different FSF profiles.

Table 7-5 I-V-parameters for the best solar cells with different front surface field diffusion profiles. Solar cells with base resistivity of 1 Ω cm and pitch of 1800 µm are presented. Results in the table are the designated cell area (2×2 cm^2) measurements.

Cell no.	FSF Profile	Type	ρ_{sheet} [Ω/sq]	J_{SC} [mA/cm^2]	V_{OC} [mV]	FF [%]	η [%]
BC47-2b	FSF2	erfc	73	34.1	647	81.7	18.0
BC47-6b	FSF3	erfc	96	36.1	657	81.9	19.5
BC47-11b	FSF4	erfc	353	37.8	651	81.1	20.0
BC47-16b	FSF5	Gauss	148	38.1	663	82.3	20.8
BC47-22b	no FSF	-	-	36.4	659	82.0	19.7

7.4.2 Analysis of the open-circuit voltage

The influence of the sheet resistance of the FSF doping on the V_{OC} is presented in Figure 7-10. The J_{0e} values of the planar and textured lifetime samples are plotted together with the liner fits (dotted lines). The results for the deep diffused Gaussian profile are marked with the closed symbols. The thin solid line represents the limit in V_{OC} imposed by the solar cell structure, i.e. by the bulk recombination, rear side recombination in the highly doped emitter, the back-surface field, in the gap areas and in the metal contact areas. For the analyzed solar cell structure this limit equals around 670 mV. Thus, if the front surface recombination would be eliminated ($J_{0e} = 0$), then the solar cells would have V_{OC} of 670 mV. However, due to non-zero front surface recombination the V_{OC} is decreased to values presented in Table 7-5.

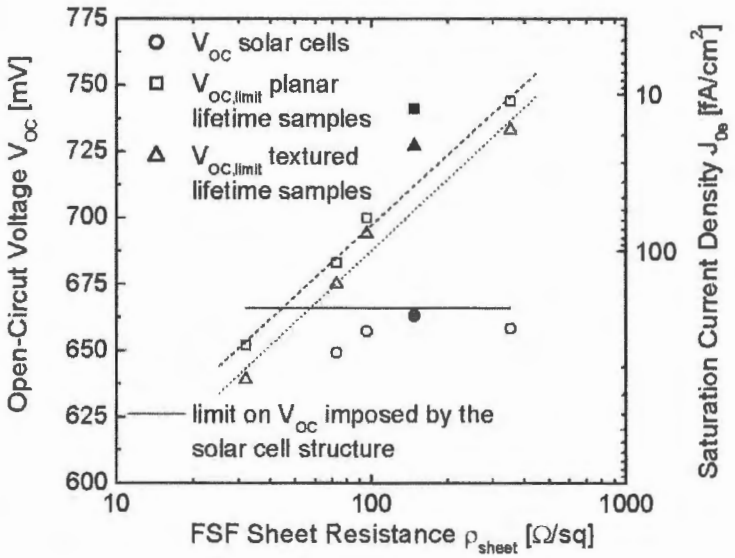


Figure 7-10 Open-circuit voltage of the processed solar cells with different sheet resistance of the FSF diffusions. Results for deep diffused Gaussian FSF profile (FSF5) are marked with closed symbols. $V_{OC,limit}$ imposed by the J_{0e} of the FSF diffusions for the planar and textured lifetime samples are shown as well.

7.4.3 Internal quantum efficiency

The internal quantum efficiency of the BC-BJ solar cells with different FSF diffusion profiles is presented in Figure 7-11. Again, the deeply diffused FSF profile results in the highest IQE, which explains the highest J_{SC} of these cells.

When the doping concentration of the front n^+ diffusion increases, the IQE decreases in the whole wavelength range. However, the most severe degradation of the IQE can be observed in the short wavelength range of 300 to 500 nm when increasing the FSF doping concentration. This effect can be well seen for the IQE of a solar cell with FSF2 doping profile (ρ_{sheet} = 73 Ω/sq). The light of this wavelength is absorbed at the front cell side, inside and in the vicinity of the highly doped FSF region. In this region the high surface recombination velocity, which increased with the surface doping concentration, and the low carrier lifetime due to Auger recombination leads to recombination of a significant percentage of the minority carriers.

Reduction of the surface doping concentration and reduction of the depth of the phosphorus doping profile leads to the strong increase of the spectral response in the short wavelength range as can be seen for the solar cells with FSF3, FSF4 and FSF5 doping profiles.

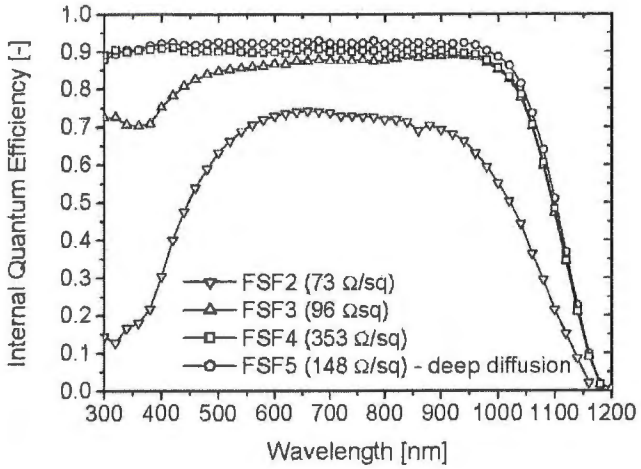


Figure 7-11 Internal quantum efficiency of the BC-BJ solar cells with different FSF diffusion profiles. Results of the solar cells with base resistivity of 1 Ω cm and pitch of 1800 μm are presented.

A strongly reduced IQE in the long wavelength range of 1000 to 1200 nm for the solar cell with highly doped front diffusion profile (FSF2) is believed to be caused by the enhanced free carrier absorption (FCA) process. Details of the free carrier's absorption process are given in section 6.2. A very good light trapping of the analyzed BC-BJ cells causes the weakly absorbed long wavelength light to travel many times through the wafer thickness and at the same time through the highly doped front phosphorus diffusion. In the case of the highly doped FSF2 diffusion profile each pass of the long wavelength light through the highly doped FSF region causes a parasitic absorption of the light, which in turn decreases the photogeneration of the electron-hole pairs in this wavelength range. Due to significantly lower surface doping and the depth of the diffusion profiles of the other analyzed FSF profiles, the FCA process is not causing any significant reduction of the spectral response in the long wavelength range of the spectrum.

7.5 Stability of the front surface passivation under UV-light exposure

7.5.1 UV-light influence on the front surface passivation

Already in 1988 Gruenbaum et al. [164], [165] reported that the efficiency of some of the point-contact concentrator solar cells developed by the Stanford University [16], decreased after exposure to concentrated sunlight. The decrease in solar cell performance was caused by the increase of the front surface recombination velocity.

The studies of Gruenbaum et al. showed that the ultraviolet (UV) component of the incident light spectrum caused damage on the front surface.

Gruenbaum et al. [166] performed the UV-exposure and photoinjection experiments. It was discovered that the UV light of energy greater than 3.1 eV causes increase of the surface recombination velocity ($S_{0,front}$) and interface state densities of the surfaces passivated with oxide. The energy of 3.1 eV corresponds to light with wavelength shorter than 400 nm. In the terrestrial solar spectrum there is a significant amount of photons with such energy. The absorption of the UV photons with wavelength shorter than 400 nm could inject electrons from the conduction band in Si into the conduction band of oxide. This photoinjection could be creating defects at the Si/SiO_2 interface.

However, Gruenbaum et al. [167] and Ruby et al. [168] showed that not all cell structures are prone to degradation under UV light. The formation of the diffused phosphorus region on the front side creates a high field which repels the minority carriers away from the recombination centers at the interface. Therefore even if the $S_{0,front}$ increases, the effective surface recombination velocity (S_{eff}) may remain low and not influence the efficiency of the solar cell. Thus, the additional positive effect of the FSF could be a significant improvement of the UV-light stability of the front side passivation, which is very important for the long term operation of the solar cells. The effect of the influence of the FSF diffusion on the UV stability of the solar cell performance is analyzed in the present section.

7.5.2 Lifetime test structures

The UV-stability of the front surface passivation with and without FSF was examined by exposing the n^+nn^+ lifetime samples to UV light (Xenon lamp) at one sun light intensity and a temperature of 50 °C. The tested samples were not covered with the module glass during the exposure, therefore the illumination spectrum absorbed by the test structures was rich in the high energy UV spectrum. The tested symmetrical lifetime samples were textured with random pyramids and the both surfaces were passivated with a thin thermal SiO_2 layer and an antireflection-SiN_X coating. The samples were annealed in a forming gas atmosphere prior to the exposure test. After each exposure step the saturation current density J_{0e} was determined.

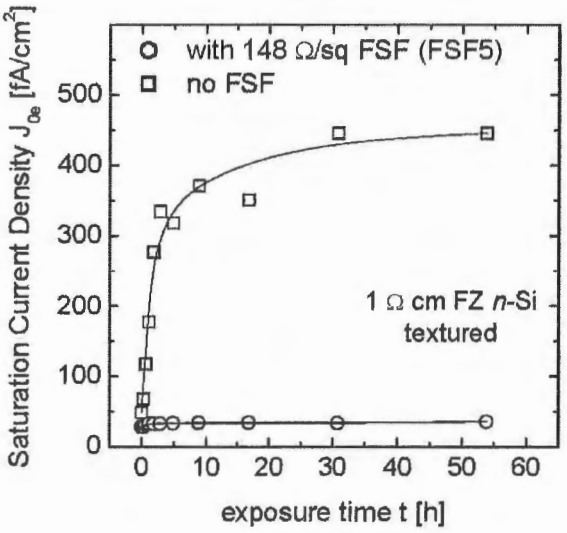


Figure 7-12 Passivation stability of textured n^+nn^+ lifetime samples with (circles) and without (squares) FSF during 55 hours of exposure to UV light. Lines are guides-to-the-eye.

Results of the UV exposure tests are shown in Figure 7-12. The lifetime of samples without FSF degrades significantly already after the first few hours of exposure. For the samples without the FSF, J_{0e} increases from initial value of ~30 fA/cm^2 to almost 450 fA/cm^2 after 55 hours of UV light exposure. Such a high increase of J_{0e}, which corresponds to $S_{0,front}$ of ~140 cm/s, will lead to a significant cell performance degradation, as already shown in section 2.3. Samples with FSF show no significant degradation. J_{0e} increases from ~30 to 35 fA/cm^2 in the case of the deep diffused 148 Ω/sq FSF diffusion. This proves that passivation using a FSF is stable and therefore appropriate for industrial applications in contrast to unstable passivation without FSF. Similar results were already obtained by Gruenbaum et al. [165].

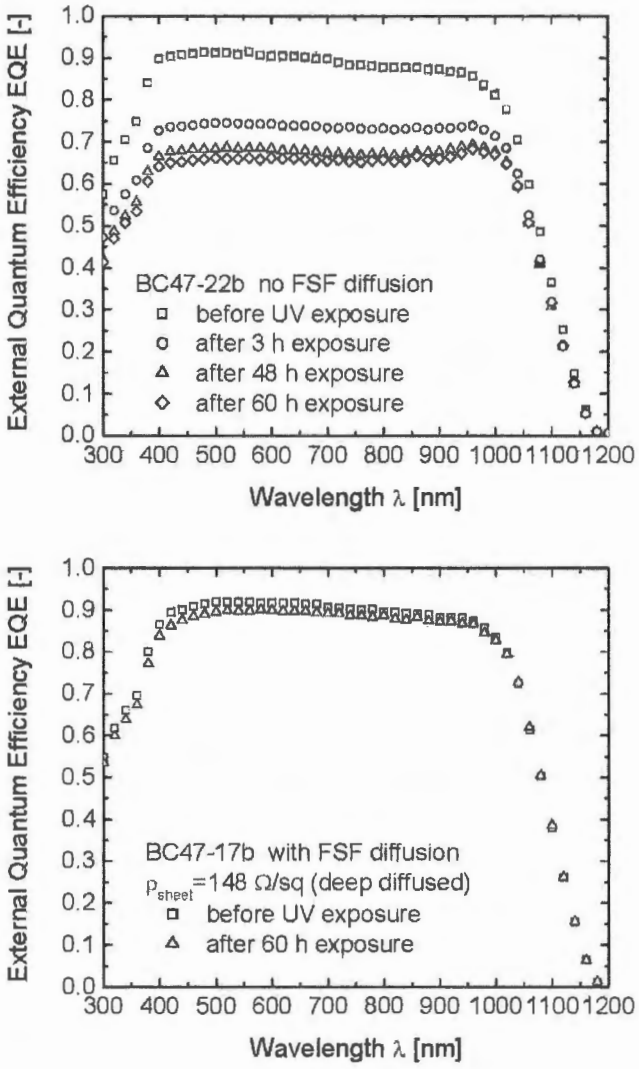


Figure 7-13 External quantum efficiency of the BC-BJ solar cells with (bottom) and without (top) the front surface field phosphorus diffusion after exposure to UV light. Duration of the UV exposure is shown in the graph. Both analyzed solar cells have base resistivity of 1 Ωcm and pitch of 1800 μm.

7.5.3 Solar cell results

Solar cells with and without the front n^+ diffusion were selected for the analysis of the performance stability under UV exposure (Xenon lamp) with illumination intensity of one sun and temperature of 50 °C. Solar cells with high starting performance (performance before UV light exposure) were analyzed in this test. The selected cells had efficiencies in the range of 19 to 20.5 %.

In Figure 7-13 the external quantum efficiency of the solar cell with (bottom) and without (top) the FSF measured after stepwise exposure to UV light. EQE of the solar cell without FSF degrades rapidly from 92 % to 75 % at wavelength of 500 nm already after 3 hours of exposure to UV light. After 60 hours of UV exposure the EQE of the solar cell without FSF decreases even further to 65 %. Thus, an EQE decrease of nearly 30 % absolute was caused by 60 hours of exposure to UV light in the case of the cell without the FSF. At the same time, the EQE of the solar cell with deep diffused FSF (FSF5) showed only minimal degradation after 60 hours of UV exposure: The EQE dropped from 92 % to 88 % at wavelength of 500 nm. Thus, the presence of the n^+ diffused layer on the front cell side drastically improves the stability of the solar cell under the UV exposure.

Table 7-6 *Front surface recombination velocity before and after exposure to UV light determined by (left column) analysis of the lifetime structures exposed to UV light and (right column) by fitting of the measured EQE using the PC1D model of the back-junction solar cell.*

	$S_{0,front}$ measured using lifetime samples [cm/s]	$S_{0,front}$ determined by PC1D fitting of the measured EQE of the solar cell [cm/s]
before UV exposure	16	18
after 60 h of UV exposure	138	145

The influence of the UV exposure on the EQE of the solar cell without FSF was analyzed in more detail with the results of the lifetime test structures and using PC1D simulations. First, the $S_{0,front}$ of the textured lifetime samples was measured before and after UV exposure. Secondly, the measured EQEs were fitted using the PC1D model presented in section 3.2.2. In order to fit the EQE results in the short wavelength range the $S_{0,front}$ was varied. The PC1D fit in the long wavelength range is not in a very good agreement with measured data due to strong influence of the two-dimensional effects, which could not be described by the one-dimensional PC1D simulation. The results are summarized in Table 7-6 and graphically presented in Figure 7-14. A very good agreement between the $S_{0,front}$ determined by analysis of the lifetime samples and by fitting of the EQE of the solar cells was obtained. This proves that the increase of

$S_{0,front}$ during the UV exposure is responsible for the degradation of the solar cell performance.

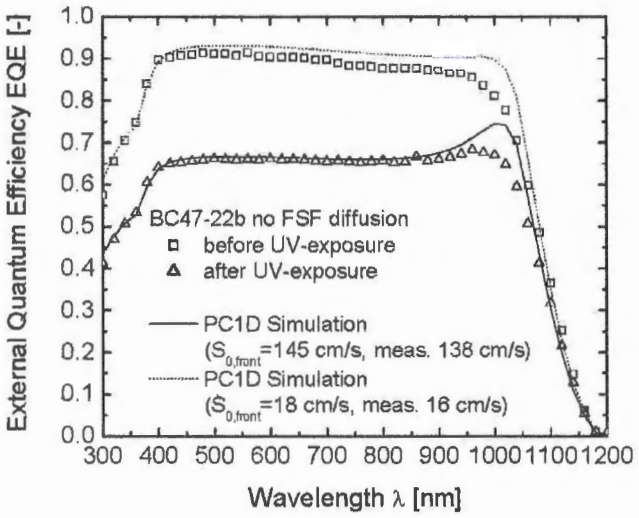


Figure 7-14 External quantum efficiency of the BC-BJ solar cell without the front surface field measured before and after 60 hours of exposure to UV light. PC1D simulations of the measured EQE with fitted $S_{0,front}$ are shown as well (thin lines).

7.5.4 Regeneration of the UV-degraded solar cells

During the illumination of the solar cell with UV light, the photoinjection of the electrons from the conduction band in silicon to the conduction band of oxide creates interface states. Increase of the interface states density at the Si/SiO_2 leads to significant reduction of the solar cell performance as shown in the previous sections.

The solar cell without FSF after UV degradation was exposed to the anneal process in the forming gas (N_2H_2) atmosphere (FGA) at the temperature of 425 °C and process duration time of 25 minutes. The elevated temperature and the hydrogen rich atmosphere leads to strong reduction of the interface states of the Si/SiO_2 interface during the FGA process [169]. This way the interface states that were created by the UV exposure can be passivated, leading to the reduction of the surface recombination velocity. In Figure 7-15 the external quantum efficiency of the BC-BJ solar cell without the FSF is shown before and after UV exposure and after FGA process. The FGA process performed after the UV exposure almost perfectly reduces the detrimental effect of the UV exposure, and regenerates the front surface passivation to the stadium as before the exposure.

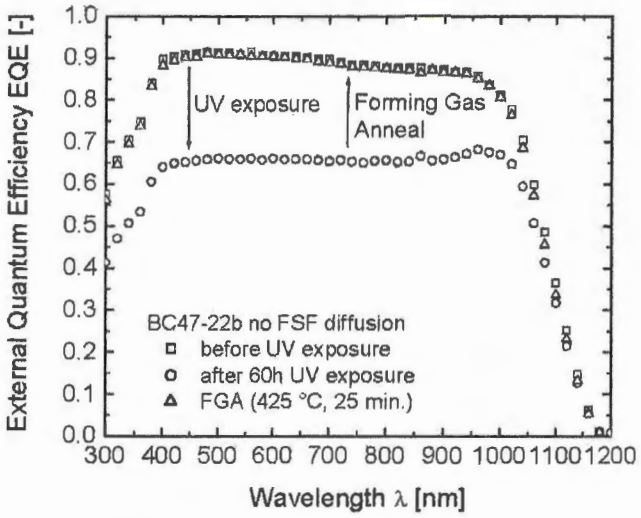


Figure 7-15 External quantum efficiency of the BC-BJ solar cell without the front surface field phosphorus diffusion before and after exposure to UV light and after regeneration of the UV damage by a forming gas anneal step.

Thus, the degradation effect of the UV exposure is not permanent and can be fully reversed by the passivation of the created interface states during the FGA process. The effect of the efficiency degradation under UV exposure and the subsequent regeneration under FGA process is shown schematically in Figure 7-16. The $S_{0,front}$ of the solar cells was determined using the lifetime test structures before and after UV exposure. The efficiency of the solar cells with and without FSF was measured after each UV exposure step and is plotted together with the $S_{0,front}$ determined by analyzing the lifetime samples. For the solar cell without the FSF the efficiency degradation follows the PC1D simulation line. However after the FGA the $S_{0,front}$ decreases and the efficiency increases as marked with a closed symbol.

The solar cell with the FSF diffusions do not show any significant performance degradation after UV exposure as marked with open symbols (circles and squares).

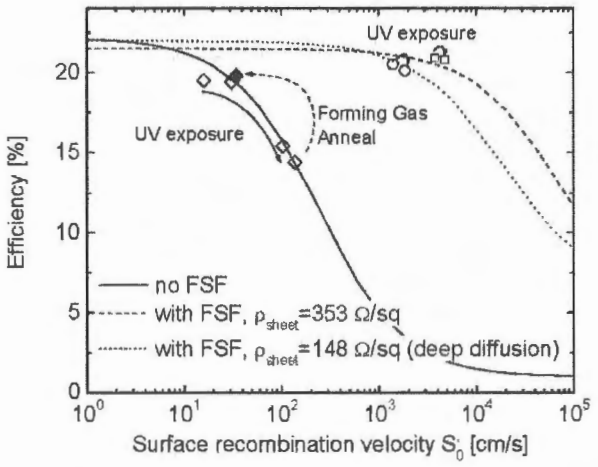


Figure 7-16 Efficiency of the back-junction solar cells as a function of the front surface recombination velocity simulated with PC1D for solar cell with and without FSF diffusion profile (thin lines). Open symbols represent the efficiency of the BC-BJ solar cells measured after UV exposure steps, as marked with arrows. The $S_{0,front}$ of was determined by analyzing the lifetime test samples with and without FSF respectively. The closed symbol represents the efficiency of the solar cell which was regenerated in forming gas anneal process after the degradation under UV illumination.

7.6 Conclusion

The front surface passivation quality is one of the most critical parameters of the back-contact back-junction solar cell structure. The phosphorus-doped front surface field can improve the front surface passivation and was therefore analyzed in details.

The saturation current density of different FSF phosphorus diffusion profiles passivated with SiO_2/SiN_X stack system was determined under low and high injection using the n^+nn^+ test structures. J_{0e} values determined using two different evaluation methods (under low injection and using *slope method* under high injection) are in a good agreement. The presence of the random pyramids texture increases the J_{0e} by a factor of 1.3 to 1.7 in comparison to the planar samples. This enhancement factor corresponds to the surface increase when going from planar to textured surfaces by a factor of 1.73.

The best solar cell efficiency of 20.8 % was obtained with deep diffused Gaussian profile of the FSF. Moreover the distribution of the efficiency of solar cells with the deep diffused FSF was lowest, proving the processing stability of the deep diffused

phosphorus profiles. The efficiency of the analyzed solar cells decreased to 18.0 % for solar cell with the FSF doping profiles with the lowest sheet resistance. Increased doping concentration and depth of the FSF diffusion reduced J_{SC} and V_{OC} of the analyzed cells.

Lifetime samples and solar cells without the front surface field showed a significant performance reduction when exposed to ultraviolet light spectrum. The lifetime samples and the solar cells with FSF diffusion are stable under UV exposure. Regeneration of the solar cell performance after degradation under UV exposure is possible by forming gas anneal.

8 Lateral current transport via front n^+ diffused layer

The application of the low-cost structuring technologies in the processing of the high-efficiency back-contact back-junction silicon solar cells results in a drastic increase in pitch on the rear cell side. The pitch in the range of millimeters leads to a significant increase of the lateral base resistance. The application of a phosphorus-doped front surface field (FSF) significantly reduces the lateral base resistance losses. This additional function of the phosphorus-doped FSF was investigated experimentally and by two-dimensional device simulations. Enhanced lateral majority carrier current transport in the front n^+ diffused layer is a function of the pitch and the base resistivity. Experimental data show that the application of a FSF reduces the total series resistance of the measured n-type cells of 160 micrometer thickness with 3.5 mm pitch by 0.1 Ωcm^2 for 1 Ωcm base resistivity and 1.3 Ωcm^2 for 8 Ωcm base resistivity. Two-dimensional simulations of the electron current transport show that the electron current density in the front n^+ diffused layer is around two orders of magnitude higher than in the base of the solar cell.

8.1 Introduction

High volume manufacturing of the back-contact and back-junction solar cell structure in the industrial environment requires the application of adequate processing technologies. The use of the photolithography technique is not cost-effective. Replacement of the very accurate photolithography with industrially applicable masking steps, such as ink-jetting and screen-printing of resist masks or laser ablation, leads to a significant reduction of the resolution and positioning accuracy. This is especially critical if more than one masking step is used. The pitch on the rear cell side processed with the low-cost masking technology mentioned above increases dramatically, as schematically shown in Figure 8-1. Point-contact solar cells processed by Prof. Swanson's group at Stanford University in the 1980s, for concentrator applications with the use of photolithography, had a pitch of 45 µm [119]. Another example of back-contact Si cells also processed using photolithographic masking is the real-line contacted concentrator (RLCC) cell, developed by Mohr [170] with the pitch in the range of 120 to 400 µm. Solar cells were processed in the course of this thesis without photolithography possessing a pitch distance of around 2 mm. Thus, when

applying low-cost patterning techniques, the pitch on the rear side increases by a factor of more than 40 in comparison to point contact cells [119]. This means that for the majority carriers (electrons here), the main current transport is transformed from the vertical to the lateral direction.

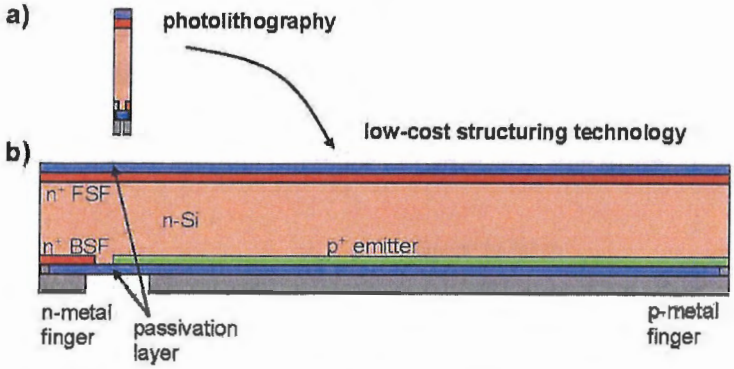


Figure 8-1 Schematic comparison of a point-contact Si solar cell processed with the use of photolithography with a pitch distance of 45 µm (a) and the solar cell with the use of low cost structuring technology with a pitch distance of 2000 µm (b). Drawings are to scale laterally. Symmetry elements of the cell structures are shown.

Depending on the base resistivity and pitch, up to 90 % of the series resistance can be attributed to the lateral majority carrier transport. Thus, the lateral current transport is the main resistance loss mechanism reducing the cell efficiency. The analyzed cells have a phosphorus diffused front surface field (FSF), which is well-known to improve the front side passivation [20]. In the case of cells with large pitch, the FSF not only improves the front side passivation, but also reduces the lateral resistance for the majority carriers and reduces the series resistance of the solar cell. This additional effect of the front n^+ layer is investigated in the present chapter.

8.2 Lateral current transport of majority carriers

The emitter coverage on the rear side should be as high as possible to reduce the required diffusion path for the light generated minority carriers to reach the p-n junction (see Figure 8-2). Increased emitter coverage on the rear cell side is linked to a reduced base doping area. As will be shown in the section 8.3, the pitch of the analyzed solar cell structures was chosen in the range of 1.3 to 3.5 mm. Therefore, the emitter coverage on the rear side is between 54 % and 83 % respectively. Due to the high emitter fraction, the majority carriers (electrons in the case of the n-type base material) need to flow lateral distances in the range of millimeters before reaching the

base contacts. This influences the fill factor of the cell. On the other hand, due to the lower base coverage on the rear cell side, the minority carriers (holes), which were photo-generated over the base contact regions, have much shorter lateral distances to diffuse to the emitter. This results in an improved carrier collection.

The lateral transport of the majority carriers causes significant series resistance losses due to the large distances. When a highly doped front n^+ layer is present, the lateral transport of the electrons can be facilitated. In the case of a high base resistivity or a large lateral distance, the diffused front n^+ layer contribution to the lateral current transport will be significant. This effect is schematically shown in Figure 8-2.

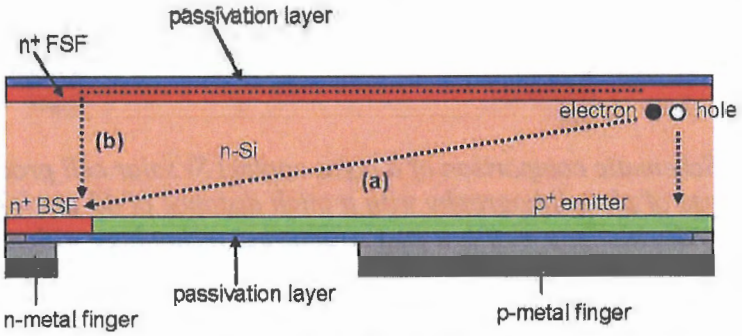


Figure 8-2 Schematic drawing of the effect of the enhanced lateral current transport of the majority carriers through the front n^+ diffused layer (a symmetry element of the cell is shown). For the sake of simplicity, the front side texture is not shown. The lateral current transport through the front diffused n^+ layer (b) can be seen as an additional transport path to the base lateral resistance (a). In this way the lateral cell resistance is reduced.

The so called *pumping* effect of floating phosphorus doped n-type emitters in the *p-type* back-contact back-junction solar cells was already investigated by Dicker et al. [33]. In the case of p-type cells with floating emitters, the minority carriers, which were photo-generated in large lateral distances from the emitter, are injected to the floating emitter, where they become majority carriers. The lateral flow of these carriers in the floating emitter is enhanced. Next, the carriers are re-injected into the base and diffuse vertically to the p-n junction. Thus, the *pumping* effect of the floating emitter reduces the electrical shading losses (described in chapter 6) in the back-contact back-junction cells. Therefore the *pumping* effect should not be confused with the effect of the enhanced lateral transport of the majority carriers in the front diffused n^+ layer, which reduces the lateral resistance losses.

The impact of the lateral cell geometry on the lateral series resistance in the base of the solar cell can be expressed by eq. (8.1), analogous to the series resistance model for the concentrator BC-BJ cells from [35]. The impact of the current transport in the front diffused n^+ layer can be described by a parallel resistance to the base lateral resistance:

$$\frac{1}{R_{Base,L}} = \frac{1}{\frac{1}{12}\frac{\rho_{Base}}{d_{wafer}}(a_{n-n})^2} + \frac{1}{\frac{1}{12}\rho_{FSF}(a_{n-n})^2} \tag{8.1}$$

Where a_{n-n} is the distance between the n^+ and n^+ doping, ρ_{Base} is the specific resistance of the base, d_{wafer} is the wafer thickness and ρ_{FSF} is the sheet resistance of the front n^+ diffused layer. The input parameters for the model described by equation (8.1) are schematically shown in Figure 8-3.

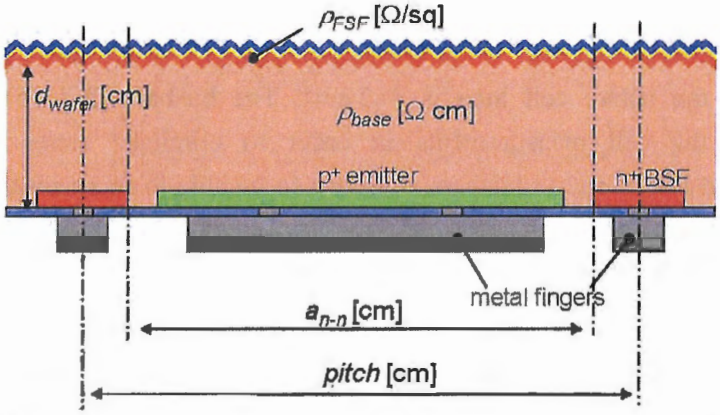


Figure 8-3 Schematic representation of the input parameters for the series resistance model presented in equation (8.1). The units of the geometry and resistance parameters are shown as well.

Due to the quadratic dependence on pitch, an increase of the pitch from 45 µm, as in the cells processed by Sinton et al. [119] with the use of photolithography, to 2000 µm, as in the cells processed in our group with low-cost masking technology, will result in the increase in the lateral series resistance by a factor of 2000. The application of the front diffused n^+ layer (FSF) will reduce the lateral base resistance, especially for cells with a higher specific base resistivity.

An analytical series resistance model of the BC-BJ solar cells was developed and presented in chapter 6.5. This model is based on the resistance model of Mohr [35]. Next to the base lateral resistance, the model also takes into account the vertical base resistance, the contact resistance and the metallization resistance losses. The impact of the lateral current transport in the front n^+ layer was incorporated as shown into

equation (8.1). The comparison of the analytical series resistance modeling with the experimental data is presented in the following sections.

8.3 Variation of the pitch

Back-contact back-junction n-type silicon solar cells with pitches of 1.3, 1.8, 2.2 and 3.5 mm were fabricated (see Table 8-1). The cell structure and its technology were already presented in 4.1. The pitch and the base and emitter width had to be selected, such that the resolution and positioning accuracy of the cell geometry can be performed using low-cost masking steps like screen-printing and laser ablation. The width of the emitter area (p^+) was varied in the range of 700 - 2900 µm in order to investigate the lateral current transport in the base and in the front n^+ layer. The width of the base doping on the rear side (undiffused gap and BSF areas) was fixed at 600 µm for all investigated pitches. The resulting emitter fraction on the rear cell side varied in the range of 54 %, for a pitch of 1.3 mm, to 83 % for a pitch of 3.5 mm.

The size of the active cell area is 2×2 cm^2. The busbars (2×0.15 cm^2) were not included in the cell measurements in order to eliminate series resistance and recombination losses due to busbars, and thus to be able to focus on the pitch-related two-dimensional effects.

Table 8-1 Photographs and the geometry parameters of the rear side of the back-contacted solar cells with different pitches. The size of the active cell area is 2×2 cm^2. The busbars' size is 2×0.15 cm^2 for each polarity.

p-bus side n-bus side				
Emitter [µm]	700	1200	1600	2900
Base [µm]	600	600	600	600
Pitch [µm]	1300	1800	2200	3500
Emitter fraction [%]	54	67	73	83

The experimental study was accompanied by two-dimensional device simulations done by M. Hermle [86] in the cooperation with the author of the present thesis. Two-dimensional simulations were done using the *Sentaurus Device* [90] program. The symmetry element of the device used in the simulations is shown in Figure 3-4. Busbars and edge effects were not included in the simulations.

8.4 Solar cell results

The best solar cell results for different pitch distances and base resistivities are summarized in Table 8-2. All results in Table 8-2 are designated cell area (2 cm × 2 cm) measurements, i.e. the busbars were not illuminated during the measurements. The edge area was also not illuminated during the cell measurements. The number of cells in each group was between 1 and 4. The best efficiency of 21.0 % for ρ_{base} = 1 Ω cm and 20.9 % for ρ_{base} = 8 Ω cm was obtained for the pitch of 2200 µm. This pitch represents the best trade-off between high carrier collection efficiency due to large emitter coverage on the rear side, and series resistance losses due to the increased lateral distances.

Table 8-2 *IV-parameters for the best solar cells with a FSF (ρ_{FSF}=148 Ω/sq) and with different pitches. Results of the cells with base resistivity of 1 and 8 Ω cm are presented. Results in the table are designated cell area (2x2cm^2) measurements.*

Cell no.	Pitch [µm]	Emitter fraction [%]	ρ_{base} [Ω cm]	J_{SC} [mA/cm^2]	V_{OC} [mV]	FF [%]	η [%]
BC47-17d	1300	54	1	37.2	662	81.6	20.1
BC47-18b	1800	67	1	38.1	663	82.6	20.9
BC47-16a	2200	73	1	38.5	663	82.2	21.0
BC47-17c	3500	83	1	38.9	661	80.7	20.7
BC47-20f	1300	54	8	39.4	654	79.9	20.6
BC47-21b	1800	67	8	40.1	656	78.3	20.6
BC47-21a	2200	73	8	40.3	658	78.8	20.9
BC47-20c	3500	83	8	40.3	658	75.4	20.0

8.5 Short-circuit current analysis

As shown in Figure 8-4, the short-circuit current increases with increasing emitter coverage and reduced base areas of lower minority carrier collection probability. The base width is 600 µm, so in the extreme case, when the photo-generation occurs in the middle of the base area, the minority carriers need to diffuse 300 µm laterally before reaching the p-n junction. This leads to recombination in the cell's base and at the surfaces. For the base resistivity of 8 Ω cm and a pitch of 3.5 mm, a maximum J_{SC} of 40.3 mA/cm^2 was obtained. Such a high J_{SC} value indicates very good optical and recombination characteristics of the cell. 2-D device simulations, also shown in Figure 8-4, are in excellent agreement with the experimental results, proving the accuracy of the model.

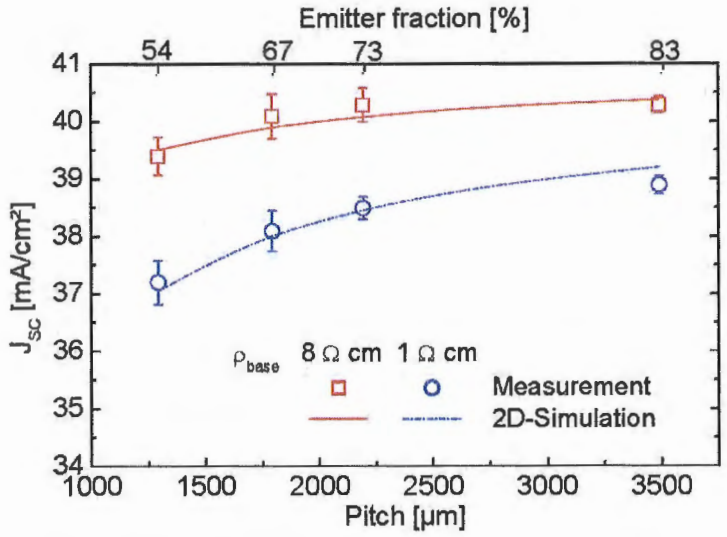


Figure 8-4 *Short-circuit current of the cells with the FSF (ρ_{FSF} = 148 Ω/sq) and with two specific base resistivities of 1 and 8 Ωcm in the investigated pitch range. The percentage of the emitter fraction on the rear side is shown on the top scale. Points represent experimental results and the lines are the two-dimensional simulation results.*

The short-circuit current of the 1 Ω cm cells is more than 1 mA/cm^2 lower than J_{SC} of the cells with 8 Ω cm specific base resistivity. In the 2D simulations, the same Shockley-Read-Hall bulk lifetime of 1 ms was assumed for both 1 and 8 Ω cm base materials. However, even with the same bulk lifetime for 1 and 8 Ω cm solar cells, the simulations show a difference in J_{SC}. The reason for the J_{SC} differences between 1 and 8 Ω cm wafers is the increased front surface recombination in the case of the 1 Ω cm

material in comparison to 8 Ω cm. A significant difference in the internal quantum efficiency (IQE) at short wavelengths between 1 and 8 Ω cm solar cells was measured. The IQE of the 1 Ω cm solar cells with pitch of 2200 μm is 94 % for wavelength of 400 nm. The IQE of the 8 Ω cm solar cells with pitch of 2200 μm equals 97 % for the same wavelength. The difference between the J_{SC} of cells with both base resistivities, determined by the integration of the solar spectrum with both measured IQEs, equals 1.8 mA/cm^2. This difference is in good agreement with the measured values presented in Figure 8-4. The effect of the increased front surface recombination in the case of the 1 Ω cm material in comparison to 8 Ω cm was investigated in section 4.5.

8.6 Fill factor and series resistance

8.6.1 Fill factor

In contrast to J_{SC}, the FF decreases as the pitch increases due to increased lateral resistance in base, as shown in Figure 8-5. The measured fill factor and 2D simulation are shown in Figure 8-5. Again, good agreement between the experimental and 2D simulation results can be observed. Results shown in Figure 8-5 clearly demonstrate that the FSF significantly reduces the series resistance losses and thus improves FF in comparison to cells without FSF. The effect of enhanced current transport in the front n^+ diffused layer is stronger for larger pitches, where the base lateral resistance dominates the resistance losses of the cell. Moreover, the additional impact of the FSF is, as expected, a function of the base doping. For higher base resistivity (8 Ω cm) and large pitch distance (3.5 mm), the FF of the cells with FSF is up to 10 % abs. higher than FF of the cells without the FSF.

8.6.2 Pseudo fill factor

In order to prove that the decrease in FF for larger pitch distances is only caused by the increased lateral series resistance and not other detrimental effects on the IV curve, the pseudo fill factor (PFF) was measured using the SunsV_{OC} measurement technique [153]. The pseudo fill factor is not influenced by series resistance; therefore, the effects of increased lateral resistance by increased pitch should not influence the PFF. The measured pseudo fill factor for the cells with varying pitch is shown in Figure 8-6. As expected, the PFF is independent of the pitch. In the pitch range analyzed, the PFF is higher than 82 % for 1 Ω cm and higher than 81 % for 8 Ω cm solar cells. Such a high PFF of the finished cells indicates that there are no significant shunting and space charge recombination losses in the analyzed solar cells. Constant PFF values in the analyzed pitch range prove that the variations in FF observed in

Figure 8-5 are caused only by the higher series resistance with increasing emitter width.

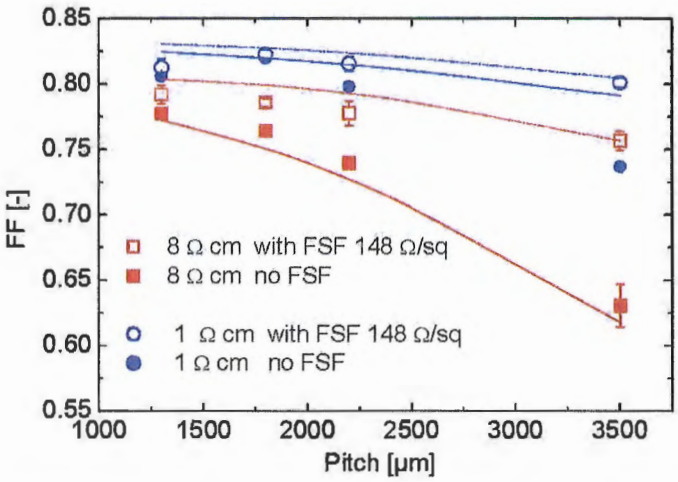


Figure 8-5 *Two-dimensional numerical simulations and measured values of the fill factor of the BC-BJ Si solar cells as a function of the pitch distance for two different base resistivities. Results for the cells with (ρ_{FSF} = 148 Ω/sq) and without FSF diffusion are shown. The data points represent a mean value of the experimental results. Lines represent 2-D simulation results.*

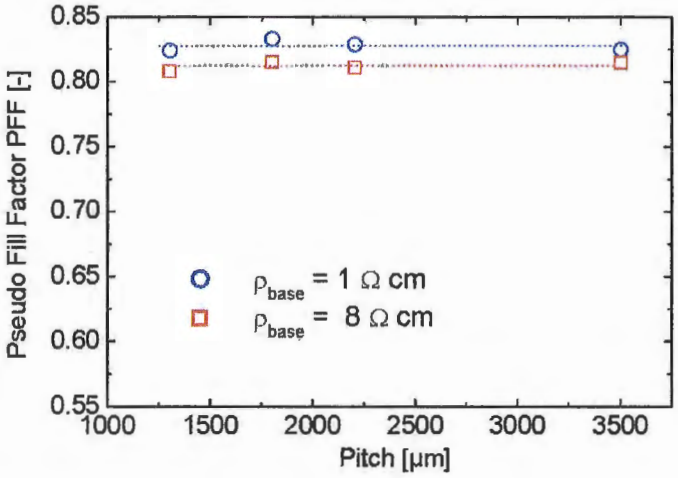


Figure 8-6 *Pseudo Fill Factor (PFF) of the BC-BJ solar cells with different pitches. Experimental results for the solar cells with FSF and base resistivity of FSF and 1 and 8 Ωcm material are shown. No reduction of the PFF over a wide pitch range was observed. Lines are guides-to-the-eye.*

8.6.3 Conductivity modulation

Since the series resistance reduces the maximum output power of the solar cell, the analytical model should describe the series resistance at the maximum power point (MPP) conditions. The base resistivity strongly depends on the density of the electrons in the base, and hence can be influenced by the cell operating conditions. Therefore, in order to correctly describe the impact of the base resistance on the total series resistance of the solar cell, the base conductivity modulation at MPP conditions should be taken into account.

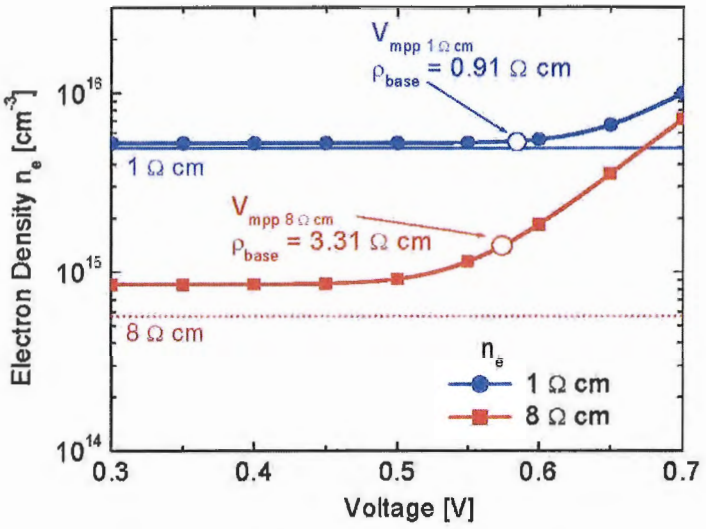


Figure 8-7 Two-dimensional simulation of the electron density in the base of the BC-BJ solar cells for two specific base resistivities of 1 and 8 Ω cm. The electron density was calculated in the voltage range of 0.3 to 0.7 V, in a distance of 100 µm from the top cell surface. The base conductivity modulation at the maximum power point is shown. Thin lines represent the base doping.

In Figure 8-7, a two-dimensional simulation of the electron density in the base in the voltage range of 0.3 to 0.7 V is presented. The voltage at maximum power point for 1 and 8 Ω cm base resistivities is marked in the graph. For both base resistivities, the electron density at MPP is higher than the base doping. ρ_{base} at MPP is therefore reduced compared to the base resistivity of the non-illuminated samples. At MPP conditions, the base resistivity equals 0.91 Ω cm for the specific base resistivity of 1 Ω cm, and 3.31 Ω cm for base resistivity of 8 Ω cm. Thus, ρ_{base} of the 8 Ω cm cells is significantly reduced under one sun illumination and operation at maximum power point. The effect of conductivity modulation at the maximum power point was taken

into account in the analytical modeling. As shown in Figure 8-8, a very good agreement between the experimental data and the analytical modeling of series resistance, adjusted for the conductivity modulation at MPP conditions, proves validity of the analytical model.

8.6.4 Series resistance

In order to investigate the pitch-related resistance losses, the total series resistance R_S of the processed cells was determined. The series resistance was obtained by comparing the SunsV_{OC} curve [153] with the one-sun IV-curve. The details of the measurement of the series resistance of the analyzed cells were presented in section 6.5. For more details on this method to determine the series resistance, see for example reference [154]. The experimentally determined series resistance is presented in Figure 8-8, together with the analytical series resistance modeling. The analytical modeling of the series resistance includes the effect of the enhanced lateral current transport in the front n^+ layer, as described by equation (8.1).

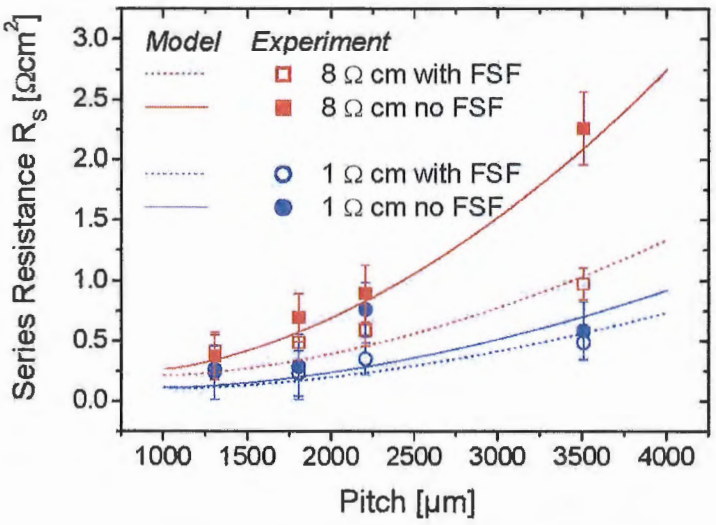


Figure 8-8 Series resistance of the BC-BJ Si solar cells with different pitches. Results of the cells on 1 and 8 Ωcm bulk resistivity and with and without the 148 Ω/sq front surface field are presented. The data points represent the mean experimental resistance values of 1 to 4 cells, determined by comparison of the measured FF and the SunsV_{OC} PFF. The lines represent the simple analytical series resistance model, in which the lateral current transport in the front diffused n^+ layer was taken into account as described by equation (8.1). In the analytical model, the base specific resistivity was adjusted for the conductivity modulation at the maximum power point.

For the 1 Ω cm cells with FSF diffusion, the series resistance R_S increases, starting from 0.2 Ω cm^2 for the lowest pitch of 1.3 mm to 0.5 Ω cm^2 for a pitch of 3.5 mm. The FF of these cells drops at the same time by about 1 % absolute, causing around 0.3 % absolute efficiency loss. For the case of the 1 Ω cm cells without FSF, the increase of R_S is higher. For the largest pitch R_S reaches 0.6 Ω cm^2.

The solar cells with a base resistivity of 8 Ω cm have a much higher lateral base resistance than the 1 Ω cm cells. This results in a lower FF for even the smallest pitch of 1.3 mm. Moreover, the fill factor drop with the increasing pitch is significantly larger than in the case of 1 Ω cm material. For the pitch distance of 1.3 mm, a maximal FF of 79 % and 78 % for 8 Ω cm cells with and without FSF respectively was measured. When reaching the largest pitch of 3.5 mm, the FF dropped to 76 % for cells with FSF and to 63 % for cells without FSF. An absolute FF drop by 3 % for the cells with FSF was caused by the increase of R_S from 0.36 Ω cm^2 for pitch of 1.3 mm to 0.96 Ω cm^2 for pitch of 3.5 mm. At the same time the FF of the 8 Ω cm cells without FSF dropped by 15 $\%_{abs}$, due to increase of R_S from 0.4 to 2.3 Ω cm^2. The drop in fill factor of our cells is consistent with the series resistance model of Mette [130] which predicts a drop of FF from 4.5 to 5.5 $\%_{abs}$ due to an increase of series resistance by 1 Ω cm^2.

8.7 Simulations of the lateral current flow of the majority carriers

The two-dimensional simulations of the majority carriers current transport are shown in Figure 8-9. Here the extreme case of the largest pitch of 3.5 mm was analyzed. The enhanced electron current density in the front n^+ diffused layer area is shown in detail (right side). The electron current density in the n^+ diffused layer area is around two orders of magnitude higher than in the base. This simulation shows that the lateral electron current transport takes place not only in the base, but also in the front diffused n^+ layer. The electrons, which were photo-generated at the front cell side in the first few micrometers of the wafer, take advantage of the high conductivity of the front n^+ layer until they are above the base contacts and then a vertical current transport through the base thickness takes place.

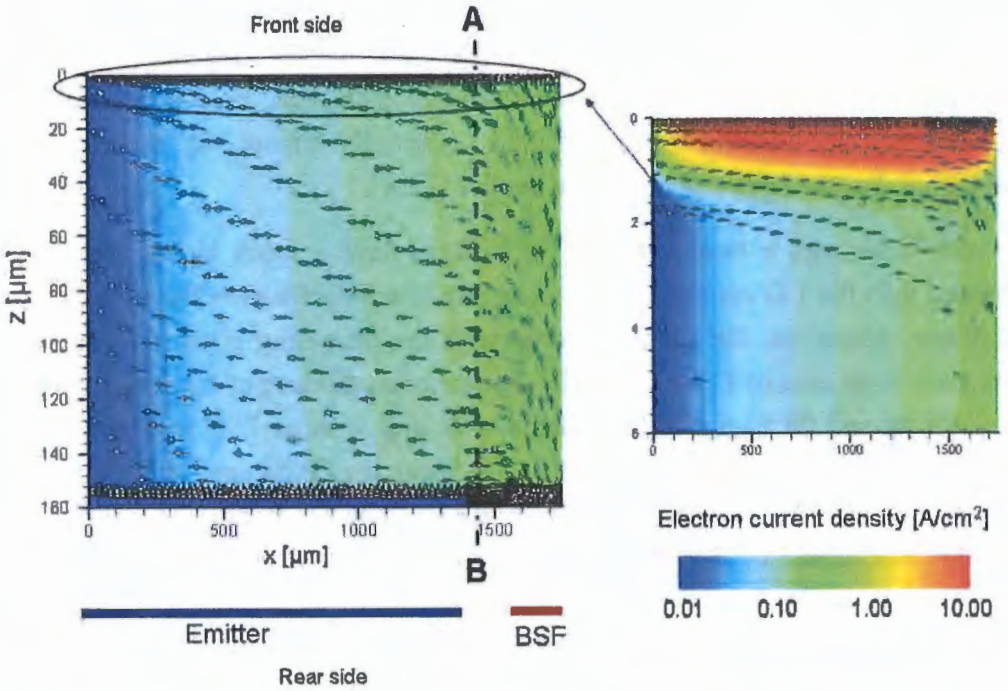


Figure 8-9 *Two-dimensional modeling results of the lateral and vertical electron current transport in the n-type BC-BJ solar cell structure with base resistivity of 8 Ω cm and pitch distance of 3.5 mm. The symmetry element of the solar cell is shown. The arrows show the direction opposite to the electron flow at V_{MPP} of a cell with front surface field (ρ_{FSF} = 148 Ω/sq). The A-B cut of the electron current density through the cell thickness is marked.*

The vertical profiles of the electron current density through the thickness of the solar cell were taken in the vicinity of the base contacts (A-B cut in Figure 8-9). These profiles for 1 and 8 Ω cm specific base resistivities are shown in Figure 8-10. A significant difference in the fraction of the current transport in the front diffused region and the base between the two base resistivities can be observed. After integrating the current density profiles, it was found that for the specific base resistivity of 1 Ω cm, 27 % of the lateral electron current transport takes place in the front n^+ layer. The remaining 73 % of the current flows laterally through the base.

A simple parallel resistance circuitry, as introduced by the analytical model in equation (8.1), can be applied to clarify the current sharing between base and n^+ front region. For the specific base resistivity of 1 Ω cm and the wafer thickness of 160 µm the wafer sheet resistance equals 42 Ω/sq. The base resistance is in parallel with n^+ sheet resistance of 148 Ω/sq. This implies a current sharing of 29 % for the front n^+ region and 71 % for the n-type base. Thus, in the case of base resistivity of 1 Ω cm, the

analytical modeling matches very well the two-dimensional modeling presented in Figure 8-10.

The analysis of the 2-D simulation of the cells with base resistivity of 8 Ω cm shows that the contribution of the front diffused area to the lateral current transport of the majority carriers becomes dominant and increases to 55 %, with 45 % of the current transport taking place in the base. The application of the same simple parallel resistance circuitry here would result in the current sharing of 77 % in the front diffused region and 23 % in the base. These results are not in agreement with 2-D simulations. However, if the same calculation is repeated for the base resistance corrected for conductivity modulation at MPP (ρ_{base}=3.31 Ω cm instead of 8 Ω cm), the base would carry 42 % of the current and the front diffused layer would carry 52% of the current. These results match the simulation results very well. The analysis presented above shows the importance of using two-dimensional modeling when describing the solar cell, which does not operate in low injection conditions.

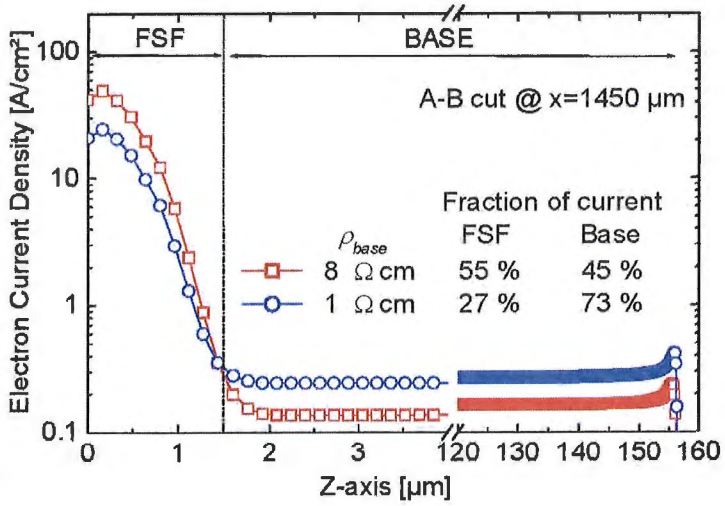


Figure 8-10 Two-dimensional simulation of the electron current density for cells with 1 and 8 Ω cm specific base resistivity and a FSF (ρ_{FSF} = 148 Ω/sq) at the maximum power point conditions. A-B cuts of the electron current density through the wafer thickness for both base resistivities are shown. Front side of the solar cell corresponds to z=0. Areas of the FSF and the base are indicated in the graph. Fractions of the current flow in the front n^+ diffused layer and the base for both specific base resitivities are shown.

8.8 Conclusions

If a low-cost structuring technology is applied in the processing of the BJ BC cell structure, the pitch on the rear side of the cell drastically increases to values in the range of millimeters. This significantly increases the lateral base resistance. The presented investigations show that the introduction of a phosphorus-doped front surface field significantly reduces the lateral base resistance losses. The majority carriers, which were photo-generated in large lateral distances from the base contacts and on the front side, take advantage of the high conductivity of the front diffused n^+ layer in order to reduce the resistance losses. The highly doped front layer can be seen as a low-resistivity *highway* for the majority carriers, which enhances its lateral transport. The front diffused n^+ layer can be seen as a parallel resistance to the lateral base resistance, and its influence on the total series resistance of the cells was successfully modeled using the parallel circuitry. In order to correctly describe the contribution of the base lateral resistance to the modeling, it is important to regard the conductivity modulation of the base resistance under the maximal power point conductions.

As expected, the enhanced lateral majority carrier's current transport in the front diffused n^+ layer is a function of the pitch and the base resistivity. The introduction of phosphorus-diffused FSF reduces the total series resistance of the measured cells with 3.5 mm pitch of 0.1 $\Omega\,cm^2$ for the base resistivity and 1.3 $\Omega\,cm^2$ for the 8 Ω cm base resistivity when compared to solar cells without the FSF. According to the two-dimensional simulations of the electron current transport, the electron current density in the front diffused n^+ layer is around two orders of magnitude higher than in the base of the solar cell. Depending on base resistivity, the lateral current transport via front n^+ diffused layer is in the range of 27 to 55 % of the total lateral current transport for 1 and 8 Ω cm base resistivity, respectively.

9 Low-illumination characteristics

The linearity of the current and voltage of three structures of high-efficiency back-junction back-contact silicon solar cells at low illumination were analyzed. Both n-type cells with non-diffused front surface and p-type cells with floating n-emitter show a pronounced current non-linearity, due to strong illumination dependence of the passivation quality of the non-diffused surface and the floating junction respectively. The quantum efficiency of this cell type drops significantly for illumination densities lower than 0.5 suns. In contrast, the quantum efficiency of n-type cells with n^+ front surface field is independent of illumination density. Thus, the n-type cell structure with n^+ front surface field enables highest energy yield at low illumination intensity conditions.

9.1 Introduction

Solar cell efficiencies are normally only reported at standard testing conditions (STC). These conditions include the so called "one sun" illumination intensity of 1000 W/m^2 with spectrum AM1.5g [171] and a device temperature of 25 °C [172]. However, over the whole year under realistic conditions, photovoltaic systems operate during cloudy days, or in the morning and evening periods of the day as well. These are the periods of strongly reduced illumination intensity. Therefore, the annual energy yield of a photovoltaic system is influenced by the low light intensity characteristics of the solar cells. Thus, in order to maximize the energy delivered by the photovoltaic system, the performance of this system should such be as high as possible, even at the low light periods of the day and the year.

The purpose of this chapter is to analyze the different back-junction back-contact solar cells structures with respect to their performance under the low-illumination intensities. Three different front surface passivation schemes are analyzed. These structures are schematically shown in Figure 9-1:

a) n-type cell with non-diffused front surface,

b) p-type cell with an n^+ floating emitter and

c) n-type cell with an n^+ front surface field (FSF).

The n-type solar cells with and without the front surface field were developed in this work and the details of their processing technology were already presented in chapter 4.

The p-type solar cells with the floating junction were developed and analyzed in the work of Dicker et al. [33] and these results are presented here for comparison with the n-type structures.

The relation between current and illumination intensity and voltage and the illumination intensity of three above mentioned solar cell structures is analyzed in the present chapter.

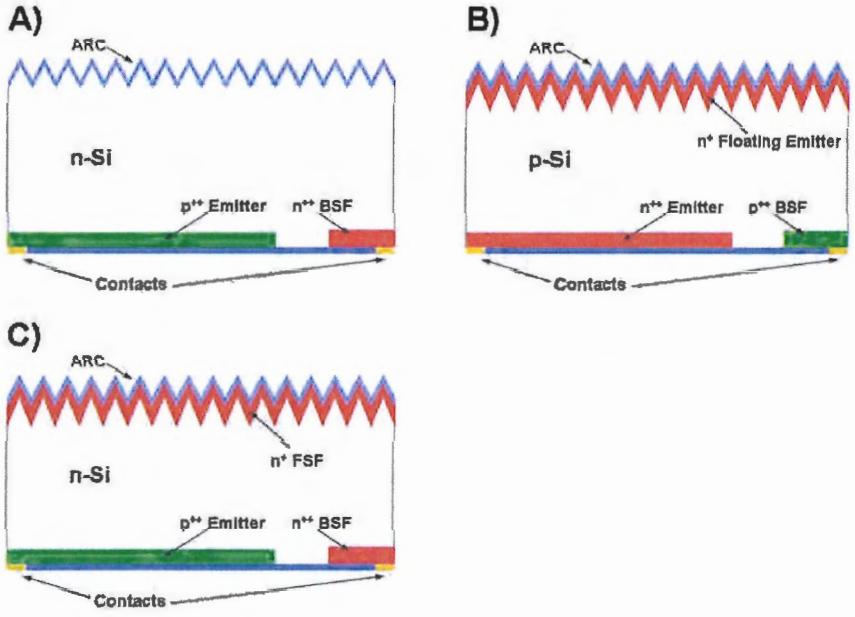


Figure 9-1 Sketch of two-dimensional symmetry elements of the back-junction solar cells: n-type with non-diffused front surface (structure A), p-type with a phosphorus doped floating emitter (structure B), and n-type with a phosphorus doped FSF (structure C).

9.2 Analyzed solar cells and methodology

Analyzed solar cells

The parameters of the solar cells chosen for the low-illumination analysis are summarized in Table 9-1. BJ BC solar cells with three structures corresponding to the notation used in Figure 9-1 were selected. The efficiency of the chosen cells was in the

range of 11.0 to 20.4 %. n-type solar cells with base resistivity of 1 and 8 Ω cm were analyzed. The results of the n-type cells with and without the FSF were compared to the p-type cell structure with the floating junction.

Table 9-1 *IV-parameters of solar cells with different front surface passivation schemes (structure types names correspond to the notation used in Figure 9-1). The presented results are measured under one sun illumination intensity and 25 °C device temperature.*

Cell No.	Structure type	Area [cm^2]	ρ_{base} [Ω cm]	V_{OC} [mV]	J_{SC} [mA/cm^2]	FF [-]	η [%]
BC47-22b *'good'*	A	4	1	649.7	35.2	0.817	18.7
BC47-23g *'bad'*	A	4	1	632.9	30.4	0.785	15.1
BC47-24b *'good'*	A	4	8	636.6	38.65	0.737	18.1
BC47-25g *'bad'*	A	4	8	598.7	29.9	0.613	11.0
RSK3-5a	B	4	1	685.0	32.1	0.792	17.4
BC47-18g	C	4	1	658.5	39.0	0.794	20.4
BC47-21g	C	4	8	653.5	39.7	0.752	19.5

External quantum efficiency

In order to examine the relation between current density and light intensity of the three cell structures described above, the external quantum efficiency (EQE) of all analyzed cells was measured in the range of 300 to 1200 nm under a bias light intensity of 0.3 and 1 sun.

Moreover, the EQE at a wavelength of 600 nm was measured as a function of bias light intensity in the illumination range of 0.01 to 1 suns. Due to the high absorption coefficient of the light with a wavelength of 600 nm, the EQE at 600 nm reflects the current of the carriers generated close to the front surface. This current is especially sensitive to the front surface recombination. Thus, any variation in the front surface recombination rate with the variation of illumination intensity can be measured well by a measurement of the solar cell response at a wavelength of 600 nm. The measured EQE at different bias light intensities was than normalized with respect to EQE at one-sun bias light intensity.

Open-circuit voltage

The V_{OC} of all cells was measured in an illumination intensity range of 0.1 to almost 10 suns. The SunsV_{OC} method [153] was used here. The dependence of the V_{OC} with illumination intensity (C for concentration) can be described with the following equation [173]:

$$V_{OC}(C) \approx \frac{kT}{q} \ln\left(\frac{CJ_{ph,one-sun}}{J_0}\right) \approx V_{OC,one-sun} + \frac{kT}{q} \ln(C) \qquad (9.1)$$

where $V_{OC,one-sun}$ and $J_{ph,one-sun}$ are the V_{OC} and photogenerated current, measured under standard reference conditions at the 1 sun illumination intensity respectively. When the saturation current J_0 is constant in the analyzed illumination intensity range, then a linear increase of voltage with the logarithm of light intensity is expected. The resulting V_{OC} dependence with illumination density can then be described by the right side of equation (9.1). The V_{OC} should show an increase of around 60 mV for each decade of increase of intensity. A deviation from the logarithmic illumination behavior could be caused if the saturation current of the cell is injection dependent.

Device simulations

In addition to solar cell measurements, two-dimensional device simulations of the symmetry elements shown in Figure 9-1 were performed. The EQE at 600 nm with varying bias light intensity was simulated and the simulation results were compared with the measured data.

9.3 Non-diffused surfaces

Two sets of parallel processed solar cells with structure A were selected for the low illumination analysis. The first pair of cells, marked as *'good'* in the Table 9-1, had EQE at one-sun bias light of about 85 %. The second pair, marked as *'bad'*, with inferior front surface passivation had an EQE of around 75 %. Cells with non-diffused front surfaces are very vulnerable to variation of front surface recombination velocity (S_{front}) as shown in section 2.3. Even a small increase of S_{front} will result in a significant current decrease. This explains the large differences between the performance of the *'good'* and *'bad'* identically processed cells. Minor and difficult-to-avoid processing imperfections, such as broken pyramid tips, local scratches or other front surface inhomogenities cause extreme differences in cell performance. Processing faults create spots on the cell front surface with locally strongly increased S_{front}. These local imperfections will, therefore, lead to a locally inhomogeneous S_{front} value.

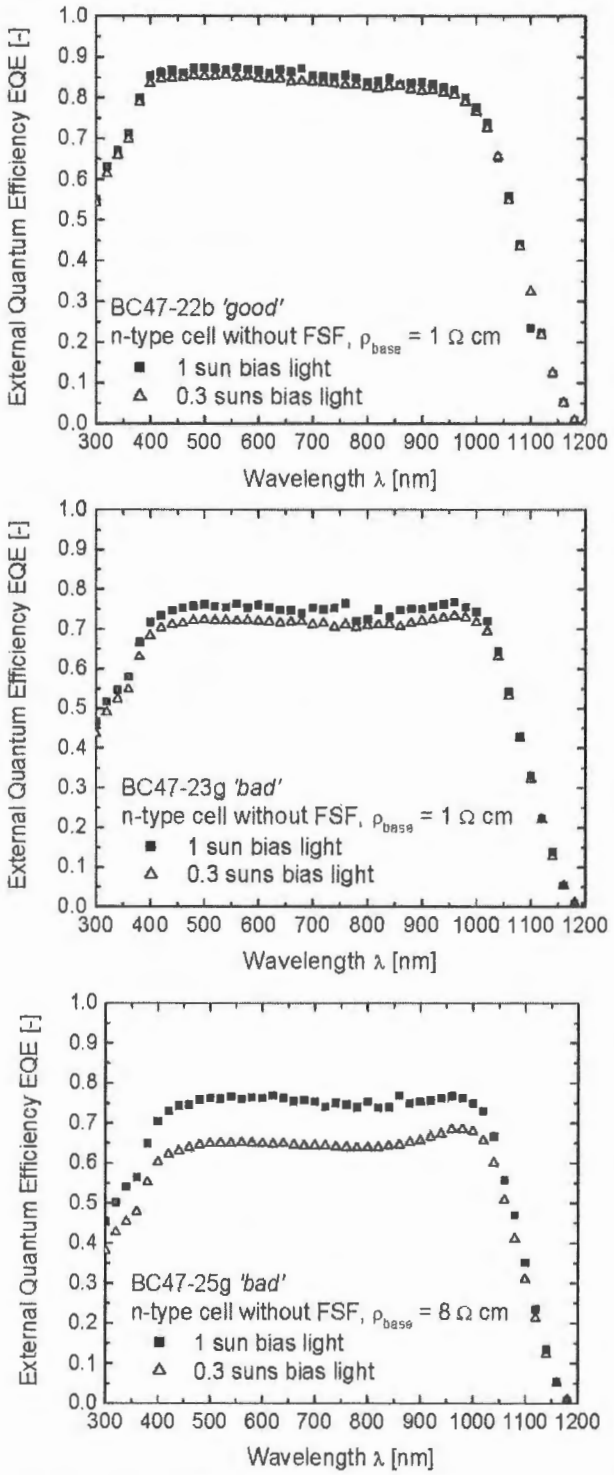


Figure 9-2 External quantum efficiency of three different n-type back-contact back-junction cells with non-diffused front surface (structure A) measured at 0.3 and 1 sun bias light intensity.

The external quantum efficiency of the structure A cells measured at a bias light intensity of 0.3 and 1 sun is shown in Figure 9-2. A strong bias light intensity dependence was observed. For the 1 Ω cm cell marked as '*good*' (BC47-22B), a 3 to 5 % absolute decrease of EQE was measured when lowering the bias light intensity from 1 to 0.3 suns. For the cells marked as *'bad'*, the decrease in EQE was even more pronounced. The EQE of the 1 Ω cm (BC47-23g) dropped by 5 to 7 % at lower bias light intensity. For the 8 Ω cm cell, the EQE dropped by 10 %.

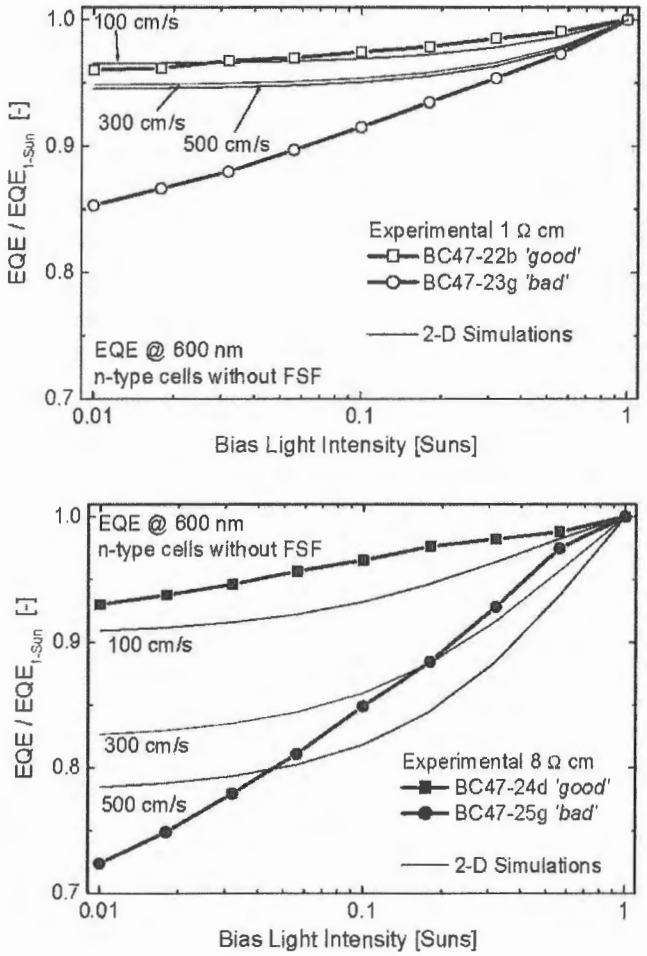


Figure 9-3 Normalized EQE for n-type back-contact back-junction cells with non-diffused front surface (structure A) measured at wavelength of 600 nm in bias light intensity range of 0.01 to 1 sun. Results for base resistivity of 1 Ω cm (top) and 8 Ω cm (bottom) are shown. Sets of two-dimensional simulations for different S_{front} values (S_{front} is shown next to simulation results) are plotted next to experimental results.

All four analyzed cells exhibit a very strong current non-linearity under low illumination. The non-linearity is much larger for the cells with lower performance. Normalized EQE of the *'bad'* cells drops down to 85 % for 1 Ω cm base resistivity, and to 72 % for 8 Ω cm base resistivity at 0.01 suns due to injection-dependent effects of the front surface recombination.

Two-dimensional device simulations (thin lines in Figure 9-3) with a set of S_{front} values as input parameters also predict a strong non-linearity of the structure A cells. A fixed S_{front} was assumed for the whole area of the front surface. However, the simulation results also show that the injection dependence cannot be described with a single S_{front} value, although injection dependence of $S_{front} = S_n = S_p$ and bulk lifetime ($\tau_{n0} = \tau_{p0} =$ 1 ms) were taken into account in the simulation. A possible explanation of these differences may be the fact that the *local* surface imperfections have to be taken into account. The combination of locally distributed S_{front} values could then result in more complex injection dependence as expected from the simulation with a single homogeneous S_{front} value.

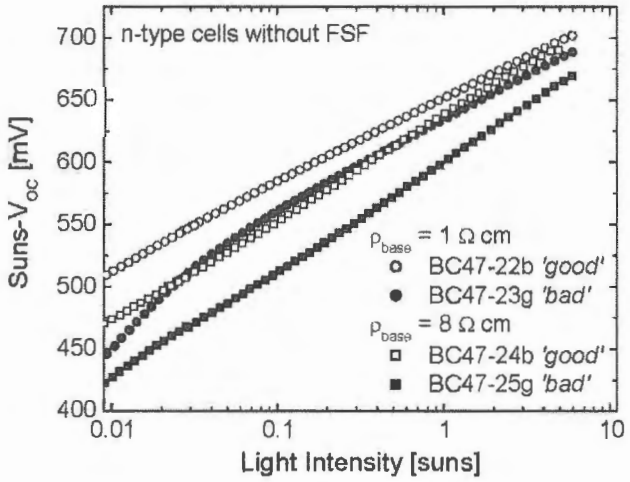


Figure 9-4 Open-circuit voltage of the n-type back-contact back-junction cells with non-diffused front surface (structure A) measured in bias light intensity range of 0.01 to 10 suns. Results for 1 and 8 Ω cm base resistivity are shown.

The open-circuit voltage of the analyzed cells measured in the light intensity range of 0.01 to 10 suns is shown in Figure 9-4. The V_{OC} of all 4 analyzed cells shows a linear decrease with logarithm of light intensity as predicted by equation (9.1) until 0.1 suns. However, for light intensities lower than 0.1 suns, a deviation from this linear decrease can be observed for the '*bad*' cells (BC47-23g and BC47-25g). The decrease of V_{OC}

under low illumination intensities is stronger than theoretically predicted. This is believed to be caused by a increase of S_{front} and thus increase of $J_{0,front}$, under low injection operating conditions.

The solar cell operates under V_{OC} conditions at a much higher injection level than in the case of J_{SC}. Therefore, the effect of increased recombination caused by a transition from high injection to low injection operating conditions occurs in the case of V_{OC} at much lower light intensities than in the case of J_{SC}. That is why the EQE of the structure A cells already decreased significantly at light intensity of 0.3 suns, and the V_{OC} at the same time shows non-linearity first at illumination lower than 0.1 suns.

9.4 Floating emitters

The p-type solar cells with floating emitter (structure B) were processed with the use of photolithography. The solar cell selected for the present analysis had an efficiency of 17.4 %. The thin metallization grid on the cell rear side covers only a small fraction of the cell rear side, thus enabling bifacial illumination of the cell structure. This feature was used during the measurements of the open-circuit voltage. The structure B solar cell was illuminated form the rear cells side during the open-circuit voltage measurements, due to problems with proper contacting of the metal grid during front side illumination.

The external quantum efficiency of the cell RSK3-5a measured at bias light intensity of 1 and 0.3 suns is shown in Figure 9-5. A decrease of the EQE by 2 to 3 % absolute when lowering the bias light from 1 to 0.3 suns was measured. As in the case of the cells without front diffusion described in the previous section, the current of the structure B cell is also non-linear, i.e. the short circuit current density decreases with decreasing bias light illumination intensity. This effect is even stronger for lower bias light intensities, as shown in Figure 9-6.

Normalized EQEs of p-type cell with floating emitter, measured in the bias light intensity range 0.01 to 1 suns, are shown in Figure 9-6. The EQE decreases rapidly for the bias light intensity lower than 0.5 suns. The effects responsible for this behavior are imperfections of the floating junction (see Figure 9-7). The diffusion inhomogenities and introduction of crystal defects lead to formation of an internal shunt element ($R_{p,floating}$) across the junction and to recombination in the space charge region, which causes diode saturation current ($J_{02,p}$) [174]. Both elements strongly reduce the voltage across the floating junction ($V_{floating}$), which is necessary to obtain a good surface passivation. The shunt resistance and a diode with ideality factor of 2 were implemented across the front side floating junction into PC1D simulations of the

floating emitter cell structure. The PC1D simulation results plotted in Figure 9-6 are in good agreement with the experimental data, indicating a reasonable model for the imperfections of the floating emitter.

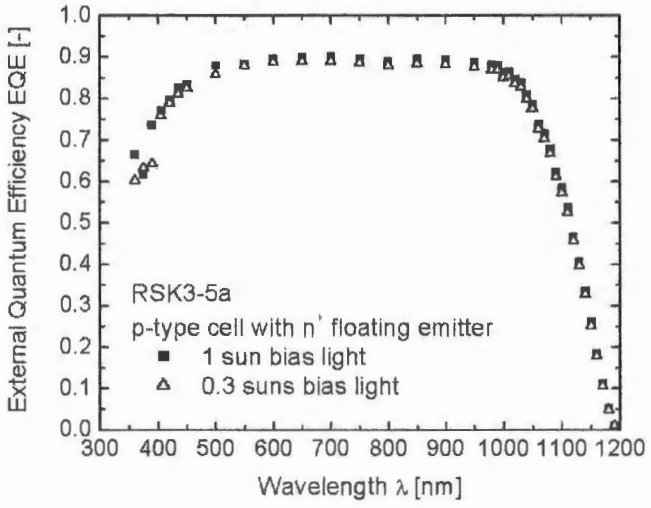


Figure 9-5 External quantum efficiency of three different p-type back-contact back-junction cells with floating emitter (structure B) measured at 0.3 and 1 sun bias light intensity.

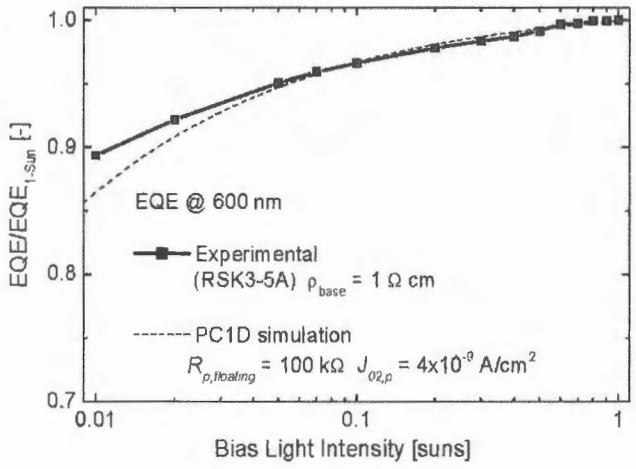


Figure 9-6 Normalized EQE for a p-type cell with floating emitter (structure B) measured at wavelength of 600 nm in bias light intensity range of 0.01 to 1 sun. The dotted line shows a PC1D simulation using $R_{p,floating}$ and $J_{02,p}$ values as shown in the graph.

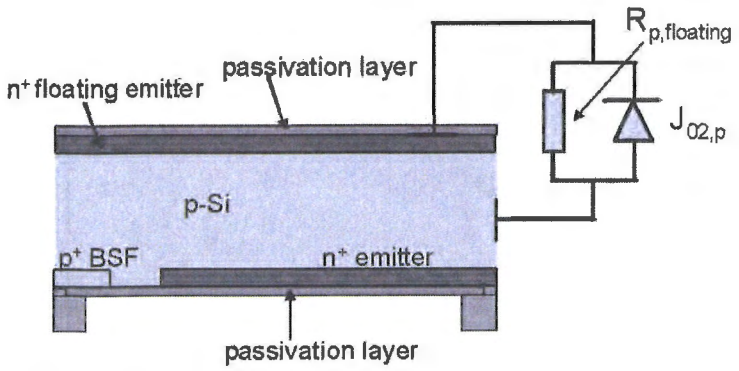


Figure 9-7 Equivalent circuit diagram for shunting effects across the floating junction used in PC1D simulations.

In the presence of the structure imperfections mentioned above, a $V_{floating}$ of about 600 mV is needed to passivate the surface. $V_{floating}$ is a function of the bias light intensity and increases with the logarithm of the light intensity, as shown in equation (9.1). Such a high voltage across the floating junction on the front side is only achieved at the light intensity higher than 0.5 suns. Thus, the surface passivation with floating junction is a very effective passivation scheme for medium to high illumination. At the same time, its passivation quality in realistic structures is poor at low illumination, due to low $V_{floating}$ and consequently high S_{front}.

The V_{OC} of the p-type cell with floating emitter was measured in illumination intensity range of 0.01 to 10 suns and is shown in Figure 9-8. In contrast to the quantum efficiency, the V_{OC} shows an approximately logarithmic behaviour with lowering of the illumination intensity. The different bias light dependence between EQE and V_{OC} of the structure B cell can be also explained by different cell operation conditions. At V_{OC} conditions, the solar cell operates under significantly higher injection level in comparison to the J_{SC} conditions, as already explained in the previous sections.

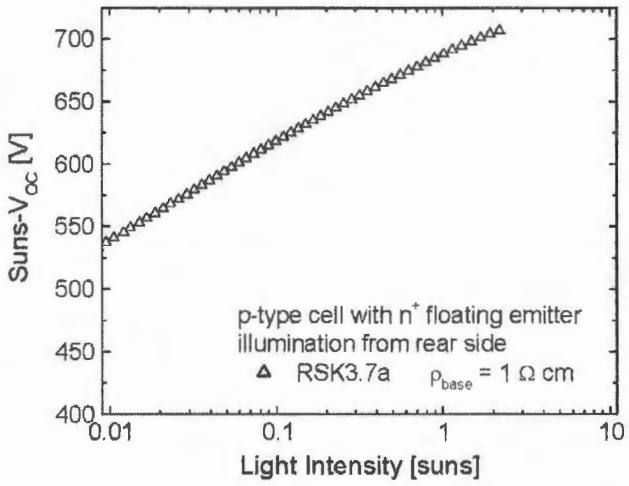


Figure 9-8 Open-circuit voltage of the p-type back-contact back-junction cell with floating emitter (structure B) measured in bias light intensity range of 0.01 to 1 sun. Result for solar cell with 1 Ω cm base resistivity is shown. The solar cell was illuminated from the rear side during the measurement.

9.5 Front surface fields

n-type solar cells with a phosphorus-doped n^+ front surface field (structure C) with base resistivity of 1 and 8 Ω cm were selected for the low illumination analysis. As shown in Table 9-1, these cells have an efficiency of 20.4 % and 19.5 % respectively. The EQE of the 1 Ω cm cell (BC47-18g) equals 95 % at wavelength of 600 nm. The EQE of the 8 Ω cm cell (BC47-21g) is higher due to higher collection efficiency and equals 98 % at the same wavelength. Both structure C cells have an EQE independent of the bias light illumination intensity, as shown in Figure 9-9. The quantum efficiency of the analyzed cells does not decrease with lowering of the bias light intensity from 1 to 0.3 suns.

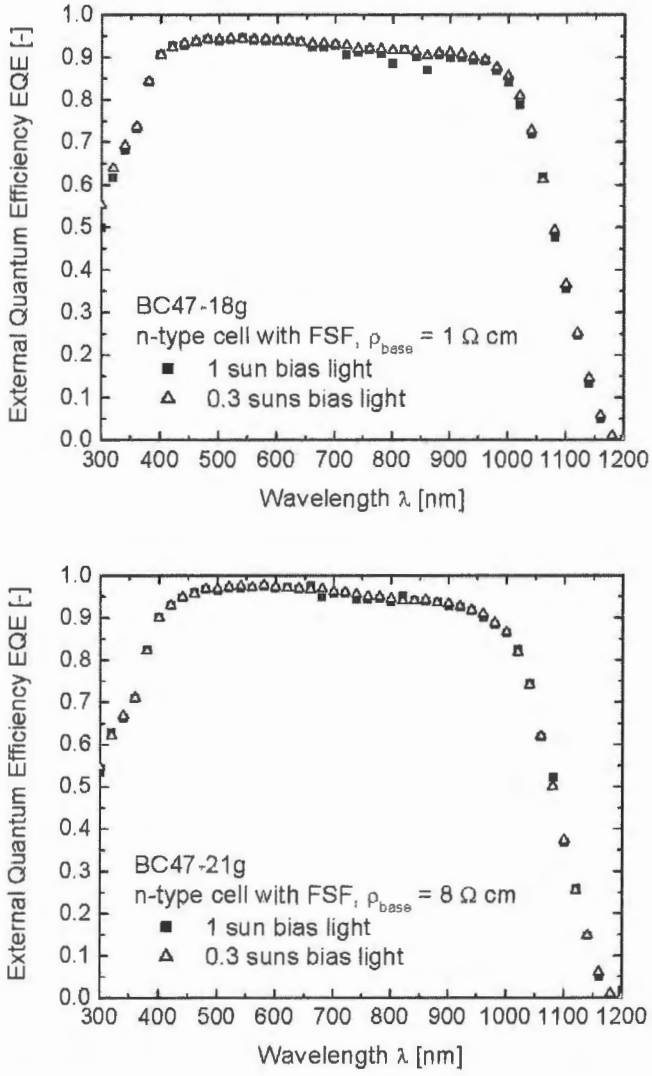


Figure 9-9 External quantum efficiency of n-type back-contact back-junction cells with front surface field (structure C) measured at 0.3 and 1 suns bias light intensity. Results for solar cells with base resistivity of 1 Ω cm (top) and 8 Ω cm (bottom) are shown.

The measurements of the normalized EQE for n-type cells with FSF are shown in Figure 9-10. The normalized EQE for both 1 and 8 Ω cm base doping is constant in the analyzed bias light intensity range. Therefore the current of the structure C is linear with bias light. Device simulations predict only a very weak injection dependence of the FSF cells. Within the measurement error, the experimental results are in good agreement with simulations.

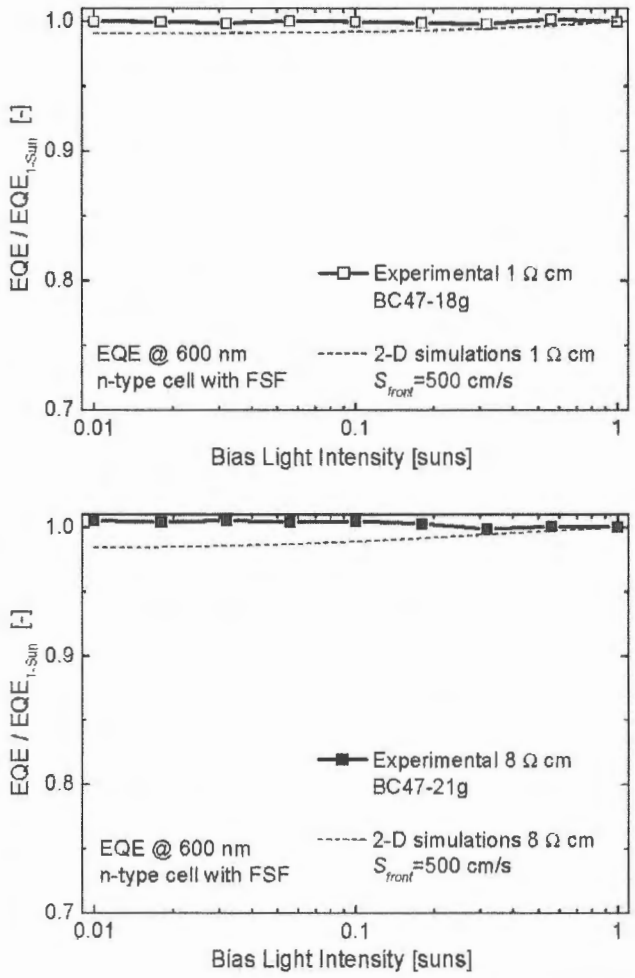


Figure 9-10 Normalized EQE for n-type cells with front surface field (structure C) measured at wavelength of 600 nm in bias light intensity range of 0.01 to 1 sun. Two-dimensional simulation results are shown as well (lines). Results for solar cells with base resistivity of 1 Ω cm (top) and 8 Ω cm (bottom) are shown.

The front surface of the FSF cell (structure C) always operates in the investigated illumination intensity range for both base resistivities under low-injection, due to high doping surface concentration of the phosphorus diffusion profile ($N_{peak} = 5 \times 10^{18}$ cm^{-3}). Thus, the high-injection effects do not occur at the physical surface as in the case of structure A and B cells, which showed a strong current injection dependence. A good passivation quality is achieved due to the high-low junction at the front surface, which is not affected by the illumination level, in contrast to the floating emitter passivation shown in the previous section. The front surface passivation with FSF is thus well suited also for low-illumination power generation.

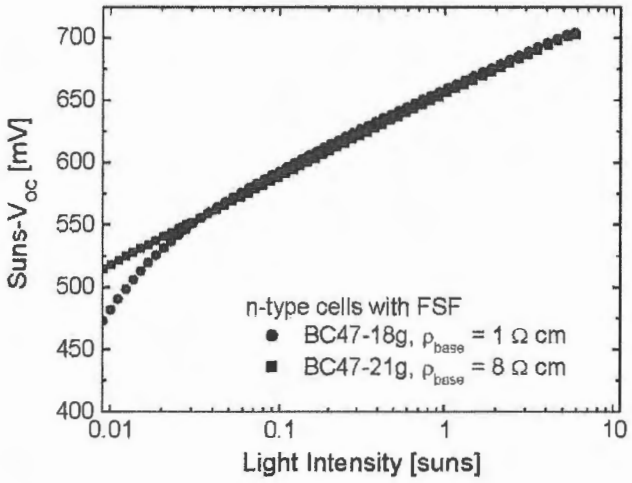


Figure 9-11 . Open-circuit voltage of the n-type back-contact back-junction cells with front surface field (structure C) measured in bias light intensity range of 0.01 to 10 suns. Results for base resistivity of 1 and 8 Ω cm are shown.

The open-circuit voltage of the structure C cells measured in wide illumination intensity range is shown in Figure 9-11. Both measured cells show a linear decrease in voltage with lowering of the illumination intensity down to 0.1 suns. However, for illumination intensity lower than 0.1 suns, the V_{OC} of both cells becomes non-linear with illumination. This effect is much stronger for the cells with base resistivity of 1 Ω cm than for the cells with base resistivity of 8 Ω cm. A further analysis of this effect is needed in order to fully explain observed non-linearity of the voltage of the structure C cells. However, since the current of the n-type cells with FSF is independent of the illumination intensity and the voltage shows non-linear behavior only at the illumination intensities lower than 0.1 suns, it may be concluded that the structure C is best suited for low illumination applications from all three analyzed cell structures.

9.6 Conclusions

The quantum efficiency and open-circuit voltage of the three back-contact back-junction solar cell structures was analyzed under low illumination conditions. Among the analyzed cell structures, it was shown that the current of only n-type cells with n^+ front surface field is linear with light intensity. The quantum efficiency of the n-type cells with non-diffused front surfaces and the p-type cells with floating emitter decreases with lower illumination intensity. This leads to a reduced cell performance under lower illumination.

In practical terms, non-perfect processing of the front surface, including diffusion inhomogenities, introduction of crystal defects, broken pyramid tips, and local scratches introduce injection dependence behavior of the n-type cells with non-diffused front surfaces and the p-type cells with floating emitter. On the other hand, front surface recombination of the n-type solar cells with FSF has much lower influence on the cell performance, due to the passivation effect of the high-low junction. Therefore, the performance of the n-type cells with FSF is not affected by low-injection effects. Thus, the passivation of the front surface of the BC-BJ cells with FSF seem to be the best one suited for achieving a high energy yield when also operating under low illumination intensity.

As expected from the physical model, the V_{OC} of all cell structures decreases linearly with the logarithm of illumination until intensity of 0.1 suns. The injection level of a solar cell under V_{OC} conditions is much higher than under the J_{SC} conditions. Therefore the low injection effects cannot be seen at lower illumination intensities, in contrast to the case of quantum efficiency analysis.

10 Summary and outlook

Summary

In this thesis high-efficiency back-contact back-junction (BC-BJ) silicon solar cells for one-sun applications were studied. The focus was put on the development of a low-cost and industrially feasible manufacturing technology in order to utilize the full cost reduction potential of this elegant cell structure. At the same time the performance of the developed solar cells was investigated in details by experimental work, analytical modeling and numerical device simulations.

The BC-BJ solar cell structure requires multiple *structuring steps*, to form an interdigitated grid of p- and n-diffusions, contact openings and metal grids. In this work, the complex and costly photolithography masking steps were replaced by techniques which are of low cost and relevant for mass production. Screen-printing of the masking layers, as well as the local laser ablation of the dielectric and silicon layers, were developed and successfully applied to the solar cell processing sequence. The highest solar cell efficiency of 21.1 % (J_{SC} = 38.6 mA/cm^2, V_{OC} = 668 mV, FF = 82.0 %) was achieved on 160 µm thick 1 Ω cm n-type FZ Si with the designated area of 4 cm^2. No photolithography was applied in the processing sequence of this solar cell.

High-temperature diffusion of boron is applied for *emitter formation* of the n-type BC-BJ solar cells. However, this process needs to take place at strongly elevated temperatures and requires an additional masking step in order to define the areas for local diffusion. Therefore an alternative low temperature and mask less process to create p-type emitters, namely the local laser-fired aluminium emitter (LFE) process, was investigated in detail. It was found that the injection-dependent Shockley-Read-Hall recombination in the laser-induced damage zone located in the direct vicinity of the local back junction negatively influences the cell performance. Based on this disadvantage of the LFE process, the application of the LFE in the manufacturing of the high-efficiency back-junction solar cells was not followed further in the course of this thesis.

A *detailed study of the loss mechanisms* limiting the efficiency of the developed back-contact back-junction silicon solar cell was performed. The reduction of the cell efficiency was determined to be 3.9 % abs. due to recombination processes, 2.0 % abs. due to optical losses, 0.3 % abs. due to series resistance effects and 0.7 % due to electrical shading. The developed model of the loss mechanisms is a powerful tool for

the further optimization study of the solar cell structure. Based on this model it was found that the solar cell efficiencies of up to 23 % could be reached by improving the solar cell optics, reduction of the overall recombination losses, minimization of the electrical shading and optimization of the cell and grid geometry, which is limited by the industrial structuring technologies.

Positive effects of the phosphorus doped n^+ *front surface field* (FSF) on the performance of the BC-BJ solar cells were studied in details. These positive effects of FSF include: (i) passivation of the front cell surface and improvement of the stability of the cell performance under UV exposure, (ii) reduction of the series resistance and (iii) improvement of the solar cell performance under low illumination.

The best solar cell results were obtained with a deep diffused Gaussian phosphorus FSF doping profile with sheet resistance of 148 Ω/sq. The saturation current density of the passivated and textured surface with this FSF diffusion profile equals 21 fA/cm^2. In contrast to solar cells without the FSF diffusion, the solar cells with the FSF diffusion profile did not show any performance degradation under *exposure to UV radiation.*

Phosphorus doped FSF not only improves the front surface passivation of the analyzed solar cells. The highly doped front n^+ layer can be also seen as a highly conductive *highway* for the majority carriers, which enhances its lateral transport. The front diffused n^+ layer can be seen as a parallel conductor to the lateral base resistance. This way the lateral base resistance can be reduced. Lateral pitch is in the case of the developed cells in the range of millimeters, due to the application of the low-cost screen-printing and laser ablation structuring. Experimental data show that the application of a FSF reduces the total series resistance of the measured n-type cells of 160 micrometer thickness with 3.5 mm pitch by 0.1 Ω cm^2 for 1 Ω cm base resistivity and 1.3 Ω cm^2 for 8 Ω cm base resistivity.

Next to improvement of the front surface passivation and reduction of the lateral base resistance, the front surface field improves the *performance* of the BC-BJ solar cells *under low illumination intensity.* Among different analyzed cell structures, it was shown that the current only of n-type cells with n^+ front surface field is linear with light intensity. Due to the fact that the front surface passivation of the n-type BC-BJ cells with FSF is not affected by low-injection effects, the quantum efficiency of these cells does not decrease in the bias light intensity range down to 0.01 suns. Therefore the BC-BJ cells with FSF seem to be these best suited for achieving a high energy yield when also operating under low illumination intensity.

Outlook

In the present thesis a base-line technological process for processing of back-contact back-junction Si solar cells was established. In order to further increase its economical competitiveness and fully utilize the potential of this cell structure, the *future research* should focus on the further optimization of the device efficiency and reduction of the manufacturing costs.

The *optimization of the solar cell geometry* should be pursued with the focus on increasing the emitter coverage on the rear side and at the same time reducing the overall device pitch. This can be obtained by careful optimization of the resolution and the positioning accuracy of the masking processing steps. Ideally these activities should be performed rather in the pilot-line environment than in the low-throughput laboratory conditions.

In parallel to the optimization of the device geometry, the electrical properties of the solar cell should be further optimized. The free carrier absorption losses and the high contribution of the rear side diffusions to the overall solar cell recombination point out the need of further *optimization of the emitter and back surface field diffusion profiles*. Also the *rear side passivation scheme* should be improved in order to reduce the recombination in the non-diffused gap areas.

An application of a pin-hole free passivation layer on the rear side, would enable *decoupling of the metallization geometry from the diffusion geometry*, without the risk of local shunt formation. This way the resistance losses in the thin base metallization fingers, which are especially important for the large size solar cells, would be reduced. Also the sizes of the diffused busbars could be reduced significantly. This way the electrical shading losses can be reduced. Further reduction of the processing costs could be obtained by replacing of the metallization using silver, by metallization scheme based on copper.

Next to the optimization of the solar cell structure, the *appropriate module technology* for the back-contacted solar cells should be applied. This technology should enable high packaging density of the solar cells and could use interconnection sheets with a pre-defined metallization pattern, which would further reduce the series resistance losses in the metallization grid.

Zusammenfassung und Ausblick

Zusammenfassung

Im Rahmen dieser Arbeit wurden hocheffiziente rückseitig kontaktierte Silicium-Solarzellen analysiert, bei denen der pn-Übergang ebenfalls auf der Rückseite ausgebildet wurde (sogenannte back-contact back-junction (BC-JC) Solarzellen). Ausgelegt waren diese Zellen für eine Beleuchtungsintensität von einer Sonne. Der Schwerpunkt dabei lag auf der Entwicklung eines preiswerten und industriell umsetzbaren Herstellungsprozesses, um das Kosteneinsparpotential dieser neuartigen Zellstruktur auszunutzen. Im Rahmen dieser Arbeit wurden ebenfalls die elektrische Effizienz der Zellen und die zugrunde liegenden physikalischen Effekte mittels verschiedener Experimente und analytischen und numerischen Simulationen detailliert untersucht.

Die Struktur der BC-BJ Solarzellen erfordert mehrere Ablaufschritte, um die ineinander greifende Struktur der p- und der n-Diffusionen, der Kontaktöffnungen und der Metallkontakte zu realisieren. In Rahmen dieser Arbeit wurden die komplexen und kostspieligen photolithographischen Prozessschritte durch einfachere und preiswertere Schritte ersetzt, welche auch industriell eingesetzt werden können. Sowohl siebgedruckte Maskierungsschichten als auch lokale lasergestützte Abtragung von dielektrischen Schichten und Silicium wurden erfolgreich entwickelt und angewandt. Das beste Zellergebnis mit einer Effizienz von 21.1 % (Kurzschlussstromdichte 38.6 mA/cm^2, Offenklemmspannung 668 mV, Füllfaktor 82.0 %) wurden bei einer 160 µm dicken, auf 1 Ω cm n-typ FZ Silicium prozessierten Solarzelle ermittelt, welche eine Aperturfläche von 4 cm^2 besaß. Bei der Prozessierung dieser hocheffizienten Solarzelle wurde komplett auf photolithographische Schritte verzichtet.

Bei den n-typ BC-JC Solarzellen wurde der Emitter durch eine Diffusion von Bor hergestellt. Allerdings sind dazu hohe Temperaturen und zusätzliche Maskierungsschritte notwendig, um die Bereiche für die lokale Diffusion einzugrenzen. Daher wurde im Rahmen dieser Arbeit ein alternativer Prozess eingehende analysiert, bei dem auf die hohen Temperaturen verzichtet werden kann und welcher ohne zusätzliche Maskierungen funktioniert. Der p-typ Emitter wird dabei durch das sogenannte „laser-fired aluminium emitter (LFE)"-Verfahren ausgebildet. Es konnte gezeigt werden, dass die injektionsabhängige Shockley-Read-Hall-Rekombination in der laserbedingten Schädigungszone in der direkten Umgebung der

lokalen rückseitigen Raumladungszone die Zelleffizienz negativ beeinflusst. Bedingt durch diesen Nachteil des LFE-Prozesses wurde dieser Ansatz im Verlauf dieser Arbeit nicht weiter verfolgt.

Ausführlich wurden die Verlustmechanismen, welche die Effizienz der untersuchten BC-BJ Solarzellen limitieren, analysiert. Dabei konnte gezeigt werden, dass die Zelleffizienz aufgrund von Rekombinationsprozessen um 3.9 % absolut, aufgrund von optischen Verlusten um 2.0 %, aufgrund von Serienwiderstands-Effekten um 0.3 % und aufgrund von elektrischen Abschattungen um 0.7 % reduziert ist. Es hat sich gezeigt, dass das entwickelte Modell der Verlustmechanismen ein mächtiges Werkzeug war, um die Struktur der hocheffizienten Solarzellen weiter zu verbessern. Darauf basierend konnte gezeigt werden, dass Zelleffizienzen von bis zu 23 % realisiert werden können, wenn die Zelloptik, Rekombinationsverluste, elektrische Abschattung und das Kontaktgrid weiter optimiert werden.

Im Rahmen dieser Arbeit wurden weiter die positiven Effekte eines Phosphor-dotierten n^+ „front surface fields (FSF)" untersucht. Diese Effekte beinhalten (i) Passivierung der Zellvorderseite und Langzeitstabilität bei Beleuchtung mittels UV-Licht, (ii) Reduzierung des Serienwiderstandes und (iii) Verbesserung der Solarzelleffizienz unter Schwachlichtverhältnissen.

Die besten Solarzellergebnisse wurden mit einem tief eingetriebenen Gauss-förmigen Phosphor FSF Dotierprofil mit einem Schichtwiderstand von 148 Ω/sq erreicht. Die Dunkelstromdichte der passivierten und texturierten Oberfläche lag dabei bei 21 fA/cm^2. Im Vergleich zu Solarzellen ohne das zusätzliche FSF konnte keine Degradation der Solarzellen unter UV-Licht nachgewiesen werden.

Ein Phosphor-dotiertes FSF verbessert nicht nur die Vorderseitenpassivierung der analysierten Solarzellen. Die hochdotierte n^+-Schicht verbessert zusätzlich den lateralen Transport der Majoritäts-Ladungsträger. In dieser Weise kann der Widerstand der Basis reduziert werden. Der laterale Abstand (Pitch) der Kontaktfinger lag bei den untersuchten Solarzellen im Bereich von Millimetern, bedingt durch die Verwendung von industriell tauglichen preiswertem Siebdruck und Laserstrukturierung. Experimentelle Daten zeigen, dass das zusätzliche FSF den gesamten Serienwiderstand der untersuchten n-typ Solarzellen mit einer Dicke von 160 µm und einem Pitch von 3.5 mm um 0.1 Ω cm^2 bei einem Basiswiderstand von 1 Ω cm und um 1.3 Ω cm^2 bei einem Basiswiderstand von 8 Ω cm reduziert.

Auch wurde im Rahmen dieser Arbeit untersucht, in wie weit das zusätzliche FSF die Zelleffizienz der BC-JC Solarzellen unter Schwachlichtbedingungen verbessert.

Mittels unterschiedlicher Zellstrukturen konnte gezeigt werden, dass bei einer n-typ Solarzelle mit einem zusätzlichen n^+ FSF der Strom linear mit der Lichtintensität ansteigt. Da diese Vorderseitenpassivierung nicht durch Niedriginjektionseffekte beeinflusst ist, ist die Quanteneffizienz der untersuchten BC-JC Solarzellen mit zusätzlichem FSF nicht verringert bis hin zu einer Lichtintensität von 0.01 Sonnen. Daher sind diese hier untersuchten BC-JC Solarzellen mit zusätzlichem FSF hervorragend geeignet, um eine hohe Stromausbeute auch unter Schwachlichtbedingengen zu erreichen.

Ausblick

In der vorliegenden Arbeit wurde ein technologischer Prozess für die Herstellung von rückseitig sammelnden und rückseitig kontaktierten Silizium-Solarzellen entwickelt. Um die Steigerung der ökonomischen Wettbewerbsfähigkeit und um das Potential dieser Zellstruktur weiter auszuschöpfen, sollten sich die zukünftige Forschungsaktivitäten auf eine weitere Optimierung des Solarzellewirkungsgrades und der Senkung der Herstellungskosten fokussieren.

Die Optimierung der Solarzellengeometrie sollte mit dem Schwerpunkt der Steigerung der Emitterbedeckung auf der Rückseite und der gleichzeitigen Verringerung der gesamten lateralen Solarzellendemensionen (Pitch) weiterverfolgt werden. Dies kann durch eine sorgfältige Optimierung der Auflösungs- und Positionierungsgenauigkeit der Maskierungsschritte erreicht werden. Ideellerweise, sollten diese Aktivitäten jedoch eher in einer Pilotlinie als in einer Laborumgebung mit geringem Durchsatz durchgeführt werden.

Parallel zur Optimierung der Solarzellengeometrie, sollten die elektrischen Eigenschaften der Solarzelle weiter verbessert werden. Die Verluste durch die Absorption freier Ladungsträger und der hohe Beitrag der Diffusionen auf der Rückseite zur gesamten Rekombination der Solarzelle haben gezeigt, dass eine Anpassung der Diffusionsprofile von Emitter und Back-Surface-Field erforderlich ist. Das rückseitige Passivierungssystem sollte ebenfalls verbessert werden, um die Rekombination im undiffundierten Bereich zu reduzieren.

Die Anwendung von „pin-hole"-freien Passivierungsschichten auf der Rückseite, würden die Entkopplung der Metallisierungsgeometrie und der Geometrie der Diffusionen ermöglichen, ohne lokale Kurzschlüsse zu erzeugen. Dadurch würden die Widerstandsverluste in den dünnen Fingern der Basismetallisierung, welche besonders wichtig für Solarzellen im Großformat sind, reduziert werden. Auch lässt sich die

Fläche der diffundierten Busbars signifikant verringert. Eine weitere Verringerung der Herstellungskosten könnte erreicht werden, indem die Metallisierung mit Silber durch die Verwendung eines Metallisierungsverfahrens mit Kupfer ersetzt wird.

Neben der Optimierung der Solarzellenstruktur, sollte eine geeignete Modultechnologie für rückseitig kontaktierte Solarzellen bereitgestellt werden. Diese Technologie sollte eine hohe Packungsdichte der Solarzellen ermöglichen und könnte durch die Verwendung einer Folien mit einem vordefinierten Metallisierungsmuster zum Zusammenschalten der Solarzellen, die Serienwiderstandsverluste im Metalisierungsgitter weiter senken.

Symbols, acronyms and physical constants

Symbols

Symbol	Description	Unit
A	area	cm^2
A_F	pitch of the solar cell	µm
a_{n+n}	distance between n^+ and n^+ doping	µm
B_F	width of the metal fingers	µm
B_R	radiative recombination coefficient	
C	concentration	
C_A	Auger coefficient	$cm^{-3}\ s^{-1}$
d_{wafer}	wafer thickness	µm
E_i	intrinsic Fermi level	eV
FF	fill factor	
H_F	height of the metal fingers	µm
J_0	saturation current density	$A\ cm^{-2}$
J_{01}, J_{02}	dark saturation current densities in a two-diode model	$A\ cm^{-2}$
J_{0s}	surface recombination current density	$A\ cm^{-2}$
J_{mpp}	current at maximum power point	$A\ cm^{-2}$
J_{ph}	photogeneratred current	$A\ cm^{-2}$
J_{SC}	short-circuit current density	$A\ cm^{-2}$
l	average path length of incoming light within silicon wafer	
L_{eff}	effective diffusion length of the minority carriers	µm

Symbol	Description	Unit
L_F	length of the metal fingers	µm
n_0	equilibrium concentration of electrons	cm^{-3}
N_A	concentration of acceptor atoms	cm^{-3}
N_D	concentration of donor atoms	cm^{-3}
n_e	electron density	cm^{-3}
n_i	intrinsic carrier density	cm^{-3}
N_{peak}, N_S	surface doping concentration	cm^{-3}
n_{Si}	refractive index of silicon	
N_{st}	number of surface states	cm^{-2}
p_0	equilibrium concentration of holes	cm^{-3}
PFF	pseudo fill factor	
P_{RP}	photon recycling rate	
$R_{CE\text{-}Auger}$	Columb-enhanced Auger recombination rate	$cm^{-3}s^{-1}$
R_p	parallel resistance	Ω
R_{rad}	radiative recombination rate	$cm^{-3}s^{-1}$
R_S	series resistance	Ω
S	surface recombination rate	$cm\ s^{-1}$
S_{eff}	effective surface recombination velocity	$cm\ s^{-1}$
S_{front}	front surface recombination velocity	$cm\ s^{-1}$
T	temperature	K or °C
t	time	h
U_S	net recombination rate at surface	$cm^{-2}\ s^{-1}$
V	voltage	mV
V_{mpp}	voltage at maximum power point	mV

Symbol	Description	Unit
V_{OC}	open-circuit voltage	mV
W	wafer thickness	µm
x_j	junction depth	µm
Δn	excess carrier density	cm^{-3}
α_{FCA}	free carrier absorption coefficient	cm^{-1}
α_{Si}	absorption coefficient of silicon	cm^{-1}
η	efficiency	%
λ	wavelength	nm
ρ	resistivity	Ω cm
ρ_{base}	resistivity of the base material	Ω cm
ρ_{FSF}	sheet resistance of the front surface field	Ω/sq
ρ_{sheet}	sheet resistance	Ω/sq
σ_n	capture cross section for electrons	cm^2
σ_p	capture cross section for holes	cm^2
τ_A	minority carrier lifetime of Auger recombination	µs
τ_{bulk}	minority carrier lifetime in bulk	µs
τ_{eff}	effective minority carrier lifetime	µs
τ_{rad}	minority carrier lifetime of radiative recombination	µs
τ_S	minority carrier lifetime of surface recombination	µs
τ_{SRH}	Shockley-Read-Hall recombination lifetime	µs
υ_{th}	thermal velocity of charge carriers	$cm\ s^{-1}$

Acronyms

Acronym	Description
AM1.5g	air mass 1.5 global spectrum
ARC	anti-reflection coating
BC-BJ	back-contact back-junction solar cell
BSF	back surface field
Cz-Si	monocrystalline silicon produced with the Czochralsky method
EQE	external quantum efficiency
EWT	emitter wrap through solar cell
FCA	free carrier absorption
FGA	forming gas anneal
FZ-Si	monocrystalline silicon produced with the floating zone method
FSF	front surface field
IQE	internal quantum efficiency
IBC	interdigitated back contact solar cell
LBSF	local back surface field
LBIC	light beam induced current
LFE	laser-fired aluminium emitters
LFC	laser-fired contacts
LIP	light-induced plating
mc-Si	multicrystalline silicon
MWT	metallization warp through solar cell
PCD	photoconductance decay
PECVD	plasma enhanced chemical vapour deposition
PERL	passivated emitter real locally diffused solar cell

Acronym	Description
PERC	passivated emitter and rear cell solar cell
QSSPC	quasi-steady state photoconductance
SIMS	secondary ion mass spectroscopy
SEM	scanning electron microscope
STC	standard testing conditions

Physical constants

Constant	Description	Value
k	Boltzmann's constant	1.3806×10^{-23} J K^{-1}
c	velocity of light	299792458 m s^{-1}
h	Planck constant	6.62607×10^{-34} J s
n_i	intrinsic carrier density	1.00×10^{10} cm^{-3}
q	elementary charge	1.6022×10^{-19} C

Bibliography

[1] EPIA and Greenpeace, *Solar Generation V – 2008. Solar electricity for over one billion people and two million jobs by 2020*, (2008).

[2] R.M. Swanson, *A vision for crystalline silicon photovoltaics*, Progress in Photovoltaics: Research and Applications, **14** (5), 443-53, (2006).

[3] D. De Ceuster, P. Cousins, D. Rose, D. Vicente, P. Tipones, and W. Mulligan, *Low Cost, high volume production of >22% efficiency silicon solar cells*, in *Proceedings of the 22nd European Photovoltaic Solar Energy Conference*, Milan, Italy, 816-9 (2007).

[4] M.A. Green, *Solar cells: operating principles, technology and system applications*. 1986, Kensington: UNSW.

[5] P. Würfel, *Physics of Solar Cells*. 2005, Weinheim: Wiley.

[6] A. Luque and S. Hegedus, *Handbook of Photovoltaic Science and Engineering*. 2003, West Sussex: John Wiley & Sons Ltd.

[7] M. Späth, P.C. de Jong, and J. Bakker, *A novel module assembly line using back contact solar cells*, in *Technical Digest of the 17th International Photovoltaic Solar Energy Conference*, Fukuoka, Japan, 436 (2007).

[8] J. Zhao, A. Wang, and M.A. Green, *24·5% Efficiency silicon PERT cells on MCZ substrates and 24.7% efficiency PERL cells on FZ substrates*, Progress in Photovoltaics: Research and Applications, **7** (6), 471-4, (1999).

[9] O. Schultz, S.W. Glunz, and G. Willeke, *Multicrystalline Silicon Solar Cells Exceeding 20 % Efficiency*, Progress in Photovoltaics: Research and Applications, **12** (7), 553-8, (2004).

[10] S.W. Glunz, *New concepts for high-efficiency silicon solar cells*, Solar Energy Materials and Solar Cells, **90** (18-19), 3276-84, (2006).

[11] S.W. Glunz, *High-efficiency crystalline silicon solar cells*, Advances in OptoElectronics, **2007**, 97370/1-15, (2007).

[12] E. Van Kerschaver and G. Beaucarne, *Back-contact solar cells: a review*, Progress in Photovoltaics: Research and Applications, **14** (2), 107-23, (2006).

[13] R.J. Schwartz and M.D. Lammert, *Silicon solar cells for high concentration applications*, in *Technical Digest of the International Electron Devices Meeting*, Washington, DC, 350-2 (1975).

[14] M.D. Lammert and R.J. Schwartz, *The interdigitated back contact solar cell: a silicon solar cell for use in concentrated sunlight*, IEEE Transactions on Electron Devices, **ED-24** (4), 337-42, (1977).

[15] R.M. Swanson, A.K. Beckwith, R.A. Crane, W.D. Eades, Y.H. Kwark, and R.A. Sinton, *Point-contact silicon solar cells*, IEEE Transactions on Electron Devices, **31** (5), 661-4, (1984).

[16] R.A. Sinton, Y. Kwark, J.Y. Gan, and R.M. Swanson, *27.5-percent silicon concentrator solar cells*, IEEE Electron Device Letters, **EDL-7** (10), 567-9, (1986).

[17] R.A. Sinton and R.M. Swanson, *Design criteria for Si point-contact concentrator solar cells*, IEEE Transactions on Electron Devices, **ED-34** (10), 2116-23, (1987).

[18] R.A. Sinton, P. Verlinden, D.E. Kane, and R.M. Swanson, *Development efforts in silicon backside-contact solar cells*, in *Proceedings of the 8th European Photovoltaic Solar Energy Conference*, Florence, Italy, 1472-6 (1988).

[19] P. Verlinden, F. Van de Wiele, G. Stehelin, and J.P. David, *Optimized interdigitated back contact (IBC) solar cell for high concentrated sunlight*, in *Proceedings of the 18th IEEE Photovoltaic Specialists Conference*, Las Vegas, Nevada, USA, 55-60 (1985).

[20] R.R. King, R.A. Sinton, and R.M. Swanson, *Front and back surface fields for point-contact solar cells*, in *Proceedings of the 20th IEEE Photovoltaic Specialists Conference*, Las Vegas, Nevada, USA, 538-44 (1988).

[21] P. Verlinden, R.A. Sinton, and R.M. Swanson, *High efficiency large area back contact concentrator solar cells with a multilevel interconnection*, International Journal of Solar Energy, **6** (6), 347-66, (1988).

[22] P. Verlinden, R.M. Swanson, R.A. Sinton, and D.E. Kane, *Multilevel metallization for large area point-contact solar cells*, in *Proceedings of the 20th IEEE Photovoltaic Specialists Conference*, Las Vegas, Nevada, USA, (1988).

[23] R.R. King, R.A. Sinton, and R.M. Swanson, *One-Sun, Single-Crystalline Silicon Solar Cell Research*. Solid State Electronics Laboratory, Stanford University, Stanford, (1991).

[24] R.A. Sinton and R.M. Swanson, *Simplified backside-contact solar cells*, IEEE Transactions on Electron Devices, **37** (2), 348-52, (1990).

[25] R.A. Sinton, P.J. Verlinden, R.A. Crane, R.M. Swanson, C. Tilford, J. Perkins, and K. Garrison, *Large-area 21% efficient Si solar cells*, in *Proceedings of the 23rd IEEE Photovoltaic Specialists Conference*, Louisville, Kentucky, USA, 1490, 157-61 (1993).

[26] P.J. Verlinden, R.M. Swanson, and R.A. Crane, *7000 high efficiency cells for a dream*, Progress in Photovoltaics: Research and Applications, **2** (2), 143, (1994).

[27] P.J. Verlinden, R.A. Sinton, K. Wickham, R.A. Crane, and R.M. Swanson, *Backside-contact silicon solar cells with improved efficiency for the `96 world solar challenge*, in *Proceedings of the 14th European Photovoltaic Solar Energy Conference*, Barcelona, Spain, 96-9 (1997).

[28] M.J. Cudzinovic and K. McIntosh, *Process simplifications to the Pegasus solar cell - Sunpower's high-efficiency bifacial solar cell*, in *Proceedings of the 29th IEEE Photovoltaics Specialists Conference*, New Orleans, Louisiana, USA, 70-3 (2002).

[29] W.P. Mulligan, D.H. Rose, M.J. Cudzinovic, D.M. De Ceuster, K.R. McIntosh, D.D. Smith, and R.M. Swanson, *Manufacture of solar cells with 21% efficiency*, in *Proceedings of the 19th European Photovoltaic Solar Energy Conference*, Paris, France, 387-90 (2004).

[30] K.R. McIntosh, M.J. Cudzinovic, D.D. Smith, W.P. Mulligan, and R.M. Swanson, *The choice of silicon wafer for the production of low-cost rear-contact solar cells*, in *Proceedings of the 3rd World Conference on Photovoltaic Energy Conversion*, Osaka, Japan, 971-4 (2003).

[31] K.R. McIntosh, N.C. Shaw, and J.E. Cotter, *Light trapping in Sunpower's A-300 solar cell*, in *Proceedings of the 19th European Photovoltaic Solar Energy Conference*, Paris, France, 844-7 (2004).

[32] R.M. Swanson, *Device physics for backside-contact solar cells*, in *Proceedings of the 33rd IEEE Photovoltaic Specialists Conference*, San Diego, USA, (2008).

[33] J. Dicker, J.O. Schumacher, W. Warta, and S.W. Glunz, *Analysis of one-sun monocrystalline rear-contacted silicon solar cells with efficiencies of 22.1%*, Journal of Applied Physics, **91** (7), 4335-43, (2002).

[34] J. Dicker, *Analyse und Simulation von hocheffizienten Silizium-Solarzellenstrukturen für industrielle Fertigungstechniken*, Dissertation, Universität Konstanz, (2003).

[35] A. Mohr, *Silicon concentrator cells in a two-stage photovoltaic system with a concentration factor of 300x*, Dissertation, Universität Freiburg, (2005).

[36] A. Mohr, T. Roth, and S.W. Glunz, *BICON: High concentration PV using one-axis tracking and silicon concentrator cells*, Progress in Photovoltaics: Research and Applications, **14**, 663-74, (2005).

[37] J.-H. Guo, *High-efficiency n-type laser-grooved buried contact silicon solar cells*, Dissertation, University of New South Wales, (2004).

[38] J.-H. Guo, B.S. Tjahjono, and J.E. Cotter, *19.2% efficiency n-type laser-grooved silicon solar cells*, in *Proceedings of the 31st IEEE Photovoltaic Specialists Conference*, Orlando, USA, 983-6 (2005).

[39] P. Engelhart, N.-P. Harder, R. Grischke, A. Merkle, R. Meyer, and R. Brendel, *Laser structuring for back junction silicon solar cells*, Progress in Photovoltaics: Research and Applications, **15**, 237-43, (2006).

[40] P. Engelhart, *Lasermaterialbearbeitung als Schlüsseltechnologie zum Herstellen rückseitenkontaktierter Siliciumsolarzellen*, Dissertation, Universität Hannover, (2007).

[41] D. Huljic, *et al.*, *Development of a 21 % back-contact monocrystalline silicon solar cell for large-scale production*, in *21st European Photovoltaic Solar Energy Conference*, Dresden, Germany, 765-8 (2006).

[42] D. Huljic, *et al.*, *Q-Cells' High-Efficiency Back Junction Solar Cell for Large-Scale Production - Main Results of the QUEBEC Project*, in *22nd European Photovoltaic Solar Energy Conference*, Milano, Italy, (2007).

[43] R. Stangl, M. Bivour, E. Conrad, I. Didschuns, L. Korte, K. Lips, and M. Schmidt, *Recash - A novel high efficiency buried grid rear contact amorphous/crystalline silicon heterojunction solar cell concept*, in *Proceedings of the 22nd European Photovoltaic Solar Energy Conference*, Milan, Italy, 870-4 (2007).

[44] M. Tucci, *et al.*, *BEHIND (Back enhanced heterostructure with interdigitated conctacts) solar cell*, in *23rd European Photovoltaic Solar Energy Conference*, Valencia, Spain, 1749-52 (2008).

[45] L. Meijun, B. Stuart, D. Ujjwal, and B. Robert, *Interdigitated back contact silicon heterojunction solar cell and the effect of front surface passivation.* Applied Physics Letters, **91** (6), 063507, (2007).

[46] J.M. Gee, W.K. Schubert, and P.A. Basore, *Emitter wrap-through solar cell*, in *Proceedings of the 23rd IEEE Photovoltaic Specialists Conference*, Louisville, Kentucky, USA, 265-70 (1993).

[47] J.M. Gee, M.E. Buck, W.K. Schubert, and P.A. Basore, *Progress on the emitter wrap-through silicon solar cell*, in *Proceedings of the 12th European Photovoltaic Solar Energy Conference*, Amsterdam, The Netherlands, 743-6 (1994).

[48] D. Kray, *Hocheffiziente Solarzellenstrukturen für kristallines Silicium-Material industrieller Qualität*, Dissertation, Universität Konstanz, (2004).

[49] J.M. Gee, P. Hacke, M.W. Sumner, and R.R. Schmit, *Towards a manufacturable back-contact emitter-wrap-through silicon solar cell*, in *Photovoltaic Specialists Conference, 2005. Conference Record of the Thirty-first IEEE*, 1663-6 (2005).

[50] A. Kress, O. Breitenstein, S. Glunz, P. Fath, G. Willeke, and E. Bucher, *Investigations on low-cost back-contact silicon solar cells*, Solar Energy Materials and Solar Cells, **65**, 555-60, (2001).

[51] A. Kress, *Emitterverbund-Rückkontaktsolarzellen für die industrielle Fertigung*, Dissertation, Universität Konstanz, (2001).

[52] D. Kray, *et al.*, *Progress in high-efficiency emitter-wrap-through cells on medium quality substrates*, in *Proceedings of the 3rd World Conference on Photovoltaic Energy Conversion*, Osaka, Japan, 1340-3 (2003).

[53] S.W. Glunz, *et al.*, *High-efficiency cell structures for medium-quality silicon*, in *Proceedings of the 17th European Photovoltaic Solar Energy Conference*, Munich, Germany, 1287-92 (2001).

[54] S. Hermann, *et al.*, *21.4 %-efficient emitter wrap-through RISE solar cell on large area and picosecond laser processing of local contact openings*, in *Proceedings of the 22nd European Photovoltaic Solar Energy Conference*, Milan, Italy, 970-5 (2007).

[55] C. Peters, *et al.*, *ALBA – Development of high-efficiency mulit-crystalline Si EWT solar cells for industrial fabrication at Q-Cells*, in *Proceedings of the 23rd European Photovoltaic Solar Energy Conference*, Valencia, Spain, 1010-13 (2008).

[56] E. van Kerschaver, R. Einhaus, J. Szlufcik, J. Nijs, and R. Mertens, *A novel silicon solar cell structure with both external polarity contacts on the back surface*, in *Proceedings of the 2nd World Conference on Photovoltaic Energy Conversion*, Vienna, Austria, 1479-82 (1998).

[57] H. Knauss, H. Haverkamp, W. Jooss, S. Steckemetz, and H. Nussbaumer, *Industrially applicable metallisation wrap through solar cell process resulting in efficiencies exceeding 16 %*, in *Proceedings of the 21st European Photovoltaic Solar Energy Conference*, Dresden, Germany, 1192-5 (2006).

[58] E. Van Kerschaver, C. Allebé, B. Devreese, L. Frisson, and J. Szlufcik, *Record high performance modules based on screen printed MWT solar cells*, in *Proceedings of the 29th IEEE Photovoltaics Specialists Conference*, New Orleans, Louisiana, USA, 78-81 (2002).

[59] J.H. Bultman, M.W. Brieko, A.R. Burgers, J. Hoornstra, A.C. Tip, and A.W. Weeber, *Interconnection through vias for improved efficiency and easy module manufacturing of crystalline silicon solar cells*, Solar Energy Materials and Solar Cells, **65**, 339-45, (2001).

[60] A.W. Weeber, R. Kinderman, C.J.J. Tool, F. Granek, and P.C. De Jong, *How to achieve 17% cell efficiencies on large back-contacted mc-Si solar cells*, in

Proceedings of the 4th World Conference on Photovoltaic Energy Conversion, Hawaii, USA, 1048-51 (2006).

[61] F. Clement, *et al.*, *Industrially feasible MC-Si metal wrap through (MWT) solar cells with high emitter sheet resistances exceeding 16% efficiency*, in *Proceedings of the 23rd European Photovoltaic Solar Energy Conference*, Valencia, Spain, in print (2008).

[62] W. Jooss, H. Knauss, F. Huster, P. Fath, E. Bucher, R. Tölle, and T.M. Bruton, *Back contact buried contact solar cells with metallization wrap around electrodes*, in *Proceedings of the 28th IEEE Photovoltaics Specialists Conference*, Anchorage, Alaska, USA, 176-9 (2000).

[63] D.A. Clugston and P.A. Basore, *PC1D version 5: 32-bit solar cell modeling on personal computers*, in *Proceedings of the 26th IEEE Photovoltaic Specialists Conference*, Anaheim, California, USA, 207-10 (1997).

[64] W. Shockley and H.J. Queisser, *Detailed balance limit of efficiency of p-n junction solar cells*, Journal of Applied Physics, **32** (3), 510-9, (1961).

[65] T. Tiedje, E. Yablonovitch, G.D. Cody, and B.G. Brooks, *Limiting efficiency of silicon solar cells*, IEEE Transactions on Electron Devices, **31** (5), 711-6, (1984).

[66] R.M. Swanson, *Approaching the 29% limit efficiency of silicon solar cells*, in *Proceedings of the 31st IEEE Photovoltaic Specialists Conference*, Orlando, USA, 889-94 (2005).

[67] R. Brendel, *Thin-film silicon solar cells: Physics and Technology*. 2003, Weinheim: Wiley-VCH.

[68] M.J. Kerr, *Surface, emitter and bulk recombination in silicon and development of silicon nitride passivated solar cells*, Dissertation, Australian National University, (2002).

[69] M.J. Kerr and A. Cuevas, *General parameterization of Auger recombination in crystalline silicon*, Journal of Applied Physics, **91** (4), 2473-80, (2002).

[70] M.J. Kerr, A. Cuevas, and P. Campbell, *Limiting efficiency of crystalline silicon solar cells due to Coulomb-enhanced Auger recombination*, Progress in Photovoltaics: Research and Applications, **11** (2), 97-104, (2003).

[71] M.A. Green, *Limits on the open-circuit voltage and efficiency of silicon solar cells imposed by intrinsic Auger processes*, IEEE Transactions on Electron Devices, **ED-31** (5), 671-8, (1984).

[72] T. Trupke, M.A. Green, P. Würfel, P.P. Altermatt, A. Wang, J. Zhao, and R. Corkish, *Temperature dependence of the radiative recombination coefficient of intrinsic crystalline silicon*, Journal of Applied Physics, **94** (8), 4930-7, (2003).

[73] Sinton-Consulting-Inc., *http://www.sintonconsulting.com/*.

[74] H. Nagel, C. Berge, and A.G. Aberle, *Generalized analysis of quasi-steady-state and quasi-transient measurements of carrier lifetimes in semiconductors*, Journal of Applied Physics, **86** (11), 6218- 21, (1999).

[75] R.A. Sinton, A. Cuevas, and M. Stuckings, *Quasi-steady-state photoconductance, a new method for solar cell material and device characterization*, in *Proceedings of the 25th IEEE Photovoltaic Specialists Conference*, Washington DC, USA, 457-60 (1996).

[76] B. Fischer, *Loss analysis of crystalline silicon solar cells using photoconductance and quantum efficiency measurements*, Dissertation, Universität Konstanz, (2003).

[77] W. Shockley and W.T.J. Read, *Statistics of the recombinations of holes and electrons*, Physical Review, **87** (5), 835-42, (1952).

[78] R.N. Hall, *Electron-hole recombination in germanium*, Physical Review, **87**, 387, (1952).

[79] J. Dziewior and W. Schmid, *Auger coefficients for highly doped and highly excited silicon*, Applied Physics Letters, **31** (5), 346-8, (1977).

[80] A.B. Sproul and M.A. Green, *Intrinsic carrier concentration and minority-carrier mobility of silicon from 77 to 300 K*, Journal of Applied Physics, **73** (3), 1214-25, (1993).

[81] A. Cuevas, *The effect of emitter recombination on the effective lifetime of silicon wafers*, Solar Energy Materials and Solar Cells, **57** (3), 277-90, (1999).

[82] A. Cuevas and D. Macdonald, *Measuring and interpreting the lifetime of silicon wafers*, Solar Energy, **76** (1-3), 255-62, (2004).

[83] A.B. Sproul, *Dimensionless solution of the equation describing the effect of surface recombination on carrier decay in semiconductors*, Journal of Applied Physics, **76** (5), 2851-4, (1994).

[84] J. del Alamo, J. Van Meerbergen, F. D'Hoore, and J. Nijs, *High-low junctions for solar cell applications*, Solid-State Electronics, **24**, 533-8, (1981).

[85] D.E. Kane and R.M. Swanson, *Measurement of the emitter saturation current by a contactless photoconductivity decay method (silicon solar cells)*, in *Proceedings of the 18th IEEE Photovoltaic Specialists Conference*, Las Vegas, Nevada, USA, 578-83 (1985).

[86] M. Hermle, *Analyse neuartiger Silizium- und III-V Solarzellen mittels Simulation und Experiment*, Dissertation, Universität Konstanz, (2008).

[87] M. Hermle, F. Granek, O. Schultz-Wittmann, and S.W. Glunz, *Shading effects in back-junction back-contacted silicon solar cells*, in *Proceedings of the 33rd IEEE Photovoltaic Specialists Conference*, San Diego, USA, (2008).

[88] J.O. Schumacher, *Charakterisierung texturierter Silicium-Solarzellen*, Diplomarbeit, Universität Freiburg, (1994).

[89] *DESSIS Manual 7.0.*

[90] S. Synopsis Zurich, *SDEVICE Manual Release: Z-2007.03*, *www.synopsys.com*, (2007)

[91] J.O. Schumacher, *Numerical simulation of silicon solar cells with novel device structures*, PhD, University of Konstanz, (2000).

[92] P.A. Basore and D.A. Clugston, *PC1D version 4 for Windows: from analysis to design*, in *Proceedings of the 25th IEEE Photovoltaic Specialists Conference*, Washington D C, 377-81 (1996).

[93] R. Brendel, *Sunrays: A versatile ray tracing program for the photovoltaic community*, in *Proceedings of the 12th European Photovoltaic Solar Energy Conference*, Amsterdam, The Netherlands, 1339-42 (1994).

[94] A. Cuevas, G. Giroult-Matlakowski, P.A. Basore, C. DuBois, and R.R. King, *Extraction of the surface recombination velocity of passivated phosphorus-doped silicon emitters*, in *Proceedings of the 1st World Conference on Photovoltaic Energy Conversion- WCPEC*, Waikoloa, Hawaii, USA, **2**, 1446-9 (1994).

[95] A. Cuevas, M. Stuckings, J. Lau, and M. Petravic, *The recombination velocity of boron diffused silicon surfaces*, in *Proceedings of the 14th European Photovoltaic Solar Energy Conference*, Barcelona, Spain, 2416-9 (1997).

[96] R.A. Sinton, P.J. Verlinden, R.M. Swanson, R.A. Crane, K. Wickham, and J. Perkins, *Improvements in silicon backside-contact solar cells for high-value one-sun applications*, in *Proceedings of the 13th European Photovoltaic Solar Energy Conference*, Nice, France, 1586-9 (1995).

[97] J. Benick, B. Hoex, M.C.M. Van de Sanden, W.M.M. Kessels, O. Schultz, and S. Glunz, *Effective passivation of boron emitters with Al_2O_3 for high-efficiency n-type solar cells*, Applied Physics Letters, **92** (24), 253504-1, (2008).

[98] J. Benick, B. Hoex, O. Schultz, and S.W. Glunz, *Surface passivation of boron diffused emitters for high efficiency solar cells*, in *Proceedings of the 33rd IEEE Photovoltaic Specialists Conference*, San Diego, USA, (2008).

[99] V.D. Mihailetchi, Y. Komatsu, and L.J. Geerligs, *Nitric acid pretreatment for the passivation of boron emitters for n-type base silicon solar cells*, Applied Physics Letters, **92**, 063510, (2008).

[100] J. Libal, *et al.*, *N-type multicrystalline silicon solar cells: BBr_3-diffusion and passivation of P^+-diffused silicon surfaces*, in *Proceedings of the 20th European Photovoltaic Solar Energy Conference*, Barcelona, Spain, 793-6 (2005).

[101] C.J.J. Tool, H.C. Rieffe, R. Kinderman, R. Kopecek, K. Wambach, and L.J. Geerligs, *Solar cells on n-type multicrystalline silicon wafers by industrial processing techniques*, in *Proceedings of the 19th European Photovoltaic Solar Energy Conference*, Paris, France, (2004).

[102] A. Cuevas, C. Samundsett, M.J. Kerr, D.H. Macdonald, H. Mäckel, and P.P. Altermatt, *Back junction solar cells on n-type multicrystalline and CZ silicon wafers*, in *Proceedings of the 3rd World Conference on Photovoltaic Energy Conversion*, Osaka, Japan, **1**, 963-6 (2003).

[103] J. Zhao and A. Wang, *High Efficiency Real Emitter PERT Solar Cells on n-type FZ Single Crystalline Silicon Substrates*, in *20th European Photovoltaic Solar Energy Conference and Exhibition*, Barcelona, Spain, (2005).

[104] C. Schmiga, M. Hermle, and S.W. Glunz, *Towards 20 % efficient n-type silicon solar cells with screen-printed aluminium-alloyed rear emitter*, in *Proceedings of the 23rd European Photovoltaic Solar Energy Conference and Exhibition*, Valencia, Spain, (2008).

[105] E. Maruyama, *et al.*, *Sanyo's challenges to the development of high-efficiency HIT solar cells and the expansion of HIT business*, in *Proceedings of the 4th World Conference on Photovoltaic Energy Conversion*, Waikoloa, Hawaii, USA, 1455-60 (2006).

[106] J. Schmidt, A.G. Aberle, and R. Hezel, *Investigation of carrier lifetime instabilities in Cz-grown silicon*, in *Proceedings of the 26th IEEE Photovoltaic Specialists Conference*, Anaheim, California, USA, 13-8 (1997).

[107] J. Schmidt and A. Cuevas, *Electronic properties of light-induced recombination centers in boron-doped Czochralski silicon*, Journal of Applied Physics, **86** (6), 3175- 80, (1999).

[108] S.W. Glunz, S. Rein, J.Y. Lee, and W. Warta, *Minority carrier lifetime degradation in boron-doped Czochralski silicon*, Journal of Applied Physics, **90** (5), 2397-404, (2001).

[109] D. Macdonald and L.J. Geerligs, *Recombination activity of interstitial iron and other transition metal point defects in p- and n-type crystalline silicon*, Applied Physics Letters, **85** (18), 4061-3, (2004).

[110] L.J. Geerligs and D. Macdonald, *Base doping and recombination activity of impurities in crystalline silicon solar cells*, Progress in Photovoltaics: Research and Applications, **12** (4), 309-16, (2004).

[111] A. Cuevas, M.J. Kerr, C. Samundsett, F. Ferrazza, and G. Coletti, *Millisecond minority carrier lifetimes in n-type multicrystalline silicon*, Applied Physics Letters, **81** (26), 4952-4, (2002).

[112] T. Trupke, R.A. Bardos, F. Hudert, P. Würfel, J. Zhao, A. Wang, and M.A. Green, *Effective excess carrier lifetimes exceeding 100 milliseconds in float zone silicon determined from photoluminescence*, in *Proceedings of the 19th European Photovoltaic Solar Energy Conference*, Paris, France, **1**, 758-61 (2004).

[113] S.W. Glunz, D. Biro, S. Rein, and W. Warta, *Field-effect passivation of the SiO_2-Si interface*, Journal of Applied Physics, **86** (1), 683-91, (1999).

[114] W. Kern, *Handbook of semiconductor wafer cleaning technology*. 1993, Park Ridge, New Jersey: Noyes.

[115] D.L. King and M.E. Buck, *Experimental optimization of an anisotropic etching process for random texturization of silicon solar cells*, in *Proceedings of the 22nd Photovoltaic Specialists Conference* Las Vegas, Nevada, USA, (1991).

[116] R. Hezel and K. Jaeger, *Low-temperature surface passivation of silicon for solar cells*, Journal of the Electrochemical Society, **136** (2), 518-23, (1989).

[117] A. Cuevas, M.J. Kerr, and J. Schmidt, *Passivation of crystalline silicon using silicon nitride*, in *Proceedings of the 3rd World Conference on Photovoltaic Energy Conversion*, Osaka, Japan, 913-8 (2003).

[118] C. Leguijt, *et al.*, *Low temperature surface passivation for silicon solar cells*, Solar Energy Materials and Solar Cells, **40** (4), 297-345, (1996).

[119] R.A. Sinton, Y. Kwark, P. Gruenbaum, and R.M. Swanson, *Silicon point contact concentrator solar cells*, in *Proceedings of the 18th IEEE Photovoltaic Specialists Conference*, Las Vegas, Nevada, USA, 61-5 (1985).

[120] S.M. Sze, *Semiconductor devices, physics and technology*, ed. M.H. AT&T Bell Laboratories, New Jersey. 1985, New York, Chichester, Brisbane, Toronto, Singapore: John Wiley & Sons.

[121] M.A. Green, *Silicon solar cells: Advanced principles and practice*. 1995, Sydney, UNSW: Centre for Photovoltaic Devises and Systems UNSW.

[122] R.M. Swanson, *Point-contact solar cells: modeling and experiment*, Solar Cells, **17** (1), 85-118, (1986).

[123] A. Wang, J. Zhao, and M.A. Green, *24% efficient silicon solar cells*, Applied Physics Letters, **57** (6), 602-4, (1990).

[124] D.K. Schroder and D.L. Meier, *Solar cell contact resistance - a review*, IEEE Transactions on Electron Devices, **ED-31** (5), 637-47, (1984).

[125] A. Grohe, *Einsatz von Laserverfahren zur Prozessierung von kristallinen Silizium-Solarzellen*, Dissertation, Universität Konstanz, (2007).

[126] D.L. Meier and D.K. Schroder, *Contact resistance: its measurement and relative importance to power loss in a solar cell*, IEEE Transactions on Electron Devices, **ED-31** (5), 647-53, (1984).

[127] A. Teppe, P. Engelhart, and J. Müller, *Method for the contact separation of electrically-conducting layers on the back contacts of solar cells and corresponding solar cells* in US Patent, USA, WO 2006/042698 A1, (2006).

[128] W.P. Mulligan, M.J. Cudzinovic, T. Pass, D. Smith, N. Kaminar, K. McIntosh, and R.M. Swanson, *Solar cell and method of manufacture*, in US Patent, USA, US 7,339,110 B1, (2008).

[129] J. Nijs, F. Dhoore, R. Mertens, and R. van Overstraeten, *Lift-off: A very fine front metallization geometry technique for high efficiency solar cells*, ESA Photovoltaic Generators in Space, 37-42, (1982).

[130] A. Mette, *New concepts for front side metallization of industrial silicon solar cells*, Dissertation, Universität Freiburg, (2007).

[131] A. Mette, C. Schetter, D. Wissen, S. Lust, S.W. Glunz, and G. Willeke, *Increasing the efficiency of screen-printed silicon solar cells by light-induced silver plating*, in *Proceedings of the 4th World Conference on Photovoltaic Energy Conversion*, Waikoloa, Hawaii, USA, 1056-9 (2006).

[132] M. Hermle, F. Granek, O. Schultz, and S.W. Glunz, *Analyzing the effects of front-surface fields on back-junction silicon solar cells using the charge-collection probability and the reciprocity theorem*, Journal of Applied Physics, **103** (054507), 054507/1-7, (2008).

[133] W. Warta, J. Sutter, B.F. Wagner, and R. Schindler, *Impact of diffusion length distributions on the performance of mc-silicon solar cells*, in *Proceedings of the 2nd World Conference on Photovoltaic Energy Conversion*, Vienna, Austria, 1650-3 (1998).

[134] E. Schneiderlöchner, R. Preu, R. Lüdemann, and S.W. Glunz, *Laser-fired rear contacts for crystalline silicon solar cells*, Progress in Photovoltaics: Research and Applications, **10**, 29-34, (2002).

[135] S.W. Glunz, E. Schneiderlöchner, D. Kray, A. Grohe, H. Kampwerth, R. Preu, and G. Willeke, *Laser-fired contact solar cells on p- and n-type substrates*, in *Proceedings of the 19th European Photovoltaic Solar Energy Conference*, Paris, France, **1**, 408-11 (2004).

[136] S.W. Glunz, *et al.*, *Analysis of laser-fired local back surface fields using n+np+ cell structures*, in *Proceedings of 3rd World Conference on Photovoltaic Energy Conversion*, Osaka, Japan, **2**, 1332-5 (2003).

[137] D. Nobili, *Solubility of P in Si in Properties of Silicon*. 1987.

[138] D. Nobili, *Solubility of B in Si in Properties of Silicon*. 1987.

[139] M. Abbott, P. Cousins, F. Chen, and J. Cotter, *Laser-induced defects in crystalline silicon solar cells*, in *Proceedings of the 31st IEEE Photovoltaic Specialists Conference*, Orlando, USA, 1241-4 (2005).

[140] S. Baumann, D. Kray, K. Mayer, A. Eyer, and G.P. Willeke, *Comparative study of laser induced damage in silicon wafers*, in *Proceedings of the 4th World Conference on Photovoltaic Energy Conversion*, Waikoloa, Hawaii, USA, 1142-5 (2006).

[141] S. Rein, T. Rehrl, W. Warta, and S.W. Glunz, *Lifetime spectroscopy for defect characterization: Systematic analysis of the possibilities and restrictions*, Journal of Applied Physics, **91** (4), 2059-70, (2002).

[142] J. Zhao and A. Wang, *Rear emitter n-type passivated emitter, rear totally diffused silicon solar cell structure*, Applied Physics Letters, **88**, 242102-1-3, (2006).

[143] D.K. Schroder, R.N. Thomas, and J.C. Swartz, *Free carrier absorption in silicon*, IEEE Transactions on Electron Devices, **ED-25** (2), 254-61, (1978).

[144] J. Isenberg and W. Warta, *Free carrier absorption in heavily doped silicon layers*, Applied Physics Letters, **84** (13), 2265-7, (2004).

[145] R.M. Swanson and R.A. Sinton, *High-efficiency silicon solar cells*, in *Advances in solar energy*, K.W. Böer, Editor, Plenum Press, New York, 427-84 (1990).

[146] A. Slade, *Boron Triboromide Sourced Boron Diffusions for Silicon Solar Cells*, PhD Thesis, UNSW, Sydney, (2003).

[147] A. Cuevas, P.A. Basore, G. Giroult-Matlakowski, and C. Dubois, *Surface recombination velocity of highly doped n-type silicon*, Journal of Applied Physics, **80** (6), 3370-5, (1996).

[148] R.R. King, R.A. Sinton, and R.M. Swanson, *Studies of diffused phosphorus emitters: saturation current, surface recombination velocity, and quantum efficiency*, IEEE Transactions on Electron Devices, **37** (2), 365-71, (1990).

[149] A.G. Aberle, *Crystalline silicon solar cells: advanced surface passivation and analysis of crystalline silicon solar cells*. 1999, Sydney, Australia.

[150] F. Dross, E. Van Kerschaver, and G. Beaucarne, *Minimization of the shadow-like losses for inter-digitated back-junction solar cells*, in *Proceedings of the 15th International Photovoltaic Science & Engineering Conference*, Shanghai. China, 971-2 (2005).

[151] N.-P. Harder, V. Mertens, and R. Brendel, *Buried emitter solar cell structures: Decoupling of metallisation geometry and carrier collection geometry of back contacted solar cells*, physica status solidi (RRL) - Rapid Research Letters, **2** (4), 148-50, (2008).

[152] F. Granek, M. Hermle, C. Reichel, O. Schultz-Wittmann, and S.W. Glunz, *High- efficiency back-contact back-junction silicon solar cell research at Fraunhofer ISE*, in *Proceedings of the 23rd European Photovoltaic Solar Energy Conference*, Valencia, Spain, 991-5 (2008).

[153] R.A. Sinton and A. Cuevas, *A quasi-steady-state open-circuit voltage method for solar cell characterization*, in *Proceedings of the 16th European Photovoltaic Solar Energy Conference*, Glasgow, UK, 1152-5 (2000).

[154] D. Pysch, A. Mette, and S.W. Glunz, *A review and comparison of different methods to determine the series resistance of solar cells*, Solar Energy Materials & Solar Cells, **91**, 1698-706, (2007).

[155] A.G. Aberle, *Surface passivation of crystalline silicon solar cells: a review*, Progress in Photovoltaics: Research and Applications, **8** (5), 473-87, (2000).

[156] A.G. Aberle, S. Glunz, and W. Warta, *Field effect passivation of high efficiency silicon solar cells*, Solar Energy Materials and Solar Cells, **29** (2), 175-82, (1993).

[157] J.A. del Alamo and R.M. Swanson, *The physics and modeling of heavily doped emitters*, IEEE Transactions on Electron Devices, **ED-31** (12), 1878-88, (1984).

[158] G. Masetti, M. Severi, and S. Solmi, *Modeling of carrier mobility against carrier concentration in arsenic-, phosphorus-, and boron-doped silicon*, IEEE Transactions on Electron Devices, **30** (7), 764-9, (1983).

[159] P.B. Moynagh and P.J. Rosser, *Thermal oxidation of Si*, in *Properties of silicon*, INSPEC, The Institution of Electrical Engineers, 469-79 (1987).

[160] J. del Alamo and R.M. Swanson, *Measurement of heavy doping parameters in n-type silicon solar cells*, in *Proceedings of the 18th IEEE Photovoltaic Specialists ConferenceCA Conference Paper*, Las Vegas, Nevada, USA, 584-9 (1985).

[161] S.W. Glunz, S. Sterk, R. Steeman, W. Warta, J. Knobloch, and W. Wettling, *Emitter dark saturation currents of high-efficiency solar cells with inverted pyramids*, in *Proceedings of the 13th European Photovoltaic Solar Energy Conference*, Nice, France, 409-12 (1995).

[162] M.J. Kerr, J. Schmidt, A. Cuevas, and J.H. Bultman, *Surface recombination velocity of phosphorus-diffused silicon solar cell emitters passivated with*

plasma enhanced chemical vapor deposited silicon nitride and thermal silicon oxide, Journal of Applied Physics, **89** (7), 3821-6, (2001).

[163] J.D. Moschner, P. Doshi, D.S. Ruby, T. Lauinger, A.G. Aberle, and A. Rohatgi, *Comparison of front and back surface passivation schemes for silicon solar cells*, in *2nd World Conference and Exhibition on Photovoltaic Solar Energy Conversion*, Vienna, Austria, 1984-7 (1998).

[164] P.E. Gruenbaum, R.A. Sinton, and R.M. Swanson, *Light-induced degradation at the silicon/silicon dioxide interface*, Applied Physics Letters, **52** (17), 1407-9, (1988).

[165] P.E. Gruenbaum, R.A. Sinton, and R.M. Swanson, *Stability problems in point contact solar cells*, in *Proceedings of the 20th IEEE Photovoltaic Specialists Conference*, Las Vegas, Nevada, USA, 423-8 (1988).

[166] P.E. Gruenbaum, R.R. King, and R.M. Swanson, *Photoinjected hot-electron damage in silicon point-contact solar cells*, Journal of Applied Physics, **66** (12), 6110-4, (1989).

[167] P.E. Gruenbaum, J.Y. Gan, R.R. King, and R.M. Swanson, *Stable passivations for high-efficiency silicon solar cells*, in *Proceedings of the 21st IEEE Photovoltaic Specialists Conference*, Kissimmee, Florida, USA, 317-22 (1990).

[168] D.S. Ruby and W.K. Schubert, *The effects of concentrated ultraviolet light on high-efficiency silicon solar cells*, in *Proceedings of the 22nd IEEE Photovoltaic Specialists Conference*, Las Vegas, Nevada, USA, 111-7 (1991).

[169] H. Nagayoshi, *et al.*, *Effect of hydrogen-radical annealing for SiO_2 passivation*, Japanese Journal of Applied Physics, **35** (8B), L1047-9, (1996).

[170] A. Mohr, M. Hermle, T. Roth, and S.W. Glunz, *Influence of grid finger and busbar structure on the performance of rear-line-contacted silicon concentrator cells*, in *Proceedings of the 19th European Photovoltaic Solar Energy Conference*, Paris, France, **1**, 721-4 (2004).

[171] Bird R., Hulstrom R., and R. C., *Normalization of direct spectral irradiance data for photovoltaic cell performance analysis*, Solar Cells, **14** (2), 193-5, (1985).

[172] K. Emery, *The Rating of Photovoltaic Performance*, IEEE Transactions on Electron Devices, **46** (10), 1928-31, (1999).

[173] A. Luque, *Solar Cells and Optics for Photovoltaic Concentration*. 1989.

[174] J. Dicker, *Charakterisierung von hocheffizienten Rückseitenkontaktzellen*. Diplomarbeit, Albert-Ludwigs-Universität, Freiburg, (1998).

List of publications

Refereed journal papers

1. F. Granek, T. Zdanowicz, „Advanced system for calibration and characterization of solar cells", *Opto-Electronics Review* **12**(1), 57–67 (2004)

2. M. Hermle, F. Granek, O. Schultz, and S. W. Glunz, „Analyzing the effects of front-surface fields on back-junction silicon solar cells using the charge-collection probability and the reciprocity theorem", *Journal of Applied Physics* **103**, 054507 (2008)

3. F. Granek, M. Hermle and S. W. Glunz, „Analysis of the current linearity at low illumination of high-efficiency back-junction back-contact silicon solar cells", *physica status solidi. - Rapid Research Letters* **2**, No. 4, 151–153 (2008)

4. F. Granek, M. Hermle, D. M. Huljić, O. Schultz-Wittmann and S. W. Glunz, „Enhanced lateral current transport via the front n^+ diffused layer of n-type high-efficiency back-junction back-contact silicon solar cell", *Progress in Photovoltaics* **17**, 47-56 (2009)

Refereed papers presented at international conferences

1. J. Hoornstra, A. van der Heide, A. Weeber, F. Granek, „New approach for firing optimization in crystalline silicon solar cell technology", 19th European Photovoltaic Solar Energy Conference, Paris, France, pp. 1044-7 (2004).

2. C.J.J. Tool, G. Coletti, F. Granek, J. Hoornstra, M. Koppes, E.J. Kossen, H.C. Rieffe, I.G. Romijn, A.W. Weeber, „Straightforward in-line processing for 16.8% efficient mc-Si solar cell", 31st IEEE Photovoltaic Specialists Conference, Orlando Florida, pp. 1324-7 (2005).

3. J. Hoornstra, G. Schubert, K. Broek, F. Granek, C. LePrince , „Lead free metallization paste for crystalline silicon solar cells: From model to results", 31st IEEE Photovoltaic Specialists Conference, Orlando Florida, pp. 1293-6 (2005).

4. C.J.J. Tool, G. Coletti, F. Granek, J. Hoornstra, M. Koppes, E.J. Kossen, H.C. Rieffe, I.G. Romijn, A.W. Weeber, „17% mc-Si solar cell efficiency using full in-

line processing with improved texturing and screen-printed contacts on high-ohmic emitters", 20th European Photovoltaic Solar Energy Conference and Exhibition, Barcelona, Spain, pp. 578-83 (2005).

5. J. Hoornstra, G. Schubert, C. LePrince, G. Wahl, K. Broek, F. Granek, B. Lenkeit, J. Horzel, „Lead free metallization for silicon solar cells: results the EC2Contact project", 20th European Photovoltaic Solar Energy Conference and Exhibition, Barcelona, Spain, pp. 651-4 (2005).

6. F. Granek, A. Weeber, Kees Tool, R. Kinderman, P. de Jong , „A systematic approach to reduce process-induces shunts in back-contact mc-Si solar cell", 32nd IEEE Photovoltaic Specialists Conference, Hawaii, pp. 1319-22 (2006).

7. F. Granek, M. Hermle, B. Fleischhauer, A. Grohe, O. Schultz, S.W. Glunz, G. Willeke, „Optimization of laser-fired aluminum emitters for high-efficiency n-type Si solar cells", 21st European Photovoltaic Solar Energy Conference, Dresden, Germany, pp. 777-80 (2006).

8. D. M. Huljić, T. Zerres, A. Mohr, K. v. Maydell, K. Petter, J. W. Müller, H. Feist, N.-P. Harder, P. Engelhart, T. Brendemühl, R. Grischke, R. Meyer, R. Brendel, F. Granek, A. Grohe, M. Hermle, O. Schultz, S. W. Glunz, „Development of a 21% back-contact monocrystalline silicon solar cell for large scale production", 21st European Photovoltaic Solar Energy Conference, Dresden, Germany, pp. 765-8 (2006).

9. F. Granek, C. Reichel, M. Hermle, D. M. Huljić, O. Schultz, S.W. Glunz, „Front surface passivation of n-type high-efficiency back-junction back-contact silicon solar cells using front surface field", 22nd European Photovoltaic Solar Energy Conference, Milano, Italy, pp.1454-7 (2007).

10. D. M. Huljić, A. Mohr, K. v. Maydell, T. Zerres and J. W. Müller, F. Granek, A. Grohe, M. Hermle, O. Schultz, S. W. Glunz, N.-P. Harder, P. Engelhart, T. Brendemühl, R. Grischke and R. Brendel, „Q-Cells' High-efficiency back junction silicon solar cell for large-scale production –Main results of the QUEBEC project", 22nd European Photovoltaic Solar Energy Conference, Milano, Italy (2007).

11. F. Granek, C. Reichel, M. Hermle, O. Schultz, . Glunz, „Function of front surface field in n-type high-efficiency back-junction back-contact silicon solar cells", Technical Digest of the International PVSEC-17, Fukuoka, Japan, pp. 723-724 (2007).

12. F. Granek, M. Hermle, C. Reichel, A. Grohe, O. Schultz-Wittmann, S. Glunz, „Positive effects of front surface fielding high-efficiency back-contact back-junction n-type silicon solar cells", 33rd IEEE Photovoltaic Specialist Conference, San Diego, CA, in print (2008).

13. M. Hermle, F. Granek, O. Schultz-Wittmann, S. W. Glunz, „Shading Effects in Back-Junction Back-Contacted Silicon Solar Cells", 33rd IEEE Photovoltaic Specialist Conference, San Diego, CA, in print (2008).

14. C. Reichel, F. Granek, J. Benick, O. Schultz-Wittmann, S. W. Glunz, „ Comparison of emitter saturation current densities determined by quasi-steady-state photoconductance measurements of effective carrier lifetimes at high and low injections", 23rd European Photovoltaic Solar Energy Conference, Valencia, Spain, pp. 1664-1669 (2008).

15. S. Kluska, F. Granek, H. Hermle, S.W. Glunz, „Loss analysis of high-efficiency back-contact back-junction silicon solar cells", 23rd European Photovoltaic Solar Energy Conference, Valencia, Spain, pp.1590-1595 (2008).

16. Kasemann M., Kwapil W., Walter B., Giesecke J., Michl B., The M., Wagner J.-M., Bauer J., Schütt A., Carstensen J., Kluska S., Granek F., Kampwerth H., Gundel P., Schubert M.C., Bardos R.A., Föll H., Nagel H., Würfel P., Trupke T., Breitenstein O., Hermle M., Warta W., Glunz S.W., „Progress in Silicon Solar Cell Characterization with Infrared Imaging Methods", 23rd European Photovoltaic Solar Energy Conference, Valencia, Spain, pp. 965-973 (2008).

17. F. Granek, M. Hermle, C. Reichel, O. Schultz-Wittmann, S. W. Glunz, „High-efficiency back-contact back-junction solar cell: Research at Fraunhofer ISE", 23rd European Photovoltaic Solar Energy Conference, Valencia, Spain, pp. 991-995 (2008).

Oral presentations

1. F. Granek, M. Hermle, B. Fleischhauer, A. Grohe, O. Schultz, S.W. Glunz, G. Willeke "Optimisation of laser-fired aluminum emitters for high-efficiency n-type Si solar cells21st European Photovoltaic Solar Energy Conference, Dresden, Germany, 4.–8.9.2006

2. F. Granek, "Analyse der Vorderseitenpassivierung von Back-junction-Solarzellen", SiliconFOREST Workschop, Falkau, Germany, 25-25.02.2008

3. F. Granek, C. Reichel, O. Schultz, S. Glunz, "Analysis of the front surface passivation of the back-junction back-contact silicon solar cells", Q-Cells AG, Thalheim, Germany, 19.03.2008

4. F. Granek, M. Hermle, C. Reichel, A. Grohe, O. Schultz; S. W. Glunz, "Positive Effects of Front Surface Field in High-efficiency Back-contact Back-junction N-Type Silicon Solar Cells", 33rd IEEE Photovoltaic Specialists Conference, San Diego, CA, USA, 11.–16.5.2008

5. F. Granek, M. Hermle, C. Reichel, O. Schultz-Wittmann, S. W. Glunz, "High-efficiency back-contact back-junction silicon solar cell - Research at Fraunhofer ISE", 23rd European Photovoltaic Solar Energy Conference and Exhibition, Valencia, Spain, 1.–5.9.2008

6. F. Granek, "Positive effects of Front Surface Field in high-efficiency back-contact back-junction silicon solar cells", ISFH Seminar, Institut für Solarenergieforschung Hameln (ISFH), Hameln, Germany, 25.11.2008

Acknowledgements

I want to express my gratitude to my thesis advisors Prof. Dr. Oliver Paul and PD Dr. Andreas Gombert for their warm encouragement and guidance.

I am grateful to Dr. Stefan Glunz for enabling me to work on the exciting topic of the back-contact back-junction solar cells, for his support and stimulating discussions, and for sharing his experience and enthusiasm.

Special thanks to Dr. Oliver Schultz, my direct supervisor at Fraunhofer ISE, for his constant encouragement during the course of this work, for sharing of his knowledge with me and for his good advices. I am also grateful to him for providing valuable suggestions in the writing-up phase which improved the quality of this thesis.

I am happy to acknowledge close and very fruitful co-operation with Dr. Martin Hermle in the field of the numerical simulations of the solar cells.

I was very lucky to be able to work with two highly motivated diploma students Christian Reichel and Sven Kluska. I thank both of them for their contribution to this thesis and for many valuable discussions.

Processing and characterization of the complex structure of the back-contact back-junction solar cell would not be possible without the help of Antonio Leimenstoll, Sonja Seitz, Harald Lautenschlager, Dr. Andreas Grohe, Annerose Knorz, Christian Harmel, Anke Herbolzheimer, Christian Shetter, Elisabeth Schäffer, Thomas Roth, Daniela Grote, Denis Erath, Norbert Kohn, Jochen Hohl-Ebinger. I thank all of you.

The frequent meetings of the *Quebec* project enabled many useful discussions of the back-contact solar cell structure and technology, for which I am grateful to all of the *Quebec* project team members. Especially my thanks goes to Dominik Huljić, Dr. Andeas Mohr, Dr. Peter Engelhart from Q-Cells and to Dr. Nils-Peter Harder form ISFH.

My time at Fraunhofer ISE was made enjoyable in large part also due to my colleagues Mónica Alemán, Jan Benick, Nicola Mingirulli, Marek Miara, Dr. Ansgar Mette, Luca Gautero, Matthias Hörteis.

To my wife Agnieszka, thank you for your patience, love and encouragement.

GRANEK07

https://web.archive.org/web/20160101000000*/http://beacon.no/resources/PhD_Granek_Filip.pdf July 26, 2024

INTERNET ARCHIVE

SIGN UP | LOG IN UPLOAD Search

ABOUT BLOG PROJECTS HELP DONATE CONTACT JOBS VOLUNTEER PEOPLE

DONATE

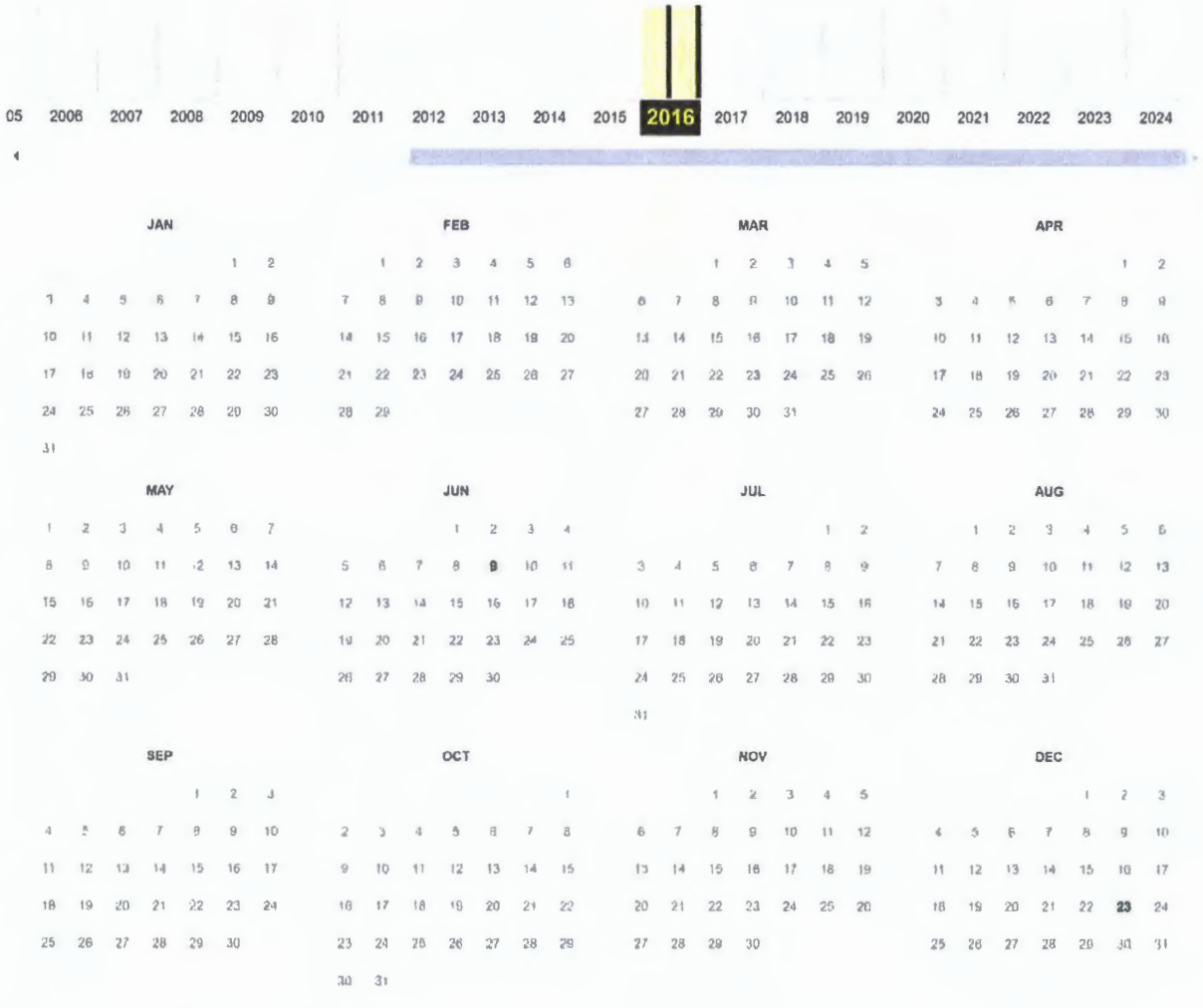
INTERNET ARCHIVE WaybackMachine

Explore more than 866 billion web pages saved over time

http://beacon.no/resources/PhD_Granek_Filip.pdf

Calendar · Collections · Changes · Summary · Site Map · URLs

Saved **2 times** between June 9, 2016 and December 23, 2016.



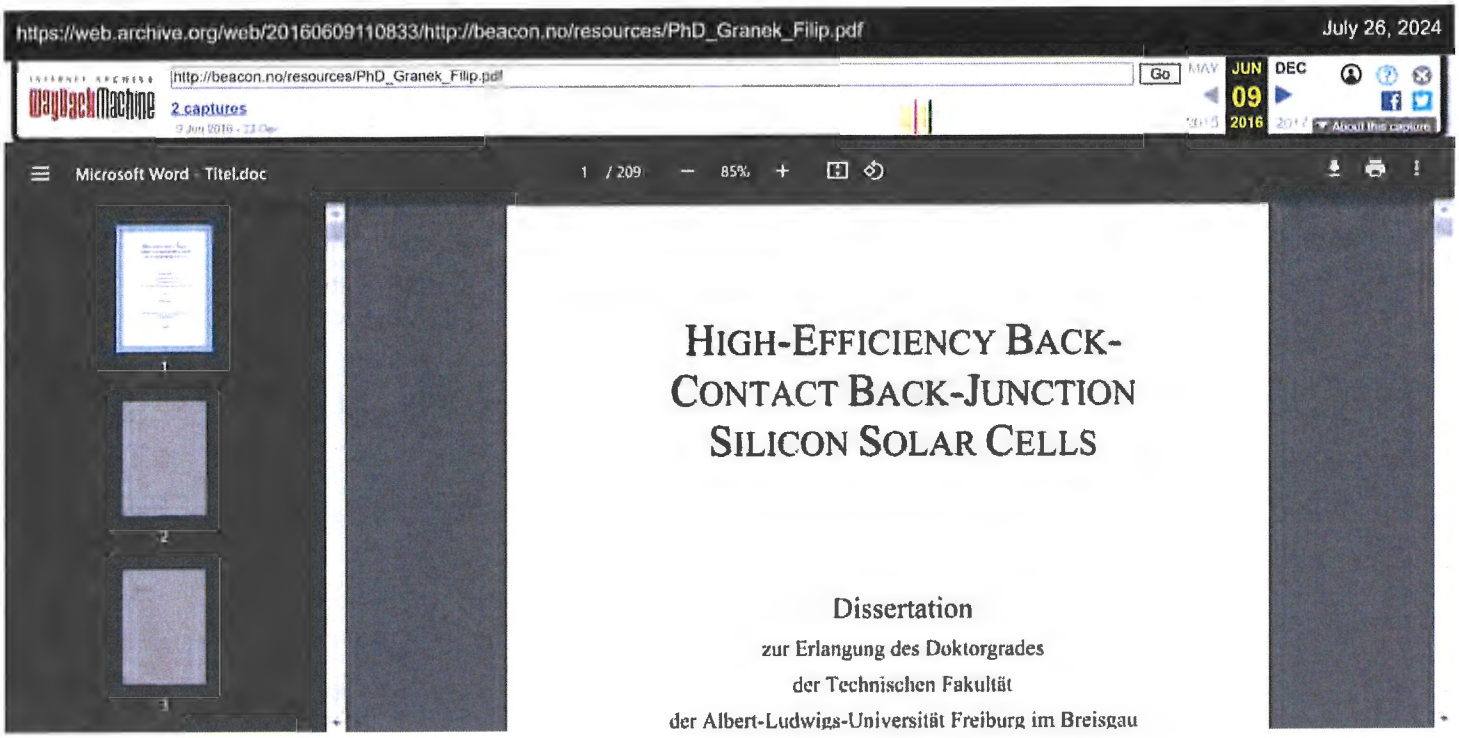
Note

This calendar view maps the number of times **http://beacon.no/resources/PhD_Granek_Filip.pdf** was crawled by the Wayback Machine, *not* how many times the site was actually updated. More info in the FAQ.

FAQ | Contact Us | Terms of Service (Dec 31, 2014)

The Wayback Machine is an initiative of the Internet Archive, a 501(c)(3) non-profit, building a digital library of Internet sites and other cultural artifacts in digital form. Other projects include Open Library & archive-it.org

Your use of the Wayback Machine is subject to the Internet Archive's Terms of Use.


https://web.archive.org/web/20160609110833/http://beacon.no/resources/PhD_Granek_Filip.pdf
July 26, 2024
http://beacon.no/resources/PhD_Granek_Filip.pdf
Go
JUN
09
2016
DEC
2 captures
Microsoft Word - Titel.doc
1 / 209
85%
HIGH-EFFICIENCY BACK-CONTACT BACK-JUNCTION SILICON SOLAR CELLS
Dissertation
zur Erlangung des Doktorgrades
der Technischen Fakultät
der Albert-Ludwigs-Universität Freiburg im Breisgau

HIGH-EFFICIENCY BACK-CONTACT BACK-JUNCTION SILICON SOLAR CELLS

Dissertation

zur Erlangung des Doktorgrades

der Technischen Fakultät

der Albert-Ludwigs-Universität Freiburg im Breisgau

vorgelegt von

Filip Granek

Fraunhofer Institut für Solare Energiesysteme (ISE)

Freiburg im Breisgau

2009

Dekan:	Prof. Dr. Hans Zappe
Hauptreferent:	Prof. Dr. Oliver Paul
Koreferent:	PD. Dr. Andreas Gombert
Datum der Prüfung:	31 Juli 2009

Table of contents

Table of contents 3

Abstract 9

1 Introduction 11

1.1 Thesis motivation 11

1.2 Thesis outline 12

2 Back-contact silicon solar cells 15

2.1 Introduction 15

2.2 Review of back-contact silicon solar cells 17

2.2.1 Back-contact back-junction (BC-BJ) solar cells 18

2.2.2 Emitter Wrap Through (EWT) solar cells 24

2.2.3 Metallization Wrap Through (MWT) solar cells 25

2.3 Critical parameters of the back-contact back-junction solar cells 26

2.4 Conversion efficiency limitations by intrinsic losses 28

2.4.1 Intrinsic loss mechanisms in silicon 28

2.4.2 Short-circuit current limit 29

2.4.3 Open-circuit voltage limit 31

2.4.4 Efficiency limit 33

3 Measurement methods and numerical simulations 35

3.1 Surface saturation current density 35

3.1.1 Injection dependent lifetime measurements 35

3.1.2 Determination of J_{0s} at low injection 37

3.1.3 Determination of J_{0s} at high injection 38

3.2 Device simulation 39

3.2.1 Two-dimensional numerical simulation 39
3.2.2 One-dimensional numerical simulation 41
3.2.3 Simulation parameters 41
3.3 Measurement table for laboratory size solar cell 43
4 Design and technology 45
4.1 Device structure 45
4.2 n-type bulk Si material 47
4.2.1 Minority carrier diffusion length 49
4.2.2 Influence of the surface potential on the minority carrier lifetime 50
4.3 Processing technology 54
4.4 Metallization 58
4.4.1 Formation of the interdigitated metal grid 59
4.4.2 Thickening of the thin seed metal layer 68
4.5 Solar cell results 70
4.5.1 Laboratory-scale solar cells 70
4.5.2 Industrial-scale solar cells 72
4.6 Conclusions 74
5 Analysis of the laser-fired aluminium emitters 77
5.1 Introduction 77
5.2 Fabrication of LFE and boron emitter cells 78
5.3 Solar cell results 79
5.4 Laser-induced damage zone 80
5.5 Quantum efficiency of the LFE cells 81
5.6 Recombination in the damage zone 82
5.7 Comparison of boron diffusion and LFE emitters 86

5.8 SunsV_{OC} and implied voltage 88
5.9 Optimization of the LFE cells 89
5.10 Conclusion 91
6 Analysis of the loss mechanisms 93
6.1 Introduction 93
6.2 Optical losses 94
6.2.1 Optical losses in the back-contact solar cell 94
6.2.2 Modeling of the optical losses 94
6.2.3 Free carrier absorption 95
6.2.4 Distribution of optical losses 97
6.2.5 Influence of optical losses on the cell efficiency 99
6.3 Recombination losses 100
6.3.1 Modeling of the saturation current densities 100
6.3.2 Influence of recombination losses on the short-circuit current 102
6.3.3 Influence of recombination losses on cell efficiency 103
6.4 Electrical shading 104
6.4.1 Increased lateral transport distance for the minority carriers 104
6.4.2 Light beam induced current mapping 105
6.4.3 LBIC line scans 106
6.4.4 Influence of the electrical shading on the cell efficiency 107
6.5 Resistive losses 107
6.5.1 Modeling of series resistance losses 107
6.5.2 Influence of series resistance losses on cell efficiency 110
6.6 Adding up the individual loss mechanisms 111

6.7 Conclusions 115

7 Front surface passivation using a front surface field 117

7.1 Introduction 117

7.1.1 Surface recombination 117

7.1.2 Surface passivation methods 119

7.2 Influence of the front surface field diffusion profile on the solar cell performance 120

7.3 Surface passivation quality for different FSF diffusion profiles 123

7.3.1 Processing of test structures for the determination of J_{0e} 124

7.3.2 Determination of J_{0e} under high and low injection 127

7.3.3 J_{0e} for different FSF diffusion profiles 128

7.4 Solar cells with different FSF diffusion profiles 131

7.4.1 Solar cell results 131

7.4.2 Analysis of the open-circuit voltage 132

7.4.3 Internal quantum efficiency 133

7.5 Stability of the front surface passivation under UV-light exposure 134

7.5.1 UV-light influence on the front surface passivation 134

7.5.2 Lifetime test structures 135

7.5.3 Solar cell results 137

7.5.4 Regeneration of the UV-degraded solar cells 139

7.6 Conclusion 141

8 Lateral current transport via front n^+ diffused layer 143

8.1 Introduction 143

8.2 Lateral current transport of majority carriers 144

8.3 Variation of the pitch 147

8.4 Solar cell results 148

8.5 Short-circuit current analysis 149
8.6 Fill factor and series resistance 150
8.6.1 Fill factor 150
8.6.2 Pseudo fill factor 150
8.6.3 Conductivity modulation 152
8.6.4 Series resistance 153
8.7 Simulations of the lateral current flow of the majority carriers 154
8.8 Conclusions 157
9 Low-illumination characteristics 159
9.1 Introduction 159
9.2 Analyzed solar cells and methodology 160
9.3 Non-diffused surfaces 162
9.4 Floating emitters 166
9.5 Front surface fields 169
9.6 Conclusions 172
10 Summary and outlook 175
Zusammenfassung und Ausblick 179
Symbols, acronyms and physical constants 183
Bibliography 189
List of publications 203
Acknowledgements 207

Abstract

In this thesis high-efficiency back-contact back-junction (BC-BJ) silicon solar cells for one-sun applications were studied. The focus was put on the development of a low-cost and industrially feasible manufacturing technology in order to utilize the full cost reduction potential of this elegant cell structure. At the same time the performance of the developed solar cells was investigated in details by experimental work, analytical modeling and numerical device simulations. The complex and costly photolithography masking steps were replaced by techniques which are of low cost and relevant for mass production, such as screen-printing of the masking layers and local laser ablation of the dielectric and silicon layers. The highest solar cell efficiency of 21.1 % (J_{SC} = 38.6 mA/cm^2, V_{OC} = 668 mV, FF = 82.0 %) was achieved on 160 µm thick 1 Ω cm n-type FZ Si with the designated area of 4 cm^2. A detailed study of the loss mechanisms limiting the efficiency of the developed back-contact back-junction silicon solar cell was performed. The reduction of the cell efficiency was determined to be 3.9 % abs. due to recombination processes, 2.0 % abs. due to optical losses, 0.3 % abs. due to series resistance effects and 0.7 % abs. due to electrical shading. The developed model of the loss mechanisms is a powerful tool for the further optimization study of the solar cell structure. Positive effects of the phosphorus doped n^+ front surface field (FSF) on the performance of the BC-BJ solar cells were studied in details. These effects are: (i) *Surface passivation and passivation stability:* The optimal surface passivation was obtained with a deep diffused Gaussian phosphorus FSF doping profile with sheet resistance of 148 Ω/sq. In contrast to solar cells without the FSF diffusion, the solar cells with the FSF diffusion profile did not show any performance degradation under exposure to UV illumination. (ii) *Lateral current transport:* The front diffused n^+ layer can be seen as a parallel conductor to the lateral base resistance. This way the lateral base resistance losses can be reduced. (iii) *Low-illumination performance:* The front surface field improves the performance of the BC-BJ solar cells under low illumination intensity. Therefore the BC-BJ cells with FSF seem to be the best ones suited for achieving a high energy yield when also operating under low illumination intensity.

1 Introduction

1.1 Thesis motivation

Today's most used form of energy is fossil energy. However this form of energy is based on limited resources and produces harmful emissions. The climate change caused by the emission of the greenhouse gases, as well as the potential of military conflicts over the remaining limited reserves of the fossil fuels, are two of the major problems, which the humanity is facing at the moment. Therefore the transition from the fossil energy sources to the clean and renewable energy sources is at present one of the greatest challenges for the mankind.

The Earth receives incoming solar radiation with the power of 174×10^{15} W from the Sun. Thus, in just one hour our planet receives enough energy from the Sun, to cover the present global annual energy consumption. Solar irradiation energy is an abundant and widely available source of energy. The solar light can be directly converted into electricity by the photovoltaic cells. During its operation, a solar cell does not produce any emissions or noise. Therefore photovoltaics is a very promising technology in satisfying the future demand for the environmentally friendly energy in a sustainable way.

The production of solar cells is growing rapidly, with an average annual growth rate of 35 % since 1998 [1]. By the end of 2007 the cumulative installed capacity of the photovoltaic systems reached 9.2 GW. Silicon solar cells dominate the market of photovoltaic solar cells and are likely to maintain its dominant market share in the coming years [2]. However the costs of energy produced by photovoltaics are still too high. Therefore the successful dissemination of photovoltaics can be only achieved by further reduction of the manufacturing costs of the photovoltaic systems.

A high impact on the lowering of the manufacturing costs is achieved by improving the efficiency of the silicon solar cells. The progress in the technology of the silicon solar cell enables manufacturing of more advanced and highly-efficient cells. In mass production of the solar cells for one-sun applications, the highest conversion efficiencies of above 22 % are achieved using a structure of a back-contact back-junction solar cells [3]. However since this cell structure is complex, its production is challenging and involves multiple masking steps, which should be able to create small feature sizes and be very well aligned to each other. Photolithography masking, a technology widely used in microelectronics, would meet the above mentioned

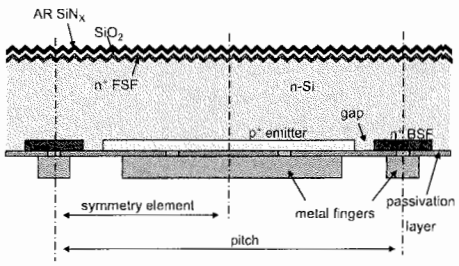
requirement perfectly. However due to its high costs, the application of photolithography is only allowed to the production of the small area concentrator solar cells. Production of the large-area one-sun back-contact back-junction solar cells requires an appropriate low-cost manufacturing technology in order to be able to produce it cost effectively.

Due to the potential of reaching the high-device efficiencies with the low-cost manufacturing technology, the present thesis focuses on the back-contact back-junction silicon solar cell structure. An industrially feasible manufacturing technology of this cell structure is developed. Moreover, based on the presented advanced characterization and modeling of the developed solar cells, further increase of the device efficiency and lowering of its manufacturing costs is possible.

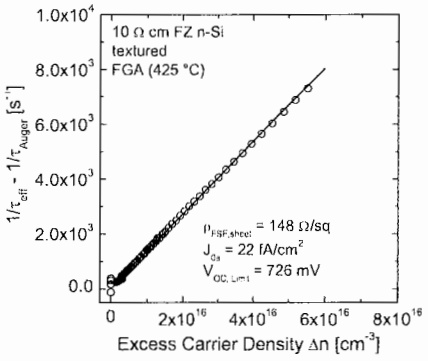
1.2 Thesis outline

The operating principles and the technology of the silicon solar cell are presented in references [4], [5], [6].

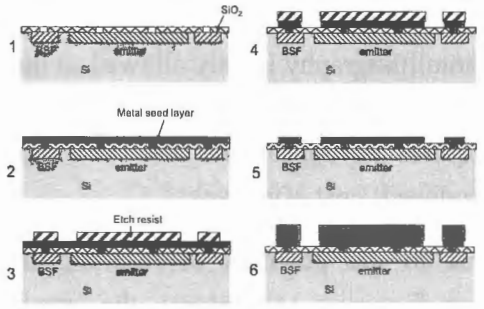
Chapter 2: The thesis starts with a review of advantages and challenges related to the back-contact solar cell structures. Different types of the back-contact solar cells are introduced and a review of the state-of-the-art technology is given. The critical parameters of the back-contact back-junction solar cells are discussed.



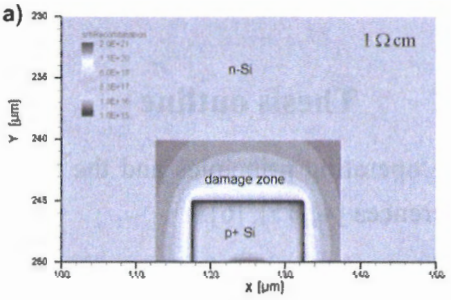
In **chapter 3** two methods for determination of the surface saturation current density under low and high injection are presented. Moreover, the process of the numerical simulations of the back-contact back-junction solar cells using one and two-dimensional simulations is described.



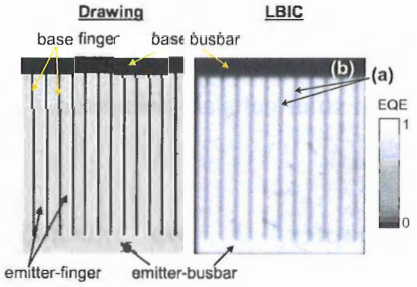
Chapter 4: The technology of the back-contact back-junction silicon solar cells, developed in this work, is presented. The starting material for the cells, n-type silicon material is characterized. Different methods for the formation of the interdigitated contact grid are described in detail. The best results of the developed small, laboratory-size and large, industrial-size solar cells are presented.



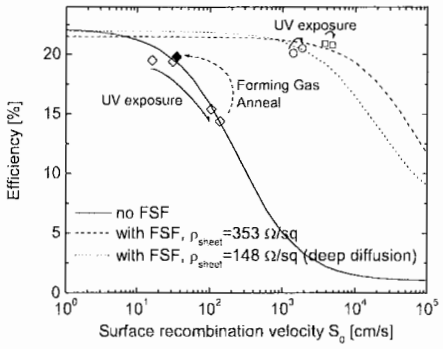
In **chapter 5** the local laser-fired aluminium emitter (LFE) process, an alternative process to boron emitter diffusion, is investigated. The model of the LFE emitters, which includes a laser-induced damage zone, is analysed using a two-dimensional simulation and compared with the experimental solar cell results.



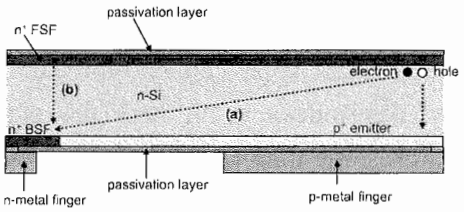
A detailed analysis of the loss mechanisms in the back-contact back-junction silicon solar cells is presented in **chapter 6**. Four main loss mechanisms in the BC-BJ solar cells are described: series resistance, optical losses, recombination losses and electrical shading. The influence of each of the loss mechanisms on the cell efficiency is studied.



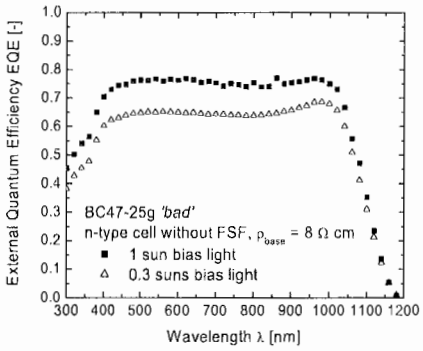
Passivation quality of the different phosphorus-doped front surface field diffusion profiles is analyzed in **chapter 7**. The dark saturation current density of different FSF diffusion profiles is determined under low and high injection. Stability of the test samples and the solar cells under UV exposure is investigated.



Chapter 8: The influence of the large pitch of the n- and p-contact fingers, which is in the range of millimetres, on the series resistance is studied. The application of a phosphorus-doped front surface field (FSF) reduces significantly the lateral base resistance losses. This additional function of the phosphorus-doped FSF is analysed using a comparison between numerical simulation and experimental results.



Chapter 9: The dependence of current and voltage output of three structures of high-efficiency back-junction back-contact silicon solar cells on illumination densities was analyzed in detail. It was shown that, the n-type cell structure with n^+ front surface field enables highest energy yield at low illumination intensity conditions.



2 Back-contact silicon solar cells

The advantages and challenges related to the back-contact solar cell structures are presented. Different types of the back-contact solar cells are introduced and a review of the state-of-the-art technology is given. The influence of the bulk lifetime and the front surface recombination velocity on the efficiency of the back-contact solar cells is discussed. The calculation of the conversion efficiency limit of crystalline silicon solar cells is presented.

2.1 Introduction

Back-contact solar cells exhibit both polarities of the metal electrodes (emitter and base electrodes) on the back cell side. Due to this fact the back-contact solar cells exhibit some major advantages over the conventional solar cell with metal contact on the front side. The advantages are:

- Zero shading due to absence of the metallization grid on the front side. This leads to an increased short-circuit current (J_{SC}) of the cell;
- Due to the absence of the front side metal grid, the front surface can be optimized for optimum light trapping and surface passivation properties, without having to allow for the low contact resistance. This way the front surface recombination can be reduced and light trapping improved;
- Reduction of the series resistance of the metallization grid. Both contact grids are placed on the rear side, therefore the metal finger width is not limited by its shading properties;
- Potentially easier and fully automated co-planar interconnection of the back-contact solar cells in the module assembly process. Recently a novel inline assembly of the solar modules with the back-contact solar cells has been introduced by Späth et al. [7];
- The solar cell packaging density in the solar module can simultaneously be increased, thereby increasing the total area efficiency of the module. A module with back-contact solar cells with a record efficiency of 20.1 % was recently presented by De Ceuster et al. [3].
- Attractive, uniform appearance of the finished modules, which is especially of importance in the building integrated photovoltaics (BIPV).

Thanks to the above mentioned advantages the conversion efficiency of the back-contact solar cells is potentially increased compared to conventional solar cells. Also the costs of the photovoltaic energy produced by the module with back-contact solar cells can be therefore reduced.

However, there are also some challenges and risks related to the back-contact solar cell structure. There challenges and risks are:

- The processing of back-contact solar cells requires a few structuring steps. This makes the processing procedure more challenging and complicated than in the case of the conventional solar cells;
- Risk of fatal shunting between the p- and n- electrodes due to errors in the masking processes. Therefore the requirements of high positioning accuracy and resolution are imposed on the masking steps. That results in an increase of the cost of these processes;
- If the analyzed back-contact solar cell structure possesses all collecting p-n junction on the back side (back-contact back-junction solar cell structure), then a high minority carrier lifetime in the base material is required in order to enable high solar cell efficiencies. Therefore the starting silicon material needs to be of high quality and its quality needs to be maintained during the whole solar cell processing sequence;
- Simultaneously the front surface recombination velocity needs to be kept low in the finished device in order to enable high efficiencies. More information on the issues of the minority carrier lifetime in the base material and the surface recombination velocity are presented in section 2.3.

The high material quality and the complicated processing technology result in the increase of the manufacturing costs. Therefore the efficiency of the processed back-contact solar cell needs to be high, in order to balance the increased costs.

The issues of the complicated processing technology and the requirement of reaching high conversion efficiencies are addressed in this work. In the following chapters a development of a high-efficiency back-contact back-junction solar cell structure using industrially applicable processing technology, including the masking technology, together with an advanced solar cell characterization are presented. However before going into the results of the solar cells developed in this work, a review of the back-contact silicon solar cell will be given in the next section.

2.2 Review of back-contact silicon solar cells

A conventional solar cell is presented in Figure 2-1. This solar cell possesses metal contact on both cell sides. The cell structure shown in Figure 2-1 is a passivated emitter rear locally diffused (PERL) solar cell structure, which enabled reaching the highest efficiency of the silicon solar cell under one-sun illumination intensity. The record efficiency of 24.7 % was demonstrated by Zhao et al. [8] on monocrystalline silicon. Using mulitcrystalline silicon the record efficiency of 20.3 % was obtained by Schultz et al. [9]. These cells feature: a selective doping profiles underneath metal contacts for low contact recombination, passivated front and rear surfaces, well textured front surface with an antireflection coating for low front surface reflection and flat, highly reflective rear for light-trapping, low front contact shading. These are the required ingredients for a high-efficiency design and they are also applicable for the back-contact back-junction cell structure. A review of the recent activities in the industrial application of high-efficiency silicon solar is given by Glunz [10], [11].

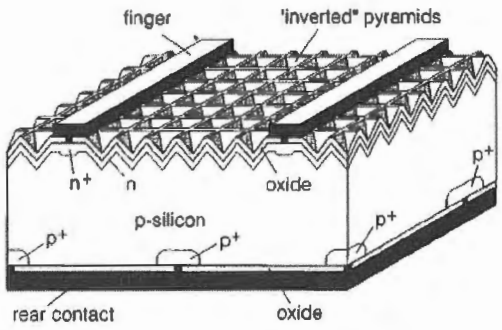


Figure 2-1 The passivated emitter, rear locally-diffused PERL cell which reached record efficiency of 24.7 % (from [8]).

The backside contacted solar cells, which exhibits both polarities of metal contacts on the back side, can be divided into three major categories:

- Back-Contact Back-Junction (BC-BJ) solar cells (section 2.2.1), also called Interdigitated Back Contact (IBC) solar cells, which have both contacts and the collecting junction placed on the back side of the cell;
- Emitter Wrap Through (EWT) solar cells (section 2.2.2), in which the front surface collecting junction is connected to the interdigitated contacts on the back surface via laser-drilled holes;

- Metallization Wrap Through (MWT) solar cells (section 2.2.3), in which the front surface collecting junction and the front metallization grid are connected to the interconnection pads on the back surface via laser-drilled holes.

A short review of the above mentioned categories of the back-contact solar cells is presented in the following subsections. For a more detailed review of back-contact solar cells the reader is refered to the paper of Van Kerschaver and Beaucarne [12]. The topic of this work are back-contact back-junction solar cells. Therefore a detailed review of the development efforts in the field of this solar cell structure done by different groups will be given here.

2.2.1 Back-contact back-junction (BC-BJ) solar cells

The concept of the back-contact back-junction solar cells, also called interdigitated back contact (IBC), was introduced in 1975 by Schwartz and Lammert [13], [14]. This cell structure is shown in Figure 2-2.

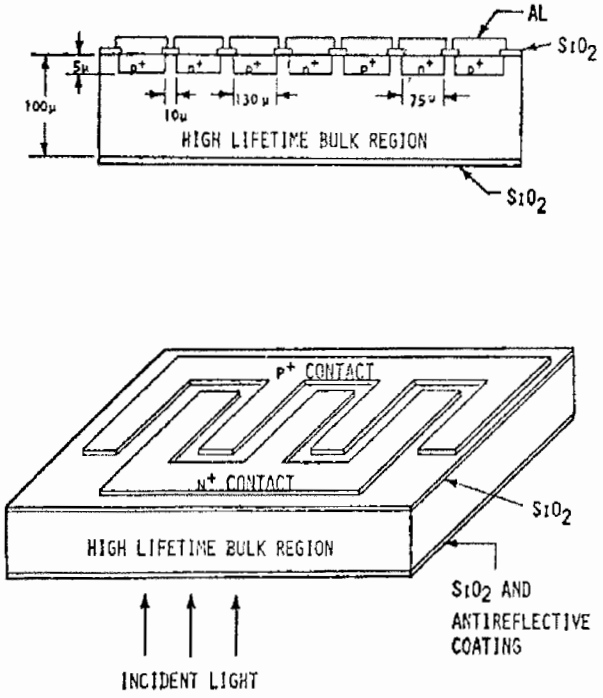


Figure 2-2 The structure of the interdigitated back contact IBC solar cell (from [13]).

Both emitter and base metal contacts are placed on the back cell side in a form of an interdigitated grid. Also the emitter and back surface field diffusions are in the form of the interdigitated grid. Due to such design this device possesses all of the above

mentioned advantages. At first the IBC solar cells were designed for operating in the high-concentration systems. An efficiency of 17 % was achieved under 50-suns concentration [13].

In 1984 Swanson et al. [15] introduced a point contact silicon solar cell, which is similar to the IBC solar cell. The main difference is that in the point contact solar cell the rear side diffusions are limited to an array of small points, as schematically shown in Figure 2-3. By reducing of the area of the highly diffused regions on the back cell side, the dark saturation current of the doped areas could be reduced significantly. Thus, the output voltage and the efficiency of the cell could be increased.

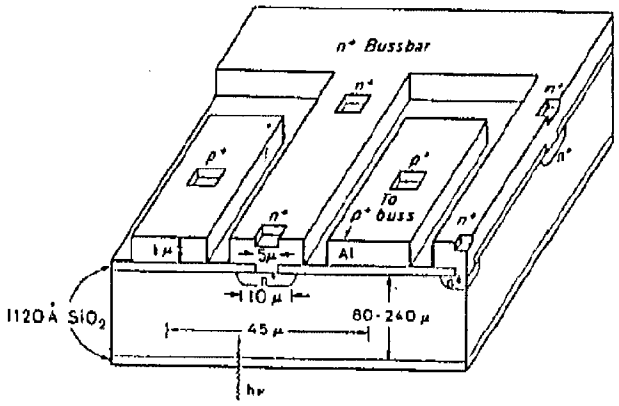


Figure 2-3 Structure of a point contact solar cell (from [15]).

The photovoltaic group at Stanford University led by Prof. Swanson has made the most significant contributions in the field of the IBC cells. Thus, the developments of the back-side contacted cells made by this group are presented in the following:

Non-textured point contact *concentrator solar cell* achieved an efficiency of 19.7 % under 88-suns concentration in 1984 [15]. In 1986 a further optimized point contact solar cell with an efficiency of 27.5 % under 100 suns concentration was achieved by Sinton et al. [16]. Shortly after, an increased device cell efficiency up to 28 % under 150 suns was after presented by Sinton et al. [17]. In 1988 Sinton et al. [18] reported point contact solar cells with an efficiency of 28.4 % at power densities up to 200 suns. The area of these solar cells was 0.15 cm^2.

The back-contact back-junction solar cell structure was also optimized for the applications under standard *one-sun illumination*. In 1985 Verlinden et al. [19] presented an IBC solar cell with a one-sun illumination efficiency of 21 %. One year later Sinton et al. [16] introduced a point contact solar cell with 22.2 % one-sun

efficiency with the area of 0.15 cm^2. However this efficiency was corrected down to 21.7 % after the publication [20].

King et al. [20] presented a first medium-area (8.5 cm^2) point contact solar cell with the front and back surface fields with the top efficiency of 22.3 %. In this solar cell a novel *multi-level metallization scheme*, introduced by Verlinden et al. [21], [22], was applied. This metallization scheme allowed for realization of large-area solar cells in which series resistance is not dependent on solar cell area. In 1991 a record one-sun efficiency of 22.7 % on a 37.5 cm^2 point contact solar cell was reported by King et al. [23].

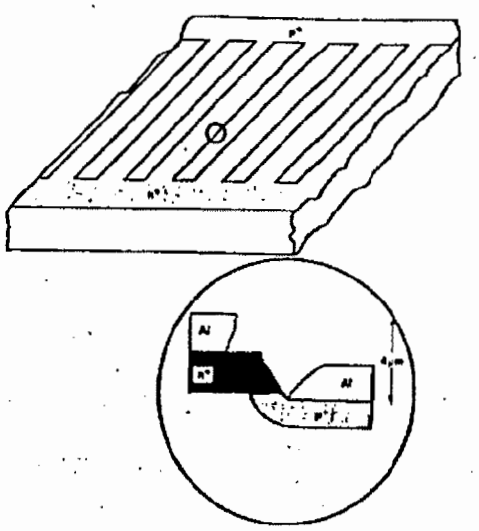


Figure 2-4 Simplified back-side solar cell. The illuminated side is on the bottom in this figure. The mesa trench, which allows for self-aligned metal contact separation is shown in the inset (from [24]).

The processing of the interdigitated grid of the rear side diffusions, contact openings and the metal grid of the point contact solar cells requires four to six patterning steps [24]. Thus, this processing sequence is complex, which results in high manufacturing costs. In 1988 a *self-aligned method* to for an interdigitated contact grid was introduced [18]. In 1990 Sinton et al. [24] presented a simplified back-side solar cell (schematically shown in Figure 2-4), which used this self-aligned contact separation and allowed for reduction of the masking steps to one. For the simplified processing sequence a 10.5 cm^2 one-sun solar cell with an efficiency of 21.9 % was reported.

The Sunpower Corporation was founded in 1985 by Prof. Swanson in order to commercialize to high-efficiency back-contact silicon solar cells developed by the

research group of Stanford University. A pilot production of large area (35 cm^2) back-contacted solar cells with an efficiency of 21 % was reported by Sinton et al. [25]. 7000 solar cells of this type, with an average efficiency of 21.1 %, were manufactured for the Honda solar-car *Dream*, which won the World Solar Challenge race in 1993 [26]. The processing of these solar cells required five photolithography masking steps.

In a following study of Sunpower the back-contact solar cell design, especially the *edge passivation* and the *substrate doping*, were optimized. This resulted in a record one-sun efficiency of 23.2 % reported in 1997 by Verlinden et al. [27]. In 2002 the process simplifications, which eliminated one third of the major processing steps and resulted in reduction of the fabrication costs by 30 %, were reported by Cudzinovic et al. [28]. The process simplifications led to 0.6 % absolute efficiency decrease.

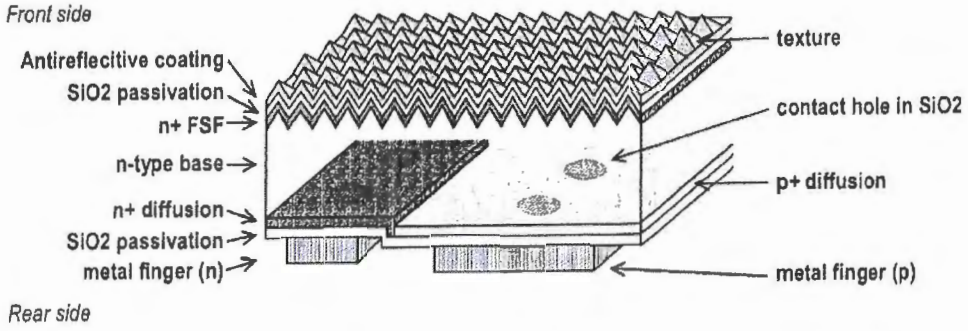


Figure 2-5 Schematic diagram of the Sunpower's A-300 solar cell (from [29]).

In 2004 a manufacture of the large-area (149 cm^2) *A-300 back-contact solar cells* was introduced by Mulligan et al. [29]. A maximum cell efficiency of the A-300 solar cells of 21.5 % was achieved. A schematic diagram of the Sunpower's A-300 solar cell is shown in Figure 2-5. McIntosh et al. [30] found that the n-type silicon material with thickness of 160 to 280 μm and resistivity of 2 to 10 Ω cm was optimal for the A-300 cells. Also the light trapping of this cell type was studied in details by McIntosh et al. [31].

A high volume production of a *new generation of the A-300* back-contact cells with an record average efficiency of 22.4 % was introduced in 2007 by De Ceuster et al. [3]. The new generation back-contact solar cells achieve the highest efficiency silicon solar cells in mass production up to date. In the same paper a record module efficiency of 20.1 % using back-contact solar cells was reported.

In a recent lecture Prof. Swanson [32] announced a new record efficiency of 23.4 % of a large area (149 cm^2) back-contact solar cell developed by the R&D department of Sunpower. Details of the improvements that have been applied to this solar cell design and to the processing technology are not known.

Simultaneously to the development efforts at Stanford University and Sunpower, there other groups which are working on the high-efficiency back-contact back-junction solar cell devices. At Fraunhofer ISE a rear-contacted (RCC) silicon solar cell with line contacts were processed using the photolithography masking. A schematic diagram of a RCC cell is shown in Figure 2-6. An efficiency of 22.1 % was reported by Dicker et al. [33], [34].

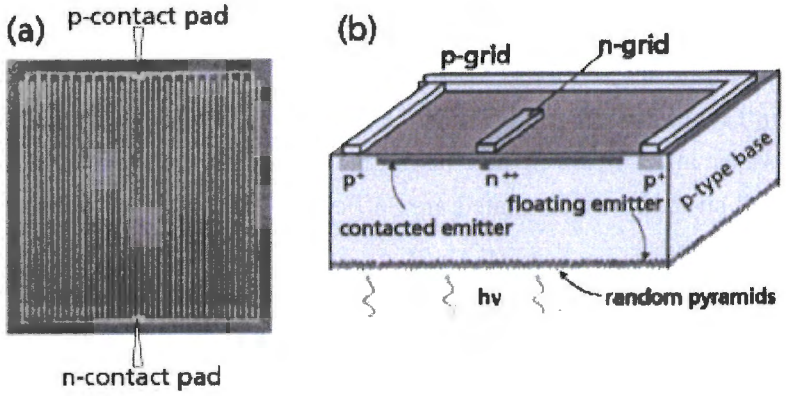


Figure 2-6 Structure of the RCC fabricated at Fraunhofer ISE. (a) View of the rear side of the RCC showing the interdigitated contact pattern. (b) Details of the solar cell structure, with the cell shown upside down (from [33]).

For the applications under concentrated sunlight a rear-line-contacted concentrator cell (RCLL) was developed by Mohr [35]. This cell structure is based on the RCC solar cell design. A maximum efficiency of 25 % at illumination intensity of 100 suns was achieved [36].

A low-cost approach to the BC-BJ solar cell structure was developed by Guo [37] from the UNSW. The *Interdigitated Backside Buried Contact* (IBBC) solar cell, shown in Figure 2-7, is processed without the use of photolithography. The laser-grooved buried contact technology is applied. A maximum one-sun efficiency of 19.2 % was reported by Guo et al. [38].

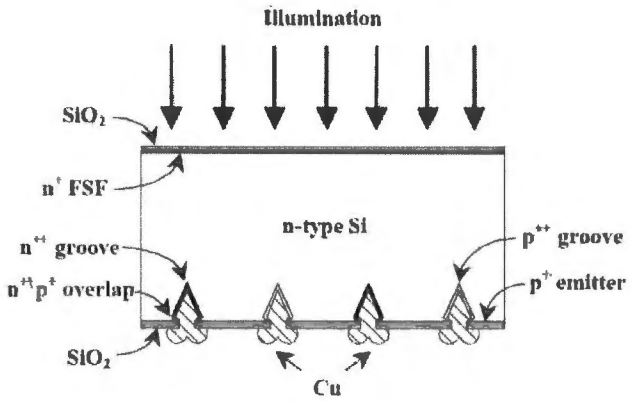


Figure 2-7 Schematic cross section of the n-type IBBC solar (from [38]).

Another very promising low-cost BC-BJ solar cell structure was developed by Engelhart at al. [39], [40] from the ISFH. The *RISE* (*Rear Interdigitated contact scheme, metalized by a Single Evaporation*) solar cell structure is schematically presented in Figure 2-8. The RISE solar cell is fabricated using a mask-free process, in which the laser ablation of Si and laser ablation of protective coatings are applied. With this cell structure a designated area efficiency of 22 % was achieved on a 4 cm^2 laboratory solar cell.

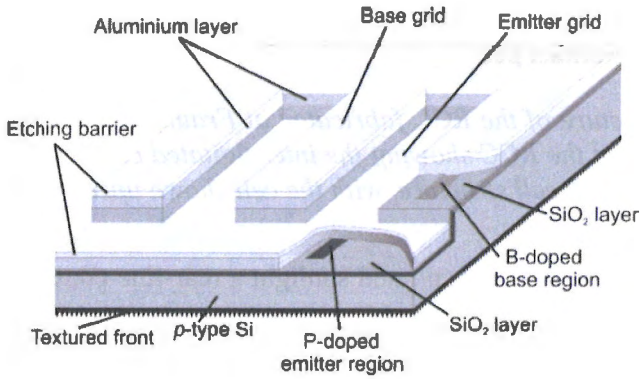


Figure 2-8 Schematics of the RISE back junction solar cell. (from [39]). The illuminated side is on the bottom in this drawing.

Furthermore, large-area high-efficiency back-contact solar cells for a mass production are being developed by Q-Cells within the *Quebec* project. In 2006 Huljic et al. [41] reported maximum efficiency of 21 % for laboratory scale 4 cm^2 on low cost Cz-Si wafers. In 2007 Huljic et al. [42] presented large area (100 cm^2) BC-BJ solar cell with an efficiency of 20.5 %. In the same presentation plans for a technology transfer to a pilot production were announced.

One of the very promising developments in the field of back-contact solar cells, is the application of the of *amorphous/crystalline silicon* (a-Si/c-Si) *hetero-junction structures*. Due to its superior surface passivation properties the a-Si/c-Si hetero-junctions have the potential to significantly increase the voltage of a solar cell. Hetero-junction back-contact solar cells are being developed by a number of research groups [43], [44], [45].

2.2.2 Emitter Wrap Through (EWT) solar cells

The concept of the emitter wrap through EWT solar cell was introduced by Gee et al. [46], [47]. The concept is based on an emitter which is diffused on the front and back side of the cell. The front and back emitters and connected through laser-drilled and emitter-diffused holes. The EWT cell concept is schematically shown in Figure 2-9.

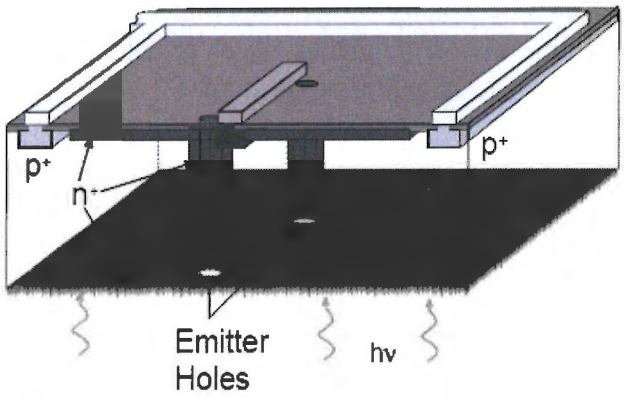


Figure 2-9 Schematic diagram of an emitter wrap through EWT solar cell. The illuminated side is facing down in the picture (from [48]).

The advantages of the EWT solar cell are comparable to the ones of back-contact back-junction solar cells: (i) complete elimination of front contact grid shading, and (ii) the possibility of the co-planar interconnection. However there exists one major advantage of the EWT cells over the BC-BJ cells. Due to the presence of the p-n junction on the front and on the back cells side, the average distance of the minority carriers to the emitter is significantly reduced. This results in the much lower required minority carrier lifetime in the bulk than in the case of BC-BJ cells. It is therefore possible to reach high efficiencies with EWT cells even with a low quality bulk Si, what is not possible in the case of BC-BJ cells. A comparison of the influence of the bulk lifetime on the solar cell efficiency for the BC-BJ and EWT solar cells is presented by Kray [48] and Engelhart [40].

Advent Solar reported manufacturable EWT solar cells with efficiencies of 14 % on mc-Si and 16 % on mono-Si using only low-cost processing [49]. At the University of Konstanz a low-cost EWT solar cell process was developed and an efficiency of 13.6 % on Cz-Si was achieved [50], [51]. At Fraunhofer ISE an EWT solar cell processed using photolithography masking achieved 18.7 % on Cz-Si [52] and 21.4 % on FZ-Si [53]. At ISFH a large area (92 cm^2) RISE-EWT (Rear Interdigitated Single Evaporation Emitter Wrap-Through) solar cell was developed. A maximum efficiency of 21.4 % on FZ-Si was reported by Hermann et al. [54]. Q-Cells presented a large area (92 cm^2) EWT solar cell on mc-Si with an efficiency of 17.1 % [55].

2.2.3 Metallization Wrap Through (MWT) solar cells

The metallization wrap through (MWT) solar cell concept [56] shows the closest similarity to a conventional solar cell structure. The emitter and the front side metallization fingers are located on the front surface. However, the busbars are placed on the back side of the cell. The front side metal fingers are connected to the busbar on the rear side through the laser drilled holes, which are filled with the metal. The MWT cell concept is schematically shown in Figure 2-10.

Due to the fact that in the processing of the MWT solar cells standard screen-printing technology can be applied, the transition from the processing sequence of a conventional soar cell to a MWT solar cell is not complicated. Furthermore, the MWT cell concept offers advantages over the conventional solar cell. Thanks to the removal of the front side busbars, the front contact shading is reduced. Simultaneously, the co-planar interconnection is possible since both contact polarities are placed on the back side.

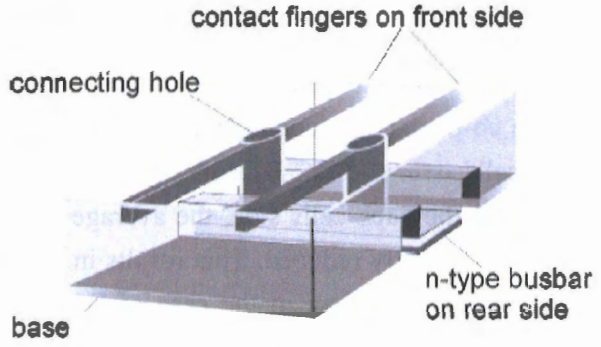


Figure 2-10 Schematic drawing of a MWT cell (from [57]).

The MWT cell structure is being successfully developed by different groups: Van Kerschaver et al. [58] from IMEC presented a module based on screen-printed MWT solar cells with an efficiency of 14.7 %. At ECN a pin-up module concept was introduced by Bultman et al. [59]. Weeber et al. [60] from the ECN group presented mc-Si MWT cells with an area of 225 cm^2 and an efficiency of 16.7 %. At Fraunhofer ISE a mc-Si MWT solar cell with an area of 156 cm^2 and an efficiency of 16.2 % was presented by Clement et al. [61]. Joos et al. [62] from the group of University of Konstanz presented Cz-Si MWT solar cells with an area of 25 cm^2 and an efficiency of 17.5 % and Knauss et al. [57] presented large area (243 cm^2) Cz-Si MWT cells with an efficiency up to 16.7 %.

2.3 Critical parameters of the back-contact back-junction solar cells

As already mentioned in section 2.1, one of the challenges related to the back-contact back-junction solar cell structure is the requirement of a high minority carrier lifetime in the silicon bulk (τ_{bulk}) and a low front surface recombination velocity (S_{front}). Without fulfilling these requirements, high device efficiencies cannot be achieved.

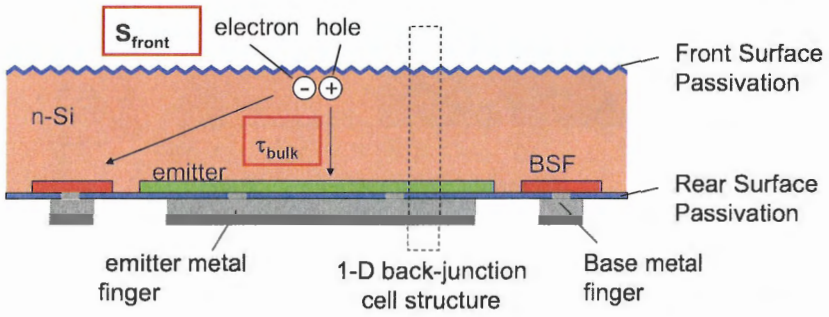


Figure 2-11 *Schematic cross-section of an n-type high-efficiency back-contact back-junction silicon solar cell (sketch not to scale). Two most critical parameters for this cell type, namely the front surface recombination velocity (S_{front}) and the minority carriers lifetime in bulk (τ_{bulk}) are also shown.*

In silicon solar cells most of the photogeneration occurs at the front side of the cell (schematically shown in the Figure 2-11). But in the back-junction cell structure, the p-n junction is located on the back cell side. Therefore the light generated carriers can be easily lost by recombining at a poorly passivated front surface, instead of reaching the back junction. Moreover, even if the front surface is well passivated, a risk of recombination within the bulk silicon exists. The carriers which need to diffuse

through the wafer thickness can recombine in the bulk silicon before reaching the back junction if the bulk lifetime of the minority carriers is insufficient. Therefore, τ_{bulk} and S_{front} are the two most critical parameters in the back-contact back-junction solar cell structure.

In order to show the importance of these two critical parameters in the back-contact back-junction solar cell structure, a one-dimensional back-junction cell structure (marked in Figure 2-11) was simulated using simulation program PC1D [63]. Both critical parameters τ_{bulk} and S_{front} were varied in a wide range in order to analyze their influence on the solar cell efficiency. In the simulations the device thickness of 200 µm was chosen. The simulation results are shown in Figure 2-12.

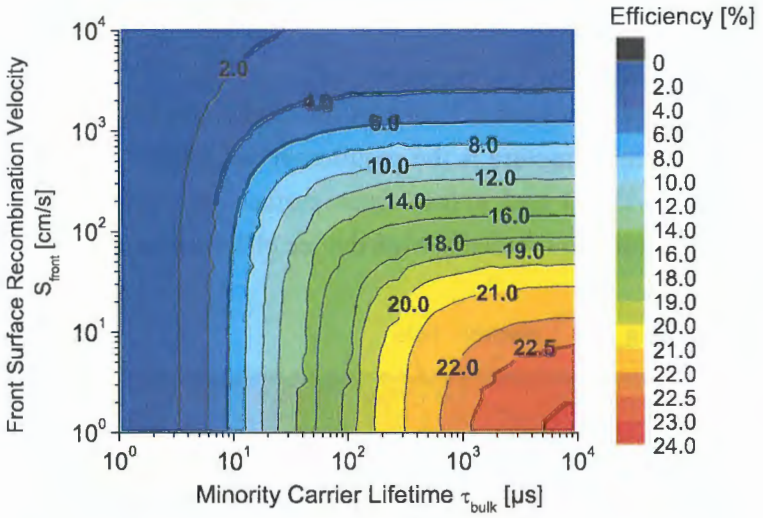


Figure 2-12 Simulations of the efficiency of a one-dimensional back-junction solar cell structure in a wide range of carriers lifetime and front surface recombination velocity. The thickness of the simulated device is 200 µm. The resistivity of the n-type base is 1 Ω cm and the p-type rear emitter has a sheet resistance of 30 Ω/sq. Simulations were performed using PC1D [63].

Based on the simulation results presented in Figure 2-12 the requirements on the τ_{bulk} and S_{front} can be quantified. In order to achieve conversion efficiencies above 22 %, the front surface recombination velocity should be less than 10 cm/s. At the same time the minority carrier lifetime in the bulk material should be higher than 700 µs, which for the base resistivity of 1 Ω cm corresponds to a diffusion length of 900 µm. As a rule of thumb it can be assumed that the diffusion length of the minority carriers in the bulk should be at least four times greater than the wafer thickness in order to allow for high efficiencies in this solar cell concept. As can be seen in Figure 2-12 the conditions of

low S_{front} and high τ_{bulk} need to be fulfilled simultaneously in order to reach high device efficiencies. Even a minor deterioration of one of the critical parameters will lead to a significant efficiency decrease.

It is therefore essential to be able to fulfill the above mentioned requirements when developing a back-contact back-junction solar cell structure. Without having realized the conditions of low S_{front} and high τ_{bulk}, any other developments and optimization efforts on the BC-BJ structure will be fruitless. The analysis of the minority carrier lifetime in the bulk is presented in section 4.2. The front surface recombination velocity of the analyzed solar cell structure was investigated in chapter 7.

2.4 Conversion efficiency limitations by intrinsic losses

The thermodynamic limit of the conversion efficiency of a single bang-gap photovoltaic converter was found to be 33 % [64], [65] for a band-gap of silicon (1.12 eV) and the AM1.5 spectrum. Using actual parameters for intrinsic recombination the efficiency limit is reduced to 30 % [65]. Swanson [66] calculated a theoretical limit of efficiency of a silicon solar cell of 29 %.

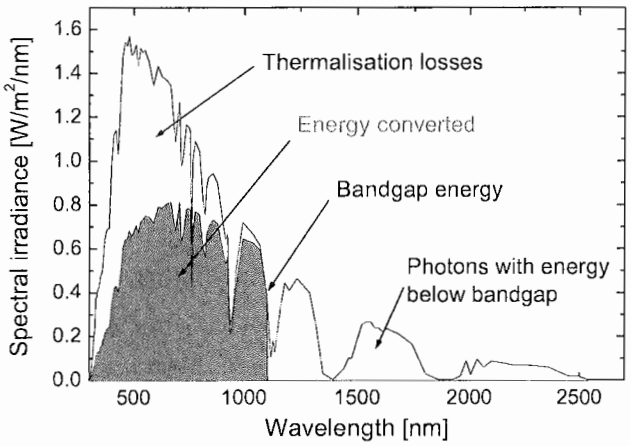


Figure 2-13 Spectral irradiance of the AM1.5G spectrum. The fraction of the spectrum that can be converted by a single-junction silicon solar cell is marked with dark grey.

2.4.1 Intrinsic loss mechanisms in silicon

The above mentioned conversion efficiency of a single junction silicon solar cell is primarily limited due to the following intrinsic loss mechanisms:

- Photons with energy smaller than the band gap (1.12 eV) of silicon do not have enough energy to generate electron hole pairs.
- Photons with energy equal or exceeding the band gap will generate electron-hole pairs. However, photon energy exceeding 1.12 eV will be lost due to the thermalization process. These two effects are schematically shown in Figure 2-13.
- The maximum open-circuit voltage is smaller than 1.12 V (band gap in Si). This is caused by the fact that not the separation of band gap, but the separation of the quasi-Fermi levels defines the open-circuit voltage [5].
- The maximum power that can be generated by a solar cell is smaller than the product of open-circuit voltage and short-circuit current. The current-voltage (IV) curve of a solar cell does not have a rectangular shape (see for example Figure 4-23). Due to the exponential dependence of current with voltage, which is caused by the non-avoidable recombination currents, the fill factor (FF) is limited to about 85 %.

Moreover, the absorption of incoming photons in silicon strongly depends on the energy of the photons (see Figure 2-13). For the low energy photons ($\lambda > 1000$ nm) the absorption coefficient is very low, and the absorption length increases strongly. Therefore, even with optimal light trapping schemes, for a finite thickness of the silicon wafer not all incoming photons with appropriate energy will generate electron-hole pairs (see section 2.4.2).

In the following sections a calculation of the efficiency limit of an ideal single junction silicon solar cell with finite thickness and a particular base doping will be presented. In the ideal solar cell only the recombination mechanisms which are intrinsic and non-avoidable in silicon will be considered. These are: radiative and Auger recombination. The technology related recombination losses such as surface recombination, recombination in the highly doped regions of the solar cell or the recombination through the defect and/or impurities in a non-perfect silicon bulk are not taken into account here.

2.4.2 Short-circuit current limit

Short-circuit current (J_{SC}) of a solar cell is a function of the absorption of the incoming photons within the solar cell. In an ideal solar cell the technology related optical effects are not considered. These effects are front surface reflection, metallization grid

shading, transmission through the silicon wafer and parasitic absorption in the dielectric layers or in the highly doped silicon regions.

For the calculation of the limit to the short-circuit current only the intrinsic optical loss effect in the silicon wafer is considered. This effect is the finite maximal average path length of the incoming photons within the silicon wafer. Tiedje et al. [65] and Brendel [67] showed that for the optimal light trapping, the maximal average path length of the incoming light within the silicon wafer (l) can be approximated with:

$$l \approx 4\, n_{Si}(\lambda) W \tag{2.1}$$

where W is the wafer thickness, λ is the wavelength of light and $n_{Si}(\lambda)$ is the wavelength dependent refraction index of silicon.

Knowing the maximum average path length of the incoming light in silicon, the maximum limit on the short-circuit current ($J_{SC,limit}$) as a function of the wafer thickness can be calculated. In order to calculate $J_{SC,limit}$, the solar spectrum needs to be integrated with the absorption coefficient in silicon, assuming the maximum average path of the incoming light calculated with equation (2.1):

$$J_{SC,limit}(W) = \frac{q}{hc} \int \lambda\, I_{AM1.5G}(\lambda) \left[1 - \exp\left(-4\alpha_{Si}(\lambda)\, n_{Si}(\lambda) W\right)\right] d\lambda \tag{2.2}$$

where q is the elementary charge, h is the Planck constant, c is velocity of light in vacuum, $\alpha_{Si}(\lambda)$ is the wavelength dependent absorption coefficient of silicon, $I_{AM1.5G}(\lambda)$ is the energy flux density of the incoming light.

In Figure 2-14 the calculated maximal short-circuit current as a function of wafer thickness is presented. For the complete AM1.5G spectrum a maximal J_{SC} of nearly 46 mA/cm^2 is possible. However, due to the finite path length of the incoming light, the actual J_{SC} limit is lower. The calculations of J_{SC} limit for the case of optimal light trapping (as obtained using the maximal average path length calculated with Eq. 2.1 and then with Eg. 2.2) and for the case of no light trapping (i.e. the path length of the incoming light in silicon equals wafer thickness $l=W$) are shown as well. For the optimum light trapping and a wafer thickness of 150 µm the J_{SC} limit equals 44 mA/cm^2. However, if no light trapping is applied, then the J_{SC} limit is reduced to 38.6 mA/cm^2.

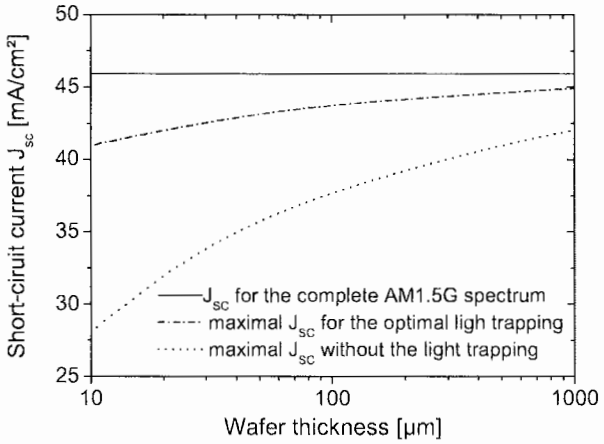


Figure 2-14 Maximum possible short-circuit current in the silicon solar cell under AM1.5G spectrum, as a function of wafer thickness.

2.4.3 Open-circuit voltage limit

Open-circuit voltage (V_{OC}) of a solar cell is limited by the recombination rate of the electron-hole pairs. In an ideal solar cell only the recombination mechanisms, which are intrinsic and non-avoidable in silicon, take place. These intrinsic recombination mechanisms in silicon are the radiative recombination and the Coulomb-enhanced Auger (CE Auger) recombination.

The influence of the intrinsic recombination processes, as well as the limitations of short-circuit current, on the V_{OC} and efficiency of the ideal solar cell can be modelled using the approach of Kerr [68]. The following equation enables calculation of the current –voltage (J-V) characteristics of an ideal solar cell:

$$J(V,W,N_D) = J_{\mathrm{SC,limit}}(W) - qWR_{\mathrm{int}}(V,W,N_D) \tag{2.3}$$

where J is the current and V is the voltage of the solar cell, N_D is the doping concentration of the silicon wafer, R_{int} is the intrinsic recombination rate and the $J_{SC,limit}$ is the short-circuit current calculated in the previous section.

The intrinsic recombination rate can be calculated using the parameterisation of the radiative (R_{rad}) and CE-Auger ($R_{CE\text{-}Auger}$) recombination by Kerr and Cuevas [69], [70] using the following equation:

$$\begin{aligned} &R_{\mathrm{int}}(V,W,N_D) = R_{CE\text{-}Auger} + R_{Rad} = \\ &= n_i^2 e^{\frac{qV}{k_B T}} \left(1.8\times10^{-24} n_0^{0.65} + 6\times10^{-25} p_0^{0.65} + 3\times10^{-27}[\Delta n(V)]^{0.8} + (1-P_{PR}(W))B_R\right) \end{aligned} \tag{2.4}$$

where n_0 and und p_0 are the equilibrium concentrations of electron and holes expressed in units of cm^{-3}, Δn is the injection density and B_R is the radiative recombination coefficient. The photon recycling (i.e. the re-absorption of the radiatve recombination radiation in the solar cell and generation of an electron-hole pair) is considered, with P_{PR} describing the photon recycling rate.

Derivation of the equation (2.4) is done under assumption of the Narrow-Base approximation of Green [71]. Assuming that Fermi levels of electrons and holes are constant within the solar cell base. Then the equation (2.5) is valid

$$np = (n_0 + \Delta n)(p_0 + \Delta n) = n_i^2 e^{\frac{qV}{k_B T}} \tag{2.5}$$

For the calculations of the recombination rate of the intrinsic recombination mechanism the parameters summarized in Table 2-1 were applied. The limit to the open-circuit voltage can be then calculated using the equation (2.3) for the condition of $J(V_{OC}) = 0$.

Table 2-1 Parameters used for the modeling of the intrinsic recombination in silicon.

Parameter	Value
T	300 K
n_i	1.0×10^{10} cm^{-3} [80]
B_R	4.73×10^{-15} cm^3s^{-1} [72]
P_{PR}	0.79 @ W= 150 µm [70]
p_0	$p_0 = \frac{n_i^2}{N_D}$
n_0	N_D
Δn	$\Delta n(V) = \frac{1}{2}\sqrt{\left(n_0^2 + p_0^2\right)^2 - 4\left((n_0 - p_0) - n_i^2 e^{\frac{qV}{k_B T}}\right)} - \frac{1}{2}(n_0 - p_0)$

The limit of the open-circuit voltage calculated for different wafer thicknesses and different base doping density of an n-type solar cell is shown in Figure 2-15. For the cell thickness of 150 µm and an n-type base with doping of N_D=5.0×10^{15} cm^{-3} the V_{OC} limit equals 742.5 mV.

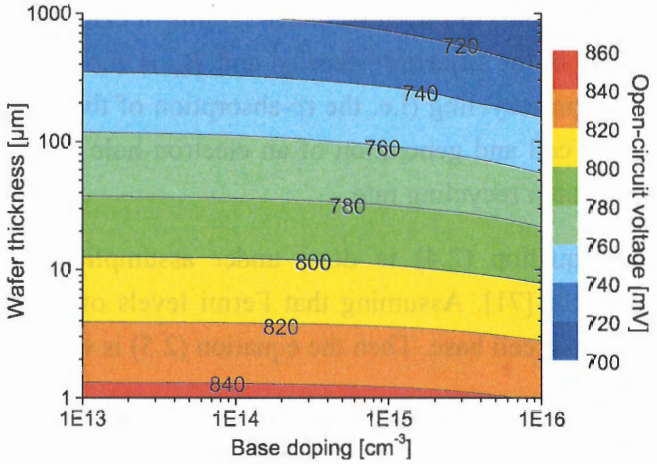


Figure 2-15 The open-circuit voltage of an n-type silicon solar cell imposed by the intrinsic (radiative and Auger) recombination loss mechanisms. Calculations were done for a wide range of the wafer thicknesses and base doping range.

Table 2-2 Efficiency limit of a silicon solar cell with optimal light trapping and only intrinsic recombination mechanisms. Calculations assuming the cell thickness of 150 µm and the n-type base with doping of $N_D=5.0\times10^{15}$ cm^{-3} (base resistivity of 1 Ω cm).

Cell parameter	Limit by intrinsic losses
efficiency η [%]	28.3
fill factor FF [%]	86.5
open-circuit voltage V_{OC} [mV]	742.5
short-circuit current J_{SC} [mA/cm^2]	44.0

2.4.4 Efficiency limit

By applying the calculated short-circuit current limit and the open-circuit limit into equation (2.3), it is possible to calculate current-voltage characteristics of an illuminated ideal solar cell. Thus, the efficiency limit can be determined.

In Table 2-2 the calculated parameters of an ideal silicon solar cell, with optimal light trapping and only Auger and radiative recombination mechanisms, are shown. The efficiency limit of 28.3 % was calculated assuming the cell thickness of 150 µm and

the n-type base with doping of N_D=5.0×10^{15} cm^{-3} (base resistivity of 1 Ω cm). This wafer thickness and the base doping correspond to the back-contact back-junction solar cells developed in this work. The fill factor was calculated using the one-diode model described by equation (6.8).

The technology related loss mechanisms, which are introduced during the manufacturing of the silicon wafers and the following solar cell processing, will lead to strongly reduced efficiencies of the real solar cells. A detailed comparison of the efficiency limit and the maximal achieved efficiency of the back-contact back-junction solar cell is presented in chapter 6.

3 Measurement methods and numerical simulations

In this chapter, two methods for the determination of the surface saturation current density under low and high-injection are presented. In addition, the process of the numerical simulations of the back-contact back-junction solar cells using one- and two-dimensional simulations is described. The measurement table developed for the electrical characterization of the analyzed solar cells is presented.

3.1 Surface saturation current density

The analysis of the surface passivation quality using different passivation layers (e.g. thermally grown SiO_2, PECVD SiN_X) in the combination with the dopant diffusion requires determination of the surface recombination velocity S and surface saturation current density J_{0s}. The measurement of the saturation current density of the applied diffusion profile is especially required in chapter 7 for the optimization of the n^+ front surface diffusion profile (the so called front surface field - FSF). The method presented below is used to determine the surface saturation current density and can also be applied in order to characterize and optimize both rear side diffusion profiles of the BC-BJ solar cell, i.e. the emitter diffusion, and the back surface field (BSF) diffusion profiles.

3.1.1 Injection dependent lifetime measurements

A direct measurement of the surface recombination velocity S and surface saturation current density J_{0s} is not possible. It is, however, possible to measure the so-called effective lifetime τ_{eff} of minority carriers, which takes into account the recombination mechanisms at the surfaces of the measured sample as well as within its bulk.

The effective lifetime was measured using the photoconductance tool WTC-120 from Sinton Consulting [73]. In this experimental setup, the measured silicon wafer is illuminated by a Xenon flash lamp, which has its spectrum distributed mainly at the wavelengths of 900 to 1000 nm. This near infrared light source allos for a fairly uniform profile of the excess carrier density Δn along the wafer thickness. During the lamp flash, the photoconductance of the measured wafer $\Delta\sigma$ is measured contactlessly by using inductive coupling. At the same time, the light intensity is measured using a reference solar cell, which is placed very close to the measured sample. The excess

carrier density Δn in the sample is calculated from the measured $\Delta\sigma$. Knowing the optical properties of the measured sample allows for the determination of the photogeneration rate within the sample measuring the illumination intensity with a monitor solar cell. After determination of both Δn and photogeneration, τ_{eff} can be calculated as a function of Δn (see for example Figure 3-2). This is possible by applying the generalized evaluation method, which is valid for quasi-steady-state and quasi-transient measurement conditions [74]. The quasi-steady–state photoconductance (QSSPC) method was introduced by Sinton et al. [75].

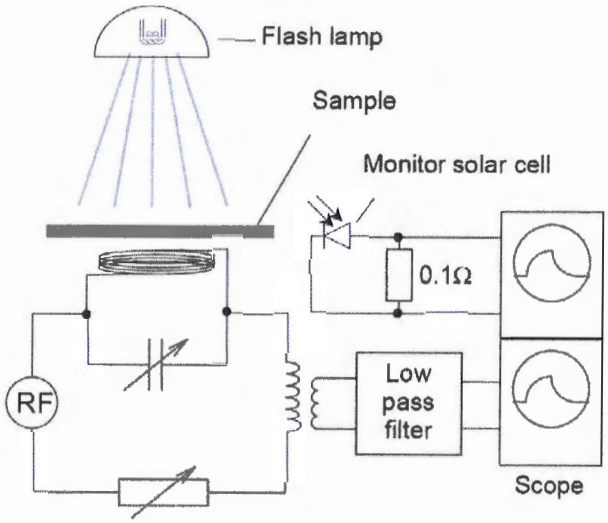


Figure 3-1 Schematic sketch of the photoconductance measurement setup (picture taken from [76])

The measured effective lifetime of the carriers is a function of the recombination in the bulk and at the surfaces of the sample, as shown in equation (3.1).

$$\frac{1}{\tau_{eff}} = \frac{1}{\tau_s} + \frac{1}{\tau_{SRH}} + \frac{1}{\tau_A} + \frac{1}{\tau_{rad}} \tag{3.1}$$

The surface recombination can be described by the surface lifetime τ_s. The volume lifetime τ_b is determined by the Shockley-Read-Hall (SRH) recombination [77], [78], described by the SRH lifetime τ_{SRH}, the Auger recombination τ_A [79] , and the radiative recombination (τ_{rad}).

The sample temperature during the measurements was set to 30°C. For the calculation of recombination parameters, the intrinsic carrier concentration value n_i=1.0 × 10^{10} cm^{-3} [80] was used. In order to determine the surface saturation current density, two methods were applied. J_{0s} was determined under low injection, where

$\Delta n << N_D$, for samples with resistivity of 1 Ω cm and under high injection, where $\Delta n >> N_D$, for 10 Ω cm samples. The same n_i value was used for both analyzed wafer resistivities of 1 and 10 Ω cm. Determination of the J_{0s} from the measured effective lifetime is presented in the next sections.

3.1.2 Determination of J_{0s} at low injection

The effective lifetime τ_{eff} measured under low injection at $\Delta n = 1\times10^{14}$ cm^{-3} was used for the calculations of the surface saturation current density. For samples with resistivity of 1 Ω cm, the dopant concentration equals $N_D = 5\times10^{15}$ cm^{-3}. Therefore, the condition of low injection $\Delta n << N_D$ is satisfied [81].

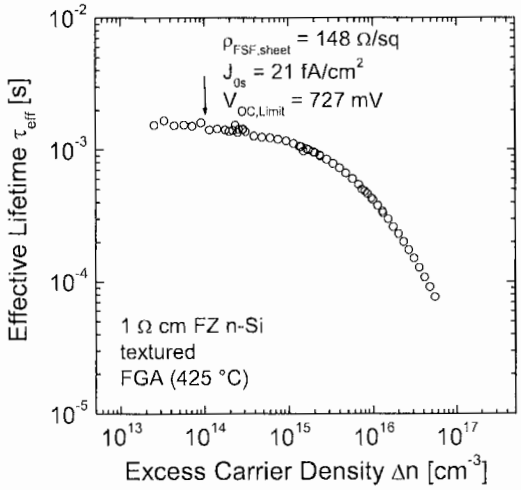


Figure 3-2 Example of QSSPC lifetime measurement of the textured symmetrical test sample with resistivity of 1 Ωcm and front surface field diffusion of 148 Ω/sq. J_{0s} and $V_{OC,\,Limit}$ determined at $\Delta n = 1\times10^{14}$ cm^{-3} are shown.

The surface lifetime τ_s was calculated using the equation (3.2) [82]. For the bulk lifetime τ_b, the intrinsic Auger and radiative recombination was used for the calculation. For the calculation of the Auger lifetime, the model of Kerr [69] was used. For the radiative recombination, the parameterization of Trupke et al. [72] was taken. Omitting the Shockley-Read-Hall bulk recombination results, the upper limit for J_{0s} value is determined as:

$$\frac{1}{\tau_{eff}} = \frac{1}{\tau_b} + \frac{1}{\tau_s} \tag{3.2}$$

For symmetrical lifetime samples, the effective surface recombination velocity S_{eff} can now be calculated using an approximation from Sproul [83]:

$$\tau_s = \frac{W}{2S_{eff}} + \frac{1}{D}\left(\frac{W}{\pi}\right)^2 \tag{3.3}$$

Where S_{eff} takes into account the recombination at the silicon surface as well as the minority carrier's behavior in the highly doped layers at the silicon surface. S_{eff} is defined by del Alamo [84] as:

$$S_{eff} = -\frac{J_p}{q\Delta n} \tag{3.4}$$

Where J_p is the minority carrier current into the surface or from the lowly doped side to the highly doped side of the high-low junction, if a front- and/or back surface field is applied. Using the following equation:

$$J_p = -J_{0s}\frac{\Delta n(N_D + \Delta n)}{n_i^2} \tag{3.5}$$

Thus S_{eff} can be calculated with:

$$S_{eff} = \frac{J_{0s}(N_D + \Delta n)}{qn_i^2} \tag{3.6}$$

With the known S_{eff} value, the J_{0s} can then be calculated using equation (3.7):

$$J_{0s} = \frac{S_{eff} qn_i^2}{(N_D + \Delta n)} \tag{3.7}$$

In Figure 3-2, the example of the measured lifetime curve over a broad injection level is shown.

3.1.3 Determination of J_{0s} at high injection

Surface saturation current density can be also determined under high injection, i.e. at excess carrier densities higher than around ten times the dopant density [81]. Under high injection, where $\Delta n >> N_D$, the recombination of the diffused surfaces together with Auger recombination in the bulk, described by the Auger lifetime τ_A, limits the effective lifetime. One can analyze the inverse effective lifetime corrected for the Auger recombination limit under high injection with the so called *'slope method'* proposed by Kane and Swanson [85]. The slope of the inverse lifetime is then proportional to $2\times J_{0s}$ according to the equation:

$$\frac{1}{\tau_{eff}} - \frac{1}{\tau_A} = \frac{1}{\tau_{SRH}} + \frac{2J_{0s}}{qn_i^2 W}\Delta n \tag{3.8}$$

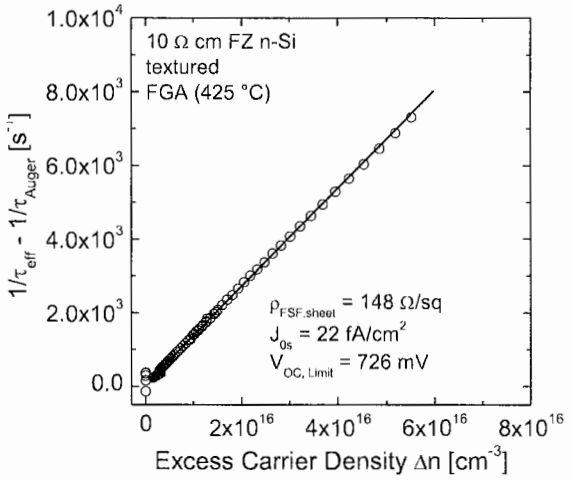


Figure 3-3 Determination of J_{0s} at high injection using the 'slope method'. Example of the determined J_{0s} and $V_{OC,\,Limit}$ for the textured samples with the resistivity of 10 Ω cm and front surface field diffusion of 148 Ω/sq is shown.

The lowly doped, 10 Ω cm samples ($N_D = 4.5\times10^{14}$ cm^{-3}) can be easily measured in high injection using QSSPC equipment. The slope of the inverse lifetime curve at $\Delta n_{hli} = 10\times N_D$ can then be calculated.

An ambipolar Auger coefficient of $C_A = 1.66\times10^{-30}$ cm^{-3}s^{-1} [17] was used for the calculation of the Auger lifetime term ($\tau_A^{-1} = C_A\Delta n^2$). For the determination of the slope of the inverse lifetime curve, a linear fit with measured data points from the range of $\Delta n_{hli} \pm 0.8\times\Delta n_{hli}$ was performed. An example of the determination of J_{0s} for the textured 10 Ω cm test sample under high injection is shown in Figure 3-3.

3.2 Device simulation

3.2.1 Two-dimensional numerical simulation

As shown in Figure 3-4, the structure of the analyzed solar cells is strongly two-dimensional due to the presence of the interdigitated grid of the p- and n-diffusions on the rear cell side. Therefore, for the correct description of the back-contact back-junction solar cell, a two-dimensional modeling and simulations of the device are required.

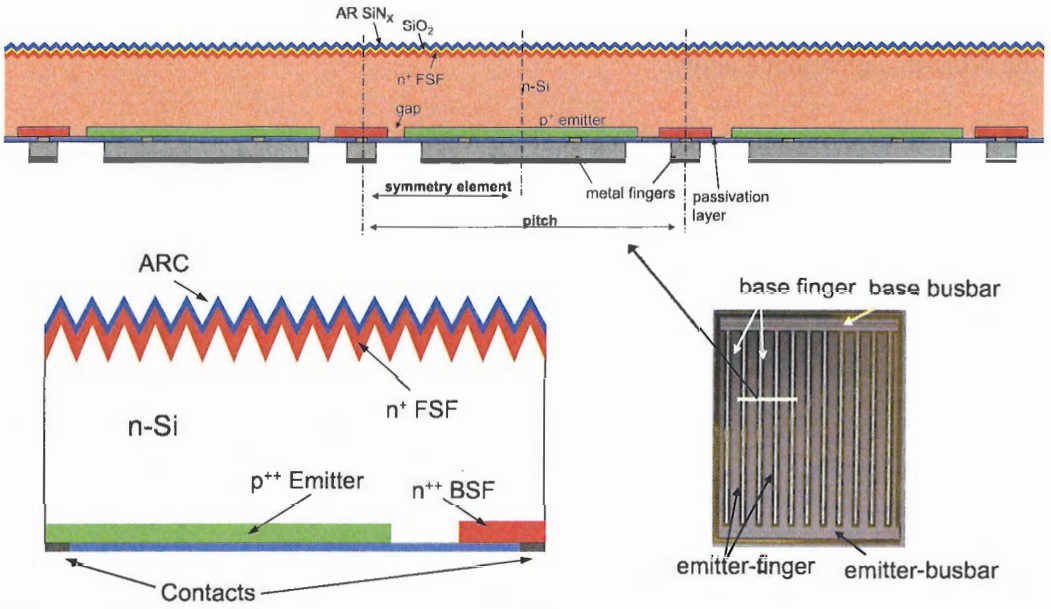


Figure 3-4 Cross-section of the back-contact back-junction silicon solar cell (top). The symmetry element used in two-dimensional simulations (left) as well as a photograph of the rear cell side (right) are shown. The white line in the photograph of the solar cell represents the direction in which the cross-section in the top picture was taken.

The two-dimensional model of the BC-BJ solar cells was developed by Martin Hermle at the Fraunhofer ISE in Freiburg [86]. The simulations of the back-contact back-junction solar cell structure were done by M. Hermle in cooperation with the author of the present thesis.

In two-dimensional simulations, the symmetry element (see Figure 3-4 left) of the solar cell is considered. Different geometry and electrical parameters of the symmetry element are also shown in the diagram. In the simulations, only the active solar cell areas were simulated. The busbar and the edge areas were not taken into account in the simulations presented in this thesis. For the simulation analysis of the influence of the busbars, see the work of M. Hermle [87], [86].

The simulation process starts with the calculation of the generation profile and the optical performance calculations. The simulations of the optical properties of the solar cell are done with the raytracing program *Rayn* [88]. Next, using the program *Mesh* [89], a discretization grid of the symmetry element is created. The semiconductor equations are solved at the nodes of the discretization grid using the *Sentaurus Device* (*SDevice*) [90] program. The whole simulation process is simplified

by the use of the *PVObjects* [91] script in Mathematica, which enables the auditing of the programs mentioned above.

3.2.2 One-dimensional numerical simulation

As previously mentioned, the BC-BJ solar cell has a strongly two-dimensional structure. In many cases, however, simulations using a simplified one-dimensional back-junction solar cell structure (see Figure 3-5) can also describe the effects which occur in the BC-BJ solar cell. The effects which occur in the BC-BJ solar cell and can be well described by the one-dimensional simulation of the back-junction solar cell include:

- Influence of the carrier lifetime on the carrier collection efficiency at the rear junction,
- Influence of the surface concentration and depth of the phosphorus doping profile on the front side (FSF) on the front surface passivation quality.

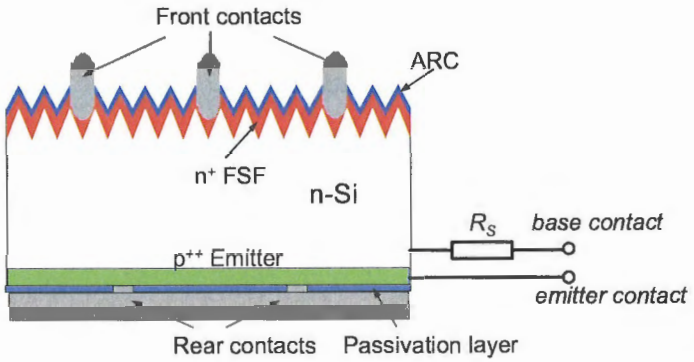


Figure 3-5 Structure of the back-junction cell used in the one-dimensional simulations using device simulation program PC1D [63], [92].

Therefore, the one-dimensional simulations were often applied throughout this thesis. The one-dimensional device simulations were done with the program *PC1D* by Basore and Clugston [63], [92]. The simulations of the optical properties, such as generation profile, reflection, and transmission spectra of the analyzed device were performed using the program *Sunrays* [93]. *Sunrays* is a raytracing program which calculates the generation in the analyzed optical device numerically using the Monte Carlo method.

3.2.3 Simulation parameters

The proper choice of the simulation parameters is essential for a correct simulation. The geometrical parameters as for example thickness and pitch are predefined and thus

easy to access. Most of the electrical parameters as for example doping profiles, bulk lifetime and resistivity have been measured and used for the simulation in this work. Some parameters such as the surface recombination velocity cannot be directly assessed and must be described by models.

The surface recombination velocity S at the doped silicon surfaces depends on the doping profile and the surface dopant concentration. In the one- and two-dimensional device simulations, the highly and lowly doped phosphorus and boron layers with a Gaussian distribution of the impurity concentrations were assumed. For these diffusion profiles with surfaces passivated with thermally grown silicon oxide, the parameterization of Cuevas et al. was taken.

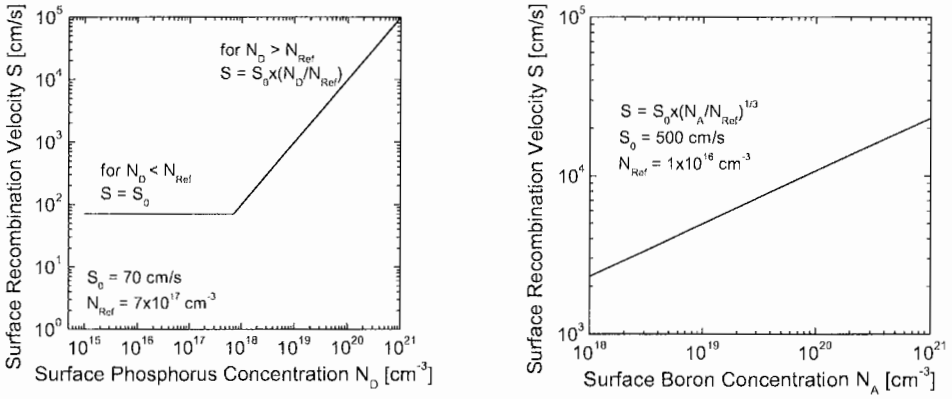


Figure 3-6 Surface recombination velocity as a function of the surface phosphorus (left) and boron (right) concentrations according to parameterization of Cuevas et al. [94], [95].

S for the phosphorus doping according to Ref. [94]:

$$\begin{aligned} S &= S_0 && \text{for } N_D < N_{ref}, \\ S &= S_0(N_D/N_{ref}) && \text{for } N_D \geq N_{ref} \end{aligned} \qquad (3.9)$$

where $S_0 = 70$ cm/s and $N_{ref} = 7\times10^{17}$ cm^{-3}

S for the boron doping according to Ref. [95]:

$$S = S_0(N_A/N_{ref})^{1/3} \qquad (3.10)$$

where $S_0 = 500$ cm/s and $N_{ref} = 1\times10^{16}$ cm^{-3}

In the left side of Figure 3-6, the surface recombination velocity of the phosphorus doped silicon surfaces and its parameterization according to [94] is shown. The surface recombination velocity dependence with the boron surface concentration and its parameterization according to [95] is shown in the right side of Figure 3-6.

3.3 Measurement table for laboratory size solar cell

Since both p- and n-electrodes of the analyzed solar cell are placed on the rear cell side, the application of the standard measurement table for the electrical characterization of the back-contact solar cells is not possible. A new measurement setup for the laboratory scale BC-BJ cells with an area of 4 cm^2 was developed by the author in the course of this work.

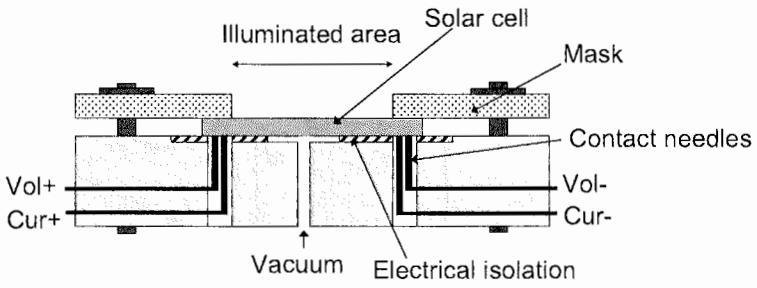


Figure 3-7 Schematic representation of the measurement table for measurement of the back-contact back-junction silicon solar cells.

A schematic drawing of the measurement table developed in this work at Fraunhofer ISE is shown in Figure 3-7. A solar cell is placed on an electrically insulating layer, in order to avoid shunting of the p- and n-electrodes. The finished solar cells are larger than the illuminated area, making it therefore possible to mechanically fix the position of the measured cell with a mask with an illumination area opening of 2×2 cm^2. The contact needles for separate measurement of the current and voltage are placed on the cell busbars from the rear side, through the holes in the measurement table. A three-dimensional AutoCAD design and a photograph of the measurement table developed in this work at Fraunhofer ISE are shown in Figure 3-8.

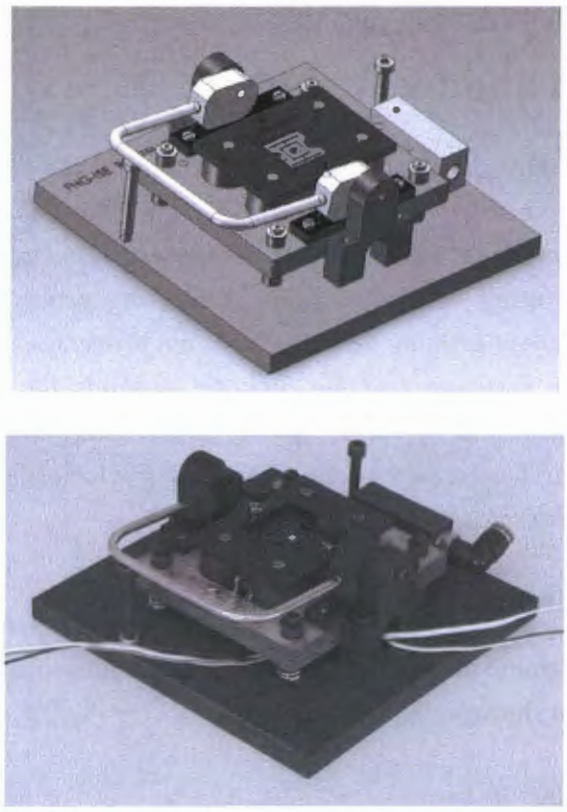


Figure 3-8 Measurement table for measurement of the illuminated and dark current-voltage characteristics of the laboratory size ($2\times2\ cm^2$) back-contact back-junction silicon solar cells. AutoCAD design is shown in top graphic and in the bottom graphic a photograph of the finished measurement table is shown.

4 Design and technology

In this chapter the structure and technology of the developed back-contact back-junction silicon solar cell is presented. The minority carrier lifetime of the applied n-type Si material is determined. The solar cell structure was fabricated using newly developed structuring processes, which are using low-cost screen-printing and laser ablation processes. The applied processes are briefly reviewed and the different methods for the formation of the interdigitated grid of the n- and p- metal grids are described in detail. Finally, the best results of the developed small, laboratory size and large, industry size solar cell are presented.

4.1 Device structure

A schematic cross-section of the back-contact back-junction solar cell developed in the frame of this work is shown in Figure 4-1.

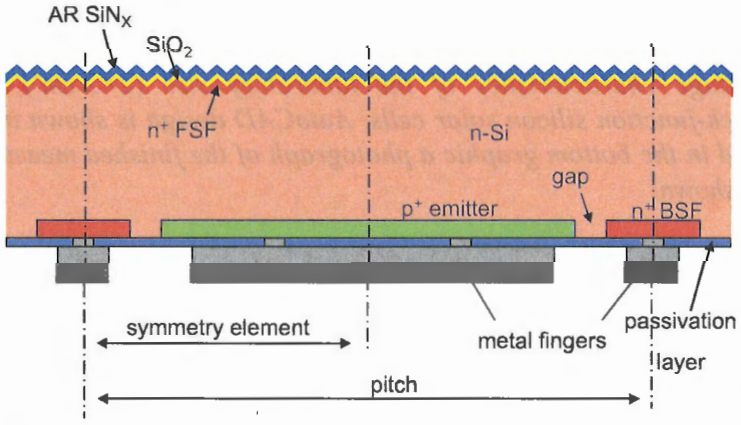


Figure 4-1 Schematic cross-section of the n-type high-efficiency back-contact back-junction silicon solar cell developed in the frame of this thesis (sketch is not to scale). Pitch and symmetry element are shown.

The cells were fabricated from n-type float-zone (FZ) silicon wafers. The thickness of the finished solar cells was about 160 µm. Specific base resistivities of 1 and 8 Ω cm were chosen. The chosen specific base resistance range is believed to be an optimum between two effects: maximization of the carrier lifetime in bulk and reduction of the series resistance losses introduced by the base material. On one hand, the carrier lifetime, which needs to be high in order to enable good collection of the minority

carriers at the rear junction, decreases with increased base doping level and reduced specific base resistance of the base material. On the other hand, the high specific base resistivity results in increased series resistance in the base material, which leads to significant efficiency losses. Details of the silicon material chosen and its characterization are presented in the next section.

The front side is textured with random pyramids and passivated with a lightly doped ($N_{peak} = 5\times10^{18}$ cm^{-3}) and deeply diffused (1.4 µm) phosphorus front surface field (FSF). The sheet resistance of the FSF (ρ_{FSF}) equals 148 Ω/sq. The diffusion profile of the FSF was optimized to achieve an optimum front side passivation quality. The presence of the phosphorus doped front surface field (FSF) is one of the key features of the developed device design. Therefore, a comprehensive analysis of the positive effects of the FSF in the BC-BJ solar cells was performed in the frame of this thesis. The presence of the FSF reduces the concentration of the minority carriers at the physical semiconductor surface and thus improves the front surface passivation (chapter 7) and strongly improves the stability of the front surface passivation under UV-light exposure (section 7.5). Furthermore, the FSF enhances the lateral majority carriers current transport and thus reduces the series resistance losses (chapter 8). Finally, the solar cells with the FSF show a linear current response at low-illumination levels, in contrast to cells without the FSF (chapter 9).

The front surface passivation is further improved by a thin thermally grown silicon dioxide layer. Finally a silicon nitride (SiN_x) antireflection (AR) layer is deposited on top of the oxide layer by means of plasma enhanced chemical vapour deposition (PECVD). Passivation properties of the applied front surface field doping profile and the stack system of the SiO_2 and SiN_X layers is investigated in section 7.3

On the cell rear side an interdigitated grid of the p- and n-diffusion areas is formed. Both emitter p^+ and back surface field n^+ diffusions are separated by an undiffused gap. The rear metallization structure also forms an interdigitated grid, as shown in Figure 4-2. The rear cell surface is passivated with silicon oxide. Metal fingers are contacted to the diffused regions via local openings in the passivation layer.

For masking steps on the rear side, such as:

- definition of boron doped emitter area,
- definition of phosphorus doped back-surface-field diffusion area,
- formation of local openings in the dielectric layer for the metal-semiconductor contacts,
- and formation of the interdigitated metal fingers grid,

only industry-relevant screen-printing and laser processes were applied. No photolithography masking steps were introduced to the processing sequence of the investigated cell structure. Due to the fact that more than one masking step was required, and the limited resolution and positioning accuracy of the applied structuring technology, the pitch of the processed cells was chosen to be in the range of 1.3 to 3.5 mm.

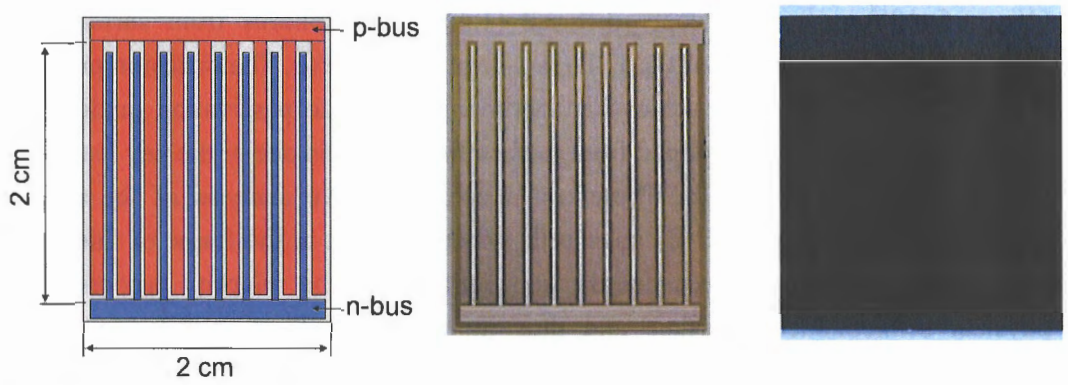


Figure 4-2 Interdigitated grid of the p- and n-metallization fingers of the back-contact back-junction Si solar cell developed in the course of this thesis. The interdigitated grid is schematically shown in the left picture and in the middle the photograph of the rear side of the actual solar cell is shown. In the right a photograph of the cell front side is shown.

Shunting between the tight p- and n-metal finger grids was avoided by a careful design of the metallization process, which is presented in section 4.4.1. The metallization is performed in a two-step process. First, a thin metal layer is deposited and structured to form an interdigitated grid. Secondly, this thin seed metal layer is thickened using an industrially feasible plating process. At the same time the series resistance losses, mainly caused by the lateral carrier transport due to large pitch, could be minimized by application of the high conductivity FSF.

Prior to measurements, the cells were annealed in a forming gas atmosphere and removed from the host wafer by the means of laser cutting. A distance of 500 μm from active cell area was chosen. This distance should allow for strong reduction of the edge recombination losses [96].

4.2 n-type bulk Si material

As previously shown in chapter 2, in order to realize high-efficiency cells using the back- junction cell structure, high minority carrier diffusion lengths are required. The carriers, most of which are generated near the front surface, need to diffuse through the

entire cell thickness in order to be collected by the back-junction. According to the simulations presented in section 2.3, the required diffusion length of the minority carriers should be at least four times larger than the wafer thickness in the back-junction cell type to enable high carrier collection efficiency. Thus, for a solar cell with a thickness of 160 μm, a diffusion length of the minority carriers of at least 640 μm is required.

Phosphorus doped n-type silicon has received increased interest in the PV research community in recent years, due to shortage of the p-type silicon feedstock and due to its high minority carrier lifetime. In many research laboratories front-junction and back-junction silicon solar cells on n-type substrates are being developed.

For example, a front-junction solar cell structure with monocrystalline FZ n-type Si with boron diffused emitter passivated using Al_2O_3 passivation layer developed by Benick et al. achieved an efficiency of 23.2 % [97]. A front-junction cell with oxide passivated boron emitter also developed by Benick et al. achieved an efficiency of 20.4 % [98]. On large area cells of 156×156 mm^2, screen-printed Cz n-type Si, the efficiency of 17.9 % was obtained by Mihailetchi et al. [99]. The application of multicrystalline n-type Si to solar cell processing is also being studied intensivley (see for example the work of Libal et al. [100], Tool et al. [101], and Cuevas et al. [102]). The application of n-type Si to the back-junction cell structure has also been investigated. Zhao et al. demonstrated an efficiency of 22.7 % for FZ n-type Si [103]. Schmiga et al. presented a rear-junction solar with aluminum emitter with an efficiency of 20.1 % [104].

Moreover, in the industry, the highest commercially available solar cells are produced on n-type Si substrates. SunPower Corp. produces back-contact back-junction n-type Si solar cells with efficiencies up to 22.7 % [3]. Sanyo Electric manufactures heterojunction solar cells on n-type c-Si with efficiency of 19.5 % [105].

The advantages of n-type Si when compared to p-type Si are as follows:

- The minority carrier lifetime in p-type boron-doped oxygen-contaminated silicon is strongly reduced under illumination or carrier injection [106], [107], [108]. Due to the lack of boron in n-type Si, no degradation occurs.
- n-type Si has a lower sensitivity to the prominent impurities (e.g. interstitial iron Fe_i,) [109], [110].This is due to strong asymmetry in capture cross section for electron and holes ($\sigma_n >> \sigma_p$).

- For reasons mentioned above, the lifetime of the minority carriers in n-type Si is higher than in the case of p-type Si. For example, extremely high minority carrier lifetime in the range of milliseconds was already reported for n-type multicrystalline silicon by Cuevas et al. [111].

4.2.1 Minority carrier diffusion length

For the determination of the minority carrier lifetime and diffusion length of the n-type FZ Si chosen for processing of the BC-BJ solar cells, lifetime samples were prepared and measured. Planar symmetrical n^+nn^+ test structures are shown in Figure 4-3. Both sides of these samples exhibit a full area shallow n^+ diffusion (ρ_{sheet} = 148 Ω/sq., N_{peak}=5×10^{18} cm^{-3}, depth 1.4 µm) and a full area thermal oxide with thickness of 105 nm. Before the measurements all samples were annealed at forming gas atmosphere (FGA) at the temperature of 425°C (15 min.).

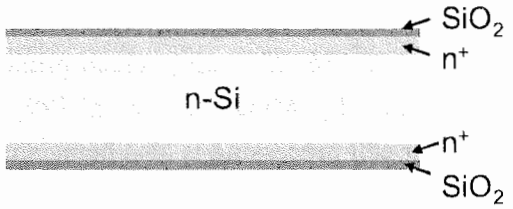


Figure 4-3 n^+nn^+ symmetrical test structures for the measurements of the minority carrier lifetime and diffusion length.

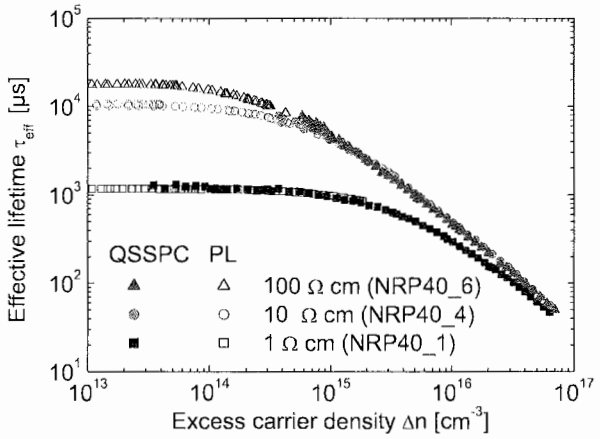


Figure 4-4 Injection-dependent minority carrier lifetime of the planar n^+nn^+ symmetrical samples on FZ n-type Si wafers with different resistivity. The effective carrier lifetime was measured in a wide excess carrier density range using quasi-steady-state photo-conductance (closed symbols) and photoluminescence (open symbols) methods.

The lifetime of all samples was measured in a wide injection density range using two measurement methods. With the quasi-steady–state photo-conductance (QSSPC) method [75], the lifetime was measured in the middle to high injection using the WTC-120 lifetime tester from Sinton Consulting [73]. In the low injection range, the lifetime was measured with the photoluminescence (PL) method [112]. The lifetime results are shown in the Figure 4-4. A good agreement between both measurement methods can be observed.

Table 4-1 *Effective minority carriers lifetime and diffusion length for n-type FZ Si with the specified base resistivity of 1, 10 and 100 Ω cm. Lifetime was measured at injection level of $\Delta n = 1 \times 10^{14}$ cm^{-3}.*

Cell no.	ρ_{base} [Ω cm]	τ_{eff} [ms]	L_{eff} [μm]
NRP40_6	100	18.3	4710
NRP40_4	10	10.1	3492
NRP40_1	1	1.2	1175

Extremely high effective lifetime values of up to 18 ms have been measured for the 100 Ω cm n-type FZ Si at an injection level of $\Delta n = 1 \times 10^{14}$ cm^{-3}. As shown in Table 4-1, the lifetime is high enough to realize perfect carrier collection by the back junction for all three investigated resistivities of 1, 10 and 100 Ω cm. Note that actual base resistivities may vary in the range of ± 20 % from the specified resistivity. Even the 1 Ω cm material exhibits lifetime values above 1 ms, resulting in an effective diffusion length (L_{eff}) of about 1200 μm, which is more than 4 times the cell thickness.

4.2.2 Influence of the surface potential on the minority carrier lifetime

In the previous section the analysis of the lifetime samples with diffused FSF and SiO_2 passivation layer was presented. However, as explained in section 3.1, the measured effective lifetime of the minority carriers is not only influenced by the bulk lifetime, but also by the quality of the surface passivation. Therefore, in order to determine the real minority carrier lifetime in the bulk of investigated n-type FZ Si, the effects of the surface recombination should not be taken into account. A significant reduction of the surface recombination can be obtained through application of the field-effect passivation using corona charging [113]. This approach is presented in the following.

Symmetrical n-type lifetime samples with resistivities of 1, 3.5 and 10 Ω cm with both surfaces passivated by a 105 nm thick thermal SiO_2 (shown in Figure 4-5) were processed and annealed at forming gas atmosphere (FGA) at the temperature fo 425°C (15 min.). The effective lifetime of the minorrity carriers was measured using quasi-steady–state photo-conductance (QSSPC) and the results are shown in Figure 4-6. In this measurement no additional corona charging was applied.

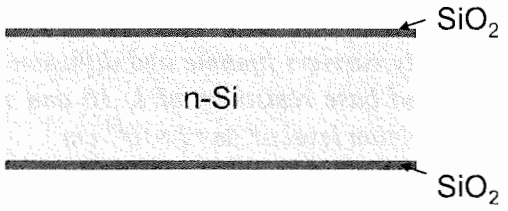


Figure 4-5 FZ n-type symmetrical test structures with thermally grown silicon dioxide passivation layer for the measurements of the minority carrier lifetime.

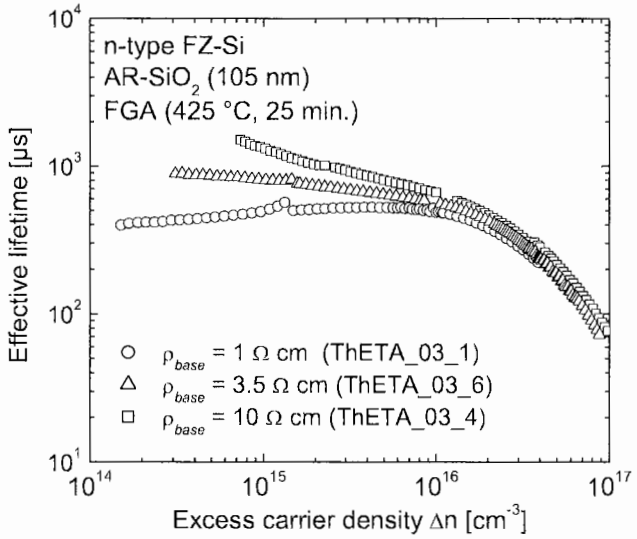


Figure 4-6 Injection-dependent minority carrier lifetime of the planar symmetrical samples on FZ n-type Si wafers with different resistivity. In this measurement no corona charging was applied.

The application of the fixed charges on top of the passivation layer strongly influences lifetime. A charge density in the range between -3×10^{12} cm^{-2} and 3×10^{12} cm^{-2} was applied on both sides of the tested samples using a corona charger. The applied charge density corresponds to a surface potential in the range of -15 V to 15 V. The resulting

voltage was measured using the Kelvin Probe technique. The results of the effective lifetime and the surface saturation current density of the tested samples in the wide range of applied charge density are shown in Figure 4-7. The surface saturation current density was determined under low injection using the method presented in section 3.1.2.

The application of the high positive surface potential of 15 V results in the highest τ_{eff} for all three samples analyzed. At the same time, the surface saturation current density is minimal for this surface potential. This is caused by the field-effect passivation of the applied surface potential. The positive charges which are present at the surface repel the positive charge carriers from the surface of the samples. Due to the depletion of the minority carrier concentration at the physical surface, the surface recombination is decreased and does not limit the effective lifetime. Therefore, the measured effective lifetime of the minority carriers is very close to the bulk lifetime.

On the other hand, the application of the negative charges on the surface of the tested samples also leads to an increase of the effective lifetime. However, the maximum lifetime when negative charges are applied is lower than in the case of the positive charges. A strong negative charge induces an accumulation of holes under the surface. Since the capture cross section of holes σ_p of the surface recombination is much smaller than the capture cross section for electrons σ_n, an accumulation of holes is not as effective as accumulation electrons to suppress surface recombination. The lifetime of the tested samples is summarized in Table 4-2.

Table 4-2 Effective minority carriers lifetime and diffusion length for n-type FZ Si with base resistivity of 1, 3.5 and 10 Ωcm for different surface charge density. Lifetime was measured under low injection at $\Delta n = 5 \times 10^{14}$ cm^{-3}.

		Surface charge density [cm^{-2}]					
		0		3×10^{12}		-3×10^{12}	
Cell name	ρ_{base}	τ_{eff}	L_{eff}	τ_{eff}	L_{eff}	τ_{eff}	L_{eff}
	[Ω cm]	[ms]	[μm]	[ms]	[μm]	[ms]	[μm]
ThETA03_1	1	0.4	682	5.1	2440	0.9	1020
ThETA03_5	3.5	0.8	980	8.3	3150	2.3	1660
ThETA03_3	10	1.7	1430	10.0	3470	3.1	1940

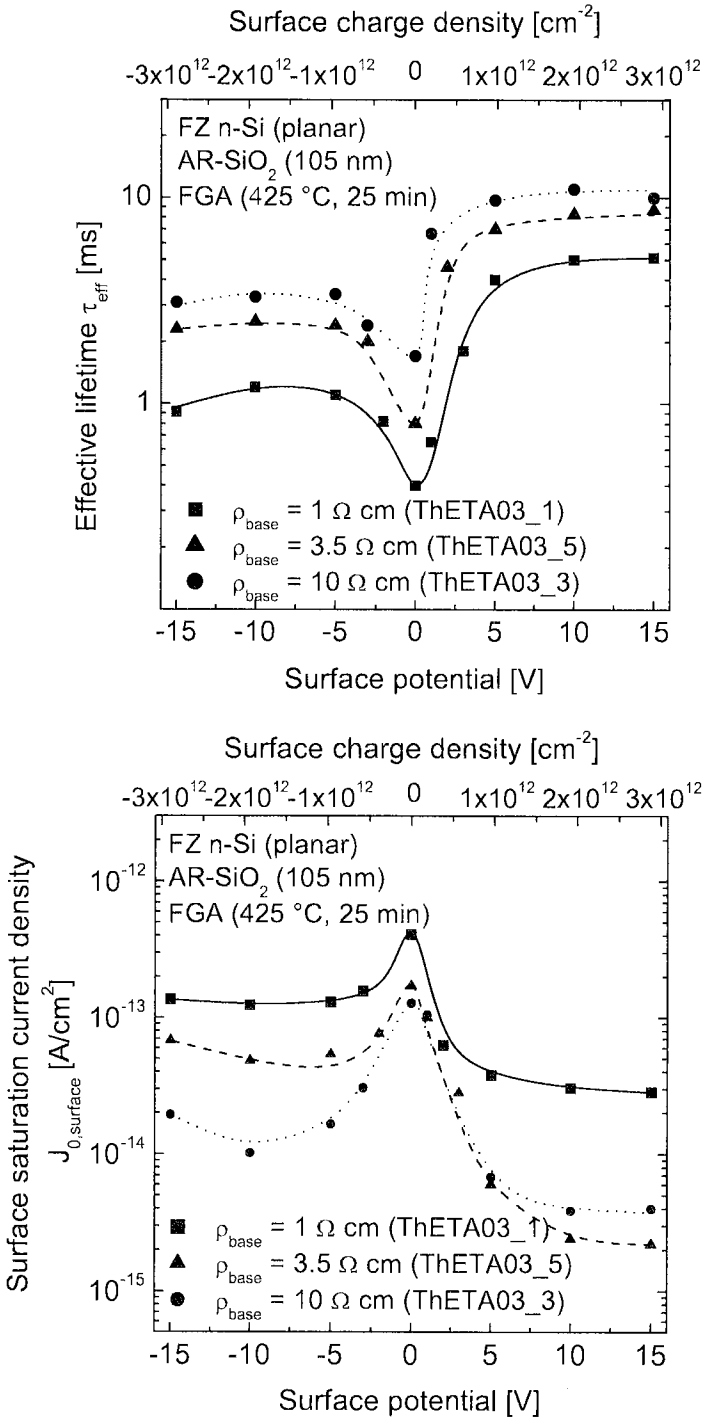


Figure 4-7 Effective lifetime of the minority carriers (top) and the surface saturation current density (bottom) of n-type FZ Si lifetime samples measured in a wide range of surface potential and surface charge density at the outer oxide surface for base resistivity of 1, 3.5 and 100 Ωcm. Lifetime was measured under low injection at $\Delta n = 5 \times 10^{14}$ cm^{-3}. Lines are guides-to-the-eye.

For the lowest surface recombination current density at the surface charge density of 3×10^{12} cm^{-2}, the effective diffusion length of the minority carriers is in the range of 2.4 to 3.5 mm for the tested n-type FZ Si. Thus, the selected Si material is of very high quality and perfectly suited for processing of high-efficiency back-junction solar cells.

4.3 Processing technology

After the selection of the silicon material, next the processing technology to form the solar cell structure, as shown in Figure 4-1 and Figure 4-2, can be to be optimized. The work of the author in the field of development of the processing technology and the sequence of the processing steps was performed in the framework of the research project *Quebec* [41] with the solar cell manufacturing company Q-Cells AG and the Institut für Solarenergieforschung Hameln (ISFH). In the present section the family of processes applied in the processing sequence of the developed back-contact back-junction solar cell is presented. The technology critical to the interdigitated solar cell structure, namely the metallization technology, is presented in more detail in the following section.

Cleaning

In the processing of the high-efficiency solar cells, much attention needs to be given to the cleaning of the processed samples. The introduction of contaminated samples into the high temperature diffusion or oxidation process would be fatal to the sample lifetime. Therefore, the so-called RCA Cleaning [114] procedure was applied. In the first step, the organic impurities and the metals are removed from the silicon surface by wet chemical oxidation in a solution of ammonium hydroxide (NH_4OH) and hydrogen peroxide (H_2O_2). Next, the formed oxide is removed in a diluted hydrofluoric acid (HF) in the so-called HF-Dip. In the second wet oxidation step, in the hydrochloric acid (HCl) and hydrogen peroxide solution, the alkali ions are removed. Again, the formed oxide is removed in a diluted hydrofluoric acid. The samples are rinsed with de-ionized (Di) water after each cleaning step.

Thermal oxidation

The role of the thermal silicon dioxide (SiO_2) layer is to:

a) reduce the surface recombination by passivation of the silicon surface, and

b) form a masking layer for the subsequent local diffusion or contact opening steps.

The typical applied oxidation temperature is 1050°C and the thickness of the applied oxide was around 200 nm for the masking oxide. In the case of the passivation oxide on the front cell side, the thickness was 10 nm and the oxidation temperature was only 850°C.

Phosphorus and boron diffusion

In the processing sequence of the analyzed high-efficiency BC-BJ solar cells, three diffusions in a quartz tube furnace are applied:

a) Formation of the boron emitter from the liquid BBr_3

b) Formation of the phosphorus back-surface field (BSF) from the gaseous $POCl_3$. From the $POCl_3$ in the atmosphere of oxygen O_2 and nitrogen N_2, a phosphorus silicate glass (PSG) is formed on the wafer surface. The phosphorus silicate glass functions as a source of phosphorus during the high temperature diffusion.

c) Formation of the low phosphorus doped front-surface field (FSF) from the gaseous $POCl_3$. A detailed analysis of the applied FSF diffusion profiles is presented in chapter 7.

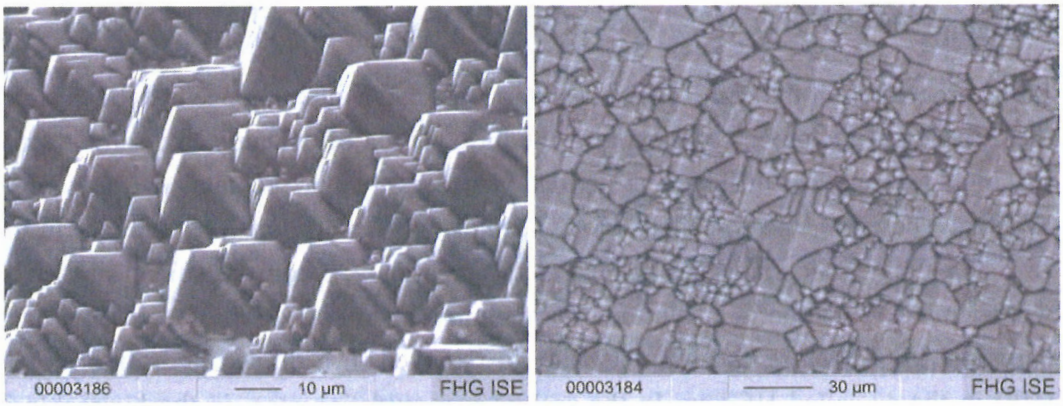


Figure 4-8 Scanning electron microscope (SEM) micrographs of the silicon surface with random pyramids texture with (111)-crystal planes. Side view (left) and top view (right) are shown.

Texture

In order to reduce the optical reflection losses of the solar cells, the front surface is textured. Due to the textured surface, the incident light that is reflected from the wafer surface has an increased chance to be absorbed by hitting the wafer surface again. To form the texture in the case of the monocrystalline silicon, the so called random pyramid texture was applied. In a low concentrated KOH solution, different crystal

planes in silicon are etched at different rates [115]. This way, the structure of the randomly distributed pyramids with different sizes is formed as shown in Figure 4-8.

Deposition of silicon nitride

An antireflection silicon nitride (SiN_X) layer with a thickness of 70 nm is deposited on the front cell side in order to further decrease the reflection losses and increase the front surface passivation quality [116], [117]. The nitride layer is deposited by means of a plasma enhanced chemical vapor deposition (PECVD) process at the temperatures around 400°C [118].

Formation of the interdigitated grid of the emitter and BSF diffusions

As already shown in Figure 4-1 and Figure 4-2, the emitter and BSF diffusions on the rear cell side form an interdigitated grid. In the solar cells, the local diffusions were performed through a masking oxide layer. For the structuring of the masking oxide only industry-relevant technology, such as screen-printing and laser ablation, were applied.

In Figure 4-9 an example of the processing sequence to create local emitter/BSF diffusion by means of laser ablation is shown. First, the whole rear surface is oxidized. Local openings in the oxide layer are then formed by local laser ablation of oxide and a thin silicon layer. Subsequently, the damage induced by the laser into the silicon crystal lattice is etched back in the KOH solution. Finally the emitter/BSF diffusion is performed. The oxide layer acts as a diffusion barrier.

In Figure 4-10 an example of the processing sequence to create local emitter/BSF diffusion by means of screen printing of the etch barrier (etch resist) is shown. First the whole rear surface is oxidized (1). Then the etch resist layer is screen-printed on the wafer surface (2). The openings in etch resist layer correspond to the places where the emitter/BSF diffusion should take place. In the next step (3), the oxide surface which was not covered with etch resist is etched in a diluted HF solution. Next (4), the etch resist layer is removed wet-chemically. Finally (5) the emitter/BSF diffusion is performed. In the developed process first the boron emitter diffusion in performed locally. Next the local phosphorus BSF diffusion is performed.

Due to the limited positioning accuracy and resolution of the applied structuring technology, the pitch of the finished solar cells was in the range of 1.3 to 3.5 mm. The pitch of concentrator solar cells processed with the use of photolithography can be as low as 50 μm [119]. Thus, the application of the low cost structuring technology

results in an increase in pitch by a factor of around 40. The impact of the pitch on solar cell performance is studied in chapters 6 and 8.

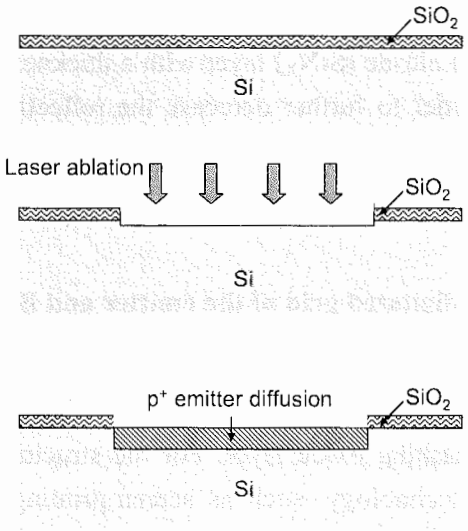


Figure 4-9 Processing sequence for the creation of the local emitter or BSF diffusions using the laser ablation of the silicon oxide layer. In the figure, the rear side of the cell is on top. The front side structure is not shown for simplification. The pictures are not to scale.

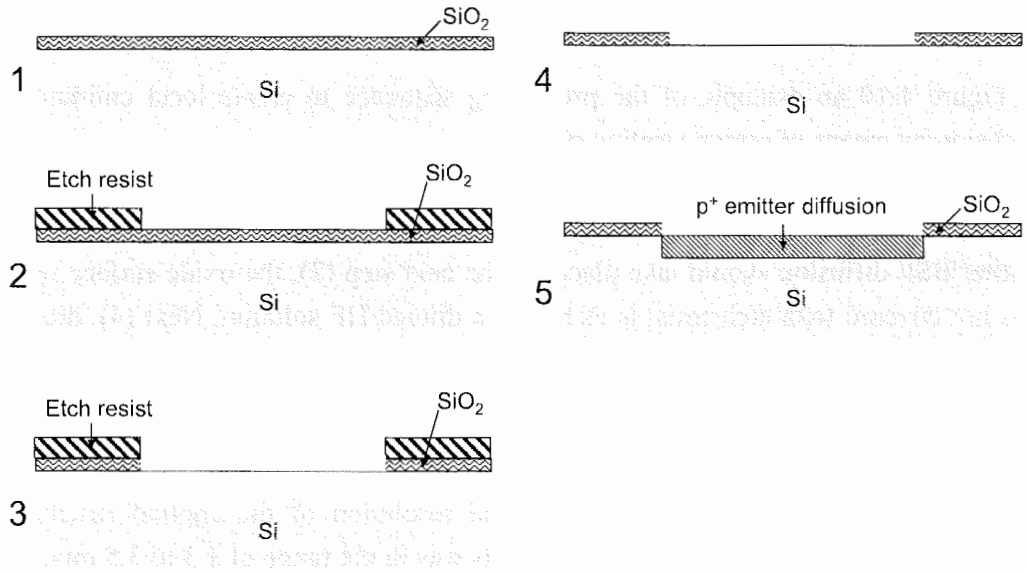


Figure 4-10 Processing sequence for the creation of the local emitter or BSF diffusions using the screen-printing of the masking layers. In the figure, the rear side of the cell is on top. The front side structure is not shown for simplification. The pictures are not to scale.

Formation of the contact openings

The surface recombination velocity of the metal contact to the intrinsic silicon is extremely high in the range of 10^6 cm/s [120] to 10^7 cm/s [121]. However, the surface recombination velocity at the metal contacts can be effectively reduced by the application of highly doped n^{++} or p^{++} silicon regions in the areas of the metal-semiconductor contacts [85]. The size and pitch of the local openings in the dielectric layer on the rear cell side through which the metal-semiconductor contacts are formed, and the diffusion profiles of the emitter and BSF diffusions, need to be carefully optimized [122], [123] in order to minimize the contact-semiconductor recombination losses and the contact resistance losses [124].

The openings of the metal-semiconductor contacts are formed in the same way as already shown in Figure 4-9 and Figure 4-10. Both screen-printing of the etch resist layer and a direct ablation of the dielectric layers were developed and applied in the processing sequence of the solar cells analyzed. The laser ablation of the dielectric layers was intensively investigated by Grohe [125]. Photographs of the rear side cell structure after emitter and BSF diffusions and after the formation of the contact openings in the rear side dielectric layer are shown in Figure 4-11.

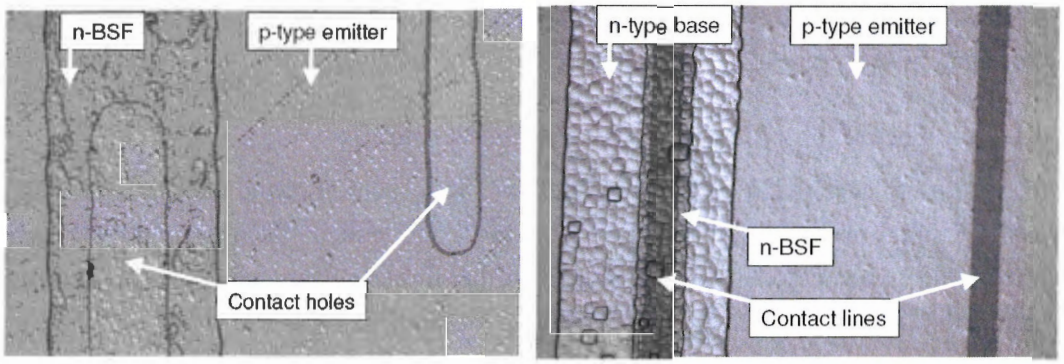


Figure 4-11 Photographs showing details of the rear side pattern prior to solar cell metallization. The emitter and BSF diffusions, as well as the contact openings are marked. The patterns were defined by (left) screen printing and (right) laser processing. For both images the same scaling is used.

4.4 Metallization

In this section the process to form an interdigitated grid of p and n metal electrodes is presented. A two-step metallization scheme was developed and successfully applied to the processing of the BC-BJ solar cells structure. In the first step a thin seed metal

layer is deposited and structured to form an interdigitated grid. In the second step the thin seed metal layer is thickened using an industrially feasible plating process.

The seed metal layer is deposited on the full rear side by the means of a vacuum evaporation process. The seed metal layer consists of a stack of aluminum and silver layers with a total thickness of less than 500 nm. The aluminum layer, which is in direct contact with the silicon wafer, enables formation of good ohmic contact to both the highly doped p-emitter and highly doped n-BSF at the same time [124], [126]. Moreover, the aluminum layer, together with the rear side passivation dielectric layer forms a very effective rear side reflector, enhancing the internal light trapping. The second layer, which is evaporated on top of the Al layer during one evaporation process, is the thin silver layer. Silver acts as a seed layer for the following silver plating process, in which the line resistance will be reduced. Moreover silver enables direct soldering on the finished cell during the solar module assembly.

After deposition of the seed metal layers on the entire rear cell surface, the interdigitated grid of non-shunted p and n-metal grids needs to be formed. Different techniques for the formation of the interdigitated metal gird are presented in section 4.4.1. Next, the thin seed metal layer needs to be thickened, in order to increase the conductivity of the metal fingers. This is accomplished by means of the plating process. The analysis of the required thickness of the finished metallization grid is presented in section 4.4.2.

4.4.1 Formation of the interdigitated metal grid

In the present section different techniques for the formation of the interdigitated metal grid, which are based on the two-step approach called 'seed and growth', are presented. Two methods were developed in the course of this work and successfully applied to the processing of solar cells. These methods are:

- Local etching of the metal layer defined by screen-printed masks
- Lift-off approach and laser-enhanced lift-off using screen-printed masks

Other interesting techniques, which are based on deposition of the thin seed metal layers and thickening them using a plating process, are presented for reference. In all presented methods both p- and n-diffusions, as well as the local contact openings, are already present on the solar cell. Thus, only the formation of the interdigitated metal grid is presented.

Self-aligned metal grid formation on steps in Si surface

A self-aligned technique to separate p- and n-contact grids after full area metal deposition was introduced by Sinton et al. in 1988 [18]. The method is schematically presented in Figure 4-12. In this method, on the rear side of the solar cell the emitter and base areas are placed on different levels on the Si surface, i.e. there is a wafer thickness difference of 5 to around 20 µm between the emitter and base areas, which was created by the local KOH etching.

After the formation of the contact openings, a full area deposition of the metal layer (e.g. Al) with a thickness of few to several tens of micrometers is performed. Next a thin (e.g. 50 nm) layer of the etch barrier (such as Ti or PECVD SiO_2) is deposited on top of the metal layer. Due to steep slopes between emitter and base regions, the thin etch barrier material is thinner and even discontinuous at the slopes. This feature is used in the following etch step, in which the aluminum layer is etched at the slopes where the etch barrier is discontinuous, e.g. in diluted HCl solution. In this manner, no alignment is required for this method. However, the solar cell structure must feature the above mentioned thickness variation structure. The self-aligned method of slopes in the Si surface was also successfully applied by Engelhart in the processing sequence of the RISE solar cell [40].

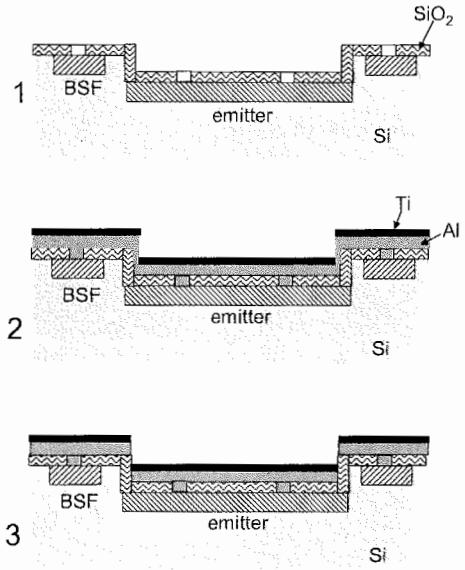


Figure 4-12 Method formation of the interdigitated p-n metal grid using the self aligned process on the high steps in the silicon surface. The method was introduced by Sinton et al. [18]. The front side structure is not shown for simplification. The drawings are not to scale.

Laser ablation of the masking layer and etching of the bulk metal

A contact separation method using a laser ablation of the thin etch barrier was recently introduced by Teppe et al. [127]. This method is schematically shown in Figure 4-13. First a full area metal deposition by means of evaporation or sputtering is applied. Secondly, a thin layer of the etch barrier (here again, a thin PECVD SiO_2 layer can be used for example) is deposited on top of the metal layer. In the next step, the etch barrier and a thin layer of the underlying metal layer is locally removed by means of laser ablation. Finally the metal layer is locally etched back, and the etch barrier is removed.

The advantage of this method is the formation of very thin separation lines between metal fingers, which enables the realization of high metal coverage on the rear cell side, which is needed for good reflection characteristics. Additionally, the application of a thick metal layer below the thin etch barrier removes the risk of introduction of laser damage to the solar cell structure, because all of the laser power will be absorbed in the etch barrier and in the top surface of the metal layer. An example of separation lines created between the metal fingers is shown in Figure 4-14.

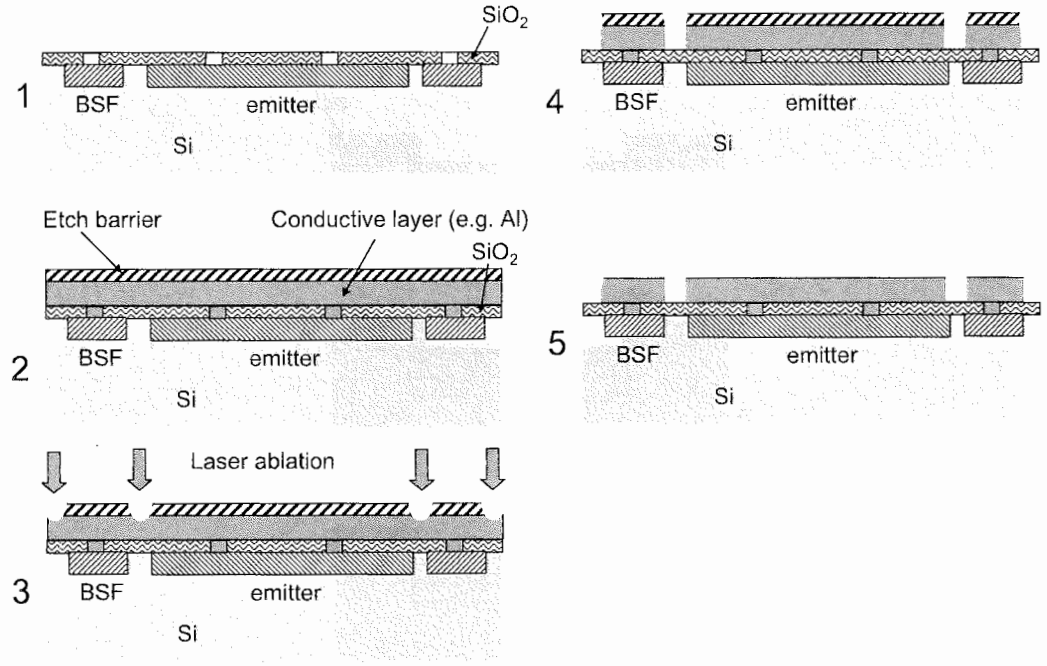


Figure 4-13 Method for contact separation using local laser ablation of an etch barrier and etching of the conductive layer. Method is patented by Teppe et al. [127]. The front side structure is not shown for simplification. The drawings are not to scale.



Figure 4-14 Example of a successfully separated p- and n-metal grid using laser ablation of the masking layer and local wet chemical etching of the Al layer. The size of the opening between the metal fingers is around 50 µm. Photograph taken with an optical microscope.

Process patented by Sunpower Corp.

A method which uses a local application of the screen-printed or inkjet plating resist layer is shown in Figure 4-15.

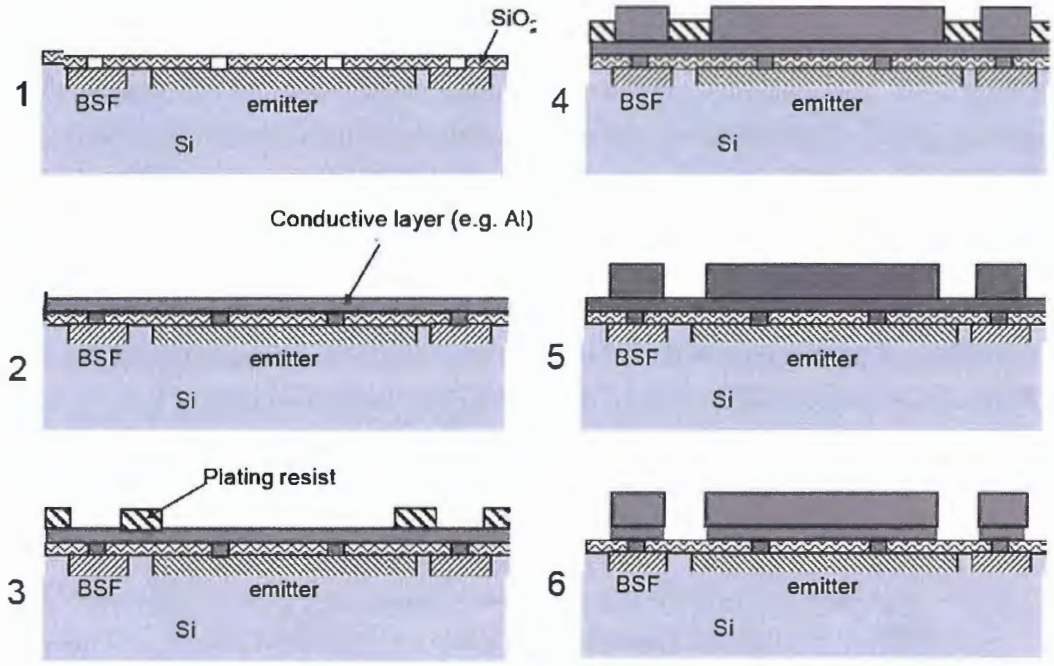


Figure 4-15 Method for contact separation using application of the screen-printed or inkjet plating resist. Method is patented by Mulligan et al. from Sunpower Corp. The front side structure is not shown for simplification. The drawings are not to scale.

This method is patented by Mulligan et al. [128] of Sunpower Co. After deposition of a thin seed metal layer, the plating resist is applied on top of the metal layer locally in the locations where the separation between the metal fingers is required. Next, the rear side metal layer is thickened in the electroplating process using Ag or Cu plating baths. The locations covered with the plating resist remain thin after the electroplating process. Next, the plating resist layer is stripped. Now, using the wet chemical etching, the thin metal layer between the thick plated metal fingers can be etched away. Since the seed metal layer is typically thinner than 1 μm, only a very small percentage of the plated metal will be etched away.

The advantage of this process is the elimination of the shunting risk through the formation of metal bridges between p- and n-electrodes during the plating process. On the other hand, if more than one metal is applied in the seed layer, as can be the case in copper plating, then multiple selective etching steps are required, which may increase the complexity of the process.

Local etching of the metal layer through the screen-printed masks (this work)

Another method which uses the screen-printed or inkjet masking layers is presented in Figure 4-16. This method, using screen-printing of the etch barriers, was developed and successfully applied during solar cell processing in the course of this thesis. After the deposition of the thin (less than 1 μm) seed metal layer (Al and Ag), the etch barrier is screen-printed locally on top of the metal layer in the locations where the metal fingers are needed. Next, the local wet chemical etching of the Ag layer is done in diluted HNO_3. In the following step the Al layer is etched back in diluted HCl (see Table 4-3). After etching the metal layer, the etch barrier is stripped and the thin metal fingers are thickened to the required thickness using the Ag plating process.

Table 4-3 Process parameters for the selective etching of the aluminum (thickness of 300 nm) and silver (thickness of 100 nm) seed metal layers, used in the formation of the interdigitated p- and n-metal grids.

Etched metal	Etching Solution	Ratio	Temperature	Time
silver	HNO_3 (69 %) : H_20	1 : 1	room T	30 sec
aluminum	HCl (32 %) : H_20	1.4 : 1	room T	2 to 10 min.

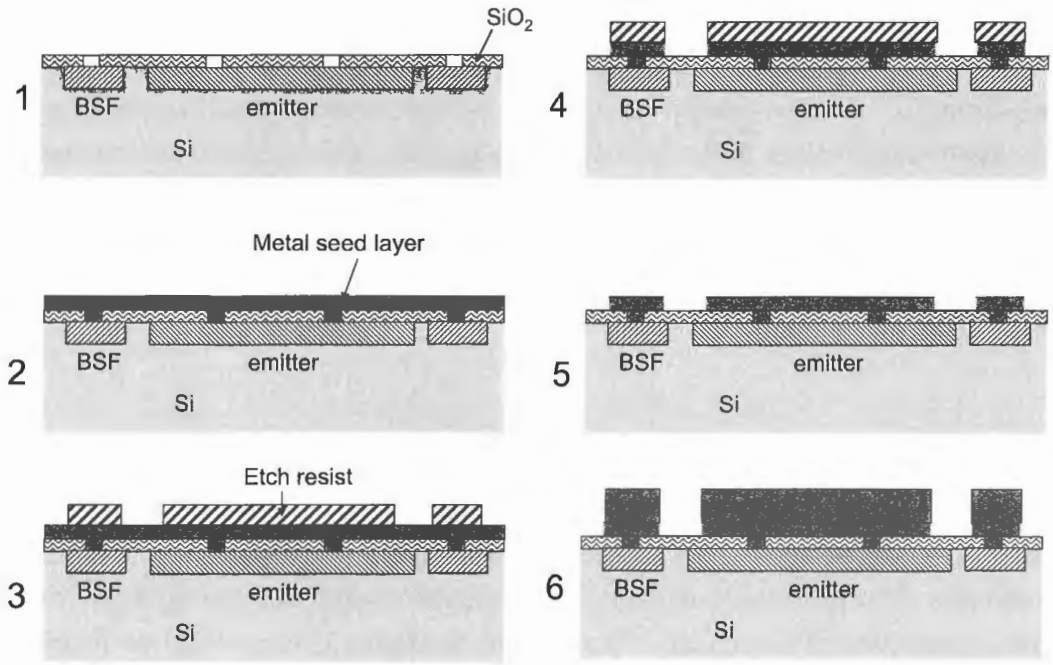


Figure 4-16 Method for contact separation using application of the screen-printed or inkjet etching masks. This method was developed in and successfully applied into the solar cells processing in the course of this thesis. The front side structure is not shown for simplification. The drawings are not to scale.

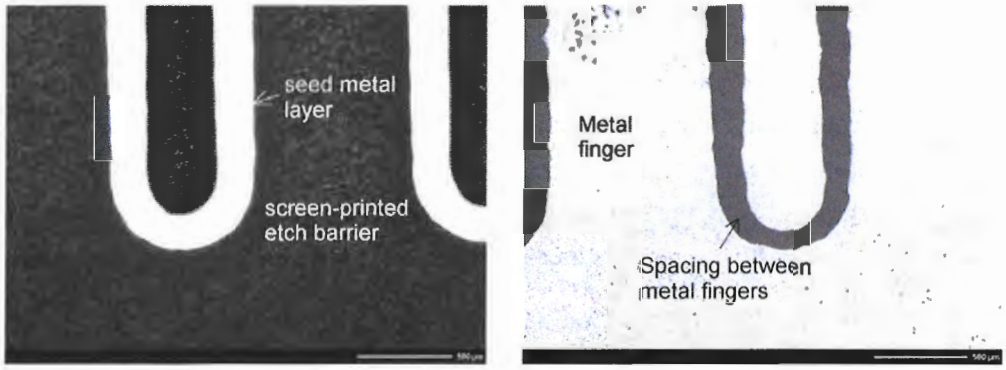


Figure 4-17 Example of the contact separation using the screen-printed etch barrier layers (left). After the local etching of the metal seed layer and etch barrier removal, the contact separation between the metal fingers is created (right). Photographs taken with optical microscope.

An example of the application of the screen-printed etch barrier and the resulting metal finger structure is shown in the Figure 4-17. The presented method has two major risks. These are:

- strong under-etching of the metal fingers underneath the etch barrier if the etching time and uniformity over the whole wafer area are not optimized carefully, and
- formation of metal bridges between the p- and n-metal grids if openings and/or local imperfections in the screen-printing process, such as locally closed opening lines, are formed.

Additionally as in the previous method, if more than one metal is applied in the seed layer, then multiple selective etching steps are required. This would increase the complexity of the process.

Lift-off approach and laser enhanced lift-off (this work)

In microelectronics and in the processing of high-efficiency solar cells, the lift-off method is widely used [129]. However, the use of photolithography to form the structures in the photoresist makes this approach too complicated and expensive for the mass production of solar cells. Therefore in the frame of this work an alternative approach, in which the photolithography was replaced with the low-cost screen-printing process, was developed. In Figure 4-18 the lift-off method is schematically presented.

The screen-printed lift-off resist is locally deposited on the rear cell surface. Next, a thin seed metal layer is deposited. If the slopes of the resist are steep enough, only a very thin layer of the metal is deposited on the slopes. In the next step, the resist is stripped in a liquid solvent. The solvent can penetrate the resist layer through the very thin and non-continuous metal layer at the slopes of the resist. After dissolution of the resist, the metal layer lying on top of the resist is removed and the contact separation is complete. In the final step, the thin seed metal layer is thickened in the plating process.

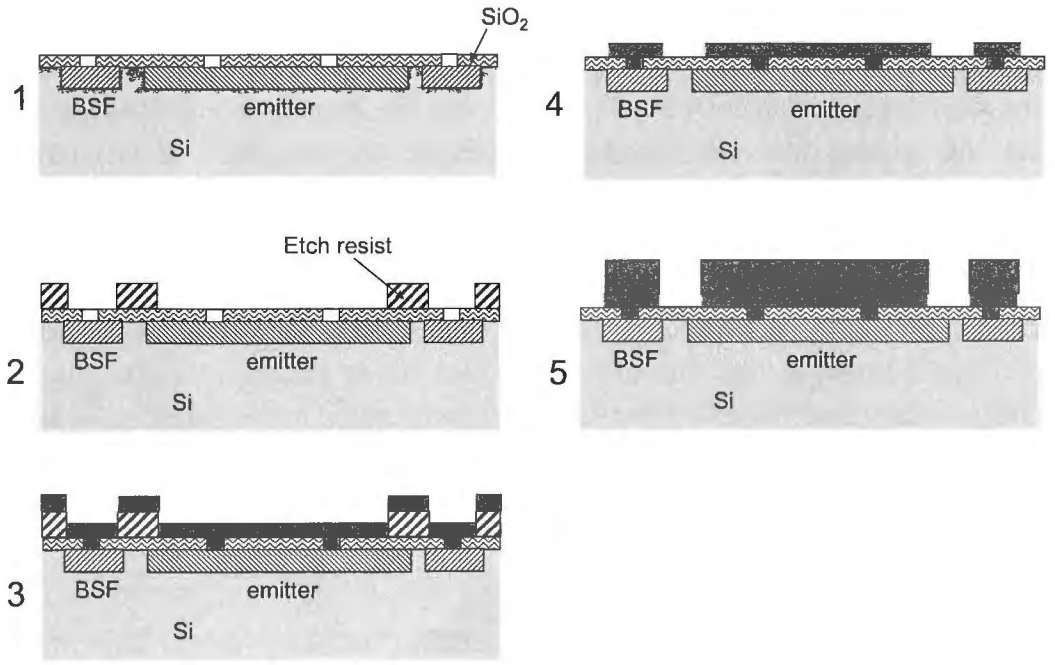


Figure 4-18 Method for contact separation using the lift-off approach with the application of the screen-printed or ink-jetted resist layer. This method was developed in and successfully applied into the solar cells processing in the frame of this thesis. The front side structure is not shown for simplification. The drawings are not to scale.

An example of the contact separation using the lift-off technique with screen-printed resist layer is shown in Figure 4-19. The same screen-printing mask was used here as in the case of Figure 4-17, which resulted in a negative structure of the metal fingers after the lift-off process.

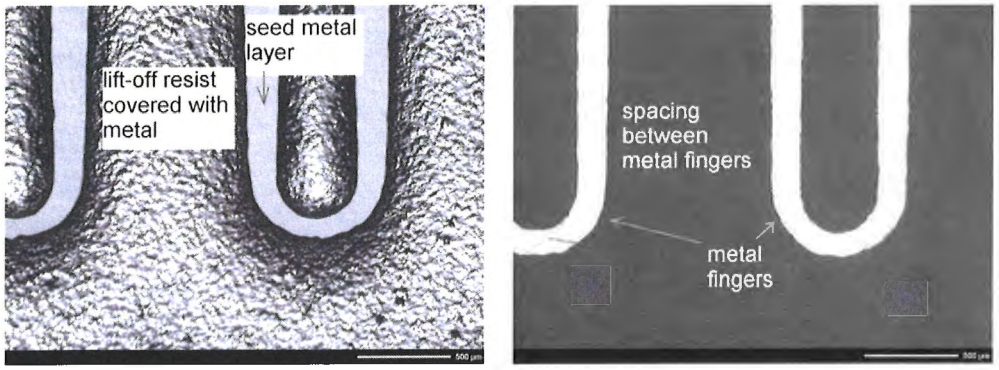


Figure 4-19 Example of the contact separation using the lift-off process with the screen-printed resist layer before (left) and after (right) the lift-off process. Photographs taken with optical microscope.

Unfortunately, due to the fact that the slopes of the screen-printed resist are not steep enough, the metal layer at these slopes is usually dense, and the solvent cannot reach the resist easily (see Figure 4-20). Due to this fact, the stripping time of the resist layer can take a long time and significantly decrease the throughput of this process. Therefore, a modification of the standard lift-off process was introduced in the course of this work. After deposition of the seed metal layer, local openings in the metal layer are formed by means of the laser ablation as schematically shown in Figure 4-20. Thus the transport of the solvent to the resist layer is greatly enhanced, at the same time reducing the process time. This process is called "Laser enhanced lift-off". The laser energy is fully absorbed in the first few micrometers of the metal and the resist layers. Therefore, due to the large thickness of the resist layer (10-30 μm), the laser energy cannot reach the silicon surface and create damage there.

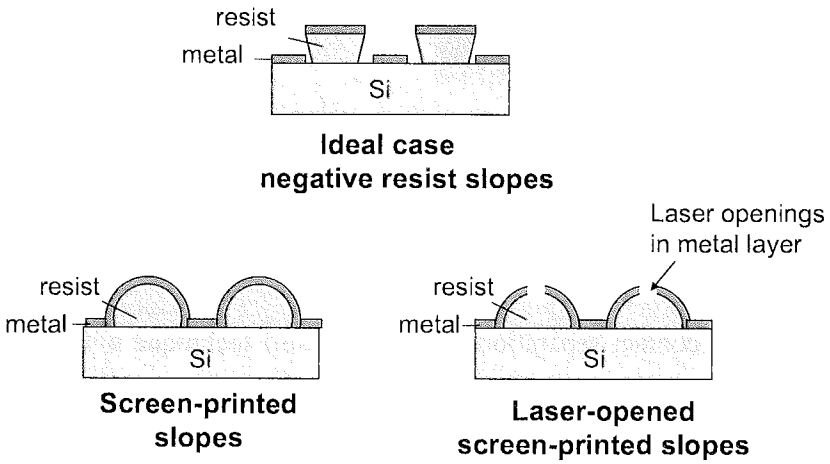


Figure 4-20 Influence of the slope of the resist edges on the lift-off process. The ideal case of the resist with negative slopes is shown in the top picture. The actual slopes of the screen-printed resist are not steep at all (left). The laser ablation process, used to open the metal layer, enhances the speed of lift off process significantly (right).

The advantages of the lift-off process are:

- No risk of under-etching of the metal fingers,
- Removal of the seed metal layers is done in one step. There is no need for selective etching of many metals in the seed layer.

On the other hand, due to the application of the screen-printing process the size of the spacing between the metal fingers is high, in the range of 100 to 300 μm. This is caused by the low positioning accuracy and the resolution of the screen-printing process. The large spacing between the metal fingers increases the optical transmission

losses of the solar cell. The application of screen-printed resist with non-steep slopes requires the introduction of the laser ablation process in order to increase the speed of the lift-off process.

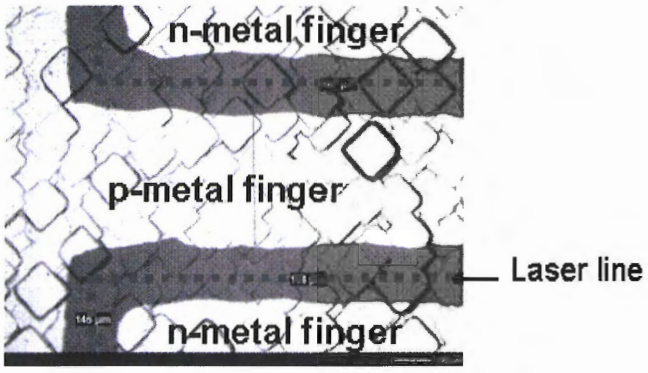


Figure 4-21 Example of the contact separation using the laser enhanced lift-off process with the screen-printed resist layer. Photographs were taken using an optical microscope.

4.4.2 Thickening of the thin seed metal layer

After formation of the interdigitated p- and n-metal seed layer, the thickening of the thin seed metal layer is required in order to increase the conductivity of the metal fingers and reduce the series resistance losses. The influence of the metal finger height on the series resistance and the resulting fill factor of the solar cell can be calculated with the following equations [121]:

$$R_s = \frac{1}{3}\frac{A_F}{B_F H_F}\rho {L_F}^2 \tag{4.1}$$

$$\Delta FF = FF_0 \frac{R_s J_{sc}}{V_{oc}} \tag{4.2}$$

where A_F is the pitch of the solar cell, B_F is the width of the metal fingers, L_F is the length of the fingers, H_F is the height of the fingers, and ρ is the resistivity of the applied metal. FF_0 is the fill factor of the solar cell not reduced by the series resistance losses and ΔFF is the fill factor loss caused by the series resistance R_S.

The calculated series resistance and the fill factor of the n- and p- metallization grid for two solar cell sizes of 2×2 cm^2 and 12×12 cm^2 with the pitch of 2200 µm are shown in Figure 4-22. For the laboratory cell size of 4 cm^2 a thickness of 2 µm of the metal

fingers is sufficient to reduce the resistance of the metal grid to 0.1 Ω cm^2, which would result in a the fill factor loss of less than 0.5 % absolute. However, for the industrial scale 144 cm^2 solar cells with the length of the metal fingers of 12 cm, the required thickness of the metal fingers is much higher. If 1 % absolute loss in fill factor due to metal resistance is allowed, than the required thickness of the metal fingers is around 35 µm in the case of the application of the silver plating. Using this metal finger thickness, the series resistance of the metallization grid equals 0.2 Ω cm^2. This calculation shows the importance of the thickening of the seed metal layer, especially for industrial size solar cells.

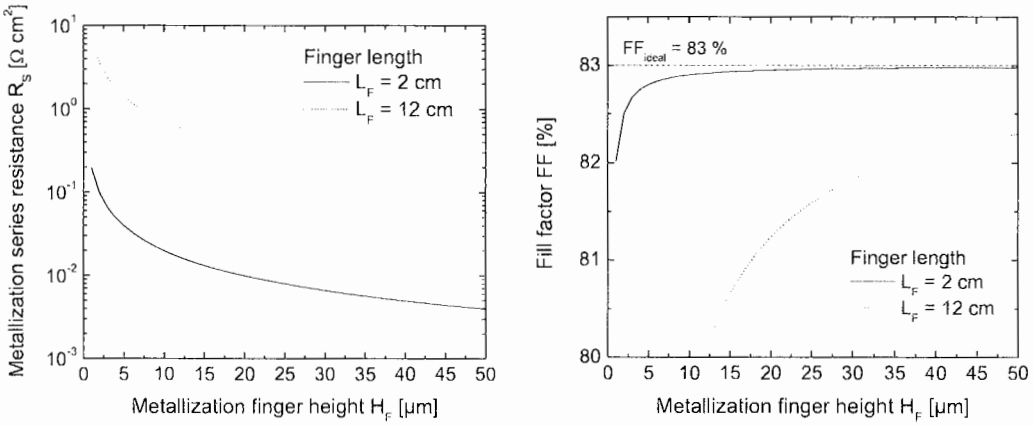


Figure 4-22 Calculated resistance of the interdigitated grid for a pitch of 2200 µm for two solar cell sizes of 2×2 cm^2 and 12×12 cm^2 (left side) for different thickness of the silver fingers. The resulting fill factor for both solar cell sizes is shown in the right graph.

In the developed solar cell process, the thickening of the structured seed metal layer was done using silver plating. A novel approach to thickening the interdigitated grid of the back-contact back-junction solar cells was introduced, in which both electrodes are thickened using different plating mechanisms. The p-electrode is contacted and thickened using the electroplating process in the potassium silver cyanide $K[Ag(CN)_2]$ bath [130]. The n-electrode is not contacted. It is plated using the light-induced plating (LIP) approach in the same chemical bath. LIP was optimized by Mette et al. [131] for the application of thickening the front surface metallization grid of the both-sides contacted solar cells. The p- and n-electrodes are of different width (see Figure 4-2), requiring therefore different thickness to achieve optimal resistance of the total metal grid. Due to the application of two different plating mechanisms during one plating process, the rate of the thickening of both electrodes can be optimized in order to achieve optimum usage of the metal material.

4.5 Solar cell results

The low-cost screen-printing and laser structuring processes described above were successfully applied to the BC-CJ solar cell processing sequence. In the present section the solar cell results, obtained using the described technologies, are presented.

4.5.1 Laboratory-scale solar cells

For laboratory-scale (4 cm^2) solar cell (see Figure 4-2), best conversion efficiency of 21.1 % (designated area measurement) was achieved on 1 Ω cm n-type FZ Si with the pitch of 2200 μm. The illuminated current-voltage characteristics together with the solar cell parameters of the best solar cell are shown in Figure 4-23.

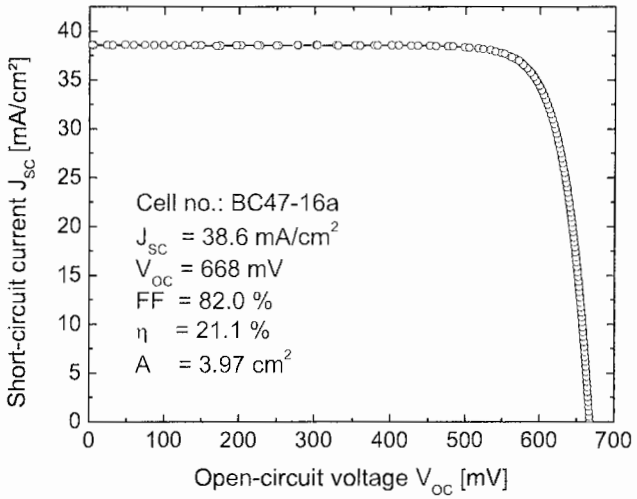


Figure 4-23 Illuminated current-voltage characteristics of the best n-type back-contact back-junction solar cell with the pitch of 2200 μm and the efficiency of 21.1 %. Designated area measurement under AM1.5G spectrum with illumination intensity of 100 mW/cm² and with device temperature of 25 °C. The efficiency was measured at Fraunhofer CalLab.

A very high fill factor value of the finished cell of 82 % indicates low resistive losses. Shunting between the tight p- and n-metal finger grids was avoided by a application of appropriate metallization process (see section 4.4.1). The series resistance losses of lateral carrier transport due to the large pitch could be minimized by application of the high conductivity FSF (see chapter 8 for more details). The total series resistance of the best solar cells is around 0.2 Ω cm^2, which proves a good device design in terms of resistive losses.

The open-circuit voltage of the best cell equals 668 mV. The rather moderate V_{OC} value indicates that a careful optimization of the rear side geometry and the diffusion profiles is required in order to further increase the device efficiency.

The short-circuit current of the best cell reaches nearly 39 mA/cm^2 for 1 Ω cm base resistivity. Analysis of the J_{SC} losses (section 6.2) shows that the optical losses (mainly front surface reflection, escape light and free carrier absorption) and the recombination losses over the base areas are limiting J_{SC}.

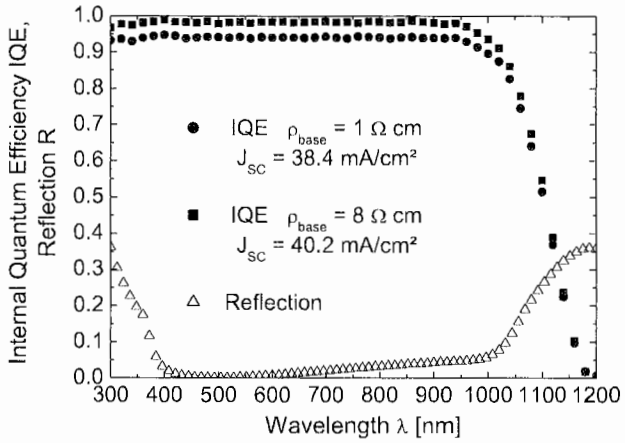


Figure 4-24 Comparison of the internal quantum efficiencies of the BC-BJ solar cells with base resistivity of 1 Ωcm and 8 Ωcm. The cells have a FSF with ρ_{sheet} = 148 Ω/sq and pitch of 2200 µm. The short-circuit current calculated by the integration of the solar spectrum with the external quantum efficiencies are shown in the graph. Note a nearly zero-reflectance at wavelength of around 550 nm due to the absence of the front side metal fingers.

The internal quantum efficiencies (IQE) and reflection (R) of the BC-BJ solar cells with a base resistivity of 1 Ω cm and 8 Ω cm are shown in Figure 4-24. The cell's reflection is very low due to the absence of the front side metallization grid. A nearly zero-reflectance is achieved for wavelengths of around 550 nm. The internal quantum efficiency for both resistivities is high, but does not reach unity. The IQE of the 1 Ω cm cells equals 95 % and for the 8 Ω cm cells it equals 98 %. The decrease of the IQE (5 % for 1 Ω cm cells and 2 % for 8 Ω cm cells) is partially caused by the front surface recombination and the bulk recombination of the minority carriers, which did not reach the rear side p-n junction. The front and rear surface recombination is higher in the case of base material with higher doping concentration [132]. This explains the differences in J_{SC} of solar cells with both base resistivities. However, the analysis presented in section 6.4 indicates that there is another cause for the decrease of IQE,

namely the recombination over the broad areas of base doping, called electrical shading.

Due to the absence of the front side metallization grid, the optical shading losses can be avoided in the BC-BJ solar cells. However, electrical shading is still present due to the rear side recombination in the regions of base busbar and base fingers [87]. A light beam induced current (LBIC) [133] map of the 2×2 cm^2 laboratory solar cell is presented in Figure 4-25. One can clearly recognize the reduced EQE signal over the base fingers and busbar. The EQE drops to nearly zero above the base busbar, even though no optical shading in this region is present. This is due to (a) large lateral distances which the minority carriers need to diffuse in order to be collected by the p-n junction and (b) due to enhanced recombination over the gap and BSF areas which have high saturation current densities. A detailed analysis of the solar cell results and the loss mechanisms is presented in chapter 6.

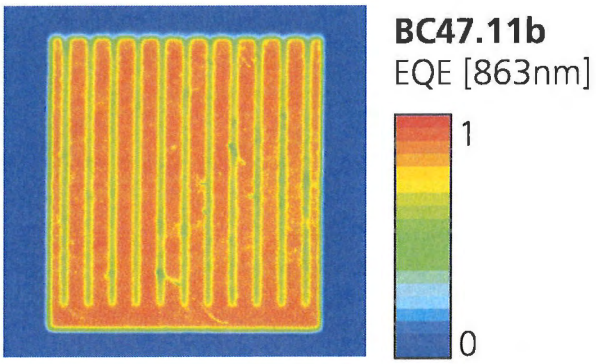


Figure 4-25 LBIC map of the BC-BJ silicon solar cell. The reduced EQE signal above the base fingers and base busbar (top side) are visible. The designated cell area is 2x2 cm^2 and the busbar area is 0.15x2 cm^2. EQE was measured at a wavelength of 863 nm.

4.5.2 Industrial-scale solar cells

In the frame of the *Quebec* [41] project, in which the author of the thesis developed the back-contact back-junction solar cell structure for mass production, large size solar cells were also manufactured. The photographs of a finished large area cell is shown in Figure 4-26.

The best efficiency of 19.2 % was achieved on n-type Cz-Si 5-inch pseudosquare wafers (cell size 147.4 cm^2) with the resistivity of 3 Ω cm. The illuminated current-voltage characteristics, together with the solar cell parameters of the best large size solar cell are shown in Figure 4-27.

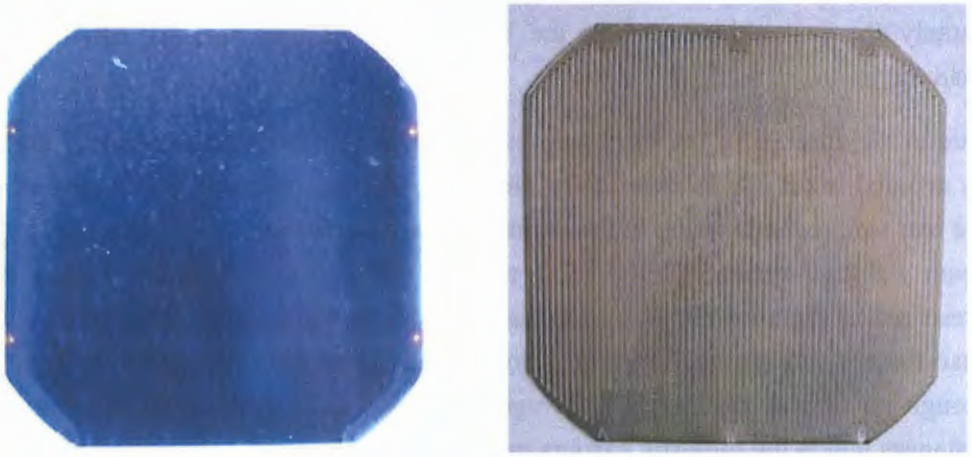


Figure 4-26 Photographs of the front (left) and rear (right) side of the large area back-contact back-junction solar cells developed in the course of the Quebec project at Fraunhofer ISE. Cell area is 147.4 cm²

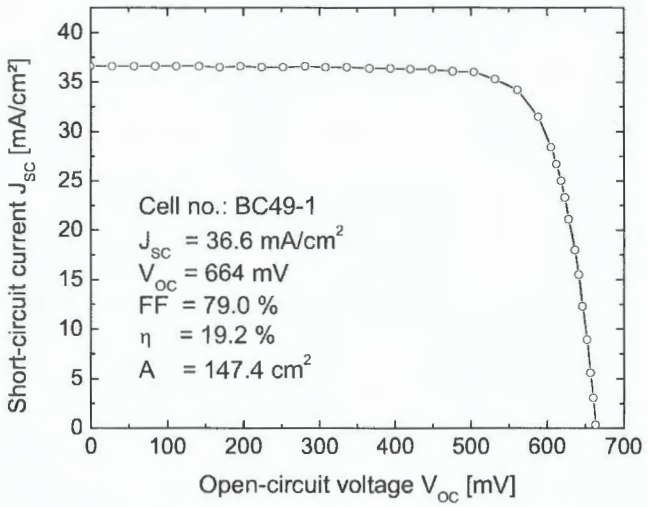


Figure 4-27 Illuminated current-voltage characteristics of the best n-type large size (147.4 cm²) back-contact back-junction solar cell developed at Fraunhofer ISE in the frame of the Quebec project [41]. The solar cell has an efficiency of 19.2 %. Measurement under AM1.5G spectrum with illumination intensity of 100 mW/cm² and with device temperature of 25 °C.

A lower efficiency (19.2 %) of the large area solar cells in comparison to the small laboratory-scale solar cells (21.1 %) is caused mainly by the lower fill factor and lower short-circuit current values. The open-circuit voltage of both solar cells is similar.

The lower FF values are caused by the significantly increased length of the metal fingers from 2 to 12 cm. The metal finger height after the silver plating process is in the range of 10 to 30 µm, which results in a FF loss of about 2 to 3 % absolute (see Figure 4-22). The rather wide spread of the metal finger thickness is caused by the fact the silver plating process of the BC-BJ solar cells was not optimized for large-area solar cells.

The difference in J_{SC} of small and large size solar cells is partially caused by the application of a different silicon material: FZ Si for small cells and Cz Si for large cells. The differences in the minority carrier's lifetime in the bulk of the fully processed cells may cause the J_{SC} differences. Moreover, in the case of the large size solar cells, local imperfections and non-uniformities, which are not avoidable due to manual handling of the large size wafers in the laboratory processing conditions, are present. These local imperfections (e.g. scratches, cracks, and passivation or diffusion non-uniformities) over the whole area of the solar cells are responsible for the locally decreased quantum efficiency of these cells (see Figure 4-28).

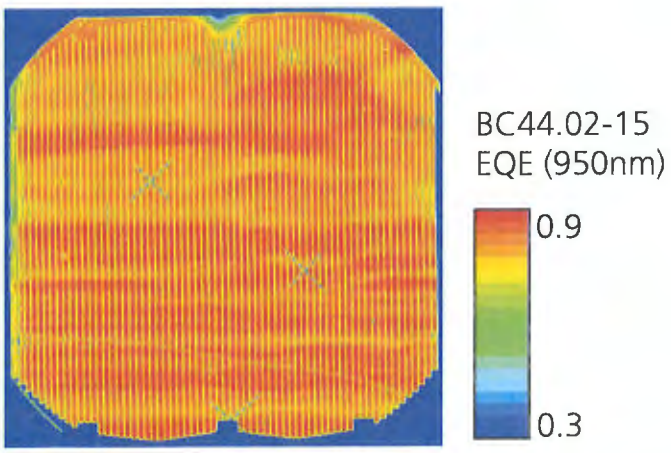


Figure 4-28 LBIC map of the large area BC-BJ silicon solar cell. The reduced EQE signal above the base fingers and base busbar (bottom side) are visible. The solar cell area is 147.4 cm^2. Local defects introduced by the manual handling of the wafer during processing can be recognized.

4.6 Conclusions

The design and the processing technology of the developed high-efficiency back-contact back-junction solar cell were presented. The structuring steps, which are required to form an interdigitated grid of p- and n-diffusions and metal grids, were done using industrially relevant low-cost techniques. Screen-printing of the masking

layers, as well as the local laser ablation of the dielectric and silicon layers, were developed and successfully applied to the solar cell processing sequence.

Solar cells were processed on n-type Si substrates. The applied n-type Si material was intensively examined. Very high minority carrier lifetimes up to 18 ms were measured for the investigated silicon substrates. The determined minority carrier lifetime is high enough to enable realization of the high-efficiency BC-BJ silicon solar cells.

Metallization technology is very critical in the case of the interdigitated metal grid structure, due to the very high risk of shunt formation between the p- and n-metal grids. A review of the existing approaches to form an interdigitated metallization grid on the rear cell side, as well as the two methods which were developed in the frame of this study, were presented. Metallization of the developed solar cells was performed using a laboratory approach consisting of two steps. First a thin (less than 1 μm) seed metal layer was evaporated and structured to form interdigitated grid geometry. Next, a silver plating process was applied to increase the metal finger height and conductivity.

The highest solar cell efficiency of 21.1 % was achieved on 1 Ω cm n-type FZ Si with the designated area of 4 cm^2. For the large area solar cells with an area of 147.4 cm^2, a maximum efficiency of 19.2 % was achieved. A detailed analysis of the solar cell results is presented in the following chapters.

5 Analysis of the laser-fired aluminium emitters

In this chapter the local laser-fired aluminium emitter (LFE) process, an alternative process to boron emitter diffusion, was investigated. The model of the LFE emitters, which includes a laser-induced damage zone, was analyzed using a two-dimensional simulation and compared with the experimental solar cell results. The injection-dependent Shockley-Read-Hall recombination in the direct vicinity of the local back junction influences negatively the cell performance and causes large cell performance differences for varying specific base resistivities of the cells.

5.1 Introduction

The Laser-Fired Contact (LFC) technology developed at Fraunhofer ISE [134] not only provides local contacts through the dielectric passivation layer at the back cell side, but also creates a local aluminium doped region. In the case of p-type cells, this region works as a high-low junction - an effective back surface field (BSF). This feature of the LFC process already enabled fabrication of a 21.9 % p-type solar cell. In addition to application of the LFC process to p-type substrates, an n-type substrate process with the use of the LFC has been introduced by Glunz et al. [135], [136]. The LFC process was used in that case to form local p-n back junctions on the *n-type* substrates, referred to as the laser-fired aluminium emitter (LFE) process.

The LFE process combines three steps in one:

1. Formation of the local openings in a dielectric layer.
2. Formation of the metal-semiconductor contacts, through the local openings.
3. Formation of the local p^+ emitter. Al is alloyed with Si, and a local p^+ emitter is created in the n-type substrate. Thus, the additional emitter diffusion process can be omitted.

Thus, the greatest appeal of the laser-fired p^+ aluminium emitter (LFE) process is the inherent opportunity to create a patterned emitter without additional masking steps. This feature of the LFE process makes it attractive for its application in the back-contact back-junction solar cell structure, where the p^+ emitter is diffused only locally.

Moreover, the LFE process enables the fabrication of high efficiency n-type cells without the use of boron diffusion. Replacement of the boron diffused emitter with the laser fired aluminium emitter could lead to significant reductions in processing time and potentially to a reduction in costs of the manufacturing of back-contact back-junction solar cells. The reason for this is that the boron diffusion is a high-temperature and time consuming process: diffusion temperatures are in the range of 800 - 1100°C, and the process requires several hours. High diffusion temperatures are required because of the low solubility of boron in Si. The solubility of phosphorus [137] is, for example, around one order of magnitude higher than the solubility of boron at the same temperatures [138]. Thus, in order to achieve high surface concentrations of boron, the diffusion process needs to take place at strongly elevated temperatures. In contrast LFE can be performed with the wafer at room temperature. Therefore, the heating of wafers to high diffusion temperatures is not required for this process, as it is in the case of boron emitter diffusion. Additionally, the LFE process is very fast, requiring a processing time in the range of seconds per wafer.

The objective of this chapter is to analyze and gain fundamental knowledge about the LFE process, an alternative process to the emitter formation using boron diffusion. Based on the analysis of the laser-fired Al emitters, the replacement of the boron diffusion with the LFE process could be potentially considered in the processing sequence of the back-contact back-junction solar cells.

5.2 Fabrication of LFE and boron emitter cells

Laser fired aluminium emitters (Figure 5-1 left) and locally diffused boron emitter (Figure 5-1 right) n^+np^+ back junction cells have been fabricated on 250 µm thick FZ n-type 1, 10 and 100 Ω cm Si substrates. The size of the cells is 2x2 cm^2. The cells exhibit a front surface with random pyramids, evaporated front contacts and a phosphorus diffusion (front surface field) with sheet resistance ρ_{sheet}=120 Ω/sq. The front surface is passivated by a 105 nm thick thermal oxide. The rear surface is covered with the same thermal oxide.

Formation of the local p-n junction on the rear side:

- LFE cell: After evaporation of 2 µm thick aluminium layer on the rear surface, the back junction is created by local laser-firing of the aluminium through the oxide layer, resulting in formation of a p^+ emitter and contact/emitter coverage of about 5 %.

- Diffused boron emitter cell: Back junction was formed by local boron diffusion through the oxide structured with photolithography on the rear side, with 1.5 % emitter coverage. The rear surface was then oxidized again and local contact openings were formed using photolithography with 0.2 % contact opening coverage. Finally, a 2 µm thick aluminium layer was evaporated on the rear surface.

The last processing step is a low temperature (425 °C) annealing under forming gas, called FGA process. The process time is 25 min and the concentration of H_2 in N_2 equals 5 %.

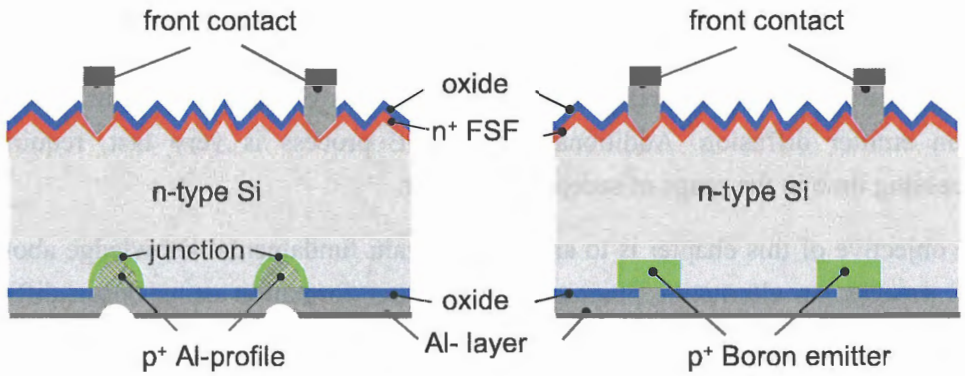


Figure 5-1 Structure of the n-type back-junction LFE cell (left) and the n-type back-junction locally boron diffused cell (right).

5.3 Solar cell results

The best results of different base resistivity n-type LFE cells are summarized in Table 5-1. The best efficiency of 19.4 % was obtained on 100 Ω cm FZ n-type material with the back-junction LFE cells. In the section 5.7, where the comparison of the results of the solar cells with LFE and boron diffused emitters is presented.

In Table 5-1 a very large difference in the performance of the LFE cells with different base resistivities can be observed. Differences of almost 10 mA/cm^2 (i.e. up to more than 20 % relative) in J_{SC} of the 1 and 100 Ω cm cells were measured. At the same time, differences of 30 mV in V_{OC} of cells with 1 and 100 Ω cm base can be seen. It is believed that the laser-induced crystal damage is responsible for limiting the performance of the LFE cells and for causing significant differences in the performance of these cells with different base resistivities. Understanding the differences in performance of the LFE solar cells with different base resistivities is an objective of the analysis presented in the following sections.

Table 5-1 I-V results of the LFE cells fabricated on n-type FZ Si substrates with different resistivities.

Cell no.	ρ_{base} [Ω cm]	V_{OC} [mV]	J_{SC} [mA/cm^2]	FF [%]	η [%]
NRP7_24.2m	100	646.5	39.8	75.1	19.4
NRP7_21.2m	10	639.8	37.9	71.9	17.4
NRP4_23.5	1	616.7	30.2	72.9	13.5

5.4 Laser-induced damage zone

In previous work [135] a concept of a laser-induced damage zone (see Figure 5-2) was introduced in order to explain the decreased V_{OC} of the p-type LFC cells in comparison to the passivated emitter rear locally diffused (PERL) cells with diffused Al BSF. Laser damage to the crystal lattice is caused by rapid melting during the absorption of a very short laser pulse [139] and a subsequent recrystallization of the silicon. The laser-induced defects are known to form recombination centers [140], [139], thus locally reducing the lifetime of the minority carriers.

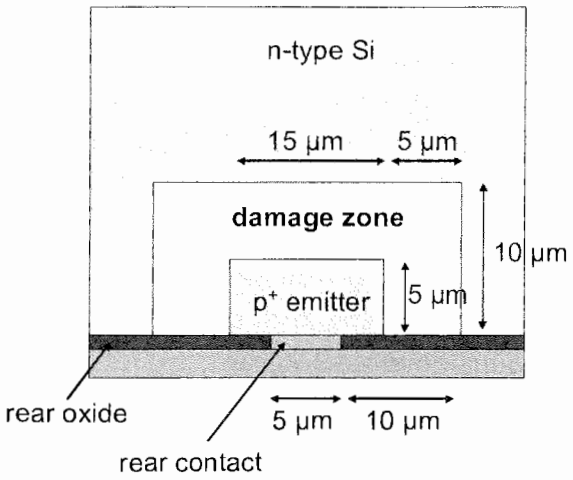


Figure 5-2 Two-dimensional simulation model of an LFC contact with a laser-induced damage zone around the local Al BSF.

The introduction of the damage zone with strongly reduced lifetime into the two-dimensional simulation model enabled very good modelling of the LFC p-type structures and modelling of their performance as a function of different base doping

concentrations. The damage zone implemented in the simulation model has a size of $15\times5\ \mu m^2$ and strongly reduced lifetime of $\tau_{local} = 0.3\ \mu s$. The size of the damage zone and the value of τ_{local} were arbitrary chosen in the simulations. The strongly reduced local lifetime in the laser damage zone models the very strong crystal defects and introduction of the metal impurities induced by the laser firing of the Al contacts.

Since in case of the n-type cell the local Al-profile functions as an emitter, the quality of this junction and the quality of the area in the direct vicinity of the junction is has a much bigger impact on the cell performance than in the case of p-type cells, where the Al-profile has the function of a local back-surface-field (LBSF).

5.5 Quantum efficiency of the LFE cells

In Figure 5-3 the measured internal quantum efficiency (IQE) of the LFE cells and the simulated IQEs are presented. Significant differences in the quantum efficiency of the LFE cells with different base doping concentrations cause very large differences in short-circuit current of the measured cells. IQE of the cell with 100 Ω cm base resistivity equals around 97%. At the same time the internal quantum efficiency of the LFE cell with 1 Ω cm base resistivity equals only around 75%. This difference in IQE explains around 20% differences in J_{SC} of these cells.

In the bottom part of Figure 5-3, the IQE of the n-type LFE cells were modeled using two-dimensional device simulation. Next to the LFE cells with the laser-induced damage zone, the IQE of the ideal case of a LFE cell without the damage zone was calculated as well. These modelling results are marked in the graph as 'Ideal Local Al-Diffusion'. In the device simulations an identical bulk lifetime $\tau_{SRH} = 1000\ \mu s$ was used for all three base doping concentrations in order to investigate the influence of the damage zone independently of the bulk effects. The damage zone model enables modeling which is in good agreement with the measured IQEs. It is believed that fine adjustments of the damage zone parameters, such as size and lifetime, may result in even better agreement with the measured values.

In Figure 5-3b, one can compare the influence of the damage zone on the quantum efficiency of the 1 and 100 Ω cm cells. The influence of the damage zone is much bigger for the 1 Ω cm material than in the case of 100 Ω cm, where the damage zone has almost no influence on the quantum efficiency. In the case of the cell with 1 Ω cm base resistivity and with the damage zone model the quantum efficiency is around 7 $\%_{abs}$ lower than the IQE of the cell without the damage zone. The next section deals with the explanation of this effect.

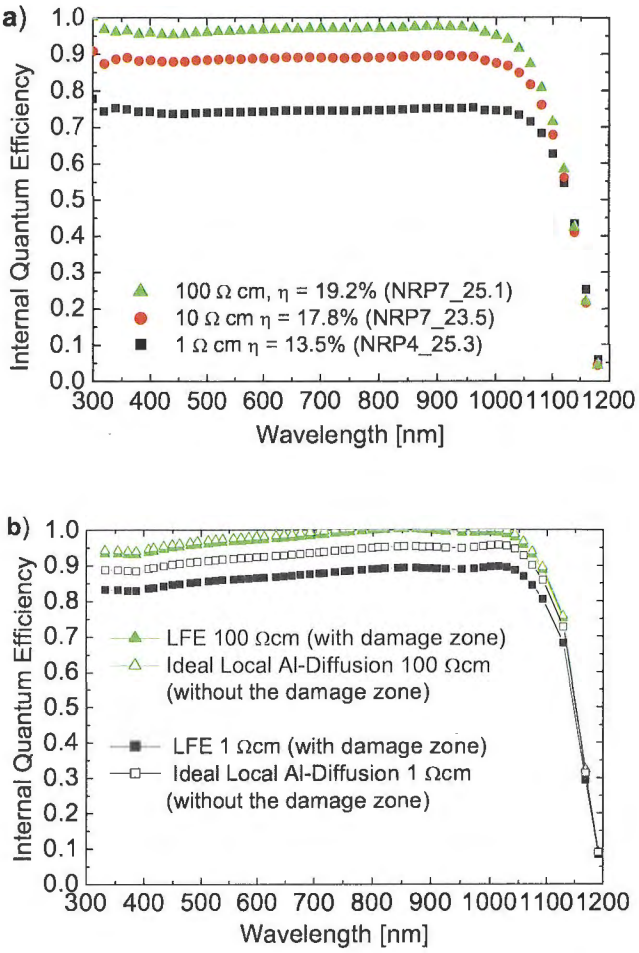


Figure 5-3 Measured (a) and two-dimensional SDEVICE [90] simulation (b) internal quantum efficiencies for the n-type LFE cells of different doping concentration.

5.6 Recombination in the damage zone

Using the damage zone model presented in the previous section, the Shockley-Read-Hall (SRH) recombination rate and the density of the electrons and holes in the direct vicinity of the rear local junction were simulated. The results of the two-dimensional simulations of the SRH recombination rate are shown in Figure 5-4. The LFE cells with base resistivities of 1 and 100 Ω cm were simulated. Additionally, the rear local junction solar cell without the damage zone and with base resistivity of 1 Ω cm was simulated for comparison.

In the results shown in Figure 5-4, a strongly increased recombination rate in the damage zone is observed. The recombination rate in damage zone is around 3 to 4

orders of magnitude higher than in the bulk Si material. Increased SRH recombination in the damage zone results from the very low lifetime of the minority carriers within this zone. In the model, the local minority carrier lifetime inside of the damage zone is set to 0.3 µs. The bulk lifetime is significantly larger and equals 1000 µs.

In the simulation of the cell without the damage zone, shown in Figure 5-4c, the recombination rate is uniform over the whole bulk area. This is the case when a p^+ emitter was created by boron diffusion or by alloying of Al, without the introduction of the stress caused by rapid thermal processing and crystal lattice defects during emitter formation using the LFE process.

An interesting effect can be observed by comparing the recombination rate in the damage zone of the LFE cells with 1 and 100 Ω cm. The recombination rate is there clearly higher in the case of the 1 Ω cm LFE cell than in the case of the 100 Ω cm cell. This effect can be analyzed better when looking at the profiles of the recombination rate taken through the wafer thickness in the middle of the rear local emitter, as shown in Figure 5-5.

The difference in the recombination rate of the cells with different base resistivity can be explained with the injection dependence of the Shockley-Read-Hall carrier lifetime (τ_{SRH}). τ_{SRH} is a function of the carrier injection level and the dopant density. In the case of the 1 Ω cm material, where the injection level is lower than the dopant density (see Figure 5-5a), a low injection level condition occurs ($\tau_{SRH,\,lli}$). However, the dopant density of the 100 Ω cm material is lower than the density of the holes (Figure 5-5 b), thus the 100 Ω cm LFE cell is under high injection ($\tau_{SRH,\,hli}$).

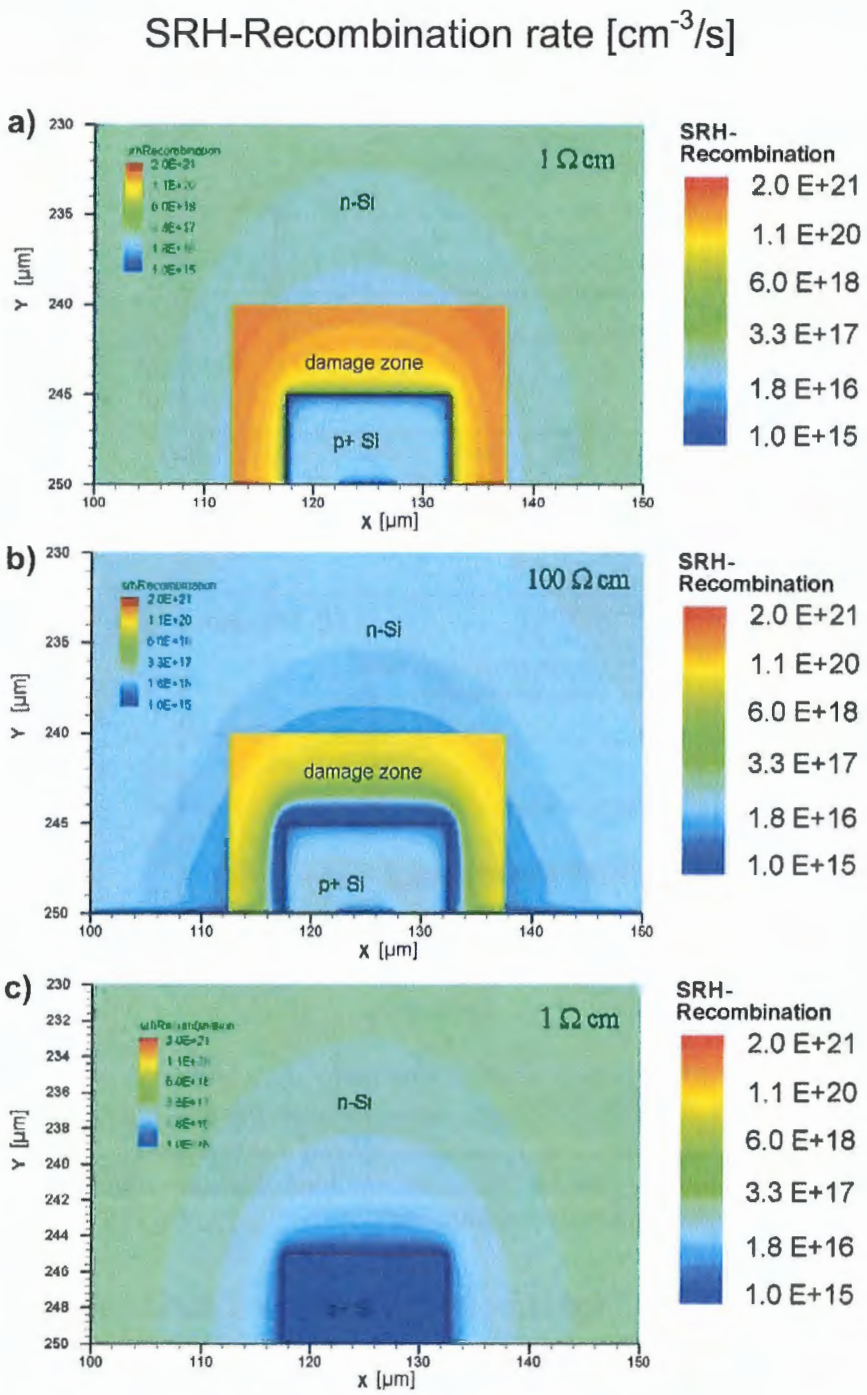


Figure 5-4 Two-dimensional simulation of the SRH-recombination rate under J_{SC} conditions of 1 Ω cm (a) and 100 Ω cm (b) LFE and 1 Ω cm LBSF (c) cells. Recombination was simulated in the vicinity of the local emitter on the rear side. Y-axis represents the thickness of the cell, with front cell surface at Y=0. SHR-recombination rate shown in the colour scale is given in cm^{-3}/s. Note strongly the increased recombination rate in the laser damage zone of the LFE cells (a and b).

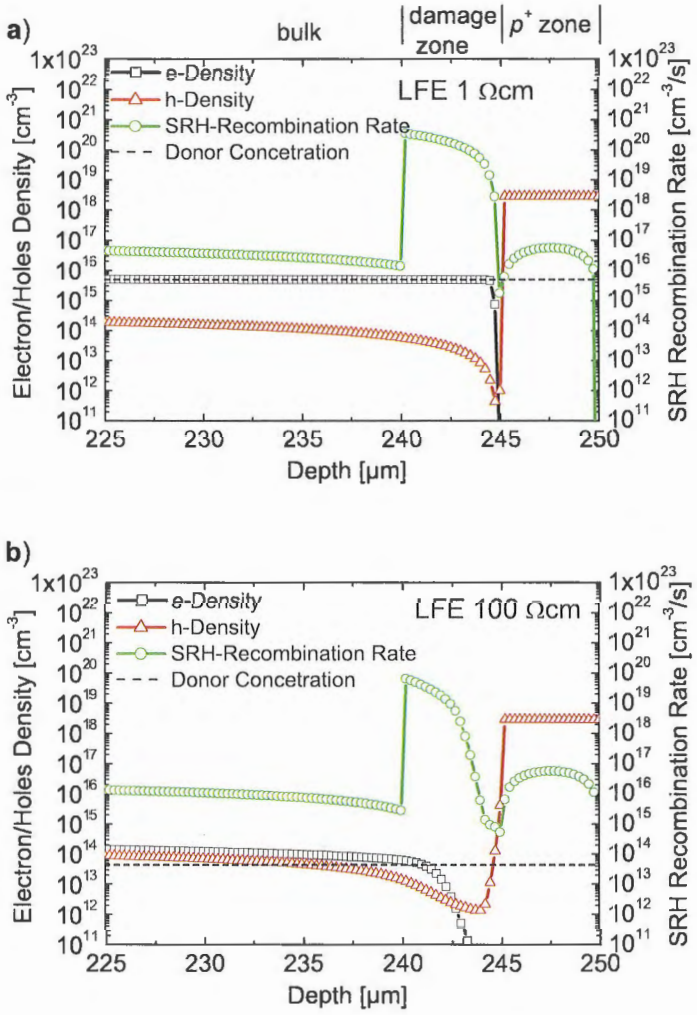


Figure 5-5 Profiles of the recombination rate under J_{SC} conditions of the 1 Ω cm (a) and 100 Ω cm (b) LFE cells taken through the cell thickness at the back surface of the cell (two-dimensional simulation). Note the high recombination rate in the laser-induced damage zone (between 240-245 µm from the cell front surface).

Using the simplified SRH lifetime models under low- and high-level injection [141] and for $\tau_{no} = \tau_{po}$, the low (lli)- and high-level injection (hli) lifetime in n-type Si is:

$$\tau_{SRH,\,\mathrm{lli}} = \tau_{po}$$
$$\tau_{SRH,\,\mathrm{hli}} = \tau_{no} + \tau_{po} \qquad (5.1)$$

Thus both bulk and damage zone lifetime of cells under high injection is significantly higher than under low injection. It is therefore believed that this significant lifetime difference, resulting in a drastic change of the diffusion length in the bulk Si and in the

damage zone, is the reason for the performance difference between the LFE cells processed on the 1 and 100 Ω cm n-type wafers. Results of the simulation prove the hypothesis to be correct. The increased recombination rate of the 1 Ω cm cell in the bulk and inside the damage zone leads to a significant current reduction of these cells compared to 100 Ω cm LFE cells.

5.7 Comparison of boron diffusion and LFE emitters

Further analysis of the influence of the injection dependence bulk and damage zone lifetime on the analyzed cell structure performance is done by direct comparison of the solar cells with LFE emitters (Figure 5-1 left) to cells with local boron diffused emitters (Figure 5-1 right). During the boron diffusion process, the damage zone in the direct vicinity of the local rear junction is not formed. It is therefore expected that, due to the absence of the damage zone, the solar cells with boron diffused emitters will show a different dependence on the current as a function of base doping than with the LFE cells.

Table 5-2 Comparison of the parameters of the LFE and boron diffusion emitter cells on different base resistivities. All cells were processed on the n-type FZ Si substrates. The area of the solar cells is 4 cm^2.

Cell no.	Emitter type	ρ_{base} [Ω cm]	V_{OC} [mV]	J_{SC} [mA/cm^2]	FF [%]	η [%]
NRP46_1d	Boron diffusion	1	599.6	35.1	60.6	12.8
NRP46_4e	Boron diffusion	10	653.1	36.0	74.7	17.6
NRP46_5e	Boron diffusion	100	658.5	37.6	74.2	18.4
NRP46_10f	LFE	1	619.2	31.7	69.8	13.7
NRP46_14b	LFE	10	625.1	35.9	78.0	17.5
NRP46_18b	LFE	100	629.0	37.6	76.3	18.0

As mentioned in section 5.2, a set of the LFE and boron diffused emitter solar cells was processed within the frame of this work. The best results are summarized in Table 5-2. The best efficiency of the back junction with locally diffused boron emitters in this experiment was 18.4 % on the 100 Ω cm substrate resistivity. For comparison, the highest reported efficiency of the n-type back junction solar cell with full area boron emitter is 22.7 %, presented by Zhao et al. [142]. Thus, the full area emitter on the rear

side has a far superior performance than the local rear emitter of this study. Coming back to Table 5-2, the performance of the cells with boron emitters is slightly higher than that of the LFE cells. The variation in FF of the boron emitter cells is caused by processing faults during the photolithography for the rear side contact formation.

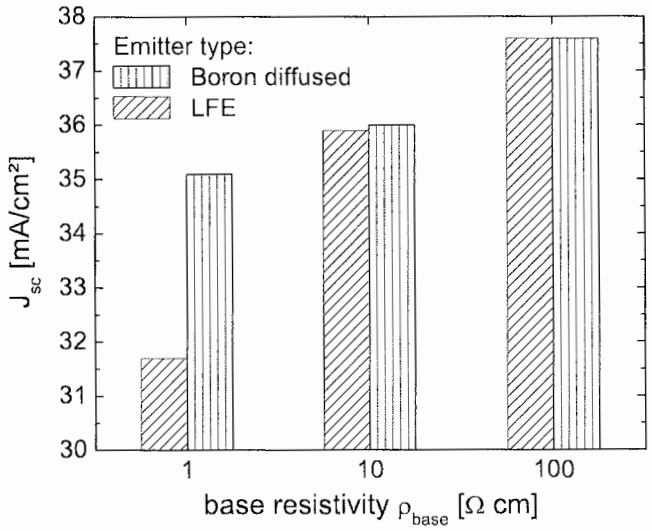


Figure 5-6 Comparison of the short-circuit current of the back-junction cells with LFE and boron diffused emitters on different resistivity substrates.

The V_{OC} values of the LFE cells are around 20 to 30 mV lower than the V_{OC} values of the boron emitter cells. The loss in V_{OC} is caused by the recombination in the damage zone of the LFE cells and by the increased metal contact coverage of LFE cells, which also results in the increased recombination of the minority carriers at the rear surface. In Figure 5-6, direct comparison of J_{SC} of the LFE and boron diffused cells on different substrate resistivities is shown. For a base resistivity of 100 Ω cm, there is no difference in J_{SC} of both cell types. The cell operates under high injection, thus the damage zone lifetime of LFE cells is high enough not to limit the device performance. This result is in good agreement with the device simulations shown in Figure 5-3b. With increasing substrate doping concentration, the J_{SC} of both cell types decreases. This effect is caused by decreased bulk lifetime in the substrate of higher doping concentration. However, for a base resistivity of 1 Ω cm there is a large J_{SC} difference of 3.4 mA/cm^2 between the LFE and boron emitter cells. This effect is again in good agreement with simulations shown in Figure 5-3 b. In the case of 1 Ω cm cells, which operate under low injection, the bulk lifetime in the damage zone is so low that it limits the minority carrier collection at the back junction.

The results mentioned above clearly prove the validity of the model of the laser fired aluminium emitter process, which includes the damage zone with significantly reduced local lifetime.

5.8 SunsV$_{OC}$ and implied voltage

The SunsV$_{OC}$ curves of the fully processed LFE cells, presented in Table 5-1, were measured for a wide light intensity range (Figure 5-7) in order to analyze the cell voltage under low and high injection level conditions.

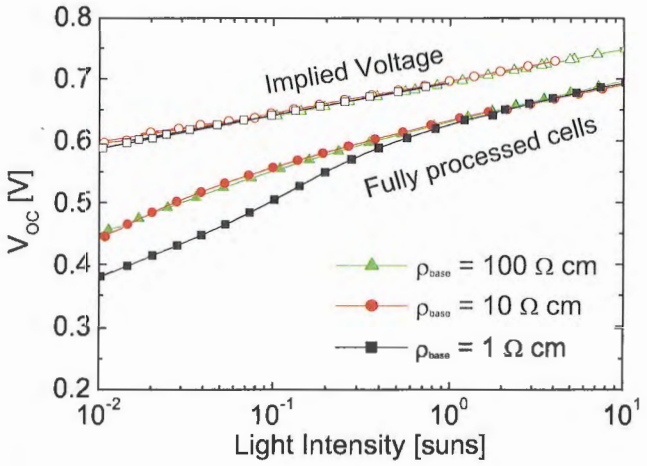


Figure 5-7 Open-circuit voltage (closed symbols) and implied voltage (open symbols) in the wide light intensity range for different resistivity n-type fully processed LFE cells and test samples for determination of the effective minority carrier lifetime.

The excess carrier density in the lifetime samples lead to the separation of the quasi Fermi levels and implies an open circuit voltage. For this experiment the n-type lifetime samples with different base resistivity have been prepared. Both sides of these samples exhibit a full area shallow n^+ diffusion (ρ_{sheet} = 120 Ω/sq.) and a full area 105 nm thick thermal oxide.

The implied voltage of the n-type FZ Si material, used for the solar cell processing, was calculated from the QSSPC lifetime curves. The calculations were performed using equation (5.2) as proposed by Sinton et al. in [75].

$$V_{OC} = \frac{kT}{q} \ln\left(\frac{\Delta p(N_D + \Delta n)}{n_i^2}\right) \tag{5.2}$$

The calculated implied voltage is plotted in Figure 5-7. The symmetrical n-Si lifetime samples, as shown in section 4.2.1, were analyzed. For all resistivities, shape and values of the implied voltage are roughly the same in the range of 700 mV at one sun light intensity. The implied voltage values represent an ideal state, where only bulk recombination (which is low for the good quality n-type material as shown in section 4.2) and the low surface recombination rate plays a role.

In the case of the fully processed LFE cells, the SunsV_{OC} curves are different than the implied voltage curves of the symmetrical lifetime samples. First of all, voltage values are lower. This is attributed to the cell structure, where additional recombination mechanisms such as: (a) front and rear side metal contacts, (b) laser-induced damage zone and (c) texturization are introduced. All these elements reduce the cell voltage to 610-630 mV at light intensity of one sun.

Additionally, one can see an interesting shape of the 1 Ω cm curve of the LFE cell. Under low-injection intensities (light intensities <0.3 Suns), the voltage decreases faster than in the case of higher resistivity cells. It is believed that this effect is caused by a strong decrease in lifetime in the laser damage zone, where under low-injection the SRH recombination dominates – as discussed above.

One would expect a larger J_{SC} vs. Suns than a V_{OC} vs. Suns dependence, because under short-circuit conditions the cells operate at much lower injection levels as compared to open-circuit conditions. Moreover, the short-circuit current of the rear junction cell structure has a much stronger bulk lifetime dependence then the cell voltage. That is why the differences in J_{SC} are much more significant than the V_{OC} differences between 100, 10 and 1 Ω cm cells, as can be seen in Table 5-1. The analysis above has another practical meaning as well. Under low illumination conditions, i.e. more realistic outdoor conditions, the LFE cells will suffer from an drop in efficiency, whereas the boron diffused cells should retain linear characteristics.

5.9 Optimization of the LFE cells

Optimization of the pitch, i.e. distance between the LFE points, was performed. The pitch of laser points was varied in order to find the optimum between two opposing trends:

a) For a smaller laser pitch, the emitter coverage on the rear side increases, which improves carrier collection at the back-junction. Moreover, the decrease of the LFE pitch should also have a beneficial influence on the fill

factor by reducing the lateral series resistance, especially for the cells with a low conductivity substrate.

b) Increasing the pitch of the LFE points results in a decrease of the damage introduced by laser, which should be as small as possible to reduce degradation of the cell performance.

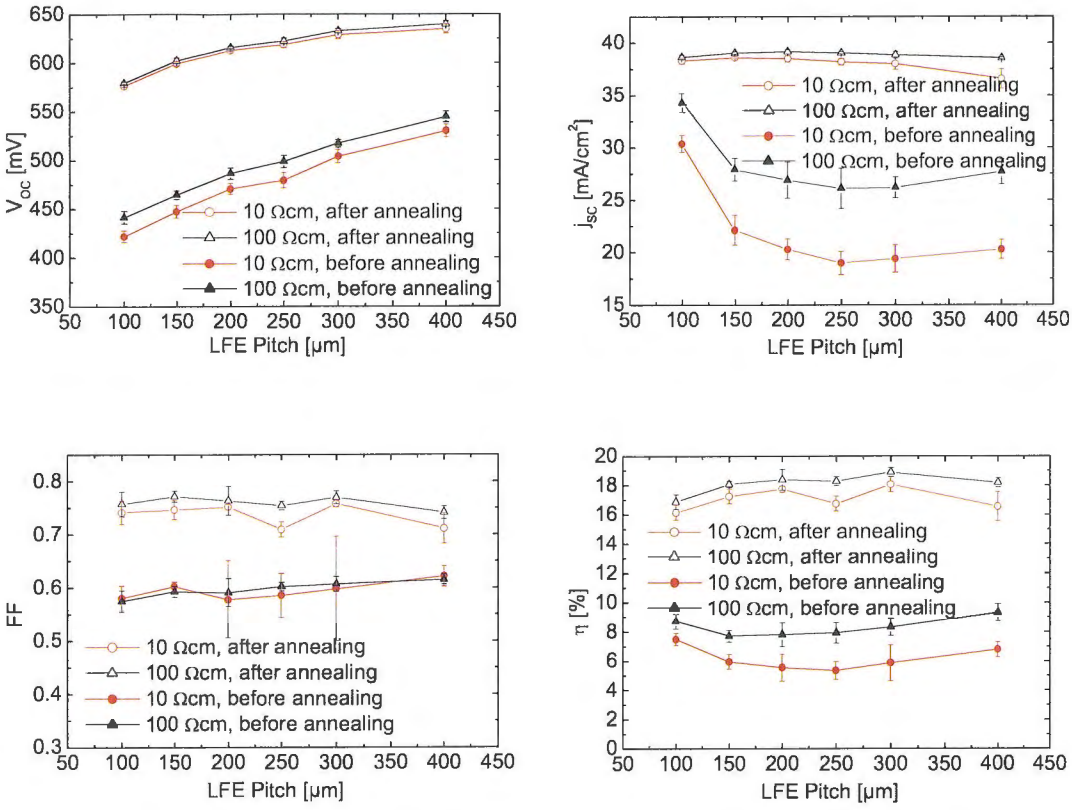


Figure 5-8 Results of the LFE cells processed with different pitch of the laser process. Cell results before and after annealing step are shown. Each data point represents the average of 7-16 cells. Standard deviation of the measurements is also plotted on the graphs.

A pitch of the LFE points in the range between 100 µm and 400 µm was chosen. The minimum pitch of 100 µm allows realization of an almost full area emitter on the rear side (each LFE point is of about 70 µm in diameter). The maximum pitch of 400 µm, on the other hand, is expected to be already too large for a good carrier collection at the back side and therefore lead to strongly reduced performance of the LFE cells. Results of the pitch optimization of the 10 and 100 Ω cm LFE cells are shown in Figure 5-8.

The solar cell parameters before and after the low-temperature (425 °C) annealing are presented. The importance of the annealing to achieve good cell results is clear, as it drastically improves all of the solar cell parameters: open-circuit voltage, short-circuit current, fill factor, and efficiency.

As expected, the cell's voltage improves with increasing pitch, because less damage is introduced by the laser. V_{OC} increased from 575 mV for the pitch of 100 µm to 630 mV for the pitch of 400 µm. Further increase of pitch of the LFE points is expected to lead to further improvement of V_{OC}.

However, with increasing pitch J_{SC} decreases. This is due to the increase of the effective diffusion path for the carriers required to reach the local back junction. When the required diffusion length becomes equal or higher than the effective diffusion length of the carriers, a significant percentage of the minority carriers, which were photogenerated in large lateral distances from the local junction, will recombine before reaching the p-n junction. Detailed analysis of the J_{SC} of the 10 and 100 Ω cm LFE cells shows that the J_{SC} of the 10 Ω cm cells is both lower and decreases more rapidly with the increasing pitch. This is caused by lower diffusion length of the minority carriers in the 10 Ω cm cells compared to 100 Ω cm n-type Si.

The fill factor of the cells is not significantly affected by the pitch in the investigated pitch range. However, a decrease of the FF for the largest pitch of 400 µm can be observed, due to increased lateral series resistance of the LFE cells. The best efficiency of 19.4 % on the 100 Ω cm was realized for the LFE pitch of 300 µm. Both voltage and current of the 100 Ω cm is only slightly better than 10 Ω cm cells, since both cell groups operate under medium- to high- injection and the low-injection conditions do not occur significantly.

5.10 Conclusion

The appealing benefit of the laser-fired p^+ aluminium emitter (LFE) process is the inherent opportunity to create a patterned emitter without additional masking steps. This feature of the LFE process makes it attractive for the application in the back-contact back-junction solar cell structure, where the p^+ emitter is diffused only locally. Therefore, in this chapter the LFE process was investigated and its influence on the solar cell parameters was compared to the solar cells with the traditional boron diffused p^+ emitter.

N-type solar cells with local back-junction were processed on 1, 10 and 100 Ω cm resistivity n-type FZ-Si. Differences in J_{SC} of up to 20 % between 1 and 100 Ω cm

cells were observed. An explanation, based on the experimental and simulation analysis of this effect, was proposed. It is concluded that the injection-dependent Shockley-Read-Hall recombination in the bulk Si and in the laser-induced damage zone determines the LFE cell performance and leads to strong performance differences between cells on different resistivity substrates.

By directly comparing the back-junction cells with LFE and boron diffused emitters, it was shown that the LFE process limits the open-circuit voltage and the short-circuit current of the LFE cells in comparison to the back-junction cells with locally diffused boron emitters. Moreover, due to non-linear behavior of the voltage under low illumination conditions, at the low light intensities the LFE cells will suffer drops in efficiency, whereas the boron diffused cells should remain linear.

Based on the above disadvantages of the LFE emitter formation process, the application of the LFE in the manufacturing of the high-efficiency back-junction solar cells was not further followed in the course of this thesis. On the other hand, if lower device efficiencies are allowed, then it might be interesting to consider the replacement of the boron diffusion by the LFE process in order to reduce the device processing thermal budget and time.

6 Analysis of the loss mechanisms

A detailed analysis of the loss mechanisms in the back-contact back-junction silicon solar cells is presented. Four main loss mechanisms in the BC-BJ solar cells are described: series resistance, optical losses, recombination losses and electrical shading. The influence of each of the loss mechanisms on the cell efficiency is studied. The reduction of the cell efficiency due to the analyzed loss processes was determined to be 3.9 % abs. due to recombination processes, 2.0 % abs. due to optical losses, 0.3 % abs. due to series resistance effects and 0.7 % abs. due to electrical shading.

6.1 Introduction

A back-contact back-junction n-type Si solar cell processed without the use of photolithography with a top efficiency of 21.1 % was developed and demonstrated in the course of this work. In order to better understand the paramcters of the best solar cell and to further optimize the cell design, it is crucial to perform a detailed loss analysis. Therefore, the focus of this chapter is to quantify the main loss mechanisms of the developed solar cells and to analyze their influence on the cell efficiency. The loss mechanisms, such as optical, recombination, and resistance losses are analyzed and discussed in the following sections.

Table 6-1 *Solar cell parameters of the best solar cell demonstrated within this work. The parameters of an ideal solar cell with only the intrinsic loss mechanisms are shown for comparison. Cell thickness (W), pitch and base resistivity (ρ_{base}) are given as well.*

	Cell no	ρ_{base}	W	Pitch	V_{OC}	J_{SC}	FF	η
		[Ω cm]	[µm]	[µm]	[mV]	[mA/cm2]	[%]	[%]
best	BC47-16a	1	160	2200	668	38.6	82.0	21.1
ideal	-	1	160	2200	742	44.0	86.5	28.3

The calculated loss mechanisms limiting device efficiency are compared to the parameters of the best solar cell results achieved experimentally. The best solar cell results were already presented in section 4.5, and are used in this chapter in Table 6-1

for reference. In addition to the experimental results of the best solar cell, the ideal solar cell parameters limited only by intrinsic loss processes are shown in the Table 6-1 as well. The analysis of the intrinsic loss mechanisms in the silicon solar cells, such as radiative and Auger recombination processes and the optical losses due to finite absorption coefficient of the incoming light, were already presented in section 2.4.

6.2 Optical losses

6.2.1 Optical losses in the back-contact solar cell

One of the major advantages of BC-BJ solar cells is the reduction of optical losses due to the absence of the metal finger grid on the front side. This results in a reduction of the front side reflectance and enables an increase of the short-circuit current of this cell type. However, there are still other remaining optical losses in BC-BJ solar cells. These include: (a) primary surface reflectance, (b) escape light, (c) transmission, and (d) parasitic absorption. The parasitic absorption occurs in front side antireflection layers, rear side passivation layers, at the metal contacts and as free-carrier absorption (FCA) in highly doped cell regions (see section 6.2.3 for more details on FCA). All these parasitic absorption effects are non-generating absorption processes and therefore do not contribute to current generation of the solar cell. The analysis of the contribution of each of the optical loss mechanisms to the overall optical losses is the goal of this section.

6.2.2 Modeling of the optical losses

The optical processes which occur in the solar cell, like absorption, reflection, transmission and parasitic absorption, can be simulated with the optical simulation tool *Sunrays* [93]. *Sunrays* is a three dimensional ray tracing program that simulates the optical effects in stack systems of layers with different optical characteristics. It uses a Monte Carlo approach to simulate reflectance, transmission, absorption, and parasitic absorption spectra of the modeled structures. With *Sunrays* it is possible to model optical systems with variable textures and multiple layers. *Sunrays* allows modeling of layers which are varied only vertically. However the BC-BJ solar cells have a strongly two-dimensional structure of the rear cell side. Therefore the modeling of this structure requires a modified simulation approach.

In order to enable simulation of the BC-BJ cell structure with the *Sunrays* program, the analyzed device was split into different, optically one-dimensional unit-cells, as shown in Figure 6-1. Each optical unit-cell was simulated separately. Finally, the individual

optical simulation results of each unit-cell were averaged using area weighted averaging factors. For simplicity reasons of this model, it is assumed that the arrangement of the unit cells is not relevant in this averaging. In reality however it is definitely a more complex problem. With this approach the analysis of the optical effects in different regions of the solar cell is performed.

All of the optical unit-cells (Figure 6-1) have the same optical characteristics on the front surface of the cell and in the bulk of the silicon wafer. The differences among the unit-cells are in the rear surface layer stack systems. The structure of the rear side layers of the chosen unit-cells is as follows:

1. bulk Si / BSF doping / rear passivation layer / Aluminum metallization
2. bulk Si / rear passivation layer
3. bulk Si / emitter doping / rear passivation layer / Aluminum metallization
4. bulk Si / emitter doping / Aluminum metallization
5. bulk Si / emitter doping / rear passivation layer / Aluminum metallization
6. bulk Si / BSF doping / Aluminum metallization

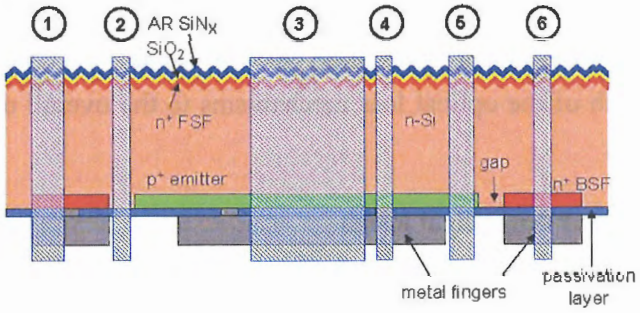


Figure 6-1 Schematic diagram of the different optical unit-cells in back-contact back-junction solar cell structure. Six different optical unit-cells with different rear side structures are shown.

6.2.3 Free carrier absorption

In silicon solar cells there are different light absorption mechanisms. To maximize the conversion efficiency of a photovoltaic device, the desired absorption process is the intrinsic absorption, also called bandgap absorption. In this process, if the energy of the incoming photon is higher than the band gap, then an electron-hole pair can be generated. However, in heavily doped silicon layers, in addition to the bandgap absorption, free carrier absorption (FCA) also occurs. FCA is a process in which the

photon energy is absorbed by free carriers in either conduction or valence bands [143], [144]. In the solar cell the FCA is a parasitic process, which reduces the useful photon flux and reduces the photogenerated current, leading to a reduction in the device's performance. As mentioned above, the FCA process is especially significant in highly doped silicon layers, where the concentration of free carriers is high. The absorption coefficient for the intrinsic silicon and absorption coefficient of the FCA process in highly doped silicon are shown in Figure 6-2. The free carrier absorption coefficient can be calculated using the modeling proposed by Green [121]:

$$\alpha_{FCA} = 2.6\times10^{-18} N_D \lambda^3 + 2.7\times10^{-18} N_A \lambda^2 \tag{6.1}$$

where N_D and N_A are the doping densities of the n- and p-doped region in cm^{-3} respectively and λ is the wavelength in micrometers.

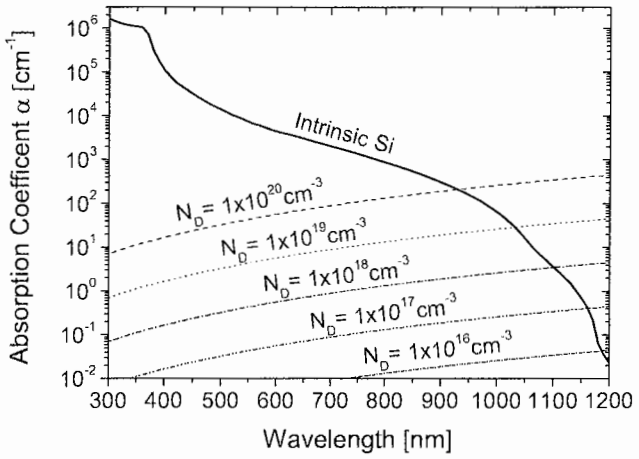


Figure 6-2 Absorption coefficient of intrinsic silicon (thick line) and absorption coefficients of the free carrier absorption process for different donor concentrations (thin lines) calculated with equation (4.1) as a function of wavelength. For the calculated free carrier absorption coefficients, the corresponding donor concentrations are shown.

As can be seen in Figure 6-2, the effect of FCA is especially significant for long wavelengths in the range of 1000 to 1200 nm. In solar cells with good light trapping properties, the light in this wavelength range may pass many times through the wafer thickness and through the highly doped regions at the same time. Thus, the FCA process can significantly contribute to the reduction of the amount of low energy photons available for the photogeneration of electron-hole pairs.

In the *Sunrays*, the FCA process in highly doped cell regions, such as front surface field, back surface field, and emitter doping is not taken into account. In order to analyze the influence of this effect on the optical losses of the BC-BJ cell, an additional layer on the back cell side, possessing the refractive index (n) of silicon, but an absorption coefficient (α_{FCA}) calculated with equation (4.1), was introduced.

6.2.4 Distribution of optical losses

The resulting simulation spectra of reflectance and transmission for a BC-BJ solar cell are shown in Figure 6-3. The experimental results are shown as well. A good agreement between the measured and simulated results indicates that the simulation approach, introduced in the previous section, allows a good description of the device. Note that the reflection is nearly zero at a wavelength of 500 to 600 nm due to the absence of the front side metallization. Another important feature of the analyzed device is the non-zero transmission at long wavelength ranges. Transmission of 5-10 % at 1200 nm is caused by the not fully metalized rear surface. The interdigitated metallization grid covers around 60 % of the rear cell surface. The remaining 40 % of the rear surface is not covered with metal. Therefore the weakly absorbed light can pass through the cell without being absorbed.

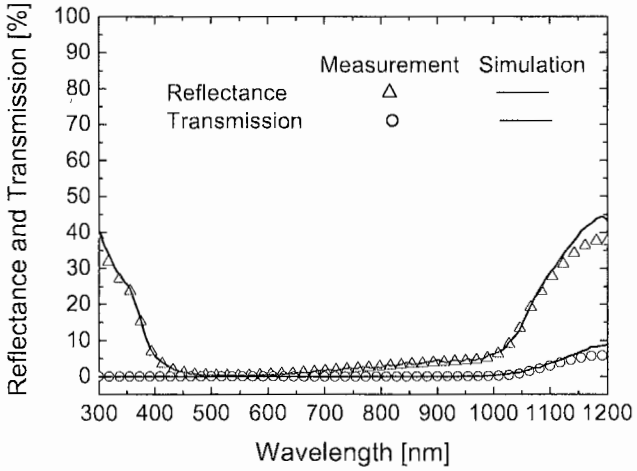


Figure 6-3 Measured and simulated reflectance and transmission spectra of a back-contact back-junction cell with a pitch of 2200 µm and base resistivity of 1 Ω cm. The simulated reflectance shows good agreement with the measured data. The measurements were done using an integrating sphere set-up.

According to the optical simulations of the device, the maximal short-circuit current density $J_{SC,opt}$ of 41.1 mA/cm^2 can be generated assuming no recombination and

resistance losses. By comparing the ideal short-circuit current ($J_{SC,ideal}$) shown in Table 6-1 with the $J_{SC,opt}$, a loss in short-circuit current due to the non-intrinsic optical loss mechanisms ($J_{opt,loss}$) can be determined. For a BC-BJ solar cell with 1 Ω cm base resistivity and thickness of 160 µm under AM1.5g illumination, the $J_{opt,loss}$ is 2.93 mA/cm^2.

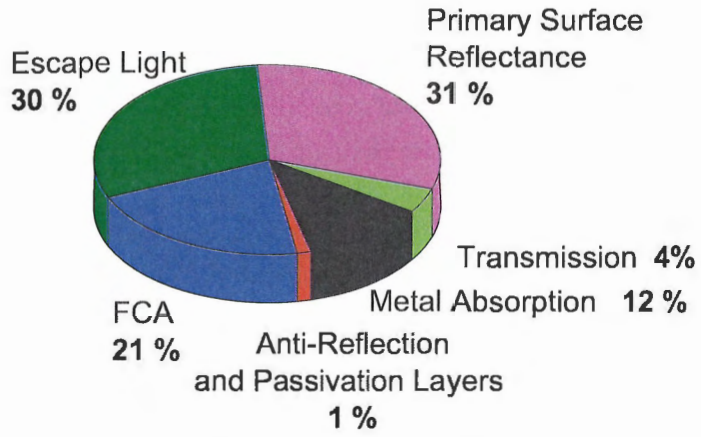


Figure 6-4 Distribution of the modeled optical loss mechanisms in BC-BJ cells with pitch 2200 µm and 1 Ωcm base resistivity under AM1.5g illumination with 0.1 W/cm². Note the significant influence of the free carrier absorption caused by the presence of the highly doped emitter and BSF regions.

In order to quantify the effect of every single layer and process, two simulations are required: one with normal absorption coefficients of every layer, and the other one with an absorption coefficient of a specific layer set to zero for all wavelengths. The difference of the two spectra equals the parasitic absorption in the specific layer. Figure 6-4 shows the modeled distribution of the optical loss mechanisms in the BC-BJ solar cell. The largest loss mechanism is the primary surface reflectance, which accounts for 31 % of all optical losses. The primary surface reflectance is caused by the non-optimal properties of a single layer antireflection coating. The second largest contribution to the optical losses is the escape light (30 %). Escape light is a result of non-ideal light trapping, where light rays are reflected out of the cell after multiple internal reflections in the cell. The next largest loss mechanisms are the free-carrier absorption (21 %) in the highly doped emitter and BSF regions and absorption in the metal layer (12 %). The influence of the FCA process is significant and caused by the large coverage of the highly doped regions (BSF, emitter) on the rear cell side and very good light trapping properties, which result in multiple passes of the long wavelength

light through the highly doped regions. The impact of transmission (4 %) and absorption in antireflection and passivation layers (1 %) is only minor.

One remark about the optimization of the optical device design has to be made. The reduction of one of the optical loss mechanisms will not lead to the increase of the generated photocurrent by the same amount. The increase in J_{SC} will be smaller, because the gain resulting from reduction of one of the optical loss mechanisms will be partially distributed between the other optical loss effects. For example, the replacement of the partial metal coverage on the rear cell side with full area aluminum would lower the transmission losses to zero. However, the reduction of transmission losses will result in the increase of the parasitic absorption in the aluminum.

Table 6-2 *Modeled reduction of the solar cell parameters due to optical losses, for a 160 μm thick n-type BC-BJ cell with pitch of 2200 μm and 1 Ωcm base resistivity under AM1.5g illumination with intensity of 0.1 W/cm². The influence of non-intrinsic recombination losses and series resistance losses were not included in the modeling.*

		Limit imposed by	
		intrinsic losses	optical losses
J_{SC}	[mA/cm²]	44.0	41.1
V_{OC}	[mV]	742.5	741.3
FF	[%]	86.5	86.5
η	[%]	28.3	26.3
Δη	[%]		**-2.0**

6.2.5 Influence of optical losses on the cell efficiency

Optical losses reduce the amount of the photo-generated electron-hole pairs, which mainly reduces the short-circuit current density. However, a reduction of J_{SC} causes a reduction in the open-circuit voltage and the fill factor as well. The effect of the reduced V_{OC}, FF and efficiency can be calculated similarly to the calculations made in section 2.4, using the equations below:

$$J(V) = J_{SC,opt} - qWU_{rec,\text{int}} \tag{6.2}$$

$$\Delta\eta_{opt} = \eta_{opt} - \eta_{\text{int}} \tag{6.3}$$

$J_{sc,opt}$ is the short-circuit current density modeled considering the optical losses. The recombination and resistive losses are not taken into account in this calculation. η_{opt} is the cell efficiency limit imposed by the intrinsic recombination and optical losses and non-intrinsic optical losses calculated with equation (6.2). $\Delta\eta_{opt}$ is the reduction in the cell efficiency due to optical losses. The influence of the non-intrinsic optical losses on the solar cell parameters is summarized in Table 6-2. In the device analyzed, the optical losses cause 2.0 % absolute efficiency loss.

6.3 Recombination losses

6.3.1 Modeling of the saturation current densities

The non-intrinsic recombination losses include the surface recombination, the Auger recombination in highly doped regions of the solar cell, the bulk recombination, and the recombination at metal-semiconductor contacts. Each of the recombination processes can be described by its individual value of the saturation current density J_0. The total saturation current density of the solar cell can then be calculated as an area-weighted sum of the saturation current densities of the different cell regions.

The saturation current densities of the highly doped regions (emitter, BSF) for both passivated and metalized case were taken from the literature. The references used for different doping types are listed in Table 6-3. The published values of J_0 for highly doped regions with different sheet resistance were fitted. According to the fit function, the J_0 values for the sheet resistance of the doping profiles applied in the analyzed cell structure were calculated.

The saturation current densities of the bulk [145] and the gap regions can be calculated analytically by using the equations (3.2) and (6.5) respectively:

$$J_{0,Bulk} = \frac{qWn_i^2}{N_{Bulk}\tau_{Bulk}} \tag{6.4}$$

$$J_{0,Gap} = \frac{qn_i^2 S_{Gap}}{N_{Bulk}} \tag{6.5}$$

where n_i is the intrinsic carrier concentration, N_{base} is the doping density of the bulk, τ_{bulk} is the lifetime of the minority carriers in the bulk and S_{Gap} is the surface recombination velocity of the gap region. S_{Gap} was calculated according to the model of Cuevas et al. [94] and for a base doping of N_{base}=5×10^{15} cm^{-3}, which corresponds to base resistivity of 1 Ω cm, thus S_{Gap}= 70 cm/s. The saturation current density of the

front surface field doping was experimentally determined in section 7.3. Therefore, the experimental result for $J_{0,FSF}$ obtained in this work was applied here.

The area weighted results are summarized in Table 6-3. The total saturation current density of the solar cell equals 227 fA/cm^2. The largest contribution is due to passivated and metalized emitter doping, which account for 47.1 % of the total J_0. Such a high emitter saturation current contribution is caused by the large coverage of the emitter on the rear cell side and high doping level of the emitter profile. The relatively small contribution of the highly recombinative contacted areas is caused by the very small area coverage of the metal-semiconductor contacts, which totals 5 % for both contact polarities.

Table 6-3 *Modeled saturation current densities and their contributions to the overall J_0. Calculations were made for an n-type BC-BJ cell with 1 Ωcm base resistivity and 148 Ω/□ sheet resistance of the FSF. The saturation current densities were area weighted proportionally to their coverage on respective surfaces. Literature sources for the saturation current densities are given. J_0 values were calculated for $n_i=1\times10\ cm^{-3}$ and T=25°C.*

	Reference	Area weighted J_0 [fA/cm^2]	Fraction of $J_{0,total}$ [%]
Boron Emitter (passivated)	[95], [85], [146]	98	43.3
Boron Emitter (metallized)	[85]	8.6	3.8
Phosphorus BSF (passivated)	[147], [148]	30	13.1
Phosphorus BSF (metallized)	[147]	7	2.9
Bulk	[145]	26	11.3
Gap regions	[94]	37	16.4
Phosphorus FSF (passivated)	this work	21	9.2
$J_{0,total}$		**227**	**100**

6.3.2 Influence of recombination losses on the short-circuit current

A general analysis of the influence of the two most important parameters of the back-junction solar cell structure, namely the front surface recombination S_{front} and the diffusion length of the carriers L, on the short-circuit current was already presented in section 2.3. Here the specific calculations of the J_{SC} losses due to measured S_{front} and L are presented. The 1-dimensional expression for the short-circuit current of the back-junction solar cell structure in the case of n-type base doping and monochromatic illumination with light of absorption coefficient α is given by [149]:

$$J_p(\alpha) = qF_{ph}(1-R)\left(\frac{\alpha L_p}{\alpha^2 L_p^{\,2}-1}\right)\cdot \left[\frac{\left(\frac{S_{front}L_p}{D_p}+\alpha L_p\right)-e^{-\alpha W}\left[\frac{S_{front}L_p}{D_p}\cosh\left(\frac{W}{L_p}\right)+\sinh\left(\frac{W}{L_p}\right)\right]}{\frac{S_{front}L_p}{D_p}\sinh\left(\frac{W}{L_p}\right)+\cosh\left(\frac{W}{L_p}\right)}-\alpha L_p e^{-\alpha W}\right] \tag{6.6}$$

where J_p is the hole current density, q the elementary charge, D_p the electron diffusion coefficient, F_{ph} the incident monochromatic photon flux density, R is the reflection coefficient, S_{front} is the front surface recombination velocity, L_p is the hole diffusion length, W is the wafer thickness. Integration of J_p for the whole light spectrum results in a short-circuit current density as a function of L_p and S_{front}.

Table 6-4 *Influence of the non-perfect collection efficiency of the carriers in on the short-circuit current density of the back-junction solar cell structure. J_{SC} losses due non-zero front surface recombination velocity and finite carrier lifetime was calculated for S_{front}=6.6 cm/s, τ_{bulk}=1 ms, ρ_{base}=1 Ω cm, W=160 µm.*

τ_{bulk} [ms]	S_{front} [cm/s]	J_{SC} [mA/cm^2]	ΔJ_{SC} [mA/cm^2]
∞	0	41.1	-
1	0	40.6	-0.5
∞	6.6	40.8	-0.3
1	6.6	40.3	**-0.8**

Using the equation (6.6) and the light absorption simulated with *Sunrays* as described in section 6.2.2, the short-circuit current losses due to non-zero recombination at the front surface and due to finite bulk lifetime of the carriers were calculated. Calculations were performed for base resistivity of 1 Ω cm, wafer thickness of 160 µm, S_{front}=6.6 cm/s was calculated using equation (6.7) and the measured saturation current density of the front surface field $J_{0,FSF}$=21 fA/cm^2 as shown in Table 6-3.

$$S_{front} = \frac{J_{0,FSF} N_{Bulk}}{q n_i^2} \tag{6.7}$$

The carrier lifetime in bulk τ_{bulk}=1 ms was assumed. The results are summarized in Table 6-4. The finite carrier lifetime causes 0.5 mA/cm^2 loss in J_{SC}. The non-zero front surface recombination results in another 0.3 mA/cm^2 loss in J_{SC}. Together both effects lead to 0.8 mA/cm^2 loss in J_{SC} and the maximal short-circuit current, resulting from optical and recombination losses ($J_{SC,rec}$), equals 40.3 mA/cm^2.

6.3.3 Influence of recombination losses on cell efficiency

The effect of the modeled saturation current densities on the open-circuit voltage and the cell efficiency can be calculated with the one-diode model:

$$J(V) = J_{SC,rec} - J_{0,total}\left(e^{qV/kT} - 1 \right) \tag{6.8}$$

Where $J_{SC,rec}$ is the maximal short-circuit current resulting in optical and recombination losses. The influence of the $J_{0,total}$ on the V_{OC} can be calculated by transforming the one-diode equation:

$$V_{OC} = \frac{kT}{q} \ln\left(\frac{J_{SC,rec}}{J_{0,total}} + 1 \right) \tag{6.9}$$

A good agreement between the analytically determined and measured V_{OC} can be observed. The open-circuit voltage calculated with equation (6.9) for T=25°C equals 666.3 mV. This result is very close to the V_{OC} of the best solar cell, which as shown in Table 6-1 equals 668 mV.

When the total saturation current density $J_{0,total}$ is determined, it is possible to calculate the influence of the recombination losses on the efficiency of the solar cell. Two calculations are needed. First, the efficiency limit (η_{opt}) due to intrinsic recombination losses and due to optical losses needs to be calculated (as shown in previous section).

Secondly, using equation (6.8), the efficiency limit imposed by non-intrinsic recombination losses (η_{rec}) can be determined. The difference between both efficiency limits is the efficiency reduction, which is caused only by the non-intrinsic recombination losses:

$$\Delta\eta_{rec} = \eta_{rec} - \eta_{opt} \tag{6.10}$$

where $\Delta\eta_{rec}$ is the reduction of the cell efficiency caused by the non-intrinsic recombination processes. The influence of the non-intrinsic recombination processes on the solar cell parameters is summarized in Table 6-5. The non-intrinsic recombination losses are causing an efficiency loss of 3.8 % absolute. However, it should be noted that the influence of the recombination losses in form of electrical shading on the short circuit current was not taken into account here. The influence of electrical shading losses on the short-circuit current was determined experimentally in section 6.4.

Table 6-5 Modeled reduction of the cell parameters caused by the non-intrinsic recombination processes for the BC-BJ cell of this thesis with pitch 2200 µm and 1 Ω cm base resistivity under AM1.5g illumination.

		Limit imposed by	
		intrinsic and optical losses	recombination losses
J_{SC}	[mA/cm^2]	41.1	40.3
V_{OC}	[mV]	741.3	666.3
FF	[%]	86.5	84.1
η	[%]	26.3	22.5
$\Delta\eta$	[%]		**-3.8**

6.4 Electrical shading

6.4.1 Increased lateral transport distance for the minority carriers

In back-contact solar cells, optical shading losses of the metallization grid can be avoided. However, electrical shading losses [150], [87] are still present due to the large

lateral dimensions on the rear cell side and due to the increased recombination rate in the regions of base busbar and base. The impact of this recombination on V_{OC} was already modeled in the previous section. In this section the impact of electrical shading on J_{SC} losses will analyzed. In Figure 6-5, a symmetry element of the BC-BJ solar cell is shown schematically. For the minority carriers that were photogenerated far away form the p-n junction, the large lateral dimensions of the BSF and non-diffused gap regions increase the required diffusion length before reaching the emitter. If the lateral dimensions of the base areas on the rear side are too large, or if the minority carrier lifetime is too low, then the carriers generated far away from the emitter may recombine before reaching the emitter. This results in a reduction of the quantum efficiency in the rear side regions of the solar cell that are not covered by an emitter.

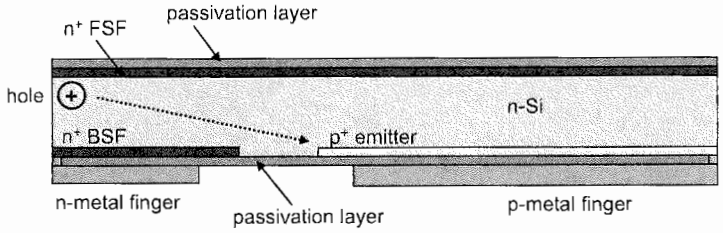


Figure 6-5 *Increased lateral diffusion path for the minority carriers which were photogenerated far away from the p-n junction can lead to the recombination of these carriers before reaching the emitter. A symmetry element of the BC-BJ solar cell is shown.*

6.4.2 Light beam induced current mapping

A light beam induced current (LBIC) [133] map of the 2×2 cm^2 laboratory solar cell is presented in Figure 6-6. One can clearly recognize the reduced EQE signal over the base fingers and busbar. The EQE drops down to nearly zero above the base busbar, even though no optical shading in this region is present. This effect is caused by (a) large lateral distances which the minority carriers need to diffuse in order to be collected by the p-n junction and (b) by the enhanced recombination over the gap and BSF areas which have high saturation current densities.

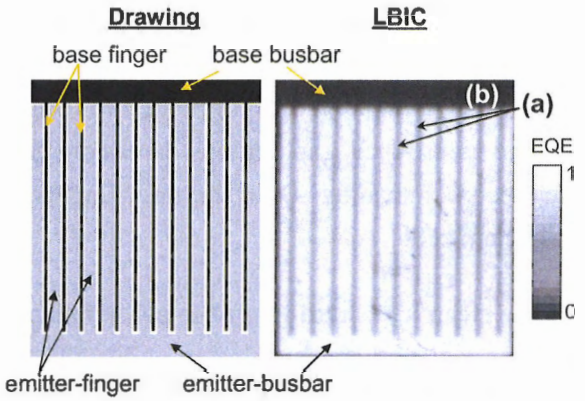


Figure 6-6 *Sketch (left) and LBIC map (right) of the rear side of the BC-BJ silicon solar cell. The reduced EQE signal above the base fingers (a) and base busbar (b) are visible. The active cell area is 2x2 cm^2 and the busbar area is 0.15x2 cm^2.*

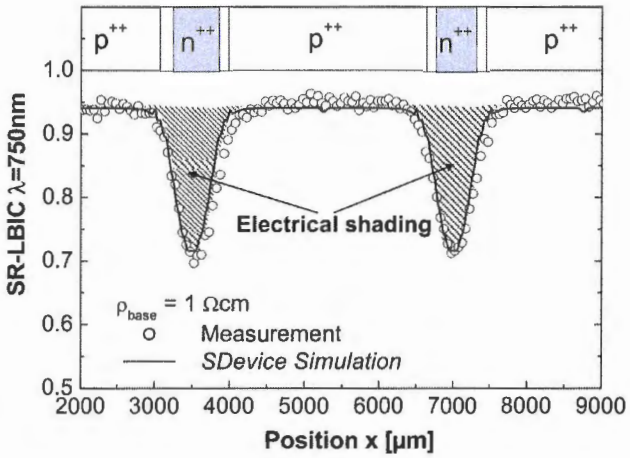


Figure 6-7 *Measured and simulated external quantum efficiency line scans of a BC-BJ solar cells with 1 Ωcm base resistivity and a pitch of 3500 µm. Line scans were measured perpendicular to the p-n grid. The width of the p^{++} (emitter) diffusion and the n^{++} (BSF) diffusion are shown in the graph. The EQE was measured at a wavelength of 750 nm. The influence of electrical shading on the quantum efficiency is marked with thin lines.*

6.4.3 LBIC line scans

In order to quantify the influence of the electrical shading over the base fingers (gap and BSF areas) on the solar cell efficiency, light beam induced current (LBIC) line scans were measured perpendicular to the p-n grid at a wavelength of 750 nm. The results are shown in Figure 6-7. A solar cell with a base resistivity of 1 Ω cm was

measured. The pitch of the cell analyzed was 3500 μm. The width of the p^{++} (emitter) diffusion and the n^{++} (BSF) diffusion are shown in the graph. Next to the measured LBIC signal, the 2D device simulation results are plotted in the graph. The EQE drops down above the BSF and undiffused gap regions (areas marked with thin lines in Figure 6-7) due to the electrical shading. Over the base fingers, the EQE drops from 0.95 down to 0.70 for 1 Ω cm cells.

6.4.4 Influence of the electrical shading on the cell efficiency

In order to determine the influence of the electrical shading losses on the solar cell's efficiency, the LBIC line scans shown in Figure 6-7 were integrated. The LBIC signal reduction over the base doping causes a 3.3 % absolute reduction of internal quantum efficiency for $\rho_{base} = 1\ \Omega$ cm. By making a simplified assumption that the electrical shading is equal for all wavelengths in the absorbed light spectrum, the short circuit current loss of 1.4 mA/cm^2 caused by electrical shading can be assumed. The maximal J_{SC} reduces from 40.3 to 38.9 mA/cm^2. The resulting efficiency loss caused by the reduction of J_{SC} equals 0.7 % absolute. Thus, the minority carrier recombination in the area of the rear side BSF and undiffused gap causes a significant efficiency loss in the analyzed device. Novel structures of a back-contact back-junction solar cells is which the electrical shading losses can be significantly reduced or even eliminated were recently proposed by Harder et al. [151] and Granek et al. [152].

6.5 Resistive losses

6.5.1 Modeling of series resistance losses

The series resistance (R_S) of BC-BJ solar cells can be described analytically by a network of several resistance elements connected in series as shown in Figure 6-8. The analyzed solar cells operate close to high-injection or under high-injection at maximum power point (MPP) conditions. Therefore both carrier types have to be included in the analysis of the series resistance.

In Figure 6-8, the extreme case for an electron and a hole is shown, where the lateral distance to the metal contacts is at a maximum. The resulting model is a quasi-one-dimensional model of the series resistances in the BC-BJ solar cell. This model is built of the lateral and vertical resistances in the bulk, the lateral resistance of the emitter and the back surface field, the metal-semiconductor contact resistances, and the resistance of the metallization fingers and busbar. The influence of the front n^+ diffused layer on the lateral current transport of the majority carriers was taken into account as parallel resistances to the base lateral resistance. A detailed analysis of the

influence of the front n^+ diffused layer on the lateral current transport is given in chapter 8. The descriptions of the individual resistance elements, as shown in Figure 6-8, are given in Table 6-6. The resistance of the individual resistance elements was calculated similarly to the series resistance model of the concentrator BC-BJ solar cells described in [35].

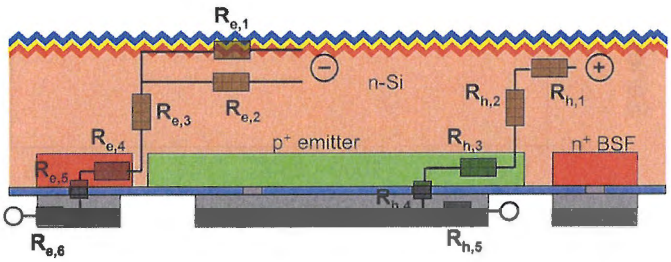


Figure 6-8 *Schematic diagram of the series resistance elements in BC-BJ solar cell that contribute to the analytical resistance model. The influence of the front surface field on the minority carriers (holes) lateral current transport was modeled using a parallel connection of lateral base and front surface field resistances.*

Table 6-6 *Explanation of the resistance symbols used in the quasi-one-dimensional resistance model shown in Figure 6-8.*

electrons		holes	
$R_{e,1}$	lateral FSF resistance	$R_{h,1}$	lateral base resistance
$R_{e,2}$	lateral base resistance	$R_{h,2}$	vertical base resistance
$R_{e,3}$	vertical base resistance	$R_{h,3}$	lateral emitter resistance
$R_{e,4}$	lateral BSF resistance	$R_{h,4}$	p-contact resistance
$R_{e,5}$	n-contact resistance	$R_{h,5}$	p-metal finger resistance
$R_{e,6}$	n-metal finger resistance		

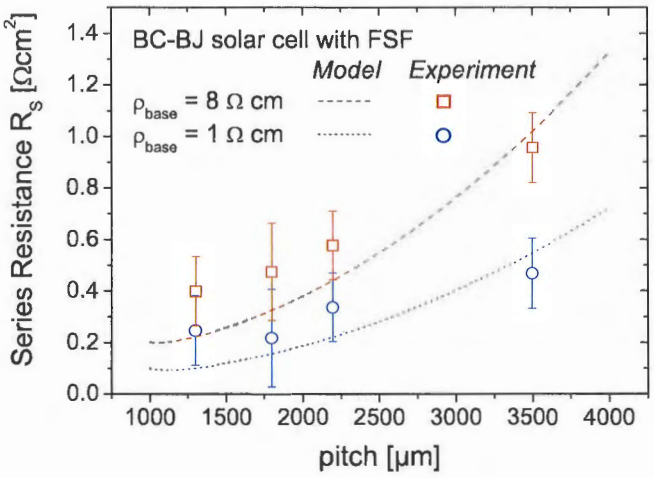


Figure 6-9 *Series resistance of the BC-BJ solar cells with FSF (ρ_{sheet} = 148 Ω/□) and base resistivity of 1 and 8 Ωcm for different pitches. Analytical modeling results (lines) and the experimentally determined series resistance (points) together with the error bars are shown. The conductivity modulation in the base under the maximum power point was taken into account. The size of the solar cells was 2×2 cm^2.*

The series resistance of the BC-BJ solar cells calculated analytically, using the series resistance model presented above, was compared to the experimentally determined series resistance of the processed solar. The series resistance of the fully processed solar cells was determined by comparing the SunsV_{OC} curve [153] with the one-sun IV-curve. For more details on this method to determine series resistance, see for example Ref. [154]. The analytical and experimentally determined series resistance of the BC-BJ solar cells with different base resistivity and pitch are shown in Figure 6-9. A good agreement between the analytical model and experimental data can be observed, proving the accuracy of the analytical model. The increase of R_S with increasing pitch is caused by a strong increase of the lateral base resistance with increasing pitch. See chapter 8 for more details on lateral base resistance issues.

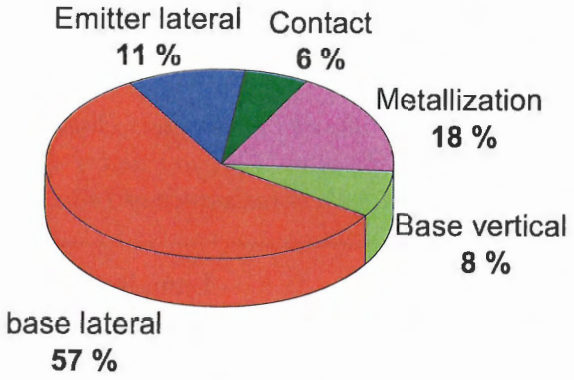


Figure 6-10 Distribution of the modeled series resistance in BC-BJ cells with pitch of 2200 µm, sheet resistance of the FSF of 148 Ω/□ and 1 Ω cm base resistivity. A solar cell with a size of 2×2 cm² was modeled. The total series resistance equals 0.18 Ω cm².

The distribution of the series resistance components in a BC-BJ cell with 1 Ω cm base resistivity, front surface field ($\rho_{FSF,sheet}$ = 148 Ω/□) and pitch of 2200 µm is shown in Figure 6-10. The lateral base resistance is the dominat resistance loss mechanism, contributing to 57 % of the total series resistance. The impact of lateral base resistance is very high due to the large lateral current transport distances required in the solar cell with a pitch of 2200 µm. A smaller pitch would decrease the lateral paths of the charge carriers and therefore reduce the lateral base resistance. It would be difficult, however, to decrease the pitch while using the low cost structuring technology. The impact of the metal fingers equals only 18 %, due to the small finger length in the cell size of 2×2 cm². The contribution of the metallization losses to the total series resistance will increase with an upscaling of the cell design to the production standard sizes of 12.5×12.5 cm² or larger. The total series resistance equals 0.18 Ω cm².

6.5.2 Influence of series resistance losses on cell efficiency

The series resistance causes a reduction of voltage at the maximum power point and therefore reduces the fill factor of the solar cell. The effect of the reduction of FF caused by R_S can be described using an approximation proposed by Green [4]:

$$FF_{Rs} = FF_{rec}\left(1 - R_S \frac{J_{SC}}{V_{OC}}\right) \tag{6.11}$$

where FF_{Rs} is the fill factor resulting from series resistance, optical and recombination losses, FF_{rec} is the fill factor limit imposed by the optical and recombination losses, not affected by resistance losses, R_S is the series resistance given in Ω cm², J_{sc} is the short-

circuit current density limited by the optical losses, and V_{OC} is the reduced open-circuit voltage limited by optical and recombination losses.

Table 6-7 Modeled reduction of the cell parameters caused by the series resistance for a BC-BJ cell with pitch 2200 µm and 1 Ωcm base resistivity and front surface field with sheet resistance of 148 Ω/□.

		Limit imposed by	
		intrinsic, optical and recombination (including electrical shading) losses	resistance losses
J_{SC}	[mA/cm^2]	38.9	38.9
V_{OC}	[mV]	666	666
FF	[%]	84.1	83.0
η	[%]	21.8	21.4
Δη	[%]		**-0.3**

Due to the low value of the series resistance, its influence on the short-circuit current was not taken into account. The reduction of the solar cell parameters resulting from the influence of the series resistance is summarized in Table 6-7. Series resistances of 0.18 Ω cm^2 causes fill factor loss of 1.1 % absolute; in this case, this results in a efficiency reduction of 0.3 % absolute.

6.6 Adding up the individual loss mechanisms

The presented model gives an overview of the different loss mechanisms in the back-contact back-junction solar cell structure developed in this work. The main results of the modeled solar cell efficiency are schematically shown in Figure 6-11 and summarized in Table 6-8. The evolution of the calculated current-voltage characteristics of the solar cell structure after stepwise introduction of the different loss mechanisms is presented in Figure 6-12.

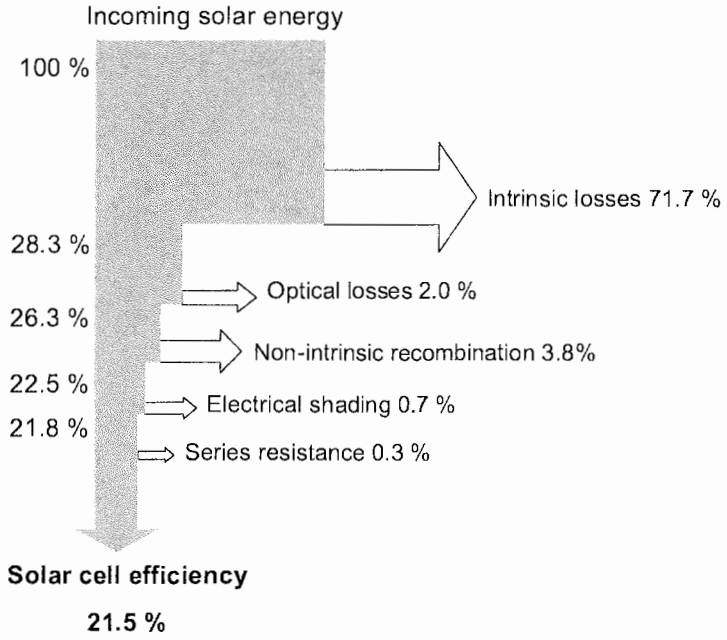


Figure 6-11 Schematic drawing showing the influence of different loss mechanisms on the reduction of the efficiency of the analyzed back-contact back-junction solar cell.

As can be seen in Table 6-8, a very good agreement between the modeled solar cell parameters and the experimental results of the best solar cell can be observed, proving the accuracy of the developed model. Both the modeled short-circuit current and the modeled open-circuit voltage are very close to the measured solar cell parameters. A slightly higher modeled fill factor may be a result of the fact that the edge effects, shunt resistance losses and the recombination in the space charge region were not taken into account in the calculations. These effects have a detrimental influence on the fill factor, thus introduction of these effects into modelling could result in a lower fill factor, with values closer to the measured one. The modelled overall cell efficiency equals 21.5 %, which is very close to the efficiency of the best solar cell (21.1 %).

The presented model is a powerful tool for the further optimization study of the solar cell structure. Improving the solar cell optics, reduction of the overall recombination losses and minimization/elimination of the electrical shading could enable reaching a solar cell efficiency of above 23 %.

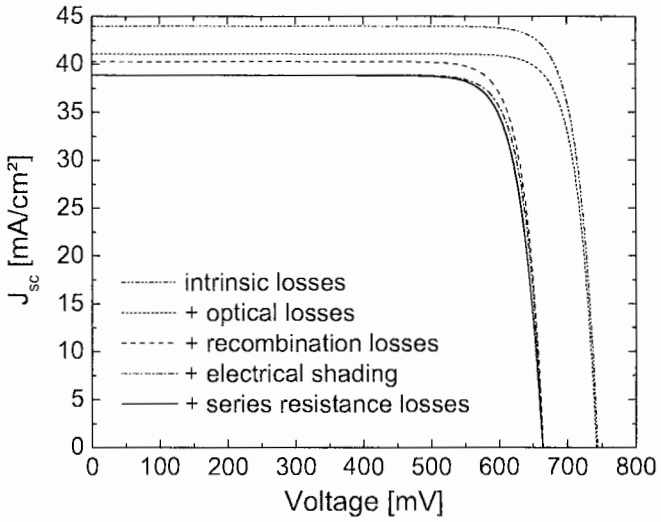


Figure 6-12 Evolution of the current-voltage characteristics of the analyzed BC-BJ solar cell structure after introduction of the different loss mechanisms.

Table 6-8 Summary of the modeled cell parameters of a 160 µm thick n-type BC-BJ silicon solar cell with pitch of 1800 µm, base resistivity of 1 Ω cm and the FSF with sheet resistance of 148 Ω/□. The influence of different loss mechanisms on the solar cell parameters is shown. The results of the best experimental solar cell are shown for comparison.

Parameter	Unit	Intrinsic losses	+Optical losses	+Non-intrinsic recombination losses	+Electrical shading losses	+Series resistance losses	Best measured solar cell
J_{SC}	mA/cm^2	44.0	41.1	40.3	38.9	38.9	38.6
ΔJ_{SC}	mA/cm^2	-	-2.9	-0.8	-1.4	0.0	
V_{OC}	mV	742	741	666	666	666	668
ΔV_{OC}	mV	-	-1	-75	0	0	
FF	%	86.5	86.5	84.1	84.1	83.0	82.0
ΔFF	%	-	0.0	-2.6	0.0	-0.91	
η	%	28.3	26.3	22.5	21.8	21.5	21.1
Δη	%	-	-2.0	-3.8	-0.7	-0.3	

6.7 Conclusions

A detailed study of loss mechanisms limiting the efficiency of the back-contact back-junction silicon solar cell developed in this work was presented. The analytical model included the intrinsic, optical, recombination and resistance losses occurring in the actual cell design. The experimental analysis of the electrical shading losses was also introduced to the modeling of the overall solar cell characteristics.

A very good agreement between the modeled solar cell parameters and the experimental results of the best solar cell was obtained, proving the accuracy of the developed model. The main loss sources in the analyzed solar cell structure are the recombination losses, accounting for the absolute efficiency loss of 3.8 %; the optical losses, which cause 2.0 % absolute efficiency loss; and the electrical shading, which causes 0.7 % absolute efficiency loss. Altogether, the analyzed loss mechanisms reduce the solar cell efficiency by 6.8 % absolute from 28.3 % to 21.5 %.

The presented model is a powerful tool for the further optimization study of the solar cell structure. The performed analysis showed that improving the solar cell optics, reduction of the overall recombination losses, and minimization of the electrical shading could enable reaching the solar cell efficiency of 23 %.

7 Front surface passivation using a front surface field

The passivation quality of different phosphorus-doped front surface field diffusion profiles was analyzed. J_{0e} values of different FSF diffusion profiles determined under low and high injection are in a good agreement. The presence of the random pyramids texture increased the J_{0e} by a factor of 1.3 to 1.7. The best solar cell efficiency of 20.8 % was obtained with a deep diffused Gaussian profile of the FSF. Increased doping concentration and depth of the FSF diffusion reduced J_{SC} and V_{OC} of the analyzed cells. The lifetime samples and the solar cells with FSF diffusion are stable under UV exposure in opposition to test structures and solar cells without FSF. The regeneration of the performance of the solar cells without FSF after degradation under UV exposure is possible by a forming gas anneal.

7.1 Introduction

Due to the fact that the p-n junction is placed on the rear surface of the back-contact back-junction solar cells developed and analyzed in the frame of this work, the requirements on the front surface passivation of this cell type are very high. Most of the photo-generation occurs close to the front surface, where the carriers can easily be lost by recombining at a poorly passivated surface. Thus, a low front surface recombination (S_{front}) is one of the critical factors influencing the efficiency of the back-junction cell type. The importance of the high quality of the front surface passivation in the case of the back-junction solar cells was already presented in more details in section 2.3. In the present chapter the quality of the front surface field passivation and its influence on the solar cell stability with respect to ultraviolet light is studied.

7.1.1 Surface recombination

The crystal lattice is severely disturbed at the surface. This results in a large density of the non-saturated bonds, also called 'dangling' bonds. Moreover at the surface the material defects related processing technology such as residues of chemicals and metals depositions are present. At the crystal surface these effects result in a high density of surface states within the bandgap, which cause surface recombination.

In this section the fundamentals of surface recombination are given following Aberle [155]. The recombination rate U_S via a single-level surface state, which is located at an energy E_t, is described by the Shockley-Read-Hall (SRH) theory [77], [78]:

$$U_S = \frac{n_S p_S - n_i^2}{\frac{n_S + n_1}{S_{p0}} + \frac{p_S + p_1}{S_{n0}}} \tag{7.1}$$

with

$$\begin{aligned} n_1 &= n_i \exp\left(\frac{E_t - E_i}{kT}\right), \qquad p_1 = \frac{n_i^2}{n_1}, \\ S_{n0} &= \sigma_n \upsilon_{th} N_{st}, \qquad S_{p0} = \sigma_p \upsilon_{th} N_{st} \end{aligned} \tag{7.2}$$

n_S and p_S are the electron and hole concentrations at the surface, S_{n0} and S_{p0} are the surface recombination velocity parameters of electron and holes, σ_n and σ_p are the capture cross sections for electrons and holes, N_{st} is the number of surface states per unit area, E_i is the intrinsic Fermi energy, n_i is the intrinsic carrier density, υ_{th} is the thermal velocity of the charge carriers, k is the Boltzman constant, T is the temperature.

The surface recombination velocity S is defined as $U_S = S\Delta n$, with Δn being the excess carrier density at the surface. In the case of the equal excess densities of electrons and holes at the surface ($\Delta n_S = \Delta p_S$), S can be expressed as [149] :

$$S(\Delta n_S) = \frac{n_0 + p_0 + \Delta n_S}{\frac{n_0 + n_1 + \Delta n_S}{S_{p0}} + \frac{p_0 + p_1 + \Delta n_S}{S_{n0}}} \tag{7.3}$$

Thus, the surface recombination velocity is also influenced by the injection level at the surface (Δn_S) and by the wafer doping (n_0 and p_0).

For the recombination velocity of the p-n junctions and high-low junctions, an effective surface recombination velocity S_{eff} can be defined at a virtual surface. This virtual surface is positioned at the edge of the surface space charge region, located at $x=d$:

$$S_{eff} = \frac{U_S}{\Delta n(x = d)} \tag{7.4}$$

The quality of the emitter or the highly diffused region is expressed using the emitter saturation current density J_{0e}. The relation between S_{eff} and J_{0e} for n^+ diffused regions equals:

$$S_{eff} = \frac{J_{0e}(N_A + \Delta n)}{qn_i^2} \tag{7.5}$$

7.1.2 Surface passivation methods

Analysis of the SRH theory of the surface recombination defined with equation (7.1) indicates that there are two ways to reduce the recombination rate at the silicon surface:

1. The surface recombination rate is proportional to the defect density at the surface (see equation (7.1)). Thus, it is beneficial to reduce the density of the surface states, what can be technologically achieved by growth or deposition of passivation layers. The most widely used examples of the passivation layers in silicon solar cell technology are the thermally grown silicon oxide (SiO_2) and silicon nitride (SiN_X) deposited using the plasma enhanced vapour deposition (PECVD). Both of these passivation layers are applied in the investigated solar cell structure in a form of a stack of passivation layers.

2. The SRH recombination process requires a pair of one electron and one hole. The recombination rate is the highest when the concentration of electrons and holes at the surface is equal. However, if the surface concentration of one of the carrier types is reduced, then the surface recombination rate is also reduced. There are two methods to reduce the concentration of one type of carriers:

   a. One is to implement a doping profile at the surface, which results in a reduction of one carrier type. This can be achieved by the high-temperature diffusion, which will result is a high-low junction [84] or p-n junction, depending on the polarity of the dopant and the silicon substrate. The phosphorus-doped front surface field, applied in the analyzed solar cells, is therefore a high-low junction which passivates the silicon surface by a strong reduction of holes concentration at the surface.

   b. The second method is the application of the field-effect passivation [156]. This can be achieved by electrical charges implemented in the passivation layer.

More details on surface passivation methods for silicon solar cells can be found in a review article of Aberle [155]. In the following, the front surface passivation quality of

the phosphorus doped front surface field combined with a stack system of SiO_2/SiN_X passivation layers will be analyzed.

7.2 Influence of the front surface field diffusion profile on the solar cell performance

A one-dimensional PC1D [63] simulations of a back-junction cell structure as presented in Figure 3-5 are shown in Figure 7-1. The influence of the front surface recombination velocity on the efficiency of the back-junction solar cells with and without front surface field diffusion is obvious: As already shown in section 2.3, with increasing S_{front} the efficiency of the cells without the front surface diffusion decreases rapidly. On the other hand the solar cells with front surface field diffusion profit from the reduction of the effective recombination velocity in a broad $S_{0,front}$ range. A properly designed FSF can therefore improve the efficiency of the back-unction cell for the non-perfectly passivated front surfaces, which is often the case for realistic processing conditions. However, comparing the range of $S_{0,front}$ in which the efficiency remains high for cells with and without FSF should be done carefully and consciously. It should be noted that the $S_{0,front}$ increases rapidly with increasing surface concentration of the phosphorus doping [94]. Therefore the $S_{0,front}$ of the solar cells with FSF diffusion is inherently orders of magnitude higher than in the case of solar cell without FSF diffusion.

The influence of the front surface recombination velocity is visible in the whole wavelength range of the internal quantum efficiency of the back-junction cells as can be seen in Figure 7-2. A lowly doped FSF results in high quantum efficiency. This is because the Auger recombination inside the highly doped region and the surface recombination velocity are low. A proper choice of the front surface field profile is therefore one of the most critical points in the design of the back-contact, back-junction solar cell device.

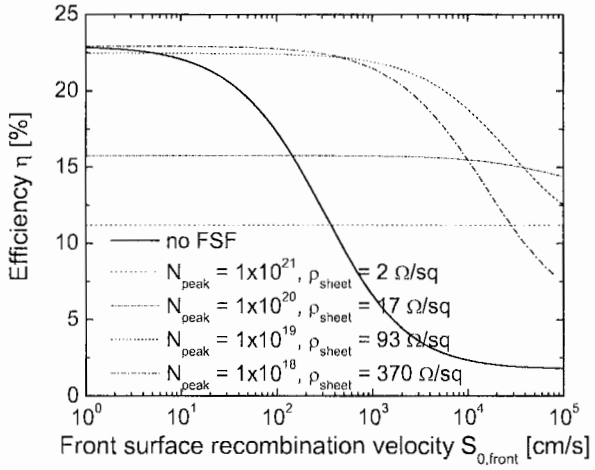


Figure 7-1 Influence of the front surface recombination velocity ($S_{0,front}$) on the efficiency of the back-junction n-type Si solar cells with different phosphorus FSF diffusion profiles (one-dimensional PC1D simulations). In simulations of the doping profiles a depth factor of 0.5 was used.

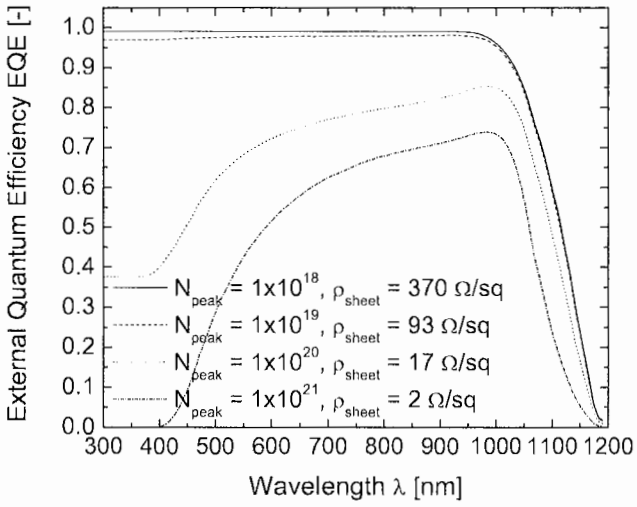


Figure 7-2 Internal quantum efficiency of an n-type back-junction solar cells for different front surface field diffusion profiles. $S_{0,front}$ calculated accordingly to model of Cuevas et al. [94] was assumed for this PC1D simulations. Depth factor of the diffusion profiles equals 0.5 in all simulations.

The importance of the selection of the appropriate diffusion profile for surface passivation is presented in the Figure 7-3. PC1D modelling results of the emitter saturation current density for both metalized and passivated Gaussian phosphorus

diffusion profiles are shown. The sheet resistance of the simulated diffusion profiles is presented in Figure 7-4.

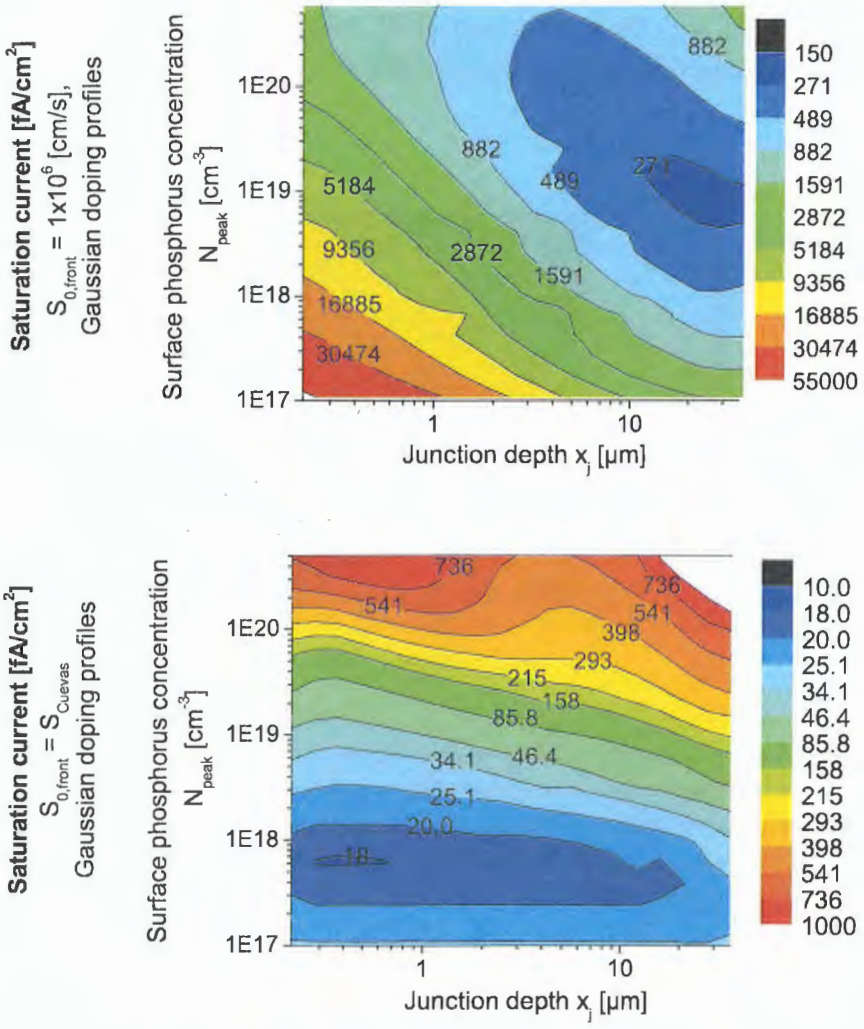


Figure 7-3 Emitter saturation current densities (J_{0e}) of the phosphorus doped Gaussian diffusion profiles calculated in a wide range of surface phosphorus concentration and junction depth. On top the case of the metalized diffusion profiles with $S_{0,front}=1\times10^6$ cm/s is presented. On the bottom graph, the case of the passivated diffusion profiles is shown. For the passivated emitter the $S_{0,front}$ was calculated using the model of Cuevas et al. [94], which was presented in 3.2.3. Note that the emitter saturation current density is presented in a logarithmic scale. The calculations were done using PC1D [63].

From the simulations it is clear that for the poorly passivated surfaces, highly doped and deep diffusion profiles are optimal in order to minimize the surface recombination (see Figure 7-3 top), with sheet resistance of about 10 Ω/sq. On the other hand, for the well passivated surfaces, an optimal diffusion profile is lowly doped and shallow (see Figure 7-3 bottom), with the sheet resistance of around 200 to 800 Ω/sq. These results are in a good agreement with the analytical modelling of del Alamo et al. [157].

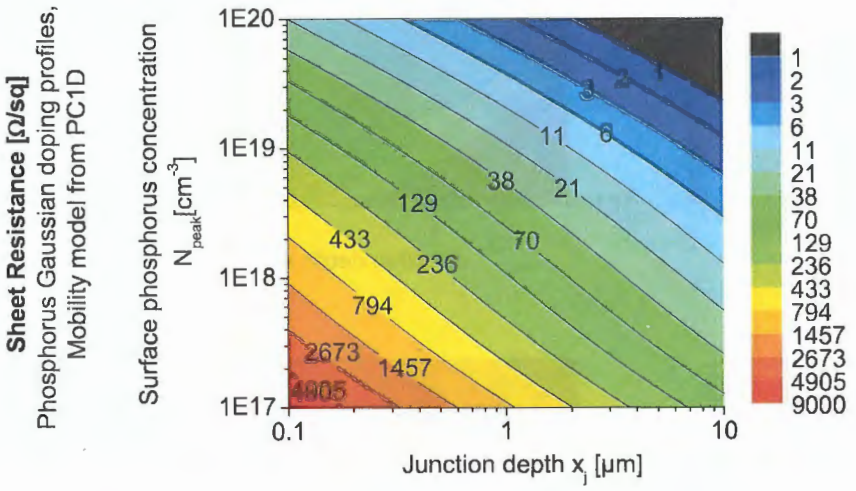


Figure 7-4 *Sheet resistance of the phosphorus doped Gaussian diffusion profiles in a wide range of surface phosphorus concentration and junction depth. For the calculation of sheet resistance an electron mobility model of PC1D program [63] was taken. Note that the sheet resistance is presented in a logarithmic scale.*

7.3 Surface passivation quality for different FSF diffusion profiles

King et al. [148], [20] and Cuevas et al. [147] studied the saturation current densities of the phosphorus doped emitters. In their work the Gaussian phosphorus profiles were analyzed using n^+pn^+ test structures. In the present work the focus is to analyze the FSF diffusion profiles on the n-type base, therefore in contrast to both authors here the n^+nn^+ samples with front surface field, without the p-n junction, were studied. Error-function diffusion profiles are formed by only a short oxidation step after phosphorus diffusion. The deep diffused Gaussian profile on the other hand, is a result of a long post diffusion oxidation process times and temperatures.

7.3.1 Processing of test structures for the determination of J_{0e}

Symmetrical n^+nn^+ test structures (see Figure 7-5) for lifetime measurements were processed on 250 µm thick n-type FZ-Si wafers. Base resistivities of 1 and 10 Ω cm were selected for this study. This base resistivity range is of interest for the high-efficiency back-junction back-contact solar cells processed in the frame of this study. The advantage of using high quality n-type FZ-Si is the very high bulk lifetime, as was already shown in section 4.2. Due to the high minority carrier lifetimes, the recombination in bulk material is minimum and the carrier lifetime is almost entirely limited by the surface recombination. This way an accurate determination of the surface recombination effects is possible.

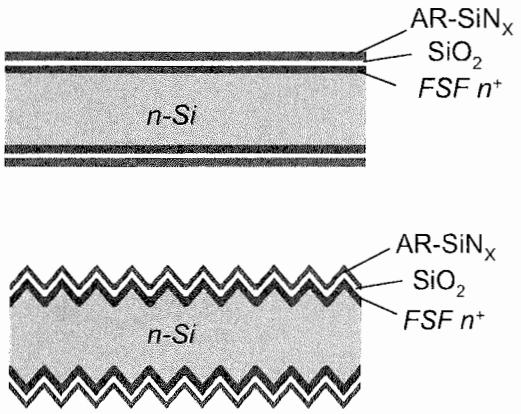


Figure 7-5 Symmetrical n^+nn^+ test structures for the lifetime measurements and the determination of the surface recombination current density. Test structures with planar (top) and textured (bottom) surfaces were processed.

Test samples with untextured (planar) and textured surfaces (random pyramids) were processed. The front surface field was created on both sample sides by a tube furnace phosphorus diffusion form liquid $POCl_3$ source. The phosphorus diffusion time was fixed for all diffusion profiles and the diffusion temperature was varied in the range from 780 to 840°C. This resulted in different n^+ error-function dopant profiles. The resulting diffusion profiles measured for planar samples are shown in Figure 7-6.

Next, the phosphorus glass was etched back in HF solution. For selected samples a deep Gaussian phosphorus profile (called 'deep diffusion') was created by a dry thermal oxidation at 1050°C to form a 105 nm thick antireflection SiO_2 layer. The high oxidation temperature caused redistribution of the phosphorus atoms and transition from the error-function dopant profile to Gaussian profile. The thick oxide was then etched-back in HF solution. Next, the thermal oxide of the planed thickness of about

10 nm for the passivation of the silicon surface was grown during a short dry oxidation process at the temperature of 850°C. Due to the short oxidation time and its low temperature, the doping profiles were not changed significantly.

The parameters such as sheet resistance (ρ_{sheet}), surface phosphorus concentration (N_S) and depths of the diffusion profile (x_j) of the resulting diffusion profiles are summarized in Table 7-1. The sheet resistance of the FSF doping was calculated by integrating the dopant profiles using the mobility model from Masetti et al. [158].

All wafers were processed in one oxidation step. However the oxide growth rate is different on differently doped surfaces [159]. This resulted in the oxide thickness variation of all samples in the range from 10 to 40 nm. Next, the antireflection 70 nm thick PECVD silicon nitride coating was deposited. Finally all samples were annealed at forming gas atmosphere (FGA) at the temperature of 425°C for 15 min.

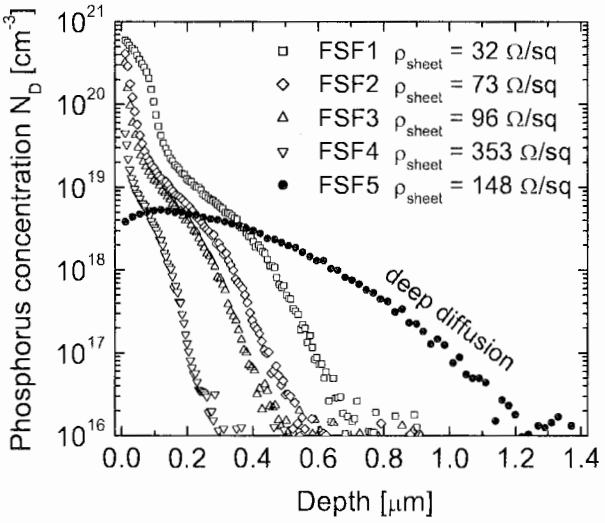


Figure 7-6 Secondary ion mass spectometry (SIMS) profiles of the studied phosphorus dopant profiles measured for untextured samples after all high temperature processing steps.

Table 7-1 Parameters of the analyzed phosphorus doped front surface field diffusion profiles.

Profile	Type	ρ_{sheet} [Ω/sq]	N_S [cm^{-3}]	x_j [μm]
FSF1	erfc	32	6.0×10^{20}	0.78
FSF2	erfc	73	4.0×10^{20}	0.66
FSF3	erfc	96	3.2×10^{20}	0.56
FSF4	erfc	353	4.5×10^{19}	0.38
FSF5	Gauss	148	3.8×10^{18}	1.44

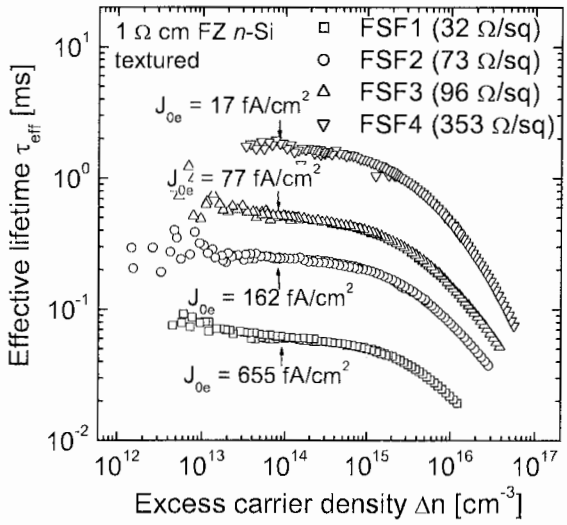


Figure 7-7 Determination of the emitter saturation current density under low injection for different front surface field diffusion profiles. J_{0e} is determined at $\Delta n = 1\times10^{14}$ cm^{-3}.

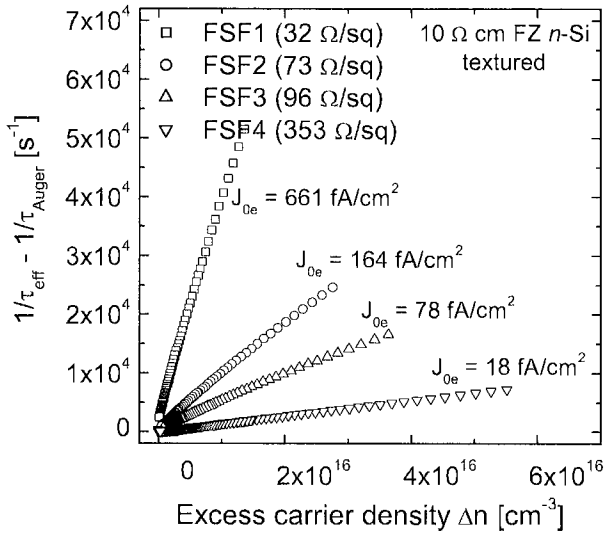


Figure 7-8 Determination of the emitter saturation current density under high injection for different front surface field diffusion profiles. J_{0e} is determined using the slope method.

7.3.2 Determination of J_{0e} under high and low injection

In order to determine the saturation current density of the phosphorus doped front surface field areas (J_{0e}) of the analyzed front surface field diffusion profiles, two methods were applied. J_{0e} was determined under low level injection for 1 Ω cm samples and using the *slope method* under high level injection for 10 Ω cm samples. This way a direct comparison of J_{0e} values determined by both methods was possible. Both methods for determination of J_{0e} under low and high injection are presented in section 3.1 Because of the different SiO_2 thicknesses of samples with different n^+ dopant profile, the optical factor required for QSSPC measurements had to be calculated for all samples. After measuring the oxide thickness, the optical factor was calculated using *SUNRAYS* [93].

Next to J_{0e}, the V_{OC} limit imposed by $J_0 = J_{0e}$ was calculated with the equation (2.1) for all determined J_{0e} (J_{SC} = 40 mA/cm^2 was assumed). For calculation of $V_{OC,\,limit}$ the standard testing temperature of 25°C was assumed. The $V_{OC,\,Limit}$ is the maximum V_{OC} that can be achieved with the used passivation. The influence of the bulk recombination was neglected in calculation of $V_{OC,\,limit}$.

$$V_{\mathrm{OC,limit}} = \frac{kT}{q}\ln\left(\frac{J_{SC}}{J_0}+1\right) \tag{7.6}$$

Examples of the determination of the emitter saturation current density of the analyzed FSF diffusion profiles are shown in Figure 7-7 for the low injection case and in Figure 7-8 for the slope method in high injection.

7.3.3 J_{0e} for different FSF diffusion profiles

The determined J_{0e} values together with the corresponding $V_{OC,\,Limit}$ are summarized in Table 7-2 for the untextured samples and in Table 7-3 for the textured samples. A very good agreement between J_{0e} results determined under high injection using the slope method for the 10 Ω cm samples and in low injection for the 1 Ω cm samples was obtained. This shows that both methods enable a very good determination of J_{0e} of the samples with front surface field. The presence of p-n junction is not required to determine the recombination currents of the n^+ diffused regions [147]. Both methods of determination of J_{0e} proved also to be independent of the base doping.

Table 7-2 Summary of the J_{0e} results for the planar lifetime samples with different FSF diffusions. J_{0e} results for the 1 and 10 Ωcm samples determined under low and high injection respectively are shown together with the corresponding $V_{OC,\,limit}$.

			ρ_{base} = 1 Ω cm low-injection		ρ_{base} = 10 Ω cm high-injection	
Profile	Type	ρ_{sheet} [Ω/sq]	J_{0e} [fA/cm²]	$V_{OC,limit}$ [mV]	J_{0e} [fA/cm²]	$V_{OC,limit}$ [mV]
FSF1	erfc	32	404	652	414	651
FSF2	erfc	73	118	683	128	681
FSF3	erfc	96	61	700	69	697
FSF4	erfc	353	11	744	12	742
FSF5	Gauss	148	12	741	16	734
no FSF	-	-	3[i]	774	3[i]	774

[i] For the non-diffused surfaces a surface saturation current density J_{0s} was determined instead of diffusion saturation currant density J_{0e}.

Table 7-3 *Summary of the J_{0e} results for the textured lifetime samples with different FSF diffusions. J_{0e} results for the 1 and 10 Ωcm samples determined under low and high injection respectively are shown together with the corresponding $V_{OC,\ limit}$.*

Profile	Type	ρ_{sheet}	ρ_{base} = 1 Ω cm low-injection		ρ_{base} = 10 Ω cm high-injection	
			J_{0e}	$V_{OC,limit}$	J_{0e}	$V_{OC,limit}$
		[Ω/sq]	[fA/cm^2]	[mV]	[fA/cm^2]	[mV]
FSF1	erfc	32	655	639	661	639
FSF2	erfc	73	162	675	166	674
FSF3	erfc	96	77	694	90	690
FSF4	erfc	353	17	733	20	729
FSF5	Gauss	148	21	727	22	726
no FSF	-	-	15[i]	736	17[i]	733

Extremely low J_{0e} = 3 fA/cm^2 for the non-diffused surface were measured. This proves that stack system of the thin (10 nm) thermal oxide and PECVD SiN_X (70 nm) passivation is very effective. Phosphorus diffusion introduces increased Auger recombination and SRH recombination due to crystal defects [147], [160]. That is why J_{0e} of samples with FSF are higher than for samples without FSF for the untextured surfaces. Of the investigated diffusions deep Gaussian diffusion (148 Ω/sq) and shallow error-function (353 Ω/sq) diffusion result as expected in the lowest J_{0e} values. These are the two doping profiles with the lowest surface phosphorus concentration.

For textured surfaces J_{0e} is as expected higher than for the untextured samples. This is due to larger surface area of the textured samples and could also be caused by a different phosphorus concentration at the tops and bottoms of the pyramids as proposed by Glunz at al. [161]. For the textured samples with FSF the V_{OC} higher than 720 mV are possible when only the front surface recombination is regarded. Such a good surface passivation with thin SiO_2 and antireflection SiN_X layers have enabled processing of back-junction back-contact solar cells with efficiencies greater than 21 % as presented in this thesis.

Table 7-4 Comparison of the J_{0e} values for textured and planar samples for different front surface field doping profiles.

Profile	Type	ρ_{sheet}	$J_{0e,planar}$	$J_{0e,textured}$	$\frac{J_{0e,textured}}{J_{0e,planar}}$
		[Ω/sq]	[fA/cm^2]	[fA/cm^2]	[mV]
FSF1	erfc	32	404	655	1.62
FSF2	erfc	73	118	162	1.37
FSF3	erfc	96	61	77	1.26
FSF4	erfc	353	11	17	1.54
FSF5	Gauss	148	12	21	1.75
no FSF	-	-	3[i]	15[i]	5.00

Comparison of the J_{0e} data in Table 7-4 of the planar and textured samples indicates that the J_{0e} increases by a factor of 1.3–1.7 when going from a planar to a textured surface. This is similar to the increase measured by Kerr et al. [162] and by Moschner et al. [163] and is consistent with the increase in surface area by a factor of 1.73 compared to a planar surface.

A strong J_{0e} dependence of the sheet resistance is shown in Figure 7-9. The J_{0e} of the error-function diffusions could be very well fitted with a linear fit in the broad sheet resistance range. Deep Gaussian diffusion seems to have a different dependence of the ρ_{sheet}. It is concluded that this effect is due to differences in surface phosphorus concentration between error function profiles and the deep diffused Gaussian profiles.

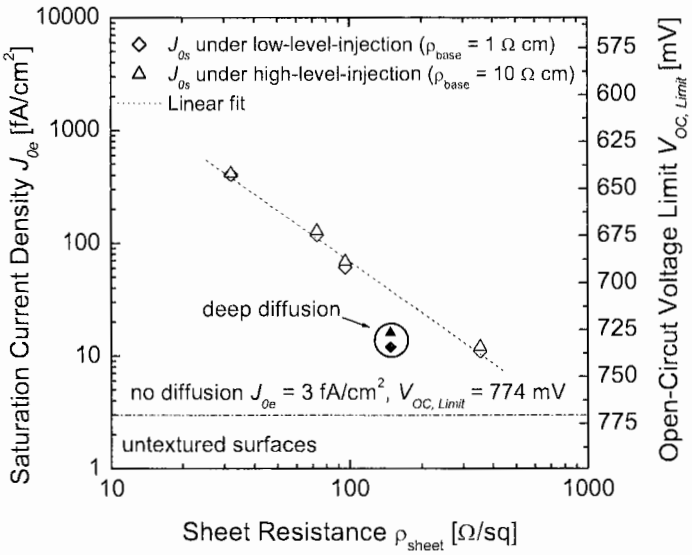


Figure 7-9 *J_{0e} and $V_{OC, Limit}$ as a function of sheet resistance of the n^+ diffusion for the untextured samples. J_{0e} of the sample without FSF is shown for comparison.*

7.4 Solar cells with different FSF diffusion profiles

Back-contact back-junction n-type silicon solar cells were processed with different FSF diffusion profiles. Thus, the influence of the FSF profile on the solar cell performance could be analyzed. The solar cells structure together with the processing technology is presented in chapter 4. Solar cells were processed on 1 Ω cm FZ n-type wafers. The thickness of the finished cells was about 160 µm. The active cell area was 4 cm^2.

7.4.1 Solar cell results

The current-voltage (I-V) parameters of the best solar cells for each FSF diffusion profile are summarized in Table 7-5. The diffusion profiles are labelled corresponding to the data presented in Table 7-1. The pitch of the analyzed cells was 1800 µm, with an emitter width of 1200 µm and a base width of 600 µm. The highest efficiency of 20.8 % was achieved on base resistivity of 1 Ω cm and deep diffused FSF (FSF5). The best efficiency of the BC-BJ solar cell processed without the FSF was 19.7 %. However, it should be noted the solar cells without the FSF diffusion had a very large distribution of the efficiency in the range of 10 to almost 20 %. This shows the importance of the stable front surface passivation quality. The distribution of the solar cell efficiency of the cells with FSF diffusion was much lower, in the range of 2 to 4 %

absolute. For the deeply diffused FSF profile the efficiency distribution was is the range of 0.5 % absolute.

The FSF doping has an influence primarily on the short-circuit current density and the open-circuit voltage as can be seen in Table 7-5. J_{SC} increases from 34.1 mA/cm^2 for the 73 Ω/sq FSF, to 38.1 mA/cm^2 for the deep diffused 148 Ω/sq FSF diffusion. At the same time V_{OC} increases from 647 mV to 663 mV due to reduction of the overall J_0 caused by reduction of the J_{0e} on the front side. The FF of the cells is on a high level of 81 to 82 % and is not being influenced by the different FSF profiles.

Table 7-5 I-V-parameters for the best solar cells with different front surface field diffusion profiles. Solar cells with base resistivity of 1 Ω cm and pitch of 1800 µm are presented. Results in the table are the designated cell area (2×2 cm^2) measurements.

Cell no.	FSF Profile	Type	ρ_{sheet} [Ω/sq]	J_{SC} [mA/cm^2]	V_{OC} [mV]	FF [%]	η [%]
BC47-2b	FSF2	erfc	73	34.1	647	81.7	18.0
BC47-6b	FSF3	erfc	96	36.1	657	81.9	19.5
BC47-11b	FSF4	erfc	353	37.8	651	81.1	20.0
BC47-16b	FSF5	Gauss	148	38.1	663	82.3	20.8
BC47-22b	no FSF	-	-	36.4	659	82.0	19.7

7.4.2 Analysis of the open-circuit voltage

The influence of the sheet resistance of the FSF doping on the V_{OC} is presented in Figure 7-10. The J_{0e} values of the planar and textured lifetime samples are plotted together with the liner fits (dotted lines). The results for the deep diffused Gaussian profile are marked with the closed symbols. The thin solid line represents the limit in V_{OC} imposed by the solar cell structure, i.e. by the bulk recombination, rear side recombination in the highly doped emitter, the back-surface field, in the gap areas and in the metal contact areas. For the analyzed solar cell structure this limit equals around 670 mV. Thus, if the front surface recombination would be eliminated ($J_{0e} = 0$), then the solar cells would have V_{OC} of 670 mV. However, due to non-zero front surface recombination the V_{OC} is decreased to values presented in Table 7-5.

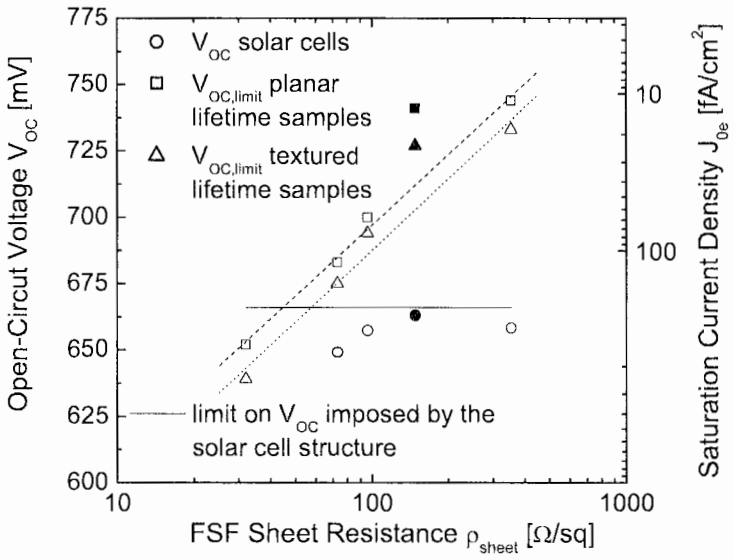


Figure 7-10 Open-circuit voltage of the processed solar cells with different sheet resistance of the FSF diffusions. Results for deep diffused Gaussian FSF profile (FSF5) are marked with closed symbols. $V_{OC,limit}$ imposed by the J_{0e} of the FSF diffusions for the planar and textured lifetime samples are shown as well.

7.4.3 Internal quantum efficiency

The internal quantum efficiency of the BC-BJ solar cells with different FSF diffusion profiles is presented in Figure 7-11. Again, the deeply diffused FSF profile results in the highest IQE, which explains the highest J_{SC} of these cells.

When the doping concentration of the front n^+ diffusion increases, the IQE decreases in the whole wavelength range. However, the most severe degradation of the IQE can be observed in the short wavelength range of 300 to 500 nm when increasing the FSF doping concentration. This effect can be well seen for the IQE of a solar cell with FSF2 doping profile (ρ_{sheet} = 73 Ω/sq). The light of this wavelength is absorbed at the front cell side, inside and in the vicinity of the highly doped FSF region. In this region the high surface recombination velocity, which increased with the surface doping concentration, and the low carrier lifetime due to Auger recombination leads to recombination of a significant percentage of the minority carriers.

Reduction of the surface doping concentration and reduction of the depth of the phosphorus doping profile leads to the strong increase of the spectral response in the short wavelength range as can be seen for the solar cells with FSF3, FSF4 and FSF5 doping profiles.

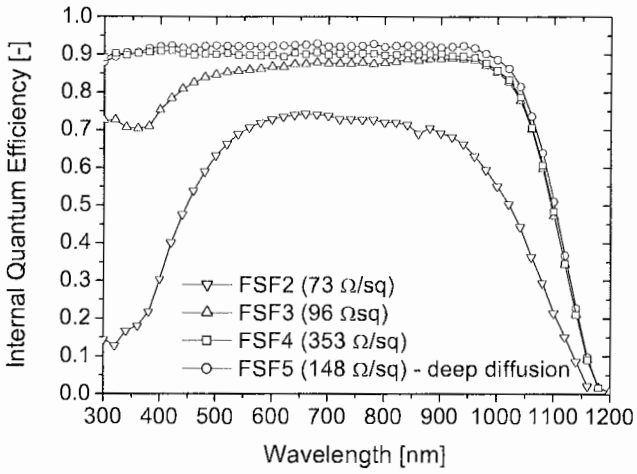


Figure 7-11 Internal quantum efficiency of the BC-BJ solar cells with different FSF diffusion profiles. Results of the solar cells with base resistivity of 1 Ω cm and pitch of 1800 μm are presented.

A strongly reduced IQE in the long wavelength range of 1000 to 1200 nm for the solar cell with highly doped front diffusion profile (FSF2) is believed to be caused by the enhanced free carrier absorption (FCA) process. Details of the free carrier's absorption process are given in section 6.2. A very good light trapping of the analyzed BC-BJ cells causes the weakly absorbed long wavelength light to travel many times through the wafer thickness and at the same time through the highly doped front phosphorus diffusion. In the case of the highly doped FSF2 diffusion profile each pass of the long wavelength light through the highly doped FSF region causes a parasitic absorption of the light, which in turn decreases the photogeneration of the electron-hole pairs in this wavelength range. Due to significantly lower surface doping and the depth of the diffusion profiles of the other analyzed FSF profiles, the FCA process is not causing any significant reduction of the spectral response in the long wavelength range of the spectrum.

7.5 Stability of the front surface passivation under UV-light exposure

7.5.1 UV-light influence on the front surface passivation

Already in 1988 Gruenbaum et al. [164], [165] reported that the efficiency of some of the point-contact concentrator solar cells developed by the Stanford University [16], decreased after exposure to concentrated sunlight. The decrease in solar cell performance was caused by the increase of the front surface recombination velocity.

The studies of Gruenbaum et al. showed that the ultraviolet (UV) component of the incident light spectrum caused damage on the front surface.

Gruenbaum et al. [166] performed the UV-exposure and photoinjection experiments. It was discovered that the UV light of energy greater than 3.1 eV causes increase of the surface recombination velocity ($S_{0,front}$) and interface state densities of the surfaces passivated with oxide. The energy of 3.1 eV corresponds to light with wavelength shorter than 400 nm. In the terrestrial solar spectrum there is a significant amount of photons with such energy. The absorption of the UV photons with wavelength shorter than 400 nm could inject electrons from the conduction band in Si into the conduction band of oxide. This photoinjection could be creating defects at the Si/SiO_2 interface.

However, Gruenbaum et al. [167] and Ruby et al. [168] showed that not all cell structures are prone to degradation under UV light. The formation of the diffused phosphorus region on the front side creates a high field which repels the minority carriers away from the recombination centers at the interface. Therefore even if the $S_{0,front}$ increases, the effective surface recombination velocity (S_{eff}) may remain low and not influence the efficiency of the solar cell. Thus, the additional positive effect of the FSF could be a significant improvement of the UV-light stability of the front side passivation, which is very important for the long term operation of the solar cells. The effect of the influence of the FSF diffusion on the UV stability of the solar cell performance is analyzed in the present section.

7.5.2 Lifetime test structures

The UV-stability of the front surface passivation with and without FSF was examined by exposing the n^+nn^+ lifetime samples to UV light (Xenon lamp) at one sun light intensity and a temperature of 50 °C. The tested samples were not covered with the module glass during the exposure, therefore the illumination spectrum absorbed by the test structures was rich in the high energy UV spectrum. The tested symmetrical lifetime samples were textured with random pyramids and the both surfaces were passivated with a thin thermal SiO_2 layer and an antireflection-SiN_X coating. The samples were annealed in a forming gas atmosphere prior to the exposure test. After each exposure step the saturation current density J_{0e} was determined.

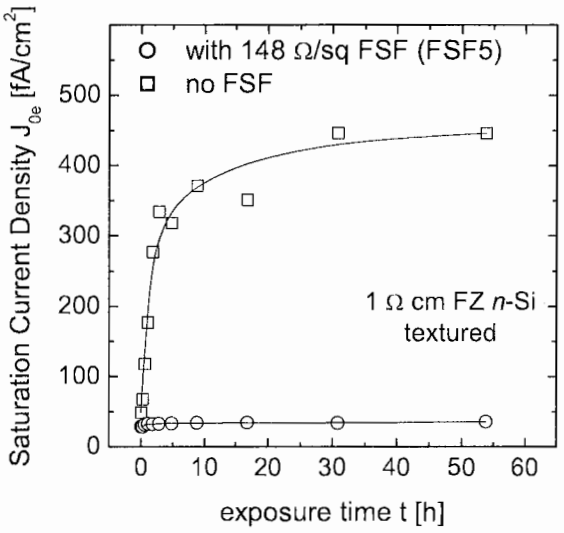


Figure 7-12 Passivation stability of textured n^+nn^+ lifetime samples with (circles) and without (squares) FSF during 55 hours of exposure to UV light. Lines are guides-to-the-eye.

Results of the UV exposure tests are shown in Figure 7-12. The lifetime of samples without FSF degrades significantly already after the first few hours of exposure. For the samples without the FSF, J_{0e} increases from initial value of ~30 fA/cm^2 to almost 450 fA/cm^2 after 55 hours of UV light exposure. Such a high increase of J_{0e}, which corresponds to $S_{0,front}$ of ~140 cm/s, will lead to a significant cell performance degradation, as already shown in section 2.3. Samples with FSF show no significant degradation. J_{0e} increases from ~30 to 35 fA/cm^2 in the case of the deep diffused 148 Ω/sq FSF diffusion. This proves that passivation using a FSF is stable and therefore appropriate for industrial applications in contrast to unstable passivation without FSF. Similar results were already obtained by Gruenbaum et al. [165].

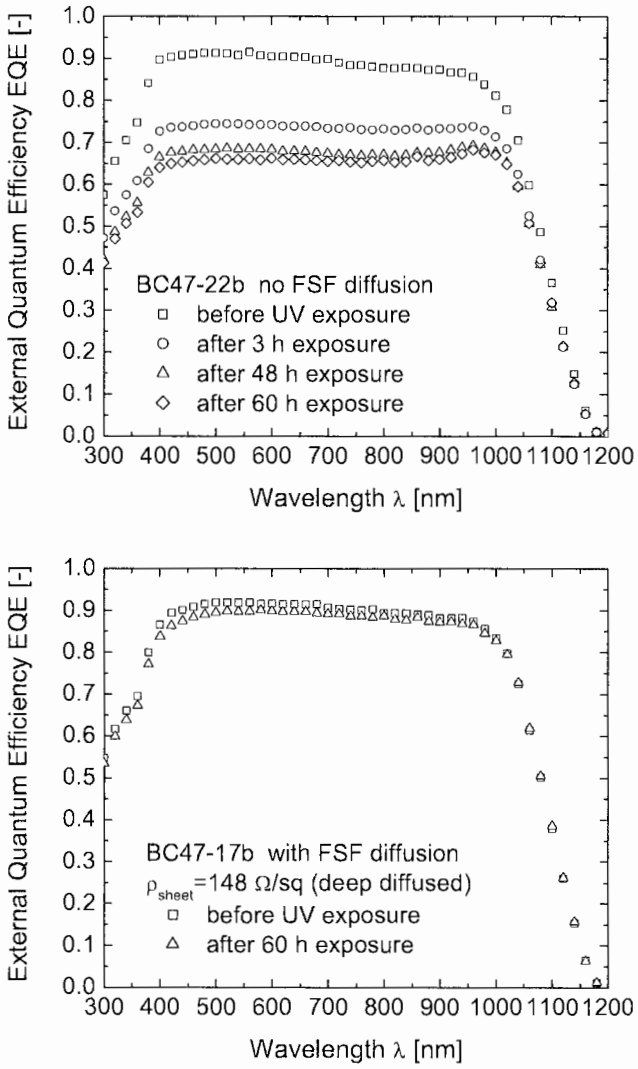


Figure 7-13 External quantum efficiency of the BC-BJ solar cells with (bottom) and without (top) the front surface field phosphorus diffusion after exposure to UV light. Duration of the UV exposure is shown in the graph. Both analyzed solar cells have base resistivity of 1 Ωcm and pitch of 1800 μm.

7.5.3 Solar cell results

Solar cells with and without the front n^+ diffusion were selected for the analysis of the performance stability under UV exposure (Xenon lamp) with illumination intensity of one sun and temperature of 50 °C. Solar cells with high starting performance (performance before UV light exposure) were analyzed in this test. The selected cells had efficiencies in the range of 19 to 20.5 %.

In Figure 7-13 the external quantum efficiency of the solar cell with (bottom) and without (top) the FSF measured after stepwise exposure to UV light. EQE of the solar cell without FSF degrades rapidly from 92 % to 75 % at wavelength of 500 nm already after 3 hours of exposure to UV light. After 60 hours of UV exposure the EQE of the solar cell without FSF decreases even further to 65 %. Thus, an EQE decrease of nearly 30 % absolute was caused by 60 hours of exposure to UV light in the case of the cell without the FSF. At the same time, the EQE of the solar cell with deep diffused FSF (FSF5) showed only minimal degradation after 60 hours of UV exposure: The EQE dropped from 92 % to 88 % at wavelength of 500 nm. Thus, the presence of the n^+ diffused layer on the front cell side drastically improves the stability of the solar cell under the UV exposure.

Table 7-6 *Front surface recombination velocity before and after exposure to UV light determined by (left column) analysis of the lifetime structures exposed to UV light and (right column) by fitting of the measured EQE using the PC1D model of the back-junction solar cell.*

	$S_{0,front}$ measured using lifetime samples [cm/s]	$S_{0,front}$ determined by PC1D fitting of the measured EQE of the solar cell [cm/s]
before UV exposure	16	18
after 60 h of UV exposure	138	145

The influence of the UV exposure on the EQE of the solar cell without FSF was analyzed in more detail with the results of the lifetime test structures and using PC1D simulations. First, the $S_{0,front}$ of the textured lifetime samples was measured before and after UV exposure. Secondly, the measured EQEs were fitted using the PC1D model presented in section 3.2.2. In order to fit the EQE results in the short wavelength range the $S_{0,front}$ was varied. The PC1D fit in the long wavelength range is not in a very good agreement with measured data due to strong influence of the two-dimensional effects, which could not be described by the one-dimensional PC1D simulation. The results are summarized in Table 7-6 and graphically presented in Figure 7-14. A very good agreement between the $S_{0,front}$ determined by analysis of the lifetime samples and by fitting of the EQE of the solar cells was obtained. This proves that the increase of

$S_{0,front}$ during the UV exposure is responsible for the degradation of the solar cell performance.

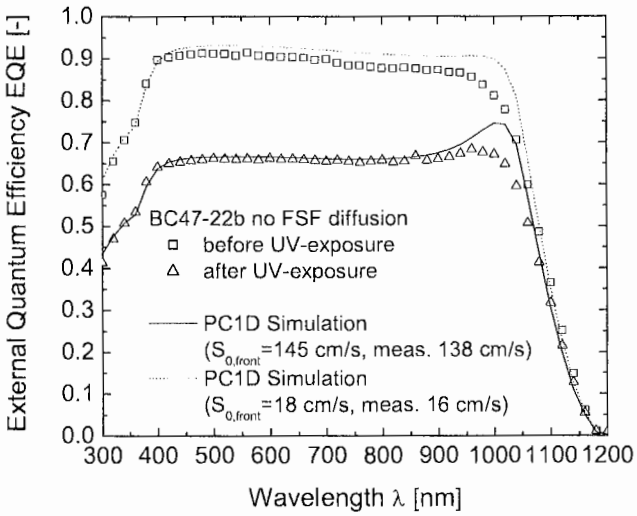


Figure 7-14 External quantum efficiency of the BC-BJ solar cell without the front surface field measured before and after 60 hours of exposure to UV light. PC1D simulations of the measured EQE with fitted $S_{0,front}$ are shown as well (thin lines).

7.5.4 Regeneration of the UV-degraded solar cells

During the illumination of the solar cell with UV light, the photoinjection of the electrons from the conduction band in silicon to the conduction band of oxide creates interface states. Increase of the interface states density at the Si/SiO_2 leads to significant reduction of the solar cell performance as shown in the previous sections.

The solar cell without FSF after UV degradation was exposed to the anneal process in the forming gas (N_2H_2) atmosphere (FGA) at the temperature of 425 °C and process duration time of 25 minutes. The elevated temperature and the hydrogen rich atmosphere leads to strong reduction of the interface states of the Si/SiO_2 interface during the FGA process [169]. This way the interface states that were created by the UV exposure can be passivated, leading to the reduction of the surface recombination velocity. In Figure 7-15 the external quantum efficiency of the BC-BJ solar cell without the FSF is shown before and after UV exposure and after FGA process. The FGA process performed after the UV exposure almost perfectly reduces the detrimental effect of the UV exposure, and regenerates the front surface passivation to the stadium as before the exposure.

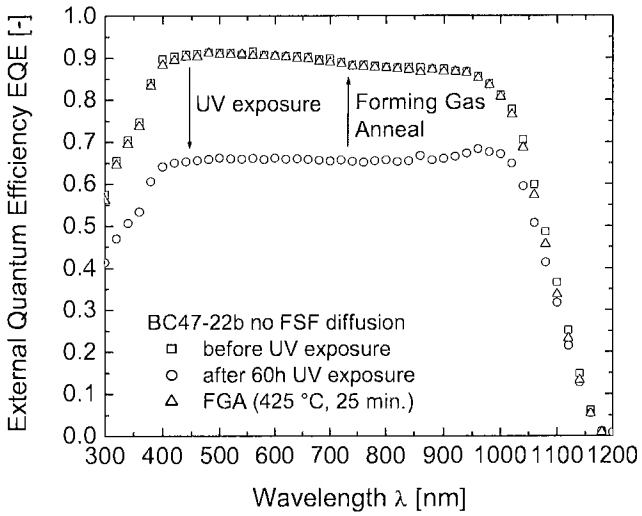


Figure 7-15 External quantum efficiency of the BC-BJ solar cell without the front surface field phosphorus diffusion before and after exposure to UV light and after regeneration of the UV damage by a forming gas anneal step.

Thus, the degradation effect of the UV exposure is not permanent and can be fully reversed by the passivation of the created interface states during the FGA process. The effect of the efficiency degradation under UV exposure and the subsequent regeneration under FGA process is shown schematically in Figure 7-16. The $S_{0,front}$ of the solar cells was determined using the lifetime test structures before and after UV exposure. The efficiency of the solar cells with and without FSF was measured after each UV exposure step and is plotted together with the $S_{0,front}$ determined by analyzing the lifetime samples. For the solar cell without the FSF the efficiency degradation follows the PC1D simulation line. However after the FGA the $S_{0,front}$ decreases and the efficiency increases as marked with a closed symbol.

The solar cell with the FSF diffusions do not show any significant performance degradation after UV exposure as marked with open symbols (circles and squares).

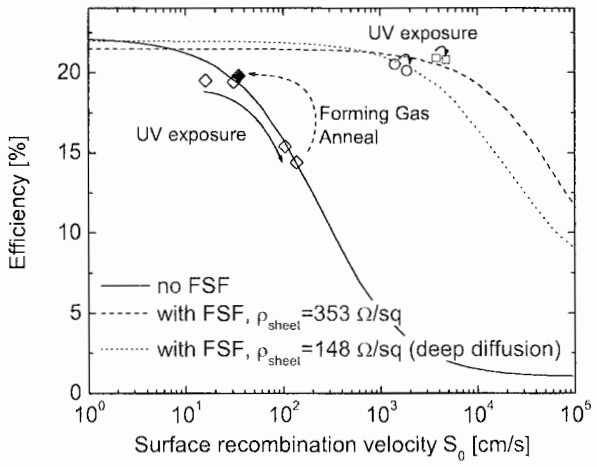


Figure 7-16 Efficiency of the back-junction solar cells as a function of the front surface recombination velocity simulated with PC1D for solar cell with and without FSF diffusion profile (thin lines). Open symbols represent the efficiency of the BC-BJ solar cells measured after UV exposure steps, as marked with arrows. The $S_{0,front}$ of was determined by analyzing the lifetime test samples with and without FSF respectively. The closed symbol represents the efficiency of the solar cell which was regenerated in forming gas anneal process after the degradation under UV illumination.

7.6 Conclusion

The front surface passivation quality is one of the most critical parameters of the back-contact back-junction solar cell structure. The phosphorus-doped front surface field can improve the front surface passivation and was therefore analyzed in details.

The saturation current density of different FSF phosphorus diffusion profiles passivated with SiO_2/SiN_X stack system was determined under low and high injection using the n^+nn^+ test structures. J_{0e} values determined using two different evaluation methods (under low injection and using *slope method* under high injection) are in a good agreement. The presence of the random pyramids texture increases the J_{0e} by a factor of 1.3 to 1.7 in comparison to the planar samples. This enhancement factor corresponds to the surface increase when going from planar to textured surfaces by a factor of 1.73.

The best solar cell efficiency of 20.8 % was obtained with deep diffused Gaussian profile of the FSF. Moreover the distribution of the efficiency of solar cells with the deep diffused FSF was lowest, proving the processing stability of the deep diffused

phosphorus profiles. The efficiency of the analyzed solar cells decreased to 18.0 % for solar cell with the FSF doping profiles with the lowest sheet resistance. Increased doping concentration and depth of the FSF diffusion reduced J_{SC} and V_{OC} of the analyzed cells.

Lifetime samples and solar cells without the front surface field showed a significant performance reduction when exposed to ultraviolet light spectrum. The lifetime samples and the solar cells with FSF diffusion are stable under UV exposure. Regeneration of the solar cell performance after degradation under UV exposure is possible by forming gas anneal.

8 Lateral current transport via front n^+ diffused layer

The application of the low-cost structuring technologies in the processing of the high-efficiency back-contact back-junction silicon solar cells results in a drastic increase in pitch on the rear cell side. The pitch in the range of millimeters leads to a significant increase of the lateral base resistance. The application of a phosphorus-doped front surface field (FSF) significantly reduces the lateral base resistance losses. This additional function of the phosphorus-doped FSF was investigated experimentally and by two-dimensional device simulations. Enhanced lateral majority carrier current transport in the front n^+ diffused layer is a function of the pitch and the base resistivity. Experimental data show that the application of a FSF reduces the total series resistance of the measured n-type cells of 160 micrometer thickness with 3.5 mm pitch by 0.1 Ωcm^2 for 1 Ωcm base resistivity and 1.3 Ωcm^2 for 8 Ωcm base resistivity. Two-dimensional simulations of the electron current transport show that the electron current density in the front n^+ diffused layer is around two orders of magnitude higher than in the base of the solar cell.

8.1 Introduction

High volume manufacturing of the back-contact and back-junction solar cell structure in the industrial environment requires the application of adequate processing technologies. The use of the photolithography technique is not cost-effective. Replacement of the very accurate photolithography with industrially applicable masking steps, such as ink-jetting and screen-printing of resist masks or laser ablation, leads to a significant reduction of the resolution and positioning accuracy. This is especially critical if more than one masking step is used. The pitch on the rear cell side processed with the low-cost masking technology mentioned above increases dramatically, as schematically shown in Figure 8-1. Point-contact solar cells processed by Prof. Swanson's group at Stanford University in the 1980s, for concentrator applications with the use of photolithography, had a pitch of 45 μm [119]. Another example of back-contact Si cells also processed using photolithographic masking is the real-line contacted concentrator (RLCC) cell, developed by Mohr [170] with the pitch in the range of 120 to 400 μm. Solar cells were processed in the course of this thesis without photolithography possessing a pitch distance of around 2 mm. Thus, when

applying low-cost patterning techniques, the pitch on the rear side increases by a factor of more than 40 in comparison to point contact cells [119]. This means that for the majority carriers (electrons here), the main current transport is transformed from the vertical to the lateral direction.

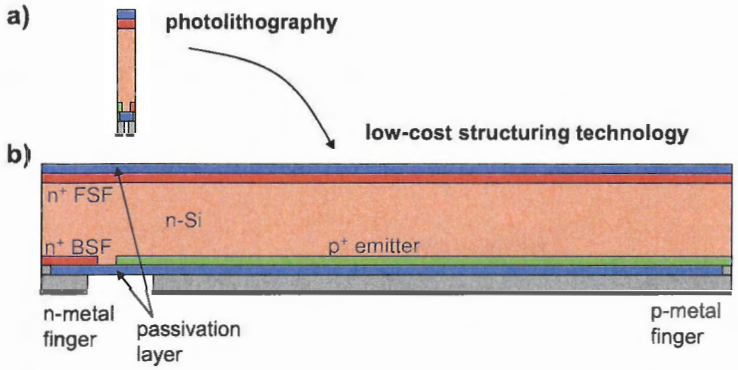


Figure 8-1 Schematic comparison of a point-contact Si solar cell processed with the use of photolithography with a pitch distance of 45 µm (a) and the solar cell with the use of low cost structuring technology with a pitch distance of 2000 µm (b). Drawings are to scale laterally. Symmetry elements of the cell structures are shown.

Depending on the base resistivity and pitch, up to 90 % of the series resistance can be attributed to the lateral majority carrier transport. Thus, the lateral current transport is the main resistance loss mechanism reducing the cell efficiency. The analyzed cells have a phosphorus diffused front surface field (FSF), which is well-known to improve the front side passivation [20]. In the case of cells with large pitch, the FSF not only improves the front side passivation, but also reduces the lateral resistance for the majority carriers and reduces the series resistance of the solar cell. This additional effect of the front n^+ layer is investigated in the present chapter.

8.2 Lateral current transport of majority carriers

The emitter coverage on the rear side should be as high as possible to reduce the required diffusion path for the light generated minority carriers to reach the p-n junction (see Figure 8-2). Increased emitter coverage on the rear cell side is linked to a reduced base doping area. As will be shown in the section 8.3, the pitch of the analyzed solar cell structures was chosen in the range of 1.3 to 3.5 mm. Therefore, the emitter coverage on the rear side is between 54 % and 83 % respectively. Due to the high emitter fraction, the majority carriers (electrons in the case of the n-type base material) need to flow lateral distances in the range of millimeters before reaching the

base contacts. This influences the fill factor of the cell. On the other hand, due to the lower base coverage on the rear cell side, the minority carriers (holes), which were photo-generated over the base contact regions, have much shorter lateral distances to diffuse to the emitter. This results in an improved carrier collection.

The lateral transport of the majority carriers causes significant series resistance losses due to the large distances. When a highly doped front n^+ layer is present, the lateral transport of the electrons can be facilitated. In the case of a high base resistivity or a large lateral distance, the diffused front n^+ layer contribution to the lateral current transport will be significant. This effect is schematically shown in Figure 8-2.

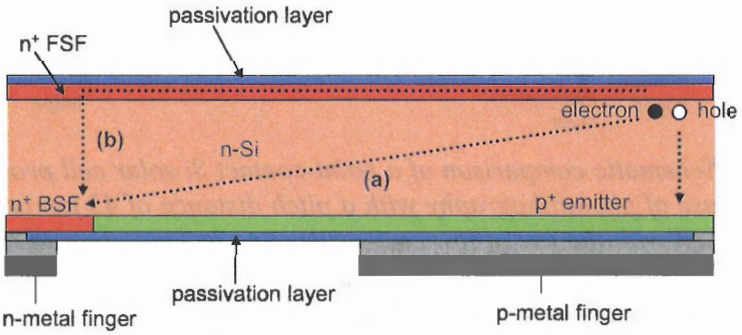


Figure 8-2 Schematic drawing of the effect of the enhanced lateral current transport of the majority carriers through the front n^+ diffused layer (a symmetry element of the cell is shown). For the sake of simplicity, the front side texture is not shown. The lateral current transport through the front diffused n^+ layer (b) can be seen as an additional transport path to the base lateral resistance (a). In this way the lateral cell resistance is reduced.

The so called *pumping* effect of floating phosphorus doped n-type emitters in the *p-type* back-contact back-junction solar cells was already investigated by Dicker et al. [33]. In the case of p-type cells with floating emitters, the minority carriers, which were photo-generated in large lateral distances from the emitter, are injected to the floating emitter, where they become majority carriers. The lateral flow of these carriers in the floating emitter is enhanced. Next, the carriers are re-injected into the base and diffuse vertically to the p-n junction. Thus, the *pumping* effect of the floating emitter reduces the electrical shading losses (described in chapter 6) in the back-contact back-junction cells. Therefore the *pumping* effect should not be confused with the effect of the enhanced lateral transport of the majority carriers in the front diffused n^+ layer, which reduces the lateral resistance losses.

The impact of the lateral cell geometry on the lateral series resistance in the base of the solar cell can be expressed by eq. (8.1), analogous to the series resistance model for the concentrator BC-BJ cells from [35]. The impact of the current transport in the front diffused n^+ layer can be described by a parallel resistance to the base lateral resistance:

$$\frac{1}{R_{Base,L}} = \frac{1}{\frac{1}{12}\frac{\rho_{Base}}{d_{wafer}}(a_{n-n})^2} + \frac{1}{\frac{1}{12}\rho_{FSF}(a_{n-n})^2} \tag{8.1}$$

Where $a_{n\text{-}n}$ is the distance between the n^+ and n^+ doping, ρ_{Base} is the specific resistance of the base, d_{wafer} is the wafer thickness and ρ_{FSF} is the sheet resistance of the front n^+ diffused layer. The input parameters for the model described by equation (8.1) are schematically shown in Figure 8-3.

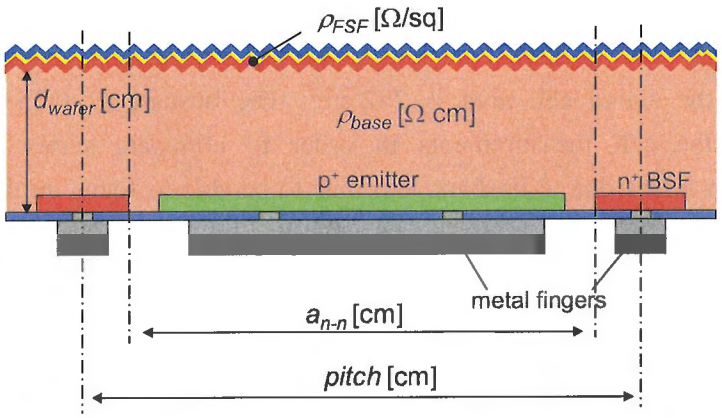


Figure 8-3 Schematic representation of the input parameters for the series resistance model presented in equation (8.1). The units of the geometry and resistance parameters are shown as well.

Due to the quadratic dependence on pitch, an increase of the pitch from 45 µm, as in the cells processed by Sinton et al. [119] with the use of photolithography, to 2000 µm, as in the cells processed in our group with low-cost masking technology, will result in the increase in the lateral series resistance by a factor of 2000. The application of the front diffused n^+ layer (FSF) will reduce the lateral base resistance, especially for cells with a higher specific base resistivity.

An analytical series resistance model of the BC-BJ solar cells was developed and presented in chapter 6.5. This model is based on the resistance model of Mohr [35]. Next to the base lateral resistance, the model also takes into account the vertical base resistance, the contact resistance and the metallization resistance losses. The impact of the lateral current transport in the front n^+ layer was incorporated as shown into

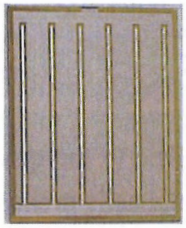
equation (8.1). The comparison of the analytical series resistance modeling with the experimental data is presented in the following sections.

8.3 Variation of the pitch

Back-contact back-junction n-type silicon solar cells with pitches of 1.3, 1.8, 2.2 and 3.5 mm were fabricated (see Table 8-1). The cell structure and its technology were already presented in 4.1. The pitch and the base and emitter width had to be selected, such that the resolution and positioning accuracy of the cell geometry can be performed using low-cost masking steps like screen-printing and laser ablation. The width of the emitter area (p^+) was varied in the range of 700 - 2900 µm in order to investigate the lateral current transport in the base and in the front n^+ layer. The width of the base doping on the rear side (undiffused gap and BSF areas) was fixed at 600 µm for all investigated pitches. The resulting emitter fraction on the rear cell side varied in the range of 54 %, for a pitch of 1.3 mm, to 83 % for a pitch of 3.5 mm.

The size of the active cell area is 2×2 cm^2. The busbars (2×0.15 cm^2) were not included in the cell measurements in order to eliminate series resistance and recombination losses due to busbars, and thus to be able to focus on the pitch-related two-dimensional effects.

Table 8-1 *Photographs and the geometry parameters of the rear side of the back-contacted solar cells with different pitches. The size of the active cell area is 2×2 cm^2. The busbars' size is 2×0.15 cm^2 for each polarity.*

p-bus side n-bus side				
Emitter [µm]	700	1200	1600	2900
Base [µm]	600	600	600	600
Pitch [µm]	1300	1800	2200	3500
Emitter fraction [%]	54	67	73	83

The experimental study was accompanied by two-dimensional device simulations done by M. Hermle [86] in the cooperation with the author of the present thesis. Two-dimensional simulations were done using the *Sentaurus Device* [90] program. The symmetry element of the device used in the simulations is shown in Figure 3-4. Busbars and edge effects were not included in the simulations.

8.4 Solar cell results

The best solar cell results for different pitch distances and base resistivities are summarized in Table 8-2. All results in Table 8-2 are designated cell area (2 cm × 2 cm) measurements, i.e. the busbars were not illuminated during the measurements. The edge area was also not illuminated during the cell measurements. The number of cells in each group was between 1 and 4. The best efficiency of 21.0 % for ρ_{base} = 1 Ω cm and 20.9 % for ρ_{base} = 8 Ω cm was obtained for the pitch of 2200 µm. This pitch represents the best trade-off between high carrier collection efficiency due to large emitter coverage on the rear side, and series resistance losses due to the increased lateral distances.

Table 8-2 *IV-parameters for the best solar cells with a FSF (ρ_{FSF}=148 Ω/sq) and with different pitches. Results of the cells with base resistivity of 1 and 8 Ω cm are presented. Results in the table are designated cell area (2x2cm^2) measurements.*

Cell no.	Pitch [µm]	Emitter fraction [%]	ρ_{base} [Ω cm]	J_{SC} [mA/cm^2]	V_{OC} [mV]	FF [%]	η [%]
BC47-17d	1300	54	1	37.2	662	81.6	20.1
BC47-18b	1800	67	1	38.1	663	82.6	20.9
BC47-16a	2200	73	1	38.5	663	82.2	21.0
BC47-17c	3500	83	1	38.9	661	80.7	20.7
BC47-20f	1300	54	8	39.4	654	79.9	20.6
BC47-21b	1800	67	8	40.1	656	78.3	20.6
BC47-21a	2200	73	8	40.3	658	78.8	20.9
BC47-20c	3500	83	8	40.3	658	75.4	20.0

8.5 Short-circuit current analysis

As shown in Figure 8-4, the short-circuit current increases with increasing emitter coverage and reduced base areas of lower minority carrier collection probability. The base width is 600 µm, so in the extreme case, when the photo-generation occurs in the middle of the base area, the minority carriers need to diffuse 300 µm laterally before reaching the p-n junction. This leads to recombination in the cell's base and at the surfaces. For the base resistivity of 8 Ω cm and a pitch of 3.5 mm, a maximum J_{SC} of 40.3 mA/cm^2 was obtained. Such a high J_{SC} value indicates very good optical and recombination characteristics of the cell. 2-D device simulations, also shown in Figure 8-4, are in excellent agreement with the experimental results, proving the accuracy of the model.

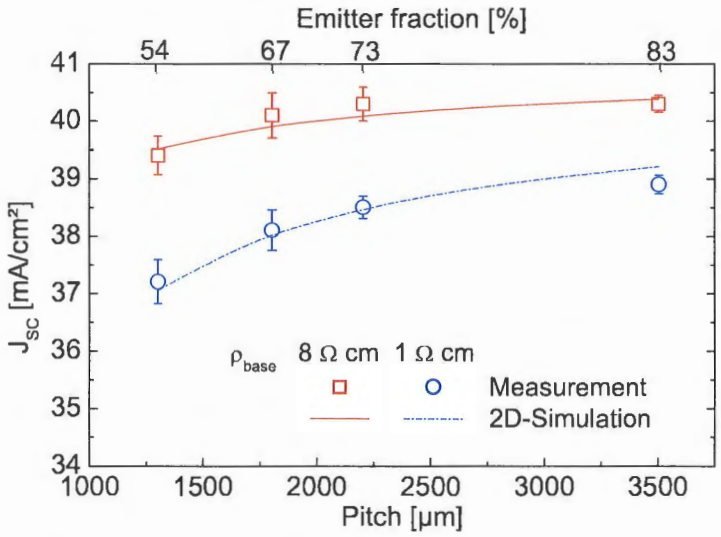


Figure 8-4 *Short-circuit current of the cells with the FSF (ρ_{FSF} = 148 Ω/sq) and with two specific base resistivities of 1 and 8 Ω cm in the investigated pitch range. The percentage of the emitter fraction on the rear side is shown on the top scale. Points represent experimental results and the lines are the two-dimensional simulation results.*

The short-circuit current of the 1 Ω cm cells is more than 1 mA/cm^2 lower than J_{SC} of the cells with 8 Ω cm specific base resistivity. In the 2D simulations, the same Shockley-Read-Hall bulk lifetime of 1 ms was assumed for both 1 and 8 Ω cm base materials. However, even with the same bulk lifetime for 1 and 8 Ω cm solar cells, the simulations show a difference in J_{SC}. The reason for the J_{SC} differences between 1 and 8 Ω cm wafers is the increased front surface recombination in the case of the 1 Ω cm

material in comparison to 8 Ω cm. A significant difference in the internal quantum efficiency (IQE) at short wavelengths between 1 and 8 Ω cm solar cells was measured. The IQE of the 1 Ω cm solar cells with pitch of 2200 µm is 94 % for wavelength of 400 nm. The IQE of the 8 Ω cm solar cells with pitch of 2200 µm equals 97 % for the same wavelength. The difference between the J_{SC} of cells with both base resistivities, determined by the integration of the solar spectrum with both measured IQEs, equals 1.8 mA/cm^2. This difference is in good agreement with the measured values presented in Figure 8-4. The effect of the increased front surface recombination in the case of the 1 Ω cm material in comparison to 8 Ω cm was investigated in section 4.5.

8.6 Fill factor and series resistance

8.6.1 Fill factor

In contrast to J_{SC}, the FF decreases as the pitch increases due to increased lateral resistance in base, as shown in Figure 8-5. The measured fill factor and 2D simulation are shown in Figure 8-5. Again, good agreement between the experimental and 2D simulation results can be observed. Results shown in Figure 8-5 clearly demonstrate that the FSF significantly reduces the series resistance losses and thus improves FF in comparison to cells without FSF. The effect of enhanced current transport in the front n^+ diffused layer is stronger for larger pitches, where the base lateral resistance dominates the resistance losses of the cell. Moreover, the additional impact of the FSF is, as expected, a function of the base doping. For higher base resistivity (8 Ω cm) and large pitch distance (3.5 mm), the FF of the cells with FSF is up to 10 % abs. higher than FF of the cells without the FSF.

8.6.2 Pseudo fill factor

In order to prove that the decrease in FF for larger pitch distances is only caused by the increased lateral series resistance and not other detrimental effects on the IV curve, the pseudo fill factor (PFF) was measured using the SunsV_{OC} measurement technique [153]. The pseudo fill factor is not influenced by series resistance; therefore, the effects of increased lateral resistance by increased pitch should not influence the PFF. The measured pseudo fill factor for the cells with varying pitch is shown in Figure 8-6. As expected, the PFF is independent of the pitch. In the pitch range analyzed, the PFF is higher than 82 % for 1 Ω cm and higher than 81 % for 8 Ω cm solar cells. Such a high PFF of the finished cells indicates that there are no significant shunting and space charge recombination losses in the analyzed solar cells. Constant PFF values in the analyzed pitch range prove that the variations in FF observed in

Figure 8-5 are caused only by the higher series resistance with increasing emitter width.

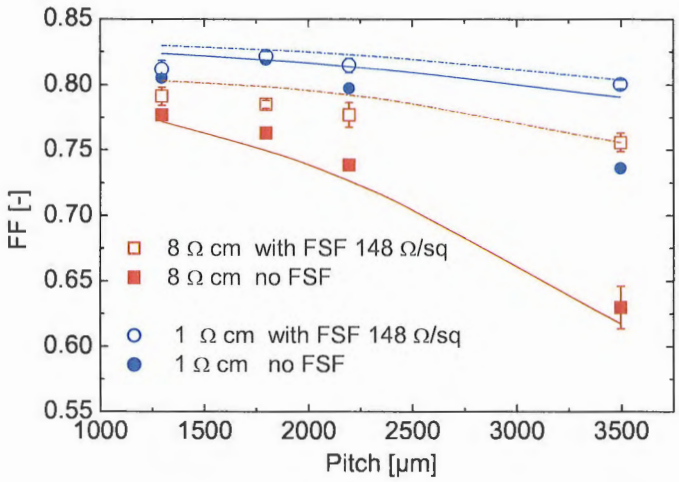


Figure 8-5 *Two-dimensional numerical simulations and measured values of the fill factor of the BC-BJ Si solar cells as a function of the pitch distance for two different base resistivities. Results for the cells with (ρ_{FSF} = 148 Ω/sq) and without FSF diffusion are shown. The data points represent a mean value of the experimental results. Lines represent 2-D simulation results.*

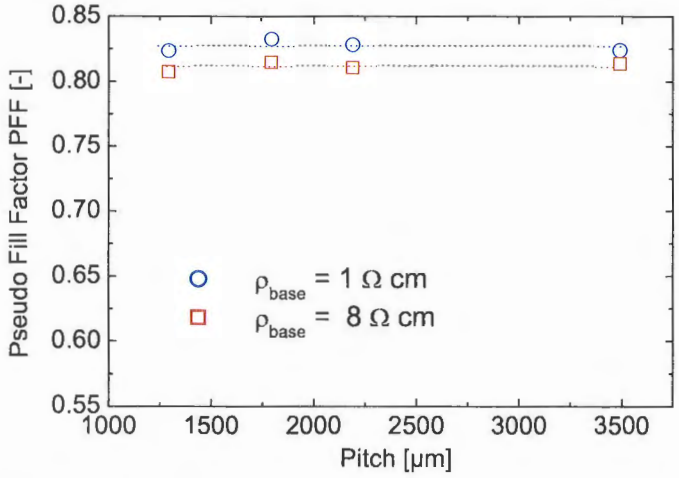


Figure 8-6 *Pseudo Fill Factor (PFF) of the BC-BJ solar cells with different pitches. Experimental results for the solar cells with FSF and base resistivity of FSF and 1 and 8 Ωcm material are shown. No reduction of the PFF over a wide pitch range was observed. Lines are guides-to-the-eye.*

8.6.3 Conductivity modulation

Since the series resistance reduces the maximum output power of the solar cell, the analytical model should describe the series resistance at the maximum power point (MPP) conditions. The base resistivity strongly depends on the density of the electrons in the base, and hence can be influenced by the cell operating conditions. Therefore, in order to correctly describe the impact of the base resistance on the total series resistance of the solar cell, the base conductivity modulation at MPP conditions should be taken into account.

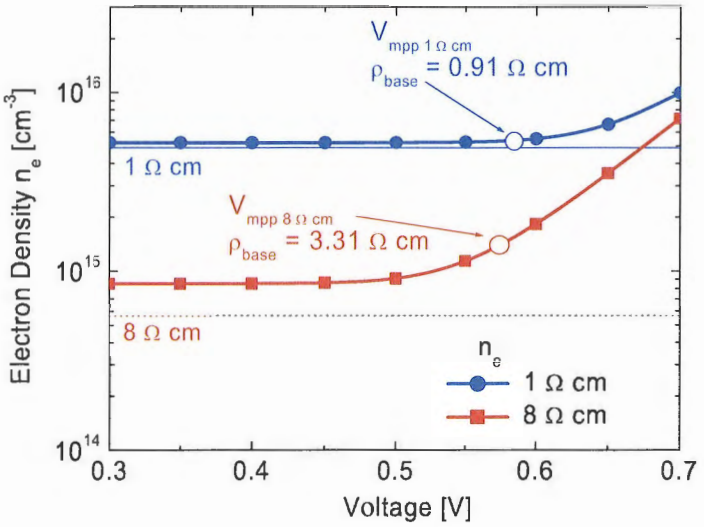


Figure 8-7 Two-dimensional simulation of the electron density in the base of the BC-BJ solar cells for two specific base resistivities of 1 and 8 Ω cm. The electron density was calculated in the voltage range of 0.3 to 0.7 V, in a distance of 100 µm from the top cell surface. The base conductivity modulation at the maximum power point is shown. Thin lines represent the base doping.

In Figure 8-7, a two-dimensional simulation of the electron density in the base in the voltage range of 0.3 to 0.7 V is presented. The voltage at maximum power point for 1 and 8 Ω cm base resistivities is marked in the graph. For both base resistivities, the electron density at MPP is higher than the base doping. ρ_{base} at MPP is therefore reduced compared to the base resistivity of the non-illuminated samples. At MPP conditions, the base resistivity equals 0.91 Ω cm for the specific base resistivity of 1 Ω cm, and 3.31 Ω cm for base resistivity of 8 Ω cm. Thus, ρ_{base} of the 8 Ω cm cells is significantly reduced under one sun illumination and operation at maximum power point. The effect of conductivity modulation at the maximum power point was taken

into account in the analytical modeling. As shown in Figure 8-8, a very good agreement between the experimental data and the analytical modeling of series resistance, adjusted for the conductivity modulation at MPP conditions, proves validity of the analytical model.

8.6.4 Series resistance

In order to investigate the pitch-related resistance losses, the total series resistance R_S of the processed cells was determined. The series resistance was obtained by comparing the SunsV_{OC} curve [153] with the one-sun IV-curve. The details of the measurement of the series resistance of the analyzed cells were presented in section 6.5. For more details on this method to determine the series resistance, see for example reference [154]. The experimentally determined series resistance is presented in Figure 8-8, together with the analytical series resistance modeling. The analytical modeling of the series resistance includes the effect of the enhanced lateral current transport in the front n^+ layer, as described by equation (8.1).

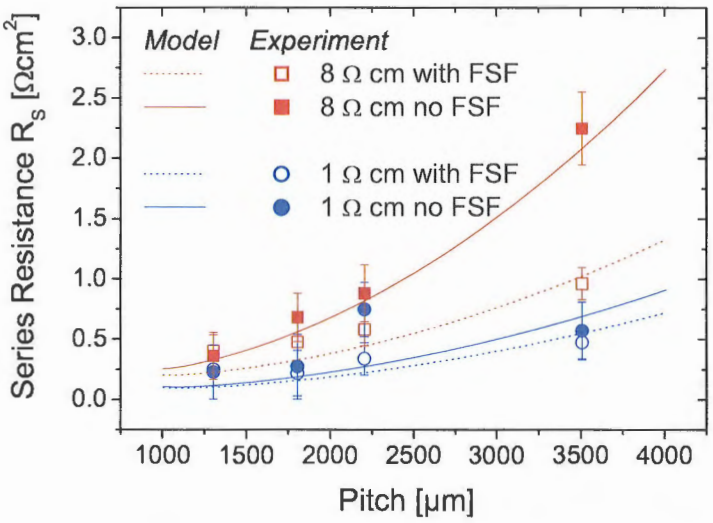


Figure 8-8 Series resistance of the BC-BJ Si solar cells with different pitches. Results of the cells on 1 and 8 Ω cm bulk resistivity and with and without the 148 Ω/sq front surface field are presented. The data points represent the mean experimental resistance values of 1 to 4 cells, determined by comparison of the measured FF and the SunsV_{OC} PFF. The lines represent the simple analytical series resistance model, in which the lateral current transport in the front diffused n^+ layer was taken into account as described by equation (8.1). In the analytical model, the base specific resistivity was adjusted for the conductivity modulation at the maximum power point.

For the 1 Ω cm cells with FSF diffusion, the series resistance R_S increases, starting from 0.2 Ω cm^2 for the lowest pitch of 1.3 mm to 0.5 Ω cm^2 for a pitch of 3.5 mm. The FF of these cells drops at the same time by about 1 % absolute, causing around 0.3 % absolute efficiency loss. For the case of the 1 Ω cm cells without FSF, the increase of R_S is higher. For the largest pitch R_S reaches 0.6 Ω cm^2.

The solar cells with a base resistivity of 8 Ω cm have a much higher lateral base resistance than the 1 Ω cm cells. This results in a lower FF for even the smallest pitch of 1.3 mm. Moreover, the fill factor drop with the increasing pitch is significantly larger than in the case of 1 Ω cm material. For the pitch distance of 1.3 mm, a maximal FF of 79 % and 78 % for 8 Ω cm cells with and without FSF respectively was measured. When reaching the largest pitch of 3.5 mm, the FF dropped to 76 % for cells with FSF and to 63 % for cells without FSF. An absolute FF drop by 3 % for the cells with FSF was caused by the increase of R_S from 0.36 Ω cm^2 for pitch of 1.3 mm to 0.96 Ω cm^2 for pitch of 3.5 mm. At the same time the FF of the 8 Ω cm cells without FSF dropped by 15 $\%_{abs}$, due to increase of R_S from 0.4 to 2.3 Ω cm^2. The drop in fill factor of our cells is consistent with the series resistance model of Mette [130] which predicts a drop of FF from 4.5 to 5.5 $\%_{abs}$ due to an increase of series resistance by 1 Ω cm^2.

8.7 Simulations of the lateral current flow of the majority carriers

The two-dimensional simulations of the majority carriers current transport are shown in Figure 8-9. Here the extreme case of the largest pitch of 3.5 mm was analyzed. The enhanced electron current density in the front n^+ diffused layer area is shown in detail (right side). The electron current density in the n^+ diffused layer area is around two orders of magnitude higher than in the base. This simulation shows that the lateral electron current transport takes place not only in the base, but also in the front diffused n^+ layer. The electrons, which were photo-generated at the front cell side in the first few micrometers of the wafer, take advantage of the high conductivity of the front n^+ layer until they are above the base contacts and then a vertical current transport through the base thickness takes place.

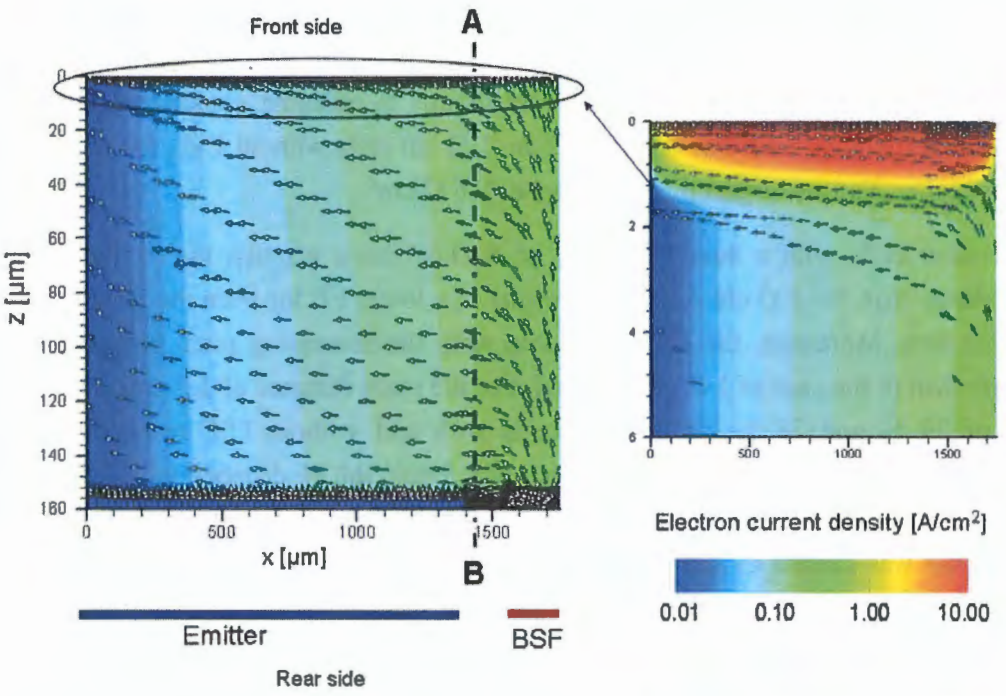


Figure 8-9 *Two-dimensional modeling results of the lateral and vertical electron current transport in the n-type BC-BJ solar cell structure with base resistivity of 8 Ω cm and pitch distance of 3.5 mm. The symmetry element of the solar cell is shown. The arrows show the direction opposite to the electron flow at V_{MPP} of a cell with front surface field (ρ_{FSF} = 148 Ω/sq). The A-B cut of the electron current density through the cell thickness is marked.*

The vertical profiles of the electron current density through the thickness of the solar cell were taken in the vicinity of the base contacts (A-B cut in Figure 8-9). These profiles for 1 and 8 Ω cm specific base resistivities are shown in Figure 8-10. A significant difference in the fraction of the current transport in the front diffused region and the base between the two base resistivities can be observed. After integrating the current density profiles, it was found that for the specific base resistivity of 1 Ω cm, 27 % of the lateral electron current transport takes place in the front n^+ layer. The remaining 73 % of the current flows laterally through the base.

A simple parallel resistance circuitry, as introduced by the analytical model in equation (8.1), can be applied to clarify the current sharing between base and n^+ front region. For the specific base resistivity of 1 Ω cm and the wafer thickness of 160 µm the wafer sheet resistance equals 42 Ω/sq. The base resistance is in parallel with n^+ sheet resistance of 148 Ω/sq. This implies a current sharing of 29 % for the front n^+ region and 71 % for the n-type base. Thus, in the case of base resistivity of 1 Ω cm, the

analytical modeling matches very well the two-dimensional modeling presented in Figure 8-10.

The analysis of the 2-D simulation of the cells with base resistivity of 8 Ω cm shows that the contribution of the front diffused area to the lateral current transport of the majority carriers becomes dominant and increases to 55 %, with 45 % of the current transport taking place in the base. The application of the same simple parallel resistance circuitry here would result in the current sharing of 77 % in the front diffused region and 23 % in the base. These results are not in agreement with 2-D simulations. However, if the same calculation is repeated for the base resistance corrected for conductivity modulation at MPP (ρ_{base}=3.31 Ω cm instead of 8 Ω cm), the base would carry 42 % of the current and the front diffused layer would carry 52% of the current. These results match the simulation results very well. The analysis presented above shows the importance of using two-dimensional modeling when describing the solar cell, which does not operate in low injection conditions.

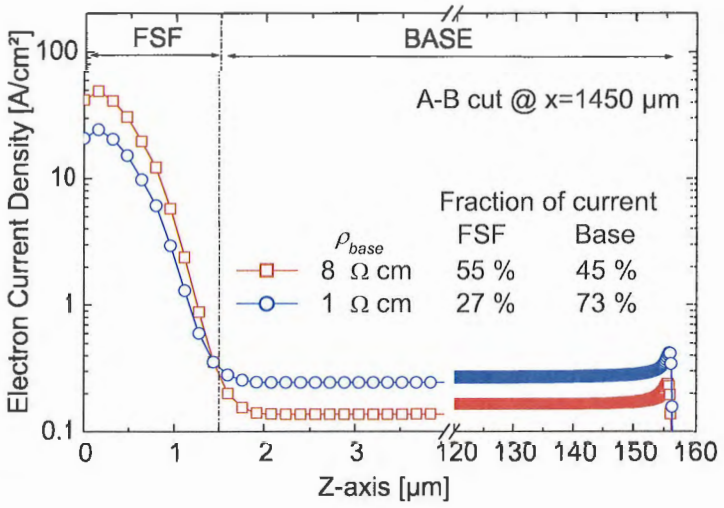


Figure 8-10 Two-dimensional simulation of the electron current density for cells with 1 and 8 Ω cm specific base resistivity and a FSF (ρ_{FSF} = 148 Ω/sq) at the maximum power point conditions. A-B cuts of the electron current density through the wafer thickness for both base resistivities are shown. Front side of the solar cell corresponds to z=0. Areas of the FSF and the base are indicated in the graph. Fractions of the current flow in the front n^+ diffused layer and the base for both specific base resitivities are shown.

8.8 Conclusions

If a low-cost structuring technology is applied in the processing of the BJ BC cell structure, the pitch on the rear side of the cell drastically increases to values in the range of millimeters. This significantly increases the lateral base resistance. The presented investigations show that the introduction of a phosphorus-doped front surface field significantly reduces the lateral base resistance losses. The majority carriers, which were photo-generated in large lateral distances from the base contacts and on the front side, take advantage of the high conductivity of the front diffused n^+ layer in order to reduce the resistance losses. The highly doped front layer can be seen as a low-resistivity *highway* for the majority carriers, which enhances its lateral transport. The front diffused n^+ layer can be seen as a parallel resistance to the lateral base resistance, and its influence on the total series resistance of the cells was successfully modeled using the parallel circuitry. In order to correctly describe the contribution of the base lateral resistance to the modeling, it is important to regard the conductivity modulation of the base resistance under the maximal power point conductions.

As expected, the enhanced lateral majority carrier's current transport in the front diffused n^+ layer is a function of the pitch and the base resistivity. The introduction of phosphorus-diffused FSF reduces the total series resistance of the measured cells with 3.5 mm pitch of 0.1 $\Omega\,cm^2$ for the base resistivity and 1.3 $\Omega\,cm^2$ for the 8 Ω cm base resistivity when compared to solar cells without the FSF. According to the two-dimensional simulations of the electron current transport, the electron current density in the front diffused n^+ layer is around two orders of magnitude higher than in the base of the solar cell. Depending on base resistivity, the lateral current transport via front n^+ diffused layer is in the range of 27 to 55 % of the total lateral current transport for 1 and 8 Ω cm base resistivity, respectively.

9 Low-illumination characteristics

The linearity of the current and voltage of three structures of high-efficiency back-junction back-contact silicon solar cells at low illumination were analyzed. Both n-type cells with non-diffused front surface and p-type cells with floating n-emitter show a pronounced current non-linearity, due to strong illumination dependence of the passivation quality of the non-diffused surface and the floating junction respectively. The quantum efficiency of this cell type drops significantly for illumination densities lower than 0.5 suns. In contrast, the quantum efficiency of n-type cells with n^+ front surface field is independent of illumination density. Thus, the n-type cell structure with n^+ front surface field enables highest energy yield at low illumination intensity conditions.

9.1 Introduction

Solar cell efficiencies are normally only reported at standard testing conditions (STC). These conditions include the so called "one sun" illumination intensity of 1000 W/m^2 with spectrum AM1.5g [171] and a device temperature of 25 °C [172]. However, over the whole year under realistic conditions, photovoltaic systems operate during cloudy days, or in the morning and evening periods of the day as well. These are the periods of strongly reduced illumination intensity. Therefore, the annual energy yield of a photovoltaic system is influenced by the low light intensity characteristics of the solar cells. Thus, in order to maximize the energy delivered by the photovoltaic system, the performance of this system should such be as high as possible, even at the low light periods of the day and the year.

The purpose of this chapter is to analyze the different back-junction back-contact solar cells structures with respect to their performance under the low-illumination intensities. Three different front surface passivation schemes are analyzed. These structures are schematically shown in Figure 9-1:

a) n-type cell with non-diffused front surface,

b) p-type cell with an n^+ floating emitter and

c) n-type cell with an n^+ front surface field (FSF).

The n-type solar cells with and without the front surface field were developed in this work and the details of their processing technology were already presented in chapter 4.

The p-type solar cells with the floating junction were developed and analyzed in the work of Dicker et al. [33] and these results are presented here for comparison with the n-type structures.

The relation between current and illumination intensity and voltage and the illumination intensity of three above mentioned solar cell structures is analyzed in the present chapter.

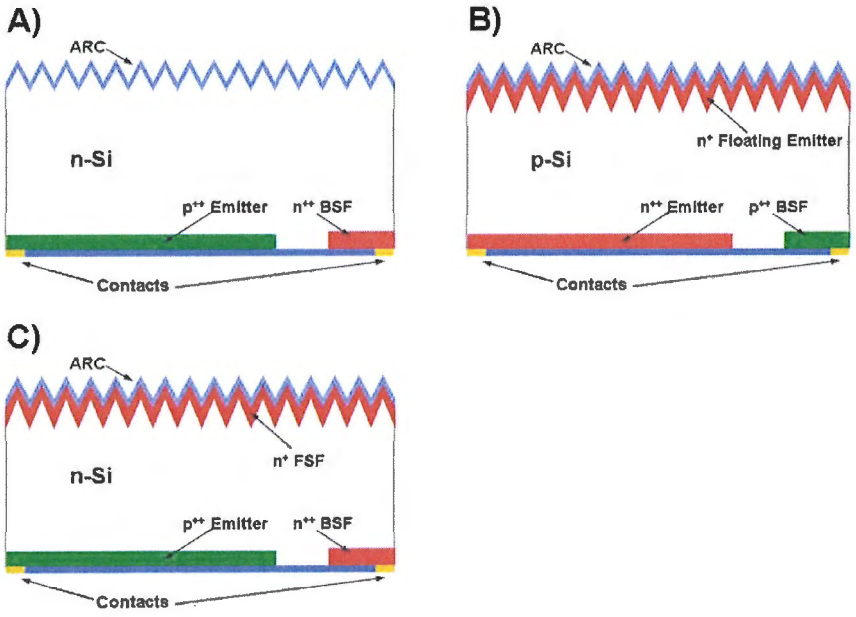


Figure 9-1 Sketch of two-dimensional symmetry elements of the back-junction solar cells: n-type with non-diffused front surface (structure A), p-type with a phosphorus doped floating emitter (structure B), and n-type with a phosphorus doped FSF (structure C).

9.2 Analyzed solar cells and methodology

Analyzed solar cells

The parameters of the solar cells chosen for the low-illumination analysis are summarized in Table 9-1. BJ BC solar cells with three structures corresponding to the notation used in Figure 9-1 were selected. The efficiency of the chosen cells was in the

range of 11.0 to 20.4 %. n-type solar cells with base resistivity of 1 and 8 Ω cm were analyzed. The results of the n-type cells with and without the FSF were compared to the p-type cell structure with the floating junction.

Table 9-1 *IV-parameters of solar cells with different front surface passivation schemes (structure types names correspond to the notation used in Figure 9-1). The presented results are measured under one sun illumination intensity and 25 °C device temperature.*

Cell No.	Structure type	Area [cm^2]	ρ_{base} [Ω cm]	V_{OC} [mV]	J_{SC} [mA/cm^2]	FF [-]	η [%]
BC47-22b '*good*'	A	4	1	649.7	35.2	0.817	18.7
BC47-23g '*bad*'	A	4	1	632.9	30.4	0.785	15.1
BC47-24b '*good*'	A	4	8	636.6	38.65	0.737	18.1
BC47-25g '*bad*'	A	4	8	598.7	29.9	0.613	11.0
RSK3-5a	B	4	1	685.0	32.1	0.792	17.4
BC47-18g	C	4	1	658.5	39.0	0.794	20.4
BC47-21g	C	4	8	653.5	39.7	0.752	19.5

External quantum efficiency

In order to examine the relation between current density and light intensity of the three cell structures described above, the external quantum efficiency (EQE) of all analyzed cells was measured in the range of 300 to 1200 nm under a bias light intensity of 0.3 and 1 sun.

Moreover, the EQE at a wavelength of 600 nm was measured as a function of bias light intensity in the illumination range of 0.01 to 1 suns. Due to the high absorption coefficient of the light with a wavelength of 600 nm, the EQE at 600 nm reflects the current of the carriers generated close to the front surface. This current is especially sensitive to the front surface recombination. Thus, any variation in the front surface recombination rate with the variation of illumination intensity can be measured well by a measurement of the solar cell response at a wavelength of 600 nm. The measured EQE at different bias light intensities was than normalized with respect to EQE at one-sun bias light intensity.

Open-circuit voltage

The V_{OC} of all cells was measured in an illumination intensity range of 0.1 to almost 10 suns. The SunsV_{OC} method [153] was used here. The dependence of the V_{OC} with illumination intensity (C for concentration) can be described with the following equation [173]:

$$V_{OC}(C) \approx \frac{kT}{q} \ln\left(\frac{CJ_{ph,one-sun}}{J_0}\right) \approx V_{OC,one-sun} + \frac{kT}{q} \ln(C) \tag{9.1}$$

where $V_{OC,one\text{-}sun}$ and $J_{ph,one\text{-}sun}$ are the V_{OC} and photogenerated current, measured under standard reference conditions at the 1 sun illumination intensity respectively. When the saturation current J_0 is constant in the analyzed illumination intensity range, then a linear increase of voltage with the logarithm of light intensity is expected. The resulting V_{OC} dependence with illumination density can then be described by the right side of equation (9.1). The V_{OC} should show an increase of around 60 mV for each decade of increase of intensity. A deviation from the logarithmic illumination behavior could be caused if the saturation current of the cell is injection dependent.

Device simulations

In addition to solar cell measurements, two-dimensional device simulations of the symmetry elements shown in Figure 9-1 were performed. The EQE at 600 nm with varying bias light intensity was simulated and the simulation results were compared with the measured data.

9.3 Non-diffused surfaces

Two sets of parallel processed solar cells with structure A were selected for the low illumination analysis. The first pair of cells, marked as *'good'* in the Table 9-1, had EQE at one-sun bias light of about 85 %. The second pair, marked as *'bad'*, with inferior front surface passivation had an EQE of around 75 %. Cells with non-diffused front surfaces are very vulnerable to variation of front surface recombination velocity (S_{front}) as shown in section 2.3. Even a small increase of S_{front} will result in a significant current decrease. This explains the large differences between the performance of the *'good'* and *'bad'* identically processed cells. Minor and difficult-to-avoid processing imperfections, such as broken pyramid tips, local scratches or other front surface inhomogenities cause extreme differences in cell performance. Processing faults create spots on the cell front surface with locally strongly increased S_{front}. These local imperfections will, therefore, lead to a locally inhomogeneous S_{front} value.

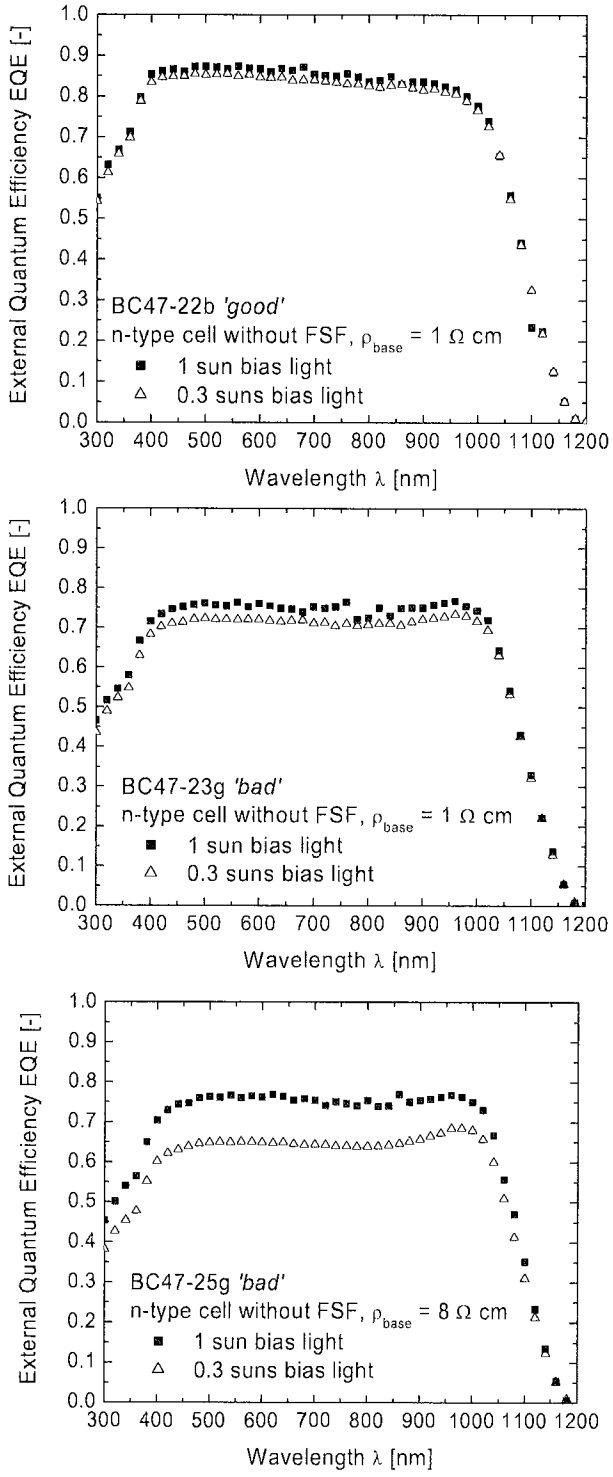


Figure 9-2 External quantum efficiency of three different n-type back-contact back-junction cells with non-diffused front surface (structure A) measured at 0.3 and 1 sun bias light intensity.

The external quantum efficiency of the structure A cells measured at a bias light intensity of 0.3 and 1 sun is shown in Figure 9-2. A strong bias light intensity dependence was observed. For the 1 Ω cm cell marked as *'good'* (BC47-22B), a 3 to 5 % absolute decrease of EQE was measured when lowering the bias light intensity from 1 to 0.3 suns. For the cells marked as *'bad'*, the decrease in EQE was even more pronounced. The EQE of the 1 Ω cm (BC47-23g) dropped by 5 to 7 % at lower bias light intensity. For the 8 Ω cm cell, the EQE dropped by 10 %.

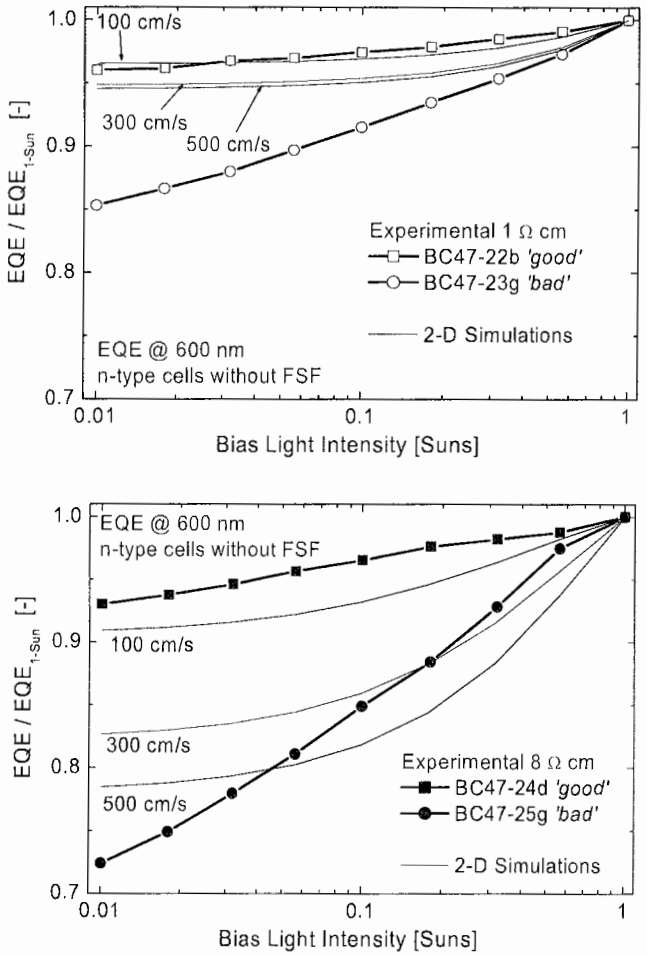


Figure 9-3 Normalized EQE for n-type back-contact back-junction cells with non-diffused front surface (structure A) measured at wavelength of 600 nm in bias light intensity range of 0.01 to 1 sun. Results for base resistivity of 1 Ω cm (top) and 8 Ω cm (bottom) are shown. Sets of two-dimensional simulations for different S_{front} values (S_{front} is shown next to simulation results) are plotted next to experimental results.

All four analyzed cells exhibit a very strong current non-linearity under low illumination. The non-linearity is much larger for the cells with lower performance. Normalized EQE of the *'bad'* cells drops down to 85 % for 1 Ω cm base resistivity, and to 72 % for 8 Ω cm base resistivity at 0.01 suns due to injection-dependent effects of the front surface recombination.

Two-dimensional device simulations (thin lines in Figure 9-3) with a set of S_{front} values as input parameters also predict a strong non-linearity of the structure A cells. A fixed S_{front} was assumed for the whole area of the front surface. However, the simulation results also show that the injection dependence cannot be described with a single S_{front} value, although injection dependence of $S_{front} = S_n = S_p$ and bulk lifetime ($\tau_{n0} = \tau_{p0} =$ 1 ms) were taken into account in the simulation. A possible explanation of these differences may be the fact that the *local* surface imperfections have to be taken into account. The combination of locally distributed S_{front} values could then result in more complex injection dependence as expected from the simulation with a single homogeneous S_{front} value.

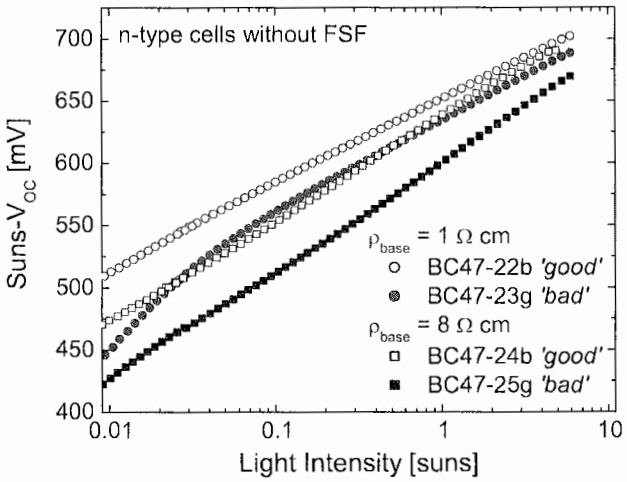


Figure 9-4 Open-circuit voltage of the n-type back-contact back-junction cells with non-diffused front surface (structure A) measured in bias light intensity range of 0.01 to 10 suns. Results for 1 and 8 Ω cm base resistivity are shown.

The open-circuit voltage of the analyzed cells measured in the light intensity range of 0.01 to 10 suns is shown in Figure 9-4. The V_{OC} of all 4 analyzed cells shows a linear decrease with logarithm of light intensity as predicted by equation (9.1) until 0.1 suns. However, for light intensities lower than 0.1 suns, a deviation from this linear decrease can be observed for the *'bad'* cells (BC47-23g and BC47-25g). The decrease of V_{OC}

under low illumination intensities is stronger than theoretically predicted. This is believed to be caused by a increase of S_{front} and thus increase of $J_{0,front}$, under low injection operating conditions.

The solar cell operates under V_{OC} conditions at a much higher injection level than in the case of J_{SC}. Therefore, the effect of increased recombination caused by a transition from high injection to low injection operating conditions occurs in the case of V_{OC} at much lower light intensities than in the case of J_{SC}. That is why the EQE of the structure A cells already decreased significantly at light intensity of 0.3 suns, and the V_{OC} at the same time shows non-linearity first at illumination lower than 0.1 suns.

9.4 Floating emitters

The p-type solar cells with floating emitter (structure B) were processed with the use of photolithography. The solar cell selected for the present analysis had an efficiency of 17.4 %. The thin metallization grid on the cell rear side covers only a small fraction of the cell rear side, thus enabling bifacial illumination of the cell structure. This feature was used during the measurements of the open-circuit voltage. The structure B solar cell was illuminated form the rear cells side during the open-circuit voltage measurements, due to problems with proper contacting of the metal grid during front side illumination.

The external quantum efficiency of the cell RSK3-5a measured at bias light intensity of 1 and 0.3 suns is shown in Figure 9-5. A decrease of the EQE by 2 to 3 % absolute when lowering the bias light from 1 to 0.3 suns was measured. As in the case of the cells without front diffusion described in the previous section, the current of the structure B cell is also non-linear, i.e. the short circuit current density decreases with decreasing bias light illumination intensity. This effect is even stronger for lower bias light intensities, as shown in Figure 9-6.

Normalized EQEs of p-type cell with floating emitter, measured in the bias light intensity range 0.01 to 1 suns, are shown in Figure 9-6. The EQE decreases rapidly for the bias light intensity lower than 0.5 suns. The effects responsible for this behavior are imperfections of the floating junction (see Figure 9-7). The diffusion inhomogenities and introduction of crystal defects lead to formation of an internal shunt element ($R_{p,floating}$) across the junction and to recombination in the space charge region, which causes diode saturation current ($J_{02,p}$) [174]. Both elements strongly reduce the voltage across the floating junction ($V_{floating}$), which is necessary to obtain a good surface passivation. The shunt resistance and a diode with ideality factor of 2 were implemented across the front side floating junction into PC1D simulations of the

floating emitter cell structure. The PC1D simulation results plotted in Figure 9-6 are in good agreement with the experimental data, indicating a reasonable model for the imperfections of the floating emitter.

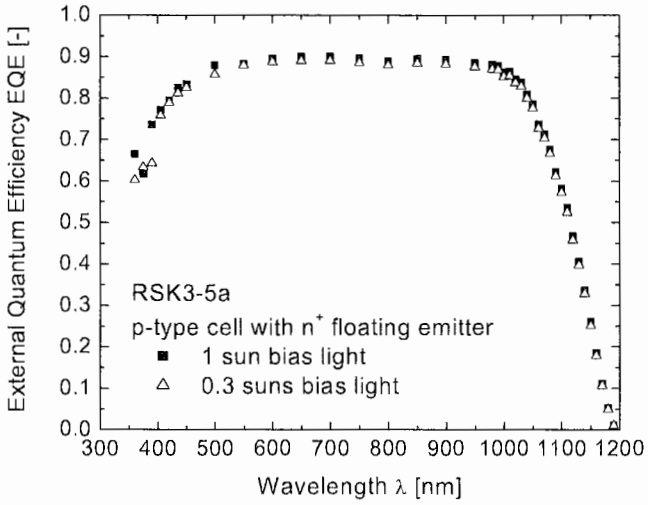


Figure 9-5 External quantum efficiency of three different p-type back-contact back-junction cells with floating emitter (structure B) measured at 0.3 and 1 sun bias light intensity.

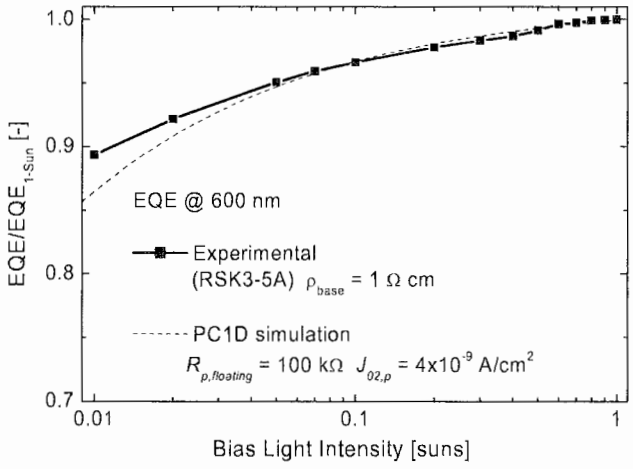


Figure 9-6 Normalized EQE for a p-type cell with floating emitter (structure B) measured at wavelength of 600 nm in bias light intensity range of 0.01 to 1 sun. The dotted line shows a PC1D simulation using $R_{p,floating}$ and $J_{02,p}$ values as shown in the graph.

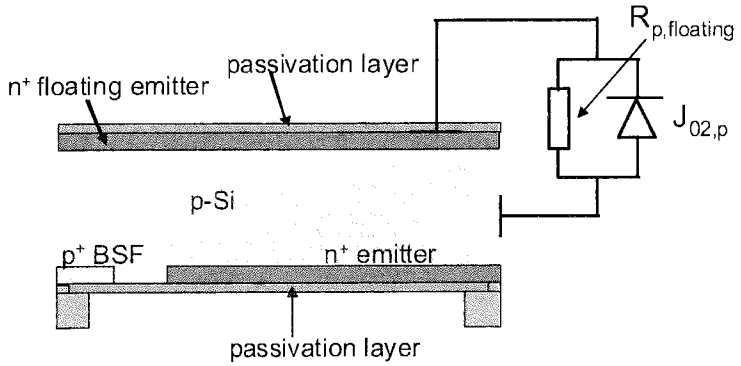


Figure 9-7 Equivalent circuit diagram for shunting effects across the floating junction used in PC1D simulations.

In the presence of the structure imperfections mentioned above, a $V_{floating}$ of about 600 mV is needed to passivate the surface. $V_{floating}$ is a function of the bias light intensity and increases with the logarithm of the light intensity, as shown in equation (9.1). Such a high voltage across the floating junction on the front side is only achieved at the light intensity higher than 0.5 suns. Thus, the surface passivation with floating junction is a very effective passivation scheme for medium to high illumination. At the same time, its passivation quality in realistic structures is poor at low illumination, due to low $V_{floating}$ and consequently high S_{front}.

The V_{OC} of the p-type cell with floating emitter was measured in illumination intensity range of 0.01 to 10 suns and is shown in Figure 9-8. In contrast to the quantum efficiency, the V_{OC} shows an approximately logarithmic behaviour with lowering of the illumination intensity. The different bias light dependence between EQE and V_{OC} of the structure B cell can be also explained by different cell operation conditions. At V_{OC} conditions, the solar cell operates under significantly higher injection level in comparison to the J_{SC} conditions, as already explained in the previous sections.

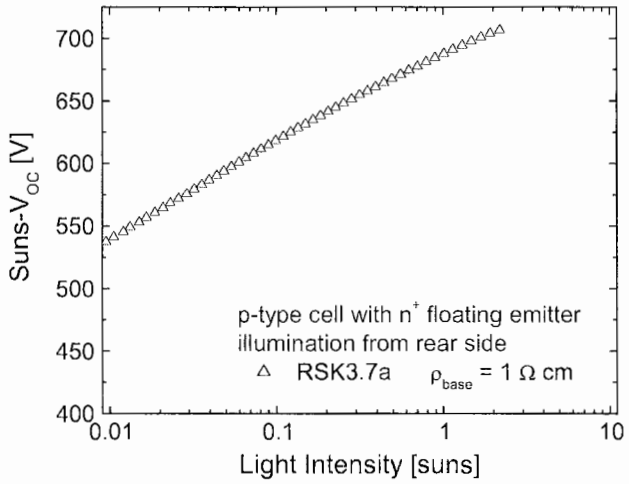


Figure 9-8 *Open-circuit voltage of the p-type back-contact back-junction cell with floating emitter (structure B) measured in bias light intensity range of 0.01 to 1 sun. Result for solar cell with 1 Ω cm base resistivity is shown. The solar cell was illuminated from the rear side during the measurement.*

9.5 Front surface fields

n-type solar cells with a phosphorus-doped n^+ front surface field (structure C) with base resistivity of 1 and 8 Ω cm were selected for the low illumination analysis. As shown in Table 9-1, these cells have an efficiency of 20.4 % and 19.5 % respectively. The EQE of the 1 Ω cm cell (BC47-18g) equals 95 % at wavelength of 600 nm. The EQE of the 8 Ω cm cell (BC47-21g) is higher due to higher collection efficiency and equals 98 % at the same wavelength. Both structure C cells have an EQE independent of the bias light illumination intensity, as shown in Figure 9-9. The quantum efficiency of the analyzed cells does not decrease with lowering of the bias light intensity from 1 to 0.3 suns.

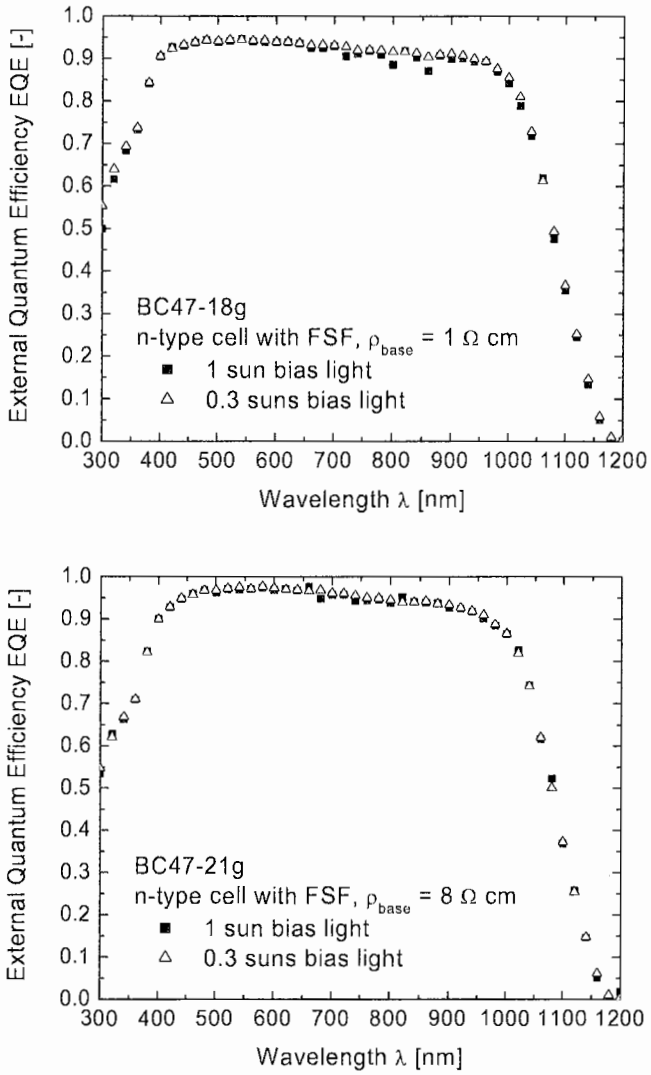


Figure 9-9 External quantum efficiency of n-type back-contact back-junction cells with front surface field (structure C) measured at 0.3 and 1 suns bias light intensity. Results for solar cells with base resistivity of 1 Ω cm (top) and 8 Ω cm (bottom) are shown.

The measurements of the normalized EQE for n-type cells with FSF are shown in Figure 9-10. The normalized EQE for both 1 and 8 Ω cm base doping is constant in the analyzed bias light intensity range. Therefore the current of the structure C is linear with bias light. Device simulations predict only a very weak injection dependence of the FSF cells. Within the measurement error, the experimental results are in good agreement with simulations.

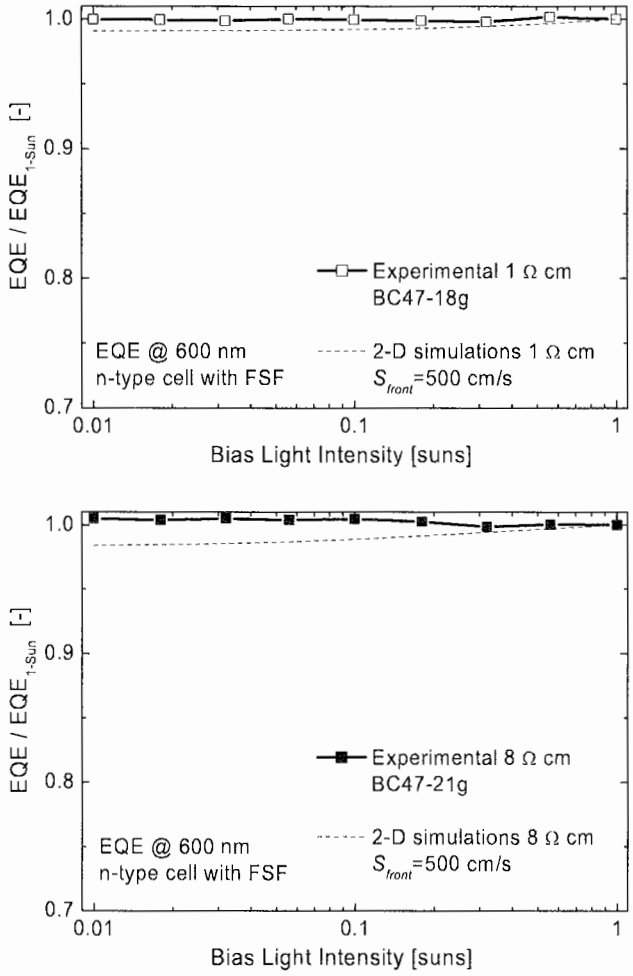


Figure 9-10 Normalized EQE for n-type cells with front surface field (structure C) measured at wavelength of 600 nm in bias light intensity range of 0.01 to 1 sun. Two-dimensional simulation results are shown as well (lines). Results for solar cells with base resistivity of 1 Ω cm (top) and 8 Ω cm (bottom) are shown.

The front surface of the FSF cell (structure C) always operates in the investigated illumination intensity range for both base resistivities under low-injection, due to high doping surface concentration of the phosphorus diffusion profile ($N_{peak} = 5\times10^{18}$ cm^{-3}). Thus, the high-injection effects do not occur at the physical surface as in the case of structure A and B cells, which showed a strong current injection dependence. A good passivation quality is achieved due to the high-low junction at the front surface, which is not affected by the illumination level, in contrast to the floating emitter passivation shown in the previous section. The front surface passivation with FSF is thus well suited also for low-illumination power generation.

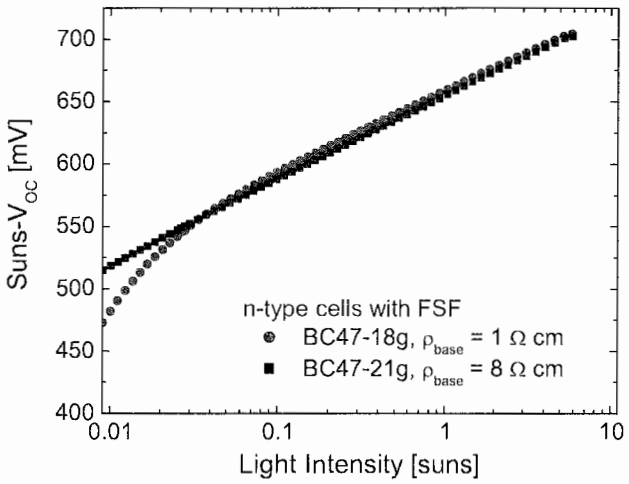


Figure 9-11 Open-circuit voltage of the n-type back-contact back-junction cells with front surface field (structure C) measured in bias light intensity range of 0.01 to 10 suns. Results for base resistivity of 1 and 8 Ω cm are shown.

The open-circuit voltage of the structure C cells measured in wide illumination intensity range is shown in Figure 9-11. Both measured cells show a linear decrease in voltage with lowering of the illumination intensity down to 0.1 suns. However, for illumination intensity lower than 0.1 suns, the V_{OC} of both cells becomes non-linear with illumination. This effect is much stronger for the cells with base resistivity of 1 Ω cm than for the cells with base resistivity of 8 Ω cm. A further analysis of this effect is needed in order to fully explain observed non-linearity of the voltage of the structure C cells. However, since the current of the n-type cells with FSF is independent of the illumination intensity and the voltage shows non-linear behavior only at the illumination intensities lower than 0.1 suns, it may be concluded that the structure C is best suited for low illumination applications from all three analyzed cell structures.

9.6 Conclusions

The quantum efficiency and open-circuit voltage of the three back-contact back-junction solar cell structures was analyzed under low illumination conditions. Among the analyzed cell structures, it was shown that the current of only n-type cells with n^+ front surface field is linear with light intensity. The quantum efficiency of the n-type cells with non-diffused front surfaces and the p-type cells with floating emitter decreases with lower illumination intensity. This leads to a reduced cell performance under lower illumination.

In practical terms, non-perfect processing of the front surface, including diffusion inhomogenities, introduction of crystal defects, broken pyramid tips, and local scratches introduce injection dependence behavior of the n-type cells with non-diffused front surfaces and the p-type cells with floating emitter. On the other hand, front surface recombination of the n-type solar cells with FSF has much lower influence on the cell performance, due to the passivation effect of the high-low junction. Therefore, the performance of the n-type cells with FSF is not affected by low-injection effects. Thus, the passivation of the front surface of the BC-BJ cells with FSF seem to be the best one suited for achieving a high energy yield when also operating under low illumination intensity.

As expected from the physical model, the V_{OC} of all cell structures decreases linearly with the logarithm of illumination until intensity of 0.1 suns. The injection level of a solar cell under V_{OC} conditions is much higher than under the J_{SC} conditions. Therefore the low injection effects cannot be seen at lower illumination intensities, in contrast to the case of quantum efficiency analysis.

10 Summary and outlook

Summary

In this thesis high-efficiency back-contact back-junction (BC-BJ) silicon solar cells for one-sun applications were studied. The focus was put on the development of a low-cost and industrially feasible manufacturing technology in order to utilize the full cost reduction potential of this elegant cell structure. At the same time the performance of the developed solar cells was investigated in details by experimental work, analytical modeling and numerical device simulations.

The BC-BJ solar cell structure requires multiple *structuring steps*, to form an interdigitated grid of p- and n-diffusions, contact openings and metal grids. In this work, the complex and costly photolithography masking steps were replaced by techniques which are of low cost and relevant for mass production. Screen-printing of the masking layers, as well as the local laser ablation of the dielectric and silicon layers, were developed and successfully applied to the solar cell processing sequence. The highest solar cell efficiency of 21.1 % (J_{SC} = 38.6 mA/cm^2, V_{OC} = 668 mV, FF = 82.0 %) was achieved on 160 µm thick 1 Ω cm n-type FZ Si with the designated area of 4 cm^2. No photolithography was applied in the processing sequence of this solar cell.

High-temperature diffusion of boron is applied for *emitter formation* of the n-type BC-BJ solar cells. However, this process needs to take place at strongly elevated temperatures and requires an additional masking step in order to define the areas for local diffusion. Therefore an alternative low temperature and mask less process to create p-type emitters, namely the local laser-fired aluminium emitter (LFE) process, was investigated in detail. It was found that the injection-dependent Shockley-Read-Hall recombination in the laser-induced damage zone located in the direct vicinity of the local back junction negatively influences the cell performance. Based on this disadvantage of the LFE process, the application of the LFE in the manufacturing of the high-efficiency back-junction solar cells was not followed further in the course of this thesis.

A *detailed study of the loss mechanisms* limiting the efficiency of the developed back-contact back-junction silicon solar cell was performed. The reduction of the cell efficiency was determined to be 3.9 % abs. due to recombination processes, 2.0 % abs. due to optical losses, 0.3 % abs. due to series resistance effects and 0.7 % due to electrical shading. The developed model of the loss mechanisms is a powerful tool for

the further optimization study of the solar cell structure. Based on this model it was found that the solar cell efficiencies of up to 23 % could be reached by improving the solar cell optics, reduction of the overall recombination losses, minimization of the electrical shading and optimization of the cell and grid geometry, which is limited by the industrial structuring technologies.

Positive effects of the phosphorus doped n^+ *front surface field* (FSF) on the performance of the BC-BJ solar cells were studied in details. These positive effects of FSF include: (i) passivation of the front cell surface and improvement of the stability of the cell performance under UV exposure, (ii) reduction of the series resistance and (iii) improvement of the solar cell performance under low illumination.

The best solar cell results were obtained with a deep diffused Gaussian phosphorus FSF doping profile with sheet resistance of 148 Ω/sq. The saturation current density of the passivated and textured surface with this FSF diffusion profile equals 21 fA/cm^2. In contrast to solar cells without the FSF diffusion, the solar cells with the FSF diffusion profile did not show any performance degradation under *exposure to UV radiation.*

Phosphorus doped FSF not only improves the front surface passivation of the analyzed solar cells. The highly doped front n^+ layer can be also seen as a highly conductive *highway* for the majority carriers, which enhances its lateral transport. The front diffused n^+ layer can be seen as a parallel conductor to the lateral base resistance. This way the lateral base resistance can be reduced. Lateral pitch is in the case of the developed cells in the range of millimeters, due to the application of the low-cost screen-printing and laser ablation structuring. Experimental data show that the application of a FSF reduces the total series resistance of the measured n-type cells of 160 micrometer thickness with 3.5 mm pitch by 0.1 Ω cm^2 for 1 Ω cm base resistivity and 1.3 Ω cm^2 for 8 Ω cm base resistivity.

Next to improvement of the front surface passivation and reduction of the lateral base resistance, the front surface field improves the *performance* of the BC-BJ solar cells *under low illumination intensity.* Among different analyzed cell structures, it was shown that the current only of n-type cells with n^+ front surface field is linear with light intensity. Due to the fact that the front surface passivation of the n-type BC-BJ cells with FSF is not affected by low-injection effects, the quantum efficiency of these cells does not decrease in the bias light intensity range down to 0.01 suns. Therefore the BC-BJ cells with FSF seem to be these best suited for achieving a high energy yield when also operating under low illumination intensity.

Outlook

In the present thesis a base-line technological process for processing of back-contact back-junction Si solar cells was established. In order to further increase its economical competitiveness and fully utilize the potential of this cell structure, the *future research* should focus on the further optimization of the device efficiency and reduction of the manufacturing costs.

The *optimization of the solar cell geometry* should be pursued with the focus on increasing the emitter coverage on the rear side and at the same time reducing the overall device pitch. This can be obtained by careful optimization of the resolution and the positioning accuracy of the masking processing steps. Ideally these activities should be performed rather in the pilot-line environment than in the low-throughput laboratory conditions.

In parallel to the optimization of the device geometry, the electrical properties of the solar cell should be further optimized. The free carrier absorption losses and the high contribution of the rear side diffusions to the overall solar cell recombination point out the need of further *optimization of the emitter and back surface field diffusion profiles*. Also the *rear side passivation scheme* should be improved in order to reduce the recombination in the non-diffused gap areas.

An application of a pin-hole free passivation layer on the rear side, would enable *decoupling of the metallization geometry from the diffusion geometry*, without the risk of local shunt formation. This way the resistance losses in the thin base metallization fingers, which are especially important for the large size solar cells, would be reduced. Also the sizes of the diffused busbars could be reduced significantly. This way the electrical shading losses can be reduced. Further reduction of the processing costs could be obtained by replacing of the metallization using silver, by metallization scheme based on copper.

Next to the optimization of the solar cell structure, the *appropriate module technology* for the back-contacted solar cells should be applied. This technology should enable high packaging density of the solar cells and could use interconnection sheets with a pre-defined metallization pattern, which would further reduce the series resistance losses in the metallization grid.

Zusammenfassung und Ausblick

Zusammenfassung

Im Rahmen dieser Arbeit wurden hocheffiziente rückseitig kontaktierte Silicium-Solarzellen analysiert, bei denen der pn-Übergang ebenfalls auf der Rückseite ausgebildet wurde (sogenannte back-contact back-junction (BC-JC) Solarzellen). Ausgelegt waren diese Zellen für eine Beleuchtungsintensität von einer Sonne. Der Schwerpunkt dabei lag auf der Entwicklung eines preiswerten und industriell umsetzbaren Herstellungsprozesses, um das Kosteneinsparpotential dieser neuartigen Zellstruktur auszunutzen. Im Rahmen dieser Arbeit wurden ebenfalls die elektrische Effizienz der Zellen und die zugrunde liegenden physikalischen Effekte mittels verschiedener Experimente und analytischen und numerischen Simulationen detailliert untersucht.

Die Struktur der BC-BJ Solarzellen erfordert mehrere Ablaufschritte, um die ineinander greifende Struktur der p- und der n-Diffusionen, der Kontaktöffnungen und der Metallkontakte zu realisieren. In Rahmen dieser Arbeit wurden die komplexen und kostspieligen photolithographischen Prozessschritte durch einfachere und preiswertere Schritte ersetzt, welche auch industriell eingesetzt werden können. Sowohl siebgedruckte Maskierungsschichten als auch lokale lasergestützte Abtragung von dielektrischen Schichten und Silicium wurden erfolgreich entwickelt und angewandt. Das beste Zellergebnis mit einer Effizienz von 21.1 % (Kurzschlussstromdichte 38.6 mA/cm^2, Offenklemmspannung 668 mV, Füllfaktor 82.0 %) wurden bei einer 160 µm dicken, auf 1 Ω cm n-typ FZ Silicium prozessierten Solarzelle ermittelt, welche eine Aperturfläche von 4 cm^2 besaß. Bei der Prozessierung dieser hocheffizienten Solarzelle wurde komplett auf photolithographische Schritte verzichtet.

Bei den n-typ BC-JC Solarzellen wurde der Emitter durch eine Diffusion von Bor hergestellt. Allerdings sind dazu hohe Temperaturen und zusätzliche Maskierungsschritte notwendig, um die Bereiche für die lokale Diffusion einzugrenzen. Daher wurde im Rahmen dieser Arbeit ein alternativer Prozess eingehende analysiert, bei dem auf die hohen Temperaturen verzichtet werden kann und welcher ohne zusätzliche Maskierungen funktioniert. Der p-typ Emitter wird dabei durch das sogenannte „laser-fired aluminium emitter (LFE)"-Verfahren ausgebildet. Es konnte gezeigt werden, dass die injektionsabhängige Shockley-Read-Hall-Rekombination in der laserbedingten Schädigungszone in der direkten Umgebung der

lokalen rückseitigen Raumladungszone die Zelleffizienz negativ beeinflusst. Bedingt durch diesen Nachteil des LFE-Prozesses wurde dieser Ansatz im Verlauf dieser Arbeit nicht weiter verfolgt.

Ausführlich wurden die Verlustmechanismen, welche die Effizienz der untersuchten BC-BJ Solarzellen limitieren, analysiert. Dabei konnte gezeigt werden, dass die Zelleffizienz aufgrund von Rekombinationsprozessen um 3.9 % absolut, aufgrund von optischen Verlusten um 2.0 %, aufgrund von Serienwiderstands-Effekten um 0.3 % und aufgrund von elektrischen Abschattungen um 0.7 % reduziert ist. Es hat sich gezeigt, dass das entwickelte Modell der Verlustmechanismen ein mächtiges Werkzeug war, um die Struktur der hocheffizienten Solarzellen weiter zu verbessern. Darauf basierend konnte gezeigt werden, dass Zelleffizienzen von bis zu 23 % realisiert werden können, wenn die Zelloptik, Rekombinationsverluste, elektrische Abschattung und das Kontaktgrid weiter optimiert werden.

Im Rahmen dieser Arbeit wurden weiter die positiven Effekte eines Phosphor-dotierten n^+ „front surface fields (FSF)" untersucht. Diese Effekte beinhalten (i) Passivierung der Zellvorderseite und Langzeitstabilität bei Beleuchtung mittels UV-Licht, (ii) Reduzierung des Serienwiderstandes und (iii) Verbesserung der Solarzelleffizienz unter Schwachlichtverhältnissen.

Die besten Solarzellergebnisse wurden mit einem tief eingetriebenen Gauss-förmigen Phosphor FSF Dotierprofil mit einem Schichtwiderstand von 148 Ω/sq erreicht. Die Dunkelstromdichte der passivierten und texturierten Oberfläche lag dabei bei 21 fA/cm^2. Im Vergleich zu Solarzellen ohne das zusätzliche FSF konnte keine Degradation der Solarzellen unter UV-Licht nachgewiesen werden.

Ein Phosphor-dotiertes FSF verbessert nicht nur die Vorderseitenpassivierung der analysierten Solarzellen. Die hochdotierte n^+-Schicht verbessert zusätzlich den lateralen Transport der Majoritäts-Ladungsträger. In dieser Weise kann der Widerstand der Basis reduziert werden. Der laterale Abstand (Pitch) der Kontaktfinger lag bei den untersuchten Solarzellen im Bereich von Millimetern, bedingt durch die Verwendung von industriell tauglichen preiswertem Siebdruck und Laserstrukturierung. Experimentelle Daten zeigen, dass das zusätzliche FSF den gesamten Serienwiderstand der untersuchten n-typ Solarzellen mit einer Dicke von 160 µm und einem Pitch von 3.5 mm um 0.1 Ω cm^2 bei einem Basiswiderstand von 1 Ω cm und um 1.3 Ω cm^2 bei einem Basiswiderstand von 8 Ω cm reduziert.

Auch wurde im Rahmen dieser Arbeit untersucht, in wie weit das zusätzliche FSF die Zelleffizienz der BC-JC Solarzellen unter Schwachlichtbedingungen verbessert.

Mittels unterschiedlicher Zellstrukturen konnte gezeigt werden, dass bei einer n-typ Solarzelle mit einem zusätzlichen n^+ FSF der Strom linear mit der Lichtintensität ansteigt. Da diese Vorderseitenpassivierung nicht durch Niedriginjektionseffekte beeinflusst ist, ist die Quanteneffizienz der untersuchten BC-JC Solarzellen mit zusätzlichem FSF nicht verringert bis hin zu einer Lichtintensität von 0.01 Sonnen. Daher sind diese hier untersuchten BC-JC Solarzellen mit zusätzlichem FSF hervorragend geeignet, um eine hohe Stromausbeute auch unter Schwachlichtbedingengen zu erreichen.

Ausblick

In der vorliegenden Arbeit wurde ein technologischer Prozess für die Herstellung von rückseitig sammelnden und rückseitig kontaktierten Silizium-Solarzellen entwickelt. Um die Steigerung der ökonomischen Wettbewerbsfähigkeit und um das Potential dieser Zellstruktur weiter auszuschöpfen, sollten sich die zukünftige Forschungsaktivitäten auf eine weitere Optimierung des Solarzellewirkungsgrades und der Senkung der Herstellungskosten fokussieren.

Die Optimierung der Solarzellengeometrie sollte mit dem Schwerpunkt der Steigerung der Emitterbedeckung auf der Rückseite und der gleichzeitigen Verringerung der gesamten lateralen Solarzellendemensionen (Pitch) weiterverfolgt werden. Dies kann durch eine sorgfältige Optimierung der Auflösungs- und Positionierungsgenauigkeit der Maskierungsschritte erreicht werden. Ideellerweise, sollten diese Aktivitäten jedoch eher in einer Pilotlinie als in einer Laborumgebung mit geringem Durchsatz durchgeführt werden.

Parallel zur Optimierung der Solarzellengeometrie, sollten die elektrischen Eigenschaften der Solarzelle weiter verbessert werden. Die Verluste durch die Absorption freier Ladungsträger und der hohe Beitrag der Diffusionen auf der Rückseite zur gesamten Rekombination der Solarzelle haben gezeigt, dass eine Anpassung der Diffusionsprofile von Emitter und Back-Surface-Field erforderlich ist. Das rückseitige Passivierungssystem sollte ebenfalls verbessert werden, um die Rekombination im undiffundierten Bereich zu reduzieren.

Die Anwendung von „pin-hole"-freien Passivierungsschichten auf der Rückseite, würden die Entkopplung der Metallisierungsgeometrie und der Geometrie der Diffusionen ermöglichen, ohne lokale Kurzschlüsse zu erzeugen. Dadurch würden die Widerstandsverluste in den dünnen Fingern der Basismetallisierung, welche besonders wichtig für Solarzellen im Großformat sind, reduziert werden. Auch lässt sich die

Fläche der diffundierten Busbars signifikant verringert. Eine weitere Verringerung der Herstellungskosten könnte erreicht werden, indem die Metallisierung mit Silber durch die Verwendung eines Metallisierungsverfahrens mit Kupfer ersetzt wird.

Neben der Optimierung der Solarzellenstruktur, sollte eine geeignete Modultechnologie für rückseitig kontaktierte Solarzellen bereitgestellt werden. Diese Technologie sollte eine hohe Packungsdichte der Solarzellen ermöglichen und könnte durch die Verwendung einer Folien mit einem vordefinierten Metallisierungsmuster zum Zusammenschalten der Solarzellen, die Serienwiderstandsverluste im Metalisierungsgitter weiter senken.

Symbols, acronyms and physical constants

Symbols

Symbol	Description	Unit
A	area	cm^2
A_F	pitch of the solar cell	µm
a_{n-n}	distance between n^+ and n^+ doping	µm
B_F	width of the metal fingers	µm
B_R	radiative recombination coefficient	
C	concentration	
C_A	Auger coefficient	$cm^{-3}\ s^{-1}$
d_{wafer}	wafer thickness	µm
E_i	intrinsic Fermi level	eV
FF	fill factor	
H_F	height of the metal fingers	µm
J_0	saturation current density	$A\ cm^{-2}$
J_{01}, J_{02}	dark saturation current densities in a two-diode model	$A\ cm^{-2}$
J_{0s}	surface recombination current density	$A\ cm^{-2}$
J_{mpp}	current at maximum power point	$A\ cm^{-2}$
J_{ph}	photogeneratred current	$A\ cm^{-2}$
J_{SC}	short-circuit current density	$A\ cm^{-2}$
l	average path length of incoming light within silicon wafer	
L_{eff}	effective diffusion length of the minority carriers	µm

Symbol	Description	Unit
L_F	length of the metal fingers	µm
n_0	equilibrium concentration of electrons	cm^{-3}
N_A	concentration of acceptor atoms	cm^{-3}
N_D	concentration of donor atoms	cm^{-3}
n_e	electron density	cm^{-3}
n_i	intrinsic carrier density	cm^{-3}
N_{peak}, N_S	surface doping concentration	cm^{-3}
n_{Si}	refractive index of silicon	
N_{st}	number of surface states	cm^{-2}
p_0	equilibrium concentration of holes	cm^{-3}
PFF	pseudo fill factor	
P_{RP}	photon recycling rate	
$R_{CE\text{-}Auger}$	Columb-enhanced Auger recombination rate	$cm^{-3}s^{-1}$
R_p	parallel resistance	Ω
R_{rad}	radiative recombination rate	$cm^{-3}s^{-1}$
R_S	series resistance	Ω
S	surface recombination rate	$cm\ s^{-1}$
S_{eff}	effective surface recombination velocity	$cm\ s^{-1}$
S_{front}	front surface recombination velocity	$cm\ s^{-1}$
T	temperature	K or °C
t	time	h
U_S	net recombination rate at surface	$cm^{-2}\ s^{-1}$
V	voltage	mV
V_{mpp}	voltage at maximum power point	mV

Symbol	Description	Unit
V_{OC}	open-circuit voltage	mV
W	wafer thickness	µm
x_j	junction depth	µm
Δn	excess carrier density	cm^{-3}
α_{FCA}	free carrier absorption coefficient	cm^{-1}
α_{Si}	absorption coefficient of silicon	cm^{-1}
η	efficiency	%
λ	wavelength	nm
ρ	resistivity	Ω cm
ρ_{base}	resistivity of the base material	Ω cm
ρ_{FSF}	sheet resistance of the front surface field	Ω/sq
ρ_{sheet}	sheet resistance	Ω/sq
σ_n	capture cross section for electrons	cm^2
σ_p	capture cross section for holes	cm^2
τ_A	minority carrier lifetime of Auger recombination	µs
τ_{bulk}	minority carrier lifetime in bulk	µs
τ_{eff}	effective minority carrier lifetime	µs
τ_{rad}	minority carrier lifetime of radiative recombination	µs
τ_S	minority carrier lifetime of surface recombination	µs
τ_{SRH}	Shockley-Read-Hall recombination lifetime	µs
υ_{th}	thermal velocity of charge carriers	$cm\ s^{-1}$

Acronyms

Acronym	Description
AM1.5g	air mass 1.5 global spectrum
ARC	anti-reflection coating
BC-BJ	back-contact back-junction solar cell
BSF	back surface field
Cz-Si	monocrystalline silicon produced with the Czochralsky method
EQE	external quantum efficiency
EWT	emitter wrap through solar cell
FCA	free carrier absorption
FGA	forming gas anneal
FZ-Si	monocrystalline silicon produced with the floating zone method
FSF	front surface field
IQE	internal quantum efficiency
IBC	interdigitated back contact solar cell
LBSF	local back surface field
LBIC	light beam induced current
LFE	laser-fired aluminium emitters
LFC	laser-fired contacts
LIP	light-induced plating
mc-Si	multicrystalline silicon
MWT	metallization warp through solar cell
PCD	photoconductance decay
PECVD	plasma enhanced chemical vapour deposition
PERL	passivated emitter real locally diffused solar cell

Acronym	Description
PERC	passivated emitter and rear cell solar cell
QSSPC	quasi-steady state photoconductance
SIMS	secondary ion mass spectroscopy
SEM	scanning electron microscope
STC	standard testing conditions

Physical constants

Constant	Description	Value
k	Boltzmann's constant	1.3806×10^{-23} J K^{-1}
c	velocity of light	299792458 m s^{-1}
h	Planck constant	6.62607×10^{-34} J s
n_i	intrinsic carrier density	1.00×10^{10} cm^{-3}
q	elementary charge	1.6022×10^{-19} C

Bibliography

[1] EPIA and Greenpeace, *Solar Generation V – 2008. Solar electricity for over one billion people and two million jobs by 2020*, (2008).

[2] R.M. Swanson, *A vision for crystalline silicon photovoltaics*, Progress in Photovoltaics: Research and Applications, **14** (5), 443-53, (2006).

[3] D. De Ceuster, P. Cousins, D. Rose, D. Vicente, P. Tipones, and W. Mulligan, *Low Cost, high volume production of >22% efficiency silicon solar cells*, in *Proceedings of the 22nd European Photovoltaic Solar Energy Conference*, Milan, Italy, 816-9 (2007).

[4] M.A. Green, *Solar cells: operating principles, technology and system applications*. 1986, Kensington: UNSW.

[5] P. Würfel, *Physics of Solar Cells*. 2005, Weinheim: Wiley.

[6] A. Luque and S. Hegedus, *Handbook of Photovoltaic Science and Engineering*. 2003, West Sussex: John Wiley & Sons Ltd.

[7] M. Späth, P.C. de Jong, and J. Bakker, *A novel module assembly line using back contact solar cells*, in *Technical Digest of the 17th International Photovoltaic Solar Energy Conference*, Fukuoka, Japan, 436 (2007).

[8] J. Zhao, A. Wang, and M.A. Green, *24·5% Efficiency silicon PERT cells on MCZ substrates and 24.7% efficiency PERL cells on FZ substrates*, Progress in Photovoltaics: Research and Applications, **7** (6), 471-4, (1999).

[9] O. Schultz, S.W. Glunz, and G. Willeke, *Multicrystalline Silicon Solar Cells Exceeding 20 % Efficiency*, Progress in Photovoltaics: Research and Applications, **12** (7), 553-8, (2004).

[10] S.W. Glunz, *New concepts for high-efficiency silicon solar cells*, Solar Energy Materials and Solar Cells, **90** (18-19), 3276-84, (2006).

[11] S.W. Glunz, *High-efficiency crystalline silicon solar cells*, Advances in OptoElectronics, **2007**, 97370/1-15, (2007).

[12] E. Van Kerschaver and G. Beaucarne, *Back-contact solar cells: a review*, Progress in Photovoltaics: Research and Applications, **14** (2), 107-23, (2006).

[13] R.J. Schwartz and M.D. Lammert, *Silicon solar cells for high concentration applications*, in *Technical Digest of the International Electron Devices Meeting*, Washington, DC, 350-2 (1975).

[14] M.D. Lammert and R.J. Schwartz, *The interdigitated back contact solar cell: a silicon solar cell for use in concentrated sunlight*, IEEE Transactions on Electron Devices, **ED-24** (4), 337-42, (1977).

[15] R.M. Swanson, A.K. Beckwith, R.A. Crane, W.D. Eades, Y.H. Kwark, and R.A. Sinton, *Point-contact silicon solar cells*, IEEE Transactions on Electron Devices, **31** (5), 661-4, (1984).

[16] R.A. Sinton, Y. Kwark, J.Y. Gan, and R.M. Swanson, *27.5-percent silicon concentrator solar cells*, IEEE Electron Device Letters, **EDL-7** (10), 567-9, (1986).

[17] R.A. Sinton and R.M. Swanson, *Design criteria for Si point-contact concentrator solar cells*, IEEE Transactions on Electron Devices, **ED-34** (10), 2116-23, (1987).

[18] R.A. Sinton, P. Verlinden, D.E. Kane, and R.M. Swanson, *Development efforts in silicon backside-contact solar cells*, in *Proceedings of the 8th European Photovoltaic Solar Energy Conference*, Florence, Italy, 1472-6 (1988).

[19] P. Verlinden, F. Van de Wiele, G. Stehelin, and J.P. David, *Optimized interdigitated back contact (IBC) solar cell for high concentrated sunlight*, in *Proceedings of the 18th IEEE Photovoltaic Specialists Conference*, Las Vegas, Nevada, USA, 55-60 (1985).

[20] R.R. King, R.A. Sinton, and R.M. Swanson, *Front and back surface fields for point-contact solar cells*, in *Proceedings of the 20th IEEE Photovoltaic Specialists Conference*, Las Vegas, Nevada, USA, 538-44 (1988).

[21] P. Verlinden, R.A. Sinton, and R.M. Swanson, *High efficiency large area back contact concentrator solar cells with a multilevel interconnection*, International Journal of Solar Energy, **6** (6), 347-66, (1988).

[22] P. Verlinden, R.M. Swanson, R.A. Sinton, and D.E. Kane, *Multilevel metallization for large area point-contact solar cells*, in *Proceedings of the 20th IEEE Photovoltaic Specialists Conference*, Las Vegas, Nevada, USA, (1988).

[23] R.R. King, R.A. Sinton, and R.M. Swanson, *One-Sun, Single-Crystalline Silicon Solar Cell Research*. Solid State Electronics Laboratory, Stanford University, Stanford, (1991).

[24] R.A. Sinton and R.M. Swanson, *Simplified backside-contact solar cells*, IEEE Transactions on Electron Devices, **37** (2), 348-52, (1990).

[25] R.A. Sinton, P.J. Verlinden, R.A. Crane, R.M. Swanson, C. Tilford, J. Perkins, and K. Garrison, *Large-area 21% efficient Si solar cells*, in *Proceedings of the 23rd IEEE Photovoltaic Specialists Conference*, Louisville, Kentucky, USA, 1490, 157-61 (1993).

[26] P.J. Verlinden, R.M. Swanson, and R.A. Crane, *7000 high efficiency cells for a dream*, Progress in Photovoltaics: Research and Applications, **2** (2), 143, (1994).

[27] P.J. Verlinden, R.A. Sinton, K. Wickham, R.A. Crane, and R.M. Swanson, *Backside-contact silicon solar cells with improved efficiency for the '96 world solar challenge*, in *Proceedings of the 14th European Photovoltaic Solar Energy Conference*, Barcelona, Spain, 96-9 (1997).

[28] M.J. Cudzinovic and K. McIntosh, *Process simplifications to the Pegasus solar cell - Sunpower's high-efficiency bifacial solar cell*, in *Proceedings of the 29th IEEE Photovoltaics Specialists Conference*, New Orleans, Louisiana, USA, 70-3 (2002).

[29] W.P. Mulligan, D.H. Rose, M.J. Cudzinovic, D.M. De Ceuster, K.R. McIntosh, D.D. Smith, and R.M. Swanson, *Manufacture of solar cells with 21% efficiency*, in *Proceedings of the 19th European Photovoltaic Solar Energy Conference*, Paris, France, 387-90 (2004).

[30] K.R. McIntosh, M.J. Cudzinovic, D.D. Smith, W.P. Mulligan, and R.M. Swanson, *The choice of silicon wafer for the production of low-cost rear-contact solar cells*, in *Proceedings of the 3rd World Conference on Photovoltaic Energy Conversion*, Osaka, Japan, 971-4 (2003).

[31] K.R. McIntosh, N.C. Shaw, and J.E. Cotter, *Light trapping in Sunpower's A-300 solar cell*, in *Proceedings of the 19th European Photovoltaic Solar Energy Conference*, Paris, France, 844-7 (2004).

[32] R.M. Swanson, *Device physics for backside-contact solar cells*, in *Proceedings of the 33rd IEEE Photovoltaic Specialists Conference*, San Diego, USA, (2008).

[33] J. Dicker, J.O. Schumacher, W. Warta, and S.W. Glunz, *Analysis of one-sun monocrystalline rear-contacted silicon solar cells with efficiencies of 22.1%*, Journal of Applied Physics, **91** (7), 4335-43, (2002).

[34] J. Dicker, *Analyse und Simulation von hocheffizienten Silizium-Solarzellenstrukturen für industrielle Fertigungstechniken*, Dissertation, Universität Konstanz, (2003).

[35] A. Mohr, *Silicon concentrator cells in a two-stage photovoltaic system with a concentration factor of 300x*, Dissertation, Universität Freiburg, (2005).

[36] A. Mohr, T. Roth, and S.W. Glunz, *BICON: High concentration PV using one-axis tracking and silicon concentrator cells*, Progress in Photovoltaics: Research and Applications, **14**, 663-74, (2005).

[37] J.-H. Guo, *High-efficiency n-type laser-grooved buried contact silicon solar cells*, Dissertation, University of New South Wales, (2004).

[38] J.-H. Guo, B.S. Tjahjono, and J.E. Cotter, *19.2% efficiency n-type laser-grooved silicon solar cells*, in *Proceedings of the 31st IEEE Photovoltaic Specialists Conference*, Orlando, USA, 983-6 (2005).

[39] P. Engelhart, N.-P. Harder, R. Grischke, A. Merkle, R. Meyer, and R. Brendel, *Laser structuring for back junction silicon solar cells*, Progress in Photovoltaics: Research and Applications, **15**, 237-43, (2006).

[40] P. Engelhart, *Lasermaterialbearbeitung als Schlüsseltechnologie zum Herstellen rückseitenkontaktierter Siliciumsolarzellen*, Dissertation, Universität Hannover, (2007).

[41] D. Huljic, *et al.*, *Development of a 21 % back-contact monocrystalline silicon solar cell for large-scale production*, in *21st European Photovoltaic Solar Energy Conference*, Dresden, Germany, 765-8 (2006).

[42] D. Huljic, *et al.*, *Q-Cells' High-Efficiency Back Junction Solar Cell for Large-Scale Production - Main Results of the QUEBEC Project*, in *22nd European Photovoltaic Solar Energy Conference*, Milano, Italy, (2007).

[43] R. Stangl, M. Bivour, E. Conrad, I. Didschuns, L. Korte, K. Lips, and M. Schmidt, *Recash - A novel high efficiency buried grid rear contact amorphous/crystalline silicon heterojunction solar cell concept*, in *Proceedings of the 22nd European Photovoltaic Solar Energy Conference*, Milan, Italy, 870-4 (2007).

[44] M. Tucci, *et al.*, *BEHIND (Back enhanced heterostructure with interdigitated conctacts) solar cell*, in *23rd European Photovoltaic Solar Energy Conference*, Valencia, Spain, 1749-52 (2008).

[45] L. Meijun, B. Stuart, D. Ujjwal, and B. Robert, *Interdigitated back contact silicon heterojunction solar cell and the effect of front surface passivation*, Applied Physics Letters, **91** (6), 063507, (2007).

[46] J.M. Gee, W.K. Schubert, and P.A. Basore, *Emitter wrap-through solar cell*, in *Proceedings of the 23rd IEEE Photovoltaic Specialists Conference*, Louisville, Kentucky, USA, 265-70 (1993).

[47] J.M. Gee, M.E. Buck, W.K. Schubert, and P.A. Basore, *Progress on the emitter wrap-through silicon solar cell*, in *Proceedings of the 12th European Photovoltaic Solar Energy Conference*, Amsterdam, The Netherlands, 743-6 (1994).

[48] D. Kray, *Hocheffiziente Solarzellenstrukturen für kristallines Silicium-Material industrieller Qualität*, Dissertation, Universität Konstanz, (2004).

[49] J.M. Gee, P. Hacke, M.W. Sumner, and R.R. Schmit, *Towards a manufacturable back-contact emitter-wrap-through silicon solar cell*, in *Photovoltaic Specialists Conference, 2005. Conference Record of the Thirty-first IEEE*, 1663-6 (2005).

[50] A. Kress, O. Breitenstein, S. Glunz, P. Fath, G. Willeke, and E. Bucher, *Investigations on low-cost back-contact silicon solar cells*, Solar Energy Materials and Solar Cells, **65**, 555-60, (2001).

[51] A. Kress, *Emitterverbund-Rückkontaktsolarzellen für die industrielle Fertigung*, Dissertation, Universität Konstanz, (2001).

[52] D. Kray, *et al.*, *Progress in high-efficiency emitter-wrap-through cells on medium quality substrates*, in *Proceedings of the 3rd World Conference on Photovoltaic Energy Conversion*, Osaka, Japan, 1340-3 (2003).

[53] S.W. Glunz, *et al.*, *High-efficiency cell structures for medium-quality silicon*, in *Proceedings of the 17th European Photovoltaic Solar Energy Conference*, Munich, Germany, 1287-92 (2001).

[54] S. Hermann, *et al.*, *21.4 %-efficient emitter wrap-through RISE solar cell on large area and picosecond laser processing of local contact openings*, in *Proceedings of the 22nd European Photovoltaic Solar Energy Conference*, Milan, Italy, 970-5 (2007).

[55] C. Peters, *et al.*, *ALBA – Development of high-efficiency mulit-crystalline Si EWT solar cells for industrial fabrication at Q-Cells*, in *Proceedings of the 23rd European Photovoltaic Solar Energy Conference*, Valencia, Spain, 1010-13 (2008).

[56] E. van Kerschaver, R. Einhaus, J. Szlufcik, J. Nijs, and R. Mertens, *A novel silicon solar cell structure with both external polarity contacts on the back surface*, in *Proceedings of the 2nd World Conference on Photovoltaic Energy Conversion*, Vienna, Austria, 1479-82 (1998).

[57] H. Knauss, H. Haverkamp, W. Jooss, S. Steckemetz, and H. Nussbaumer, *Industrially applicable metallisation wrap through solar cell process resulting in efficiencies exceeding 16 %*, in *Proceedings of the 21st European Photovoltaic Solar Energy Conference*, Dresden, Germany, 1192-5 (2006).

[58] E. Van Kerschaver, C. Allebé, B. Devreese, L. Frisson, and J. Szlufcik, *Record high performance modules based on screen printed MWT solar cells*, in *Proceedings of the 29th IEEE Photovoltaics Specialists Conference*, New Orleans, Louisiana, USA, 78-81 (2002).

[59] J.H. Bultman, M.W. Brieko, A.R. Burgers, J. Hoornstra, A.C. Tip, and A.W. Weeber, *Interconnection through vias for improved efficiency and easy module manufacturing of crystalline silicon solar cells*, Solar Energy Materials and Solar Cells, **65**, 339-45, (2001).

[60] A.W. Weeber, R. Kinderman, C.J.J. Tool, F. Granek, and P.C. De Jong, *How to achieve 17% cell efficiencies on large back-contacted mc-Si solar cells*, in

Proceedings of the 4th World Conference on Photovoltaic Energy Conversion, Hawaii, USA, 1048-51 (2006).

[61] F. Clement, *et al.*, *Industrially feasible MC-Si metal wrap through (MWT) solar cells with high emitter sheet resistances exceeding 16% efficiency*, in *Proceedings of the 23rd European Photovoltaic Solar Energy Conference*, Valencia, Spain, in print (2008).

[62] W. Jooss, H. Knauss, F. Huster, P. Fath, E. Bucher, R. Tölle, and T.M. Bruton, *Back contact buried contact solar cells with metallization wrap around electrodes*, in *Proceedings of the 28th IEEE Photovoltaics Specialists Conference*, Anchorage, Alaska, USA, 176-9 (2000).

[63] D.A. Clugston and P.A. Basore, *PC1D version 5: 32-bit solar cell modeling on personal computers*, in *Proceedings of the 26th IEEE Photovoltaic Specialists Conference*, Anaheim, California, USA, 207-10 (1997).

[64] W. Shockley and H.J. Queisser, *Detailed balance limit of efficiency of p-n junction solar cells*, Journal of Applied Physics, **32** (3), 510-9, (1961).

[65] T. Tiedje, E. Yablonovitch, G.D. Cody, and B.G. Brooks, *Limiting efficiency of silicon solar cells*, IEEE Transactions on Electron Devices, **31** (5), 711-6, (1984).

[66] R.M. Swanson, *Approaching the 29% limit efficiency of silicon solar cells*, in *Proceedings of the 31st IEEE Photovoltaic Specialists Conference*, Orlando, USA, 889-94 (2005).

[67] R. Brendel, *Thin-film silicon solar cells: Physics and Technology*. 2003, Weinheim: Wiley-VCH.

[68] M.J. Kerr, *Surface, emitter and bulk recombination in silicon and development of silicon nitride passivated solar cells*, Dissertation, Australian National University, (2002).

[69] M.J. Kerr and A. Cuevas, *General parameterization of Auger recombination in crystalline silicon*, Journal of Applied Physics, **91** (4), 2473-80, (2002).

[70] M.J. Kerr, A. Cuevas, and P. Campbell, *Limiting efficiency of crystalline silicon solar cells due to Coulomb-enhanced Auger recombination*, Progress in Photovoltaics: Research and Applications, **11** (2), 97-104, (2003).

[71] M.A. Green, *Limits on the open-circuit voltage and efficiency of silicon solar cells imposed by intrinsic Auger processes*, IEEE Transactions on Electron Devices, **ED-31** (5), 671-8, (1984).

[72] T. Trupke, M.A. Green, P. Würfel, P.P. Altermatt, A. Wang, J. Zhao, and R. Corkish, *Temperature dependence of the radiative recombination coefficient of intrinsic crystalline silicon*, Journal of Applied Physics, **94** (8), 4930-7, (2003).

[73] Sinton-Consulting-Inc., *http://www.sintonconsulting.com/.*

[74] H. Nagel, C. Berge, and A.G. Aberle, *Generalized analysis of quasi-steady-state and quasi-transient measurements of carrier lifetimes in semiconductors*, Journal of Applied Physics, **86** (11), 6218- 21, (1999).

[75] R.A. Sinton, A. Cuevas, and M. Stuckings, *Quasi-steady-state photoconductance, a new method for solar cell material and device characterization*, in *Proceedings of the 25th IEEE Photovoltaic Specialists Conference*, Washington DC, USA, 457-60 (1996).

[76] B. Fischer, *Loss analysis of crystalline silicon solar cells using photoconductance and quantum efficiency measurements*, Dissertation, Universität Konstanz, (2003).

[77] W. Shockley and W.T.J. Read, *Statistics of the recombinations of holes and electrons*, Physical Review, **87** (5), 835-42, (1952).

[78] R.N. Hall, *Electron-hole recombination in germanium*, Physical Review, **87**, 387, (1952).

[79] J. Dziewior and W. Schmid, *Auger coefficients for highly doped and highly excited silicon*, Applied Physics Letters, **31** (5), 346-8, (1977).

[80] A.B. Sproul and M.A. Green, *Intrinsic carrier concentration and minority-carrier mobility of silicon from 77 to 300 K*, Journal of Applied Physics, **73** (3), 1214-25, (1993).

[81] A. Cuevas, *The effect of emitter recombination on the effective lifetime of silicon wafers*, Solar Energy Materials and Solar Cells, **57** (3), 277-90, (1999).

[82] A. Cuevas and D. Macdonald, *Measuring and interpreting the lifetime of silicon wafers*, Solar Energy, **76** (1-3), 255-62, (2004).

[83] A.B. Sproul, *Dimensionless solution of the equation describing the effect of surface recombination on carrier decay in semiconductors*, Journal of Applied Physics, **76** (5), 2851-4, (1994).

[84] J. del Alamo, J. Van Meerbergen, F. D`Hoore, and J. Nijs, *High-low junctions for solar cell applications*, Solid-State Electronics, **24**, 533-8, (1981).

[85] D.E. Kane and R.M. Swanson, *Measurement of the emitter saturation current by a contactless photoconductivity decay method (silicon solar cells)*, in *Proceedings of the 18th IEEE Photovoltaic Specialists Conference*, Las Vegas, Nevada, USA, 578-83 (1985).

[86] M. Hermle, *Analyse neuartiger Silizium- und III-V Solarzellen mittels Simulation und Experiment*, Dissertation, Universität Konstanz, (2008).

[87] M. Hermle, F. Granek, O. Schultz-Wittmann, and S.W. Glunz, *Shading effects in back-junction back-contacted silicon solar cells*, in *Proceedings of the 33rd IEEE Photovoltaic Specialists Conference*, San Diego, USA, (2008).

[88] J.O. Schumacher, *Charakterisierung texturierter Silicium-Solarzellen*, Diplomarbeit, Universität Freiburg, (1994).

[89] *DESSIS Manual 7.0.*

[90] S. Synopsis Zurich, *SDEVICE Manual Release: Z-2007.03, www.synopsys.com*, (2007)

[91] J.O. Schumacher, *Numerical simulation of silicon solar cells with novel device structures*, PhD, University of Konstanz, (2000).

[92] P.A. Basore and D.A. Clugston, *PC1D version 4 for Windows: from analysis to design*, in *Proceedings of the 25th IEEE Photovoltaic Specialists Conference*, Washington D C, 377-81 (1996).

[93] R. Brendel, *Sunrays: A versatile ray tracing program for the photovoltaic community*, in *Proceedings of the 12th European Photovoltaic Solar Energy Conference*, Amsterdam, The Netherlands, 1339-42 (1994).

[94] A. Cuevas, G. Giroult-Matlakowski, P.A. Basore, C. DuBois, and R.R. King, *Extraction of the surface recombination velocity of passivated phosphorus-doped silicon emitters*, in *Proceedings of the 1st World Conference on Photovoltaic Energy Conversion- WCPEC*, Waikoloa, Hawaii, USA, **2**, 1446-9 (1994).

[95] A. Cuevas, M. Stuckings, J. Lau, and M. Petravic, *The recombination velocity of boron diffused silicon surfaces*, in *Proceedings of the 14th European Photovoltaic Solar Energy Conference*, Barcelona, Spain, 2416-9 (1997).

[96] R.A. Sinton, P.J. Verlinden, R.M. Swanson, R.A. Crane, K. Wickham, and J. Perkins, *Improvements in silicon backside-contact solar cells for high-value one-sun applications*, in *Proceedings of the 13th European Photovoltaic Solar Energy Conference*, Nice, France, 1586-9 (1995).

[97] J. Benick, B. Hoex, M.C.M. Van de Sanden, W.M.M. Kessels, O. Schultz, and S. Glunz, *Effective passivation of boron emitters with Al_2O_3 for high-efficiency n-type solar cells*, Applied Physics Letters, **92** (24), 253504-1, (2008).

[98] J. Benick, B. Hoex, O. Schultz, and S.W. Glunz, *Surface passivation of boron diffused emitters for high efficiency solar cells*, in *Proceedings of the 33rd IEEE Photovoltaic Specialists Conference*, San Diego, USA, (2008).

[99] V.D. Mihailetchi, Y. Komatsu, and L.J. Geerligs, *Nitric acid pretreatment for the passivation of boron emitters for n-type base silicon solar cells*, Applied Physics Letters, **92**, 063510, (2008).

[100] J. Libal, *et al.*, *N-type multicrystalline silicon solar cells: BBr_3-diffusion and passivation of P^+-diffused silicon surfaces*, in *Proceedings of the 20th European Photovoltaic Solar Energy Conference*, Barcelona, Spain, 793-6 (2005).

[101] C.J.J. Tool, H.C. Rieffe, R. Kinderman, R. Kopecek, K. Wambach, and L.J. Geerligs, *Solar cells on n-type multicrystalline silicon wafers by industrial processing techniques*, in *Proceedings of the 19th European Photovoltaic Solar Energy Conference*, Paris, France, (2004).

[102] A. Cuevas, C. Samundsett, M.J. Kerr, D.H. Macdonald, H. Mäckel, and P.P. Altermatt, *Back junction solar cells on n-type multicrystalline and CZ silicon wafers*, in *Proceedings of the 3rd World Conference on Photovoltaic Energy Conversion*, Osaka, Japan, **1**, 963-6 (2003).

[103] J. Zhao and A. Wang, *High Efficiency Real Emitter PERT Solar Cells on n-type FZ Single Crystalline Silicon Substrates*, in *20th European Photovoltaic Solar Energy Conference and Exhibition*, Barcelona, Spain, (2005).

[104] C. Schmiga, M. Hermle, and S.W. Glunz, *Towards 20 % efficient n-type silicon solar cells with screen-printed aluminium-alloyed rear emitter*, in *Proceedings of the 23rd European Photovoltaic Solar Energy Conference and Exhibition*, Valencia, Spain, (2008).

[105] E. Maruyama, *et al.*, *Sanyo's challenges to the development of high-efficiency HIT solar cells and the expansion of HIT business*, in *Proceedings of the 4th World Conference on Photovoltaic Energy Conversion*, Waikoloa, Hawaii, USA, 1455-60 (2006).

[106] J. Schmidt, A.G. Aberle, and R. Hezel, *Investigation of carrier lifetime instabilities in Cz-grown silicon*, in *Proceedings of the 26th IEEE Photovoltaic Specialists Conference*, Anaheim, California, USA, 13-8 (1997).

[107] J. Schmidt and A. Cuevas, *Electronic properties of light-induced recombination centers in boron-doped Czochralski silicon*, Journal of Applied Physics, **86** (6), 3175- 80, (1999).

[108] S.W. Glunz, S. Rein, J.Y. Lee, and W. Warta, *Minority carrier lifetime degradation in boron-doped Czochralski silicon*, Journal of Applied Physics, **90** (5), 2397-404, (2001).

[109] D. Macdonald and L.J. Geerligs, *Recombination activity of interstitial iron and other transition metal point defects in p- and n-type crystalline silicon*, Applied Physics Letters, **85** (18), 4061-3, (2004).

[110] L.J. Geerligs and D. Macdonald, *Base doping and recombination activity of impurities in crystalline silicon solar cells*, Progress in Photovoltaics: Research and Applications, **12** (4), 309-16, (2004).

[111] A. Cuevas, M.J. Kerr, C. Samundsett, F. Ferrazza, and G. Coletti, *Millisecond minority carrier lifetimes in n-type multicrystalline silicon*, Applied Physics Letters, **81** (26), 4952-4, (2002).

[112] T. Trupke, R.A. Bardos, F. Hudert, P. Würfel, J. Zhao, A. Wang, and M.A. Green, *Effective excess carrier lifetimes exceeding 100 milliseconds in float zone silicon determined from photoluminescence*, in *Proceedings of the 19th European Photovoltaic Solar Energy Conference*, Paris, France, **1**, 758-61 (2004).

[113] S.W. Glunz, D. Biro, S. Rein, and W. Warta, *Field-effect passivation of the SiO_2-Si interface*, Journal of Applied Physics, **86** (1), 683-91, (1999).

[114] W. Kern, *Handbook of semiconductor wafer cleaning technology*. 1993, Park Ridge, New Jersey: Noyes.

[115] D.L. King and M.E. Buck, *Experimental optimization of an anisotropic etching process for random texturization of silicon solar cells*, in *Proceedings of the 22nd Photovoltaic Specialists Conference* Las Vegas, Nevada, USA, (1991).

[116] R. Hezel and K. Jaeger, *Low-temperature surface passivation of silicon for solar cells*, Journal of the Electrochemical Society, **136** (2), 518-23, (1989).

[117] A. Cuevas, M.J. Kerr, and J. Schmidt, *Passivation of crystalline silicon using silicon nitride*, in *Proceedings of the 3rd World Conference on Photovoltaic Energy Conversion*, Osaka, Japan, 913-8 (2003).

[118] C. Leguijt, *et al.*, *Low temperature surface passivation for silicon solar cells*, Solar Energy Materials and Solar Cells, **40** (4), 297-345, (1996).

[119] R.A. Sinton, Y. Kwark, P. Gruenbaum, and R.M. Swanson, *Silicon point contact concentrator solar cells*, in *Proceedings of the 18th IEEE Photovoltaic Specialists Conference*, Las Vegas, Nevada, USA, 61-5 (1985).

[120] S.M. Sze, *Semiconductor devices, physics and technology*, ed. M.H. AT&T Bell Laboratories, New Jersey. 1985, New York, Chichester, Brisbane, Toronto, Singapore: John Wiley & Sons.

[121] M.A. Green, *Silicon solar cells: Advanced principles and practice*. 1995, Sydney, UNSW: Centre for Photovoltaic Devises and Systems UNSW.

[122] R.M. Swanson, *Point-contact solar cells: modeling and experiment*, Solar Cells, **17** (1), 85-118, (1986).

[123] A. Wang, J. Zhao, and M.A. Green, *24% efficient silicon solar cells*, Applied Physics Letters, **57** (6), 602-4, (1990).

[124] D.K. Schroder and D.L. Meier, *Solar cell contact resistance - a review*, IEEE Transactions on Electron Devices, **ED-31** (5), 637-47, (1984).

[125] A. Grohe, *Einsatz von Laserverfahren zur Prozessierung von kristallinen Silizium-Solarzellen*, Dissertation, Universität Konstanz, (2007).

[126] D.L. Meier and D.K. Schroder, *Contact resistance: its measurement and relative importance to power loss in a solar cell*, IEEE Transactions on Electron Devices, **ED-31** (5), 647-53, (1984).

[127] A. Teppe, P. Engelhart, and J. Müller, *Method for the contact separation of electrically-conducting layers on the back contacts of solar cells and corresponding solar cells* in US Patent, USA, WO 2006/042698 A1, (2006).

[128] W.P. Mulligan, M.J. Cudzinovic, T. Pass, D. Smith, N. Kaminar, K. McIntosh, and R.M. Swanson, *Solar cell and method of manufacture*, in US Patent, USA, US 7,339,110 B1, (2008).

[129] J. Nijs, F. Dhoore, R. Mertens, and R. van Overstraeten, *Lift-off: A very fine front metallization geometry technique for high efficiency solar cells*, ESA Photovoltaic Generators in Space, 37-42, (1982).

[130] A. Mette, *New concepts for front side metallization of industrial silicon solar cells*, Dissertation, Universität Freiburg, (2007).

[131] A. Mette, C. Schetter, D. Wissen, S. Lust, S.W. Glunz, and G. Willeke, *Increasing the efficiency of screen-printed silicon solar cells by light-induced silver plating*, in *Proceedings of the 4th World Conference on Photovoltaic Energy Conversion*, Waikoloa, Hawaii, USA, 1056-9 (2006).

[132] M. Hermle, F. Granek, O. Schultz, and S.W. Glunz, *Analyzing the effects of front-surface fields on back-junction silicon solar cells using the charge-collection probability and the reciprocity theorem*, Journal of Applied Physics, **103** (054507), 054507/1-7, (2008).

[133] W. Warta, J. Sutter, B.F. Wagner, and R. Schindler, *Impact of diffusion length distributions on the performance of mc-silicon solar cells*, in *Proceedings of the 2nd World Conference on Photovoltaic Energy Conversion*, Vienna, Austria, 1650-3 (1998).

[134] E. Schneiderlöchner, R. Preu, R. Lüdemann, and S.W. Glunz, *Laser-fired rear contacts for crystalline silicon solar cells*, Progress in Photovoltaics: Research and Applications, **10**, 29-34, (2002).

[135] S.W. Glunz, E. Schneiderlöchner, D. Kray, A. Grohe, H. Kampwerth, R. Preu, and G. Willeke, *Laser-fired contact solar cells on p- and n-type substrates*, in *Proceedings of the 19th European Photovoltaic Solar Energy Conference*, Paris, France, **1**, 408-11 (2004).

[136] S.W. Glunz, *et al.*, *Analysis of laser-fired local back surface fields using n+np+ cell structures*, in *Proceedings of 3rd World Conference on Photovoltaic Energy Conversion*, Osaka, Japan, **2**, 1332-5 (2003).

[137] D. Nobili, *Solubility of P in Si in Properties of Silicon*. 1987.

[138] D. Nobili, *Solubility of B in Si in Properties of Silicon*. 1987.

[139] M. Abbott, P. Cousins, F. Chen, and J. Cotter, *Laser-induced defects in crystalline silicon solar cells*, in *Proceedings of the 31st IEEE Photovoltaic Specialists Conference*, Orlando, USA, 1241-4 (2005).

[140] S. Baumann, D. Kray, K. Mayer, A. Eyer, and G.P. Willeke, *Comparative study of laser induced damage in silicon wafers*, in *Proceedings of the 4th World Conference on Photovoltaic Energy Conversion*, Waikoloa, Hawaii, USA, 1142-5 (2006).

[141] S. Rein, T. Rehrl, W. Warta, and S.W. Glunz, *Lifetime spectroscopy for defect characterization: Systematic analysis of the possibilities and restrictions*, Journal of Applied Physics, **91** (4), 2059-70, (2002).

[142] J. Zhao and A. Wang, *Rear emitter n-type passivated emitter, rear totally diffused silicon solar cell structure*, Applied Physics Letters, **88**, 242102-1-3, (2006).

[143] D.K. Schroder, R.N. Thomas, and J.C. Swartz, *Free carrier absorption in silicon*, IEEE Transactions on Electron Devices, **ED-25** (2), 254-61, (1978).

[144] J. Isenberg and W. Warta, *Free carrier absorption in heavily doped silicon layers*, Applied Physics Letters, **84** (13), 2265-7, (2004).

[145] R.M. Swanson and R.A. Sinton, *High-efficiency silicon solar cells*, in *Advances in solar energy*, K.W. Böer, Editor, Plenum Press, New York, 427-84 (1990).

[146] A. Slade, *Boron Triboromide Sourced Boron Diffusions for Silicon Solar Cells*, PhD Thesis, UNSW, Sydney, (2003).

[147] A. Cuevas, P.A. Basore, G. Giroult-Matlakowski, and C. Dubois, *Surface recombination velocity of highly doped n-type silicon*, Journal of Applied Physics, **80** (6), 3370-5, (1996).

[148] R.R. King, R.A. Sinton, and R.M. Swanson, *Studies of diffused phosphorus emitters: saturation current, surface recombination velocity, and quantum efficiency*, IEEE Transactions on Electron Devices, **37** (2), 365-71, (1990).

[149] A.G. Aberle, *Crystalline silicon solar cells: advanced surface passivation and analysis of crystalline silicon solar cells*. 1999, Sydney, Australia.

[150] F. Dross, E. Van Kerschaver, and G. Beaucarne, *Minimization of the shadow-like losses for inter-digitated back-junction solar cells*, in *Proceedings of the 15th International Photovoltaic Science & Engineering Conference*, Shanghai, China, 971-2 (2005).

[151] N.-P. Harder, V. Mertens, and R. Brendel, *Buried emitter solar cell structures: Decoupling of metallisation geometry and carrier collection geometry of back contacted solar cells*, physica status solidi (RRL) - Rapid Research Letters, **2** (4), 148-50, (2008).

[152] F. Granek, M. Hermle, C. Reichel, O. Schultz-Wittmann, and S.W. Glunz, *High- efficiency back-contact back-junction silicon solar cell research at Fraunhofer ISE*, in *Proceedings of the 23rd European Photovoltaic Solar Energy Conference*, Valencia, Spain, 991-5 (2008).

[153] R.A. Sinton and A. Cuevas, *A quasi-steady-state open-circuit voltage method for solar cell characterization*, in *Proceedings of the 16th European Photovoltaic Solar Energy Conference*, Glasgow, UK, 1152-5 (2000).

[154] D. Pysch, A. Mette, and S.W. Glunz, *A review and comparison of different methods to determine the series resistance of solar cells*, Solar Energy Materials & Solar Cells, **91**, 1698-706, (2007).

[155] A.G. Aberle, *Surface passivation of crystalline silicon solar cells: a review*, Progress in Photovoltaics: Research and Applications, **8** (5), 473-87, (2000).

[156] A.G. Aberle, S. Glunz, and W. Warta, *Field effect passivation of high efficiency silicon solar cells*, Solar Energy Materials and Solar Cells, **29** (2), 175-82, (1993).

[157] J.A. del Alamo and R.M. Swanson, *The physics and modeling of heavily doped emitters*, IEEE Transactions on Electron Devices, **ED-31** (12), 1878-88, (1984).

[158] G. Masetti, M. Severi, and S. Solmi, *Modeling of carrier mobility against carrier concentration in arsenic-, phosphorus-, and boron-doped silicon*, IEEE Transactions on Electron Devices, **30** (7), 764-9, (1983).

[159] P.B. Moynagh and P.J. Rosser, *Thermal oxidation of Si*, in *Properties of silicon*, INSPEC, The Institution of Electrical Engineers, 469-79 (1987).

[160] J. del Alamo and R.M. Swanson, *Measurement of heavy doping parameters in n-type silicon solar cells*, in *Proceedings of the 18th IEEE Photovoltaic Specialists ConferenceCA Conference Paper*, Las Vegas, Nevada, USA, 584-9 (1985).

[161] S.W. Glunz, S. Sterk, R. Steeman, W. Warta, J. Knobloch, and W. Wettling, *Emitter dark saturation currents of high-efficiency solar cells with inverted pyramids*, in *Proceedings of the 13th European Photovoltaic Solar Energy Conference*, Nice, France, 409-12 (1995).

[162] M.J. Kerr, J. Schmidt, A. Cuevas, and J.H. Bultman, *Surface recombination velocity of phosphorus-diffused silicon solar cell emitters passivated with*

plasma enhanced chemical vapor deposited silicon nitride and thermal silicon oxide, Journal of Applied Physics, **89** (7), 3821-6, (2001).

[163] J.D. Moschner, P. Doshi, D.S. Ruby, T. Lauinger, A.G. Aberle, and A. Rohatgi, *Comparison of front and back surface passivation schemes for silicon solar cells*, in *2nd World Conference and Exhibition on Photovoltaic Solar Energy Conversion*, Vienna, Austria, 1984-7 (1998).

[164] P.E. Gruenbaum, R.A. Sinton, and R.M. Swanson, *Light-induced degradation at the silicon/silicon dioxide interface*, Applied Physics Letters, **52** (17), 1407-9, (1988).

[165] P.E. Gruenbaum, R.A. Sinton, and R.M. Swanson, *Stability problems in point contact solar cells*, in *Proceedings of the 20th IEEE Photovoltaic Specialists Conference*, Las Vegas, Nevada, USA, 423-8 (1988).

[166] P.E. Gruenbaum, R.R. King, and R.M. Swanson, *Photoinjected hot-electron damage in silicon point-contact solar cells*, Journal of Applied Physics, **66** (12), 6110-4, (1989).

[167] P.E. Gruenbaum, J.Y. Gan, R.R. King, and R.M. Swanson, *Stable passivations for high-efficiency silicon solar cells*, in *Proceedings of the 21st IEEE Photovoltaic Specialists Conference*, Kissimmee, Florida, USA, 317-22 (1990).

[168] D.S. Ruby and W.K. Schubert, *The effects of concentrated ultraviolet light on high-efficiency silicon solar cells*, in *Proceedings of the 22nd IEEE Photovoltaic Specialists Conference*, Las Vegas, Nevada, USA, 111-7 (1991).

[169] H. Nagayoshi, *et al.*, *Effect of hydrogen-radical annealing for SiO_2 passivation*, Japanese Journal of Applied Physics, **35** (8B), L1047-9, (1996).

[170] A. Mohr, M. Hermle, T. Roth, and S.W. Glunz, *Influence of grid finger and busbar structure on the performance of rear-line-contacted silicon concentrator cells*, in *Proceedings of the 19th European Photovoltaic Solar Energy Conference*, Paris, France, **1**, 721-4 (2004).

[171] Bird R., Hulstrom R., and R. C., *Normalization of direct spectral irradiance data for photovoltaic cell performance analysis*, Solar Cells, **14** (2), 193-5, (1985).

[172] K. Emery, *The Rating of Photovoltaic Performance*, IEEE Transactions on Electron Devices, **46** (10), 1928-31, (1999).

[173] A. Luque, *Solar Cells and Optics for Photovoltaic Concentration*. 1989.

[174] J. Dicker, *Charakterisierung von hocheffizienten Rückseitenkontaktzellen*, Diplomarbeit, Albert-Ludwigs-Universität, Freiburg, (1998).

List of publications

Refereed journal papers

1. F. Granek, T. Zdanowicz, „Advanced system for calibration and characterization of solar cells", *Opto-Electronics Review* **12**(1), 57–67 (2004)

2. M. Hermle, F. Granek, O. Schultz, and S. W. Glunz, „Analyzing the effects of front-surface fields on back-junction silicon solar cells using the charge-collection probability and the reciprocity theorem", *Journal of Applied Physics* **103**, 054507 (2008)

3. F. Granek, M. Hermle and S. W. Glunz, „Analysis of the current linearity at low illumination of high-efficiency back-junction back-contact silicon solar cells", *physica status solidi. - Rapid Research Letters* **2**, No. 4, 151–153 (2008)

4. F. Granek, M. Hermle, D. M. Huljić, O. Schultz-Wittmann and S. W. Glunz, „Enhanced lateral current transport via the front n^+ diffused layer of n-type high-efficiency back-junction back-contact silicon solar cell", *Progress in Photovoltaics* **17**, 47-56 (2009)

Refereed papers presented at international conferences

1. J. Hoornstra, A. van der Heide, A. Weeber, F. Granek, „New approach for firing optimization in crystalline silicon solar cell technology", 19th European Photovoltaic Solar Energy Conference, Paris, France, pp. 1044-7 (2004).

2. C.J.J. Tool, G. Coletti, F. Granek, J. Hoornstra, M. Koppes, E.J. Kossen, H.C. Rieffe, I.G. Romijn, A.W. Weeber, „Straightforward in-line processing for 16.8% efficient mc-Si solar cell", 31st IEEE Photovoltaic Specialists Conference, Orlando Florida, pp. 1324-7 (2005).

3. J. Hoornstra, G. Schubert, K. Broek, F. Granek, C. LePrince , „Lead free metallization paste for crystalline silicon solar cells: From model to results", 31st IEEE Photovoltaic Specialists Conference, Orlando Florida, pp. 1293-6 (2005).

4. C.J.J. Tool, G. Coletti, F. Granek, J. Hoornstra, M. Koppes, E.J. Kossen, H.C. Rieffe, I.G. Romijn, A.W. Weeber, „17% mc-Si solar cell efficiency using full in-

line processing with improved texturing and screen-printed contacts on high-ohmic emitters", 20th European Photovoltaic Solar Energy Conference and Exhibition, Barcelona, Spain, pp. 578-83 (2005).

5. J. Hoornstra, G. Schubert, C. LePrince, G. Wahl, K. Broek, F. Granek, B. Lenkeit, J. Horzel, „Lead free metallization for silicon solar cells: results the EC2Contact project", 20th European Photovoltaic Solar Energy Conference and Exhibition, Barcelona, Spain, pp. 651-4 (2005).

6. F. Granek, A. Weeber, Kees Tool, R. Kinderman, P. de Jong , „A systematic approach to reduce process-induces shunts in back-contact mc-Si solar cell", 32nd IEEE Photovoltaic Specialists Conference, Hawaii, pp. 1319-22 (2006).

7. F. Granek, M. Hermle, B. Fleischhauer, A. Grohe, O. Schultz, S.W. Glunz, G. Willeke, „Optimization of laser-fired aluminum emitters for high-efficiency n-type Si solar cells", 21st European Photovoltaic Solar Energy Conference, Dresden, Germany, pp. 777-80 (2006).

8. D. M. Huljić, T. Zerres, A. Mohr, K. v. Maydell, K. Petter, J. W. Müller, H. Feist, N.-P. Harder, P. Engelhart, T. Brendemühl, R. Grischke, R. Meyer, R. Brendel, F. Granek, A. Grohe, M. Hermle, O. Schultz, S. W. Glunz, „Development of a 21% back-contact monocrystalline silicon solar cell for large scale production", 21st European Photovoltaic Solar Energy Conference, Dresden, Germany, pp. 765-8 (2006).

9. F. Granek, C. Reichel, M. Hermle, D. M. Huljić, O. Schultz, S.W. Glunz, „Front surface passivation of n-type high-efficiency back-junction back-contact silicon solar cells using front surface field", 22nd European Photovoltaic Solar Energy Conference, Milano, Italy, pp.1454-7 (2007).

10. D. M. Huljić, A. Mohr, K. v. Maydell, T. Zerres and J. W. Müller, F. Granek, A. Grohe, M. Hermle, O. Schultz, S. W. Glunz, N.-P. Harder, P. Engelhart, T. Brendemühl, R. Grischke and R. Brendel, „Q-Cells' High-efficiency back junction silicon solar cell for large-scale production –Main results of the QUEBEC project", 22nd European Photovoltaic Solar Energy Conference, Milano, Italy (2007).

11. F. Granek, C. Reichel, M. Hermle, O. Schultz, . Glunz, „Function of front surface field in n-type high-efficiency back-junction back-contact silicon solar cells", Technical Digest of the International PVSEC-17, Fukuoka, Japan, pp. 723-724 (2007).

12. F. Granek, M. Hermle, C. Reichel, A. Grohe, O. Schultz-Wittmann, S. Glunz, „Positive effects of front surface fielding high-efficiency back-contact back-junction n-type silicon solar cells", 33rd IEEE Photovoltaic Specialist Conference, San Diego, CA, in print (2008).

13. M. Hermle, F. Granek, O. Schultz-Wittmann, S. W. Glunz, „Shading Effects in Back-Junction Back-Contacted Silicon Solar Cells", 33rd IEEE Photovoltaic Specialist Conference, San Diego, CA, in print (2008).

14. C. Reichel, F. Granek, J. Benick, O. Schultz-Wittmann, S. W. Glunz, „ Comparison of emitter saturation current densities determined by quasi-steady-state photoconductance measurements of effective carrier lifetimes at high and low injections", 23rd European Photovoltaic Solar Energy Conference, Valencia, Spain, pp. 1664-1669 (2008).

15. S. Kluska, F. Granek, H. Hermle, S.W. Glunz, „Loss analysis of high-efficiency back-contact back-junction silicon solar cells", 23rd European Photovoltaic Solar Energy Conference, Valencia, Spain, pp.1590-1595 (2008).

16. Kasemann M., Kwapil W., Walter B., Giesecke J., Michl B., The M., Wagner J.-M., Bauer J., Schütt A., Carstensen J., Kluska S., Granek F., Kampwerth H., Gundel P., Schubert M.C., Bardos R.A., Föll H., Nagel H., Würfel P., Trupke T., Breitenstein O., Hermle M., Warta W., Glunz S.W., „Progress in Silicon Solar Cell Characterization with Infrared Imaging Methods", 23rd European Photovoltaic Solar Energy Conference, Valencia, Spain, pp. 965-973 (2008).

17. F. Granek, M. Hermle, C. Reichel, O. Schultz-Wittmann, S. W. Glunz, „High-efficiency back-contact back-junction solar cell: Research at Fraunhofer ISE", 23rd European Photovoltaic Solar Energy Conference, Valencia, Spain, pp. 991-995 (2008).

Oral presentations

1. F. Granek, M. Hermle, B. Fleischhauer, A. Grohe, O. Schultz, S.W. Glunz, G. Willeke "Optimisation of laser-fired aluminum emitters for high-efficiency n-type Si solar cells21st European Photovoltaic Solar Energy Conference, Dresden, Germany, 4.–8.9.2006

2. F. Granek, "Analyse der Vorderseitenpassivierung von Back-junction-Solarzellen", SiliconFOREST Workschop, Falkau, Germany, 25-25.02.2008

3. F. Granek, C. Reichel, O. Schultz, S. Glunz, "Analysis of the front surface passivation of the back-junction back-contact silicon solar cells", Q-Cells AG, Thalheim, Germany, 19.03.2008

4. F. Granek, M. Hermle, C. Reichel, A. Grohe, O. Schultz; S. W. Glunz, "Positive Effects of Front Surface Field in High-efficiency Back-contact Back-junction N-Type Silicon Solar Cells", 33rd IEEE Photovoltaic Specialists Conference, San Diego, CA, USA, 11.–16.5.2008

5. F. Granek, M. Hermle, C. Reichel, O. Schultz-Wittmann, S. W. Glunz, "High-efficiency back-contact back-junction silicon solar cell - Research at Fraunhofer ISE", 23rd European Photovoltaic Solar Energy Conference and Exhibition, Valencia, Spain, 1.–5.9.2008

6. F. Granek, "Positive effects of Front Surface Field in high-efficiency back-contact back-junction silicon solar cells", ISFH Seminar, Institut für Solarenergieforschung Hameln (ISFH), Hameln, Germany, 25.11.2008

Acknowledgements

I want to express my gratitude to my thesis advisors Prof. Dr. Oliver Paul and PD Dr. Andreas Gombert for their warm encouragement and guidance.

I am grateful to Dr. Stefan Glunz for enabling me to work on the exciting topic of the back-contact back-junction solar cells, for his support and stimulating discussions, and for sharing his experience and enthusiasm.

Special thanks to Dr. Oliver Schultz, my direct supervisor at Fraunhofer ISE, for his constant encouragement during the course of this work, for sharing of his knowledge with me and for his good advices. I am also grateful to him for providing valuable suggestions in the writing-up phase which improved the quality of this thesis.

I am happy to acknowledge close and very fruitful co-operation with Dr. Martin Hermle in the field of the numerical simulations of the solar cells.

I was very lucky to be able to work with two highly motivated diploma students Christian Reichel and Sven Kluska. I thank both of them for their contribution to this thesis and for many valuable discussions.

Processing and characterization of the complex structure of the back-contact back-junction solar cell would not be possible without the help of Antonio Leimenstoll, Sonja Seitz, Harald Lautenschlager, Dr. Andreas Grohe, Annerose Knorz, Christian Harmel, Anke Herbolzheimer, Christian Shetter, Elisabeth Schäffer, Thomas Roth, Daniela Grote, Denis Erath, Norbert Kohn, Jochen Hohl-Ebinger. I thank all of you.

The frequent meetings of the *Quebec* project enabled many useful discussions of the back-contact solar cell structure and technology, for which I am grateful to all of the *Quebec* project team members. Especially my thanks goes to Dominik Huljić, Dr. Andeas Mohr, Dr. Peter Engelhart from Q-Cells and to Dr. Nils-Peter Harder form ISFH.

My time at Fraunhofer ISE was made enjoyable in large part also due to my colleagues Mónica Alemán, Jan Benick, Nicola Mingirulli, Marek Miara, Dr. Ansgar Mette, Luca Gautero, Matthias Hörteis.

To my wife Agnieszka, thank you for your patience, love and encouragement.

GRANEK08

DONATE

INTERNET ARCHIVE WayBackMachine

Explore more than 866 billion web pages saved over time

https://www.beacon.no/resources.html

Calendar · Collections · Changes · Summary · Site Map · URLs

Saved 13 times between July 23, 2013 and March 22, 2023.



Tue, 23 Jul 2013 16:33:45 GMT (why: survey_00000, survey_crawl, webwidecrawl)

JAN

	1	2	3	4	5	
6	7	8	9	10	11	12
13	14	15	16	17	18	19
20	21	22	23	24	25	26
27	28	29	30	31		

FEB

					1	2
3	4	5	6	7	8	9
10	11	12	13	14	15	16
17	18	19	20	21	22	23
24	25	26	27	28		

MAR

					1	2
3	4	5	6	7	8	9
10	11	12	13	14	15	16
17	18	19	20	21	22	23
24	25	26	27	28	29	30
31						

APR

	1	2	3	4	5	6
7	8	9	10	11	12	13
14	15	16	17	18	19	20
21	22	23	24	25	26	27
28	29	30				

MAY

		1	2	3	4	
5	6	7	8	9	10	11
12	13	14	15	16	17	18
19	20	21	22	23	24	25
26	27	28	29	30	31	

JUN

						1
2	3	4	5	6	7	8
9	10	11	12	13	14	15
16	17	18	19	20	21	22
23	24	25	26	27	28	29
30						

JUL

	1	2	3	4	5	6
7	8	9	10	11	12	13
14	15	16	17	18	19	20
21	22	**23**	24	25	26	27
28	29	30	31			

AUG

				1	2	3
4	5	6	7	8	9	10
11	12	13	14	15	16	17
18	19	20	21	22	23	24
25	26	27	28	29	30	31

SEP

1	2	3	4	5	6	7
8	9	10	11	12	13	14
15	16	17	18	19	20	21
22	23	24	25	26	27	28
29	30					

OCT

		1	2	3	4	5
6	7	8	9	10	11	12
13	14	15	16	17	18	19
20	21	22	23	24	25	26
27	28	29	30	31		

NOV

					1	2
3	4	5	6	7	8	9
10	11	12	13	14	15	16
17	18	19	20	21	22	23
24	25	26	27	28	29	30

DEC

1	2	3	4	5	6	7
8	9	10	11	12	13	14
15	16	17	18	19	20	21
22	23	24	25	26	27	28
29	30	31				

Note

This calendar view maps the number of times **https:/www.beacon.no/resources.html** was crawled by the Wayback Machine, *not* how many times the site was actually updated. More info in the FAQ.

FAQ | Contact Us | Terms of Service (Dec 31, 2014)

The Wayback Machine is an initiative of the Internet Archive, a 501(c)(3) non-profit building a digital library of Internet sites and other cultural artifacts in digital form. Other projects include Open Library & archive-it.org

Your use of the Wayback Machine is subject to the Internet Archive's Terms of Use

https://web.archive.org/web/20130723163345/https://www.beacon.no/resources.html July 26, 2024

Resources

This page contains resources available for direct download as well as links to externally hosted material. New resources will be added from time to time, so make sure to check back in regularly or follow Beacon on LinkedIn for updates.

All material available through this page can be downloaded free of charge. Please observe that the copyright to the documents belong to the corresponding author and/or publisher, and that further distribution or reproduction of any content should only be done with permission from the author and with full reference to the original work. If you would like to have your material (e.g., thesis, research paper, technical note, etc.) hosted or referenced on this page, please use the details found on the contact page for correspondence.

Presentations

Andreas Bentzen, "Kerf-less Silicon Technologies", Presented at the Norwegian Solar Cell Conference, 14. March 2013 [pdf]

Theses

Andreas Bentzen, "Phosphorus Diffusion and Gettering in Silicon Solar Cells", Ph.D. Thesis, University of Oslo, Norway, 2006 [pdf]

Lode Carnel, "Thin-Film Polycrystalline Silicon Solar Cells With Lowly-Active Grain Boundaries and With a High Absorbance", Ph.D. Thesis, University of Leuven, Belgium, 2007 [pdf]

Filip Granek, "High-Efficiency Back Contact Back-Junction Silicon Solar Cells", Ph.D. Thesis, University of Freiburg, Germany, 2009 [pdf]

Sara Olibet, "Properties of Interfaces in Amorphous / Crystalline Silicon Heterojunctions", Ph.D. Thesis, University of Neuchatel, Switzerland, 2009 [pdf]

Roman Petres, "Amorphous Silicon Compound Films for Surface Passivation and Antireflection Coating of Crystalline Silicon Solar Cells", Ph.D. Thesis, University of Konstanz, Germany, 2010 [pdf]

Gunnar Schubert, "Thick Film Metallisation of Crystalline Silicon Solar Cells - Mechanisms, Models and Applications", Ph.D. Thesis, University of Konstanz, Germany, 2006 [link]

Recommend 3 Tweet

Copyright © 2013 Bentzen Consulting. All rights reserved.

APPENDIX CV

June A. Munford
Curriculum Vitae

Education

University of Wisconsin-Milwaukee - MS, Library & Information Science, 2009
Milwaukee, WI

- Coursework included cataloging, metadata, data analysis, library systems, management strategies and collection development.
- Specialized in library advocacy, cataloging and public administration.

Grand Valley State University - BA, English Language & Literature, 2008
Allendale, MI

- Coursework included linguistics, documentation and literary analysis.
- Minor in political science with a focus in local-level economics and government.

Professional Experience

Researcher / Expert Witness, October 2017 – present
Freelance • Pittsburgh, Pennsylvania & Grand Rapids, Michigan

- Material authentication and public accessibility determination. Declarations of authenticity and/or public accessibility provided upon research completion. Experienced with appeals and deposition process.

- Research provided on topics of public library operations, material publication history, digital database services and legacy web resources.

- Past clients include Alston & Bird, Arnold & Porter, Baker Botts, Fish & Richardson, Erise IP, Irell & Manella, O'Melveny & Myers, Perkins-Coie, Pillsbury Winthrop Shaw Pittman and Slayden Grubert Beard.

Library Director, February 2013 - March 2015
Dowagiac District Library • Dowagiac, Michigan

- Executive administrator of the Dowagiac District Library. Located in

Southwest Michigan, this library has a service area of 13,000, an annual operating budget of over $400,000 and total assets of approximately $1,300,000.

- Developed careful budgeting guidelines to produce a 15% surplus during the 2013-2014 & 2014-2015 fiscal years while being audited.

- Using this budget surplus, oversaw significant library investments including the purchase of property for a future building site, demolition of existing buildings and building renovation projects on the current facility.

- Led the organization and digitization of the library's archival records.

- Served as the public representative for the library, developing business relationships with local school, museum and tribal government entities.

- Developed an objective-based analysis system for measuring library services - including a full collection analysis of the library's 50,000+ circulating items and their records.

November 2010 - January 2013
Librarian & Branch Manager, Anchorage Public Library • Anchorage, Alaska

- Headed the 2013 Anchorage Reads community reading campaign including event planning, staging public performances and creating marketing materials for mass distribution.

- Co-led the social media department of the library's marketing team, drafting social media guidelines, creating original content and instituting long-term planning via content calendars.

- Developed business relationships with The Boys & Girls Club, Anchorage School District and the US Army to establish summer reading programs for children.

June 2004 - September 2005, September 2006 - October 2013
Library Assistant, Hart Area Public Library
Hart, MI

- Responsible for verifying imported MARC records and original MARC

cataloging for the local-level collection as well as the Michigan Electronic Library.

- Handled OCLC Worldcat interlibrary loan requests & fulfillment via ongoing communication with lending libraries.

Professional Involvement

Alaska Library Association - Anchorage Chapter
- Treasurer, 2012

Library Of Michigan
- Level VII Certification, 2008
- Level II Certification, 2013

Michigan Library Association Annual Conference 2014
- New Directors Conference Panel Member

Southwest Michigan Library Cooperative
- Represented the Dowagiac District Library, 2013-2015

Professional Development

Library Of Michigan Beginning Workshop, May 2008
Petoskey, MI
- Received training in cataloging, local history, collection management, children's literacy and reference service.

Public Library Association Intensive Library Management Training, October 2011
Nashville, TN
- Attended a five-day workshop focused on strategic planning, staff management, statistical analysis, collections and cataloging theory.

Alaska Library Association Annual Conference 2012 - Fairbanks, February 2012
Fairbanks, AK
- Attended seminars on EBSCO advanced search methods, budgeting, cataloging, database usage and marketing.

Depositions

2019 • Fish & Richardson

Apple v. Qualcomm (IPR2018-001281, 39521-00421IP, IPR2018-01282 and 39521-00421IP2)

2019 • Erise IP

Implicit, LLC v. Netscout Systems, Inc (Civil Action No. 2:18-cv-53-JRG)

2019 • Perkins-Coie

Adobe Inc. v. RAH Color Technologies LLC (Cases IPR2019-00627, IPR2019-00628, IPR2019-00629 and IPR2019-00646)

2020 • O'Melveny & Myers

Maxell, Ltd. v. Apple Inc. (Case No. 5:19-cv-00036-RWS)

2021 • Pillsbury Winthrop Shaw Pittman LLP

Intel v. SRC (IPR2020-1449)

2022 • Perkins-Coie

Realtek v. Future Link (IPR2021-01182)

2023 • Fish & Richardson

Neuroderm Ltd. v. Abbvie, Inc (Case No. PGR2022-00040)

2023 • Fish & Richardson

Nearmap US Inc. v. Pictometry International Corp. (IPR2022-00735)

2023 • Fish & Richardson

Samsung Electronics v. MemoryWeb LLC (Case No. 39843-0136PS1)

2023 • Pillsbury Winthrop Shaw Whitman LLP

Gravel Rating Systems v. Costco Wholesale Corp. (Civil Action No. 4:21-cv-149-ALM)

Limited Case and Clientele History

Alston & Bird

- Ericsson

  v. Collision Communications (IPR2022-01233)

- Nokia

  v. Neptune Subsea, Xtera (Case No. 1:17-cv-01876)

- Universal Electronics Inc

  v. Roku Inc (IPR2022-00818)

Arnold & Porter

- Ivantis

  v. Glaukos (Case No. 8:18-cv-00620)

- Samsung

  v. Jawbone (Case No. 2:21-cv-00186)

Benesch Friedlander Coplan & Aronoff

- Voyis

  v. Cathx (Case No. 5:21-cv-00077-RWS)

Erise I.P.

- Apple
  - v. Ericsson Inc. (IPR2022-00715)
  - v. Future Link Systems (IPRs 6317804, 6622108, 6807505, and 7917680)
  - v. INVT (Case No. 20-1881)
  - v. Navblazer LLC (IPR2020-01253)
  - v. Qualcomm (IPR2018-001281, 39521-00421IP, IPR2018-01282, 39521-00421IP2)
  - v. Quest Nettech Corp (Case No. 2:19-cv-00118-JRG)
  - v. Telefonaktiebolaget LM Ericsson (IPR2022-00275)
- Fanduel
  - v. CGT (Case No. 19-1393)
- Garmin
  - v. Phillips North America LLC (Case No. 2:19-cv-6301-AB-KS)
- Netscout
  - v. Longhorn HD LLC (Case No. 2:20-cv-00349)
  - v. Implicit, LLC (Civil Action No. 2:18-cv-53-JRG)
- Sony Interactive Entertainment LLC
  - v. Bot M8 LLC (IPR2020-01288)
  - v. Infernal Technology LLC (Case No. 2:19-CV-00248-JRG)
- Unified Patents

v. GE Video Compression (Civil Action No. 2:19-cv-248)

Fish & Richardson

- Apple

  v. AliveCor (3:21-cv-03958)

  v. LBS Innovations (Case No. 2:19-cv-00119-JRG-RSP)

  v. Koss Corporation (IPR2021-00305)

  v. Masimo (IPR 50095-0012IP1, 50095-0012IP2, 50095-0013IP1, 50095-0013IP2, 50095-0006IP1, 50095-0135IP1)

  v. Neonode (Case No. 21-cv-08872-EMC)

  v. Qualcomm (IPR2018-001281, 39521-00421IP, IPR2018-01282, 39521-00421IP2)

- Dell

  v. Neo Wireless (IPR2022-00616)

- Dish Network

  v. Entropic Communications, LLC (Case No. 2:2023-CV-01043)

  v. Realtime Adaptive Streaming (Case No. 1:17-CV-02097-RBJ)

  v. TQ Delta LLC (Case No. 18-1798)

- Evapco Dry Cooling

  v. SPG Dry Cooling (IPR2021-00688)

- Genetec

  v. Sensormatic Electronics (Case No. 1:20-CV-00760)

- Huawei

v. Bell Northern Research LLC (IPR2019-01174)

- Kianxis

  v. Blue Yonder (Case No. 3:20-cv-03636)

- LG Electronics

  v. Bell Northern Research LLC (Case No. 3:18-cv-2864-CAB-BLM)

- Metaswitch

  v. Sonus Networks (IPR2018-01719)

- Microsoft

  v. Throughputer Inc (IPR2022-00757)

- Mom Enterprises

  v. Ddrops Company (Case No. 1:22-cv-00332)

- MLC Intellectual Property

  v. MicronTech (Case No. 3:14-cv-03657-SI)

- Nearmap Inc

  v. EagleView Technologies (IPR2022-01009)

- Neuroderm Ltd.

  v. Abbvie, Inc (Case No. PGR2022-00040)

- Realtek Semiconductor

v. Future Link (IPR2021-01182)

- Quectel

  v. Koninklijke Philips (Case No. 1:20-cv-01710)

- Samsung

  v. Aire Technology (IPR2022-00877)

  v. Bell Northern Research (Case No. 2:19-cv-00286-JRG)

  v. Communication Technologies Inc (IPR2022-01221)

  v. Jawbone Innovations (IPR2022-00865)

  v. MemoryWeb LLC (IPR2022-00885)

  v. Dodots Licensing Solutions (IPR2023-00701)

  v. Telefonaktiebolaget LM Ericsson (IPR2021-00615)

- Texas Instruments

  v. Vantage Micro LLC (IPR2020-01261)

- Xilinx

  v. Sentient Sensors LCC (Case No. 1:22-cv-00173)

Irell & Manella

- Curium

O'Melveny & Myers

- Apple

  v. Maxell (Case No. 5:19-cv-00036-RWS)

- Micron Technology Inc.

  v. Besang Inc (IPR2023-00900)

- Samsung

  v. Daedalus Prime LLC (1335 Investigation)

Perkins-Coie

- Heru Industries

  v. The UAB Research Foundation (IPR2022-01148)

- Intel Corporation

  v. BitMICRO (Case No. 5:23-cv-00625)

- Realtek Semiconductor

  v. Future Link (IPR2021-01182)

- Twitter Inc

  v. VOIP-Pal.com (Case No. 3:20-cv-02397-JD)

- TCL Industries

  v. Koninklijke Philips NV (IPR2021-00495, IPR2021-00496 and IPR2021-00497)

Pillsbury Winthrop Shaw Pittman

- Intel

  v. FG SRC LLC (Case No. 6:20-cv-00315)

- Gravel Rating Systems

v. Costco (Case No. 4:21-cv-149)
v. Lowe's Home Centers (Case No. 4:21-cv-150)
v. T-Mobile USA (Case No. 4:21-cv-152)
v. Kohl's Inc. (Case No. 4:21-cv-258)
v. Under Armor (Case No. 4:21-cv-356)

Quinn Emanuel

- Wolfspeed

  v. The Trustees of Purdue University (Case No. 1:2021-cv-00840)

Stern, Kessler, Goldstein & Fox

- Preliminary Research

Sheppard, Mullin, Richter & Hampton LLP

- Cadence Design Systems Inc.

  v. Semiconductor Design Technologies (Case No. 3:23-cv-01001)